Award Number: W81XWH-07-1-0428

TITLE:
Nanotechnology-Enabled Optical Molecular Imaging of Breast Cancer

PRINCIPAL INVESTIGATOR: Rebekah Drezek, Ph.D.

CONTRACTING ORGANIZATION: Rice University, Houston, TX 77005

REPORT DATE: September 2013

TYPE OF REPORT: Final

PREPARED FOR: U.S. Army Medical Research and Material Command
Fort Detrick, Maryland 21702-5012

DISTRIBUTION STATEMENT:

Approved for public release; distribution unlimited

# REPORT DOCUMENTATION PAGE

*Form Approved*
*OMB No. 0704-0188*

**1. REPORT DATE** *(DD-MM-YYYY)*
September 2013

**2. REPORT TYPE**
Final

**3. DATES COVERED** *(From - To)*
06/15/2007 - 06/14/2013

**4. TITLE AND SUBTITLE**

Nanotechnology-
Enabled Optical Molecular Imaging of Breast Cancer

**5a. CONTRACT NUMBER**

**5b. GRANT NUMBER**
W81XWH-07-1-0428

**5c. PROGRAM ELEMENT NUMBER**

**6. AUTHOR(S)**

Rebekah Drezek, Ph.D.

drezek@rice.edu

**5d. PROJECT NUMBER**

**5e. TASK NUMBER**

**5f. WORK UNIT NUMBER**

**7. PERFORMING ORGANIZATION NAME(S) AND ADDRESS(ES)**

Rice University
PO Box 1892
Houston, TX 77251-1892

**8. PERFORMING ORGANIZATION REPORT NUMBER**

**9. SPONSORING / MONITORING AGENCY NAME(S) AND ADDRESS(ES)**

DOD CDMRP in Breast Cancer
U.S. Army Medical Research and Material
Fort Detrick, Maryland 21702-5012

**10. SPONSOR/MONITOR'S ACRONYM(S)**
DOD CDMRP in Breast Cancer

**11. SPONSOR/MONITOR'S REPORT NUMBER(S)**

**12. DISTRIBUTION / AVAILABILITY STATEMENT**
Approved for public release; distribution unlimited

**13. SUPPLEMENTARY NOTES**

**14. ABSTRACT**
This project focuses on development of nanotechnology-enabled optical molecular imaging technologies for applications in both breast cancer diagnosis and monitoring therapeutic response. The project consists of two major efforts: (1) optical instrumentation technology development and (2) development of complementary engineered nanomaterials for use in conjunction with the instrumentation created to provide molecular specificity. A particularly significant effort is underway to develop needle-compatible fiber optic probes to enable in vivo imaging of tumors with micron resolution in order to provide a new microscopic, high resolution imaging modality. These microscopic devices will complement the macroscopic, wide-field optical imaging devices being developed in this project.

**15. SUBJECT TERMS**
nanotechnology, molecular imaging, optical imaging

| **16. SECURITY CLASSIFICATION OF:** | | | **17. LIMITATION OF ABSTRACT** | **18. NUMBER OF PAGES** | **19a. NAME OF RESPONSIBLE PERSON** |
|---|---|---|---|---|---|
| **a. REPORT**<br>U | **b. ABSTRACT**<br>U | **c. THIS PAGE**<br>U | UU | 333 | **19b. TELEPHONE NUMBER** *(include area code)* |

**Standard Form 298**

# Table of Contents

## Introduction

There is a critical need to develop new imaging technologies which bridge the gap between our rapidly developing fundamental molecular understanding of breast carcinogenesis and our ability to rationally harness this understanding to develop more effective diagnostic and treatment strategies. Bridging that gap requires developing new tools which can rapidly detect, diagnose, and at times, intervene in the disease process based on recognition of specific molecular signatures of breast cancer *in vivo*. In this project, we focus on the development of photonics-based imaging technologies (SOW, Project 1 and Project 2) and complementary nanoscale molecular-targeted imaging agents for detection and monitoring applications (SOW, Project 3) in order to provide a new approach to molecular imaging of breast cancer. Medical imaging plays a prominent role in all aspects of the screening, detection, and management of breast cancer today. A variety of imaging methods including screening and diagnostic x-ray mammography and resonance imaging (MRI) are currently used to evaluate and monitor breast lesions. Although existing imaging technologies provide a useful approach to delineating the extent of tumors, these methods offer only low resolution, non-specific issues of tissue and cannot provide a detailed picture of the molecular profile of a tumor. In addition, techniques such as x-ray imaging and MRI are not able to detect small early cancers or pre-cancerous breast lesions and are difficult to use in settings such as the operating room where near real-time dynamic images are required. Thus, there is a substantial clinical need for novel imaging methods for the detection and monitoring of breast cancers which offer improved sensitivity, specificity, portability, and cost-effectiveness. In this project we develop portable optical technologies which promise high resolution, noninvasive functional imaging of tissue at competitive costs. Optical approaches can detect a broad range of morphological, biochemical, and architectural tissue features directly relevant to characterizing breast lesions including sub-cellular physical parameters such as nuclear size and nuclear to cytoplasm (N/C) ratios and biochemical indicators such as hemoglobin concentration, metabolic rate, and collagen cross-linking levels. To make these technologies even more powerful we are expanding the current capabilities of photonics-based imaging approaches with the additional capacity to quantitatively and dynamically detect molecular markers of breast cancer *in vivo* without tissue removal or directly after removal in a surgical environment (SOW, Project 3). While initial work focused on agents best classified as pure imaging agents (quantum dots, nanorods, and other gold based materials), a particular focus during the final year of the award will be on gold-based agents also incorporating therapeutic functionalities through delivery of peptides, oligonucleotides, or drugs. We have now completed six years of effort on this project. The SOW has been modified once to reflect revised goals at the time of a major change in the project directions (discontinuation of radiation project (SOW, Project 4) and replacement with macroscopic imaging project (SOW, Project 2)). More minor changes including the particular nanomaterials worked with (shift from high aspect nanorods to spherical materials for the gold work and additional biomolecule attachments beyond antibodies) have been described in the annual reports. In addition, an exempt protocol was approved by Rice University's IRB and DoD for acquisition of human breast cancer tissue specimens so that work could extend beyond the cell level studies originally proposed.

## Progress Report Body

The sections below contain annual progress reports on the project for each year of the award. Additionally, a final section contains new work completed during the no cost extension period. Figures have been renumbered from prior reports to provide consistent numbering throughout the overall final report.

## Year 1

### Project 1: Needle-Based Biopsy System Development

*In the section which follows we provide background on our motivation for developing a needle-compatible fiber optic system for breast cancer diagnostic and monitoring applications, information regarding the optical techniques and image analysis strategies we will use, and a description of how our system would interact with the technologies which are standard of care today. We then present our results to date. As described in the Statement of Work, Year 1 plans focused on design of this system and beginning initial construction. It was expected that the first system would be completed approximately 20 months after the design phase. We are significantly ahead of schedule on this project. In this section we present initial data for the system which is already providing micron resolution imaging capability through a needle probe. As we are ahead of schedule of Project 1, in Year 2 we will seek permission to modify our program of work to include much more extensive clinical evaluation of this instrument than originally anticipated. Plans which note tissue studies and other clinical efforts below will only proceed presuming these modifications to our SOW are accepted and regulatory paperwork is approved.*

#### *Background*

The survival rate of cancer increases significantly with earlier diagnosis; the 5-year survival rate of breast cancer, for example, is greater than 90% when it is diagnosed and treated while still localized but drops to 25% after metastasis. However, an accurate diagnosis often requires an invasive procedure that is sufficiently unpleasant that sometimes patients and even doctors are reluctant to undergo it. This coupled to the fact that early signs of cancer are frequently difficult to distinguish from benign lesions by routine examination lead to delayed diagnosis that cost lives. As a result, new techniques in cancer diagnosis have traditionally sought a balance between accuracy and invasiveness. Nevertheless, the gold standard for cancer diagnosis remains the biopsy slides read by a trained pathologist. Not surprisingly, this is also the most invasive diagnostic procedure available.

Recent advances in miniaturized optics and electronic systems have opened the way to a new kind of cancer diagnosis: optical biopsy. Optical biopsy permits a direct examination of the tissue of suspicion without any invasive tissue removal while maintaining much of the sensitivity and specificity that make biopsy reading the gold standard for cancer diagnosis. Such advancement is possible because the diagnosis of cancer from surgical biopsy focuses on a few key observations: the greatly enlarged nucleus of uncontrollably dividing cells and the visibly disrupted tissue morphology of unregulated cell expansion. Although the miniature optics used for optical biopsy sacrifices some resolving power for smaller size, they retain sufficient resolution and field of view to image the key features that make surgical biopsy work. This technique therefore makes the gold standard of cancer diagnosis much more accessible and much less unpleasant.

On the other hand, research into alternative methods of cancer diagnosis that rely on spectroscopic information has also progressed at a robust pace. Recent publications have reported significant differences in the fluorescence and reflectance spectra of normal versus dysplastic tissue. Although the analysis of these spectra require the aid of computers and spectroscopy has not proven itself equal to biopsy, the ability to probe chemical and structural information that are not available for visualization offers an entirely new set of diagnostic tools that can at the very least compliment the visual information from biopsies.

Starting from the development of physical imaging hardware that can produce images of sufficient quality for optical biopsy, efforts will be directed to the subsequent development of a complimentary software system that can at the minimum accentuate the key visual characteristics that indicate cancer; every effort will be made to move a step further from simply enhancing the images to automated analysis. The whole system will then be packaged for clinical testing. After the optical biopsy system has been largely completed, the second major thrust of the project will involve the integration of optical biopsy information with spectroscopy information. Ultimately, this project hopes to produce an automated system that uses both optical biopsy and spectroscopy to diagnose breast cancer. It will have sensitivity, specificity, and minimal invasiveness that surpass or rival the diagnostic tools available to doctors today.

To that end, the following tasks will be accomplished in sequence:

> **Development and testing of an optical biopsy system for breast cancer applications with digital image enhancement and analysis**
>
> This part of the project focuses on the development and testing of the optical biopsy system. Appropriate hardware will be selected to test the feasibility of the physical system to generate an image of sufficient quality for the software to process. Specifically, the hardware development will be considered a success if (1) the system clearly demonstrates sufficient resolution to image cellular features relevant to cancer diagnosis and (2) there is clear evidence that the images contain information about those relevant cell feature (though it need not be clear enough for a diagnosis as is). After the hardware has been successfully developed, a software system will be designed that can extract relevant information from the hardware images to generate a pseudo image useful to pathologists for diagnosis and to make an automated diagnosis based on that information. Specifically, the software development will be considered a success if (1) the relevant cellular information can be extracted from the hardware image and (2) the information can be used to generate a useful pseudo image to accentuate the relevant features. If an automated diagnostic algorithm can be developed, it will be considered a major success. This stage will be deemed successful if the two specific criteria for both hardware and software are met.

### Development and testing of an optical biopsy system for use with molecular imaging agents in either reflectance or fluorescence mode (to be completed in conjunction with Project 2)

This part of the project focuses on the development and testing of an optical biopsy system specifically designed to take advantage of contrast agents for improved imaging capability. There are two distinct areas where efforts will be focused. One area of research will focus on the development of a contrast agent suitable for the imaging of breast tissue. Two specific goals have been set: (1) the contrast agent can be used to improve the visibility of key cellular features in breast tissue including but not limited to the cell membrane and the nucleus; (2) the contrast agent can specifically target cancer cells and distinguish them from normal cells by color or other means. If either goal can be met in reflectance or fluorescence mode, this area would be considered a success. The other area compliments the first by focusing on the development of a hardware system that can deliver contrast agents directly to the imaging site. There are also two goals specific to this area: (1) the optical biopsy system has a mechanism to deliver precise amounts of contrast agents directly to the imaging site without adversely affecting the imaging capability of the system; (2) if necessary, the optical biopsy system has a mechanism to remove either unbound or excess contrast agent from the imaging site without inflicting additional pain and suffering on the patient. The first goal is considered the more important and feasible; however, if the situation arises where the second goal becomes necessary, all efforts will be spend to achieve it.

### Evaluation: Investigation of combining structural information with spectroscopic information for improved cancer diagnosis

Although it has not yet show sufficient quality to rival the gold standard of biopsy, spectroscopy has been shown to distinguish normal and dysplastic cells based on non-visual information in many experiments. Efforts at this stage will focus first on validating the diagnostic value of spectroscopy in breast tissue. Should the validation be positive, structural information such as the nuclear-to-cytoplasmic ratio will be manually extracted from a tissue sample that will also be probed spectroscopically. A statistical software algorithm will be developed to combine the structural and spectroscopic information, and its sensitivity and specificity will be evaluated. A suitable spectroscopic component will be added to the optical biopsy system and integrated in such a way that the data from both can be acquired and analyzed in the same setting. Specifically, the integrated system will be considered a success if (1) the spectroscopic component of the system can acquire spectroscopic information from breast tissue and distinguish them with sensitivity and specificity comparable to published results and (2) the final integrated system can stage breast cancer with higher sensitivity and specificity than is possible with either method in isolation.

## *Background on biopsy and fiber optical imaging*

### Excisional biopsy, core needle biopsy, and fine needle aspiration biopsy

To this day, biopsy slides read by a pathologist remain the gold standard for cancer diagnosis. The most informative type of biopsy is excisional biopsy. During this procedure, the piece of tissue containing the entire suspect lesion is removed. The removed tissue is then cut into very thin slices, stained with dyes, and examined under the microscope by a pathologist [1]. The pathologist looks for structural and morphological abnormalities when assessing whether cancer is present in the tissue. The most prominent structural feature associated with cancerous cells is an enlarged cell nucleus, which may occupy as much as 80% of the total cell area when observed under the microscope. In addition, the rapid and unregulated division of cancer cells creates distinctive morphological characteristics in a cancerous lesion that separate it from normal tissue. Although a single cell could potentially be observed during cell division, a cancerous lesion will contain many more dividing cells than normal tissue. Furthermore, cancerous lesions will show a clear breakdown in cell organization because the regulators that controls cell organization in normal tissue do not correctly affects cancer cells. (Fig. 1.1) These structural and morphological changes are the primary symptoms that pathologists use to diagnose cancer in a biopsied tissue.

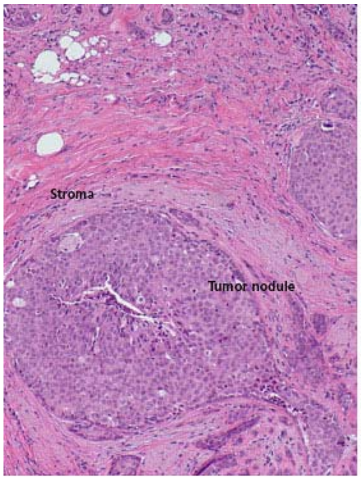

Figure 1.1 [2]: Dye stained breast tissue slide showing cancer cells (blue-purple, labeled “Tumor nodule”) surrounded by normal cells (pink, labeled “Stroma”). The cancer cells show a high density of nucleus stained blue-purple. They are also rounded and crowded. The normal cells are elongated, striated, and have much lower nucleus visibility.

Besides being the gold standard for cancer diagnosis, excisional biopsy is also the primary method for monitoring the surgical margin, the region of normal tissue surrounding the cancerous lesion in the removed sample, in breast conservation surgery. Primarily a gauge for the success of breast cancer resection surgery, a clear margin means there is no cancerous tissue bordering the edges of the tissue sample, indicating a high probability that the entire cancerous lesion has been removed. The traditional method for mapping the surgical margins in an excisional biopsy sample is the paraffin-embedded histology method; this requires a lengthy preparation in which the tissue is embedded in paraffin and sectioned into thin slices with a microtome. The slices are then examined for clear surgical margins [3].

In order to better visualize the various structures in a tissue sample, the tissue is normally stained with dyes that add artificial color to different structures. The most common dyes used are hematoxylin and eosin (H&E). The hematoxylin stains the nucleic acid-rich regions of the cells, primarily the nucleus, blue-purple and the protein-rich regions, mainly the cytoplasm and extracellular matrix, pink [4]. It is uncommon for a diagnosis to be based on raw tissue.

Despite the powerful diagnostic value of the excisional biopsy, its high cost compels a simpler and cheaper alternative in cases where only the diagnosis of disease, not the mapping of surgical margins, is necessary. The magnitude of the operation to remove a piece of tissue containing the entire suspect lesion ranges from a minor to a major surgery. The pain and suffering of the patient, the time and medical resourced consumed, and the monetary cost necessary for such procedures are imposed on patients and doctors alike. Because the diagnosis of cancer is based on cellular and morphological features present even in a limited sample, it is frequently sufficient to remove only a small piece of suspect lesion for examination by a pathologist.

One of the most widely used alternatives to excisional biopsy is core needle biopsy. Although needle core biopsy had been performed on other organ sites, the procedure for successfully applying it to breast cancer diagnosis was first established by Parker et al. in 1990 [5]. In that study, commercial core biopsy needles ranging in size from 14-gauge to 18-gauge were used to remove tissue samples from suspect lesions identified by mammography. The mammography system also served as the stereotactic mapping system for the guided core biopsies. The biopsied tissues were prepared for standard pathological evaluation. A total of 103 patients underwent stereotactic breast core biopsy followed by surgical biopsy at the same site. In all, the histology results from the core biopsies agreed with that of the surgical biopsies in 89 of the 103 cases (87% agreement). For the 29 cases in which a 14-gauge needle was used, the histology agreement between core and surgical biopsies reached an impressive 97%. Parker et al. subsequently reported in 1993 a study of breast core biopsies using 14-gauge needles guided by ultrasound [6]. In that setup, both the ultrasound transducer and the biopsy needle were positioned by hand. The 14-gauge needle was also established as having most suitable size for core needle biopsy of breast tissue. Of the 181 biopsies performed in that investigation, the core biopsy results agreed 100% with surgical biopsy results in the 49 cases in which surgical biopsy was performed after the core biopsy. Among the other 132 cases that had a benign core biopsy result, patients were followed-up for 12-36 months after the core biopsy, and no patient was diagnosed with breast cancer during that period. The success of the simpler ultrasound-guided core biopsy continues to this day. As recently as 2008, Schueller et al. reported a study involving 1352 US-guided needle core-biopsies, of which 1061 case were followed by surgical biopsy and the other 291 benign results were followed up for at least two years [7]. The agreement between the needle core biopsy results and either the surgical or follow up results agreed 95.8% of the time. Needle core biopsies have been validated over the past 20 years as a viable but cheaper and simpler alternative to surgical biopsy.

The other widely used needle-based alternative to excisional biopsy is the fine needle aspiration biopsy. This technique was introduced to the US earlier than core needle biopsy [8]. FNAB uses a much smaller needle, 18-27 gauge depending on position and size of lesion, compared to the 14-gauge needle used for reliable CNB. Such a small needle size is possible because FNAB is based on cytopathological (cell-level) instead of histopathological (tissue level) examinations. Cells gathered from FNAB is typically smeared directly on slides and stained for better visualization. Different smearing methods can be used; the most common are alcohol-fixed Papanicolaou/H&E stains and air-dried Romanowsky-type stains. However, the success rate of this technique is heavily dependent on user proficiency. The reported sensitivity of FNAB varied widely from trial to trial until a uniform approach was adopted as during a FNAB conference in 1996 [9]. The conference concluded that by properly correlating FNAB with initial physical examination and imaging of suspect lesion, the sensitivity and specificity of FNAB in diagnosing breast cancer can reach 97%-100% and 98%-100%, respectively.

Barra et al. reported in a 2007 study that by employing both the ultrasound-guided CNB technique established by Parker et al. in 1993 and the uniform approach to FNAB recommended by the 1996 FNAB conference, FNAB still performed poorly compared to CNB [10]. Of 264 suspect lesions that were biopsied using both CNB and FNAB in the same setting and then excisional biopsy, FNAC results had an absolute sensitivity and specificity of 68.5 and 66.7, respectively, compared to the excsional biopsy results. CNB results had an absolute sensitivity and specificity of 88.3 and 95.2, respectively. The result of this study resembles that of a seminal investigation more than 15 years earlier, in which Dowlatshahi et al. reported FNAB having a sensitivity of 32% compared to 41% for CNB [11]. These results indicate that despite having a uniform guideline for maximizing the performance of FNAB, this method remains more challenging than CNB. The user's ability to follow the guidelines influences the results much more than in for CNB.

It is not surprising that FNAB is more challenging than CNB. FNAB results are based on cytopathology, whereas the CNB results are based on histopathology. While it is relatively easy to acquire cellular information from a tissue sample; the reverse is not true. When suctioning out cells, FNAB cannot preserve the morphological features of the tissue that contained those cells. The subsequently cytopathology relies on cellular information only. Although this is sufficient in some cases, the range of disease to which FNAB is applicable is less than CNB because it inherently possesses less information.

### *Fiber optical imaging systems*

Based on existing trends in making the diagnosis of cancer as un-invasive as possible, one logical next step could be to perform pathological examination without physically removing the suspicious tissue: an optical biopsy. Trying to look inside the body is an age-old goal of physicians; one of the first successful medical endoscopes was developed by Desormeaux in 1853, although physicians from much earlier times have tried to probe into various orifices of the body [12]. Since those early days of crude endoscopes, advances in miniaturized optics and optical fibers have enabled tremendous advances in the field of in-vivo optical imaging, especially in the last 20 years [13]. Today's fiber optical in-vivo imaging systems can penetrate solid tissue, employ a wide variety of contrast agents, and visualize their target using techniques ranging from physical image formation to interferometry.

The first fiber optical imaging systems were single fiber scanning confocal microscopes designed to extend the reach of confocal microscopy to otherwise inaccessible sites [14, 15]. This single fiber approach has one severe limitation: in order to form an image the distal tip of the fiber needs to scan across the surface of interest. The light it gathers at each point is re-assembled into an image of that surface. Therefore, a scanning mechanism is needed at the distal end of the fiber. Over the years, numerous techniques and mechanisms have been developed to allow a single optical fiber to scan a surface, including microfabricated mirrors [16-18], piezoelectric transducers [19], and electromagnetic actuators [20-22]. However, due to current limitations in microfabrication technology, the smallest of these probes that produce an image suitable for pathological analysis is several mm in diameter [18]. Yelin et al. have proposed a spatial encoding scheme using different wavelengths of light to remove the need for a scanning mechanism [23]. However, this technology has only been tested in the imaging of peritoneum surface topology in mouse. It is unclear whether a spectrally divergent beam of light possesses sufficient sensitivity to distinguish the small difference in reflectivity between cell nucleus and cell cytoplasm without significant variation in surface topology. Such is the case of imaging suspicious lesion inside bulk tissue using an inserted probe that is pressed against the tissue. Despite their limitations, however, single fiber optical imaging systems remain a promising tool for in vivo imaging because of the simple fact that the fiber itself can as small as a few hundred micrometers in diameter.

Until the scanning challenge is solved, fiber optical imaging systems are better served by a coherent fiber bundle instead of a single fiber. Although a fiber bundle is in general larger than a single fiber, it can transfer an image directly from its distal surface to its proximal surface because each individual fiber images a distinct point [24]. This capability removes the need for a scanning mechanism on the distal end of the fiber bundle so the fiber bundle becomes the limiting factor in miniaturization of the probe. Current manufacturing technology allows several thousand single fibers to be packaged in a fiber bundle with a diameter of only a few hundred micrometers [25]. This approaches the practical operational size of a single fiber because a single fiber requires sufficient size to transmit enough light for imaging and to maintain structural stability. This setup has been used successfully in both reflectance based imaging systems [26, 27] and fluorescence based imaging systems [28, 29]. These systems generally still employ a scanning system made of mirrors on the proximal side of the fiber bundle and detect the light from each fiber in the bundle using an avalanche photodiode. The advantage of the APD is its high sensitivity, so even low signals can be detected. The disadvantages of this method include the need for scanning mechanism, which is frequently complex, and the time needed for the scanning. To decrease the time required to scan a complete image, Sabharwal et al. have developed a slit scanning mechanism that scans a whole line of the image at once [30]. Despite their many benefits, the current fiber bundle based fiber optical imaging systems still suffer from an often complicated scanning mechanism at the proximal end. Although the scanning mechanism no longer affects the size of probe tip and the speed of scan has been gradually increasing, the need for moving parts decreases the robustness and increases the size of final system. This makes packaging the system into a device suitable for clinical applications in harsh environments difficult.

In a direct effort to make a fiber optical imaging device that is robust, fast, and suitable for routine clinical use in a variety of settings, Muldoon et al. have developed a fiber bundle fluorescence imaging system that has no scanning components [31]. (Fig. 1.2) Image from the fiber bundle is directly acquired by a commercial CCD camera and displayed on a computer screen using commercial image capture software. The system is capable of imaging 4.4 um-wide bars on the USAF resolution target and human oral mucosal cells with visible nuclei after application of medical grade acriflavin. The promising results of this setup in in-vivo human cell imaging and its targeted application for clinical use makes it the ideal inspiration for the hardware aspect of an optical biopsy system for breast cancer diagnosis and monitoring. A complete optical biopsy system, however, will require simultaneous development in image processing and analyzing software and very likely a contrast agent delivery system suitable for use in bulk tissue.

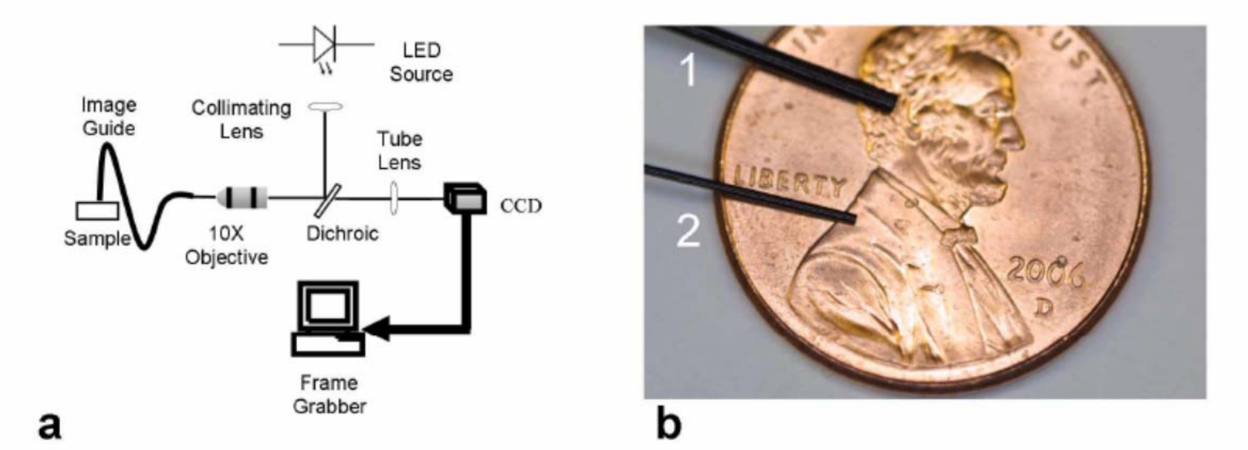

Figure 1.2 [31]: (a) System diagram of a CCD-based non-scanning fiber bundle optical imaging system. (b) Potential 1 mm and 0.5 mm diameter commercial fiber bundles that can be used.

***Digital image processing and analysis***

**Digital image processing and thresholding**

Concurrent to the development of hardware systems for in vivo fiber optical imaging, software algorithms to process and analyze the raw images from hardware are also a major area of research. The ultimate motivation for the high amount of interest is two-fold. If optical biopsy is to become a viable alternative to incisional or perhaps even excisional biopsy, the quality of the image produced by the system must convey the same level of information available from physical biopsy slides examined under the microscope. This is challenging from a purely hardware point of view because despite the advances made in miniaturized optics and imaging electronics during recent years, these components still lag behind high precision microscopy optics in performance. Compounding the problem is the fact that the staining agents used in many pathological examinations cannot be readily applied inside in bulk tissue in vivo. Therefore, imaging using optical fiber systems benefit from and sometimes require digital enhancements to accentuate structural features essential for pathological assessment. The other factor that motivates the development of digital processing and analyzes of medical images is the drive for quantitative analysis. Despite being the gold standard in cancer diagnosis, pathology today remains predominantly a qualitative process. The human brain can quickly survey a large area of cells and make an almost immediate estimation of quantitative characteristics such as the overall nuclear-to-cytoplasmic ratio and the proportion of cells undergoing cell division. However, for a human being to precisely quantify this information is nearly impossible due to the sheer # of cells involved and the difficulty of calculating the area of irregularly shaped objects. On the other hand, both challenges are easily solved digitally provided that dividing and non-dividing cells can be accurately segmented and counted. Therefore, development of the software component is an important part in making an optical biopsy system.

One of the first problems encountered in the images from a fiber bundle optical imaging system is the pixilation artifact created by individual fibers in the bundle [31]. However, this is not a difficult problem to solve because the artifact is highly localized in the spatial frequency domain. By transforming the image into the Fourier domain, removing the frequency band corresponding to the pixilation artifact and transforming back to the spatial domain, the artifact can be reduced with minimal distortion to the other features of the image [32]. This basic signal processing method can be easily implemented digitally [33]. Application of this type of image processing has already been reported [34, 35].

Unfortunately, beyond removing the pixelation artifacts, subsequent processing of the image becomes much more challenging. In particular, finding the appropriate threshold to accentuate the cell membrane and the nuclear boundary, two features essential for cytopathological analysis, does not yet have an ideal solution [36] despite the fact that numerous techniques have been investigated since the 1980s [37]. The fundamental assumption of thresholding is that the features of interest in an image can be assigned numeric values that are significantly different from values in the background without or without first undergoing a mathematical transform. Furthermore, should such a significant difference exist, a suitable threshold value must be found to separate the feature values from the background values. One of the most common problems for accurate thresholding is non-uniform background; this can easily caused by non-uniform illumination or different tissue types in an optical fiber image. A threshold value suited for one part of the image is unlikely to be suitable for another part, particularly for the two extremes of the variation. Global background correction schemes exist [38, 39]. However such correction schemes usually either require a priori knowledge of the kind of non-uniformity that can occur, so the proper correction filter can be designed, or distort the interesting features of the image during correction in such a way that renders subsequent thresholding difficult. Adaptive thresholding has been proposed as a possible solution to non-uniform background without the adverse effects of global background correction [40]. Although a suitable local region size still needs to be manually defined, the algorithm automatically computes the most likely threshold value in that region by assuming the background is uniform. Therefore, as long as a reasonable region size is chosen, the exact nature of global background non-uniformity need not be known. Furthermore, because no correction is applied, there is no risk of feature distortion. Despite these techniques, straightforward thresdholding is still unsuitable to process an image for which a suitable threshold value cannot be found, a common problem when trying to detect edges in an image that show gradual instead of sharp edges [36].

### The watershed algorithm

Because gradual edge detection is such a widely demanded application of image processing and analysis, one popular method has evolved over the years specifically to perform this task without using any thresholding: the watershed algorithm, first proposed by Beucher and Lantuejoul in 1979 [41]. The watershed method works in a way analogous to water filling a landscape. (Fig. 1.3) The starting point of the algorithm is the image as an intensity map; this can be the intensity of the image directly or the intensity of a transform of the image, e.g. its gradient. If we imagine a 3D graph of the intensity map, regions of high intensities will be ridges and hills while low intensities will be represented by valleys and pits. Starting from the lowest points, we gradually fill up the valleys and pits with water; in actual terms, lowest intensities are successively discarded as background. A condition is imposed on the filling of water: no two pools of water that started separately can be joined. The intensity map will be gradually filled until it cannot be filled anymore without violating the condition just described. The remaining ridge tops will be the boundaries that need to be detected. This analogy is slightly misleading because if the water were rising uniformly throughout the map, some ridges will drown before the tips of others were approached. This is where the analogy ends; at each intensity, all points whose discarding does not violate the no-joining condition will be discarded as background. So intensities discarded as background in some parts of the map are preserved in other parts. Since it as proposed, the watershed algorithm has been used in a wide variety of image processing applications [42, 43].

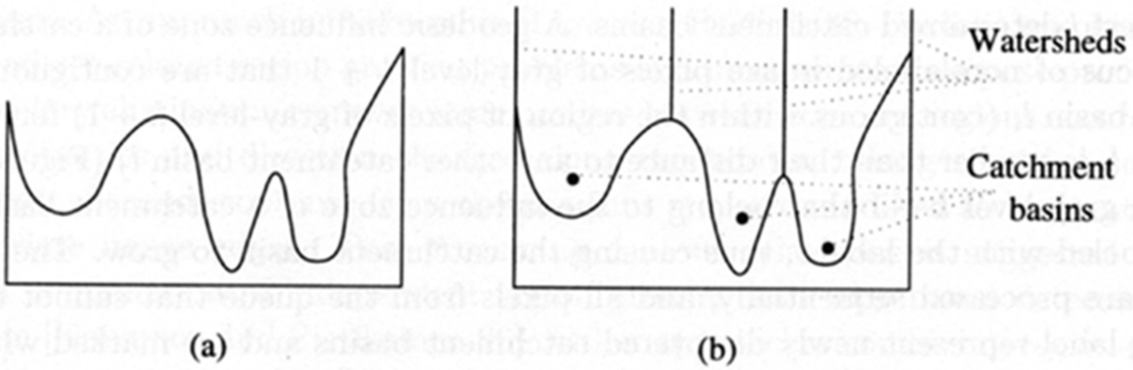

Figure 1.3: Conceptual representation of a 1D watershed algorithm. The local minima in the image (a) can be viewed as catch basins in which water accumulate. As the water rises, the highest point between two catch basins is a watershed (b), or a boundary to be detected. (Image and caption from http://iria.pku.edu.cn/~jiangm/courses/dip/html/ node139.html)

However, directly applying the basic watershed algorithm to a complex image such as that of tissue would cause significant over-segmentation. Due to the large variation present in these images, there may be many intensity local minima in a single object: a cell, a nuclei, or the background. To overcome this problem, various efforts to develop a seeded watershed algorithm have been reported [42-47]. The basis of the seeded watershed algorithm is to fill the intensity map starting from only designated locations, or seeds. All other local minima will be disregarded, and only pools that started from seeds should not touch. This method creates its own problems. Automated seeding algorithms are imperfect, frequently putting more than one seeds in one object of interest, e.g. a cell, and none in others, leading to incorrect segmentation [42]. Manual seeding, on the other hand, is an extremely laborious process for images containing a large number of objects [45]. Despite these difficulties, the watershed algorithm remains a useful image processing method because of its robustness in accurately detecting boundaries given correctly placed seeds. A useful direction of research, then, seems to be to develop a competent automated seeding algorithm to be used with the watershed algorithm for boundary detection.

### Dynamic programming and the optimal path problem

While a reliable automated seeding algorithm is being developed, alternative means of boundary detection without thresholding have emerged. One of the most promising techniques employ dynamic programming to solve a optimal path problem along the boundary of interest that would otherwise be computationally intractable. Baggett et al. reported one implementation of this technique in 2005 [48]. The problem can be broadly separated into two sub-problems of design—formulation of an optimal path problem—and implementation—solving the optimal path problem using dynamic programming. For the design sub-problem, Baggett et al. first manually designates a point near the center of the object of interest, e.g. a cell, and another point on the boundary to be detected. To detect the entire boundary, a region of the around the center point is transformed from polar coordinates to Cartesian coordinates with the designated boundary point simultaneously on both edges of the transformed image. (Fig. 1.4) The optimal path is the path of highest average intensity between the two points on the edges. In other words, in the original image, start from the boundary point and proceed either clockwise or counterclockwise and find the path of maximum average intensity until the path forms a loop and returns to the boundary point.

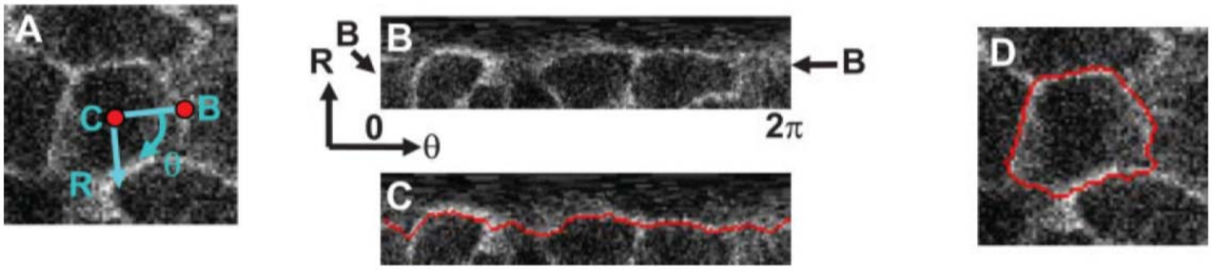

Figure 1.4 [Figures and caption from 48]: The optimal path problem to detect boundary of a cell in an image involves (A) selecting a point central to the cell and another point on the cell boundary, (B) transforming an area around the central point from polar to Cartesian coordinates, (C) finding the path of maximum average intensity in the transformed image, and finally (D) performing an inverse transformation.

To solve the optimal path problem, a gray-weighted distance transform is used to find the path of highest average intensity between the two boundary points on the edges of the polar-to-cartesian transformed image. This method is employed because it is amenable to dynamic programming. A simple example illustrates this method. (Fig. 1.5) In a simple MxN image, designate one pixel on the edge as the starting pixel. First, generate a MxN map A containing the distance of each pixel in the image from the starting pixel; map A is completely filled first. Then, generate a 2nd map MxN B containing optimal cumulative intensities of each pixel. To starting filling B, the pixels with the highest values in A have B values equal to their original intensity in the image. The we move on to pixels with A values of one less. For each of these pixels (call it P), find all adjacent pixels with A values of exactly one more; then, from those adjacent pixels find the one with highest B value; then add that B value to P's intensity in the original image; finally, set P's B value equal to that sum. After that, go to pixels with A values of one less still and iterate until the starting pixel is reached. To find the path of highest average intensity from the starting pixel to any destination pixel, simply start from the destination pixel and trace backward, in strictly decreasing A value, along adjacent pixels of highest B value until the starting pixel is reached. To prove why this method always gives the maximum average intensity, a detailed study of the theory of dynamic programming [49-51] and its application in optimal path finding [52, 53] is required.

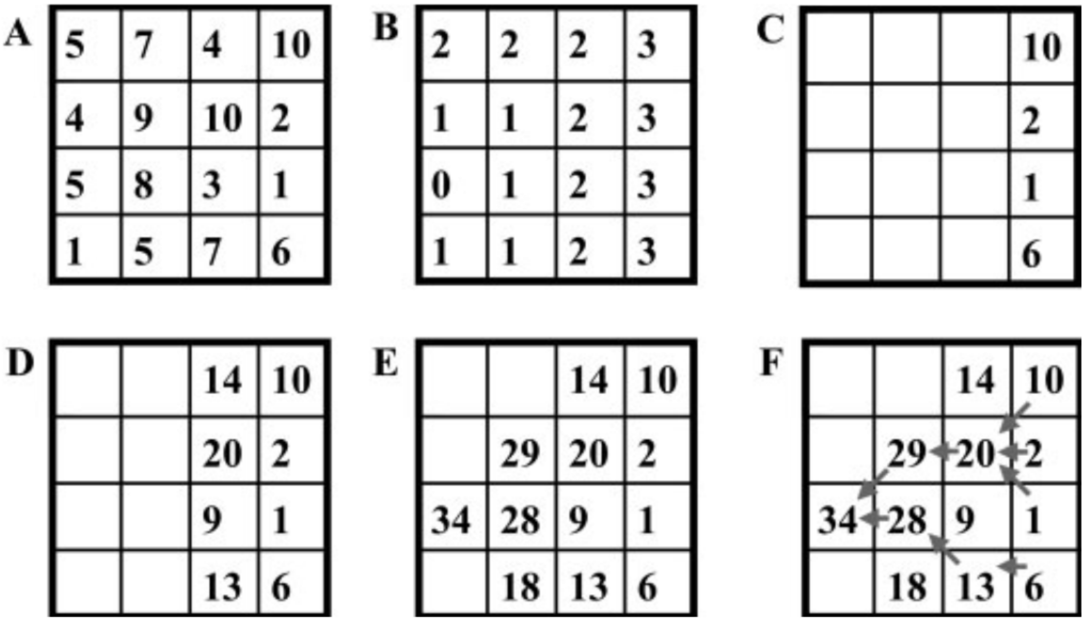

Figure 1.5 [Figures and caption from 48]: A simple figure depicting the steps in gray-weighted distance transform from (A) the intensities in the original image, (B) a map of pixel distance from the starting pixel, and (C) the optimal cumulative intensity map, through successive iterations (D) and (E) to fill the cumulative intensity map until the optimal path from the starting pixel to any non-trivial pixel can be found by backtracking through the highest adjacent cumulative intensities (F).

Since its introduction to image processing, dynamic programming has been used in a variety of projects to segment both 2D [54, 55] and 3D [56, 57] images. The main limitation of formulating cell boundary detection as an optimal path problem solved by dynamic programming, at least using the aforementioned method, is the need for manual placement of two points: one at the cell center and one on the cell boundary. To segment a large number of cells in a tissue image, the amount of user interaction can be significant. A major benefit of this technique is that given a complex image of cells, individual cells can be marked and segmented in isolation. Such high degree of control is impossible for the watershed method because to place only two seeds in a complex image, even if one is inside a cell and one is out, there is no guarantee that when the seeds begin to form pools and fill the image, the highest remaining ridge separating the two will be the correct cell boundary, especially for tissue images in which cell boundaries appear as a interconnected network of high intensity ridges. On the other hand, dynamic programming methods require a substantial amount of computation to segment just one cell, and cells need to be process individually. This requires considerably greater computational resources than the watershed method, which processes the entire image at once until only the boundaries remain.

It is clear that both the watershed algorithms and the dynamic programming methods have their benefits and limitations; however, one limitation that exists in both methods is the need to place marks in the image to indicate objects of interest, such a cell. For either method to work in an automated or fast image enhancement or analysis software package, the placement of such marks (seeds or central/boundary points) needs to be automated yet reliable. One possibility to solve this problem is by using a Hough Transform to identify the center of cells.

The Hough Transform is a technique to extract generalized features from a data set that may contain imperfections or significant noise [58, 59]. One example would be to extract a circle from an image of a circle made up of broken arcs. In the simplest terms, the Hough transform works by first defining the feature of interest using a parameter space, followed by investigating every point in the dataset for possible sets of parameters that define an acceptable feature that includes that point and adding a count to the appropriate bin in the parameter space for each set that is found, and finally picking the appropriate bins in the parameter space that has the highest number of counts. A simple case for detecting the line formed by three points is illustrated in Figure 1.6. For circles, the Hough transform typically uses three parameters: the coordinates of the center and the radius. Some groups have reported studies incorporating the Hough transform in software algorithms to segment biological images [60-62]. However, applying the Hough transform to the analysis of biological images is very challenging because (1) biological structures such as cells are frequently irregular in shape and cannot easily be parameterized and (2) biological images frequently contain too much information for Hough transform to be performed in reasonable time without a highly optimized software algorithm. Despite these limitations, the ability of the Hough transform to penetrate imperfection and noise is very attractive. With research and development, it may be possible to adapt the Hough Transform as a tool to reliably mark the cells/nuclei in a tissue so that either the watershed algorithm or a dynamic programming technique can be employed for boundary detection.

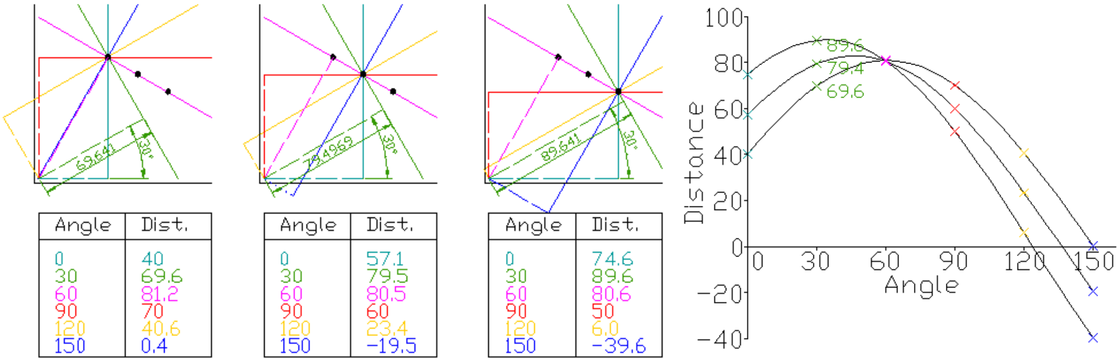

| Angle | Dist. |
|---|---|
| 0 | 40 |
| 30 | 69.6 |
| 60 | 81.2 |
| 90 | 70 |
| 120 | 40.6 |
| 150 | 0.4 |

| Angle | Dist. |
|---|---|
| 0 | 57.1 |
| 30 | 79.5 |
| 60 | 80.5 |
| 90 | 60 |
| 120 | 23.4 |
| 150 | −19.5 |

| Angle | Dist. |
|---|---|
| 0 | 74.6 |
| 30 | 89.6 |
| 60 | 80.6 |
| 90 | 50 |
| 120 | 6.0 |
| 150 | −39.6 |

Figure 1.6: To start the Hough transform, the line to be detected (target line) is described by two parameters: (1) the slope of another line (parameter line) that is both perpendicular to the target line and passing through the origin, and (2) the distance between the origin and the intersection of the parameter line with the target line. The two parameters form a two-dimensional parameter space (figure, right), called a Hough space in this case. For each of the three points, a number of potential target lines that contain that point are considered (solid lines, left top). For each of the potential target lines, the two parameters of its parameter line (dashed lines, left top) is recorded (table, left bottom). Assume that for each point, a substantial number of potential target lines are investigated and the parameters associated with each record in the parameter space, the parameter space eventually looks like the figure on the right with three lines. The intersection of the three lines represents the parameters associated with the target line that includes all three points. (Image and accompanying caption from http://en.wikipedia.org/wiki/Hough_transform)

## Results Achieved in Months 1-12

## Development and testing of a needle compatible optical biopsy system with digital image enhancement and analysis

### Preliminary work: hardware system

We have built and tested a prototype setup in order to investigate the hardware capabilities of the optical biopsy system. (Fig. 1.7) The setup maximizes simplicity and minimizes the cost while meeting the core design criteria essential to minimally invasive optical biopsy. The intentional open-air layout permits easy replacement of various components and modifications to the optical pathway. This approach allows continuous optimization of the design—to balance performance, size, cost, and robustness—while adhering to a set of pre-determined requirement.

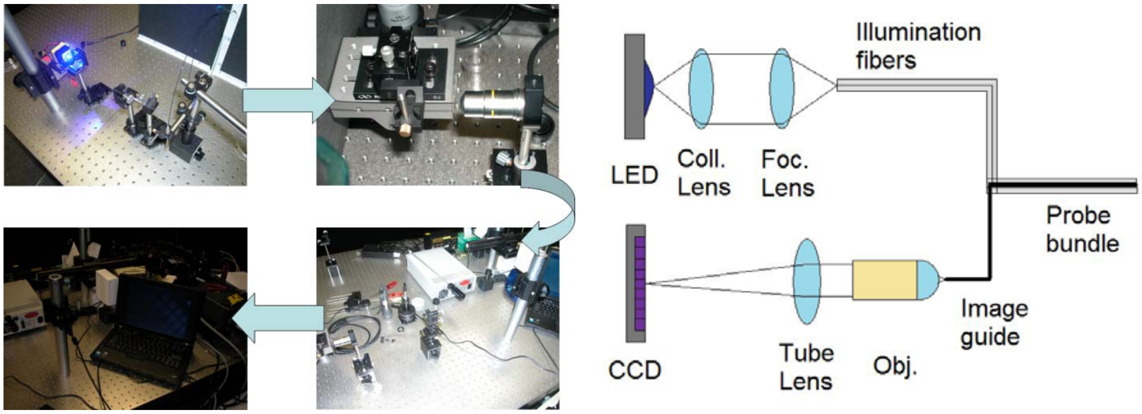

Figure 1.7: Photos (left) and schematic (right) of the optical biopsy system hardware prototype.

The optical train starts at a 455 nm peak-wavelength, 20 nm HWHM LED (Luxeon III Star, Philips). This light source was chosen because it was demonstrated in a previous study that this wavelength of excitation light is suitable for fluorescence imaging using acriflavin as contrast agent [31]. It is useful to build a prototype that possesses the flexibility to image in both reflectance and fluorescence mode to enable testing of all the agents developed in Project 2. The viability of using a single light source for both modes can then be assessed.

Light from the LED is collected by a planar-convex collimating lens (f = 25.4 mm, Newport) and transmitted to a planar-convex focusing lens (f = 62.9 mm, Newport), which focuses the light onto the proximal tip of a bundle of two illumination fibers (NA = 0.22, 200 um diameter; Thorlabs). The collimating-focusing lens pair was chosen to transmit the maximum amount of light from the LED to the illumination fibers. 25.40 mm is the shortest focal length available in a standard Newport lens set. The LED is purposely placed one focal length away from the front principle plane of the collimating lens to ensure light exiting the collimating lens is essentially parallel. Using a collimating lens with the shortest focal length means the collimating lens is as close to the LED as possible, capturing the maximum amount of light.

The focusing lens was chosen so to have the shortest focal length while keeping the light within the acceptance cone of the illumination fibers. Given NA = 0.22 for the illumination fibers, their maximum half angle θ of light acceptance in air (n = 1) can be calculated as

$$\sin^{-1}(NA/n) = \theta$$

$\sin^{-1}(0.22) = 0.222$ rad

To keep the angle of light from the focusing lens with diameter d and focal length f within the acceptance angle of the illumination fibers, it is necessary that

$\tan^{-1}(d/2f) < \theta$ or $f > d/2\tan(\theta)$

We used standard Newport lenses with diameter of 25.4 mm, so

$f > 25.4/2\tan(0.222)$ [mm]
$f > 56.3$ mm

The smallest focal length greater than 56.3 mm in the lens set was 62.9 mm. So this was chosen to be the focusing lens. The separation between the collimating and focusing lenses were based purely on setup convenience and in this particular instance measured 140 mm.

The distal ends of the illumination fibers are positioned co-axially with an image guide (3000 single fibers, 240 um outer diameter, 200 um picture area diameter, NA = 0.35; Sumitomo Electric). Both the illumination fibers and the image guide were chosen for their small size; each illumination fiber has an outer diameter of approximately 150 um after buffer stripping. Together, the two illumination fibers and the image guide were inserted into the bore of a 20-gauge needle with (584 um inner diameter, 902 um outer diameter; Sigma-Aldrich). This ensured that the needle probe of our optical biopsy system is on the large end of FNAB needles, some of the least invasive biopsy needles available.

While we paid close attention to the size of the needle probe, we also made sure that the image guide met minimum resolution and field of view requirements. Based on its picture area diameter and the number of fibers, we estimated the center-to-center spacing between the fibers to be approximately 3.7 um--200 um/sqrt(3000)—giving a Nyquist limit resolution of 7.4 um; this meets the requirement of imaging at the 10 um size scale of human blood and epithelial cells. At the same time, the field of view of the image permits simultaneous examination of some 300-400 cells—$\pi(100\text{um})^2/\pi(5\text{um})^2$, a reasonable size to examine even tissue morphology; the needle probe also has the advantage of being movable while imaging. As a consequence of these calculations, we expect the system to image at least at the cellular level while still permitting tissue morphology to be examined.

The proximal tip of the image guide is located at the focal plane of an infinity corrected objective (f = 18.2 mm, Newport). The infinity corrected objective is beneficial in a couple of ways. Because the light exiting the objective is collimated, the tube lens after the objective can be placed at an arbitrary distance from the objective, either saving space or permitting other optical components to be added. Furthermore, the image formed at the focal plane of the tube lens is magnified relative to the image at the focal plane of the objective by a factor K.

$K = f_{tube}/f_{obj}$

So the magnification can be adjusted by switching tube lenses with different focal lengths. In the prototype, the tube lens (f = 300 mm, Newport) was chosen to have the longest focal length within the space constraint of the setup.

A commercial CCD camera (AxioCam MRc5, Zeiss) is placed at the focal plane of the tube lens to capture the final image. The camera has 5 megapixels on an 8.7 mm x 6.6 mm CCD with single pixel detector size of 3.4x3.4 um$^2$. The camera is controlled by its associated software (AxioVision, Zeiss). The camera has a Nyquist limit resolution of 6.8 um, smaller than the 7.4 um resolution of the image guide even without image magnification by the tube lens. So the camera introduces no limiting factor to the prototype system.

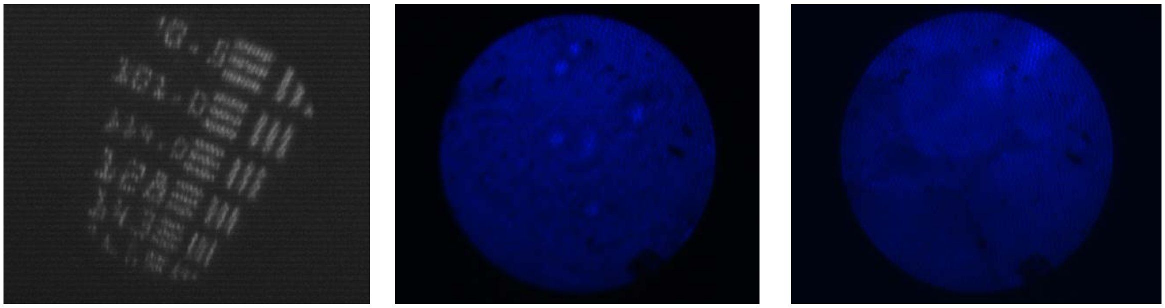

Figure 1.8: (left) Image of USAF resolution targets shows that the 128 cycles/mm bars are clearly distinguishable (grayscale done using Matlab); (center) image of SkBr3 breast cancer cells in culture; (right) image of adipose cells in bulk tissue.

Prior to the start of the project, two specific goals were set for the hardware aspect of the optical system: meeting minimum resolution requirement and acquiring cell structure information. Imaging results from the prototype indicate that the hardware accomplishes both goals. (Fig. 1.8) Imaging of the USAF resolution target showed that the system could achieve a resolution of at least 7.8 um and perhaps as high as 7 um, which is slightly better than even the estimated theoretical limit of 7.4 um. The center and right images further demonstrate the capability of the system to image both cancer cells in culture and adipose cells in bulk tissue (we are using chicken tissue from the grocery store until we receive regulatory approval and SOW modification for breast tissue protocols). The present investigation does not include the introduction of chemical agents to visualize sub-cellular structures, but the prototype system can image at the cellular level with confidence. For sub-cellular structures larger than the resolution limit of the system, such cancer cell nuclei that can occupy up to 80% of cell area, we expect no problem for our system to image them.

### Preliminary work: software program

The software program development is in some ways more challenging than for the hardware system. Unlike the hardware, for which cheap and reliable components exist commercially, most of the algorithms for the software are still being developed. However, we have identified several very promising algorithms to perform specific functions in the program: the Hough transform for cell localization, the watershed algorithm for broad feature extraction, and dynamically programmed optimal path finding for specific feature extraction. As we research and develop these techniques for the optical biopsy system, new ideas and results will continually be reported by us and many others. We are confident that like the hardware, the software program will shape up to be exactly the tool we need to perform breast optical biopsy.

As a first step, raw images from the hardware are first processed in the Fourier domain to investigate the efficiency with which pixelation artifacts caused by fibers can be removed. (Fig. 1.9) The Fourier transform of the raw images clearly shows a clearly define frequency band corresponding to the pixelation artifact, which occurs regularly in space. By removing that narrow range of frequency components using a band-stop filter, the artifact can be largely removed without significantly distorting other features of the image. By further changing the color map of the image and implementing simple histogram stretching, the raw image can be made much more visually clear with minimal effort.

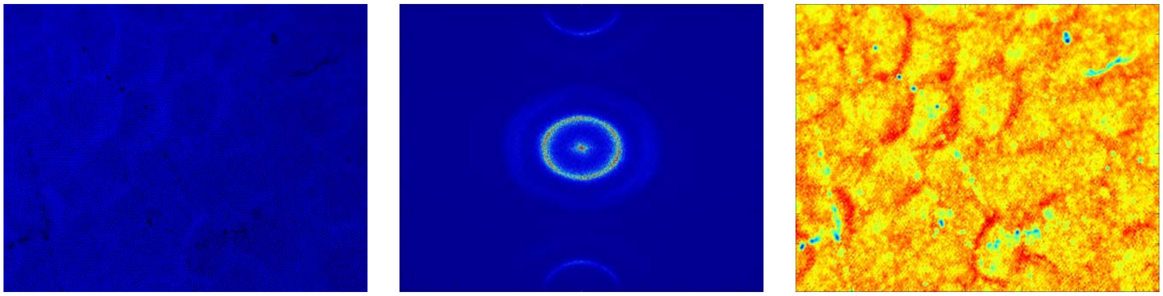

Figure 1.9: (left) A raw image of adipose cells in bulk tissue from the prototype setup using a larger image guide more suitable for software development; (center) the Fourier transform of the raw image shows a clear and bright ring (red-yellow) corresponding to the pixelation artifact; (right) the processed image using a different color map after band-stop filtering and histogram stretching.

Because we want minimize the burden on the physician when using the optical biopsy system, we started the algorithm development with the Hough transform. During our review of existing image processing methods, we noticed that both the watershed algorithm and the optimal path finding method suffer from the need for manual marking of cells in a tissue image. It is therefore logical to try and solve that problem first. We performed an initial investigation of applying the Hough transform for circles to the analysis of cells in a tissue image. (Fig. 1.10)

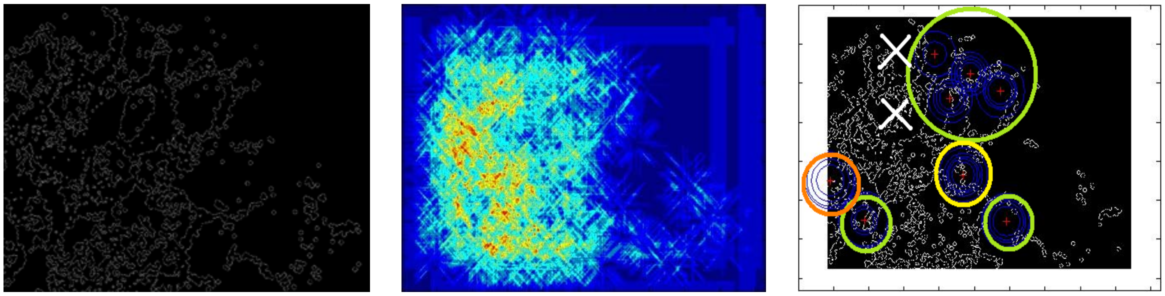

Figure 1.10: (Left) To perform the Hough transform on a tissue image, the set of points roughly corresponding to the cell boundaries must first be identified. (Center) The parameter space requires an adaptive local thresholding algorithm to identify bins with the highest counts that are most likely to represent actual cells. (Right) A simple Hough transform for detecting circles extracted 8 cells from the image, of which 6 could be confirmed as correct by visual correlation between the program output and the original image (green) and 2 could not be confirmed with

one more likely to be correct (yellow) and one more likely to be incorrect (orange). At least two cells visible in the original image were missed by the algorithm (white cross). The original image is the same one in Fig. 1.9.

Before the Hough transform can be used, it is necessary to first identify the set of points that has a reasonable probability to be the cell boundaries. This set needs not be comprehensive or completely accurate. The only requirement is that the points roughly represent where the cell boundaries are located without too much noise. We chose to use a gradient map plus thresholding approach for the initial testing because it is simple to implement and suits well the wide cell boundaries in the image. This technique is a poor choice if we wanted a precise extraction of size information because more than one boundary surrounds a cell; however, since we care mostly about locating the cells, having an extra boundary is actually helpful.

The Hough transform is subsequently performed on the set of boundary points. The boundary point plot (Fig. 1.10, left) showed a great deal of noise in the lower left region. Comparison with the source image showed that area to have some sharp edges without clearly discernable cells. This phenomenon was more trouble than the right region of the image that has no discernable cells or edges because edges not part of a cell contributes to noise. Because the boundary point plot showed a great deal more noise in the left bottom region, an adaptive local thresholding algorithm was used to pick out the most likely centers of circles from the parameter space (Fig. 1.10, center), representing cells in this case. A local thresholding method prevents high noise areas from affecting low noise areas.

In the end, the simple test algorithm we used extracted a total of eight cells, six of which have correct cell locations—judged as having the cell center mark inside the actual cell—after correlation with the original image; two extracted cells cannot be confirmed by correlation with image because there is insufficient detail in the image. (Fig. 1.10, right) At least two visible cells near the top left of the original image were missed by the algorithm. However, given that this was an initial attempt to assess how a straightforward Hough transform for circles would perform on a difficult image, the result was very encouraging. Just by testing a simple Hough transform without any modifications to account for irregularities in cell shapes or distortions in the image, we extracted most of the visibly identifiable cells fro the image with an accuracy of 75%. Most importantly, we have established that the Hough transform is a viable tool to locate the cells in a complicated tissue image.

### Next steps: hardware

The testing of the hardware has shown that the goals we set at the beginning of the project have been largely accomplished. Both the resolution of the imaging system and the ability of the system to image biological structures have been demonstrated. There remains, however, much that can to be done on the development of the hardware. Because the successful completion of Project 1 depends on the achievement of both software and hardware goals, improvements to the hardware can continue at least until the software has achieved its goals; every improvement in hardware makes the software's job that much easier.

The most logical place to start improvement is in the needle probe. So far, we have tested just one probe size based on the smallest components available. However, should smaller probes be possible, how small becomes too small? Background studies revealed that despite its superiority in size, FNAB is more challenging to use correctly because it sacrifices the ability to perform histopathology in order to employ the smallest possible needles. There is no doubt that an optical biopsy system also has a lower size limit beyond which it loses performance, which can be caused by overly small field of view or too little light being transmitted. As the needle gets smaller, safety may also become a concern; although it does not seem probable that structural failure can happen before performance reduction. In any event, a fuller investigation on the optimal size for the needle probe is a worthwhile endeavor.

While considering different needle sizes, the question of light transmission naturally comes up. The present setup uses separate illumination fibers even though the image guide is capable of simultaneous transmitting light in both directions. This was done to avoid specular reflection from the various optical-air interfaces in the optical pathway. There are certainly methods to minimize the specular reflection—index matching, polarity control, angled optics, just to name a few—but the possibilities extend further. For example, the image guide has many individual fibers. It is potentially possible to design a precise enough optical pathway that delivers light through only some of fibers, say those on the outside, and use only the inner fibers for image transmission. To accomplish this without fiber bifurcation is both an impressive challenge and very rewarding because the needle probe size in the present setup can be reduced by 50% if the illumination fibers are removed. To go smaller, these modifications are worth testing.

On the other hand, going smaller is not the only option. CNB using a 14-gauge needle remains more widely used in the US today than FNAB. If biopsies with the same quality as CNB could be performed without tissue removal , even if the same 14-gauge needle were used, that would be a positive development in itself. It would improve the lives of all CNB patients. If the quality of the optical biopsy can be made higher than CNB, then it's even better. Given this possibility, an investigation toward the larger end appears just as worthwhile as going small; on top of that, bigger is easier in optics.

These are just some of the possible ways in which our prototype optical biopsy system can be improved. Even if the current setup by some miracle performs just perfectly, investigations into the limits of the system design and the various ways different components can be modified will yield invaluable insight into the design of future medical imaging equipment, say an optical biopsy system for the brain, a very dangerous procedure today. Finally, after both the hardware and software objectives have been accomplished and the desired investigations made, the system will be packaged. While the prototype system benefits from an open and easily modifiable setup, the system must be made portable, compact, and robust for clinical testing. It must also have a clean and intuitive user interface. In short, the system should perform all the difficult tasks on its own to make the clinician's life as easy as possible.

### Future work: software

Unlike the hardware side, many challenging tasks remain on the road of software development. Although there are alternative techniques in consideration that will be investigated, these efforts are for the most part critical to the success of the optical biopsy imaging system. The best approach is to take one step at a time and gradually build up the software program until every algorithm in the sequence falls into place.

The first task in software development is the adaption of the Hough transform to a algorithm that can mark the location of cells in an image so that subsequent processing and analysis by either the watershed algorithm or the optimal path problem can be performed. Hot on the heels of a successful initial test, there is every reason to believe that a suitably modified Hough transform can accurately identify the majority of cells in a tissue image. Because the initial test resulted in two extracted cells that could not be confirmed by the original image, there is even the possibility that the Hough transform can help in the identification of important structures that are otherwise difficulty to visualize by the human eye. However, to develop a Hough transform algorithm is also best done one step at a time.

Before the Hough transform can even be applied, it is necessary to extract the cell boundaries from an image. The initial investigation showed that through pre-processing, the intensity of boundaries in the image can be greatly increased. This leads to the possibility of an adaptive local thresholding algorithm, which was used successfully in the initial testing to pick out most likely cell centers from the parameter space of the Hough transform. This method is more powerful for overcoming noise in an image, the source of difficulty with identifying the cell boundaries in our first attempt. Reducing the noise in the cell boundary plot goes a long way toward performing a successful Hough transform.

To improve the situation even more, a way to extend cell boundaries will be investigated. It is clear from Figure 1.9 that cells in a tissue image are sometimes partially blocked. So instead of a circle or an oval, they show up as a partial elliptical shape. Using geometric computation and pattern recognition, it is possible to detect a significant arc in the image and then extend that arc into an ellipse by adding false boundary points. For the cases where the detect arc really is a partial boundary of a cell, the pseudo boundary points greatly increases the chance that cell will be correctly detected by the Hough transform. In addition to the localization of cells, adding pseudo boundaries in the analysis could also aid in size estimation of structures; however, that direction of research has the risk of misleading results, and will be pursue separately and with great caution.

In the meantime, the modifications in the preprocessing have given way to the development of the Hough transform itself. One of the assumptions in the initial test was the circularity of cells. Although some cells and cells in culture are often round, cells in tissue are generally not. This is especially true for epithelial cells in highly hierarchical tissue, where they are often flattened ovals with pinching ends. Developing a Hough transform that most accurately parameterizes the shape of the cells to be detected is an important goal in the software development.

Perhaps even more importantly, there is a possibility here to aid the diagnosis of cancer using the tissue image. Because cancer cells lose tissue level control, their morphological structure often differs significantly from normal tissue, especially for cancer of otherwise highly striated cells. As seen in Figure 1.1, cancer in the breast can manifest visually as a concentration of generally round cells surrounded by largely elongated stromal cells. By employing two Hough transforms, each specifically designed to identify cancer or normal cells of the breast, it is possible that some information about the pathology of the tissue under examination can be gathered even at this early stage of image process/analysis. By having two Hough transforms, the localization of cells for subsequent algorithms may also be improved.

The previous proposed investigations are just some of the possible ways in which the image processing/analysis can be improved. As work on the Hough transform progresses, other ideas will likely reveal themselves. After the Hough transform algorithm has been satisfactorily developed, work on either the watershed method or the optimal path problem or perhaps some other new technique will commence. Because these are highly sophisticated image analysis methods, it is not resource efficient to simultaneously develop all of them. Instead, as indicated by the background study, one method will be superior to the other depending on the proportion of cells identified by the Hough transform. It is better to hold off on formulating the specifics until the Hough transform portion has been completed.

After all the above algorithms have been developed and the cells in the image segmented, the techniques to extract the relevant structural data, such as size, morphological score, etc. will be pursued. These are even further out into the future. Unlike the hardware portion, where everything can be planned ahead at once, the software development is best done in stages with the best method chosen at each stage based on the result of the stage before.

### *Project 2*

*This project develops the nanoprobes which will be used along with the optical systems created in Project 1 to enable molecular specificity. As our SOW describes, we are developing two types of materials: (1) non-cadmium luminescent dots and (2) shaped and layered gold nanoparticles. Our first year effort on this project has been focused on the basic materials chemistry development aspects as indicated the SOW. We are ahead of schedule on this project and in Year 1 provide results for both Task 1 and Task 2 rather than just Task 1 as originally anticipated. We also provide preliminary results for Task 3 which encompasses biological evaluation of several different nanoengineered probes including luminescent dots and gold-based nanoparticles (both nanorods and nanoshells). Please refer to the Appendix section for copies of one submitted and three published papers on development of molecular imaging agents for breast cancer applications.*

### *Background*

The success of an optical biopsy system that uses contrast agents will depend largely on finding the appropriate agents. Even though gold nanoshells have been the most promising candidates based on our preliminary research, other contrast agents will be evaluated. To ensure that these evaluations proceed in a thorough and consistent manner, a set of guidelines will be used to direct all investigations involving potential contrast agents to be used in the optical biopsy system.

As with all chemicals used in the human body, the foremost question about the contrast agents is whether they are safe to use. Once safety of the contrast agents has been reasonably established, factors relevant to performance will be evaluated. Based on our preliminary study of biopsy staining agents, one of the major questions will deal with time (see Task 3 results for our own work in this area). As revealed by preliminary research, current biopsy staining methods can at best work on a time scale of minutes to hours. While this is not an unreasonable reaction time, indeed appearing fast for use on physical biopsy slides, the optical biopsy system has a much higher demand on reaction efficiency. Since one goal for a contrast agent-using optical biopsy system is site-specific delivery, the imaging needs to occur quickly after the delivery of the contrast agent so that the needle probe does not need to be removed. Therefore, the time it takes for the contrast agent to begin working after delivery will be a prominent factor in evaluating its efficacy.

The other major issue related to contrast agent performance is simplicity. While the need to introduce eosin after hematoxylin in H&E staining already poses a problem for in vivo delivery of contrast agent during optical imaging, the numerous steps in the Papanicolaou stain are outright impossible. The delivery system will be too complex if it has to delivery several chemical agents into the breast with washing steps in between. Fortunately, all the nanotechnology contrast agents under investigation work by themselves. Nevertheless, it is necessary to explicitly specify all steps in applying a particular contrast agent and finding one that is facile to use clinically.

Finally, it is perhaps obvious that the optimal imaging conditions for each candidate contrast agent be thoroughly described. Some contrast agents work best in fluorescence mode; others work better in reflectance mode. Still others work well under both conditions. It is necessary to characterize the optimal imaging conditions so that the feasibility of adapting the imaging system can be assessed and the modifications made prior to testing. Naturally, the system setup is not the only condition that needs evaluation. The optimal condition of the contrast agent also needs to be clarified. It is known that pH, temperature, concentration, and even fluid mechanics can significantly affect the behavior of chemicals or nanoparticles in solution. The chemical environment and the imaging environment are both important for optimal contrast agent performance.

Other as of yet undiscovered issues may arise during the investigation of best contrast agents. They will be incorporated into the study as they arise. The aforementioned factors, however, are known questions of relevance based on the preliminary study. Whether or not other issues arise, the characterizations noted above will be performed for each contrast agent evaluated to ensure a uniform standard. However, because some factors are more important than others, e.g. safety, if a contrast agent fails a test of higher significance, subsequent tests will not be conducted because agent is no longer relevant. When at least one suitable contrast agent for clinical use has been found, the contrast agent-based optical biopsy system will be made suitable for clinical testing even while other promising agents continue to be studied.

Once a suitable contrast agent has been identified, the other major research objective is no doubt the delivery mechanism to bring the contrast agent to the imaging site inside the breast. Because our optical biopsy system uses a needle probe, it is very intuitive and logical to build the initial prototype delivery mechanism using a syringe with the needle as both the probe casing and contrast agent delivery channel. A conceptual drawing of such system is shown in Figure 1.11.

This system has at least two promising benefits. The first benefit is using the same needle for the imaging probe and the delivery mechanism. This ensures that the contrast agent is always delivery right where the imaging is happening. The second benefit is that a syringe, when coupled with a mechanical pump, can deliver very precise volumes of solution at highly regulated rate. This is crucial for the proper operation of contrast agents that require precise concentrations to balance signal strength and specificity. It is very possible that the needle syringe will end up being a suitable delivery mechanism.

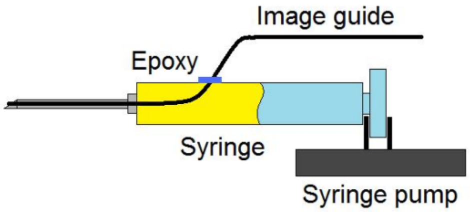

Figure 1.11: a syringe controlled by a syringe pump could be a very suitable contrast agent delivery tool. The imaging fibers (illumination not shown) are partly inserted in the syringe.

While the delivery of contrast agent is a straightforward process; the removal of excess contrast agent could be very challenging. Using a needle, there is no easy way to specifically remove excess contrast agent once it is delivered. Pulling back on the syringe with the needle tip inside the breast is simply not appropriate given that the purpose of the optical biopsy system is to minimize pain and suffering of the patient. However, one potential non-mechanical solution is to delivery just the right amount of contrast agent using the precision injection scheme described before. Under delivery is preferable to over delivery because adding additional agent is easy. Mechanical draining may not be necessary.

Another possibility to avoid having excess contrast agent distorting the image lies in molecular specific binding and activation (work underway in portions of SOW Project 2 and Project 3). There are contrast agents activated only after binding a specific molecular target. If such a contrast agent were used, then there is no problem associated with delivering excess agents into the tissue. A further modification of this strategy could involve an activating agent. It is sometimes the case that making as a single chemical that activates specifically is hard, but if a separate agent is introduced later to activate the first, the design of the two agents is easier. The syringe delivery mechanism can be modified to selective inject two different chemicals either together from separate chambers or in sequence. In any case, there are strategies available which employing a custom made delivery mechanism to help remove excess contrast agent without resorting to pulling on the syringe. If mechanical removal really is necessary, capillary action may prove to be helpful. Plants are able to pull water from their roots up to the highest branches through capillary action in special interconnected cells. By custom creation of a needle to have this kind of small channel that connects to a collecting reservoir, it may be possible to remove some contrast agent solution from the imaging site. Because no external mechanical force is applied, the chance that any cells would be severely disturbed is minimal.

## Results Over Months 1-12

Our work to date on SOW Project 2 has continued development of layered gold nanoparticles for breast imaging applications and initiated development of two additional classes of agents (cadmium-free NIR luminescent dots, Task 1, and gold nanorods, Task 2 of Project 2). We describe results of these two efforts below.

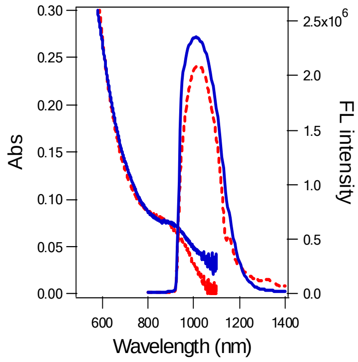

Figure 1.12. Absorption and emission data for NIR PbS quantum dots before (red) and after (blue, measured in PBS) hydrophilic modification. Optical absorption and emission properties are not significantly altered.

***Synthesis and Hydrophilic Modification of PbS NIR Quantum Dots:*** We have recently developed methods for synthesis and water solubilization of NIR nanodots described briefly here. These cadmium-free NIR emissive nanodots are appealing not only due to tunable NIR emission but also because the materials are broadly excitable from the UV through NIR. To prepare PbS nanodots, a mixture of 90 mg of PbO (0.40 mmol), 0.25 g of oleic acid (0.80 mmol), and 1-octadecene (ODE) (total weight = 5.0 g) is heated to 150°C. Upon turning colorless, the mixture is further heated to 260°C. 2mL sulfur solution (0.2 M) in ODE is then quickly injected. The temperature of the reaction mixture is allowed to cool to 200°C to allow growth of the PbS semiconductor nanocrystals. All steps in the reactions are carried out under argon. For imaging applications, the surfaces of the PbS materials must be rendered hydrophilic. The first step in this process is pretreatment with mercapto-propylmethyldimethoxysilane (MPS) and methacryl-ethylenetrimethoxysilane (Si-MA). The reaction is carried out in a 3-necked flask assembled using condenser under argon protection. 1.0 nmol of QDs is dissolved in 1.0 mL toluene followed by dropwise addition of 100 nmol of MPS and 1000 nmol of PEGS at 110°C. After 12 hrs, aminopropyldiethylethoxysilane (AES) is added under argon. The reaction is continued overnight at 100°C. After the reaction is stopped, the QDs are precipitated against n-hexane and redispersed in water. The as-prepared QD aqueous solution can then be transferred to PBS. As shown in Figure 1.12, the process to aminate the surface does not appreciably alter the optical properties.

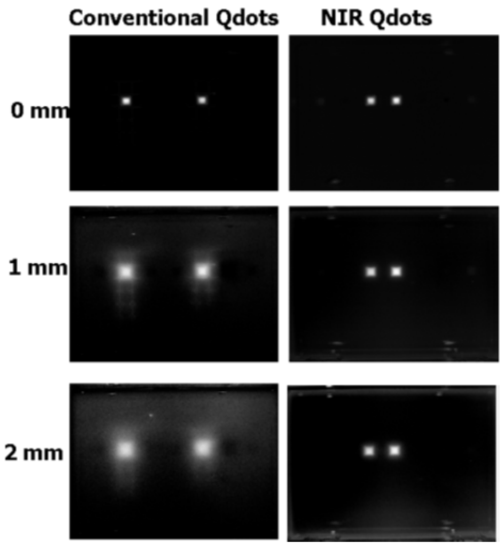

Figure 1.13. Imaging of visible (left) and NIR (right) containing tumor phantom embedded in a tissue mimic. All images were generated using the same silicon CCD with quantum dots synthesized in the Drezek lab.

***Imaging with PbS Quantum Dots:*** As a preliminary demonstration of the imaging advantages of the NIR qdots as compared to those with visible emission and to demonstrate sufficient signal for imaging these particles using a silicon CCD, we embedded tumor phantoms containing identical concentrations of visible or NIR qdots in a mouse tissue mimic and imaged the tumor phantoms as the top surface of the tumor phantom was moved deeper into the mouse tissue phantom (Figure 1.13). Decreased blur due to less scattering of NIR light is clearly apparent. After verifying signal levels were sufficient for imaging using nM concentrations, immunotargeted NIR qdots were developed and evaluated. Following quantum dot synthesis and solubilization, the surface may be conjugated to antibodies using a heterobifunctional cross-linker such as N-[p-Maleimidophenyl]isocyanate (PMPI) or (N-[ß-Maleimidopropionic acid]hydrazide•TFA) (BMPH) which reacts with the hydroxyl or carboxyl group respectively and provides a maleimide functional group on the quantum dot. The quantum dots synthesized are stable in the reagent buffer used for the cross-linker chemistry. The maleimide group is reactive to free sulfhydryl groups on antibodies. Prior to conjugation of quantum dot to antibodies, the antibody disulfide bonds are reduced to free sulfhydryls using dithiothreitol, also known as Cleland's reagent. Alternatively, we can utilize a carbodiimide such as EDC and activate carboxyl groups to react with an amine-terminus of an antibody. The quantum dots are conjugated to the antibody and isolated from unbound quantum dots and unbound antibodies by gel chromatography. In addition, antibodies may be immobilized via polymer tethering chains. This can be accomplished with difunctional polyethylene glycol derivatives. This immobilization scheme may increase the biological activity of the immobilized antibodies by enhancing their mobility and thus their ability to interact with their target ligand.

***Cytotoxicity Studies**:* It is worth noting that the quantum dots agents we propose are cadmium-free, and the lead dose we expect would be required should these particles be considered for human use in diagnostic applications is lower than the average incidental Pb daily exposure in urban environments. Initial cytotoxicity screens (Figure 1.14) of the NIR qdots have been promising. Any new formulations of conjugated NIR quantum dots developed for this project will first be evaluated for biocompatibility. Preliminary screens will determine LC50 values in cultured human dermal fibroblasts with calcein AM/ethidium homodimer staining (Molecular Probes Live/Dead Assay, lactate dehhydrogenase release, and MTT assays. Changes in proliferation rates will be monitored by staining for proliferating cell nuclear antigen (PCNA) and evaluating growth rates. Changes in adhesion, spreading and migration will be measured. TUNEL assays will also be performed to assess apoptosis. We have recently published (January 2008, *Small*) an extensive review of approaches to assessment of nanoparticle cytotoxicity which provides more detailed explanations of these methods.

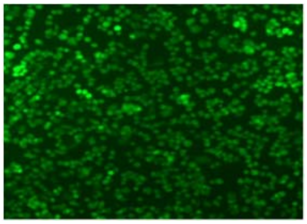

Figure 1.14. Preliminary cytotoxicity screening of PbS qdots. Green = live cells (calcein AM).

**Project 2, Task 2**

It is conceivable that the cadmium-free qdots described above still are ultimately deemed not suitable for in vivo applications. In Task 2 we focus on materials that are gold-based nanoparticles (AuNPs) which are the nanomaterials closest to clinical translation in particular gold nanorods. To facilitate future applications, it is necessary to synthesize complex AuNPs with high yield and without secondary separation steps to remove spherical or triangular contaminants. Such synthesis is particularly challenging for long nanorods. Methods for nanorods synthesis include electrochemical, photochemical, and seed-mediated approaches. In seed-mediated approaches the concentration of gold growth solution is highly dilute (0.01-0.25mM) and further purification steps are required. We are developing a modified seed-mediated synthesis approach for gram scale synthesis of *NIR* nanorods (as opposed to short nanorods readily produced using standard methods and available long nanorods methods requiring subsequent purification). To demonstrate feasibility (Figure 1.15), a seed solution was synthesized by adding freshly prepared $NaBH_4$ solution (0.3mL, 0.01M) to a solution composed of $HAuCl_4$ (2.5mL, 0.0005M) and CTAB (2.5mL, 0.2M).

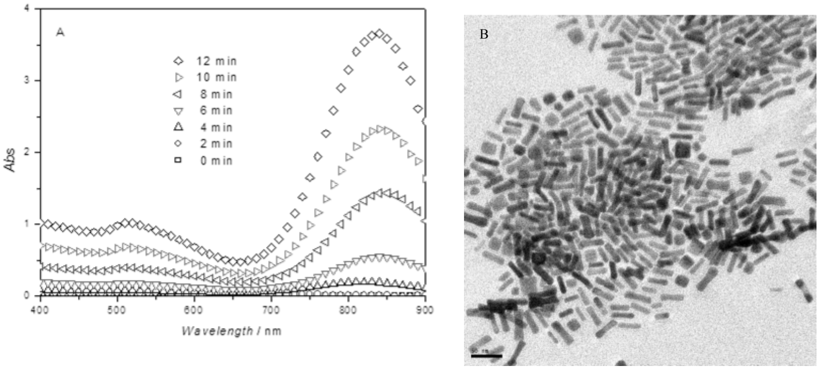

**Figure 1.15.** Preliminary results demonstrating synthesis of concentrated high aspect ratio (>800 nm peak) gold nanorods. In optimal synthetic conditions, the yield of gold nanorods is up to 0.1 g as compared to 0.02 g using conventional methods. Typical TEM image using the proposed approach *without* any further purification steps is shown on the right.

The seed solution was kept in a 40°C water bath for 15 min to decompose excess $NaBH_4$. Gold nanorod growth solution was prepared adding ascorbic acid (AA, 0.046mL, 0.1M) into a solution composed of $HAuCl_4$ (0.3mL, 0.01M), $AgNO_3$ (0.06mL, 0.01M), and CTAB (3mL, 0.2M). Nanorod growth was initiated by adding the seed solution (0.2mL) into the growth solution. After initial optimization (Figures 2.5 and 2.6), results indicate increasing the concentration of gold growth solution to 1.0mM (current reports do not exceed .25mM) and optimizing $AgNO_3$ can yield gram-scale gold nanorods with concentrations as high as 0.1g/L, a significant improvement over figures reported using standard methods (<0.02g/L). In continued work on Task 2 we will focus on further optimization of seed-mediated approaches to generate improved yields and larger quantities of NIR nanorods.

There are advantages as well as limitations to the use of gold nanorods as compared to gold nanoshells or other gold nanomaterials as in vivo imaging agents. Advantages in size, delivery, and linewidth are accompanied by disadvantages in signal strength. The biological evaluation (SOW Project 2 Task 3+) which will enable rigorous comparisons of all the material classes we are considering. Such direct comparisons of material classes are a present gap in the existing literature in molecular specific imaging agents because nanomaterial groups tend to focus on individual classes of materials within their own research labs.

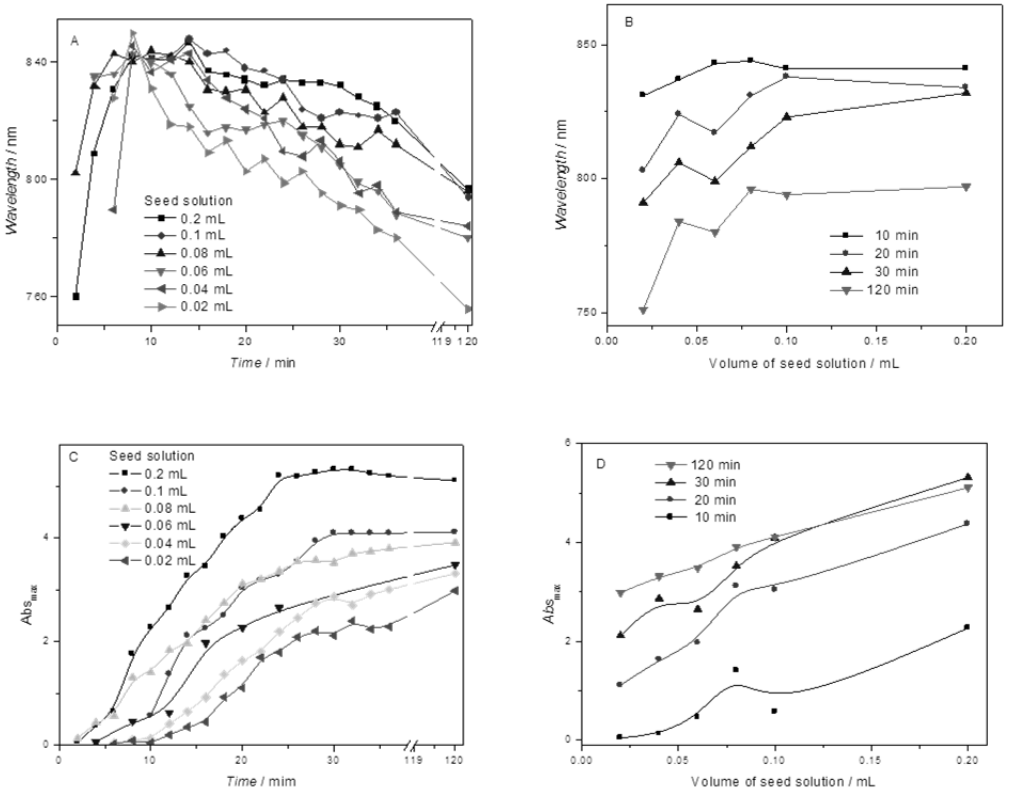

**Figure 1.16.** Preliminary results: effect of seed concentration. (a) Fluctuation of peak wavelength of Au nanorods with time under Au seed initiation. (b) Correlation between seed amount and wavelength at max absorbance. (c) Absorbance of Au nanorods with time under Au seed initiation. (d) Correlation between seed amount and absorbance. Gold nanorod growth solution: CTAB 3ml x 0.2M, $AgNO_3$ 0.01M x 0.06mL, $HAuCl_4$ 0.01M x 0.3mL, AA 0.1M x 0.046mL.

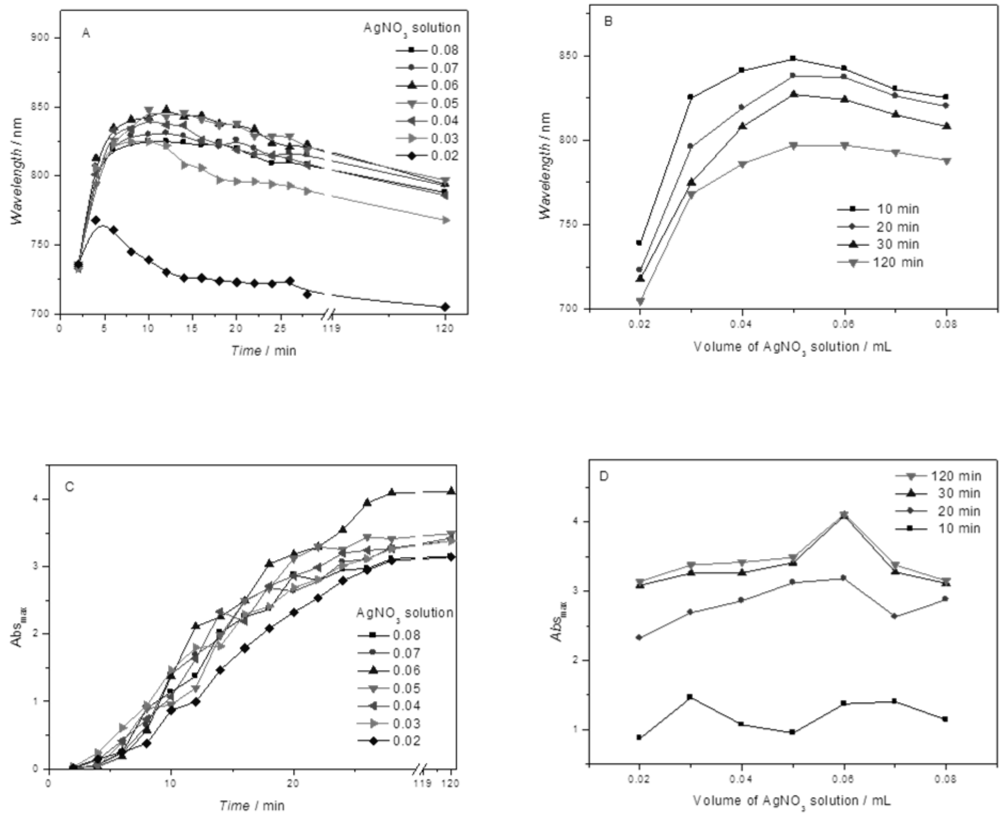

**Figure 1.17.** Preliminary results: effect of $AgNO_3$ concentration. (a) Fluctuation of peak wavelength of Au nanorods with time under Au seed initiation. (b) Correlation between $AgNO_3$ amount and wavelength of gold nanorods at maximum absorbance. (c) Absorbance of Au nanorods with time under Au seed initiation. (d) Correlation between $AgNO_3$ added and absorbance of gold nanorods. Gold nanorod growth solution: CTAB 3ml x 0.2M, add $AgNO_3$ 0.01 M x 0.06mL, $HAuCl_4$ 0.01M x 0.3mL, AA 0.1M x 0.046mL. Seed solution: 0.2mL.

***Project 2, Task 3***

Because we are ahead of schedule in imaging agent development, we have also initiated work on Task 3 which is the biological assessment aim of the imaging agent development project. This work is conducted together with MD Anderson Cancer Center and several papers co-authored with Dr. Kuan Yu, leading the MDACC efforts on this project, have resulted. Those papers may be found in the Appendix of this report which begins on Page 45. We highlight those results below.

In work published in *Nanotechnology* in January 2008, we developed a polarized light scattering method to quantify gold nanoparticle bioconjugate binding. To continue development of clinical applications using gold nanomaterials, it is critical that analytical strategies for quantification are developed. The previous method used to characterize nanoparticle binding requires the measurement of extinction spectra of cells labeled with nanoparticles. This does not result in accurate measurements of bound nanoparticles since particle-particle interaction effects are neglected using such an approach. To avoid the influence of interactions between nanoparticles when they are in close proximity to each other, we have developed a “negative” method of characterizing the binding concentration of antibody/nanoshell bioconjugates targeted specifically to breast cancer cells. Unlike previous methods, we collect unbound nanoshell bioconjugates and measure light scattering from dilute solutions of these nanoshells to achieve quantitative binding information. The interaction effects of adjacent bound nanoparticles on the cell membrane can be avoided simply by measuring light scattering from the unbound nanoshells. Specifically, we have compared the binding concentrations of anti-HER2/nanoshell and anti-IgG/nanoshell bioconjugates targeted to HER2-positive SK-BR-3 breast cancer cells using nanoshells of different sizes. The results indicate that, for anti-HER2/nanoshell bioconjugates, there are approximately 800-1600 nanoshells bound per cell. For anti-IgG/nanoshell bioconjugates, the binding concentration is significantly lower at nearly 100 nanoshells bound per cell. To the best of our knowledge this is the first paper which attempts to rigorously quantify gold nanoparticle binding.

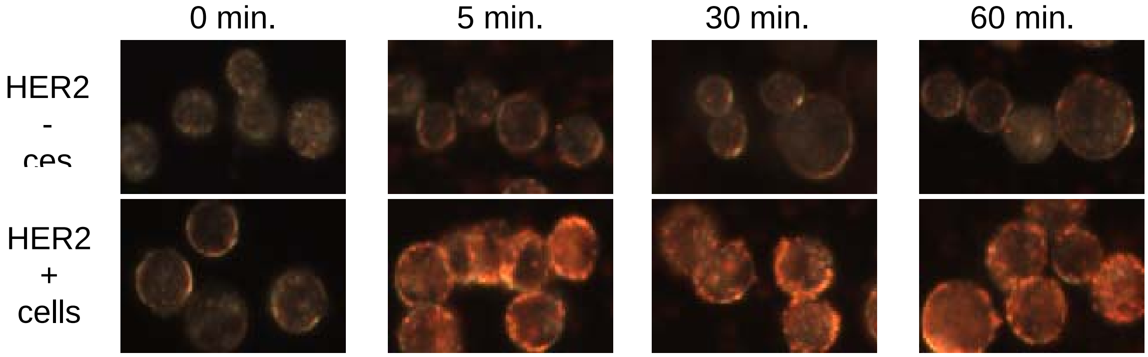

Figure 1.18 Immunotargeted gold nanoshells can produce statistically significant optical contrast in HER2+ cells within 5 minutes of incubation. Due to the patient being anesthetized while tumor margin results are pending, it is essential to minimize the amount of time spent processing the specimens.

In addition to being able to quantify binding, it is also critical we understand the time course of binding events. We ultimately would like to use these particles in clinical applications requiring rapid imaging. Almost all published protocols involving targeted nanomaterials require an incubation period of ~1 hour. This is not feasible for clinical applications which would require a read out in fifteen to twenty minutes. Thus, we conducted a study, which was recently published in *Nanobiotechnology* online and will appear in an upcoming print issue of the journal, to assess the time course of antiHER2 gold nanoparticle cellular binding (Figure 1.18). We determined we could obtain substantially equivalent results to those obtained using conventional protocols after only five minutes which greatly expands the types of clinical applications possible. While completing this study, we observed two photon luminescence from layered gold nanoparticles which had not been reported in the literature at this time we made this observation. We reported this work in a second paper in 2008 in *Nanotechnology* demonstrating for the first time the use of two photon microscopy for imaging immunotargeted (antiHER2) nanoshells. We believe using two photon imaging approaches may greatly aid in understanding biodistribution of gold nanoparticles in vivo by allowing 3D visualization of AuNPs within and surrounding tumors. Nuclear activation analysis (NAA) can provide high quality quantification of AuNPs in tissue but this is a destructive, bulk measurement method and does not allow visualization of AuNP location and distributions.

### *Project 3: Measurement of Radiation Dose Enabled by Nanoparticles*

*Project 3 is the most high risk/high yield project we proposed. The goal of the project is to investigate a strategy for real-time monitoring of delivered radiation dose rather than relying on computational modeling. Our task in Year 1 was to conduct a proof-of-principle study to assess whether our idea would work. We generated promising results concerning the potential of the overall idea: to leverage radiation breaking select bonds to cause loss of attached nanoparticles (and therefore, a measureable optical signal.) However, currently the strategy requires higher radiation dose than that used in clinical practice to work effectively. We will be conducting further experiments to determine whether it is possible to accomplish the same idea at clinically relevant radiation levels over the next year.*

Adjuvant radiation (RT) therapy in breast cancer patients is effective in reducing local-regional recurrence, and in some patients, it can improve survival. Currently, RT dose given during treatment is calculated using computer modeling which have assumptions and at times differs from actual dose delivered. Therefore, it is crucial to measure the actual dose delivered to the tumor targets to ensure proper coverage. Measuring actual dose to surrounding normal tissue is also very important to determine risk of radiation-induced toxicities, such as secondary cancers. The ability to measure RT dose delivered to breast cancer and normal tissue in vivo with high 3-dimentional spatial resolution is currently unavailable and will greatly improve current techniques used in radiation therapy.

Megavoltage ionizing RT has been shown to fragment proteins, carbohydrates, and polymers by ionization and breakage of molecular bonds directly and through free radicals generated in aqueous solution indirectly. Studies on radioisotope-conjugated antibodies also observed loss of antibody binding due to ionizing RT in dose and time dependent manner. Therefore, we use nanoparticles conjugated to antibodies through radiation-sensitive linkers and measure RT dose delivered to the tissue by measuring the release of nanoparticles caused by RT-induced breakage of the conjugation. The general concept is that since nanoparticles conjugated with disease-specific antibody can be targeted to tumor cells with great efficiency, when we link the nanoparticle with antibodies through a radiation-sensitive linker and apply these immunotargeted nanoparticle to cancer cells or tumor tissue, we would expect to observe the release of nanoparticles caused by loss of antibody binding after applying RT dose. We hope that by measuring the difference in concentration of nanoparticle binding and linker breakage, we can find some correlations between the releases of nanoparticles caused by radiation treatment to RT dose. We will also develop algorithms based on our experiments to accurately assess RT dose by measuring the optical signal and concentration of nanoparticles.

In year one of this project, we conducted in vitro studies and explored the applicability of using nanoparticle bioconjugates for RT dose measurement. We developed gold nanoshell probes conjugated with anti-HER2 antibody that specifically target HER2 overexpressed breast cancer cells. We also developed an IgG antigen and antibody based model to investigate the effects of RT treatment. By this method, we expect to relate the concentrations of nanoparticle released by

RT treatment to the RT dose applied to the cells and develop algorithms to calculate the RT dose based on our experiments. Preliminary data in Figure 1.19 shows that there is obvious nanoshell loss after RT treatment of both 50Gy and 100Gy. The bright spots in the after-RT pictures of 100Gy are nanoshell aggregates due to the detachment of nanoparticles from the slides. In contrast, for the no-RT control, the pre- and after- RT treatment images are quite similar to each other.

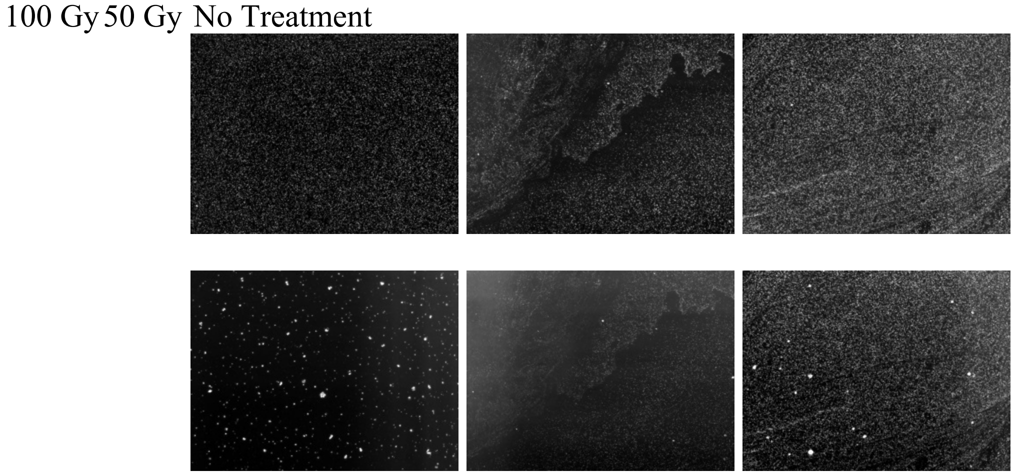

Figure 1.19. Darkfield images of IgG antigen treated slides incubated with gold nanoparticle and anti-IgG antibody conjugates, pre- (top row) and after- RT treatment (bottom row). See text for explanation of results.

## ***Year 2***

### Project 1: Needle Compatible-Optical Biopsy (NCOB) System

For background information on our motivation for developing a needle-compatible fiber optic system for breast cancer diagnostic and monitoring applications, information regarding the optical techniques and image analysis strategies we will use, and a description of how our system would interact with the technologies which are standard of care today please see our Year 1 report which covers those issues in detail. Below, we focus on progress on the instrument itself during the past reporting year. As described in the Statement of Work, Year 1 and most of Year 2 plans focused on design of this system and beginning initial construction. It was expected that the system (Figure 2.1) would be completed approximately 30 months after the design phase and evaluation would begin 2.5 years into the project. We are still ahead of schedule on this project and have built a second generation system which is modular in nature and rapidly reconfigurable – highly desirable properties as the instrument will be used in combination with imaging agents from Project 2 still under development. In this section we present initial data for the system which is already providing >10 micron resolution imaging capability through a needle probe. In Year 3 we will seek permission to modify our program of work to include more extensive clinical evaluation of this instrument than originally anticipated. Plans which note tissue studies and other clinical efforts below will only proceed presuming these modifications to our SOW are accepted and regulatory paperwork is approved.

During Year 2 of this project, to move the Needle-Compatible Optical Biopsy (NCOB) system closer to clinical applications, the needle probe has been made smaller and less invasive without sacrificing image quality. Experiments were carried out to verify the capability of the system to image individual cells.

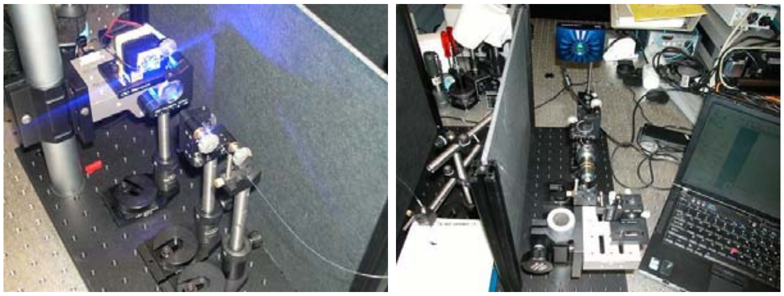

**Figure 2.1:** Our first system developed in Year 1 to evaluate a variety of different design considerations and to accommodate the CCD camera.

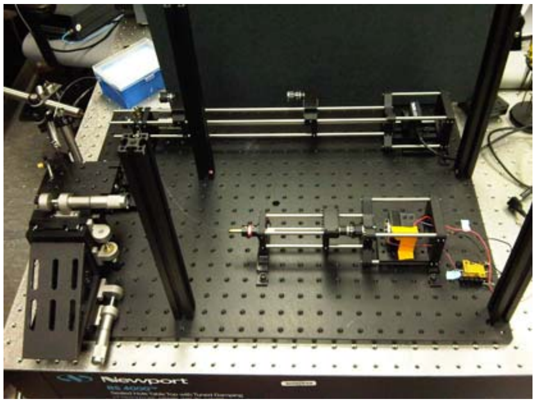

**Figure 2. 2:** The current setup using a cage system allows facile focusing of the optical components is and very stable when the parts are locked down. The optical sections are also much more compact. This setup is modular for future large section modifications (i.e. illumination section, detector section, and a currently in development fiber bundle projection section).

Ultimately, this system is intended for clinical use to provide an imaging modality with the resolution to image individual cell morphology, ultimately including nuclear morphology, without any tissue removal from the body. “Optical biopsy” refers to our ability to obtain this information optically without physically acquiring a biopsy sample. To visualize the nucleus of the cell for quantitative cancer assessment, contrast agents will be introduced to enhance nuclear contrast and more elaborate software tools will be used to automatically measure cell and tissue structural characteristics. Additionally, molecular imaging will be achieved with this system through the use of targeted imaging agents under development in Project 2.

After a year of testing out different components for the NCOB system, we have found the most suitable individual optical components to be used. It is therefore no longer necessary to use a setup where individual part can be switched out. Instead, a new cage based setup (Figure 2.2) has been constructed that emphasizes precise spatial adjustment of the optical components and stability once the fine adjustments are done. The new setup is also smaller and more easily isolated in separate compartments. Furthermore, the cage system can be easily broken down into optical sections that encompass numerous optical parts. While the parts are in locked positions relative to each other, the sections themselves can be easily modified. This is a very useful change because we are now implementing a new illumination scheme. Experiments in the last year on tissue mimics have suggested we will want to use imaging agents to improve visualization quality (both to visualize nuclear morphology and to label relevant molecular markers). This is not unexpected and is the motivation for Projects 2 and Projects 3. Because no one has built a system with the design we proposed before, we are learning as we go along what types of modifications are required to obtain images of sufficient quality. We discovered over the past year that given our intended clinical applications and imaging agents, the separate illumination and detection fiber bundles as they existed in the system design we presented last year is not ideal (too much specular reflection). Therefore, a new design has been put in place to minimize specular reflection the details of which are presented later.

**Improvement in design**: A key objective in the continuing effort to improve the NCOB system is minimizing the device's invasiveness while maintaining sufficient field of view (FOV) and resolution. At the start of the project, we set our goal to match and exceed the standards of core-needle biopsy (CNB) and fine-needle aspiration biopsy (FNAB), currently used to acquire samples for breast cancer pathology. While our first system introduced a year ago had invasiveness comparable to the CNB (though no tissue is removed from the body), our current system uses a needle probe the size of FNAB needles without the main drawback of that method.

Specifically, the size of our needle probe has been reduced from 14-gauge (2.1 mm outer diameter) to 20-gauge (0.9 mm outer diameter). The improvement has surpassed the conventional CNB needle size of 16-gauge and become comparable to the 18 to 24-gauge needles employed for FNAB (Figure 2.3). We plan to reduce this diameter further as the project progresses. . In addition, the diagnostic potential of the NCOB has advantages to that of FNAB because the imaging is performed without significantly disrupting the morphology of target tissue allowing visualization of histopathology in addition to the limited cytopathology permitted by FNAB. Furthermore, we do not remove any tissue or cells from the body using our method. The system has met our initial designs goals.

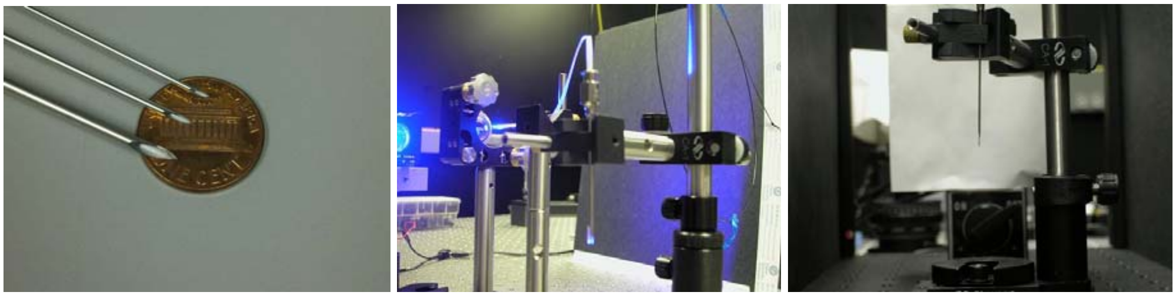

**Figure 2.3:** (left) the evolution of the needle probe for our system from 14-gauge to 20-gauge; (middle) the 14-gauge needle probe of the original system; (right) the 20-gauge needle probe of the new system.

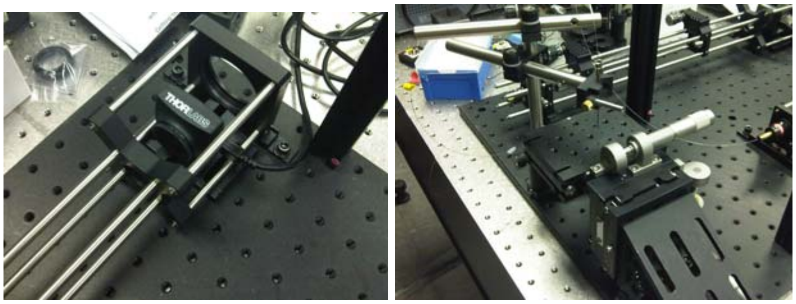

**Figure 2.4:** (Left) the new smaller and cheaper CMOS camera; (Right) the three-axis adjustable sample stage.

Besides more precise adjustment, enhanced robustness, and smaller size, the new cage based system has two other improvements (Figure 2.4) for biological experiments. One improvement is a $300 CMOS camera integrated into the cage system. This camera demonstrated comparable performance to the previous Zeiss camera but is smaller and much cheaper. Although price is not as an important consideration as quality, every bit of savings helps for a device aimed at making breast cancer screening and monitoring accessible to all patients. (We are building a tool which costs less than 5K using off the shelf parts and would cost far less than that in a manufactured setting.) A second improvement is a three-axis sample stage (Figure 2.4). Although the system will ultimate use a movable probe, the sample stage will be very useful for the imaging of NP in ex-vivo biological specimens.

**Improvement in performance**

Using higher quality image guides, the resolution of our system has actually increased as the size of the needle probe decreased. Resolution is currently well below the 10 micron average diameter of the smaller of the cells we will need to view in vivo and provides greater confidence for image the details of both normal and cancerous tissue in the breast. At the same time, the reduction in needle probe size also has raised several potential challenges. A smaller probe also means less illumination and a smaller field of view. Both could adversely affect the performance of the system. After experimentation, however, it was discovered that the current probe does not significantly increase the necessary exposure time of imaging or reduce the FOV below clinically useful levels. The exposure time was increased by only 100% to 1 second, making real time imaging still very much feasible. Although the field of view was reduced to 240 um diameter from 1 mm diameter, this smaller FOV still allows the simultaneous viewing of several hundred epithelial cells. The decrease invasiveness to the patient and the improved resolution more than make up for these marginal drawbacks.

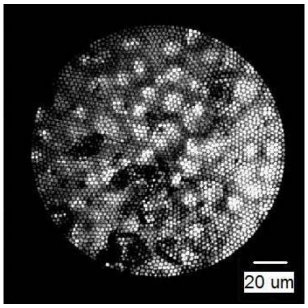

**Figure 2.5:** First images with second generation system shows the ability to detect individual breast cancer cells.

**First Imaging Results**

Our imaging work is slated to begin in Month 31 (this report covers Months 13-24). However, we are ahead of schedule and our now beginning to conduct these experiments which will be the primary focus of Year 3 of the project. The imaging of breast cancer is complicated by the need to discern specific disease features within a complex background of other breast structures. Figure 2.5 shows cultured SkBr3 breast cancer cells imaged by the NCOB system. As shown in the image, we are able to image at a cellular level visualizing individual breast cancer cells. Extensive imaging of cells in 3D constructs will be a focus of the next year with particular emphasis on using simple chemicals already in routine clinical use (toluidine blue, acetic acid, etc.) to stain nuclei for visualization and in our first assessment of the use of Project 2 imaging agents in conjunction with the Project 1 imaging system.

***Illumination/detection fiber bundle projection***

In order to improve the system to enable molecular imaging in vivo, a scheme to substitute the old probe, which consisted of separate illumination and detection fiber bundles with just an image guide is being implemented (Figure 2.6). This approach is advantageous because it strikes a good compromise between resolving specular reflection and making a small optical fiber probe. Bifurcated fiber bundles that split illumination and detection fibers at one end are hard to make and are not readily available at the sub-millimeter size we require. However, any reflectance based imaging using optical fibers would benefit greatly from separate illumination and detection fibers, especially if they can be arranged into specific shapes.

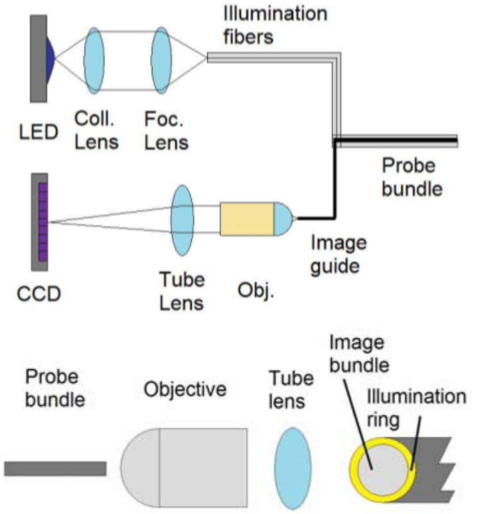

**Figure 2.6:** (Top) a schematic of the original optical pathway; (Bottom) the new illumination scheme projects an image of the old probe bundle onto the tip of another image guide, which serves as the new probe bundle; the old probe bundle, which no longer the probe, can be larger in size and of any geometry we need.

Our approach uses a single image guide for the probe, but illumination is projected onto specific fibers in the image guide separate from the detection fibers. This significantly shrinks the lateral separation of the illumination from the detection fibers and allows better distribution of illumination from the probe. While this improvement is currently being constructed, we are also working on alternative optical pathways, such as projecting illumination onto the probe image guide at an angle or separate coaxial illumination fibers polished at an angle in the probe.

***Software***

A more detailed overview of the software component of Project 1 is described in the Year 1 report. Figure 2.7 shows two diagrams of the basic and advanced tasks we are undertaking and planning to undertake as part of this effort. The first task in software development is the adaption of the Hough transform to an algorithm that can mark the location of cells in an image so that subsequent processing and analysis by either the watershed algorithm or the optimal path problem can be performed. Before the Hough transform can even be applied, it is necessary to extract the cell boundaries from an image. The initial investigation showed that through pre-processing, the intensity of boundaries in the image can be greatly increased. This leads to the possibility of an adaptive local thresholding algorithm, which was used successfully in the initial testing to pick out most likely cell centers from the parameter space of the Hough transform. This method is more powerful for overcoming noise in an image, the source of difficulty with identifying the cell boundaries in our first attempt. Reducing the noise in the cell boundary plot significantly improves the chance of a successful Hough transform.

After modifications in the preprocessing have been made, the Hough transform itself will be modified and developed. One of the assumptions in the initial test was circular cells. Although cells in culture are often round, normal cells in tissue are generally not. This is especially true for epithelial cells in highly hierarchical tissue, where they are often flattened ovals with pinching ends. A new parameter space will be developed that more accurately parameterizes cells in the human breast. To properly design the new parameter space, images of different normal human breast cells and cancerous cells will be studied. The most common features will be used to design a new parameter space for the Hough transform.

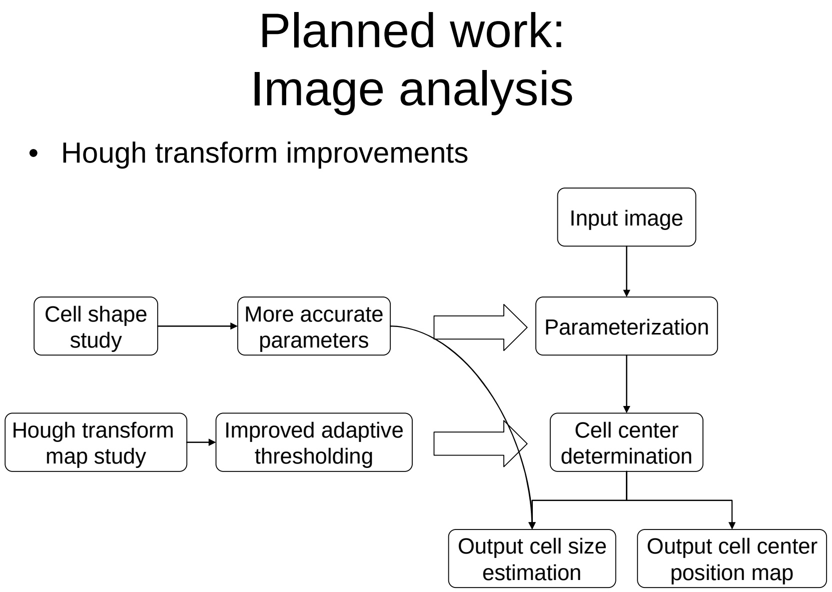

Planned work:
Image analysis

- Hough transform improvements

Input image
Cell shape study
More accurate parameters
Parameterization
Hough transform map study
Improved adaptive thresholding
Cell center determination
Output cell size estimation
Output cell center position map

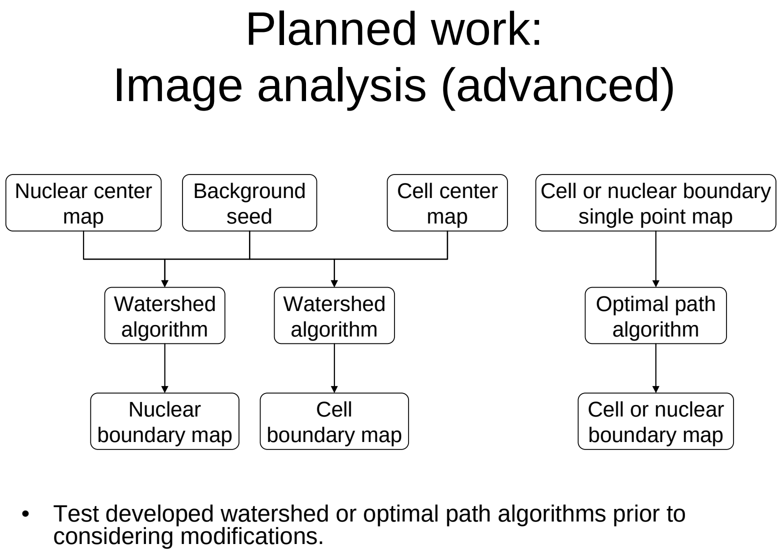

Planned work:
Image analysis (advanced)

Nuclear center map
Background seed
Cell center map
Cell or nuclear boundary single point map
Watershed algorithm
Watershed algorithm
Optimal path algorithm
Nuclear boundary map
Cell boundary map
Cell or nuclear boundary map

- Test developed watershed or optimal path algorithms prior to considering modifications.

**Figure 2.7:** (Top) flow diagram for improving the Hough transform algorithm; (Bottom) flow diagram for applying watershed algorithm and optimal path algorithm to cell boundary detection.

The previous proposed investigations are some of the ways in which the preprocessing and Hough transform can be improved. After the Hough transform algorithm has been satisfactorily developed, work on either the watershed method or the optimal path problem will commence. Because these are relatively complex image analysis methods, it is not efficient to simultaneously develop both of them. If the Hough transform demonstrates the ability to correctly locate the vast majority of cells, development of the watershed algorithm will be pursued. If the Hough transform can accurately detect only a limited number of cells, the optimal path problem method will be pursued. Because a branch point exists in the software development after the Hough transform, it is better to concentrate full effort on the investigations proposed in the preceding paragraphs and fully develop the algorithms before the branch.

***Summary to Date:*** *Project 1 seeks to develop a new tool for breast cancer imaging and monitoring applications. This is a sub-mm probe which provides micron resolution imaging (expected to be ~4 microns after full optimization) in vivo without tissue removal. To the best of our knowledge, it is unlike any tool available for breast cancer imaging today offering resolution far exceeding what would be possible by other imaging techniques not requiring removal of tissue from the body. It is also extremely inexpensive using a $300 camera and light sources based on LEDs that cost under $50. The instrumentation design is being modified to provide optimal image quality when used in conjunction with the molecular imaging agents being developed in Projects 2 and 3. The instrument will be capable of imaging both intrinsic (cellular morphology and tissue architecture) optical signals and extrinsic contrast agents used either to facilitate visualization of nuclear morphology or to highlight molecular markers of breast cancer. We are on schedule with this project having completed the vast majority of Task 1 and Task 2 and initiated Task 3. We expect to request a SOW modification to allow further clinical evaluation of the device than originally proposed.*

## Projects 2 and 3: Novel Nanoparticle-Based Imaging Probes for Breast Cancer Imaging Applications (Project 2) and for Monitoring Radiation Dose (Project 3)

We have merged the discussion of Projects 2 and 3 in this report as these two projects together encompass the two imaging agent components of the work. Projects 2 and 3 overlap in that work carried out in the first two tasks of Project 2 is also needed for Project 3. Both the imaging applications in Task 3 of Project 2 and all of the monitoring applications in Project 3, first require synthesis of appropriate nanoparticles. We describe the synthesis of these agents below and label each section to clarify whether the probes described are relevant to Projects 2, 3, or both. We also provide data from imaging (Project 2) and monitoring (Project 3) applications. We are developing two types of materials: (1) non-cadmium luminescent dots and (2) shaped and layered gold nanoparticles. The luminescent nanoparticle development work (Task 1, Months 1-12) was described in our Year 1 report. A Word copy of a submitted paper on that work was included at that time. This paper has now been published in Current Nanoscience (Sun et al, 2009) and the pdf is included in this year's Appendix and is not further discussed here. Multiple papers have appeared on the AuNP work described in the section which follows. Please refer to the Appendix section for copies of these papers. We concentrate our descriptions below only on those portions the work not yet published in final form.

## Gold Nanoparticle Imaging Agent Development (Task 2 of Project 2 to Generate Materials for Use in Both Project 2, Task 3, and Project 3, All Tasks)

Project 2 focuses on synthesis of new forms of gold-based nanoparticles (AuNPs) generating the near infrared (NIR) optical properties needed for applications in Project 2 and Project 3 through shaping (non-spherical, rod-like structures) or layering (gold-silica-gold nanoparticles). The motivation for work with gold-based nanomaterials is that these materials are the nanomaterials closest to clinical translation largely because they are consider the most suitable for human *in vivo* use from a safety standpoint. Most gold-based biomedical nanomaterial work has used either conventional nanoshell (gold-silica) or gold colloid. Gold colloid cannot be tuned into the NIR and gold-silica nanoshells are too large for effective delivery for some of the types of applications we envision. Thus, in this project, we expanded our efforts to consider newer types of nanomaterials including gold nanorods expanding on previous research using these nanomaterials in particular by developing approaches which allow scale up to the volumes required for clinical use.

To facilitate future applications, it is necessary to synthesize complex gold nanorods with high yield and without secondary separation steps to remove spherical or triangular contaminants. As we noted in our report last year, such synthesis is particularly challenging for long nanorods. We are particularly interested in these longer nanorods as these are the rods which provide the NIR properties which place them in the NIR "water window" suitable for *in vivo* biomedical applications. Last year we were ahead of schedule on Project 2 so had proceeded with the synthesis which we described in last year's project report.

At the time of last year's report we had not proceeded to bioconjugation strategies. These strategies are required since we are fabricating these materials for ultimate use as molecular imaging agents for HER2, EGFR, and potentially other markers. The image below (Figure 2.8) shows our first images from a newly proposed method for attaching antibodies to nanorods. The image in the upper left shows successful labeling of HER2+ cells. Please see (Rostro-Kohanloo et al, 2009 (in press)) included in the Appendix for technical details of this approach. As opposed to what we reported last year (nanorods in CTAB), here were use a PEGylation based stabilization approach and heterobifunctional linkers with free carboxyl groups for the antibody attachment As we moved into the last three years of the overall project, Project 1 and Project 2 will begin to come together as we apply the agents being developed in Project 2 for use with the imaging system developed in Project 1.

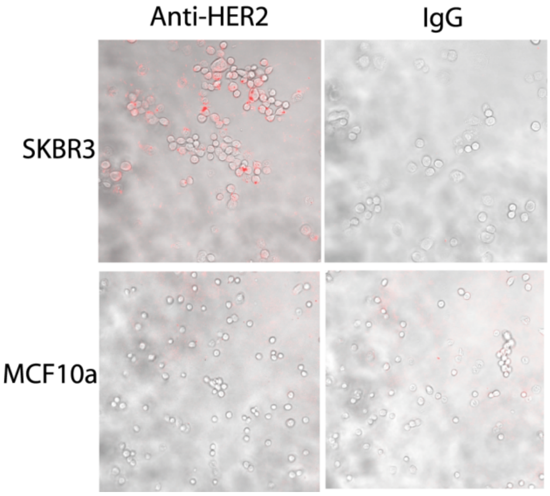

**Figure 2.8**. Nanorod conjugate targeting. Phase contrast shows the cell locations in grayscale, and two photon luminescence is displayed in red. Binding was only observed for the anti-HER2 conjugates and SKBR3 breast carcinoma cells.

As an alternative to the shaping approach considered last year, we are also investigating using a more sophisticated layering approach involving three of more layers of alternating metal and dielectric materials. The reason to consider this alternative over the shaping described above is stability. Any problem with the surface modification when working with nanorods will cause the nanorods to revert to a spherical configuration and lose their NIR properties. The method described above seems to produce by far the most stable nanorods we have developed to date. However, stability is always a hurdle when working with elongated nanoparticles. Agents inherently designed to have NIR properties while spherical will avoid this problem. An *Optics Express* paper we published in November (Hu et al, 2008) provides details on the new approach to developing tunable gold nanoparticles (NPs) for imaging (and if desired, integrated) therapy applications creating additional tunability in smaller diameter particles by addition of a small gold core into a silica-gold nanostructure (Figure 9). This approach overcomes several of the technical limitations we have encountered in our work using gold-silica nanoshells. The new gold-silica-gold NPs (1) maintain the near infrared (NIR) tunability of gold-silica NPs but will reduce the overall NP size to <100 nm to overcome delivery hurdles we have encountered with larger NPs; (2) feature narrower spectral line-widths to facilitate multiplexed labeling of molecular markers; (3) demonstrate increased extinction efficiency. The particles are formed beginning with easily synthesized gold colloid and then adding a thin silica layer followed by a final gold layer.

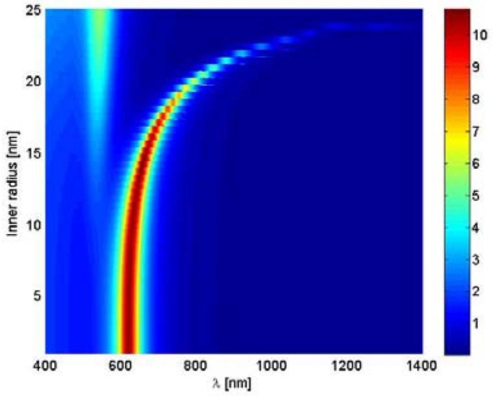

**Figure 2.9.** Extinction of *70* nm diameter multi-layer nanoshells in water as a function of inner radius.

.

Please see (Hu et al, 2008) in the Appendix for a paper describing the optical properties of gold-silica-gold materials. We do not describe the technical details of that work here as the paper covers these aspects. We have begun efforts on synthesis of these particles and describe those here. This work is not yet published and further efforts are required to bring the sizes down to a level where will we gain the advantages we seek with this class of materials. A multi-step procedure is performed to prepare gold-silica-gold nanoshells, composed of the following stages: (1) making gold colloid (15-100 nm), (2) silica coating of gold particles, (3) (3-aminopropyl)trimethoxysilane (APS) functionalization of gold-silica particles, (4) synthesis of THPC (tetrakis hydroxymethyl phosphonium chloride) gold solution composed of 1-2 nm gold colloids, and (5) finally synthesizing the complete gold-silica-gold nanoshells.

In this work, gold colloid (15-100 nm) was prepared by a standard sodium citrate reduction method. 0.86 ml of chloroauric acid solution was added to 98 ml of de-ionized water in a clean 250 ml glass flask with a stir bar, and the solution was brought to boiling temperature upon stirring. Subsequently, trisodium citrate solution was added to produce gold colloid. Particular sizes are created based on varying the amount of trisodium citrate. Upon addition of the trisodium citrate, the color of the solution changed to blue and then to red.

The preparation of the silica-coated gold nanoparticles involved priming citrate-terminated gold colloids with (3-aminopropyl)trimethoxysilane, followed by the addition of active silica to form a thin layer of silica on the gold surface. Extended growth was achieved by the Stöber method, in which silica coated gold nanoparticles were functionalized with tetraethyl orthosilicate and ammonia in ethanol. Other research groups have followed a direct coating method of citrate-stabilized gold nanoparticles with silica shells by reducing tetraethyl orthosilicate in ammonium hydroxide with isopropyl alcohol or ethanol. We are instead direct coating on citrate-stabilized gold nanoparticles with silica shells – producing thickness from 20 nm to 150 nm – by optimizing the pH of the solution via ammonium hydroxide with isopropyl alcohol, and comparably by optimizing the amount of tetraethyl orthosilicate and ammonium hydroxide. This method does not require any coupling molecules and is based on a method that our group has been using for the preparation of various thicknesses of silica particles on various radii of gold particles: 50nm (Figure 10a-1c), and 20 nm (Figure 10d). A suitable amount of 3-aminopropyl)trimethoxysilane (1 mM) from 300 – 500 µl was added to silica-coated gold nanoparticles that were vigorously stirred in ethanol solution. The mixture is allowed to react for 12 hours. To enhance covalent bonding of the 3-aminopropyl) trimethoxysilane groups to the silica shell surface, the solution was gently refluxed for one hour. The APS functionalized gold-silica nanoparticles were then collected in ethanol. A THPC gold solution composed of 1-2 nm gold colloids was prepared according to the method of Duff and Baiker. Under rapid stirring, 1.2 mL of 1 M NaOH was added to 180 mL of water, followed by the addition of 4 ml of 1.2 mM aqueous THPC solution. After 5 minutes of continuous stirring, 6.75 ml of 1 wt% aqueous chloroauric acid was added in one quick motion, after which the solution immediately turned to a medium brown color. The final solution was refrigerated for at least 2 weeks before use.

A solution containing reducible gold salt was prepared in order to grow a continuous gold layer on the gold-primed silica-coated nanoparticles. Briefly, 50 mg of potassium carbonate was dissolved in water followed by the addition of 3 ml of 1.0% wt of THPC gold solution. Gold-silica-gold nanoshells were then grown by reacting gold salt with the gold-silica-gold colloids (1-2 nm) in the presence of formaldehyde. Currently, we are focused on reducing the overall size of the nanoshells made using this approach to less than 100 nm for Project 2 and Project 3 applications. Nanoshell formation was visualized and assessed with a transmission electron microscope (TEM). We expect to be able to report fully on this new class of gold nanostructures next year.

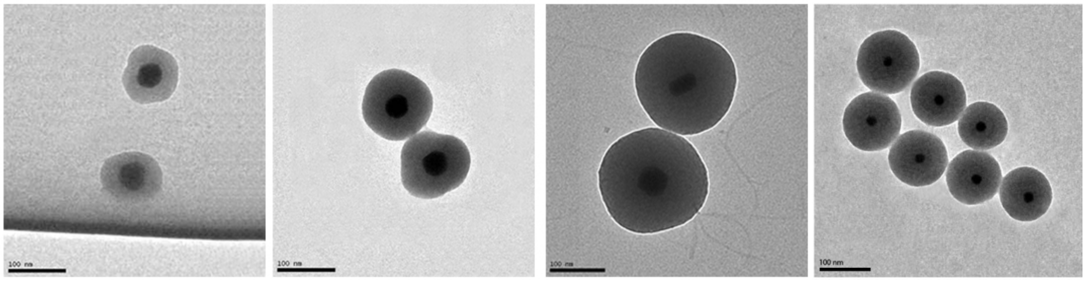

**Figure 2.10.** TEM images of silica gold (50 nm) nanoparticles with overall sizes of (a) 104 nm, (b) 125 nm, (c) 180 nm (left to right). (d) TEM image using a 20 nm gold nanoparticle as the starting point (far right).

**Biological Evaluation (Relevant to Both Projects 2 and Project 3)**

Last year we reported imaging results using darkfield microscopy for imaging. Although this method provides a facile approach to imaging cells in a laboratory setting, it is not relevant to the clinical imaging applications we are ultimately heading towards. In those applications where we will ultimately be imaging intact tissue (for example, using the needle probe device being built in Project 1), we detect reflected not transmitted optical signals. We will also ultimately be detecting reflected not transmitted optical signals in the radiation dose monitoring described in Project 3. Thus, it is important to consider how our nanomaterials perform in a reflectance-based geometry. In the work described here (paper on this work to be included in next year's progress report), we use NIR reflectance confocal microscopy. Future experiments will use the imaging system developed in Project 1.

Three breast cancer cell lines that are known to overexpress different levels of HER2 receptors were imaged: SK-BR-3, HCC1419, and JIMT-1. The normal mammary epithelial cell line, MCF10A, was also analyzed as a control that does not overexpress the HER2 antigen. All cell lines were purchased from the American Type Culture Collection with the exception of the JIMT-1 cell line, which was purchased from DSMZ (Germany). The SK-BR-3, HCC1419, and JIMT-1 cell lines were grown with medium (McCoy's 5A, RPMI-1640, and Dulbecco's Modified Essential Medium, respectively) supplemented with 10% fetal bovine serum (FBS) and 1% penicillin-streptomycin. The MCF10A cells were cultured in Mammary Epithelial Basal Medium (MEBM) supplemented with a BulletKit (Clonetics). The cells were maintained at 37ºC in 5% $CO_2$ atmosphere.

Each cell line was grown to confluency, trypsinized and then counted using a hemocytometer. The cells were then incubated with either media alone, PE anti-human CD340 (erbB2/HER-2) antibody (BioLegend), or PE mouse IgG1 isotype control antibody (BioLegend) for 30 minutes on ice in the dark. The cells were then washed, resuspended in 500 µl of cell staining buffer (BioLegend), and stored on ice until they were analyzed at The University of Texas M.D. Anderson Cancer Center (MDACC) flow cytometry core for the immunofluorescence intensity of HER2 expression levels. In order to determine the mean immunofluorescence intensity for each cell line, we used a commercially available kit including PE Anti-Human CD340 (erbB2/HER-2) Antibody, cell staining buffer, and a PE Mouse IgG1 Isotype Control (BioLegend) for background signal correction. The immunofluorescence intensity was converted into antigen binding capacity using the Quantum Simply Cellular anti-Mouse IgG kit

(Bangs Laboratories, Inc.). This kit utilizes four different samples of microbeads with a predetermined number of antigen binding sites which correlates with respective immunofluorescence intensity. A linear scale is then generated and used for the interpretation of antigen binding sites on cell samples of known intensity.

Nanoshells were fabricated using previous published procedures. Briefly, silica cores were generated using the Stöber method and surfaces were terminated with amine groups. The final silica particles were measured by scanning electron microscopy (SEM) to obtain the average diameter of 276 nm. Gold colloid of 1-3 nm in diameter was then prepared and adsorbed onto the silica cores through the amine groups (nanoshell 'seeds'). The gold shell overlay was completed by mixing the nanoshell seeds with additional gold solution, potassium carbonate and formaldehyde. A UV-vis spectrophotometer (Varian Cary 300) was used to analyze the spectrum of the completed nanoshells. Mie Theory was then used to derive the absorption, scattering, and extinction coefficients and, subsequently, the concentration of nanoshells in solution. As confirmed by SEM, the nanoshells had an average diameter of 350 nm, a peak surface plasmon resonance at 840 nm and a concentration of approximately $2.3\times10^9$ particles/mL.

To create molecularly-targeted particles, the nanoshell surfaces were first modified by the addition of either specific or non-specific antibodies (anti-HER2/neu or anti-IgG, respectively) as previously described by Loo et al. A custom made heterobifunctionalized polyethylene glycol linker, orthopyridyl-disulfide-PEG-N-hydroxysuccinimide ester (OPSS-PEG-NHS, MW = 2kD, CreativeBiochem Laboratories), was incubated with either anti-HER2 antibodies (C-erbB-2/HER-2/*neu* Ab-4, Lab Vision Corporation) or anti-rabbit-IgG (Sigma Aldrich) at a molar ratio of 3:1 in sodium bicarbonate (100 mM, pH 8.5) overnight on ice and under refrigeration. All aliquots were then stored at -80ºC. The linker permits conjugation to the antibodies via amide linkages (NHS) and conjugation to the nanoshell gold surfaces via sulfur groups (OPSS).

In order to perform biological studies, the nanoshells ($2.3\times10^9$ particles/mL) were incubated with the prepared anti-HER2-linker or anti-IgG-liker solution for 1 hour under refrigeration and further stabilized by incubation with a 10 mM polyethylene glycol-thiol solution (PEG-SH, MW = 5kD, Nektar) overnight under refrigeration. Nanoshells were then centrifuged to remove unbound antibodies and resuspended in water. Prior to experimental studies, the nanoshells were brought to room temperature and a solution of bovine serum albumin (BSA) and phosphate-buffered saline (PBS) was added at a final concentration of 1% each. Samples were vortexed briefly before use.

Approximately $6\text{x}10^5$ cells of each cell line (MCF10A, SK-BR-3, HCC1419, and JIMT-1) were isolated, washed and incubated with a 2 ml solution of either PBS alone, anti-HER2 targeted nanoshells ($2\text{x}10^9$ particles), or anti-IgG targeted nanoshells ($2\text{x}10^9$ particles). The nanoshell-cell suspensions and controls were then incubated in a hybridization chamber (VWR International) at 37ºC and 7 rpm for 15 minutes. After incubation, the suspensions were centrifuged and rinsed two times with PBS to remove unbound nanoshells. The cell pellets were resuspended in 60 μL of the appropriate cell media. This solution was then aliquoted onto a glass slide fitted with a 0.12 mm deep spacer (Invitrogen) and then coverslipped. Images of the different cell types were obtained with a Lucid VivaScope 2500 inverted confocal microscope, which employs an incident wavelength of 830 nm. The Lucid VivaScope 2500 is a portable, FDA approved system used to assess freshly excised tissue in clinics. Images were taken at the same distance from the glass surface for each condition and at a power of 1.4 mW.

The optical intensity of the reflectance of the cells was measured using ImageJ processing software. An image of pure black was designated with a value of 0 and that of pure white with a value of 255. Average intensity values for each cell line under each condition were calculated from 7 independent areas of the respective glass slide used for imaging. Images used for this component of the study contained areas where no cells were present; therefore, although the intensity of individual cells incubated with HER2-targeted nanoshells approach 255 (data not shown), this was not possible for widespread images due to the diluted sample allowing certain areas to be void of cells. Sample normality was assessed to evaluate the error distribution for all data points. A normal probability plot of the residuals verified that the samples followed a normal distribution (data not shown). F-tests were also used to determine the equality of variance before applying two-tailed paired Student's t-tests to evaluate significance in the difference in reflectance intensity of cells between two treatment conditions.

The goal of this study was to determine if gold nanoshells conjugated to anti-HER2 antibodies could optically enhance the identification of breast cancer cells that overexpress HER2 receptors. Therefore, three breast cancer cell lines (HCC1419, SK-BR-3, and JIMT-1) that are known to overexpress HER2 and a normal mammary epithelial cell line (MCF10A) were chosen to optimize the binding conditions and evaluate specificity of targeted nanoshells. Using flow cytometry, the calculated number of HER2-antigen binding sites, along with the 95% confidence interval for each cell line, was determined. Specifically, the breast cancer cell lines were found to have significantly higher (17 to 77 times more) binding sites than the normal breast epithelial cells (MCF10A).

The capacity of the nanoshells to optically image the breast cancer cell lines were then visualized using a Lucid VivoScope reflectance confocal microscope, a portable reflectance imaging system that is currently used in clinics. Since the nanoshells are made with a gold shell and have an optical peak resonance at 840 nm, the cells that are bound with the nanoshells clearly reflected more light using reflective confocal microscopy than the cells that are not bound to nanoshells. Qualitatively, the reflective confocal microscopy images in Figure 11 demonstrate that the nanoshells conjugated to anti-HER2 antibody bound the most to the three breast cancer cell lines. Most of the cell surface could be visualized. The labeling of the cancer cells was very specific against the HER2 receptor since the nanoshells conjugated with non-specific IgG resulted in only punctate labeling of the same cells. Similarly, only punctate labeling of MCF10A normal epithelial cells was imaged by the nanoshells conjugated with anti-HER2 antibody. This low level of reflectance is likely due the presence of the low level of HER2 receptors present on MCF10A cells.

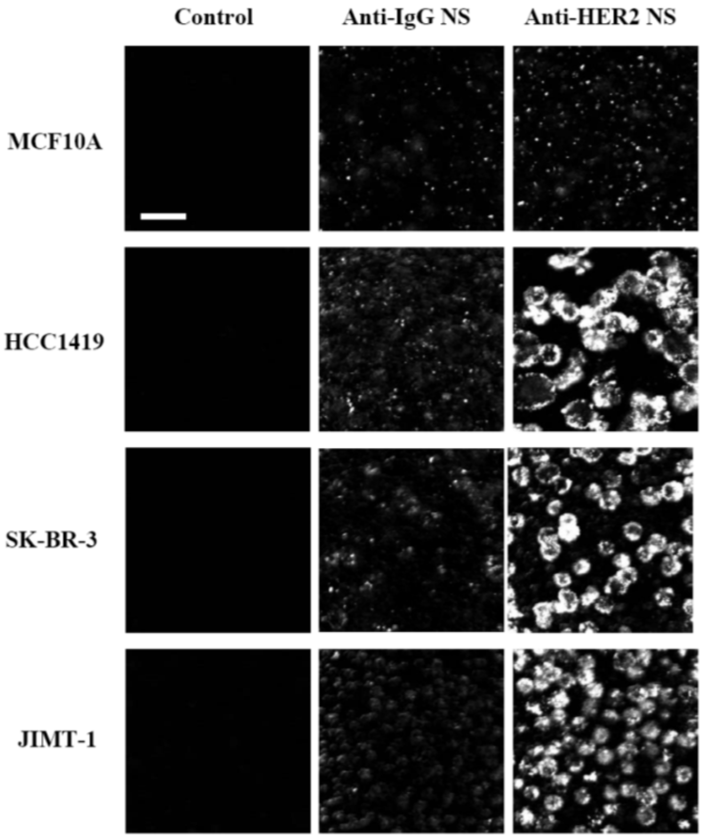

**Figure 2.11.** The right hand column shows NIR reflectance confocal imaging using targeted gold nanoparticles. Of particular interest are the 2nd and 4th rows here. These cells are herceptin resistant yet clearly we still able to achieve strong targeting. This is intriguing because these same gold nanoparticles can be used for direct photothermal ablation of cells suggesting a novel approach to treatment of HER2+, Herceptin resistant women.

Quantitatively (Figure 2.12), the reflectance intensity from each breast cancer cell line with HER2 overexpression that was treated with nanoshells conjugated with anti-HER2 antibody was 5 times higher than the reflectance from normal human breast epithelial cells (MCF10A) treated with the same nanoshells ($P<0.001$). For each cell line, the binding of nanoshells appeared to be dependent upon the anti-HER2 antibody because the reflectance intensity of the cells was 3 to 5 fold higher when the cells were treated with nanoshells conjugated to anti-HER2 antibody than to non-specific IgG ($P<0.001$). There was no difference in reflectance intensity between any cell type incubated with only PBS (the control condition) ($P>0.1$) or with IgG-targeted nanoshells ($P>0.1$).

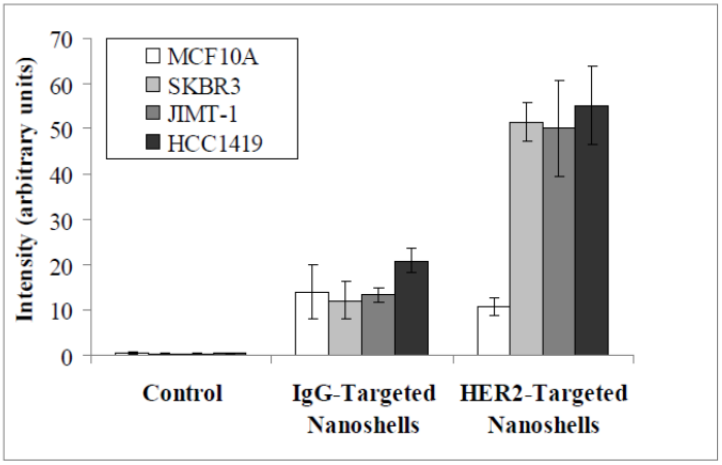

**Figure 2.12.** Quantification of imaging results.

The results obtained with RCM provide a first step towards developing these particles for the types of imaging applications we anticipate; the critical results will be those we obtain using the imaging system under construction in Project 1. We are also collaborating to investigate highly exploratory new techniques (photothermal imaging) which would dramatically increase the optical contrast achievable with gold nanoparticle based imaging agents so that the optical imaging performed will be sensitive to much lower levels of expression than what is needed using conventional approaches. A paper (Hleb et al, 2008) provides details on this work.

***Summary to Date:*** *Project 2 remains ahead of schedule. As proposed, the first two years were a basic science chemistry directed effort to create synthesis and bioconjugation strategies for the biological experiments proposed in the latter years of the projects. We have initiated imaging studies and look forward to integrating the agents being developed in this project with the imaging system developed in Project 1. We expect to submit a revised SOW request and appropriate regulatory paperwork to enable an accelerated and more ambitious set of imaging experiments to be performed. An unexpected result which may open up new avenues of work was the high level of nanoparticle targeting we were able to achieve using herceptin resistant cell lines including a line where we would have anticipated MUC interference. Because our nanoparticles inherently have both imaging and therapeutic (photothermal ablation) properties, these results suggest a possible new approach to treatment of HER2+, herceptin resistant women. Depending how the rest of the project evolves, we may in the future request a SOW modification to pursue this possibility.*

### Nanoparticle Probes to Monitor Radiation Dose (Project 3)

Project 3 is the smallest and most risk effort of the project we originally proposed. The idea underlying this project is to develop an optical approach for monitoring radiation which would provide more information than the bulk dose measurements which can be achieved today. Our MDACC coPI is a radiation oncologist by training and proposed this idea. Our work to date has been focused on the very first step towards this approach: Can we use nanoparticles to generate a change in optical signal with radiation dose? Last year we presented data demonstrating that indeed we could employ a plasmonic nanoparticle-based approach to accomplish this idea (Task 1 of Project 3). Essentially, we monitor the perturbation in optical nanoparticle as nanoparticles are released from an area after exposure to radiation. We found we could do this at a radiation dose of 100 Gy, At this point, we had a choice to make. We could move on to Task 2 which provides a more desirable signal change to measure (Our strategy in Task 1 measures *loss* of optical signal after exposure to radiation while our strategy in Task 2 measures *gain* in signal after radiation. Signal-to-background issues are already much easier to handle if we start with a probe that is dark in its original configuration. However, if we moved to Task 2 directly we would be working at radiation levels we know are not consistent with what would make this a clinically viable technique for breast cancer. (The radiation doses we are seeking to measure clinically are far lower.). Thus, it is important to examine whether it is possible to bring down sensitivity levels further. The experiment shown in Figure 13 is at a dose 50% lower than the 100 Gy data included in last year's report. For this experiment, gold colloid is prepared by using the standard sodium citrate reduction method discussed previously. Chloroauric acid solution is added to deionized water and the solution is brought to boiling temperature upon stirring. Subsequently, trisodium citrate solution is added. The size of gold can be controlled based on the amount of trisodium citrate. Based on our radiation experiments to date, 50 Gy is the lowest radiation dose for which we can potentially detect the loss of signal we are looking for as an assay (Figure 2.12). Because it has been hard to make definitive quantitative statements regarding signal loss, we are exploring the use of AFM to help us in this aspect of the work.

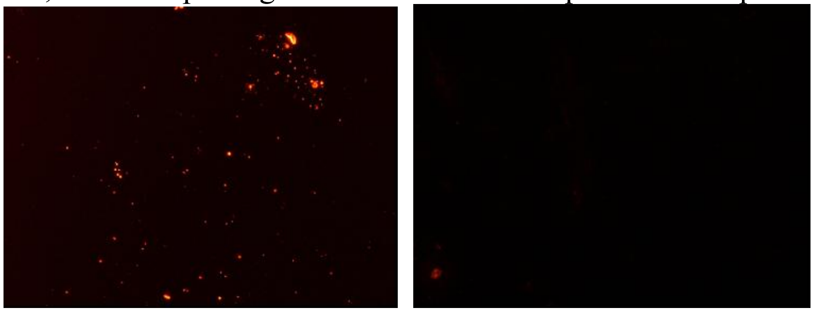

**BEFORE RADIATION AFTER 50 Gy RADIATION**

**Figure 2.13.** Gold nanoparticles (13 nm) after radiation treatment. We are seeking some level of loss of the bright spots shown in the image on the left (before treatment) after radiation. The radiation dose in these images is 50 Gy.

***Summary to Date:*** *This project is the smallest and most high risk component of our proposal. Work to date on Project 3 has indicated that idea proposed (generating an optical signal which could be measured in response to radiation dose) is fundamentally sound. However, further improvements in sensitivity are required for optical monitoring of radiation dose to become a clinically viable approach.*

## ***<u>Year 3</u>***

### Project 1: Development of a Needle-Compatible Fiber Optic System for Breast Imaging

#### ***Reflectance Mode Imaging*** (Project 1: Task 1 and Task 2)

Prior year progress reports describe the motivation behind Project 1in detail. Briefly, we believe there is significant clinical motivation for considering the use of new types of optical imaging for breast cancer detection and treatment monitoring but that the limited penetration of light into breast tissue has impeded development of some of these applications. While many studies have been conducted using ex vivo breast tissue to demonstrate the promise of emerging optical techniques, there has been very limited work in vivo translation of these methods largely because the limited light penetration makes these studies difficult. The largest project underway in our Era of Hope award has been aimed at overcoming this significant translational hurdle to the use of optical technologies in breast cancer applications. We believe that rather than be limited to applications where we bring the tissue to the light (by removing the tissue from the body), it is important we bring the light to the tissue (by developing very small diameter microendoscopes inserted through needles of the size used for fine needle aspiration or smaller). Additionally, we are focused on technologies that can provide direct high resolution images. While spectral information alone has already been shown to be of high diagnostic value, there is a need for modalities which can directly image tissue at high resolution as well. A large focus of our efforts over the past several years has been on refining our designs so the microendoscopes we develop can fit through the smallest needles possible while providing the best resolution and field of view. Although we describe these probes as "needle compatible" they do not need to be used through needle insertion in all applications (for instance, our tumor margin project is based on surface imaging).

The latest improvement to the reflectance-mode needle-compatible optical biopsy (NCOB) system has benefited from lessons learned during the development of the multimodal optical imaging (MOI) system (Project 2) for macro-scale breast imaging. As opposed to the original design created in Year 1 (Figure 3.1) and the ring based design proposed in Year 2, our current design merges the illumination and detection optical pathways (Figure 3.2) using a a simple and cheap polarizing beam splitter (PBS). The result is a probe that still has similar size to fine-needle aspiration biopsy needles. However, the signal strength and field of view (FOV) have been substantially increased. Just as importantly, these improvements have come with minimal increases in system cost and complexity. The current design of the system permits a reflectance mode imaging setup to be combined with fluorescence mode imaging setup (Project 1, Tasks 3 and 4), if desired, in a simple and straightforward manner. The two modes can then be used independently or in combination to take advantage of the potentially different information available in the images for breast cancer diagnosis and screening.

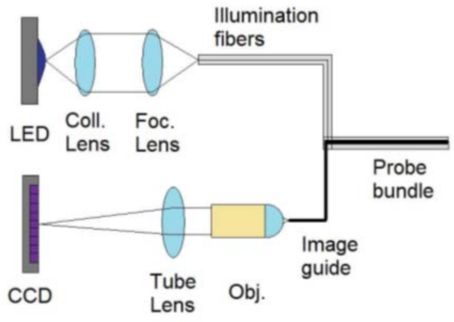

**Figure 3.1.** The original optical design proposed. Note the separate use of illumination fibers for light delivery and an image guide for light collection. While this design worked, the outer diameter of the probe was not practical for clinical applications.

### *Improvements in Design over Prior Years*

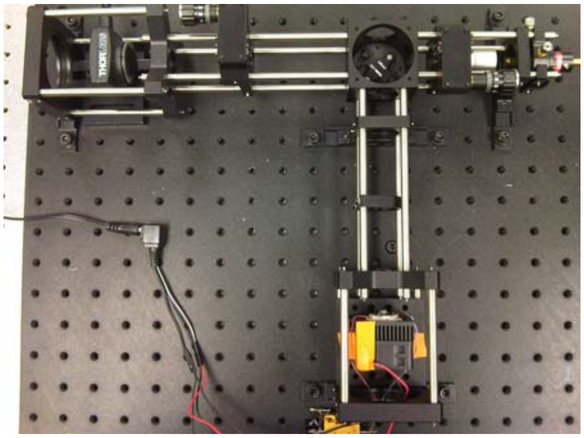

**Figure 3.2.** Photograph of the newest reflectance mode NCOB system using a polarizing beam splitter to combine the illumination and detection optical pathways at the image guide.

The key component of the NCOB system is the fiber image probe that must balance size, FOV size, signal strength, and signal-to-noise (S/N) ratio with additional considerations for cost and system complexity. One major previous obstacle was specular reflection from various optical-air interfaces in the system that overwhelmed the sample signal if one optical pathway was used for illumination and detection. However, separate illumination and detection optical pathways using separate coaxial optical fibers increased the size of the probe while reducing FOV and signal strength. Based on knowledge we acquired while building the MOI system (Project 2), the polarization of light has been used to solve the combined optical pathway problem. While in the MOI system the polarization of light is used to probe varying depths of tissue, in the NCOB system it is used to optically separate the illumination and detection optical pathways. This significantly reduces the design restrictions on the fiber probe itself. *It is important to point out that a reflectance-based single fiber needle compatible microendoscope of this type we have built in this project has never been developed before. A paper currently in press in Journal of Biomedical Optics (Sun et al, 2010) describes the design, and Rice University has filed a provisional patent on this idea.*

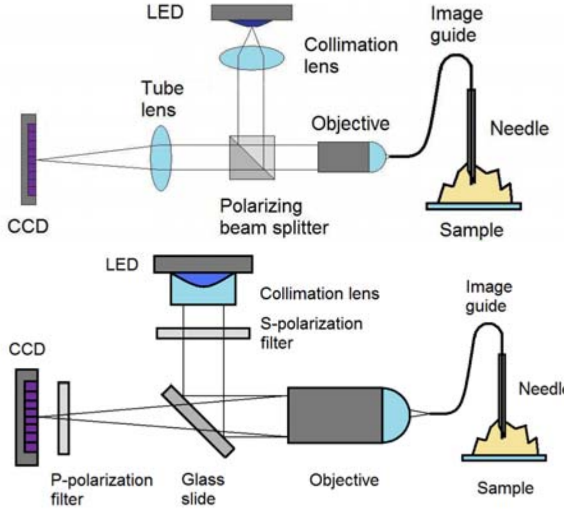

**Figure 3.3.** NCOB systems using a PBS (top) and two polarization filters and a glass slide (bottom). The PBS is more efficient at separating polarized light. The polarization filter setup is easy to customize.

The primary sources of specular reflection in the NCOB system are the air-glass interfaces of the lenses, the objective, and the image guide. Because light from specular reflection keeps its polarization, it can be separated from light scattered by the sample using a PBS or polarization filters. However, much of the light reflected by the sample also keeps its polarization and would be blocked from detector. By intentionally using a non-polarization maintaining image guide, we were able to alter the light reaching the sample so that it is no longer the same polarization as the specular reflection from sources before the image guide. This greatly increases the amount of signal that can be captured from the sample. On the other hand, there is still one more source of specular reflection from the fiber-air interface at the distal tip of the image guide probe, which is made worse by the polarization change in the image guide. This specular reflection is mitigated because the probe tip is in contact with tissue. Tissue serves as an index matching substance to reduce the specular reflection. In this way, specular reflection from all sources up to the proximal tip of the image guide probe is significantly reduced while the light scattered by the sample is attenuated much less. Furthermore, this setup is simple and cheap, requiring only an additional PBS or two polarization filters and a beamsplitter (Figure 3) to allow a single illumination-detection optical pathway in the probe.

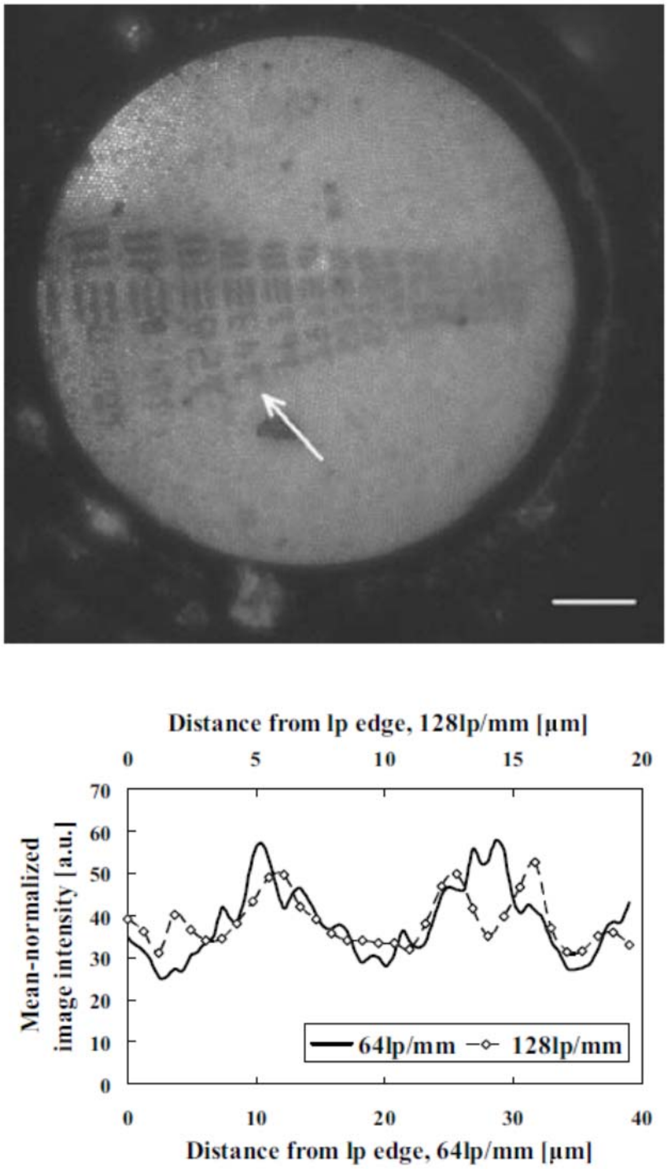

**Figure 3.4.** Demonstration of resolution obtainable using the system developed in Year 3. Note the high (several micron) resolution obtainable demonstrated by the ability to resolve the 128, 143, and 161 line pairs per inch shown in the resolution chart shown above.

### *Improvement in Performance*

Since the image guide probe was designed for simplicity and incorporates no additional optics, the probe must be in contact with the sample surface for the image to be in focus. When using separate illumination and detection fibers as we did in our prior version, the signal from the sample relies on diffusely scattered light through the sample. The signal strength is so low that it makes imaging inside bulk tissue difficult. Using our earlier probes we were able to issue visualize fatty tissue within breast, the easiest imaging target and to image suspensions of breast cancer cells but we could not image suspicious areas we were most interested in. Using the new polarization-based reflectance imaging system, the detection fibers are also the illumination fibers, and the areas of illumination are imaged directly. *As can be seen from the figures in Task 5 results, we are beginning to be able to directly image intact tissue with no sectioning, no staining, or other preparation.* This allows the system to function under the conditions for which it was originally intended, in vitro tissue imaging without sample preparation and in vivo tissue imaging without excision. In addition to the improvement in signal strength, use of the same image guide for both illumination and detection has also reduced the required probe needle size. The needle size can be selected to suit situations where a larger FOV or a smaller needle is desired. We are currently using a 20-gauge needle probe with 333 um diameter FOV. In the current design, we simply reduce FOV if we would like to use a smaller needle for a particular application. Figure 4 demonstrates the resolution obtainable with the new system dramatically improved over previous performance.

## Fluorescent-Based Needle Compatible Single Fiber Microendoscope (Project 1: Task 3 and Task 4)

To be able to consider both reflectance (scatter) and fluorescence based origins of image contrast, we have designed and constructed a complementary fluorescence based needle microscope endoscope. The design of this system is shown in Figure 5. The fiber microscope is assembled on a portable 18 × 24 × 1/2 inch$^3$ aluminum breadboard. An air-cooled royal blue batwing LED (Luxeon, model LXHL-NRR8) is selected as the illumination source. Illumination light emitted from the LED is collimated by an integrated collimation lens and reflected by a ~45°-positioned glass plate to project onto an infinitely corrected 10× objective lens (Newport, model: L-10x, 0.25NA). A multimode fiber coupler/positioner (Newport, model: F-915T) is utilized to mount the objective lens and a fiber chuck (Newport, model: FPH-DJ). With careful alignment, illumination light is focused into the incident end of a 450µm-outer-diameter fiber image guide (Sumitomo Electric, model: IGN-037/10) which is coupled by the fiber chuck. Finally, the imaging end of the image guide is inserted into the core of a 20-gauge needle and placed in contact with the samples. Light emitted by imaging samples is collected by the same illumination

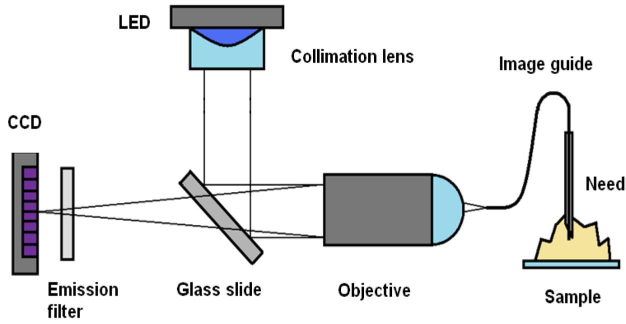

**Figure 3.5.** Schematic of the needle-compatible fluorescent fiber imaging system.

fiber and passed through the same objective lens and the glass plate as mentioned previously. A CCD color camera (Edmund Optics, model: EO-0813C) coupled with an emission filter (~540nm long-pass) is used for image acquisition. Clear fluorescent images collected from the imaging end can be obtained.

### Potential Future Design Integrating Reflectance and Fluorescence Based Detection

Fluorescence and reflectance based imaging are complementary in many ways. Reflectance-based imaging (without the use of any added contrast agent) provides information on tissue architecture and cell morphology while fluorescence based imaging generally provides information on biochemistry. Molecular imaging agents may provide either type of optical signal. It is possible to integrate the two sets of designs described above into a single system. Figure 3.6 shows a diagram for a system of this sort. This is not a system we have built but is a system we would consider in the future if we obtain imaging results suggesting we want simultaneous fluorescence and reflectance images to enhance sensitivity and specificity. If only one type of image is needed, it is more straightforward to use the design shown in Figure 3 or Figure 5 for either reflectance or fluorescence, respectively. Here, we illustrate it is possible to integrate these into a single system if needed.

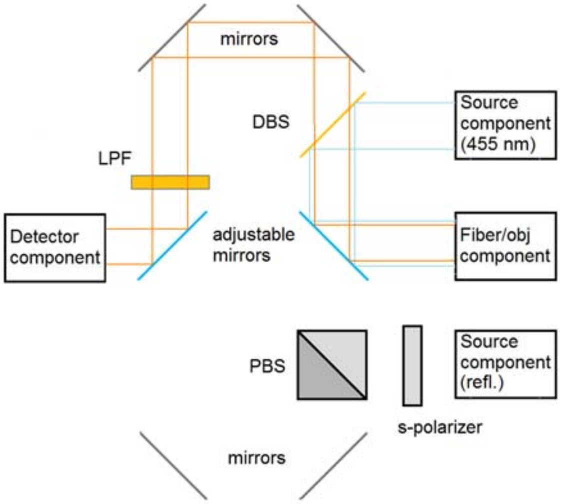

**Figure 3.6.** Preliminary design of the combined reflectance and fluorescence mode NCOB system.

### Evaluation of Needle Compatible Systems (Project 1: Task 5)

#### *Reflectance Based System*

We are in the process of evaluating system performance for imaging both cells and tissue. We first tested whether our system had sufficient resolving power and contrast to visualize individual cells (no dyes or other imaging agents of any kind.) As shown in Figure 3.7, this is possible with the current design.

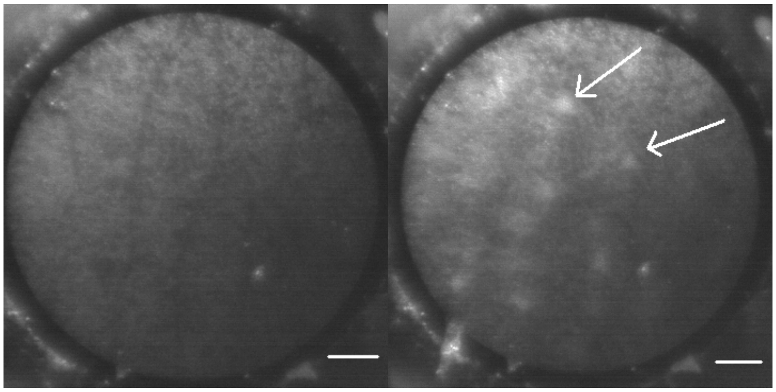

**Figure 3.9**. Cells before the application of acetic acid (left) and after the application (right). Less than 1 min elapsed between the images. The scale bars are 50 um.

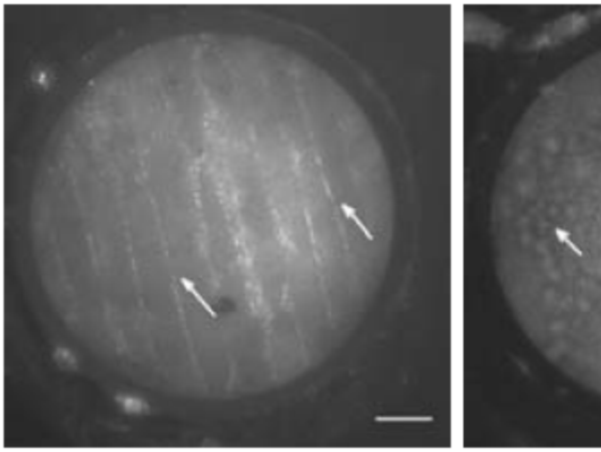

**Figure 3.7.** The microendoscope has sufficient resolving power to visualized individual cells. Left: onion cells imaged as an initial test. Right: Breast carcinoma cells.

We have also evaluated the ability of the system to image intact excised human tissue (Figure 3.8). It is critical to recognize that unlike standard histology where tissue is being removed, fixed, sectioned, stained, and then imaged days later, we are showing direct imaging of intact tissue without the use of any imaging agents. By performing only simple image processing, we are able to visualize both cell membranes (dark circular shapes) and what we believe are cell nuclei (bright dots inside dark circular shapes). The use of this tissue reveals the ability to image the cell membrane and cell nuclei, the most important structural features we want to extract for cancer screening, in tissue samples where much of the tissue morphology remains intact.

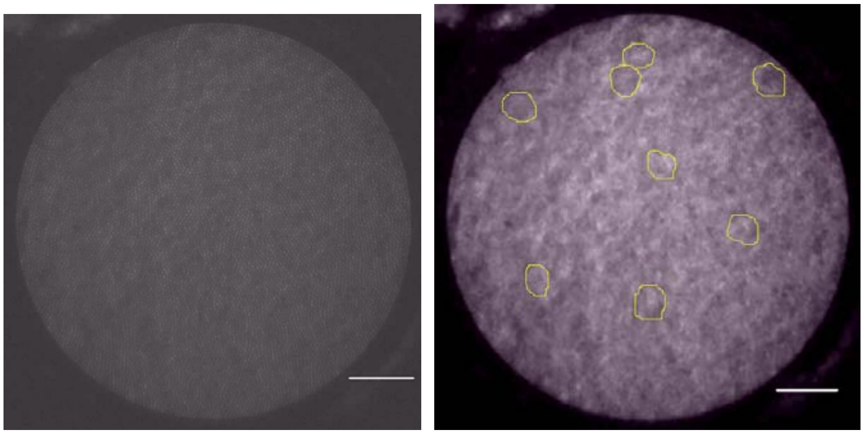

**Figure 3.8**. Human cancer tissue imaged by the NCOB system in filter setup (left). Simple image processing (right) allows the cell membranes and what we believe to be cell nuclei to stand out (right; cells marked with yellow outline). The cell membranes appear dark while the cell nuclei appear bright. The scale bars are 50 um.

In addition to the more sophisticated nanoparticle based imaging agents being considered in Project 3, we have also been exploring the use of simple contrast agents already in routine clinical use to enhance imaging capabilities. One of the first experiments we performed was the application of acetic acid to test what extent it would aid in making cell nuclei easier to visualize. Acetic acid (vinegar) is already widely used in colposcopy for cervical cancer to help establish suspicious areas by acetowhitening and is now used in dentists' offices as well with some commerical oral cancer screening devices. As can be seen in the images of cells in Figure 9, the application of acetic acid can dramatically improve nuclear visibility in cells in under a minute.

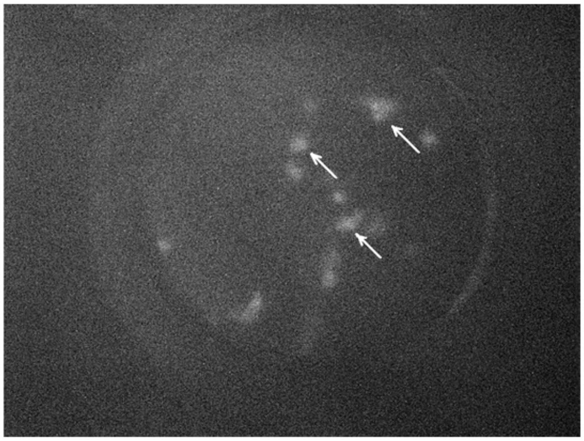

**Figure 3.10.** Endoscopic florescent image of cells incubated with 2-NBDG fluorescent dye obtained using the developed fluorescent fiber microscope, where the arrows indicate resolved single cells

### *Fluorescence Based System*

An initial test of the developed fluorescence-based fiber microscope was conducted using cultured SKBR3 human breast carcinoma cells incubated with 2-[N-(7-nitrobenz-2-oxa-1,3-diazol-4-yl)amino]-2-deoxy-d-glucose (2-NBDG). 2-NBDG is a fluorescent glucose analogue which accumulates preferentially in malignant cells. In this test study, the fiber bundle tip was immersed into PBS through a needle and focused onto a group of cells attached to the culture plate. As shown in Figure 10, cells incubated with 2-NBDG can be visualized with the florescent mode fiber microscope.

### Ongoing and Future Work Underway in Project 1, Task 5

Currently two sets of experiments using the NCOB systems are being conducted in parallel. In one, imaging without any external contrast agents is being performed on breast cancer tissue samples. The goal of these images studies is two-fold. The first is the conclusive determination of cell membranes and cell nuclei in the images (and videos). This involves both a human observer and automated processing algorithms being able to extra these features. While we have been successful in developing algorithms which allow extraction of the boundaries of some cells, it is more important than we be able to accurately estimate nuclear size. We cannot do this yet. These will require more complex image processing and possibly more optical improvements to the system. The other set of experiments involves the testing of simple contrast agents to enhance the information content of the images.

## Project 2: Development of a Macroscopic Fluorescence/Reflectance Multi-Modal Optical Imaging (MOI) System (Task 1 and Task 2)

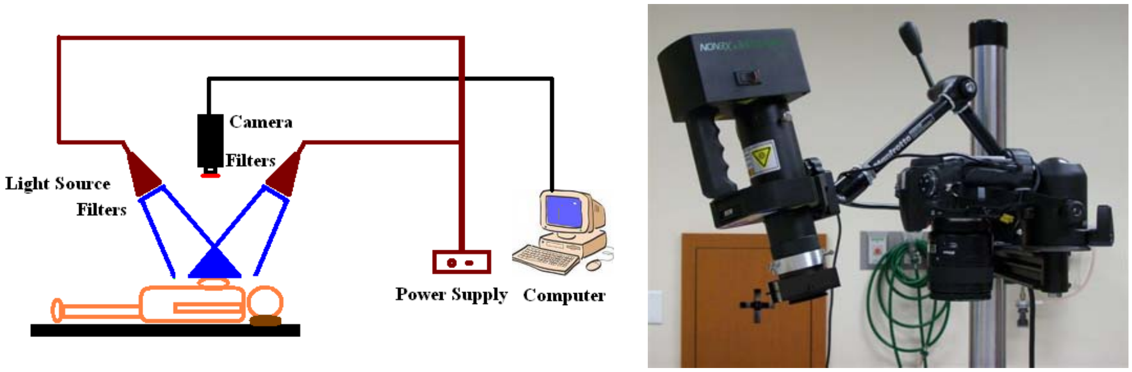

**Figure 3.11.** Multimodal optical imaging (MOI) system. Schematic (left) and constructed system (right).

Multimodal optical imaging (MOI) technology can macroscopically screen large areas of tissue to identify cancerous changes and rapidly record this optical information without the need for biopsy. Therefore, MOI technology has the potential to objectively identify and document disease related changes and aid in diagnosis or guide treatment. A multimodal optical imaging system has been designed and constructed for real-time clinical applications. Briefly, the MOI system is composed of a filtered Xenon light source (Horiba Jobin Yvon Inc., Edison, NJ) and a filtered digital CCD camera (D300, Nikon) with a selected Nikon lens (AF Micro-Nikkor, 60mm, f/2.8D) (Figure 3.11). With specific filter combinations, the MOI system provides various imaging modes, including white light imaging, polarized reflectance imaging, and fluorescence imaging. Both the light source and the camera are mounted on the same wheeled-stand to provide a fixed configuration of equipment with respect to the tissue sample or patient. This will allow easy maneuvering of the equipment in future clinical trials. In the Era of Hope project, the MOI will be used for evaluating tumor margin applications using tissue samples from CHTN.

## Project 3: Development of Novel Targeted Imaging Beacons for Breast Imaging Applications (Task 3)

Tasks 1 and 2 of Project 3 were scheduled for and completed during Years 1 and 2 of the project. A paper published on Task 1 was included in last year's project report. The working version of a paper on Task 2 was included in last year's report, and the final published *Nanotechnology* paper is included in this year's report. During Year 3, we have focused on Task 3 which is the assessment of our most promising imaging agents. We have tentatively determined not to continue assessment of the cadmium free quantum dots because we have received strong statements at both of the past two LINKS meetings that patients would be wary of clinical use of these agents even if regulatory issues were satisfactorily resolved. We had originally anticipated that by avoiding the use of cadmium, we would be able to address safety concerns. Instead, we are focusing more strongly on gold based materials.

A variety of gold imaging agents are being evaluated in this project. All of these materials are quite different than the ~115-130 nm nanoshells with dual scattering/absorption properties whose initial development was funded by a separate DoD project which ended a few years ago (PI: Halas, Innovator Award). In last year's report, we included a new method for conjugation of antibodies to AuNPs, in particular gold nanorods. We included an image demonstrating imaging of targeted gold nanorods using two photon microscopy. Although these nanoparticles may be imaged in this way, doing so requires the use of a $100K laser and is not practical for the type of clinical applications we are interested in using the instruments being developed in Project 1 and 2. A challenge with the use of nanorods is whether sufficient signal exists for scatter based applications. There is not a single answer to this question as the answer depends on the imaging system being used and the number of nanorods per targeted cell or tissue volume. Working in collaboration with two other groups at Rice University (the West lab and the Hafner lab), we have found that nanorods generally do not have sufficient contrast for the specific applications we are interested in pursuing through this Era of Hope project. This is illustrated in the darkfield images in Figure 12 of HER2+ breast carcinoma cells after incubation with either targeted or non-specific nanorods. Note that there is no clear difference between control and experimental images when visualized using darkfield microscopy while the targeting is clearly apparent when looking at the same sets of cells under two photon microscopy. Our darkfield microscope is able to collect much more scattered light than our small diameter microendoscopes. If we cannot visualize the nanorods under darkfield illumination, we will not be able to see them with our Project 1 system. For this reason, we are focusing on larger gold nanoparticles (AuNPs) designed to preferentially scatter light. We believe these nanoparticles will be the most appropriate choice for our tumor margin applications. It should be noted, however, that for applications based on systemic delivery, as opposed to the topical applications we are using for tumor margins, these AuNP would almost certainly be too large to be effectively delivered.

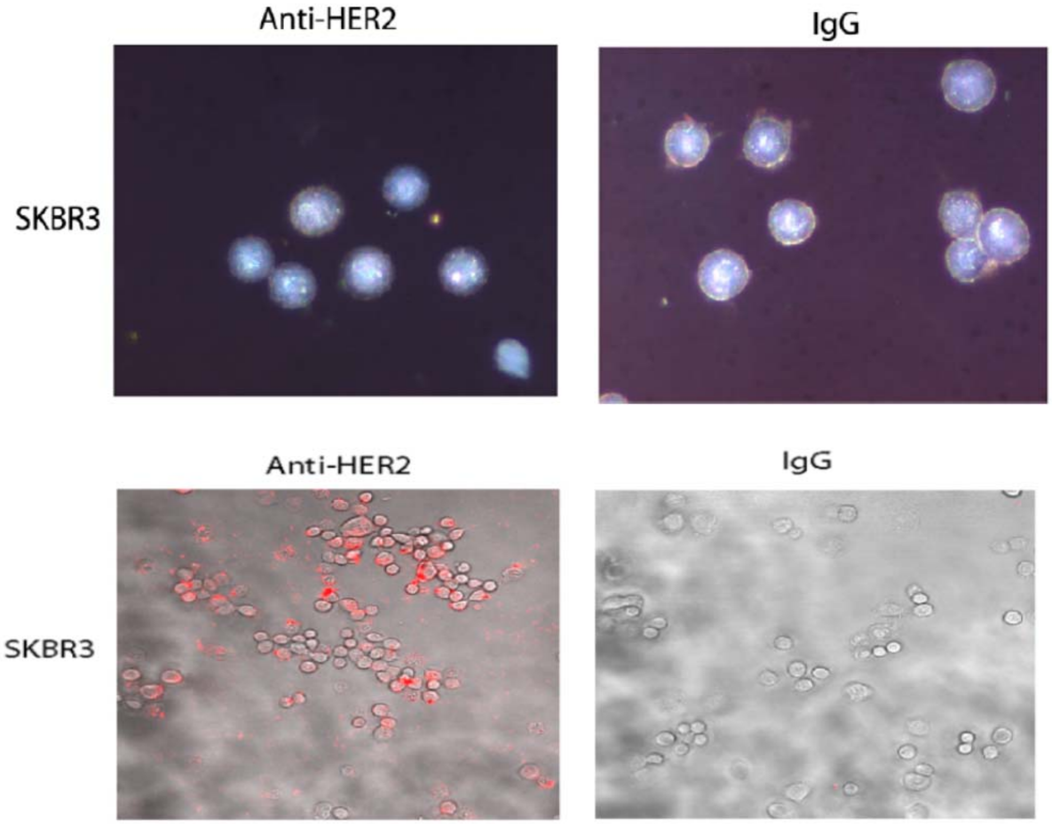

**Figure 3.12.** Top row: AntiHER2 (left) and non-specific (right) gold nanorods for imaging HER2+ cells using darkfield (scatter sensitive microscopy). Differences are not apparent comparing these images even though targeting is present. Targeting can be confirmed using a different form of imaging, two photon luminescence, shown in the bottom row (data from last year). In this image, it is clear that gold nanorods are targeting the cells as desired. They do not have strong enough optical signal to be visualized via darkfield.

As the size of the AuNP is increased, the optical scatter signal rises and it becomes much easier to use the materials as targeted contrast agents. The images below show the same SKBR3 cells, but now using larger targeted AuNPs.

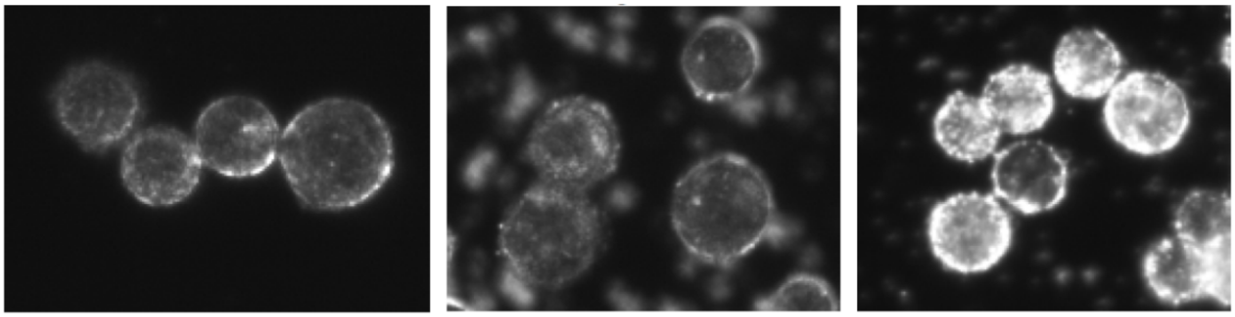

**Figure 3.13.** Left: Cells alone. Middle: Cells after incubation with AuNPs non-specifically targeted (IgG). Right: Cells after incubations with antiHER2 AuNPs.

After determining what size AuNPs provide the necessary signal for imaging, we have begun assessing the use of these immunotargeted AuNPs for tissue level molecular imaging applications initially by evaluating the enhanced optical signatures of *ex vivo* breast cancer tissue sections incubated with the nanoparticles. For these studies, we used normal breast tissue, HER2-negative cancerous tissue, and HER2-positive cancerous tissue specimens received flash frozen from the Cooperative Human Tissue Network (CHTN). Rice IRB and DoD approval was received for the use of this tissue. Specimens were thawed prior to being embedded in frozen section media. Sections were taken of all specimens at 20 microns and subsequently incubated with surface-modified AuNPs conjugated to anti-HER2 antibodies. Sequential sections were taken of all specimens at 5 microns (for standard histological processing). As shown in Figure 3.14 qualitative assessment of the imaging of normal (left column) and cancerous HER2- (middle column) tissue sections incubated with HER2-targeted AuNPs (Row B) showed little enhanced scattering. However the cancerous HER2+ tissue (right column) showed dramatically enhanced contrast after only 5 minutes of incubation with HER2-targeted AuNPs. Additional brightfield images (Row C) of the same tissue specimens validated the distribution of the AuNPs with respect to the tissue surfaces. The location and arrangement of the HER2-targeted NPs corresponded to the results obtained by performing immunohistochemistry (IHC) against HER2 (Row D). In order to demonstrate characteristic morphologic variations associated with normal and cancerous tissue, H&E stained sections (Row E) have also been included.

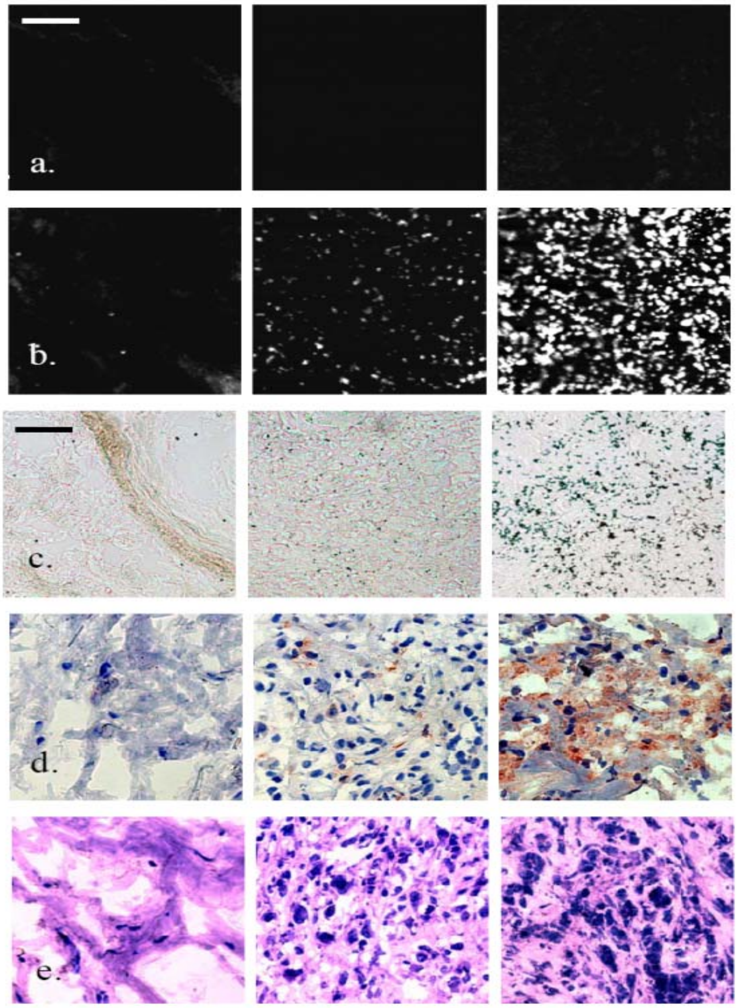

**Figure 3.14.** (a.) Reflectance (scatter based) images of normal (left), HER2- cancerous (middle), and HER2+ (right) cancerous human tissue samples incubated with HER2-targeted AuNPs for 5 minutes. (b.) Respective images from (a.) taken under brightfield microscopy under 20x magnification. Respective (c.) HER2/neu immunohistochemistry and (d.) H&E results taken under brightfield under 20x magnification. Power for (a.) at 0.4 mW. All scale bars represent 50 µm.

In order to translate these findings further into a more immediate diagnostic result in the operating room, studies are currently underway to examine the ability to enhance contrast in resected human tissue without physical sectioning. Both HER2+ cancerous tissue and HER2- cancerous tissue specimens were supplied by the CHTN and thawed prior to their use. A 5 mm (diameter) punch biopsy was used to extract samples of each tissue type in order to maintain size consistency. Sample thickness ranged from 1-2 mm. After incubation with either buffer or HER2-targeted AuNPs for 5 minutes at 37°C, samples were rinsed three times in 1xPBS and imaged without sectioning. As seen in Figure 15, reflectance intensity is greatest when HER2-overexpressing tissue is incubated with HER2-targeted AuNPs (upper right image). In contrast, only low to no levels of reflectance are evident in the buffer-only condition (upper left image) or for the negative control (lower row). These images provide preliminary evidence we should be able to use our reflectance based fiber bundle microscope (Project 1) in the manner we intend scanning around the margin regions looking for white spots indicative of areas of high HER2 (or other targeted markers in the future.)

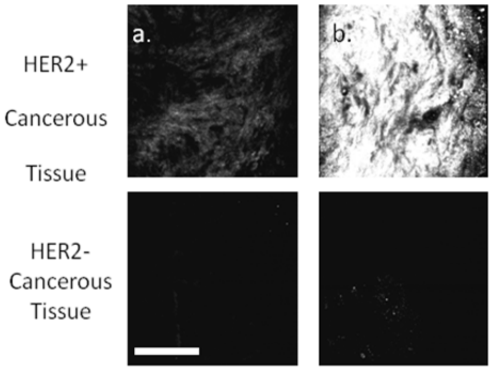

**Figure 3.15.** Preliminary results. Scatter-based images of HER2+ cancerous and HER2- cancerous human tissue samples incubated with (a.) buffer or (b.) HER2-targeted AuNPs for 5 minutes. Power at 0.4 mW. Scale bar = 0.13 mm.

In addition to using scatter based imaging for microscopic visualization of AuNP targeting and HER2-overexpression, we are also exploring the use of reflectance-based imaging for macroscopic evaluation of the same tissue. The macroscopic evaluation would visualize the entire tissue region at once and be used for guidance of the microscopic evaluation. If the number of suspicious regions that require further microscopic processing can be reduced, surgeons and pathologists can focus their attention and resources on areas that remain inconclusive. To provide a sense of what these macroscopic images would look like, we evaluated HER2+ tissue from the CHTN and analyzed thawed, 5mm diameter samples from the same specimen. Samples were incubated with either buffer or HER2-targeted AuNP at

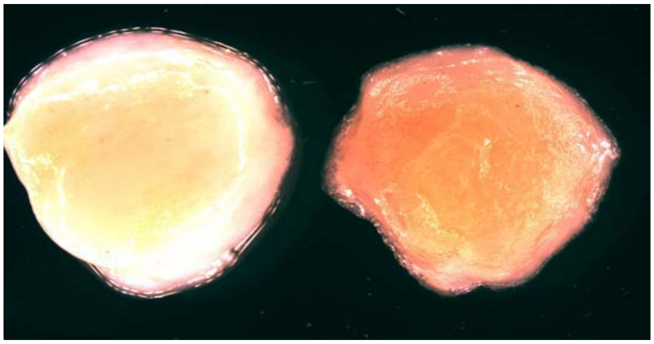

**Figure 3.16.** Macroscopic mages of HER2+ breast cancer tissue before (left) and after (right) five minute application of immunotargeted AuNPs. Magnification at 10x. This image on the right provides a sense of the type of macroscopic image we ultimately plan to obtain (although this entire sample is cancer) using the MMO imaging system being developed in Project 2 while the microscopic system being developed in Project 1 will then be used to scan around the edges of the tumor.

37°C for 5 minutes. Figure 3.16 demonstrates the enhanced contrast provided by the AuNPs after near-infrared wavelengths were enhanced through capabilities inherent in the camera's software. This supports the potential ability to visualize the nanoshell targeting, and thus HER2-overexpression, through simple macroscopic imaging of whole tissue. This supports the use of AuNPs as promising contrast agents for potential rapid imaging applications at the point of care and is a major emphasis of our work moving forward.

**Project 4: Activatable Nanoparticles for Monitoring Radiation Therapy (closed)**
This project was conducted during Years 1 and Year 2 only. When the revised Statement of Work was submitted, the work scheduled for Years 3-5 of this effort was removed. This change was made when it became clear that while the original idea behind this project was sound, the radiation levels required to create the optical signal changes needed were too high to be clinically relevant. Essentially, we had proposed to directly monitor delivered radiation through optical signal changes created when the radiation interacted with gold nanoparticles causing a signal change when particular chemical bonds were broken. We found the level of radiation required to create these changes were far higher than therapeutic levels used clinically. Rather than continue this effort, we instead added the MOI imaging project (Project 2) needed for the tumor margin effort and added tissue imaging studies throughout the project in addition to the cell based studies we had originally proposed (Projects 1 and 3).

## ***Year 4***

### (I) Combining Scattering-Based Optical Imaging Technologies and Targeted Nanoengineered Imaging Agents for Tumor Margin Detection in HER2+ Women

*Introduction*

Currently, breast cancer is the second leading cause of cancer-related deaths in women and it accounts for approximately one-third of all cancers diagnosed in women in the United States (Cancer, 2005). In order to reduce cancer recurrence and progression, cancerous tissue must be completely eliminated, regardless of grade (Steen, 1993). Surgical breast cancer therapy focuses on removing the primary tumor and identifying the possibility of disease spread through evaluation of sentinel lymph nodes. Although some patients may require modified radical mastectomy, which involves the complete removal of the entire breast, many patients with less-advanced breast cancer elect breast-conserving surgery. To reduce the likelihood of cancer recurrence, it is recommended that patients undergoing a breast conservation therapy, such as lumpectomy, receive adjuvant radiation treatment to combat potential residual cancerous cells and maintain local control (Buckman, 1997; Fisher et al., 2002). Fisher *et al.* determined that lumpectomy followed by radiation therapy is just as effective as mastectomy provided that the resected tissue specimens contain negative tumor margins (Fisher et al., 2002). Intraoperative treatment decisions are, therefore, absolutely critical. The presence of a positive surgical margin has been associated with lower rates of patient survival (Mojica CM, 2007). Due to residual cancer cells being left in many patients that undergo breast conservation therapy, as many as 40% of patients have experienced local breast cancer recurrence near the site of the original tumor (Fisher et al., 2002).

Presently, intraoperative tumor margin detection occurs only in specialized tertiary centers, such as The University of Texas M.D. Anderson Cancer Center (MDACC). In these centers, the resected tissue receives a preliminary evaluation by a pathologist while the patient remains in the operating room, and more tissue can be removed until the pathologist determines the tumor margins are negative. In community hospitals, however, pathologic analysis of excised tissue does not occur until well after the operation is complete. Those patients who consequently have positive tumor margins must return for an additional surgical procedure or receive increased doses of post-operative radiation therapy (Smitt et al., 1995; Oouchi et al., 2009). Thus, the existence of positive tumor margins subsequently portends additional risks and costs to the patient. Due to the existing limitations of current intraoperative tumor margin detection, there is an opportunity to develop superior diagnostic tools to assist in reducing the recurrence and progression of cancer due to inadequate tissue removal during primary surgery.

While histologic (and thus, microscopic) analysis remains the gold standard for tumor margin assessment, the macroscopic evaluation of tissue specimens may also be used to provide an intraoperative estimate of tumor margin status prior to subsequent processing. Currently, macroscopic evaluation occurs for breast cancer specimens that involve microcalcifications or nonpalpable masses and does not occur for palpable breast masses (Cabioglu et al., 2007). For nonpalpable masses that have been resected, the specimen is first oriented with sutures prior to delivery to pathology. The whole specimen is then radiographed and inked by pathologists to further orient the specimen as to *in situ* location. The radiographic images are used to determine the extent of the breast disease and the proximity to the resected margins. Although specimen radiography appears to increase the accuracy of tumor margin detection, limitations have been noted. For instance, microcalcifications are not always associated with malignancy and areas that appear as tumor on radiographic images may actually be areas of lymphocytic accumulation due to nonneoplastic conditions (Graham et al., 1994). In order to increase the sensitivity and specificity associated with macroscopic evaluations, the use of contrast agents targeted to specific biomarkers associated with disease may present superior opportunities.

In studies we reported in our Year 2 and Year 3 report, we confirmed that silica-based gold nanoshells targeted to the human epidermal growth factor receptor 2 (HER2) could be used for the rapid contrast enhancement of both cells (Bickford et al., 2008a) and tissue sections (Bickford et al., 2010) which overexpress HER2 biomarkers (Year 2 and Year 3, respectively). Amplification of this cell-surface bound tyrosine kinase receptor, which occurs in approximately 20-25% of all human breast cancers, is associated with increased cancer aggression, recurrence, and progression (Slamon et al., 1987; Nahta et al., 2006). Accurate tumor margin detection is thus particularly critical for patients who overexpress HER2 in order to minimize the devastating sequelae associated with this disease. To facilitate prompt tumor margin detection intraoperatively, the ability to assess tumor margins without the need for physical sectioning is highly desirable. Thus, in this study, we advance our previous findings by examining the ability to rapidly target HER2 receptors in intact *ex vivo* human breast tissue specimens without sectioning. We first confirm the predominance of the surface targeting needed to identify the tumor margins and preferential labeling of HER2-positive tissue. Then, we demonstrate the proof of concept that anti-HER2 targeted gold nanoshells can be used as rapid diagnostic imaging agents for HER2-overexpression in intact breast tissue specimens using a standard stereomicroscope and confirm these results through reflectance confocal microscopy and immunohistochemistry. In Year 5, this work will continue through similar studies this time using the optical imaging devices developed in this DoD project.

### *Nanoshell Fabrication and Antibody Conjugation*

Nanoshells were fabricated as formerly described (Loo et al., 2004; Loo et al., 2005a; Loo et al., 2005b) and only a brief summary will be provided here. Silica cores were made using the Stöber method (Stober et al., 1968) followed by subsequent termination of the silica surfaces with amine groups. The final particles were measured by dynamic light scattering (DLS) to have an average diameter of 276 nm. Next, gold colloid (diameter of ~1-3 nm) was fabricated and adsorbed onto the surface of the silica cores via the amine groups (Duff et al., 1993). After the gold shell layer over the silica cores was completed, the spectrum of the final nanoshell solution was visualized using a UV-vis spectrophotometer (Varian Cary 300) (Fig 4.1).

In order to determine the concentration of nanoshells in solution, the absorption, scattering, and extinction coefficients were determined using Mie Theory. The average size of the nanoshells, as validated by Scanning Electron Microscopy (SEM), was a diameter of 314 nm with a peak surface plasmon resonance at 840 nm (see Fig. 4.1). The concentration of the working nanoshell solution was approximately $2.0 \times 10^9$ particles/mL.

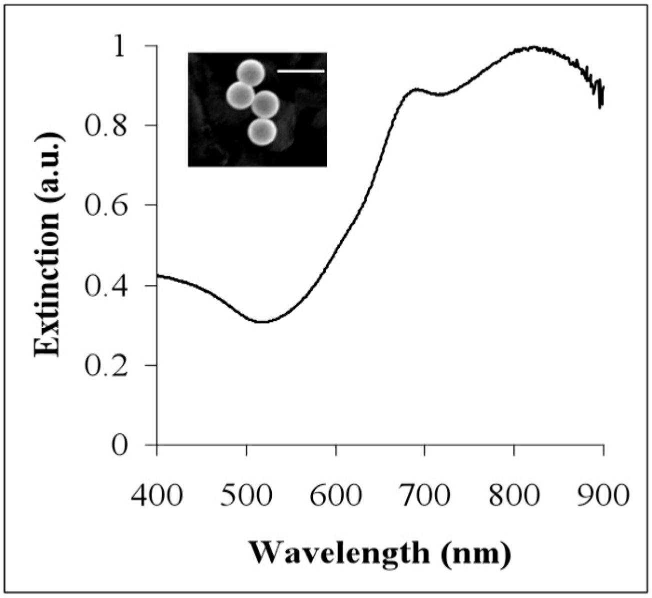

**Figure 4.1.** Measured extinction spectra of nanoshells with an average core diameter of 276 nm and average shell thickness of 19 nm. Insert depicts corresponding image from scanning electron microscopy. Scale bar represents 500 nm

Nanoshells were next targeted to biological HER2-antigens by linking the surfaces of the nanoshells to anti-HER2/neu antibodies using previously described methods (Loo et al., 2004). Prior to beginning experimental studies, nanoshells ($2.0 \times 10^9$ particles/mL) were incubated with an anti-HER2-linker cocktail (Loo et al., 2004) for 2 hours at 4°C. For the purpose of complete nanoparticle stabilization in biological media, the nanoshells were next incubated with a 1 mM polyethylene glycol-thiol solution (PEG-SH, MW = 5kD, Nektar) for 12-16 hours at 4°C. Next, unbound antibodies and excess PEG-SH were removed from the nanoshells by centrifugation. Supernatant was removed and, just prior to experimental tissue studies, the nanoshells were resuspended in antibody diluent (IHC World, pH 7.4) by gentle pipetting to a final volume of 165 μl.

### *Ex Vivo Human Breast Tissue Specimens*

Normal (nonneoplastic) and cancerous (HER2-negative and HER2-positive) breast tissue specimens were supplied by the Cooperative Human Tissue Network (CHTN) through a protocol approved by the Institutional Review Board (IRB). Tissues were previously designated as normal or cancerous by pathologists at the medical centers where the tissue samples were obtained. Additionally, HER2/neu status was also previously determined by pathologists at the respective medical centers prior to the patients undergoing any form of medical treatment. The tissues, which arrived as pre-frozen in liquid nitrogen, were immediately placed in a -80°C freezer.

Prior to use, samples were thawed briefly in a 37ºC water bath and then cut on a disposable cutting board using a 5 mm punch biopsy in order to maintain size consistency. At least two punch biopsies were taken from each specimen for control and experimental conditions. Each cut specimen used was 5 mm in diameter with an average thickness of 1 mm. Tissue samples were subsequently incubated in prewarmed antibody diluent (IHC World, pH 7.4) for 1 minute at room temperature with gentle agitation in a 24-well plate. After pre-rinsing, the samples were incubated in either antibody diluent or the aforementioned targeted-nanoshell cocktail (volume = 165 µl) in polyethylene sample vials (Sigma Aldrich). The vials were then placed on a nutator in an incubator set at 37°C for 5 minutes. After incubation, the tissue samples were removed from the vials and rinsed 3 times in 1X PBS briefly in a 24-well plate. Samples were then moved to a clean well of 1X PBS prior to imaging.

### *Two Photon Imaging of Human Breast Tissue Specimens*

For two photon imaging of intact breast tissue specimens, both HER2-negative cancerous and HER2-positive cancerous samples were evaluated for surface labeling of HER2-targeted nanoshells. Samples were placed directly on a glass coverslip (Fisher Scientific) and an additional coverslip was placed on top of the tissue in order to facilitate moderate tissue compression. For image acquisition, a Zeiss laser scanning microscope (LSM) 510 non-linear optics (NLO) META multi-photon system was used in tandem with a Coherent Chameleon femtosecond-pulsed, mode-locked Ti:sapphire laser. This system was set to operate as formerly described (Bickford et al., 2008b). Specifically, an excitation wavelength of 780 nm and a power of 10% of the maximum excitation power were used. The collected emission wavelength range spanned from 451 nm to 697 nm. Images were collected at a magnification of 20X and a z-stack (depth) increment of 5 µm. In order to calculate the percentage of area covered by nanoshells, Image J imaging software was implemented after image acquisition. An intensity threshold of 30 (on a scale of 0 to 255, where 0 represents pure black and 255 represents pure white) was used to distinguish areas with and without nanoshells. For areas that did not contain nanoshells, the associated intensities did not exceed the threshold.

### *Macroscopic Imaging of Human Breast Tissue Specimens*

Normal (nonneoplastic) and HER2-positive cancerous breast tissue specimens (from patients who had and had not received previous neoadjuvant chemotherapy) were imaged using a Zeiss Discovery.V8 stereomicroscope equipped with a VisiLED MC1000 light source. This microscope provides enhanced visualization of specimens in three dimensions ranging from 1X to 8X magnification. For macroscopic imaging of breast tissue specimens, a thin plastic black stage was placed beneath a 22 µm x 22 µm glass coverslip (Fisher Scientific) to enable ease of tissue placement and to provide a consistent black background among all samples. The specimens (controls and respective nanoshell-labeled counterparts) were placed alongside each other on top of the coverslip. Images were taken at both 1X and 2X magnification under the same lighting conditions.

### *Reflectance Confocal Microscopy Imaging of Human Breast Tissue Specimens*

Following widefield imaging, the aforementioned samples were prepared for microscopic imaging under reflectance confocal microscopy. For this component of the study, a Lucid VivaScope 2500 inverted confocal microscope was employed, which uses an 830 nm light source and has a lateral resolution of less than 2µm. Samples were placed directly on glass slides (Fisher Scientific) which were modified by the addition of an adhesive 1-mm-deep, 20-mm-diameter silicon isolator (Invitrogen). In order to compress the tissue slightly and consistently among samples, an adhesive tissue cassette (Lucid, Inc.) was placed directly on top of the silicone isolators above the tissue specimens. Multiple images were taken at a power of 0.4 mW and at the same distance from the glass surface for tissue samples incubated in either antibody diluent alone or the HER2-targeted nanoshells. After reflectance imaging, coverslips and silicone isolators were removed and the samples were prepared for histological processing. Additionally, reflectance intensity measurements were recorded using Image J processing software as described previously (Bickford et al., 2010).

### *Immunohistochemistry and Histology*

Once images were collected under both stereomicroscopy and RCM imaging systems, normal (nonneoplastic) and HER2-positive cancerous samples (with and without previous neoadjuvant chemotherapy) were embedded in OCT media (BBC Biochemical) and frozen rapidly over dry ice. Sections were then made of all specimens using a Leica CM1850 UV cryostat. At least 20 sections were cut from each specimen at a thickness of 5 μm. Cancerous specimens were sectioned at -20ºC and normal specimens were sectioned at -30ºC, as recommended by Leica for maintaining optimal tissue morphology. The sections were immediately placed on superfrost slides (Fisher Scientific) and allowed to air dry overnight. The next day, multiple sections from each specimen of interest were prepared for either immunohistochemistry (IHC) or hemotoxylin and eosin (H&E) staining. IHC for the HER2-antigen was executed using the Histostain Plus AEC Broad Spectrum Kit (Invitrogen) per manufacturer's instructions. H&E staining was also performed using the manufacturer's instructions (Sigma Aldrich) for the alcoholic Eosin Y solution. For image acquisition, a standard brightfield microscope (Zeiss Axioskop 2 equipped with a Zeiss Axiocam MRc5 color camera) was used at a magnification of 20X under the same lighting conditions.

*Results*

### *Distribution and Penetration of Gold Nanoshells in Intact Human Breast Tissue*

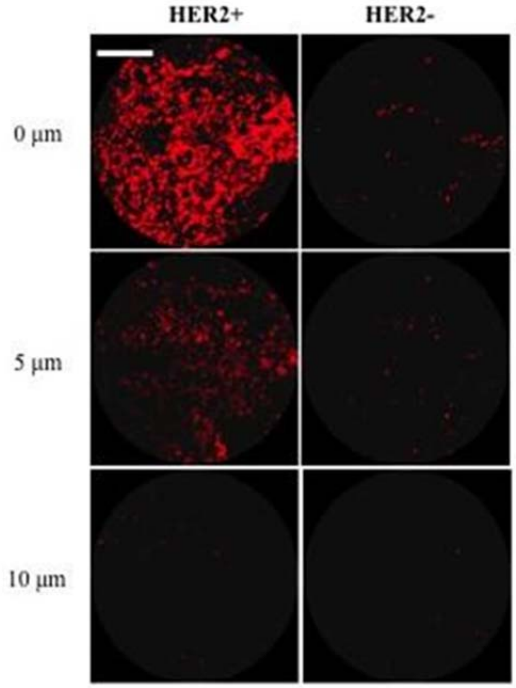

**Figure 4.2.** Z-stack two-photon luminescence images of HER2-positive and HER2-negative tissue incubated with HER2-targeted nanoshells for 5 minutes at 37°C. Each progressive image represents an increase in depth penetration of 5 µm. Magnification = 20X. Scale bar = 50 µm

The goal of this study was to evaluate the distribution of anti-HER2-conjugated gold nanoshells on resected intact tissue specimens. For comparison, the nanoshell labeling between HER2-positive and HER2-negative tissue samples was evaluated. In order to do this, a two photon imaging system was employed. As shown previously, this imaging system is capable of enhancing and capturing the luminescence signature of the gold nanoshells (Bickford et al.) while also creating a stack of images taken in the z-direction throughout the depth of the tissue of interest. It should be noted that the acquisition of images in the z-direction with this system employs the Nyquist Sampling Theorem, where images overlap by half their thickness in order to avoid missing information.

Figure 2 represents the z-stack images of HER2-positive and HER2-negative tissues incubated with HER2-targeted nanoshells. Each sequential increment in the z-direction represents 5 µm into the tissue. Qualitatively, the first image (taken at the surface, or at 0 µm) in Fig. 4.2 demonstrates that the nanoshells preferentially label HER2-receptors on the surface of the tissue. Additionally, Fig. 4.2 displays decreased signal as the focal spot from the confocal microscope penetrates further into the tissue. This is possibly due to the reduced number of nanoshells that were able to penetrate the tissue in the limited amount of incubation time, thus decreasing signal collected at each penetration depth. However, due to the optical set-up, one cannot conclusively determine if the signal seen at these depths is due to nanoshell presence, or reflection from the nanoshells attached to the surface. Future experiments, such as slicing the tissue after incubation with the nanoshells will conclusively determine the penetration depth of the nanoshells.

Additionally, a quantitative difference of the nanoshell signal at the surface of the Her2-positive and Her2-negative tissue was calculated. Using ImageJ imaging software, it was calculated that approximately 66% of the Her2-positive field of view area was covered in nanoshells versus just 2% for the Her2-negative field of view. This confirms that anti-Her2 nanoshells can be used to discriminate Her2-positive cancerous tissue from Her2-negative noncancerous tissue

### *Enhanced Optical Imaging of Intact Ex Vivo Human Breast Cancer Tissue Using Gold Nanoshells*

Based on the two-photon results demonstrating the superior labeling of HER2-targeted nanoshells on the surface of intact *ex vivo* HER2-positive tissue specimens, we assessed the potential of using a standard stereomicroscope to visualize this enhanced contrast. For this component of the study, human breast tissue specimens that over-expressed HER2 receptors at the time of patient diagnosis were evaluated and compared to normal (nonneoplastic) tissue. Due to the ultimate goal of utilizing gold nanoshells to rapidly label tumor margins intraoperatively in diverse patient populations, we examined tissue from patients who had and had not undergone neoadjuvant chemotherapy. All tissue samples were incubated with either antibody diluent buffer or the anti-HER2-targeted nanoshells for 5 minutes at 37°C. As shown in Fig. 3, which represents raw images taken with a stereomicroscope, intact tissue specimens incubated with antibody diluent alone showed no markings or features characteristic of nanoshells. However, tissue specimens incubated with the anti-HER2-targeted nanoshells demonstrate numerous particles on the surfaces of the tissues. Qualitatively, the HER2-positive tissue from the patient who did not undergo previous chemotherapy shows the greatest labeling with the targeted nanoshells. The HER2-positive tissue from the patient who did undergo neoadjuvant chemotherapy does demonstrate enriched nanoshell labeling when compared to HER2-negative normal tissue, though not to the same extent as the patient without previous chemotherapy. In contrast, the nonneoplastic tissue shows the least amount of nanoshell labeling and only a few areas of nanoshells can be visually perceived.

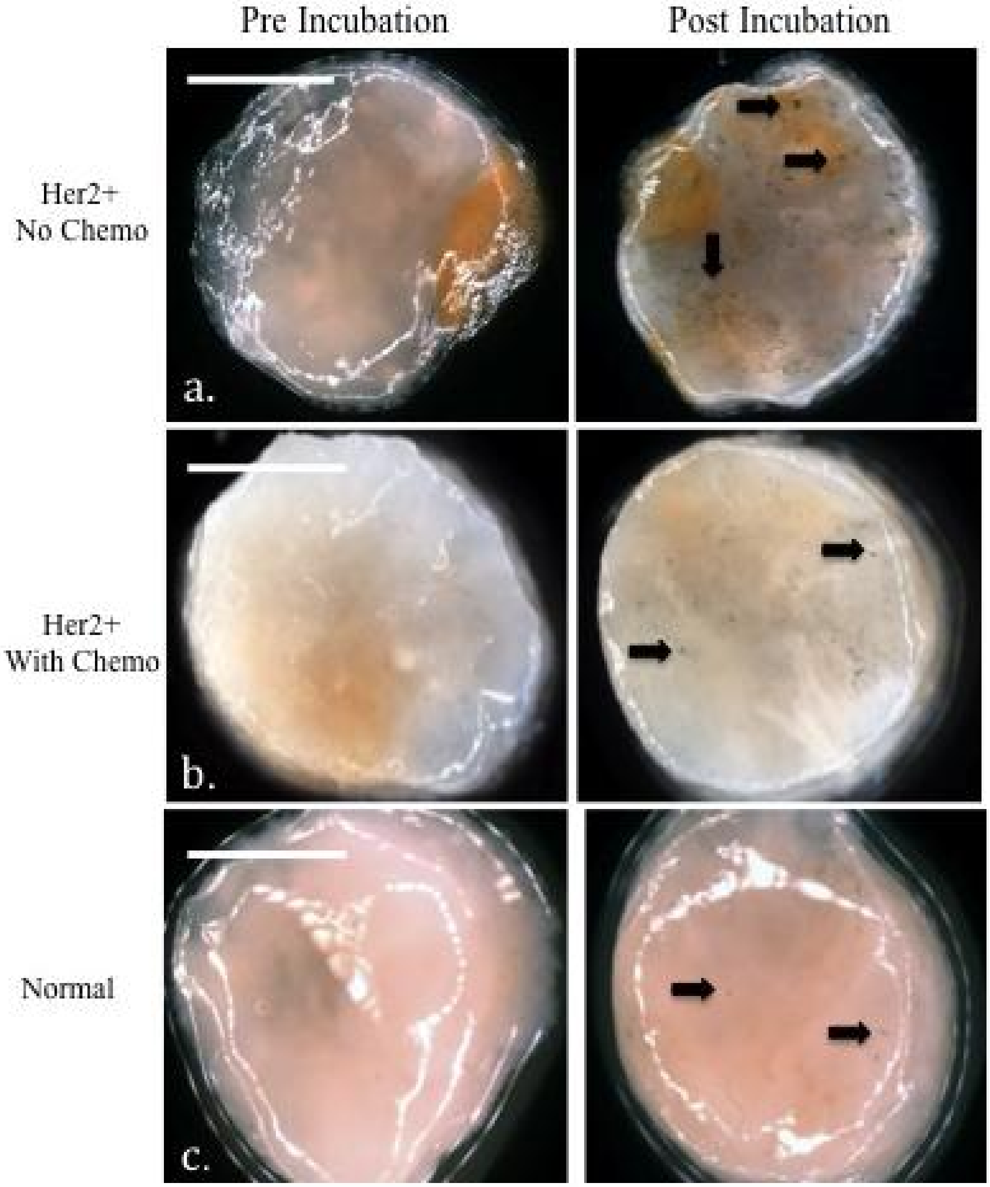

**Figure 4.3.** Raw stereomicroscope images of (a.,b.) HER2-overexpressing cancerous and (c.) nonneoplastic tissue incubated with either buffer or HER2-targeted nanoshells for 5 minutes at 37°C. Cancerous tissue taken from a patient (a.) without chemotherapy and (b.) following neoadjuvant chemotherapy. Arrows represent nanoshells. Images taken at 2X. Scale bars = 2.5 mm.

While the degree of nanoshell labeling can be visualized without image adjustments under a standard stereomicroscope, the superior extent of this labeling can be seen more clearly after a simple contrast enhancement using imaging software (Image J). As seen in Fig.4.4 (a.), the nanoshells are even more discernable against the tissue background regardless of inherent tissue constituents.

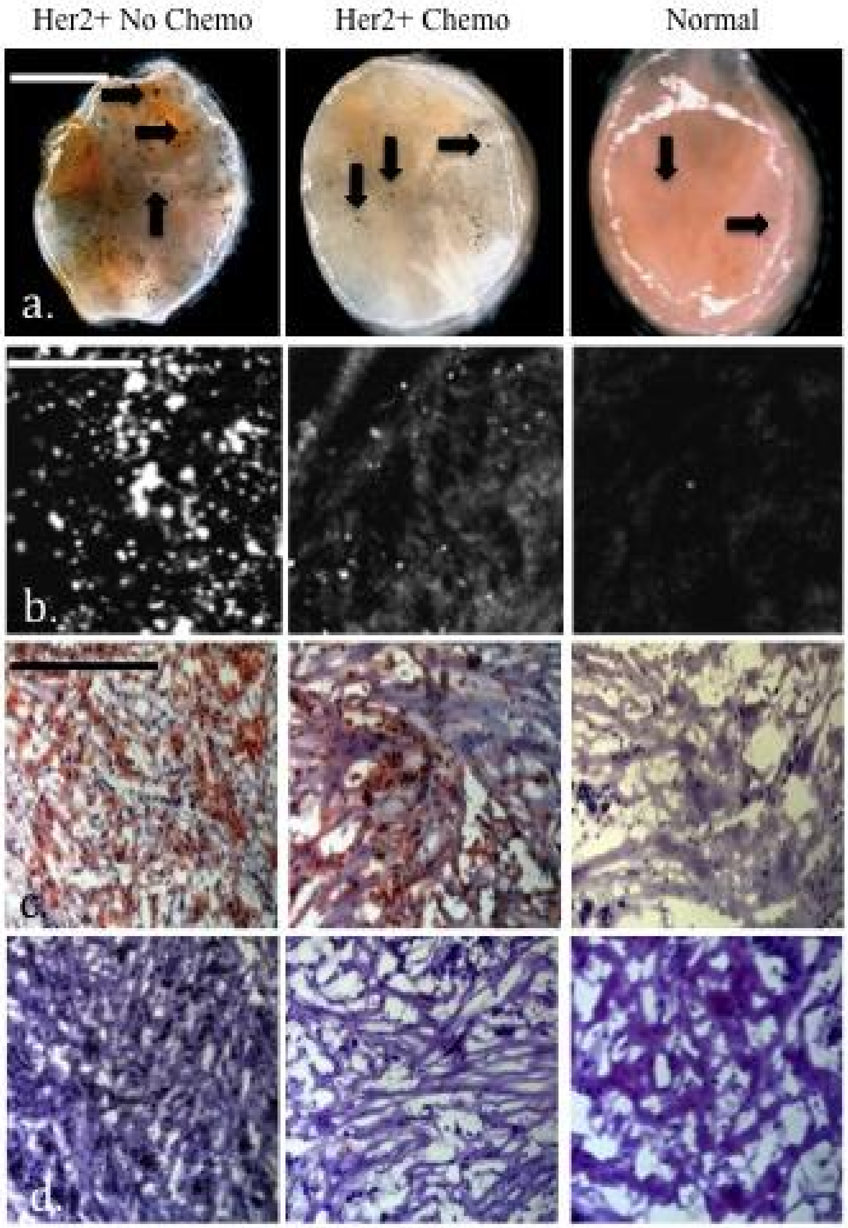

**Figure 4.4.** (a.) Stereomicroscopic images of HER2-overexpressing breast tissue (with and without neoadjuvant chemotherapy) and normal breast tissue incubated with HER2-targeted nanoshells for 5 minutes at 37°C after contrast enhancement. Magnification at 2X; scale bar = 2.5 mm. Arrows represent nanoshells. (b.) Respective reflectance confocal microscopy images of tissue samples from (a.). Power = 0.4 mW and scale bar = 75 µm. Respective (c.) HER2/neu immunohistochemistry and (d.) H&E results taken under brightfield microscopy under 20X magnification. Scale bar = 0.35 mm

In order to validate the enhanced nanoshell labeling seen by macroscopic imaging, the surfaces of the same tissue samples were also imaged using reflectance confocal microscopy (Fig.4.4 (b.)). Concurring with the stereomicroscopic images, we see dramatic nanoshell surface-labeling when using targeted nanoshells with previously untreated HER2-positive tissue.

For the HER2-positive sample, which had formerly undergone chemotherapy, we also see enhanced nanoshell labeling, though to a lesser degree than the untreated sample as suggested by the stereomicroscopy results. The normal, nonneoplastic tissue displays the least amount of surface labeling with only minimal nanoshells evident with either imaging system. Reflectance intensity measurements (data not shown) were ~2.5 to 3 times greater for both the HER2-positive tissue sample receiving chemotherapy and for the HER2-positive tissue not receiving chemotherapy when compared to the normal HER2-negative tissue sample.

Subsequent histological analysis shown in Fig. 4 (c.) reveals that the distribution of HER2 receptors seen with nanoshell-enabled contrast corresponds to that seen with IHC against HER2. The HER2 expression seen by IHC is greater for the previously untreated HER2-positive tissue sample than for the sample which had undergone neoadjuvant chemotherapy. This is believed to be due to the effects of chemotherapy. Rasbridge *et al.* previously demonstrated that patient response to chemotherapy is highly variable, with patients previously negative for HER2-overexpression occasionally becoming positive after treatment and patients previously positive for HER2-overexpression subsequently becoming negative (Rasbridge et al., 1994). In as much as patient response to chemotherapy varies, in this study both tissues which were previously identified as overexpressing HER2 receptors during initial patient diagnosis demonstrate considerably more receptors than the normal, nonneoplastic tissue. Additionally, H&E-stained sections of all tissue samples have been included (Fig. 4 (d.)) to illustrate the microscopic characteristics and differences associated with neoplastic vs. nonneoplastic conditions.

### *Summary*

The macroscopic evaluation of resected tissue is currently the standard of practice for certain patients undergoing breast conservation therapy at tertiary centers, such as MDACC. As mentioned previously, this occurs primarily for non-palpable breast cancers (Cabioglu et al., 2007). Furthermore, this extra level of evaluation is not as common in community-based hospitals. Here, we demonstrate the ability to use targeted gold nanoshells to rapidly improve visualization of a specific biomarker associated with disease aggression and progression (HER2) in intact *ex vivo* human breast tissue. By utilizing silica-gold nanoshells designed as rapid diagnostic imaging agents, surgeons and pathologists may be able to realize tumor margin status directly in the operating room after both macroscopic and microscopic assessment.

The ability to enhance contrast of malignancy using topically-applied agents has previously been demonstrated for oral tissue using fluorescently-labeled deoxy-glucose and epidermal growth factor (EGF) conjugates (Nitin et al., 2009a; Nitin et al., 2009b) as well as cervical tissue using fluorescently-labeled gold nanoparticles targeted to EGF receptors (Aaron et al., 2007). However, these studies employed incubation times ranging from 30-45 minutes, which exceeds the length of time currently needed to obtain tumor margin status using frozen section histology. Additionally, the aforementioned studies which evaluated malignancy based on EGF expression utilized optical clearing agents, which may be necessary for particles which target intracellular biomarkers (Ven et al., 2009a, b). Nevertheless, gold nanoshells targeted to extracellular biomarkers may offer more favorable opportunities for *ex vivo* intraoperative tumor margin detection without the need for lengthy incubation times or the use of optical clearing agents.

Recently, we verified that silica-based gold nanoshells could be used to enhance contrast of both HER2-overexpressing cells and tissue sections within 5 minutes of incubation time (Bickford et al., 2008a; Bickford et al., 2010). We take these findings one step further and confirm that these particles, when targeted to anti-HER2 receptors, can also be used to distinguish intact HER2-overexpressing *ex vivo* tissue from normal tissue within the same incubation time. Moreover, these results are supported by microscopic imaging with a reflectance confocal microscope as well as immunohistochemistry against HER2.

In order to translate these findings more readily to the clinic, we are presently developing a low cost widefield imaging system (Project 2) that can be used to detect the overexpression of HER2 (and other extracellular biomarkers) on account of contrast enhancement provided by gold nanoshells. In addition, we plan to collect data from diverse patient populations and assess results with fresh tissue samples. In this way, the use of gold nanoshells may demonstrate widespread efficacy or be limited only to specific patient subsets.

Our research indicates that *ex vivo* tissue specimens labeled topically with silica-based gold nanoshells can be visualized by both widefield (macroscopic) and high resolution (microscopic) imaging systems. By employing macroscopic imaging intraoperatively, clinicians may be better able to distinguish cancerous and non-cancerous breast tissue prior to further microscopic analysis and subsequent histological processing. Ultimately, this system could also be used for other diagnostic applications, for other anatomical locations, and for other biomarkers associated with disease. By facilitating fast and accurate tumor margin results intraoperatively and supplementing current diagnostic methods, the incidence of cancer progression and amount of time spent in surgery due to inadequate tissue removal is, correspondingly, expected to be reduced.

## (II) Technical Updates for Projects

### *Project 1 Technical Update*

Over the past year, the needle compatible probe system has been modified with a new illumination source arrangement, which has proved very valuable in terms of layout and ease of adjustment (Figure 4.5). Please see the included *Journal of Biomedical Optics* paper for a review of the needle-based system and prior illumination design. Three degrees of translational adjustment and two degrees of angular adjustment are now possible in the new arrangement. The major benefit to imaging relative to our prior design is that because the entire optical pathway from illumination to detection is well aligned, system sensitivity has improved greatly. The only drawback is the heat generated by the LED, which cannot be dissipated by a heat sink and a fan as was the case in the prior design. The heat is transferred to the P100-P angular adjuster (to which the LED is heat taped) which becomes hot in a matter of minutes. This issue is currently being addressed. However, as long as the LED doesn't burn out, system performance isn't affected.

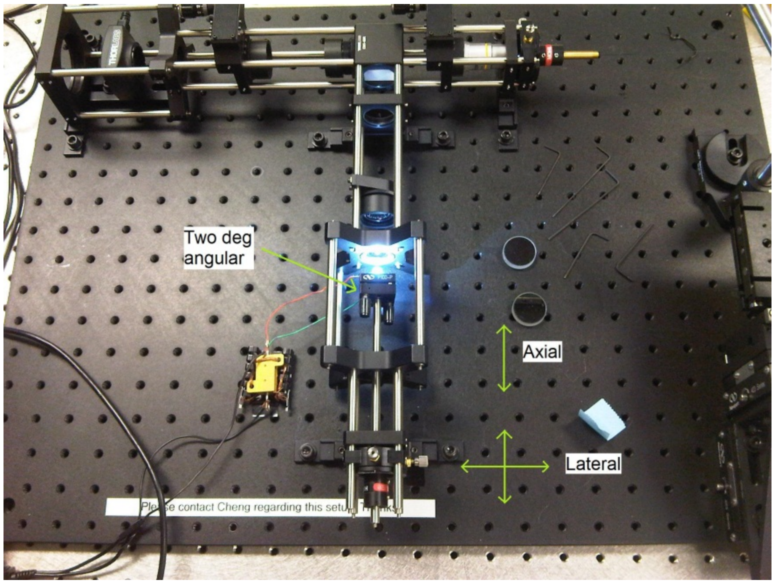

Figure 4.5: Photograph of the new illumination arrangement.

The improved performance of the system can be seen in the latest images of the USAF resolution target (Figure 4.6). With only 0.261 ms exposure time, very clear images can capture at resolutions in excess of 141 cycles/mm (~7 um). Polishing of the fiber has improved the image quality even more. However, it is still not at the point where the dark fiber cores are completely removed most likely due to an uneven image guide surface).

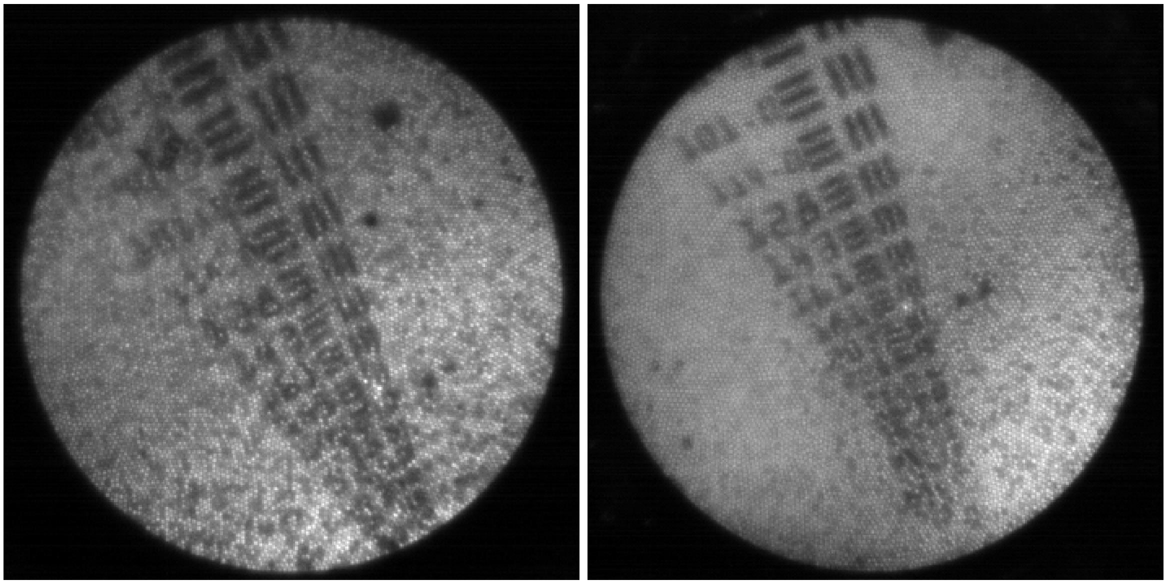

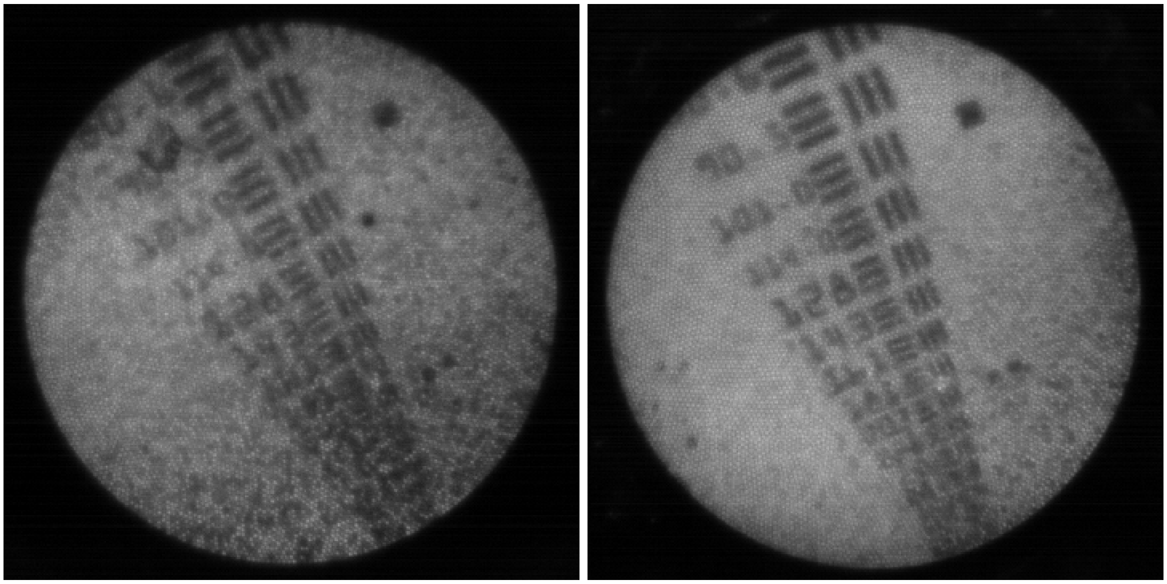

Figure 4.6: (Top left) Before polishing, with probe tip pressed against target; the dark dots corresponding to uneven image guide surface are clearly visible all over the image. (Bottom left) Before polishing, with the probe tip slightly above the target; the dark dots are not as prominent but still a major factor. (Top right) After polishing for 5 min, probe tip pressed against target; the dark dots are still present but not as intrusive. (Bottom right) After polishing and with probe tip slightly lifted, resolution as high as 181 cycles/mm (5.5 um) can be seen without interference from the black dots. Even though lifting the probe tip up slightly reduces the effect of the uneven image guide surface, the best resolution still occurs when the probe is pressed directly against the target. With a sufficiently smooth surface that removes all the black dots, even greater resolution may be attained. A droplet of water is used for index matching in all imaging cases; the exposure times are 0.261 ms in all cases.

### *Project 2 Technical Update*

In our Year 3 report, we described the design of our first generation wide-field macroscopic system. One challenge with the first system was that it was not as portable as we would like for the application we ultimately envision: guiding breast tumor resection. Here, we briefly review already existing widefield imaging system and then describe design of the second generation system. In Year 5, we will finish constructing this system and assess performance using ex vivo breast cancer specimens.

There have been several different fluorescence imaging devices developed to improve cancer diagnostics. Most have focused on improving oral cancer detection because of the ease of tissue acquisition due to patients only having to open their mouth (Lane et al., 2006; Nitin et al., 2007; Roblyer et al., 2008; Roblyer et al., 2009). Tanaka et al. developed a system that combined near infrared (NIR) fluorescence with white light to improve sentinel lymph node mapping

(Tanaka et al., 2006). Additionally, the Maestro CRI imaging system has been used for *ex vivo* margin delineation (Nitin et al., 2009b) and *in vivo* cancer detection in mice (Ntziachristos et al., 2003; Sheth et al., 2009; Zhou et al., 2009). Fluorescence spectroscopy has also been used to evaluate the excitation and emission spectrums of *ex vivo* ovarian tissue (Brewer et al., 2001).

Currently, there are only two studies that combine the use of fluorescent contrast agents with wide-field imaging systems (Nitin et al., 2007; Nitin et al., 2009b). Other current wide-field imaging systems that have been published have only been designed to detect changes in autofluorescence that are seen in neoplastic tissue. Other studies that have involved contrast agents have been used for higher resolution systems such as confocal fluorescence and fiber-optic probes (Pierce et al., 2008; Bickford et al., 2009; Rosbach et al., 2010).

The project reported on at the beginning of our Year 4 report has demonstrated that the light scattering of large anti-HER2 targeted silica-gold nanoshells can be imaged using a wide-field stereoscope to differentiate HER2+ cancerous tissue from HER2- tissue. However, the stereoscope is expensive, large, and not portable. There is a need for the development of a portable, inexpensive, wide-field imaging system that has the capability of imaging these nanoshells. This system must also address the need for a wide-field imaging system that can image fluorescent contrast agents in conjunction with the nanoshells. This system will have the capacity to image multiple markers (such as Epidermal Growth Factor Receptor and HER2), the two markers we are targeting in Project 3. The system will also be able to used so that one imaging mode (such as fluorescence) validates the findings of the other mode (i.e. targeted silica-gold nanoshells). Below, we describe the system design we propose as well as the experiments we will complete in Year 5 to assess the system.

## Design of Second Generation System

### *Camera*

In order to capture the signal from nanoshells and fluorescent contrast agents, the camera must be able to acquire signal in both the visual spectrum of light (350-750 nm) and the NIR (750-1400 nm). To satisfy this parameter and maintain a low cost, a Canon 450D digital SLR camera was purchased and the IR filter inside the camera was removed for a total cost of $1,095.00. Additionally, a camera lens with a focal length range of 18-55 mm (f/3.5-5.5) was purchased separately for a price of $215.00.

Additionally, filters will be attached to the camera so that signal from the desired contrast agents will be collected and other signal, such as tissue scattering will be blocked. A Long Pass 780 nm (LP780) filter was purchased so that signal from the targeted silica-gold nanoshells could be collected, and a Bandpass Filter (500-560 nm) was purchased to detect signal from fluorophores that emit in the green spectrum. These two filters will attach to the end of the camera lens to block light emitted from the tissue samples before signal collection by the camera. The two filters were purchased for a total price of $221.00. This leads to a total purchase price of the camera system to be $1,531.00.

### *Excitation Source*

A proper excitation wavelength and source is necessary to get maximum emission from the targeted contrast agents. In order to keep costs down and control the excitation wavelength, light emitting diodes (LEDs) were chosen to illuminate the sample and contrast agents. LEDs with different emission spectra can be purchased at a small price and arranged in a simple circuit so that the excitation sources can be controlled very simply. For the preliminary experiments, two sets of LEDs were chosen, Blue LEDs with an excitation peak of 465 nm (to excite green fluorophores such as FITC and 2-NBDG) and NIR LEDs with an emission peak of 851 nm to image the silica-gold nanoshells that have a Plasmon of 840 nm. These LEDs are available for a price of $4.55 and $3.75 each, helping to keep costs down.

Preliminary experiments have shown that unequal illumination of the samples leads to skewed results because the signal is highest where the light was hitting the sample. This has led to the concept of 360-degree illumination of the samples so that the sample is properly illuminated from all angles. Our design will follow the basic concept of the VisiLED MC1000 light source used in previous work; however, the illumination system will be modified for the camera lens. As well, our setup will have two different sets of LEDs, the Blue and the NIR, whose illumination will be controlled by a switch. The desired contrast agent and biomarker will determine which set of LED's will be illuminated.

### *Setup*

A black, non-reflective stage for the tissues will be attached to a vertical metal pole. The tissue samples will be placed in the middle of the stage for sampling. The camera will be attached to the vertical pole so that it is perpendicular to the imaging stage with the lens facing downwards. This allows for camera stability and keeps the field of view constant from sample to sample. The illumination device will be placed around the tissues and turned on, the respective filter for the desired contrast agent will be placed, and the image will then be acquired.

### *System Settings*

The system's settings will need to be tested and optimized for both the fluorophore and nanoshells that will be targeting HER2+ breast tissue. The fluorophore that we will be testing the system with is FITC (fluorescein isocyanate), a common fluorophore. To test the FITC, 1 ml of 200 μM FITC will be placed in a non-fluorescent glass embryo dish and illuminated with the Blue LEDs; excitation light will be filtered using the bandpass filter. Camera and illumination settings will be varied and the setting that gives the maximum signal will be used.

Additionally, settings for imaging non-targeted silica-gold nanoshells will also be determined by placing a 100 μl of nanoshells onto a glass slide, illuminating the particles with NIR LEDs, and filtering the scattered light using the LP780 filter. Imaging conditions and settings will be varied as with the FITC, and images will be analyzed to determine which condition produces the highest signal.

### *Tissue Testing*

Once the system's optimal settings have been determined, its imaging capability will be tested in frozen *ex vivo* breast cancer specimens. HER2-targeted silica-gold nanoshells will be used to discriminate HER2+ and HER2- tissue. These nanoshells will be synthesized following our previous work; however in place of the normal PEG-SH that has previously been added, FITC-PEG-SH will be added so that nanoshell presence can be secondary confirmation of nanoshell presence.

Tissue samples will be acquired from the Cooperative Human Tissue Network (CHTN). Both HER2+ and HER2- cancerous tissue will be acquired in addition to noncancerous tissue. The anti-HER2 nanoshells will incubate with the tissues for five minutes at 37°C then rinsed with cold PBS. Each type of tissue will also be incubated with PBS for a negative control. The tissues will be imaged using the system; each image will have one tissue incubated with nanoshells and one with PBS. The images will first be acquired using the NIR LEDs with the LP filter and then with the blue LEDs and the bandpass filter. The images will be processed using the image processing software ImageJ. The signal from the images will be converted to red (nanoshells) or green (FITC) and the images will be overlayed to compare the signal from the same tissue. The signal will also be quantitated using the values acquired from ImageJ. These values will give us quantitative confirmation to the visual evidence that the targeted nanoshells selectively bound themselves to HER2+ cancerous tissue and not to HER2- tissue. Once imaged, the tissues will be frozen and sliced using a Leica tissue slicer (Leica CM 1850 UV). They will then be stained with an H&E stain and an immunohistochemical stain will be performed to test for the presence of the HER2 receptor.

This design will yield a portable inexpensive imaging system that has the potential to image multiple contrast agents. This system will be able to use multiple agents that can help optically differentiate cancerous tissue from non-cancerous tissue, via biomarkers, metabolic activity, or other hallmarks of malignant tissue. This system can be designed to work in concert with any contrast agent/marker combination. In addition, it is portable, inexpensive, and rapid. It will give clinicians a visual representation of tissue in the amount of time to take and process a normal digital photograph.

### *Project 3 Technical Update*

#### *Alternative Approach to Synthesis of NIR quantum dots*

As noted in earlier reports, we have reduced our efforts using quantum dots as imaging agents relative to those using gold nanoparticles based on feedback from the last Era of Hope meeting suggesting that even cadmium-free quantum dots would find little patient acceptance for *in vivo* application. Because tumor margins can be checked directly after removal of the tissue, no *in vivo* use is required. This is the application of quantum dots we are still considering. We would like to compare results from both types of imaging agents being developed in this project: targeted gold nanoparticles and quantum dots. For optimal results, we require quantum dots with longer wavelength emission than those we described in the past which were originally intended for an *in vivo* imaging application. The synthesis protocol we are now using involves a reaction between lead acetate trihydrate and a sodium sulfide solution in the presence of thioglycerol and/or dithioglycerol to coat and stabilize the quantum dots. First, lead acetate was added to the solution, and thioglycerol or dithioglycerol was added to prevent the formation of sodium hydroxide in a basic solution. The pH of the solution was then increased to 11.2 by adding triethylamine, any extra dithioglycerol was added, and then a .1 molar solution of sodium sulfide was then quickly injected into the system upon vigorous stirring. Altering the amount of thioglycerol and dithioglycerol introduced into the system greatly influenced the quality of the product, as well as the location of the emission peak. Furthermore, a smaller injection of sodium sulfide reduced clumping and aggregation in the product. We found that injecting 10 μL of sodium sulfide provided a clean and usable product.

We also found that adding more dithioglycerol into the solution blueshifted the emission peak and pushed it closer to around 950 nanometers, while adding thioglycerol redshifted the emission peak and pushed it towards 1250 nanometers. However, adding too much dithioglycerol produced clumping and aggregation, especially around the sides of the test tube. Furthermore, the inclusion of a thioglycerol coating stabilized the product and produced a significantly higher emission peak. Using a .6 mmol of dithioglycerol and 60 μL of thioglycerol coating produced an emission peak around 1050 nanometers, while reducing the thioglycerol to 5 μL produced a slightly weaker emission peak around almost exactly 1000 nanometers as shown below.

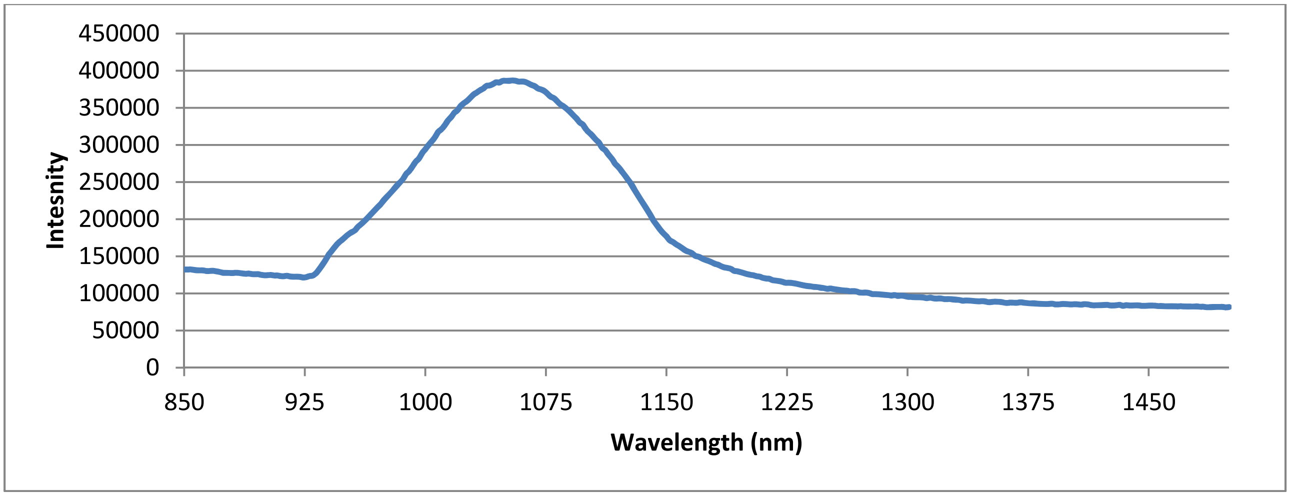

**Figure 4.7**: Emission spectra of NIR quantum dots (.6 mmol DTG, 60 μL TGL, 10 μL sodium sulfide, excited at 488 nm).

*Continued Work on Development of Gold Nanoparticle Based Molecular Imaging Agents*

An addition to our work in Project 3 over the past year was adding in an additional form of molecular contrast beyond the surface receptors originally proposed (HER2 and EGFR). This was based on a suggestion made to us at last year's LINKS meeting to broaden beyond targeting surface markers and to consider methods which could probe metabolism. Below, we provide some background on our approach to this problem, present initial data, and describe the steps we will take over the coming year to more fully assess the proposed new agents.

Targeted gold nanoparticles have been utilized to provide contrast for cell surface receptors such as Epidermal Growth Factor Receptor (EGFR) (Sokolov et al., 2003; El-Sayed et al., 2005) and for nuclear targeting (Tkachenko et al., 2003; Sun et al., 2008) for the past decade. The major means of imaging AuNPs have been demonstrated by Sokolov et al. whose work showed that gold nanoparticles could be imaged using confocal reflectance microscopy, and El-Sayed who illustrated the feasibility of darkfield imaging of gold nanoparticles (Sokolov et al., 2003; El-Sayed et al., 2005). A 2008 study by Kong et al. conjugated glucose to 10.8 nm (average) diameter AuNPs in order to improve cellular uptake of the nanoparticles to increase radiation cytotoxicity (Kong et al., 2008). Glucose-AuNP uptake was compared to bare NPs and NPs conjugated with cysteamine (AET-AuNPs) that attached to the cell surface. Results indicated that AET-AuNPs had the highest binding affinity to the cells. Transmission electron microscope (TEM) images showed that AET-NPs were localized to the cell surface whereas Glu-AuNPs had transversed the cell membrane and were found in the cytoplasm (Kong et al., 2008).

This led to an increased radiation cytotoxicity of Glu-AuNPs when compared to AET-NPs. Most importantly, Kong was able to increase the targeting rate of Glu-AuNPs versus the bare AuNPs, purportedly due to the increased metabolic activity of cancerous cells, which would mean the Glu-AuNPs would have to enter the cells via the glucose transporters (GLUTs). However, the researchers incubated the cells for a time period of 2 hours; this is more than enough time for the cells to ingest the NPs via clathrin mediated endocytosis (Connor et al., 2005; Mironava et al., 2010), phagocytosis (depending on the size of the NP) (El-Sayed et al., 2005; Mironava et al., 2010), or cell membrane mediated diffusion (Geiser et al., 2005). As well, the targeted nanoparticles had a very large size (10.8 nm) to be able to cross the cell membrane via GLUTs. Salas-Burgos et al. reports that the dimensions of the protein to be 36 X 26 Å on the extracelluar side of the protein and 46 X 27 Å on the cytosolic side (Salas-Burgos et al., 2004), much smaller than the nanoparticles reported by Kong et al. This demonstrates that there is need to examine the mechanism of entry of glucose conjugated nanoparticles and determine the maximum size of a particle that can enter via the glucose transporter. The goal of this work is to determine the mechanism of entry and determine if glucose does enhance targeting of nanoparticles to breast cancer.

### *Glucose-Gold Nanoparticle Synthesis*

AuNPs (~1.5 nm diameter) were synthesized using the following steps. 45 ml of deionized water was stirred with a stir bar at 700 rpm. 1 ml of 1M KOH was added to the water and stirred for 2 minutes. 12 µl of THPC was then added and stirred for 90 seconds. 2 ml of 1% $HAuCl_4$ was added and the solution was stirred for 5 minutes. Then, 60 µl cysteamine hydrochloride was added to the solution as a capping agent, and the solution was stirred in the dark for 2 hours. The solution was then stored at 20°C until further processing.

To remove excess cysteamine, 500 µl of the nanoparticles were pipetted into a 3,500 Dalton molecular weight cutoff dialysis membrane. The solution was then dialyzed for 48 hrs with the dialysis buffer (deionized $H_2O$) being replaced at 2, 4, 24, and 48 hours to remove excess cysteamine for the conjugation process. Once the solution was dialyzed, the absorbance of the solution was read from 240-700 nm (data presented in Figure 5). To link the glucose to the AuNP, an EDC-NHS zero length linker wasused to link the D-glucose to the cysteamine capping the particle. EDC-NHS is a common linker used to link nanostructures (Wu et al., 2007) via the amine group of the cysteamine that is covering the nanoparticle.

D-glucose was be to a solution containing EDC and sulfo-NHS. The EDC replaced the hydrogen of the –OH group bound to C1 of glucose. Sulfo-NHS was used to stabilize the product so that it did not revert to normal glucose, creating a quasi-stable active ester that reacted with the –NH group of the cysteamine on the AuNPs (Staros et al., 1986). The Glucose-EDC-NHS was then added to the AuNPs and reacted for 2 hours at room temperature in the dark. Once the reaction was completed, absorbance readings of the nanoparticles were taken (data presented in Figure 8). Preliminary data confirmed conjugation of glucose to the AuNPs because of the red shift seen in the spectrum of the particles after conjugation. However, further post conjugation steps, such as removal of excess glucose-EDC-NHS from solution need to be optimized so that the particles are ready to be added to the cells.

## Experiments to be Conducted in Year 5

### *Cellular Experiments*

After the conjugation procedure has been optimized, conjugated and non-conjugated particles will be added to the SkBr3 breast cancer cell line to test the targeting ability of glucose conjugated nanoparticles (Glu-AuNPs). Approximately 500,000 cells will be plated on a tissue culture treated microscope slide for 48 hours. After 48 hours, cell culture media will be removed and 1% bovine serum albumin in PBS will be added to the cells for 20 minutes to starve the cells. Glu-AuNPs will be added for 20 minutes at 37°C and then rinsed with PBS to remove any excess nanoparticles. A 20 minute incubation time is chosen due to previous cellular experiments with fluorescent deoxy-glucose (2-NBDG) that displayed uptake of the fluorophore within that time frame (O'Neil et al., 2005). Individual cells will be examined under a darkfield

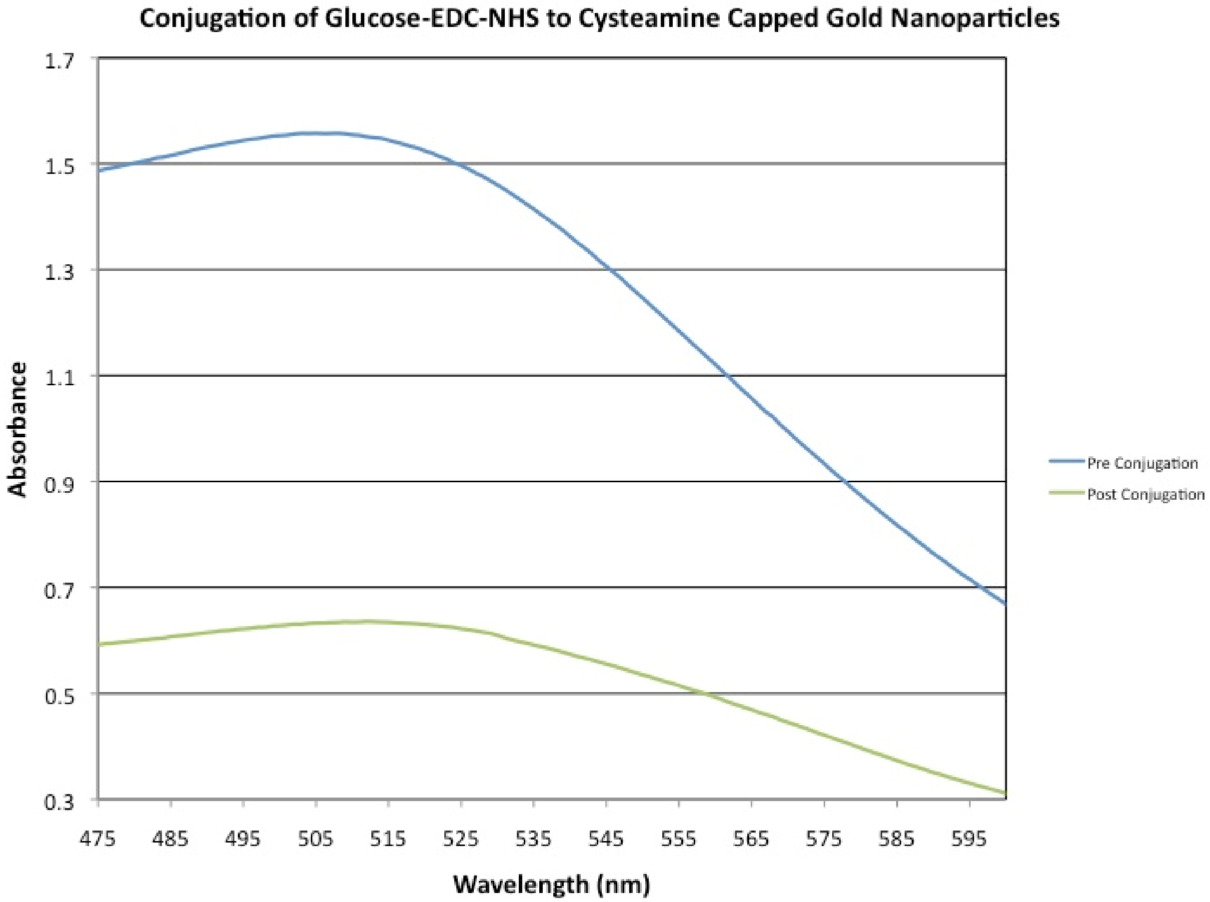

**Figure 4.8.** Absorption spectra of cysteamine capped gold nanoparticles before and after conjugation with Glucose-EDC-NHS. The absorbance peak of the particles before conjugation was 505 nm and for post conjugation it was 512 nm, confirming conjugation. The absorbance of the conjugated nanoparticles is much lower because the sample was diluted by 50% when added to the glucose-EDC-NHS solution.

microscope using a 100X objective to locate the particles' location with respect to the cell. In addition to acquiring qualitative image data, hyperspectral data of each image will also be acquired. The hyperspectral data will allow us to analyze the scattering profile of the nanoparticles and determine if the particles have entered the cell, or if they have only accumulated along the cell membrane. Hyperspectral data will also allow us to determine if particles have aggregated inside the cell. Final confirmation of cellular uptake will be completed by taking high-resolution TEM images of the cells as was presented by Kong (Kong et al., 2008). High-resolution and hyperspectral imaging will allow us to determine a difference between targeted and non-targeted particles and allow for future experiments to determine mechanism of entry.

Once cellular uptake of the targeted nanoparticles has been confirmed, multiple assays will be run to determine how the particles entered the cell. The first assay will optically determine if the Glu-AuNPs have entered the cells via endocytosis. Endosomal DNA of the SkBr3 cells will be transfected with red fluorescent protein (RFP) and cells will be prepared as previously described. Conjugated nanoparticles will be added in the same procedure as the previous step and imaged using the same darkfield setup. In addition to the normal darkfield image captured, the microscope can be switched to darkfield fluorescence mode so that the RFP labeled endosomes can be imaged. As well, hyperspectral images of both the darkfield and fluorescent images will be acquired under the same setup. The information from these images will allow us to localize nanoparticles and endosomes which will allow us to determine if nanoparticles are being endocytosed.

A second experiment to independently confirm that the Glu-AuNPs do not enter the cell via endocytosis will be to block endosomal formation using sodium azide, as presented by Chithrani et al. (Chithrani et al., 2007) In this experiment, cells will once again be cultured and plated as in previous studies, however they also will be treated with sodium azide as an endosomal blocking compound. Once the cells are treated, conjugated and non-conjugated nanoparticles will once again be added to the cells for 20 minutes and then rinsed with PBS. The cells will once again be imaged using a darkfield microscope and hyperspectral information will also be recorded. If data the shows that there are nanoparticles inside the cells, this will be a second validation that they did not enter the cells via endocytosis, and further investigation into how the particles entered the cell will be necessary.

The previous experiments will not be enough to confirm how the nanoparticles enter the cell. We hypothesize that Glu-AuNPs will enter via the GLUT1 transporter; however, to prove this hypothesis, a competition assay with D-glucose is necessary. Studies by O'Neil and Nitin have demonstrated decreased uptake of fluorescent deoxy-glucose (2-NBDG) when both 2-NBDG and D-glucose were added to the same batch of MCF-7 cancerous cells (O'Neil et al., 2005; Nitin et al., 2009a). These studies concluded that 2-NBDG entered the cells via the GLUT1 glucose transporter because the uptake of the fluorophore was competitively inhibited with the presence of D-glucose. Using this concept, glucose conjugated AuNPs and D-glucose will be added to the same batch of cells in a competition assay similar to the assay performed by O'Neil and Nitin. Cells will be plated for 48 hours and treated as in previous studies. However, this time a combination of D-glucose and Glu-AuNPs will be added to the cells; as well, there will be a control of only AuNPs and a control of D-glucose only added to cells so that a qualitative and quantitative comparison can be made. Cells will once again be imaged under darkfield microscopy; additionally hyperspectral data of the cells will be acquired for further comparison. If it is determined that D-glucose inhibited the entry of nanoparticles into the cancerous cells, then that will further elucidate the mechanism of entry for glucose conjugated gold nanoparticles. The final experiment will be to determine how the different sizes of the gold nanoparticles affects the entry of the bioconjugate into the cell. Due to the small size of GLUT1, it is hard to envision large nanoparticles being able to cross the membrane through the small pore of the GLUT1. To determine the size limit, AuNPs of varying diameter (1.5, 3, 5, 10 nm) will be synthesized and capped with cysteamine as in previous experiments. SkBr3 breast carcinoma cells will be cultured and plated as outlined in previous steps; the cells will also be treated with sodium azide to inhibit the formation of endosomes so that we can ensure the larger particles do not enter via endocytosis. D-glucose will be added to the AuNPs as outlined in previous steps, and then they will be added to the cells in the same manner as previous experiments. Cells will then be imaged and hyperspectral information will be acquired as in previous steps. Information will be compared between images to determine if larger particles were able to enter the cell.

In summary, we aim to target small (~1.5 nm) gold nanoparticles using D-glucose to target the increased GLUT1 expression seen in breast cancer. We aim to elucidate the mechanism of entry of these particles into SkBr3 breast cancer cells to determine if glucose conjugated AuNPs have a future as an additional type of molecular imaging agents. We will then be able to directly visualize this agent using the wide-field instrument being developed in Project 2.

### *Overall Future Directions*

Our previous work has demonstrated that we have the ability to differentiate cancerous breast tissue from noncancerous tissue using specific biomarker targeted nanoshells. Preliminary data also shows that large slices of *ex vivo* cancerous tissue can be incubated with contrast agents and imaged macroscopically imaged in a span of 10 minutes. One problem with the macroscopic imaging is the scattering signal from tissues is very high in the NIR range. The scattering is due to the presence of water in the tissue that leads to mismatched indices of refraction between water, protein structures, and collagen (Liu et al., 1996). Future work will involve combining a method of “tissue clearing” to lower scattering and enhance signal seen from the targeted nanoshells. Clearing methods such as mechanical and chemical clearing developed by Rylander and Vargas (Vargas et al., 1999; Vargas et al., 2001; Rylander et al., 2008) will be explored as possible answers to removing endogenous tissue scattering, needed for both Projects 1 and 2.

The portable inexpensive imaging systems being developed in Projects 1 and 2, together with the targeted imaging agents in Project 3, have great potential for use to optically identify more than just breast cancer. They are generally relevant for imaging a wide spectrum of biomarkers associated with any type of cancer. The devices provide clinicians the ability to evaluate the heterogeneity of cancerous tissue optically, noninvasively, and rapidly. They provide the potential to give clinicians a fast, macroscopic image of cancerous and noncancerous tissue intraoperatively so that an informed decision may be made about whether negative margins have been achieved during surgery.

## ***Year 5***

### *Part I: Macroscopic Tissue Level Assessment of Nanoengineered Imaging Agents (Project 2/3)*

### Introduction

In the United States (U.S.) in 2011, there were approximately 230,480 new cases of breast cancer and nearly 39,250 deaths from breast cancer (DeSantis et al. 2011). Nationally, breast cancer mortality rates have been in decline from the 1990s (2.2% per year), whereas incidence rates have been increasing. This increase is thought to be a result of the increase in the number of mammograms that has come about in the U.S (DeSantis et al. 2011).

Ninety-five percent of breast cancers are classified as adenocarcinomas; the other classifications include: squamous cell carcinomas, phyllodes tumors, sarcomas, and lymphomas (Lester 2004). There are two divisions of carcinomas: in situ and invasive. In situ indicates that the cancerous cells have not broken through the ducts or lobules in which the cancer has originated, and the cells are still limited by the basement membrane. Ductal carcinoma in situ (DCIS) is seen approximately four times more frequently (80% vs. 20%) than lobular carcinoma in situ. In situ incidences have increased recently due to technology improvements and the increased number of mammograms due to increased breast cancer awareness (DeSantis et al. 2011; Lester 2004; Nguyen et al. 2009; Atkins et al. 2012). Even though in situ carcinomas have not spread beyond the duct or lobule of origin, they can still be very dangerous because the malignant cells can spread throughout the entire duct or lobule and take up a very large volume in the breast (Lester 2004).

There are six types of invasive carcinoma, about eighty percent of all invasive carcinomas are deemed no special type (NST), also known as invasive ductal carcinoma (IDC), which can not be classified as a specific subtype (Lester 2004). These cancers have a wide variety of protein and gene expression, and there have been recent studies that have looked to classify these cancers more specifically by their expression profiles so that more specific prognoses and treatments can be accomplished. These will be explored later in the manuscript. Invasive lobular carcinoma (ILC) is the second most common breast adenocarcinoma, occurring at a rate of ten percent of all invasive carcinomas. ILC requires a different type of treatment and monitoring regiment. First ILC metastasizes to different organs than other breast cancers (Lester 2004), such as the GI tract, ovaries, and uterus. Additionally, chemotherapeutic treatment of ILC is difficult to monitor using Positron Emission Tomography and Computed Tomography scans (PET/CT) because detectors have more difficult time detecting the radioactive isotopes that target the malignant tissue (Schelling et al. 2000; Norbert Avril et al. 2001; Groheux et al. 2011; Chung et al. 2006), which may be due to the differences in cell densities between the cell types and their respective infiltration into surrounding tissues (N Avril et al. 2000; Lim et al. 2007).

Other breast adenocarcinomas include tubular carcinoma, which accounts for six percent of invasive carcinomas and ten percent of cancers less than one cm. Ninety-five percent of these cancers will express hormone receptors and they are well-differentiated (Lester 2004). Medullary carcinoma occurs in approximately two percent of invasive carcinomas. It is characterized by high nuclear grade and proliferation rates, yet despite these factors, it still has a higher prognosis than IDC. Invasive mucinous carcinoma also occurs in about two percent of invasive carcinoma and grows slowly over the course of years. It is very soft and looks like gray-blue gelatin. Two other invasive carcinomas include invasive papillary carcinoma and metaplastic carcinoma. These cases are both very rare, less than one percent of all invasive breast cancer; disease heterogeneity and rarity makes it difficult for physicians to institute patients' prognoses for these types of cancers.

There are also rare cases of stromal tumors in the breast that includes benign fibroadenomas, sarcomas, and phyllodes tumors. Fibroadenomas is the most common of benign tumors and is often presented as a palpable mass, which allows for patients to discover them with a self-examination. Phyllodes tumors originate in intra-lobular stroma that are palpable, but are rarely detected in mammography (Lester 2004). Most phyllodes tumors are benign, but those that are more aggressive have been shown to over-express epidermal growth factor receptor (EGFR), a receptor whose overexpression correlates with cell proliferation (Tse et al. 2009). Sarcomas of the breast are very rare that present as large masses. One area of concern for physicians is that there is a slight risk of angiosarcoma formation (0.3-4%) in the breast after a patient receives radiation therapy to treat the primary breast cancer (Lester 2004).

As mentioned previously, there have been studies to classify all breast carcinomas by receptor phenotype that are geared towards helping physicians determine treatment options and prognosis for patients (Lowery et al. 2011; Tamimi et al. 2008). Cell types have been broken into three main subtypes based on protein expression: luminal, HER2 overexpressing (HER2+), and basal-like. Luminal tumors are characterized by the expression of hormone receptors progesterone and estrogen (ER+/PR+) (Lowery et al. 2011; Tamimi et al. 2008). Tamimi further differentiates the luminal subtype into luminal A&B depending on the overexpression of HER2 on the surface. HER2+ cells are classified as hormone receptor negative, but the HER2 receptor is over-expressed. Finally, basal-like cells are negative for all three receptors, and are also known as triple-negative cancers (TN). Luminal tumors have been targeted with an anti-estrogen drug, Tamoxifen, that has demonstrated success in lowering recurrence and increasing long-term survival of patients that are ER+ (Shao and Brown 2004). However, tamoxifen treatment can cause endometrial cancer and cells will develop tamoxifen resistance (Shao and Brown 2004). Additionally, ER+ patients can receive oophorectomy, to remove sources of estrogen from the body. These two treatments have been recommended for combinatorial use to remove malignant tissue and lower the chances of recurrence and metastasis (Rodríguez Lajusticia, Martín Jiménez, and López-Tarruella Cobo 2008). HER2+ cancers over-express the growth factor receptor ErbB2 (Wang et al. 2011). Breast cancers of this molecular phenotype will be discussed in greater detail in a later section. TN cancers are of major concern for physicians and patients because the lack of receptors on the surface do not allow for targeted therapy that is seen with the other two subtypes of cancer (Duffy, McGowan, and Crown 2012). Lowery et al. showed that TN patients were more than likely to have a recurrence of cancer when compared to the luminal type cancers (Lowery et al. 2011). This is a result of a lack of a properly targeted therapeutic that physicians can use to treat the tumors.

There are three major treatment methods for breast cancer patients: chemotherapy, radiation therapy, and surgery. Chemotherapy involves the administration of agents to the body that will cause damage to the malignant cells. However, these compounds are also toxic to healthy cells in the body, so physicians have to balance the drugs' potential health benefits with the overall health of the patient. Chemotherapeutics can be administered pre-surgery (neoadjuvant) to reduce tumor volume before patients undergo surgery (Kaufmann et al. 2006; Margenthaler 2011). They can also be administered after surgery to control tumor recurrence and metastasis. The two main types of chemotherapeutic agents are small molecule therapeutic agents and biologically specific targets (J. H. Lee and Nan 2012).

Small molecule agents include anthracyclines and taxanes Anthracyclines' mechanisms of therapy include inhibiting DNA synthesis and creating free radicals in the cells that attack DNA (J. H. Lee and Nan 2012). Studies have shown that using multiple anthracyclines in combination raises the efficacy of the drugs (Jassem et al. 2001), but there is cardiotoxicity associated with anthracyclines that limits the amount that can be administered to the patient (Livi et al. 2009). Taxanes, which include the drug paclitaxel, disrupt microtubule formation and function to disrupt mitosis. Because taxanes and anthracyclines have different mechanisms (and therefore different mechanisms of toxicity to healthy cells), combination of these therapies has proven an effective method of prolonging survival of patients (Bria et al. 2005).

Biologically specific agents are targeted at specific receptors on the surface of cancers such as ER, PR, and HER2. VEGFR (vascular endothelial growth factor receptor) is another important surface receptor in tumor health because it stimulates angiogenesis and vasculogenesis that build blood vessels specifically for the tumor when bound with VEGF (J. H. Lee and Nan 2012). Bevacizumab is an anti-VEGFR (VEGF receptor) antibody that competitively inhibits VEGF binding and prohibits vessel formation for the tumor area. As a single therapeutic, there is a very low response (9.6%) (Cobleigh et al. 2003), but when boosted with an anthracycline, the time to disease progression in head and neck cancers more than doubles (Baselga et al. 2005). The combination of these drugs can also be used t lower toxicity of the small molecule drug. Cameron et al. showed that lapatinib (an anti-HER2 antibody) in combination with the anthracycline capecitabine raised survival time by 11 weeks in comparison to patients treated with capecitabine alone (Cameron et al. 2010). Chemotherapeutics play an important role in patients' treatment plan and have great uses both pre and post surgery. However, cytotoxicity issues will always arise with drugs because they inhibit both healthy and diseased tissue.

Whole breast radiation therapy has been used for decades as a conjunction to breast conservation therapy and has reduced the rate of recurrence and increased long-term survival of patients (Clarke et al. 2005; Vinh-Hung and Verschraegen 2004). However, it delivers a large amount of ionizing radiation to the breast that is dangerous and has potential long-term harmful effects. A newer technology is accelerated partial breast irradiation (APBI) that treats a smaller volume of breast, just around the area of excision and does not expose the whole breast to ionizing radiation. However, one disadvantage is that areas of the breast with a multi-focal tumor will not receive enough radiation and could lead to an increase in tumor recurrence (Margenthaler 2011). There have been recent advancements to improve APBI. The first is interstitial multicatheter brachytherapy that places multiple catheters around the lumpectomy cavity and then delivers radiation through these catheters to localize radiation delivery. The patients can be given high or low radiation dosages, and 5-year recurrence rates ranged from 0-6% (Arthur et al. 2008). Mammosite is very similar to interstitial multicatheter brachytherapy, but in place of multiple catheters, a single balloon catheter that is filled with saline and fills the entire tumor cavity. Radiation is delivered through this balloon twice a day. A 2008 study by Steward et al. showed a local recurrence rate of 3.8% and good cosmetic results (>90%) after a 60-month follow up. One potential downside of Mammosite is that tumors that are in the deep breast might be too close to the heart and deliver too high of a dose to the organ (Stewart et al. 2008). The final option for ABPI delivery is using a 3-dimensional external beam to treat the tumor cavity. This requires extensive planning and modeling to ensure maximized dosage delivery to the tumor cavity because there is no catheter to deliver the radiation. Multiple studies showed no local recurrence three years after treatment (L. J. Lee and Harris 2009; Vicini et al. 2003). There have been many promising developments in radiotherapy to the tumor cavity in the breast, even though whole breast therapy is still the standard therapy for BCT, APBI offers a new method of maintaining cosmesis and minimizing local recurrence.

Surgery still remains the primary method of removing the bulk of breast cancers. There are two main surgical methods, modified radical mastectomy (MRM) and breast conservation therapy (BCT). MRM involves removal total removal of the breast tissue (Yu et al. 2012) that lowers the chance of disease recurrence and removes the need for post-operative radiation therapy (Yu et al. 2012). However, one major downside of MRM is the removal of the full breast, which can be traumatic for the patient. BCT involves the surgeon removing the part of the breast with the malignant tissue and attempting to preserve as much of the breast as possible to maintain cosmesis for the patient. However, there is a higher chance of recurrence (Fisher et al. 2002; McGuire et al. 2009) with this procedure whose factors will be explored in further detail later on in this section. Because of the amount of local recurrences during BCT, surgeons sometimes have to remove larger volumes of breast tissue that has adverse effects on patient cosmesis. A new surgical specialty has developed in response to this problem, termed "onco-plastics," which involves the use of volume replacement or reconstruction of the breast during the BCT after all malignant tissue has been removed (Margenthaler 2011). These are very difficult surgical procedures and are the source of some controversy because it is thought that surgeons who are skilled enough to perform the plastics aspect of the surgery do not have enough knowledge of cancer as breast cancer surgeons and vice versa (Audisio and Chagla 2007). Because of these complications Clough et al. developed a two-tier classification system (Clough I&II) based on the percentage of tissue being removed from the breast (Clough I <20%) that helped surgical teams decide on specialty of the surgical procedure (Clough et al. 2010; Margenthaler 2011). Margenthaler defines Clough II surgeries as a surgery where two surgical specialists are present (breast and plastic) that work in tandem to complete the complicated procedure; these surgeries include radial excision lumpectomy, batwing mastopexy lumpectomy, and lumpectomy with concurrent reduction mammoplasty (Margenthaler 2011).

Technical advancements in breast cancer screening technologies have led to the detection of smaller and smaller cancerous lesions within the breast (Nguyen et al. 2009; Osborn et al. 2011). Due to the decreased size of the lesions, a higher amount of patients are opting to undergo BCT followed by radiotherapy than the more traditional MRM (Pleijhuis et al. 2009). Recent studies have shown that there is no difference in long-term survival rates for patients that undergo the respective treatments for early stage breast cancers (Veronesi et al. 2002; Fisher et al. 2002; Mahmood et al. 2012; Miles et al. 2012). While BCT is optimal for cosmesis because it preserves the original breast, many studies have shown that local recurrence occurs at a higher rate for patients receiving BCT, especially with younger patients (Beadle et al. 2009; Cabioglu et al. 2007; Tanis et al. 2012). Even though the rate of recurrence does not effect overall survival rate (Miles et al. 2012), patients must undergo re-excision and increased radiation dosage (Guidroz et al. 2011; Pleijhuis et al. 2009). Additionally, these patients undergo stress and psychological trauma that has an additive effect on the stress already seen with initial treatment (Mannell 2005; H.-C. Yang et al. 2008). Most importantly, local recurrences have been associated with increased rates of metastases in patients (Kreike et al. 2008; Voogd et al. 2005), which leads to an increased mortality rate.

Many retrospective studies have been conducted to determine the factors that lead to a local recurrence after therapy (Pleijhuis et al. 2009). These studies include patient age (Yildirim 2009; Komoike et al. 2006; Nottage et al. 2006; Cèfaro et al. 2006; Vargas et al. 2005), tumor size(Yildirim 2009; Cèfaro et al. 2006; Aziz et al. 2006), radiation treatment (Komoike et al. 2006; Nottage et al. 2006; Aziz et al. 2006), and lymph node status (Yildirim 2009; Gülben et al. 2007; Aziz et al. 2006) among many. Even though these studies found that these factors can be used as independent predictors of a local recurrence of breast cancer, tumor margin status is still thought of as the strongest predictor for recurrence (Karni et al. 2007; Ali et al. 2011; Houssami et al. 2010; Schwartz et al. 2006).

The tumor margin is the area around the edge of the resected tissue specimen of the patient. Tumor margin status refers to the question of whether or not there are microscopic cancer cells located at the edge of the excised tissue specimen; a positive status indicates microscopic disease, whereas negative indicates disease free tissue. It is generally thought that if there are cancerous cells on the edge of the tissue, then the patient has an increased chance of a local recurrence due to the increased chance of cancerous cells not being removed from the body (Houssami et al. 2010). However, this is where the consensus on margin status ends, and argument begins (Houssami et al. 2010). Many studies have argued and presented evidence as to what constitutes a proper negative margin for patients (Singletary 2002; Carlson et al. 2009; Zavagno et al. 2008; MacDonald and Taghian 2009; Luini et al. 2009). In particular, the argument over what is the proper distance from the edge of the tissue that must be disease free in order for the patient to have negative margins. For example, Zavagno used a distance of 3 mm whereas a panel led by Kauffman recommends that as long as there are no cells “touching ink” then the patient should be declared to have free margins, effectively a margin distance of 0 mm (Zavagno et al. 2008; Kaufmann et al. 2010). Additionally, some studies use a third diagnosis: a close margin. Close margins are defined as tissues that contain microscopic disease within the pre-determined margin width, but not at the edge of the tissue. This leads to the conclusion that it is very difficult to compare studies that use different indications of negative margins; however, it is still accepted the margin status (regardless of definition of distance) is still an important predictor of local recurrence.

The distance in margin status is important in BCT because surgeons are trying to strike a balance between treating the disease while also maintaining cosmesis for the patient. Studies have shown that having a more normal breast appearance has positive psychological effects for patients who have undergone breast cancer treatment (Rowland et al. 2000; Al-Ghazal, Fallowfield, and Blamey 2000; Chakravorty et al. 2012). Increasing margin width will add to the amount of excised tissue during surgery leading to a higher difficulty of maintaining cosmesis (Fentiman 2011) and perhaps leading to future psychological problems for a patient. In 2010, Houssami et al. performed a meta-analysis of 21 margin status studies to determine how well margin status and width correlated with local recurrence rates. The authors found that positive (or close) margins correlated positively with margin status and patients with a negative margin status had a lower rate of recurrence. However, the study also concluded that the increasing the tumor margin width (ranges of different studies were 1-5) did not significantly lower the rate of recurrence, especially when they considered if the patient received a radiation therapy boost (Houssami et al. 2010). However, Houssami et al. did recommend that surgeons use at least a 1 mm margin width when determining margin status in contrast to the "touching the ink" method recommended by Kaufman (Kaufmann et al. 2010; Houssami et al. 2010).

Even though proper margin width is debatable throughout the medical community, the principle of removing as much diseased tissue as possible during surgery still holds paramount to reducing local recurrence. There are many ways that physicians can increase the amount of diseased tissue removed by obtaining information about the tumor preoperatively (Pleijhuis et al. 2009).

Pre-operative imaging includes mammography, which allows the surgeon to assess the borders and a palpable tumor before the procedure begins. Additionally, physicians can determine if there are micro calcifications in the breast, an indicator of possible DCIS presence (Cho et al. 2008). A recent study by Rauscher et al. discovered that mammography has a high sensitivity in cancerous detection (94%), however it is lacking in specificity (61%) due to the presence of islands of fibroglandular or fibrocystic tissue in the breast that are indistinguishable from malignant tissue (Rauscher et al. 2008; Ikeda et al. 2003). In some patients, ultrasound is used to supplement mammography findings because it provides better information on size and growth pattern of tumors (Pleijhuis et al. 2009). Magnetic resonance imaging (MRI) is a newer technology that provides significant improvement in pre-operative imaging of cancerous tissue when compared to mammography and ultrasound (Van Goethem et al. 2007). MRI provides patients and physicians with extensive information, such as multifocality of the disease, that can help determine if a patient should even undergo BCT (Jacobs 2008). A study by Houssami et al. demonstrated that MRI helped detect additional cancer in 16% of patients, leading 1.1% of patients select a mastectomy over BCT (Houssami et al. 2008). Even though MRI can help direct patients away from a surgery in order to decrease the chance of local recurrence, its preoperative use does not have a significant impact on margin status or local recurrence (Solin et al. 2008; Pengel et al. 2009). This is probably due to there not being a means to provide an intra(peri)-operative MRI (Morrow and Freedman 2006).

Due to limitations of implementing pre-operative techniques intra-operatively and their minimal effect on overall margin status and local recurrence, methods of peri-operative tumor localization have been developed to improve resection of tissue. For 20 years the standard for intra-operative localization was wire-guided localization (WGL). WGL involves placing a pre-operative procedure in which a wire is placed in the tumor under the guidance of ultrasound, X-ray, or mammography. The surgeon would then use the wire's location during surgery to help extract diseased tissue. There were many problems with this procedure; firstly, the wire tended to move between procedure and surgery, the wire did not provide 3-dimensional information for the tumor (making edges of the tumor difficult to locate), and it was very uncomfortable for the patient (Pleijhuis et al. 2009; Kelly and Winslow 1996). Recent studies also demonstrate that WGL was ineffective, with 21-43% of patients diagnosed with positive margins (Thind et al. 2005; Burkholder et al. 2007; Medina-Franco et al. 2008) after surgeries implementing WGL. A newer technique is intra-operative ultrasound (IOUS) guided excision that uses ultrasound in the surgical suite to guide resection of both palpable and non-palpable tumors. Several studies have shown that positive margin rates for this technology range from 3 to 11% (Bennett, Greenslade, and Chiam 2005; Ngô et al. 2007; Rahusen et al. 2002; Moore et al. 2001), with Rahusen's study directly comparing IOUS to WGL and showing a much better sensitivity (11% positive margins for IOUS compared to 45% for WGL) (Rahusen et al. 2002). However, IOUS cannot detect the micro-calcifications that are associated with ductal carcinoma in situ (DCIS) which limits the usefulness of the technique. X-ray radiography of the excised tissue is another intra-operative technique to improve patients' margin status. However, this technique has very low sensitivity and is limited to detection of tumors without calcification (Huynh, Jarolimek, and Daye 1998). Cryoprobe-assisted localization (CAL) is another methodology that is helpful in resection of non-palpable tumors. An ultrasound helps guide a cryoprobe into the tumor, which then freezes the tumor into a detectable sphere that is easier to find and remove. Tafra et al. found that there was no significant difference between CAL and WGL in reducing the amount of positive margins or rates of re-excision; however, there was a significant reduction in excised tissue volume which improved cosmesis (Tafra et al. 2006). Even though these techniques have shown promise as an intra-operative technique for margin detection, each has its limitations and are still used as a supplement to surgery. They have also yet to replace the gold standard for peri-operative margin detection: intra-operative pathology.

Intra-operative pathology involves the use of an on-site pathological team that slices, stains, and analyzes the resected specimen while the patient is still under anesthesia. The pathological team will stain the different edges of the tissue to give spatial orientation of the tissue so that the physician can tell the physical location of malignant tissue with regards to the edge of the resected specimen. The tissue or cells are then stained for hematoxylin and eosin (H&E) (Rusby et al. 2008). A pathologist then reads analyzes the samples and informs the surgeon where there is still microscopic disease present. The surgical team will then decide whether to proceed with a re-excision. Hematoxylin is a blue stain that stains DNA in the nucleus, and eosin is a pink dye that stains other cellular structures. There are two different methods of intra-operative pathology, frozen section analysis (FSA) and intra-operative touch prep cytology (IOPTC).

FSA involves freezing, slicing, staining, and a pathologist analyzing samples to determine the presence of malignant cells. The pathologist will work with the surgeon while the patient is under anesthesia, and the team of physicians will determine whether or not the surgeon needs to remove more tissue from the patient. This process adds an average of 30 minutes to each surgery (Riedl et al. 2009). While there is risk with holding the patient under anesthesia for an extended amount of time, the benefits outweigh the risks because this procedure decreases the chance that patients will have to undergo a second surgery (and subsequently go under more anesthesia) and increased radiation dosage. Since 1994, M.D. Anderson Cancer Center (MDACC), a leading cancer research institution, has been performing FSA during BCT. In a 2007 article published by Cabioglu et al., the authors evaluated the effectiveness of the FSA procedure at the institution and found that the overall accuracy of the procedure was 87.4% (Cabioglu et al. 2007). Studies by Camp, Riedl, and Olson showed that 24-27% of patients undergoing lumpectomy had additional tissue resected after FSA (Camp et al. 2005; Riedl et al. 2009; Olson et al. 2007) during the same surgery, however Camp and Riedl's studies did not show an overall improvement in local recurrence (Riedl et al. 2009; Camp et al. 2005). Additionally, studies have shown that FSA has high specificity but a lower and more inconsistent sensitivity rate (Cabioglu et al. 2007; Cendán, Coco, and Copeland 2005; Olson et al. 2007). Pleijhuis et al. concludes that while FSA lowers the need for a second excision, it does not reliably improve negative margin rates (Pleijhuis et al. 2009).

IOPTC has been promoted as an alternative to FSA because of its speed, simplicity, and relative low cost (Creager et al. 2002; Bakhshandeh et al. 2007). Its process involves placing a glass slide at the edge of the tissue. Surface characteristics of the cancerous cells will allow them to stick to the slide, whereas the benign mammary cells do not. The cancerous cells are then stained with using H&E, or other cellular stains (Valdes et al. 2007; D'Halluin et al. 2009), and margin status is determined. A study by Weinberg et al. showed that IOPTC significantly lowered recurrence rates (2.8% vs. 8.8%) when compared to all other margin assessment procedures (Weinberg et al. 2004); however this study did not take differentiate between patients who received intra-operative pathology or just had permanent analysis performed post-operatively. Additionally, IOPTC is good for determining if there are malignant cells on the edge of the tissue, but does not give any indication if there are cells within the margin width, and pathologists will not be able to tell if there are close margins (Pleijhuis et al. 2009; Cabioglu et al. 2007). Additionally, there may be scarring, cell damage, and artifacts on the edge of the resected tissue as a result of the cauterization that the surgeon has to perform when the specimen is removed (Singletary 2002).

While both FSA and IOPTC are promising techniques, they still have limitations. Firstly, they require an on-site pathological team consisting of technicians and a pathologist. This is not feasible in many community hospitals due to costs and number of physicians (currently, <5% of hospitals offer this service) (Bydlon et al. 2010). There is a vast unmet need for surgeons to be able to visualize tissue peri-operatively without the use of a full pathological team. While there has been success in developing technologies and techniques that help physicians determine margin status, there is always room for improvement. We are now going to look at some future techniques that have a wide range in stages of development, from taking part in clinical trials to still being developed on the bench-top.

One device that has been developed for use in a clinical setting is the MarginProbe™ from Dune Medical Devices. The device is a spectroscope that measures the response of cells when interacting with broad range of radiofrequencies (Karni et al. 2007). The device has a detection volume of about 38.5 $mm^3$ that uses an algorithm to compare signal reflected from tissue to previously recorded signal from tissue. It gives the surgeon a simple readout of negative or positive using this algorithm. The sensitivity of the device over a range of margin widths averaged 67% sensitivity and a specificity of 68% (Karni et al. 2007). Another study by Allweis et al. demonstrated that the MarginProbe™ was effective at lowering rates of a second surgery (12.6% to 18.6%) that was not statistically significant. Additionally, the volume of excised tissue for the device was higher than that of the control group, which may have skewed the results in the device's favor (Allweis et al. 2008). Even though the device is not as effective as other options, it does show that there is potential for development of an intra-operative tool for surgeons to use as a supplement to already existing technologies.

Positron Emission Tomography (PET) has been used for imaging malignant breast tissue for many years (Pons, Duch, and Fuster 2009; Schelling et al. 2000; Wahl et al. 1991), especially as noninvasive method of monitoring chemotherapeutic response (Kumar et al. 2009). PET uses a radio-labeled glucose analog $^{18}$F-FDG that accumulates in areas of high metabolism, such as malignancies (Bos et al. 2002). PET has a high sensitivity value in detection of large lesions (>1 cm) (Minamimoto et al. 2007; Schelling et al. 2000; Kaida et al. 2008) but its specificity is low due to accumulation in non-malignant cells that are associated infection and inflammation (Gulec, Daghighian, and Essner 2006). In addition to the sensitivity and specificity concerns of PET, it originally was not a good candidate for intra-operative imaging because the device was large and not practical for a surgical suite. However, recent technological developments have enabled hand-held PET probes in colorectal (Strong et al. 2008), renal (Strong et al. 2008), ovarian (Cohn et al. 2008), and breast cancer (Hall et al. 2007). The handheld probes are a very nice proof of concept; however, for BCT implementation, there is still the issue that PET has trouble detecting lesions under 1 cm, and with recent screening technologies being able to detect lesions smaller than that, the handheld probe would not be very useful during BCT because it could not detect something below its resolution limit. Additionally, the use of a radio labeled tracer in the surgical suite not only has safety implications for the patient but for the entire surgical staff (Heckathorne, Dimock, and Dahlbom 2008), and repeated exposures may have long-term carcinogenic effects on surgeons.

Another radio labeled visualization technology is radio guided occult lesion localization (ROLL). This technology is described as a theranostic device that can both visualize and resect the desired tissue from the patient. ROLL is similar to WGL in that it uses a pre-operative procedure to inject a non-targeted radioisotope into the tumor. During the surgery, a handheld gamma probe locates the isotope in the tumor and guides excision. As with WGL, the placement of the isotope is paramount to maintain specificity and sensitivity. Studies have shown correct placement of the radiotracer in 95-100% of cases (Medina-Franco et al. 2008; Thind et al. 2005; Sarlos et al. 2009; De Cicco et al. 2002; Rampaul et al. 2004). This technique shows approximately the same clinical success as WGL, 20% of patients in the study by Sarlos et al. had positive margins post-operatively (Sarlos et al. 2009) and surgeons were able to detect the lesions at a rate of 98%. Even though, ROLL achieved the same clinical results as WGL, it was found to be more comforting for the patients and an easier technique for surgeons to perform (Rampaul et al. 2004). Even though ROLL seems to be a healthy alternative to WGL, surgeons have yet to see an improvement in re-excision rates for this technique, which probably means that the limitations seen with both technologies are probably from the pre-operative placement and the imaging device used to implant the radiotracer or wire.

The next evolution of imaging breast cancer in the clinic is through the use of optical imaging with targeted contrast agents and autofluorescent signal of tissue. Currently, near-infrared fluorescence (NIRF) has shown strong development and progress as a clinically relevant breast cancer imaging modality (Pleijhuis et al. 2009); however, most clinically relevant trials have been limited to mapping sentinel lymph nodes with incodcyanine green (ICG) (Tagaya et al. 2008; Sevick-Muraca et al. 2008; Ogasawara et al. 2008; Troyan et al. 2009) and not breast malignancies (Pleijhuis et al. 2011). NIRF is considered a strong candidate for optical imaging of breast cancer because it has resolution down to 10 μm, higher penetration depth than light in the visual range, and autofluorescence of molecules in this wavelength is reduced (Troyan et al.

2009; Pleijhuis et al. 2011; Pansare et al. 2012). Even though NIRF has shown great potential in cancer studies, it still is still limited to the use of contrast agents that must be injected into the patient, and there are still many cytotoxicity issues involved with the agents inside the patient, especially at the levels needed to differentiate tissue (Pansare et al. 2012). However, NIRF contrast agents can still be used on excised tissue which would allow physicians to use the contrast agents' positive aspects while minimizing their negative impact. This possibility will be discussed in a different section.

Other imaging modalities use the endogenous signal differences between cancerous and non-cancerous tissue to attempt to differentiate tissues without contrast agents. These signal differences arise from a difference in oxygenation of blood, hemoglobin content, and cell density (Wilke et al. 2009; Tromberg et al. 2008). One of the most successful of these technologies is Diffuse Optical Imaging (DOI). DOI has been used to measure the absorption of a broad spectrum of NIR light that is directed into specimen. Due to the presence of absorbers such as deoxy-hemoglobin, hemoglobin, lipid, and water, light will propagate through a tissue in different time lengths. These lengths can be measured, and correlated to the presence of specific absorbing molecules that characterize malignant or benign tissue (Tromberg and Cerussi 2010). This data can be combined with other imaging modalities such as mammography, and a quantitative 3-dimensional map of the breast can be created. Additionally, a study by Kurkredi et al. demonstrated tumor only spectra (650-1000 nm range) in 22 cancerous patients versus 43 normal patients (Kukreti et al. 2010). However, those studies were not used to study margin status and reconstructing an image intra-operatively would be very difficult. However, Wilke et al. developed a spectroscopic imaging device that measured β-carotene scattering coefficient in negative, close, and positive margins. The increased coefficient is due to decreased adipose tissue and higher cell density (Wilke et al. 2009). Though this study showed success, (identified 79% of positive tissues correctly), there was decreased accuracy with patients who received neoadjuvant therapy which affected physiologic and metabolic parameters that were used in their algorithm (Wilke et al. 2009); however, this device shows great potential for intra-operative margin assessment.

There are many technologies that have been developed to help physicians visualize diseased tissue intra-operatively. Whether it is through pre-operative procedures, radio-labeled tracers, or using endogenous tissue differences, there are many methods to delineate malignant tissue. As previously stated, less than 5% of BCT are completed with the use of intra-operative pathology assessment (Bydlon et al. 2010). With this in mind, the overall goal of this project has been to develop a method of differentiating malignant breast tissue that has the potential to be used in a portable, inexpensive, and rapid manner, with minimal processing performed on the tissue to maximize speed. Our aim is the construction of a system that can be used intra-operatively without the added cost and time of extra technicians or pathological staff. This system would enable the surgical team to take whole tissue at the margin area, add a targeted contrast agent, and visualize malignant tissue during surgery. Previous work has demonstrated the efficacy of using antibody targeted silica-gold nanoshells (NS) as a visual contrast agent in cells (L. Bickford, Sun, et al. 2008; L. Bickford, Chang, et al. 2008), tissue slices (L. R. Bickford et al. 2010), and even as a theragnostic (Carpin et al. 2011). These studies have demonstrated that the NS can be used in an efficient and rapid (<5 minutes) manner that can be differentiated using a variety of optical imaging techniques. However, these studies were performed on cell lines or tissues that needed to be sliced to obtain images. Tissue slicing requires an element of time, equipment, and personnel that would add to the cost and complications of the surgical procedure.

Additionally, these studies were acquired with expensive imaging equipment, and with exception of the Bickford et al. study from 2010 that utilized a Lucid VivaScope 2500, images were acquired with modalities that do not readily translate to the clinic. There is still a vast unmet need to further research into developing methods of imaging whole tissue rapidly with a portable and inexpensive system used in conjunction with targeted contrast agents.

Our previous research has used silica-gold NS linked to the anti-HER2 antibody that attaches to HER2 on the surface of cells that over-express HER2. HER2 is an EGFR that is part of the ErbB family (Tse et al. 2009), a group of four tyrosine kinase receptors expressed on the surfaces of cells in various levels. When expressed in proper levels, the receptors have an important role in cell growth, proliferation, and differentiation; however, abnormal expression levels are apparent in malignancies of a variety of organs, not just breast, and lead to uncontrolled cell growth (Altintas et al. 2009). The other three receptors include HER3 and HER4, and the commonly known EGFR. The HER2 receptor is most commonly associated with breast cancer because it is found in 25% of all breast cancers and is thought to be a more aggressive subtype of cancer (Altintas et al. 2009; Laurinavicius et al. 2012; Vanden Bempt et al.

2008; Vranic et al. 2010) that is associated with worse clinical outcomes. Even though tumors that are HER2+ are considered to be a more dangerous subtype, the over-expression of the receptor has made its cells an easier target for targeted therapy using a monoclonal antibody against the receptor either trastuzumab (Purmonen et al. 2011; Smith et al. 2007) or lapatinib (Geyer et al. 2006; Gomez et al. 2008). This has also led to research in targeting the HER2 receptor for contrast agents, such as silica-gold NS (L. Bickford, Sun, et al. 2008; L. Bickford, Chang, et al. 2008; Carpin et al. 2011) that can help physicians visualize HER2 status in tissues and cells.

Visualization of growth factor receptors at the margin status could be more important for pathologists than previously thought. As mentioned previously, cells at the tumor margin are stained for H&E, and pathologists use these slides to determine disease extent and margin status. This helps the team of physicians determine the course of action for post-operative treatment of the patient. However, a recent study of oral squamous cell carcinoma by Vosoughhosseini et al. demonstrated that there were cells that over-expressed EGFR in the samples that were deemed to be negative margins by normal H&E (Vosoughhosseini et al. 2012). This is very significant because patients who are declared cancer free, are, in fact, not, which is a possible explanation for local recurrence when patients are declared to have negative margins. Additionally, a false-negative leads to a different post-operative treatment regiment that could possibly allow the cancer to proliferate at a higher rate than if the proper diagnosis was made. Another growth factor, VEGF, has been studied as a possible marker of local recurrence, but there have only been three published studies, so conclusive evidence has yet to be established. Moran et al. found that in only a specific sub-group of patients with local relapse, was VEGF an independent indicator; however when performing multi-variate analysis with that same group, they were not able to reach statistical significance (Moran et al. 2011). Linderholm et al. found that VEGF status contributed to overall survival but did not mention VEGF as a predictor of local recurrence (Linderholm et al. 1999). A study by Manders et al. concluded that VEGF contributed to reducing the effectiveness of radiotherapy in patients with negative lymph node status (Manders et al. 2003). These studies show that physicians are delving deeper into receptor phenotype as indicators for all aspects of the treatment of breast cancer and that there is much to be gained from knowing these phenotypes.

Lowery et al. states that knowledge of the molecular phenotypes in breast cancer will not only help drive treatment decisions that will optimize patient care, but will offer valuable insight into prognosis (Lowery et al. 2011). There have been several recent reviews that have studied the relationship of tumor expression and results such as margin status and local recurrence (Tse et al. 2009; Wang et al. 2011; Miller et al. 2004). Ductal carcinoma in situ (DCIS) was of particular importance to these studies due to the increased incidence and smaller lesions that are a result of the improved screening technologies. Over-expression of HER2 occurs in up to 50% of lower grade DCIS; however, 50-100% of higher grade DCIS over-express the receptor (Altintas et al. 2009). Wang et al. found that patients that were ER-/PR- but HER2+ had a higher rate of recurrence than patients that were ER+/PR+ and HER2- (Wang et al. 2011).A 2004 study by Miller et al. states that in DCIS patients with HER2+ status it was much harder for surgeons to reach negative margins on patients with these characteristics than other types, including invasive carcinomas that were HER2+ (Miller et al. 2004). In 2011, Munirah et al. found that a higher percentage of HER2+ patients had positive lymph nodes (regardless of estrogen receptor status), indicating the aggressiveness of the subtype (Munirah et al. 2011); a 2006 study by Kim et al. showed that HER2+ cancers were the most frequent subtype found in distant metastases (Kim et al. 2006).

Due to the increasing incidence of DCIS (Virnig et al. 2010; Sørum et al. 2010), the increased number of DCIS patients choosing BCT over mastectomy for DCIS (Altintas et al. 2009), the increased prevalence of HER2+ tissue in DCIS (Tamimi et al. 2008), and increased chances of local recurrence with HER2+ DCIS (de Roos et al. 2007; Provenzano et al. 2003) there needs to be a method not only for identifying cancerous tissue at the margins, but HER2+ cells at the margin during BCT for DCIS. As stated previously, Vosoughhosseini et al. demonstrated that normal H&E might not be good enough to identify all cancerous cells at the margin (Vosoughhosseini et al. 2012), and a method to identify HER2+ cells rapidly and intra-operatively gives physicians another tool to ensure negative margins are achieved during excision.

Our aim is to use these targeted contrast agents to differentiate tissue that over-expresses HER2+ tissue from HER2- tissue optically. An imaging system that combines proper optical settings with an agent with a strong signal, such as silica-gold NS, could be an invaluable tool for surgeons intra-operatively as they attempt to achieve negative margins that have been difficult to achieve in HER2+ cancers (Miller et al. 2004). As demonstrated with earlier research, our targeted nanoshells have shown great results in being able to differentiate individual HER2+ cells from noncancerous cells because an average of 1500 nanoshells were bound to each HER2+ cell (L. Bickford, Chang, et al. 2008). This is important because studies deem patients to be HER2+ when there is strong IHC staining in greater than 10 (Kim et al. 2006; Tamimi et al. 2008) – 20% (X. R. Yang et al. 2007) of the cells being examined. During an intra-operative procedure where cells will be visually detected, such a small percentage of cells might be difficult to detect optically using fluorescent markers. This is where the strong optical scattering properties of silica-gold NS offers vast potential for use as an intra-operative contrast agent. Proper excitation light that is tuned to the optical resonance of the NS can be used in conjunction with proper emission and imaging settings to detect the NS, which, in turn, leads to proper detection of HER2+ cells and tissue.

Work described in the paper included in the appendix (currently under review) has demonstrated the ability of the silica-gold NS to differentiate whole tissue sections that were HER2+ from HER2- sections. Additionally, we believed that the localization of the nanoshells was confined to the surface of each tissue section using two-photon microscopy. In the section that follows, we take these findings further and use hyperspectral darkfield imaging to confirm the localization of the NS to the surface of the tissues. Additionally, we use the hyperspectral imaging to demonstrate the spectral changes of HER2+ tissue with nanoshells versus tissue without nanoshells to demonstrate the areas of nanoshell localization.

## Materials and Methods

### *Silica-gold Nanoshell Fabrication and Antibody Conjugation*

Silica-cores were synthesized as described in previous literature (Loo et al. 2004; Loo, Hirsch, et al. 2005; Loo, Lowery, et al. 2005). Briefly, silica cores were fabricated following the Stöber method (Stober, Fink, and Bohn 1968) whose surfaces were then terminated using amine groups. Dynamic light scattering (DLS) determined that the average diameter of the cores was 276 nm. Gold colloid (1-3 nm diameter) was then functionalized to the surface of the silica cores using the amine groups (Duff, Baiker, and Edwards 1993). Once the gold surface was formed, UV-VIS spectrophotometry (Varian Carry 300) (Fig. 1) was used to determine the final diameter and concentration of the particles in solution.

To determine concentration and size of the particles, the experimental absorption, scattering, extinction coefficients were calculated using Mie theory. The experimental theory was then compared to the spectra obtained with the spectrophotometer and final size was determined to be 305 nm peak plasmon resonance of 796 nm. The final concentration of particles was approximately was $1.25*10^9$ particles/ml.

To target the NS against cells that over-express the HER2 receptor, an antibody against HER2 was conjugated to the surface of the nanoshells using previously described methods (Loo et al. 2004). An anti-HER2 antibody was conjugated to the surface via a heterobifunctionalized polyethylene glycol orthopyridyl-disulfide-PEG-N-hyroxysuccinimide ester (OPSS-PEG-NHS) (L. Bickford, Chang, et al. 2008). 450 µl of NS in solution was incubated with 0.6 µl of anti-HER2-PEG solution for 2 hours at 4°C. Then, 2.0 µl of 1.0 mM PEG-SH was added to the solution overnight (12-16 hours) at 4°C to coat the rest of the surface of the NS with PEG to make the particle more biocompatible. Excess PEG-SH was then removed from solution by centrifugation, and the solution was resuspended in a 37°C antibody diluent buffer to a final solution of 165 µl. The nanoshells were now ready for incubation with resected tissue specimens.

### *Ex vivo breast specimens*

Cancerous (HER2+ and HER2-) and normal breast tissue were acquired from the cooperative human tissue network (CHTN) under a institutional review board (IRB) approved protocol. Tumors were classified by both tumor type and recepotor phenotype by a physician at the medical institution that provided the tissue prior to arrival in the laboratory. The tissues arrived pre-frozen in liquid nitrogen and were stored in a -80 upon arrival. They stayed in storage until sampling.

Tissues were thawed in phosphate buffered saline (PBS) at 37°C and then placed on a biopsy board where a 5 mm punch biopsy was taken to maintain consistency between samples. The biopsies were then stained with pathology ink to maintain orientation. The tissues were then incubated with the nanoshell/diluent cocktail for 5 minutes at 37°C under rotation. Samples were then rinsed in PBS 3X and placed in clean PBS prior to imaging.

After incubation, tissues were rapidly frozen in OCT media and prepared for slicing using a cryotome. 8 µm tissue slices were cut at -20°C and placed on slides to dry overnight. A coverslip was then placed on each tissue and the slides were placed under a Cytoviva™ darkfield microscope. A darkfield image of each tissue was then acquired using a Qimaging Exi blue

CCD. After this image was acquired, a hyperspectral image of the same field of view (FOV) was acquired using the Cytoviva™ hyperspectral imaging camera. This image not only gave spatial information, but also provided spectral data for each pixel in the FOV. Spectral data of slices on and below the surface of normal tissue and HER2- and HER2+ cancerous tissue was acquired. The spectra of the illumination lamp was calibrated for each image by dividing each spectral data point by the normalized data point for the lamp spectra. The fields of view were then compared between multiple specimens (n=3 for each tissue type).

## Results

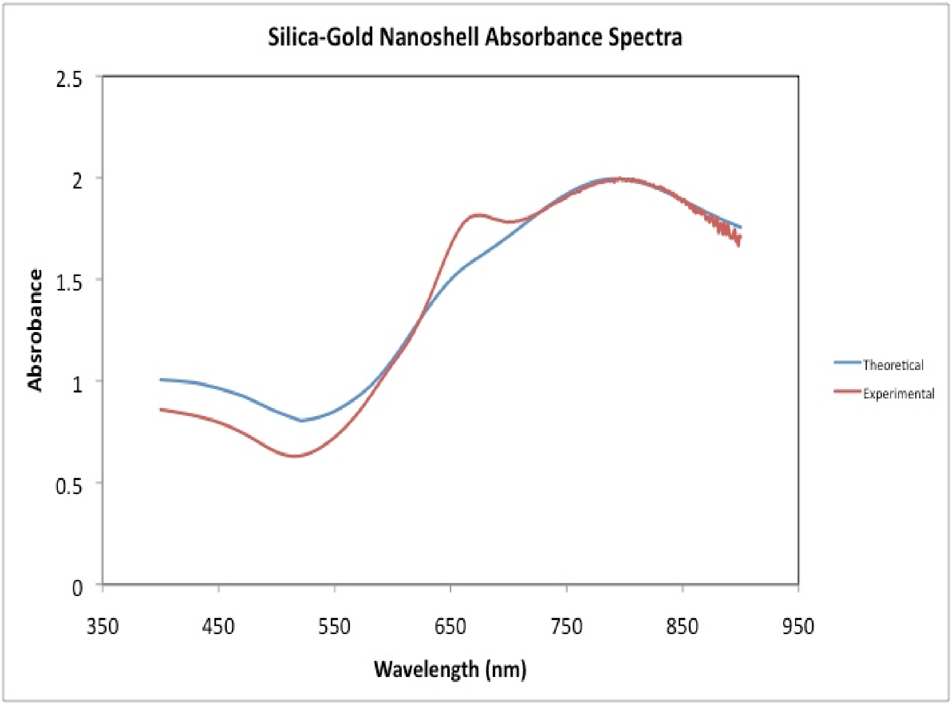

**Figure 5.1.** UV-VIS absorbance spectra of silica-gold NS with 276 nm silica-core diameter and a total diameter of 306 nm (red). The theoretical spectra as calculated by Mie Theory is displayed for comparison. Concentration of the particles in solution was calculated to be $1.25*10^9$ particles/ml.

Figure 5.1 displays the experimental (red) and theoretical (blue) UV-VIS absorbtion spectrum of silica-gold NS with a total diameter of 306 nm and a silica core diameter of 276 nm. Additionally, graphs display the plasmon resonance of the NS to be 796 nm. This is important for future experiments where we are designing an imaging system that will have optimized imaging settings for viewing silica-gold NS in excised tissue.

Figure 2 displays darkfield images of normal, HER2-, and HER2+ cancerous tissue taken with the Cytoviva hyperspectral imaging system taken on the same day and incubated with the same batch of nanoshell/antibody cocktail for 5 minutes at 37°C. 2(A) is the surface of normal mammary tissue after incubation, rinsing, and slicing in the cryotome. 2(B) displays the surface of HER2- malignant tissue (the blue ink is the pathological ink used for spatial orientation). 2(C) and 2(D) are from the same 5 mm punch biopsy of HER2+ tissue, but 2(C) represents the surface of the tissue and 2(D) represents a slice of tissue from approximately 24 μm below the surface of the same tissue. All of the tissues appear to be very different visually, but it is very difficult to visualize nanoshells on any of the tissues without the help of spectral data.

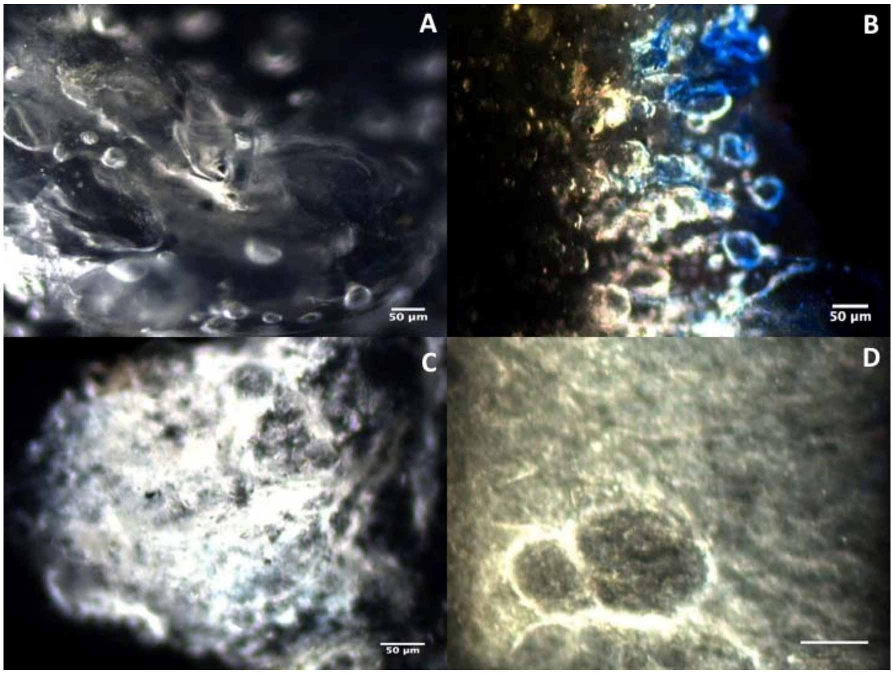

**Figure 5.2.** Darkfield images of (A) the surface of normal mammary tissue, (B) the surface of HER2- malignant tissue, (C) the surface of HER2+ tissue, and (D) 24 μm below the surface of the same tissue in 2(C). Scale bar in D represents 50 μm.

In previously submitted data, we had reported a localization of the nanoshells to the surface of the tissues. In Figure 5.3, the spectra of each of the FOV displayed in figure 2 are displayed. What is interesting is that the surface of the normal tissue and HER2- tissue seem to be more similar to the surface of the HER2+ than the HER2+ tissue below

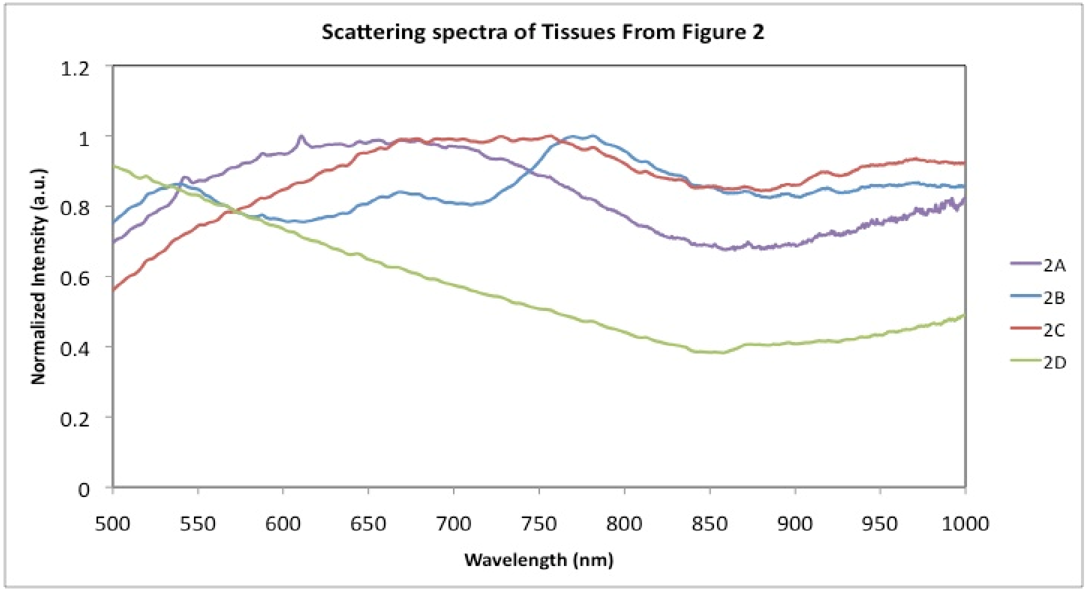

**Figure 5.3.** Scattering spectra of various tissue surfaces incubated with nanoshells that are displayed in Figure 2. 2D represents the spectra of HER2+ tissue 24 µm below the surface of the tissue displayed in 2C. The similar spectra of the surfaces of the tissue could be due to non-specific binding to the surface of the tissues that was seen in other imaging modalities.

the surface. Perhaps this is due to some non-specific binding of the nanoshells to the surface during the incubation period. Our previous data submitted (and currently in submission to a special issue "Molecular Imaging of Breast Cancer" in Journal of Oncology) showed that there were some instances of non-specific binding to the surface of these tissues after incubation, so this is not unexpected. However, there is a stark difference in scattering spectra of the surface of the HER2+ and the tissue below the surface (2C&D). Figure 5.4 is a side-by-side spectral comparison of the HER2+ tissue displayed in figure 5.2; additionally, spectra from HER2+ tissue without any nanoshells added is displayed as a negative control to show the similarity in spectra between tissue without nanoshells and the area below the surface of HER2+ tissue incubated with anti-HER2 silica-gold nanoshells. This demonstrates the localization of the NS to the surface of the tissue.

Figure 5.5 displays the spectra of the surface of three different HER2+ tissues after incubation with anti-HER2 NS and the negative control tissue spectra. Two of the specimens had very different spectra from the negative control, and surface 2 had a very similar spectra to the spectra of the negative control. One reason for this could be that there is low amount of nanoshell binding to the HER2 receptor. There were individual areas of nanoshells that were localized in the hyperspectral image, but perhaps these areas were too small to make a significant contribution to the overall signal of the FOV.

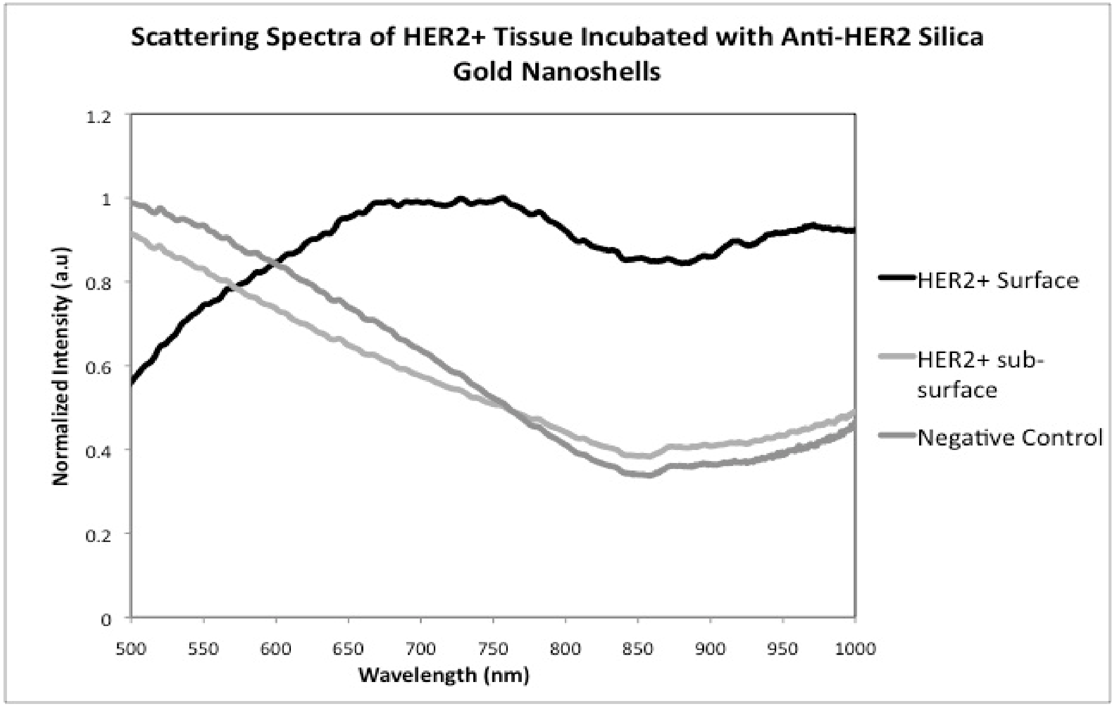

**Figure 5.4.** Scattering spectra of different areas of different localized areas of the same tissue, in addition to a negative control tissue that was not incubated with silica-gold nanoshells. The surface of the HER2+ tissue shows a much different spectra than that of the tissue 24 μm below the surface of the tissue.

Figure 5.6 displays the FOV of the slide from surface 2. 6(A) demonstrates individual areas of the tissue that were sampled and showed a different spectra than that of the overall tissue (6(B)). However, the signal from these isolated areas were not enough to create a large difference in the overall spectra of the tissue. It is interesting to note that individual areas of silica-gold NS can be pictured, but due to the limited number of binding sites, they have a very small contribution to the overall signal.

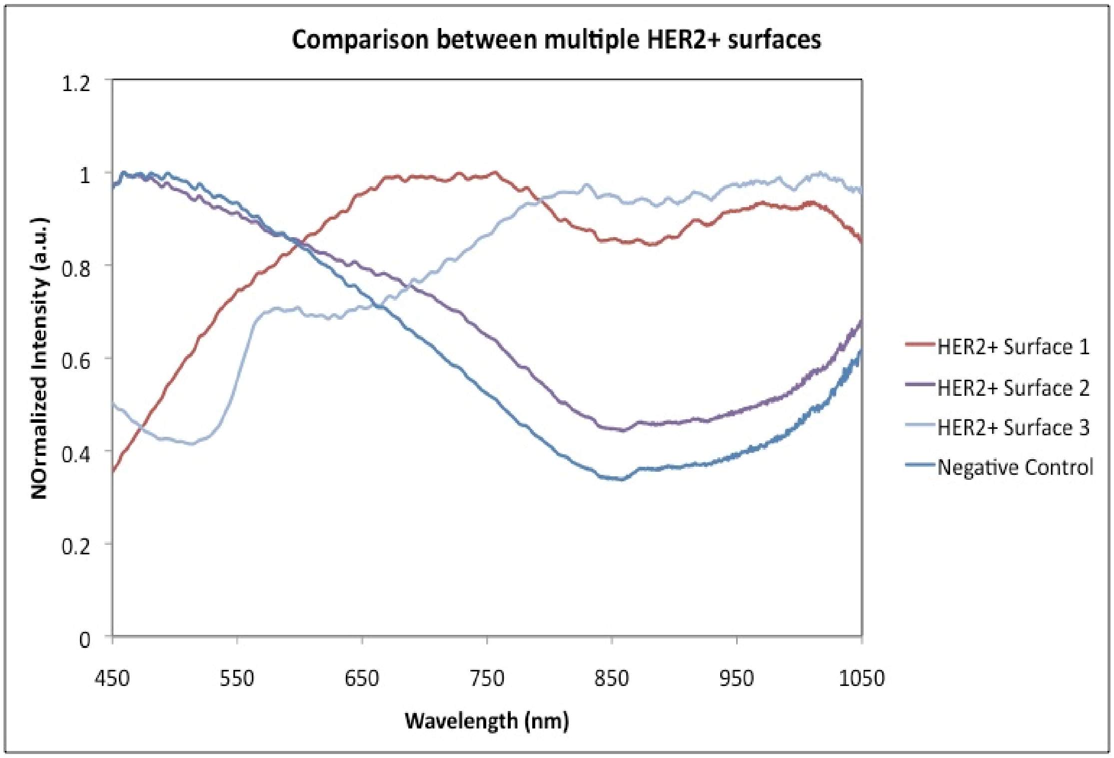

**Figure 5.5.** Scattering spectra of different HER2+ tissue surfaces that have been incubated with anti-HER2 nanoshells. Two of the three surfaces were very different from the negative control, where as surface 2 was very similar to tissue without NS.

## Discussion

The data presented here verifies previous conclusions that anti-HER2 silica-gold nanoshells were limited to the surface of excised tissue. This is important information for physicians to be aware of because it allows them to understand the information that can be obtained using this technology. Additionally, for development of our intra-operative imaging device, we need to be able to confirm that signal from tissues is either from nanoshells, thus making knowledge of the localization of the nanoshells paramount.

Even though this technology has great potential for future clinical use, there are still some pitfalls that need to be addressed. First, there is always going to be intrinsic signal from the tissue that is going to contribute the signal collected. There are ways to control for this. For this experiment we used signal from tissue that had not been incubated with nanoshells for use as a comparison between tissues. This is not the most ideal method, but for this experimental set-up it was necessary. Future whole tissue experiments will attempt to use the same tissue as its own

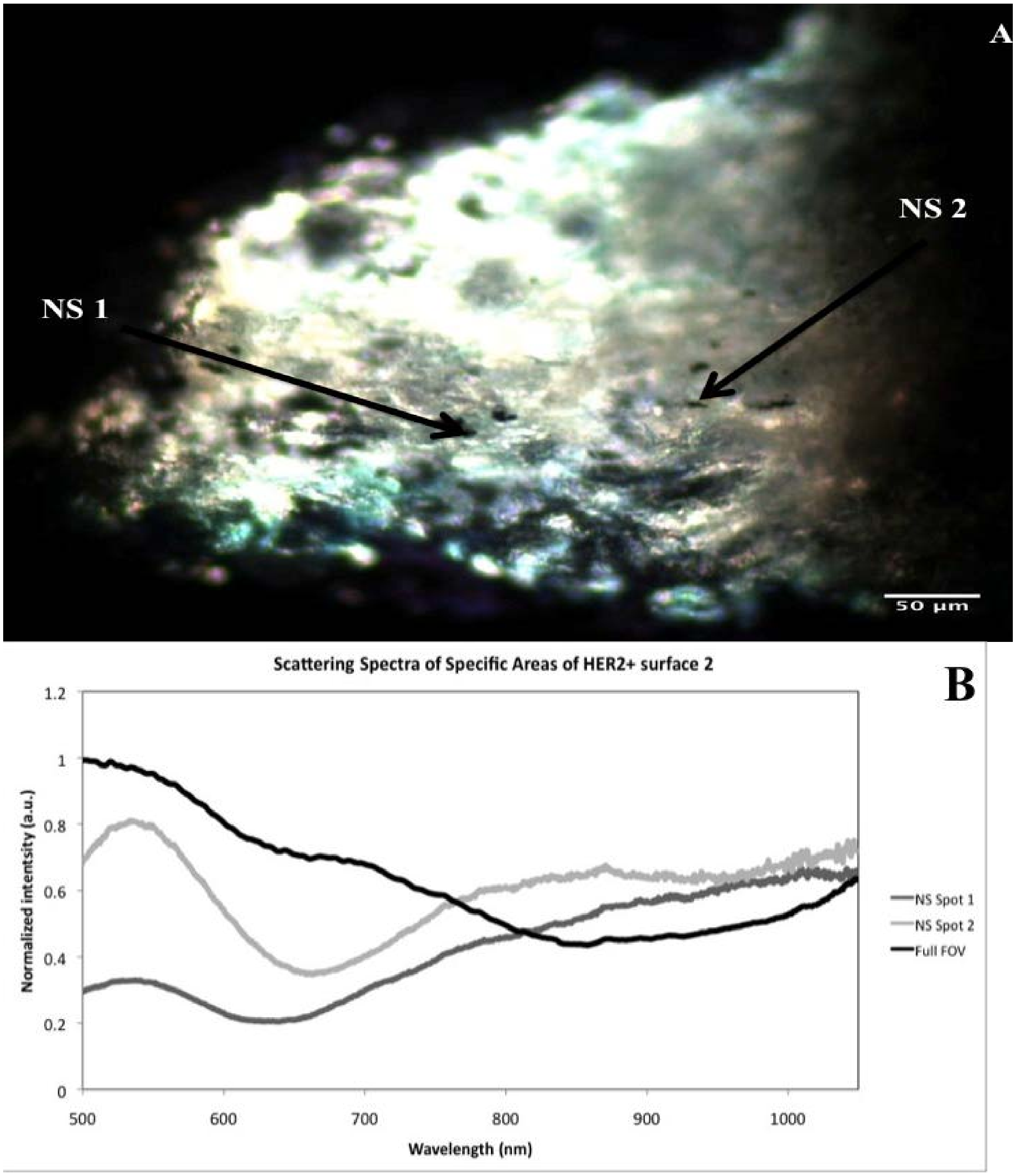

**Figure 5.6.** Darkfield image of HER2+ surface with areas of silica-gold NS pointed out with arrows. Spectral data of the individual NS spots shows different spectral data than the full FOV, showing local areas of NS. However, there was not sufficient binding of nanoshells to contribute to the signal of the full tissue changing.

control, so pre and post incubation data can be acquired from the same tissue and nanoshell effect can be measured with greater certainty.

Another result that is of some concern is from figure 5.5, which showed the spectra of "HER2+ surface 2" having a very similar spectra to that of the negative control. As stated earlier, for a breast cancer to be deemed HER2+, only 10-20% of its cells need to have a 2+/3+ score from a pathologist (Kim et al. 2006; Tamimi et al. 2008; X. R. Yang et al. 2007). This means that the tissue sampled for imaging had a low percentage of HER2+ cells that were bound with NS, meaning that there were less NS to contribute to the overall signal of the FOV. Figure 6 displays the tissue in question and the areas of localized nanoshells that had a different spectral shape than the overall FOV. However, there does not seem to be enough contribution from the NS to the overall signal of the tissue to change its spectral shape. This is important too for margin status because it would be ideal for physicians to visualize where the individual HER2+ cells are and further elucidate the areas of high concern that a surgeon might be able to focus on during the re-excision procedure. Additionally, this shows that there is great difference in tissues' expression of HER2 in just one field of view, which means that areas that scan large volumes, (i.e., the MarginProbe™) might be obtaining inaccurate results due to the subtle tissue changes in a small area. This is a prime example of the heterogeneity of malignancies that all intra-operative margin technologies have to worry about and is one of the downsides of using receptor expression as a target for diagnostic imaging.

### Conclusion

There are many elements that contribute to the discovery, treatment, and complete removal of breast cancer. The heterogeneity of the disease makes a difficult task even more treacherous. From tumor site to protein expression, each type of cancer has presents challenges to the team of physician trying to eradicate the disease. Our focus is on the development of a system that will help surgeons performing breast conserving therapy to remove as much diseased tissue as possible to decrease the chances of a patient having a recurrence of the disease. In this section, we used the over-expression of HER2+ cancerous cells in resected specimens to target an antibody targeted contrast agent that has strong optical properties in the NIR. We were able to confirm the location of these nanoshells to the surface of the tissues which gives valuable information as we move to the next section of our research development: the fabrication of a portable, intra-operative device that can visualize these targeted particles.

## *Part 2: Design and development of a portable, inexpensive macroscopic breast tissue imaging system (Project 2)*

### Introduction

There has been recent development in the field of optical imaging to develop low cost, portable imaging systems that use endogenous fluorescence of cancerous tissues as a screening tool for easy to reach areas such as the mouth, esophagus, and colon (Pierce et al. 2010; Pierce et al. 2011; Nadhi Thekkek, Anandasabapathy, and Richards-Kortum 2011; Roblyer et al. 2009). Additionally, the use of contrast agents to differentiate breast cancer and lymph nodes has also been recently published for both *in vivo* and *ex vivo* tissue specimens (Langsner et al. 2011; Rosbach et al. 2010; H. Lee et al. 2011; Mieog et al. 2011; Aoyama et al. 2011; Sano et al. 2012); however, only the studies by Rosbach and Mieog used a system that was portable and could be readily translated to a clinical setting. However, both of these studies were performed on lymph nodes of the breast. Our goal in this section is to develop an inexpensive and portable imaging system that is optimized for multi-marker imaging. As discussed previously, breast cancers can express certain hormone or tyrosine kinase receptors (ER/PR or HER2) that have been used as targets for monoclonal antibodies as therapeutics. We aim to build a system that can image both estrogen and HER2 in resected specimens that over-express these receptors using targeted anti-HER2 gold silica NS that have shown great efficacy in differentiating HER2+ tissue slices (L. R. Bickford et al. 2010) and in whole tissue specimens using a stereoscope (submitted to J of Oncology). This optical imaging system will be built with off-the-shelf imaging components to minimize cost; additionally, the system will be assembled so that the components all will fit into a standard backpack for ease of transport. In this section, we will show preliminary results of tissue incubated with nanoshells (both targeted and non-specific) that have been acquired with the first design prototype revision and discuss future studies and methods to improve the device so that it can be ready to use in the clinic.

## System Design

Our goal is to fabricate a system that can image multiple markers on excised tissue so that tissues that over-express these markers can be differentiated from tissue that does not express these surface markers. Because of our past experience targeting HER2 over-expression in multiple tissues with silica-gold NS, we decided to optimize our system to visualize the NS signal in the tissue. The other marker we chose to visualize is the estrogen receptor (ER). We choose to image this receptor because, like HER2, its expression leads to treatment with a monoclonal antibody, Tamoxifen. Additionally, as discussed earlier, HER2+ that express ER have a different clinical prognosis than ER- tumors. The ability to image two markers at once might also have significant impact on issues with false-negatives because physicians will be searching for two specific markers, and not just one. If there are low expression levels of one marker, physicians might still be able to identify malignant tissue using the other marker.

In addition to targeting the anti-HER2 antibody with silica-gold NS that can be imaged in the IR, estrogen needs to be tagged with a fluorescent marker to visualize binding in the tissue, in this case we are planning to use fluorescein (FITC), which can be excited with light in the blue spectra (460-500) and be imaged in the green (500-560). The device needs to be able to acquire both visible and NIR light to display the contrast agents. Additionally, excitation light must be filtered so that there is no bleed through into the emission filter, skewing the image. Finally, the tissues must receive 360° illumination so that not only one side of the tissue receives illumination light and signal is only collected from one area of the tissue.

We have built a prototype that accounts for all of these design parameters. Firstly, a Canon 450D digital SLR camera with its internal IR filter removed was purchased for $1,095. Two sets of LEDs (light emitting diodes) that were centered on 780 nm and 488 nm wavelength light, respectively, were purchased for $4.40 each. Short pass (800 and 500 nm) excitation filters for each set of excitation LEDs at a price of $73 each. A lens to attach to the camera was purchased for $215.00. Finally, an emission filter was attached to the end of the lens that transmits green light (500-560 nm) and any light above 825 nm. The LEDs and filters were arranged around an imaging station (design in figure 5.7a), and the LEDs were placed in a circuit with proper resistances and an on-off switch. The camera with emission filter and lens was then placed above the imaging acquisition and images are acquired.

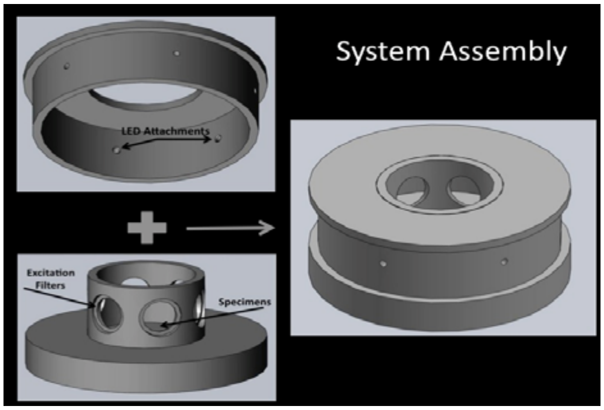

**Figure 5.7.** Two-piece assembly of imaging system to image multiple cell markers in resected specimens. The camera is attached to the top and images are acquired.

### Materials and Methods

Anti-HER2 silica-gold nanoshells and tissues were prepared in the same method as stated in section 1. Pre-incubation images were taken of both tissues that were incubated with NS and the negative control. The tissues were then incubated with nanoshells for 5 minutes at 37°C and then rinsed 3X in PBS and stored in clean PBS until post-incubation images were acquired (<10 minutes after completion of incubation). All images were acquired with the same settings on the camera. The image acquisition settings include: an f-number of 5.6, exposure time 6 seconds, and a gain setting of 800. Images of tissues were collected side-by-side for comparison and individually. Additionally, different types of tissue that were incubated with NS were compared to determine if there was a higher signal from HER2+ than HER2- tissue.

### Results

Figure 5.8 shows pre(A) and post(B) incubation images of HER2+ tissue from the same patient. 5.8(C) shows the average pixel intensity of the tissues and shows the difference between the tissues. 5.8(B) shows that the tissue incubated with nanoshells is much brighter than the negative control. However, the quantitative data is quite interesting in that the tissue incubated with nanoshells kept the same intensity while the negative control lost intensity. This could be due to the camera's internal dynamic range normalizing the signal it is acquiring, or it could be due to a change in the intensity of the signal coming from the LEDs. For future experiments, a optical power meter will be placed in the same location of the imaging system to ensure that the signal being seen by the tissues is consistent.

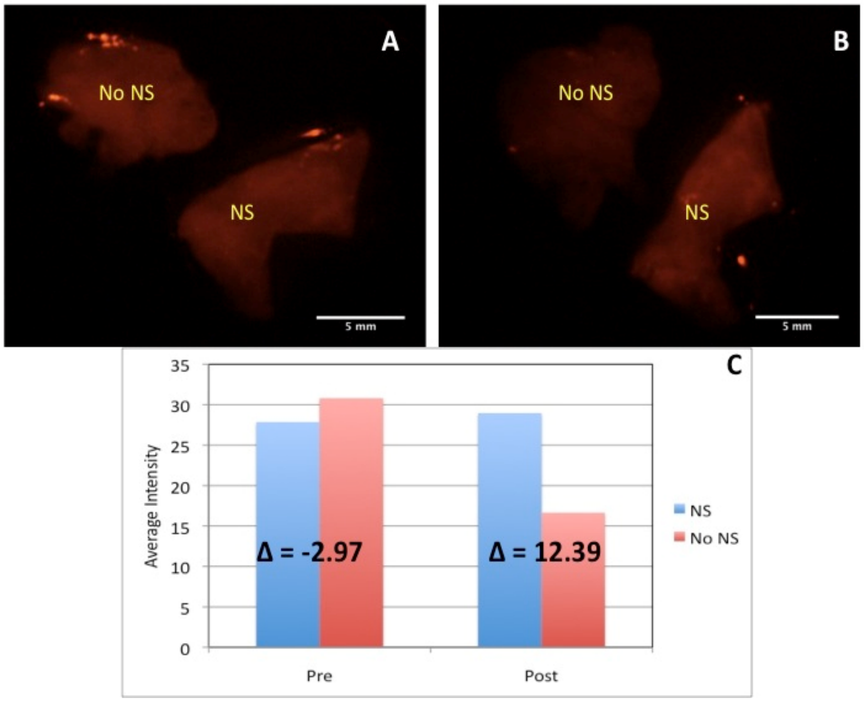

**Figure 5.8.** Pre (A) and Post (B) incubation images of HER2+ tissue that has been incubated with anti-HER2 silica-gold Nanoshells in addition to a negative control. 8(C) shows the pixel intensity of the tissues for both pre and post images and the differences between the two. The NS seem to increase the signal difference in the tissues, but not the actual signal of the tissue itself.

Figure 5.9 shows HER2- cancerous tissue from the same day with pre (A) and post (B) images of tissue incubated with nanoshells and its own control. Even though the tissue incubated with NS has a much brighter signal than the negative control, 9(C) shows that the signal difference was inherent in the tissues before the addition of nanoshells and that there was not much change due to incubation with nanoshells, which we hypothesize, implies that there was little to no nanoshell binding on the tissue that was incubated with nanoshells. Figure 10 shows the post incubation images of HER2+ tissue compared to normal (A) and HER2- tissue (B). While the normal tissue had a much lower signal than the HER2+ tissue, the HER2- was much higher than the HER2+ (Fig. 9(C)).

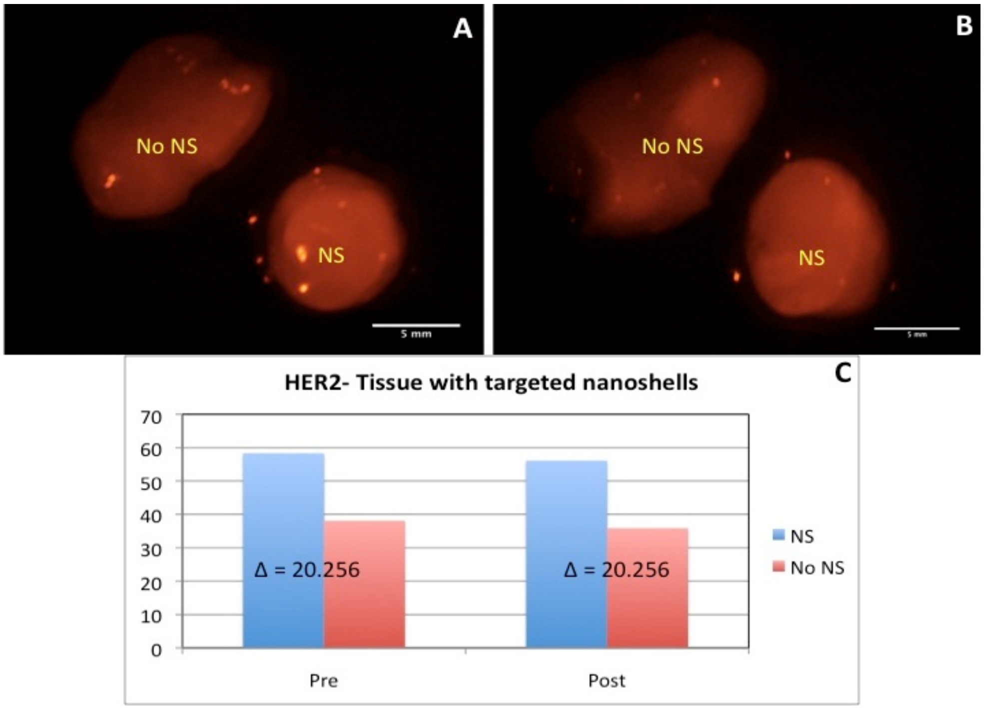

**Figure 5.9.** Pre (A) and Post (B) incubation images of HER2- tissue incubated with anti-HER2 silica gold NS. No signal difference between the tissues implies that there was no binding of anti-HER2 nanoshells to the tissue and that the signal difference is due to inherent tissue signal.

Figure 5.11 shows the results of a further experiment that acquired images of the tissues taken individually to ensure that the second tissue was not interfering with the excitation light coming from the excitation sources. It shows the difference in signal from nanoshells in tissues that were acquired individually so that there was no contributing signal from a separate tissue that might have affected the signal collected. This is interesting because it goes against the hypothesis that the nanoshells will enhance the NIR signal from the tissue, but the HER2+ tissue does have the smallest change in signal, which might mean that the nanoshells have an effect. However, this signal decrease might also be due to a change in signal from the excitation source, and further experiments will need to be completed to investigate what is happening.

These are promising results that show that incubation with anti-HER2 nanoshells seems to have a qualitative effect on the signal seen from the tissue. There are still many settings and optical set-ups that need to be considered before large amounts of quantitative data can be acquired. Additionally, a control for signal intensity needs to be acquired to confirm that the excitation light is staying within a consistent range during image acquisition.

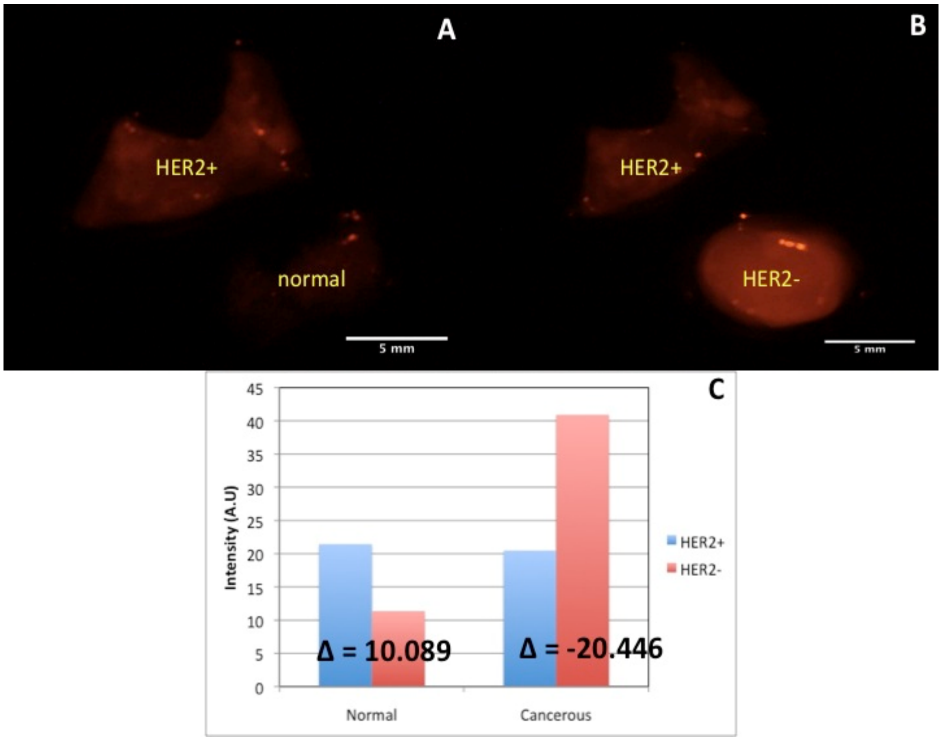

**Figure 5.10.** Post incubation images comparing HER2+ tissue to normal (A) and HER2- cancerous (B) tissue. The HER2- tissue was much brighter than the HER2+ tissue, but data from Fig. 9 shows that their was inherent signal tissue. Unfortunately, there was not pre incubation comparison images acquired to compare the signals of the tissue.

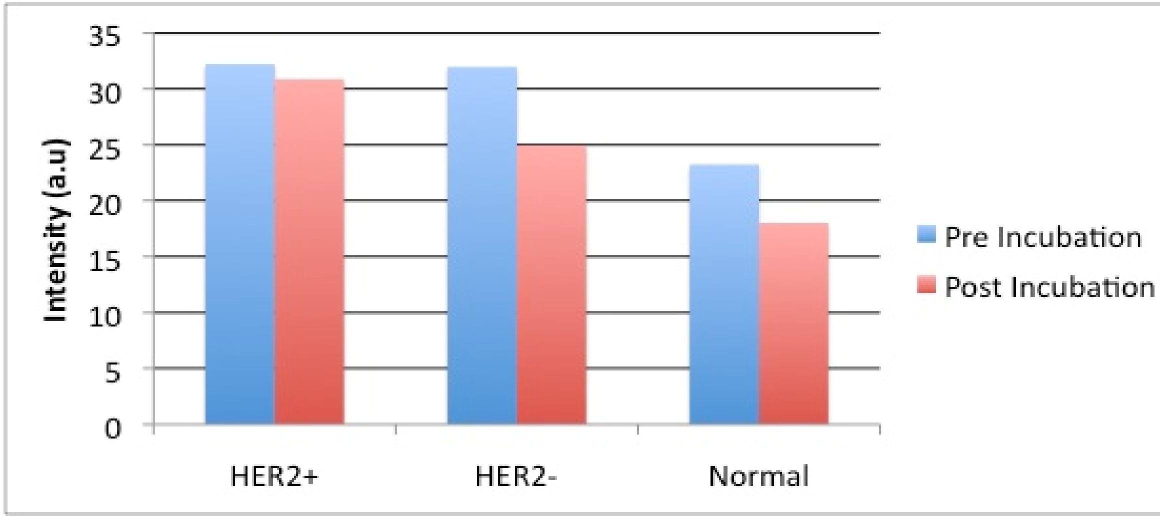

**Figure 5.11.** Signal intensities of individual tissues before and after incubation with silica-gold nanoshells. HER2+ tissue had the lowest signal drop of the three tissues.

## Discussion

So far there have been promising results in using a portable, inexpensive imaging system in conjunction with anti-HER2 silica-gold nanoshells to differentiate HER2+ tissue from normal tissue. Most promising was the data presented in Figure 5.8. Good qualitative data showed little difference in tissue from the same patient before incubation with nanoshells, which was backed up with quantitative data confirming the difference after incubation with nanoshells. However, we are hesitant to add any specific value to any quantitative data for each of the graphs displayed currently because there seems to be inconsistencies between pre and post images, where the negative controls seem to have lost signal between incubations. Some possible explanations for this include the excitation light losing intensity between images, the camera performing some automated change in the signal being collected we have not yet been able to identify, or perhaps the presence of two tissues interfering with the excitation light that interacts with tissue. There are still many settings to optimize that will provide a more definite answer in the coming year.

Future experiments will include taking multiple images with the tissues at various angles inside the imaging system. Additionally, in order for good quantitative data to be obtained, signal interacting with the tissue from the excitation light has to be measured with every experiment to properly maintain a control. Finally, future experiments might include slicing the tissue and acquiring images using a reflectance confocal microscope or darkfield hyperspectral imaging to confirm binding of nanoshells to the tissue.

Additionally, future experiments include optimizing imaging settings for estrogen receptor labeled with FITC. When optimal settings have been acquired for both markers, then both contrast agents will be applied to the same tissues to demonstrate our ability to show multiple markers in a rapid, inexpensive, and portable system. This system will not only have the capability to improve margin status in breast cancer surgeries, but it can be applied to other organ systems and molecular markers as well such as the additional agents being developed as part of Project 3.

### *Part 3: Glucose conjugated gold nanoparticles as a new imaging agent and additional theranostic agents to be assessed*

*As described in the Year 4 report, based on suggestions received at the LINKS meetings about ouy heavy reliance on HER2 and estrogen receptor status, we have expanded the range of molecular markers being considered through this project. Here, we report on not yet published data using glucose targeted gold nanoparticles. As described in the prior section, we have not ended the work using established markers but rather continue to expand beyond those.*

#### Introduction

Chemical agents have been conjugated to glucose with the purpose of targeting those agents to tissue that over-express glucose transporters (GLUTs), such as cancer (Macheda, Rogers, and Best 2005). These agents are then imaged and can be used to help differentiate cancerous tissue from non-cancerous tissue. These agents include $^{18}$F-fluorodeoxyglucose ($^{18}$FDG), a radioactive labeled agent that emits positrons and is used to monitor chemotherapeutic response and stage breast cancer (Kumar et al. 2009; Lim et al. 2007). Additionally, a fluorescent deoxy-glucose, 2-[N-(7-nitrobenz-2-oxa-1,c-diazol-4-yl)amino]-2-deoxy-d-glucose (2-NBDG), accumulates in the cytoplasm of cells because after entering the cells through the GLUTs, it undergoes the first step of glycolysis but no further processing. The optical properties of 2-NBDG allow it to be detected fluorescently (excitation maximum 475, emission maximum 550 nm) (Yoshioka et al. 1996). Studies have demonstrated the ability of 2-NBDG to differentiate cancerous tissue from non-cancerous tissue in as little as 20 minutes for oral, esophageal, and breast cancer (Nitin et al. 2009; N Thekkek et al. 2011; Langsner et al. 2011). Glucose has already been shown as a new targeting agent to enhance contrast for malignant tissue We aim to take these findings further by targeting small (~2 nm diameter) gold nanoparticles (AuNPs) by capping them with glucose and using the GLUTs to deliver nanoparticles to the cells, rather than the traditional method of endocytosis.

A 2008 study by Kong et al. demonstrated that AuNPs (~10 nm diameter) capped with thioglucose could be used to enhance radiation cytotoxicity because the thioglucose allowed the AuNPs to enter the cytoplasm of the cell, rather than staying on the cell surface such as other cysteamine-capped AuNPs did (Kong et al. 2008). The authors supposed that the capping with glucose enhanced the entrance of the nanoparticles; however, if the glucose were to help with targeting of the AuNPs, then the particles would have entered the cells via the GLUTs. The GLUTs are very small (36 X 26 Å on the extracellular side, 46 X 27 Å on the cytosolic side)

(Salas-Burgos et al. 2004) and having a 10 nm diameter AuNP go through the transporter seems to be very difficult. Additionally, the authors did not present any endocytosis inhibition or glucose inhibition studies to show that the glucose targeting was the reason for the enhanced amount of AuNPS inside the cell. Finally, the authors incubated the cells for 2 hours, which is a significant amount of time for particles to enter the cell via receptor mediated endocytosis (Connor et al. 2005; Mironava et al. 2010). Previous studies have shown that 2-NBDG offers enhanced contrast in as short of a time as 10 minutes (O'Neil, Wu, and Mullani 2005) and that adding D-glucose (which enters cells through GLUT1) to cells with 2-NBDG decreases the amount of 2-NBDG entering the cell, demonstrating 2-NBDG's mechanism of entry (O'Neil, Wu, and Mullani 2005; Nitin et al. 2009).

The aim of this study is to demonstrate that 2 nm AuNPs can be capped with thioglucose and targeted to enter the cells via the GLUTs over-expressed in the cancerous cell line Sk-Br-3. We aim to show the mechanism of entry of 2 nm particles capped with thioglucose by doing both a D-glucose competitive inhibition assay and inhibiting endocytosis. Additionally, a final assay will be performed using varying sizes of AuNPs to demonstrate the size specificity of targeting AuNPs with thioglucose. Original research done with cells was done with colloid made in lab. However, transmission electron microscope (TEM) images showed that the size of the colloid was on average 2 nm, the same size of commercially available AuNPs from Ted Pella, Inc. To standardize between experiments, all future experiments will be done using Ted Pella particles. This will allow us to know the concentration of particles for all experiments.

## Materials and Methods

Gold colloid was synthesized by spinning 45 mls of distilled $H_2O$ in a glass beaker at 800 RPM. 1 ml of 1 N KOH was then added; 1 minute later, 12 ul of THPC (Tetrakis(hydroxymethyl)phosphonium chloride) was added; 2 mls of 1% $HAuCl_4$ (gold salt was added) for 2 minutes to form the colloid solution. 10 mls of colloid solution was then combined with 10 mls of 10 mM thioglucose and spun at 800 RPM for 15 minutes. The solution was then rinsed using a centrifugal dialysis filter (10,000 Dalton cutoff) spun 3X for 20 minutes at 2500 g. The final solution was then resuspended to a total of 10 ml and kept at 4°C. TEM images of the particles were acquired using a JEOL 2010 TEM; figure 12 (A) depicts a zoomed out view of the nanoparticles and 12(B) features a zoomed in version. Colloid from Ted Pella Inc ($1.25X\ 10^{14}$ particles/ml) was combined and filtered in the same manner as the "home-made" colloid.

However, TEM images were acquired with a JEMF-2100 Field Emission Gun Transmission Electron Microscope that is equipped with Energy Dispersive Spectroscopty (EDS) that uses electron energies to confirm the presence of certain atoms. EDS is a powerful tool because it can confirm the thiol binding of thioglucose to the surface of the nanoparticle. Figure 13 depicts the TEM images and subsequent EDS data.

The first experiment to demonstrate that thioglucose can be used to target AuNPs involved comparing different cappings of particles and showing that thioglucose preferentially entered the cells. 175,000 cells of the cancerous cell line Sk-Br-3 were plated onto two-well chamber slides for 48 hours at 37°C. Three different cappings (thioglucose, citrate, and no cap) and one negative control were added with fresh media to the cells for 20 minutes at 37°C. The cells were then rinsed with PBS, and imaged on a Cytoviva™ darkfield microscope. Figure 14 demonstrates images of the different cells from this experiment.

The next experiment involved the use of D-glucose as a competitive inhibitor with glucose AuNPs. For this experiment, the same number of cells were plated in the same type of well plates for the previous experiment. This time, there were two controls: cells only and cells with D-glucose added; then, glucose AuNPs were added to cells with and without D-glucose. Figure 15 depicts images from this experiment.

**Results**

Figure 12(A) depicts a zoomed out view of gold colloid with thioglucose conjugated on the outer core of the particle. 12(B) is a high zoom image depicting an area of AuNPs. As one can tell from the images, the solution of colloid seems to be very monodisperse; there does not seem to be any aggregates of particles in the solution. However, the particles are of an approximate size of 2 nm in diameter. This is no better than the size of particle that can be commercially bought and is fabricated with a more consistent process. Additionally, there is a known stock concentration of particles that are commercially available that allows us to control volume and number of particles added to cells at a more consistent rate than with the lab made colloid. Therefore, a switch was made to the particles visible in Figure 13. As well, figure 13 shows spectroscopic data that displayed the amount of an atom that was present in the area of interest. For this sample we compared the amount of sulfur to gold present on the inside and the outside (lighter) part of the particle. The inside (spot 1) had almost four times as

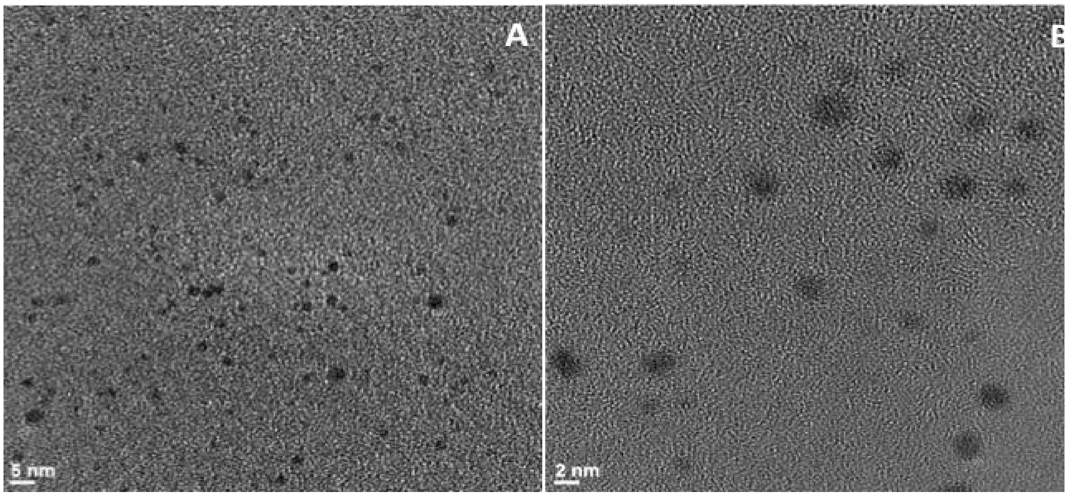

**Figure 5.12.** TEM images of gold colloid made in lab and then capped with thioglucose. These types of AuNPs were then added to the cells that are seen in Figs. 14&15

much gold present as sulfur and the outside, where the thioglucose was bound had almost 3 times as much sulfur. TEM-EDS is very powerful tool that we will be able to use to visualize and confirm thioglucose (or any molecule) binding to the surface of the particle. This technology will be used in future studies when TEM images of cells with nanoparticles are obtained.

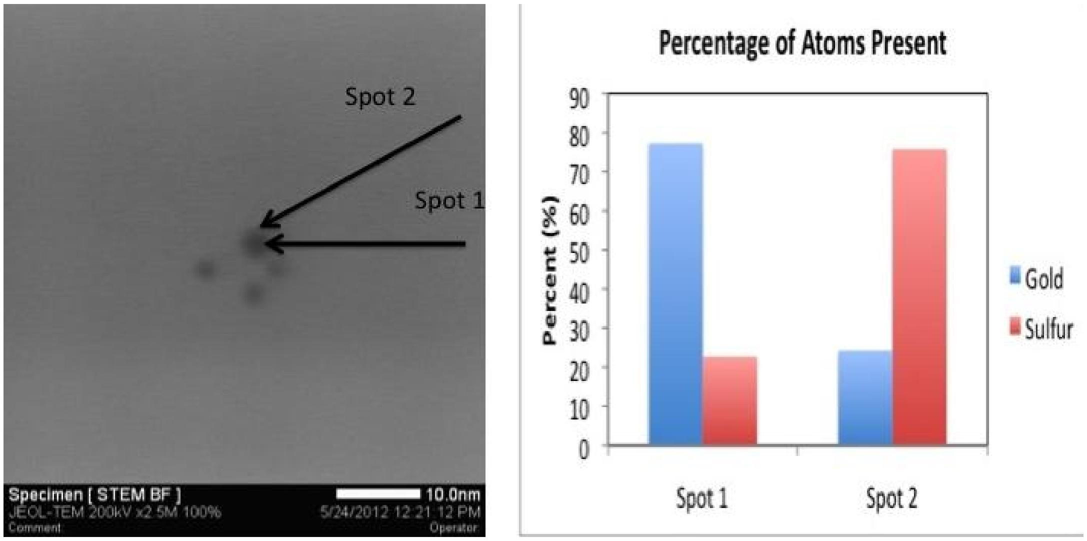

**Figure 5.13.** Gold colloid purchased from Ted Pella, Inc and then capped with thioglucose. EDS data acquired from spots delineated in the image demonstrate the concentration of sulfur and gold atoms with respect to each other at their respective locations of depicted in by the arrows. Spot 2 represents the area where the thioglucose has bound to the surface of the particle, whereas spot 1 represents the center of the particle.

Figure 5.14 displays darkfield images of Sk-BR-3 cells that were treated in four different manners (A) cells only, (B) bare AuNPs, (C) citrate capped AuNPs, and (D) thioglucose capped AuNPs. From the images, there are very obvious differences between each of the cells. What is quite interesting is that there seems to be a lot of signal from inside the cells that were treated with the thioglucose-AuNPs. We hypothesize that this is due to the increased amount of AuNPs that were able to cross the GLUT and settle into the cytoplasm. Even though we do not see individual particles due to the limitations of microscopy, the increased signal might be due to the accumulation of a high number of particles in the cells. Additionally, it appears as if there is a dark circle in each cell that represents the nucleus. The cells treated with the other types of AuNPs seem to have increased signal on the edges of the cells which may be due to electrostatic or non-specific binding of the cells to the membrane. However, none of these can be concluded until controlled TEM images of the cells are acquired, a task currently underway.

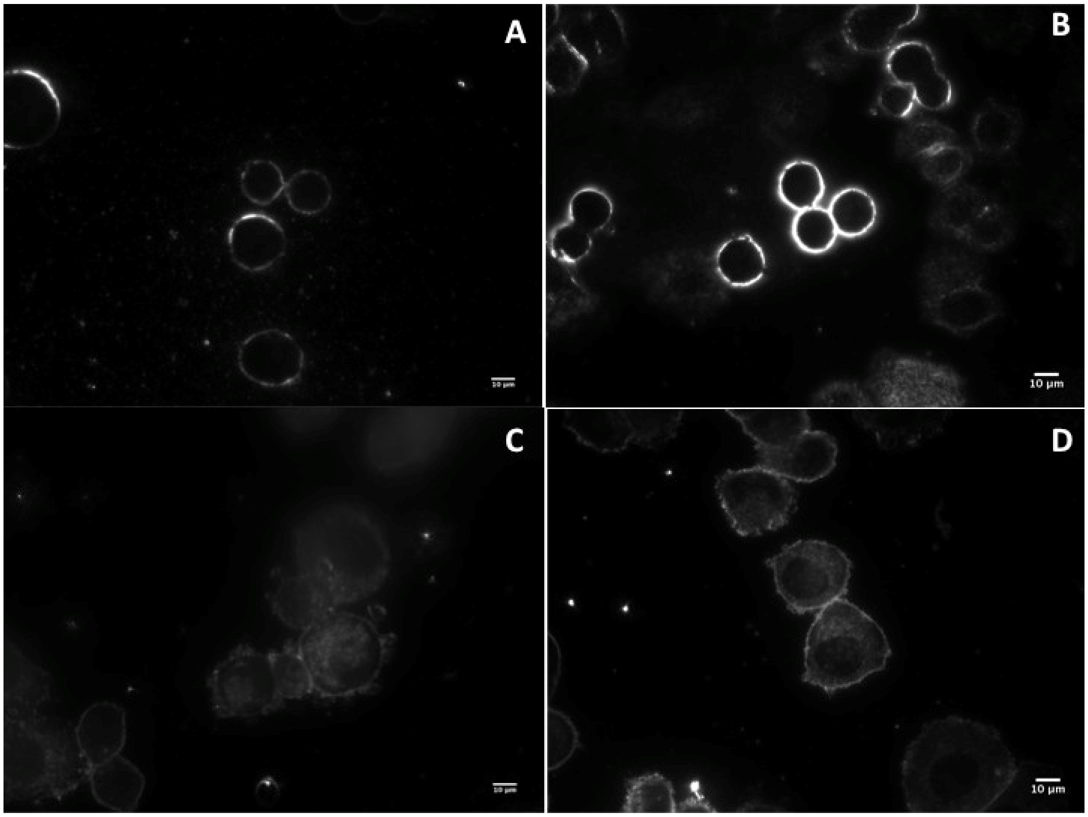

**Figure 5.14.** Darkfield images of Sk-Br-3 cells only (A), incubated with uncapped AuNPs (B), citrate AuNPs (C), and thioglucose capped AuNPs (D). 14(D) shows high signal inside the cell that is thought to be from gold AuNP accumulation. However, further tests are needed to verify this conclusion.

Once it was established that thioglucose-capped AuNPs interacted with the cancerous cell line Sk-Br-3 differently than other capped AuNPs, we hypothesized that the AuNPs were entering the cells via the GLUTs and not via endocytosis. Our first experiment to determine this was using a competitive inhibition assay using D-glucose. Figure 15 displays the darkfield images that were results of this experiment. Fig. 15(A) is the negative control of no cells, 15(B) displays cells incubated with 40 µM D-glucose only, (C) displays the cells after incubation with both D-glucose and AuNPs(D) displays the cells after incubation with AuNPs only. Once again, there is good qualitative data displaying the high scatter signal from the cells that were incubated with AuNPs only, but very little signal from inside the cells where there was competitive inhibition. However, as with previous results, this cannot be confirmed until higher resolution images with TEM are acquired.

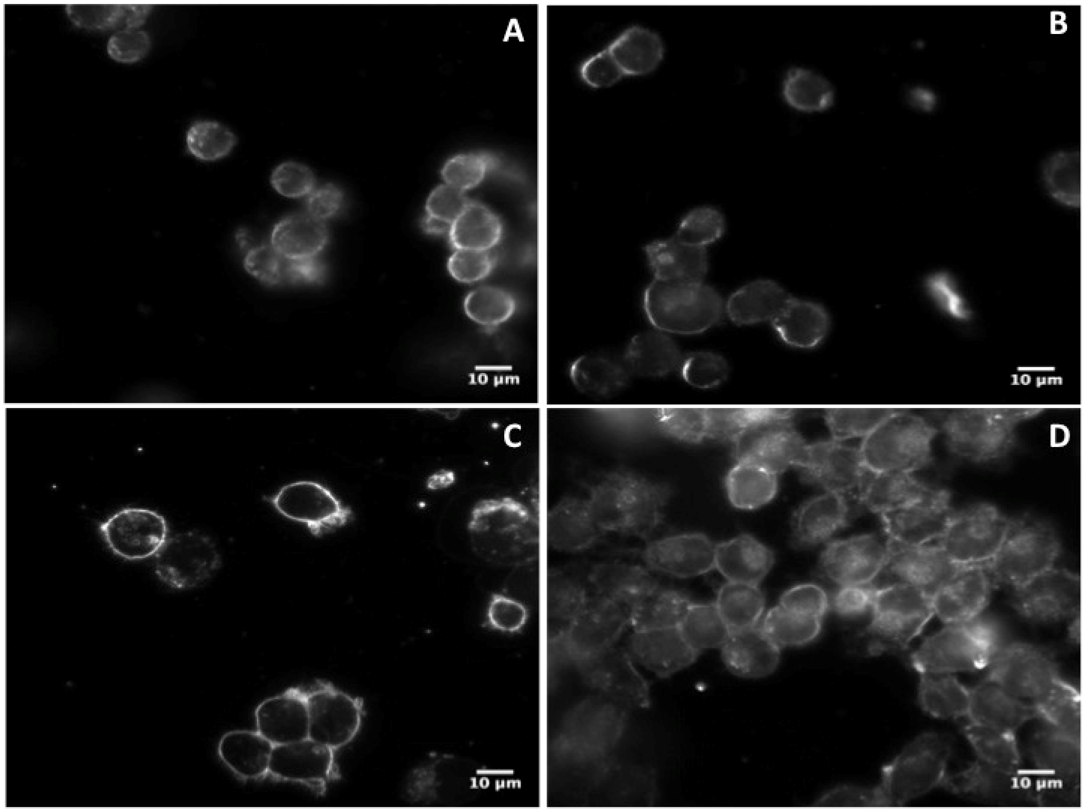

**Figure 5.15.** Sk-Br-3 breast cancer cells after incubation with (A) media only, (B) D-glucose, (C) D-glucose and thioglucose capped AuNPs, and (D) thioglucose capped AuNPs only. High scatter signal can be seen from the cells in (D) leading to the conclusion that there is gold colloid inside the cell membrane.

## Discussion

Preliminary tests and results that show glucose capped AuNPs can enter cells in a twenty minute time frame are very promising. There is good qualitative data that shows enhanced signal from inside the cytoplasm of cells that have incubated with these particles and there is very little signal from cells that were incubated with something different. Additionally, there is strong scatter signal on the cell membrane of some of the samples that have been incubated with non glucose AuNPs which could mean that the particles are being localized to the cell membrane but have yet to enter the cell. This could be because of the time it takes to form endosomes to engulf these other AuNPs or it could be due to electrostatic interactions between the membranes and the particles.

There are many more experiments that need to be run before any solid conclusions can be reached. First, there needs to be confirmation from TEM showing the AuNPs localized to the cell cytoplasm. Additionally, further experiments need to be completed to confirm the mechanism of entry for the particles. Inhibiting both clathrin dependent and independent endocytosis and then incubating the cells with the thioglucose AuNPs would show a different mechanism of entry of the particles into the cells. Second, the use of cells with RFP labeled endosomal DNA could also be used to show where endosomes have been forming inside the cell. If there are no endosomes formed, yet there is still high scatter signal coming from inside the cell, then that would be a secondary confirmation of entry into the cell via other mechanisms. Third, showing that larger AuNPs do not enter the cells as rapidly as the smaller AuNPs would also show that there is some size restriction for the NPs to enter the cells in a time frame of 20 minutes which would also imply that the AuNPs were entering via a non-endocytotic pathway.

## Summary and Future Work

We have made significant progress on three aspects of using nanotechnology enabled contrast agents to improve diagnostic imaging in breast cancer. First, we used hyperspectral imaging to demonstrate localization of anti-HER2 silica gold NS to the surface of excised tissue. Second, we furthered our research in the development of a portable diagnostic imaging system that can be readily translated to clinical use for diagnostic imaging of tissues with multiple markers by tuning an optical set-up that is optimized to visualize certain contrast agents. Finally, we provided an important proof of concept that thioglucose can be used to target small (~2 nm diameter) gold nanoparticles in a rapid (<20 minute) manner. We hope to further develop this contrast agent and understand its mechanism of entry into cancerous cells, and further develop its use to enhance contrast in excised breast tissue.

In addition to the nanoparticles described in our reporting to date, over the past few years we have also developed a number of newer gold-based materials through other awards with significant potential as theranostic agents for breast cancer applications. In the final year of the DoD award, we plan to continue to develop these materials and assess both imaging and therapeutic potential for breast cancer applications. We have dedicated a portion of the remaining personnel funding to the supply category to enable this and purchased needed supplies for this work prior to the original award end date in case of delays in processing the no cost extension request for the coming year. Specific materials to be included are dendrimer decorated gold nanoparticles, gold nanoparticles decorated with peptides or oligonucleotides (each offering potential delivery/therapeutic functionalities in addition to imaging), and gold nanoparticles also carrying a drug (paclitaxol). Finally, we have very recently discovered a potential method for generating a luminescent nanoparticle which would overcome the limitations of the cadmium-free luminescent nanocrystals (quantum dots) we had worked with in the early years of the award but abandoned largely on safety concerns. If we are able to validate our initial experiments, this will prove an additional material which we will test with the macroscopic imaging system we have already created. Throughout our DoD award we have focused most heavily on gold based nanomaterials. These materials can be imaged through scattering, absorption, and is some cases, two photon luminescence. Additionally, facile conjugation to biomolecules is enabled through the gold surface. It is this unique combination of optical and chemical properties which render these materials so powerful. Toxicity of these materials will continue to be assessed with an added emphasis on potential immune system impacts. By the conclusion of our award, we seek to have conclusively demonstrated the potential for targeted imaging and treatment of breast cancer, moving beyond the combined imaging/photothermal applications considered in the award early years to more sophisticated materials in which imaging potential is coupled with delivery of oligonucleotides, peptides, and chemotherapeutic agents, broadening the range of applications of these materials beyond the breast tumor margin area we have focused on to date.

One final small area of investigation is using the gold nanoparticles already developed for imaging applications for detection via a compressive sensing strategy using a random probes concept, which we are investigating together with collaborators at Rice. This concept removes the individual probe for each target restriction typically associated with array based analysis. Although very much at a proof of concept stage now, in the future such an approach could potentially be used to provide a more cost-effective approach to targeted large scale genetic screening valuable in applications such as determining more optimal chemotherapeutic regimens for breast cancer treatment. This effort was initiated based on the panel discussion at the 2011 LINKS meeting noting the difficulties in identifying optimal, and at times even reasonable, patient populations for drug studies and the need for new technologies to address this challenge.

B l aP na

***Year 6 No Cost Extension Period***

## ***Section 1: Development of a Portable and Inexpensive Imaging Device to Visualize Topically Applied Contrast Agents in Cells and Tissue***

### Introduction

In this section we discuss the development of a portable and cost effective imaging device designed to visualize both 2-NBDG and anti-HER2 NS in cells and tissue specimens. Previous studies have reported the use of visualization techniques that required expensive equipment and software that could not be easily transported (Langsner et al. 2011; L. R. Bickford et al. 2012), or the samples required preparation to localize the NS (L. R. Bickford et al. 2012). In this chapter, we describe the design, development, and characterization of a low cost portable imaging system to visualize 2-NBDG and anti-HER2 silica-gold nanoshells in cell lines and excised tissue.

### Background

Optical imaging can improve cancer diagnostics via minimal acquisition time and high lateral resolution. The addition of contrast agents can increase the specificity of optical imaging by improving contrast between cancerous and normal cells due to differences in molecular expression. We have demonstrated the enhanced specificity of both 2-NBDG and anti-HER2 NS in separate studies, and we aim to combine their properties to demonstrate the ability of multi-wavelength imaging to visualize cancerous tissue. Multi-wavelength NIRF imaging has been demonstrated *in vivo* in two studies by Baeten and Montet et al. (Baeten et al. 2009; Montet et al. 2007). In the study by Baerten et al., the authors used enzyme-cleavable fluorophores to indicate protease activity and vascularization of tumors. The authors were able to use the intensity values from these two measurements to correlate cathepsin expression with tumor size. Another multi-wavelength imaging system, the multi-spectral digital microscope (MDM), was developed by Roblyer et al. (Roblyer et al. 2008; Nitin et al. 2010). This device uses white light, orthogonal polarized reflectance (OPR) imaging, and multiple visible range wavelengths for visualization of neoplasia in the oral cavity (Roblyer et al. 2008) or molecularly targeted NPs in tissue phantoms (Nitin et al. 2010). The multiple wavelength approach provided the researchers with information on the best wavelength for interrogating the autofluorescent changes that are consistent with neoplastic tissue (Bedard et al. 2010)

In addition to multiple wavelength imaging, there has been a shift towards the combination of wide-field imaging followed by high resolution probes to interrogate areas of interest (Muldoon et al. 2007; Bedard et al. 2010). Another study by Lam et al. demonstrated the utility of using an endoscope to obtain wide-field autofluorescent images of the bronchi, followed by high resolution optical coherence tomography (OCT) of suspicious lesions to differentiate invasive carcinoma from carcinoma *in situ* based on the thickness of the epithelial layer (Lam et al. 2008). A recent study by Patel et al. demonstrated the use of wide-field imaging followed by confocal fluorescence to visualize specific areas of breast cancer on histopathological slides (Patel et al. 2012). In this study, slides were incubated with methylene blue (MB) and accumulated preferentially in malignant areas after 10 minutes. Wide-field images of the tissue were first acquired followed by fluorescence imaging at high-resolution. The researchers were able to separate the malignant from normal cells on the slices by the increased fluorescent signal in the cancerous areas (Patel et al. 2012).

Most multi-modal and multi-wavelength imaging systems still rely on endogenous contrast or contrast provided by non-specific contrast agents such as MB. Additionally, there is little work reported on the use of multiple specific contrast agents in one sample to enhance specificity. In a study by Xie et al., the authors used two IRdyes, 2-DG (deoxyglucose) and EGF for visualization of tumors in a murine model (Xie et al. 2012). However, in this study, the authors used contrast agents in separate animals. As the optical agent for the biomarkers was the same (IRDye), they would have been unable to resolve the differences between the contrast agents in one animal. Additionally, the authors used the Maestro© system that is both non-portable and costly. This study is the first to approach using multiple molecularly specific contrast agents, and the authors were able to show for their particular model that the EGF dye had higher signal than the DG dye. However, this result will vary due to the varied expression of molecular markers, especially across breast cancer subtypes (Vermeulen et al. 2012). A recent study by Vermeulen et al. demonstrated that increasing the number of interrogated biomarkers improved the detection of cancer on immunohistochemical slides (Vermeulen et al. 2012). Detection of multiple markers in one sample is also important due to the heterogeneity of expression levels in one tumor (Shipitsin et al. 2007; Liotta and Petricoin 2000; Milas and Hittelman 2009). The device presented in this chapter aims to use multiple contrast agents as the heterogeneity in expression profiles could lead to the system obtaining a false negative if only one contrast agent is used.

In this chapter, we aim to develop a method to visualize multiple molecular contrast agents that are used to visualize HER2-positives cells and tissue. The ultimate goal of this research is to develop a system that can be translated for use in the clinic as an *ex vivo* imaging device that provides surgeons with rapid results regarding the molecular expression of GLUT1 and HER2. Our previous experiments have shown that the expression of these proteins can be imaged using 2-NBDG and anti-HER2 NS in a rapid manner (20 and 5 minutes, respectively) (Langsner et al. 2011; L. R. Bickford et al. 2012). We further this research by designing, fabricating, and characterizing a portable, inexpensive imaging designed to visualize 2-NBDG fluorescence and anti-HER2 NS. We show that the device can visualize 2-NBDG and anti-HER2 NS in the cancerous Sk-Br-3 cell line. Additionally, we present data characterizing the performance of the system in visualizing the contrast agents in *ex vivo* tissue.

## Materials and Methods

### *Design of imaging system*

The system was designed to visualize and illuminate 2-NBDG fluorescence and NS scattering without displacing the tissue or camera to capture a composite image of both fluorescence and scattering. Preliminary studies demonstrated that 360° illumination of tissues with NS was necessary because the varying height in the tissue blocked illumination light when there was a single illumination source. This led to the design of placing three separate illumination sources placed on the diameter of a circle at an angle of 120° from each other and all facing the center of the circle (Fig. 1(A)). We chose the use of high-power LEDs as our illumination sources as they have low cost and specific wavelengths are available for our contrast agents. LEDs were purchased from Marubeni Corporation (FL-470-06, FL760-03-80)). Additionally, we placed excitation filters in front of the LEDs to control the wavelength of light interacting with the tissue (Fig. 1(B)). Short-pass (SP) 500 and 800 nm filters were purchased from Thor and Chroma (FES0500, E800sp). Once the filters and LED circuits were assembled, the two parts were placed together and held together with a setscrew to create one modular piece in which the holes for the LED attachments are lined up with the excitation filters (Fig. 1(C)). The aperture at the top of the device was designed to match the outer diameter of the filters that attach to the lens of the camera (58 mm).

As we are using our system to visualize two different contrast agents, two different circuits were designed and are controlled through an On-Off-On switch. Each circuit was soldered so that the LEDs were connected in series with a 12V battery (GP 23-AE 12V) as the voltage source and a resistor so that the LEDs would not burn out.

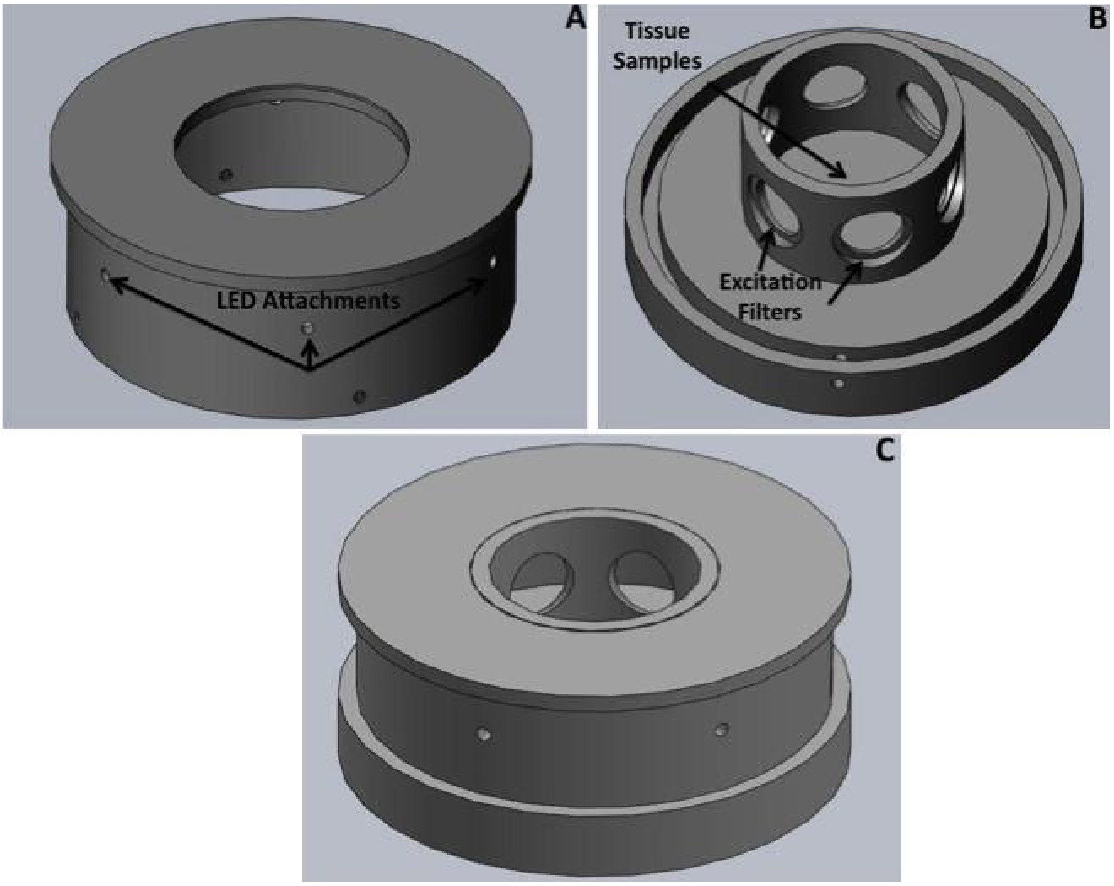

**Figure 6.1.** Schematic drawings of portable inexpensive imaging device used to visualize molecular contrast agents in cells and tissue. (A) Schematic of the outside cover in which the LEDs are attached and pointed towards the center of the device. (B) Base attachment of the device displaying placement of tissue samples and excitation filters. (C) Assembled device with holes for LED attachments lined up with large holes for excitation filters.

To capture tissue signal, a camera was attached to the device so that the lens of the camera was perpendicular to the tissue in order to capture the side scattering of the NS. Camera selection is an important design parameter as our aim was to visualize signal in both the visible and NIR wavelengths, our system required a device to detect both signals. RGB (red, green blue) sensors in digital cameras have the ability to sense in the NIR; as a result, most cameras have an internal IR blocking filter so that the sensors do not detect IR light and translate it to a color. Removal of the IR filter would allow for sensing of both NIR and visual light from NS and 2-NBDG given that the proper emission filter was placed in front of the camera lens. In addition to their versatility in sensing, digital cameras are also relatively inexpensive, another important design parameter for the system. A digital single-lens reflex camera (DSLR) with the NIR filter removed was purchased from LDP LLC for $1,095.00 (Xnite Canon450D Rebel Xsi). Additionally, a variable zoom lens from Canon was purchased for $199.00 (EF-S 18-55 mm, F/3.5-5.6 IS II). Multiple 58 mm lens filters were purchased to help further characterize the ability of the system including a 500-550 nm bandpass (BP) and two LP filters (720 and 780 nm). Additionally, the BP filter transmits light above 800 nm. The cost of the filters ranged between $70-$145.

The system was fabricated with black delrin using a variety of machinist tools, including a mill, lathe, and a CNC (computer numerical control) mill. Threaded holes were tapped so screws could be used to attach the machined pieces. An optical post was attached to the top of the system to anchor the DSLR during image acquisition to minimize camera movement. Finally, a one-inch diameter circle was etched into the center of the tissue specimen area as a scaling reference. With all components attached (Fig. 6.2), the system weighs 8.2 lbs and has a foot-space of 55.25 in$^2$.

*Characterization of system*

There are three imaging modes for this system. In white light imaging, the LEDs are not turned on and there is no emission filter; the only illumination is

**Figure 6.2.**Side view of fully assembled imaging device. An optical pole was attached to the top of the device for camera stabilization and adjustable height. A son-off-on witch allows for easy control of the two circuits.

from

the overhead lights in the room. When the term "blue light imaging" is used, we refer to the setup used to image 2-NBDG: blue LEDs illuminated with a BP 525 emission filter for the lens. For "NIR imaging", the NIR LEDs were illuminated and a LP720 emission filter is used (unless otherwise noted). The overhead lights were turned off during the latter two imaging modes so that no background signal is captured by the camera

Preliminary experiments demonstrated the importance of camera settings such ISO speed, aperture size, and exposure time. These preliminary studies led us to use the same aperture size (f/5.6) and ISO setting (800) for all experiments presented in this chapter. Different exposure times were used for all three imaging modes and for different lighting settings. These different settings will be indicated in the materials and methods section. However, any quantitative analysis performed between images was performed with images acquired at the same exposure. Additionally, an optical power meter (Newport Optics) was placed in the system during different days to confirm that illumination power did not decrease between days. We did not see any measurable change between days. However, as a precaution, any quantitative analysis was performed between samples that were acquired during the same experiment so that any difference between experiments did not affect the analysis.

To demonstrate the ability of the system to visualize NS and quantify signal intensity changes with the number of particles, 1 mL of a serial dilution (2 X$10^9$ particles to 31.25 X $10^6$ particles per mL) of NS was placed in a quartz cuvette in the same orientation in the imaging device. Images were acquired in the NIR imaging mode at an exposure time of 10 ms. After image acquisition, ImageJ was used to draw a ROI around the NS area and the average intensity for each concentration was calculated and plotted in Figure 3(A). Additionally, a serial dilution of 2-NBDG (156 mM to 15.6 nM) was characterized in the blue light imaging settings at an exposure time of 1 s and is displayed in Figure 3(B).

*Performance of system in vitro*

To demonstrate the ability of the system to visualize both contrast agents, the Sk-Br-3 cell line was chosen as previous experiments have demonstrated increased contrast with both optical agents. Cells were incubated with 2-NBDG only, anti-HER2 NS only, or both contrast agents (along with a negative control). NS were incubated with antibodies and PEG-SH in the same ratios as previously described (L. R. Bickford et al. 2012). Briefly, 2.25 mLs of NS (at a concentration of 2.0 X $10^9$ particles/mL) were incubated with 3 μL of antibody-PEG-linker and 237 μL of deionized (DI) water at 4°C. After 2 hours, 10 μL of 1mM PEG-SH was added to stabilize the particles. Particles were then centrifuged at 2500 RPM for 5 minutes and resuspended in 500 μL of antibody buffer. 2-NBDG was diluted to a concentration of 500 μM in 1X PBS.

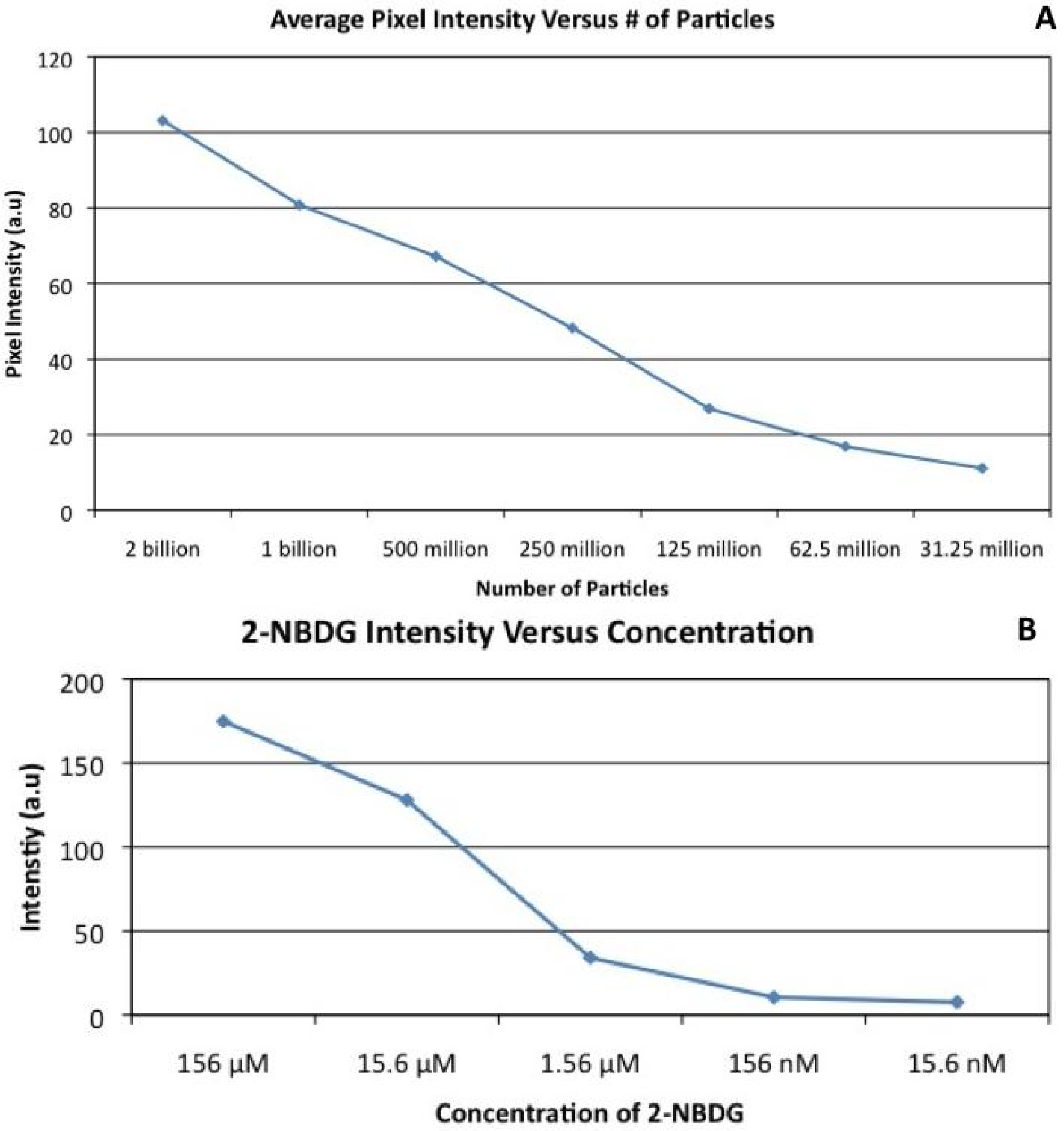

**Figure 6.3.**Pixel intensity versus number of silica-gold NS (A) and concentration of 2-NBDG (B).

Sk-Br-3 cells were grown at 37°C and 5% $CO_2$ until reaching confluency. Trypsin was added to the cells to detach from the flask and centrifuged into a pellet at 120g for 3 minutes. Supernatant was aspirated and cells were resuspended in 1X PBS to a concentration of 1.77 X $10^6$ cells/ml. 150,000 cells were added to a flat bottom centrifuge tube (Fisher 05-406-16) and 500 µL of contrast agent was added to the cells and 1X PBS was added to each centrifuge tube so each tube had a total volume of 1 mL. Samples were then placed in a rotating hybridization chamber (VWR 23050 TV) for 20 minutes. Samples were then centrifuged to remove any unbound 2-NBDG or NS and fixation buffer (Enzo ADI-950-011) was added to the cells for 20 minutes.

Cells were then transferred to coverslips and placed into the center of the device and white light, blue light, and NIR images were acquired at exposure times of 5 ms, 6 s, and 66.6 ms respectively. Results for each wavelength of imaging are shown in Figure 4. As the signal in the 2-NBDG only (Fig. 4(D)) image was faint, the images were further processed into respective RGB channels and contrast for the green channel was enhanced to demonstrate the higher 2-NBDG signal in cells with 2-NBDG versus cells with NS only. These resulting images are displayed in Figure 6.5.

*2-NBDG in ex vivo specimens*

All tissue used in this chapter was supplied by the CHTN in an IRB approved protocol as described in the previous chapter. To characterize the ability of the system to differentiate 2-NBDG signal from autofluorescent signal in tissue, a HER2-positive IDC was incubated with 1.56 mM 2-NBDG for 10 minutes at 37°C. Pre and post incubation images were acquired in both white light and blue light settings at an exposure time of 100 ms and 1 s respectively. Resulting images are displayed in Figure 6. To quantify the difference between the blue light images, ROIs were drawn around the tissues and average intensities were calculated for both the RGB composite and green channel image.

*Anti-HER2 NS in ex vivo specimens*

The same HER2-positive tissue was also incubated with anti-HER2 NS after the 2-NBDG. Pre and post incubation images with NIR LEDs, 780 LP filter and an exposure time of 1 ms are shown in Figure 6(C&F). 1 ms was chosen as the exposure time as this was the lowest exposure setting in which there was no endogenous signal from the tissue in the pre incubation image.

As shown in Figure 6, there is very little signal from the tissue in both pre and post incubation NIR images, due to the low exposure. Using a different HER2-positive tissue, we varied the exposure time for both pre and post imaging from 10 to 50 ms to visualize the NS more effectively (Figure 7). However, increasing exposure also increased the signal from the tissue, and it became difficult to differentiate the signal from the tissue and the NS.

To reduce the signal from the tissue and increase contrast between the NS and tissue, the tissue was incubated with glycerol for 10 minutes at 37°C. Glycerol is known as an optical clearing agent that reduces scattering of tissue through dehydration (Vargas et al. 1999; Rylander et al.; Elina A Genina et al.; E. A. Genina et al. 2010) or reversible disassociation of collagen fibers in the extracellular matrix (Hirshburg et al.; Yeh et al. 2003; E. A. Genina et al. 2010). Pre and post incubation images were acquired in the NIR imaging setup with a LP 780 filter at an exposure time of 20 ms (Fig. (8(A&B)). To demonstrate enhanced signal in tissue with NS after glycerol incubation, a different HER2-positive tissue was incubated with glycerol for 10 minutes at 37°C, followed by a 5 minute incubation with anti-HER2 NS at 37°C and results are presented in Figure 7.8(C&D).

*Application of FITC-functionalized NS to co-localize NS in tissue*

As we were unable to demonstrate enhanced signal in tissue after glycerol and NS incubation (Fig. 8), we chose to examine if the NS were present in tissue using PEG functionalized with FITC so that the NS could be localized using the blue light imaging settings. In this experiment HER2-negative tissue from the same patient was incubated with non-targeted NS functionalized with FITC-PEG or PEG for 10 minutes at 37°C. Tissues were not rinsed, as we did not want to remove the NS that were bound by electrostatic interactions. Pre and post incubation images and side-by-side images were acquired at an exposure of 1 s and 40 ms (Blue light and NIR). Representative images are displayed in Figure 9(A&B); the blue light images were split into RGB components and the average intensity of the green channel for each tissue was calculated with a hand-drawn ROI.

After establishing that FITC-PEG NS could be visualized in the blue light imaging settings of our system, we aimed to use targeted anti-HER2 NS that were backfilled with FITC-PEG on HER2-positive tissue. 2.25 mLs of silica-gold NS were incubated with 2.4 μL of anti-HER2-PEG linker and 189.6 μL of DI water for 2 hours at 4°C. Following incubation 8 μL of 1 mM FITC-PEG-SH were incubated with the NS overnight. NS were then centrifuged at 2500 RPM for 5 minutes and supernatant was aspirated. Finally, the NS were re-suspended in 165 μL of antibody diluent buffer. HER2-positive tissue was thawed at 37°C in PBS and pre incubation images were taken in white light, blue light, and NIR imaging settings (with a LP 720 filter). Exposure times for imaging were 66.6 ms, 1 s, and 10 ms respectively. Tissues were then incubated for 10 minutes in 99.9% glycerol and images were acquired under the same conditions. Next, 165 μL of NS were incubated with the tissue for 10 minutes at 37°C. Post incubation images were acquired. Blue imaging pictures were processed in ImageJ to visualize signal from the FITC particles. Images were split into RGB components and the contrast in the green channel was enhanced by 0.05%.

*Application of NIR Fluorescent Dye*

Anti-EGFR IRDye 800CW was purchased from LI-COR Biosciences (926-08446) and resuspended in 1.5 mLs of 1X PBS to a final concentration of 133.3 mM. HER2-positive tissue was incubated with 99.9% glycerol for 10 minutes at 37°C and pre incubation images were acquired in the NIR setting with a LP500 filter at an exposure time of 5 s. Tissue was then incubated 165 μL NIR dye (or PBS) for 10 minutes at 37°C. Post incubation images were acquired at the same imaging settings.

## Results

Our results show that we were able to design, build, and characterize a portable system to image multiple contrast agents in resected tissue specimens. Concentration versus intensity graphs are shown for silica-gold NS and 2-NBDG in Figure 3. Both graphs show that pixel intensity decreases logarithmically with the decreasing concentration, demonstrating the concentration dependence of the device.

*Performance of system in vitro*

Figure 4 demonstrates the ability of our system to capture both 2-NBDG and NS signal in separate imaging settings.. Images of SK-Br-3 cells incubated with contrast agents are presented in Figure 4. Cells with 2-NBDG only (A,D&G), anti-HER2 NS only (B,E,&H), and both contrast agents (C,F,&I). are presented. In the blue light imaging mode, there is faint green signal in cells incubated with 2-NBDG only that is not seen in the NS only cells. However, this green signal is very strong in cells incubated with both NS and 2-NBDG. Also, the cells with 2-NBDG have no signal in the NIR imaging setting, which was expected as there were no NS present. Cells incubated with NS only had no signal in the blue light imaging, which was consistent with the negative control. There is signal from the cells in the NIR imaging that is also seen in the cells incubated with both 2-NBDG and NS.

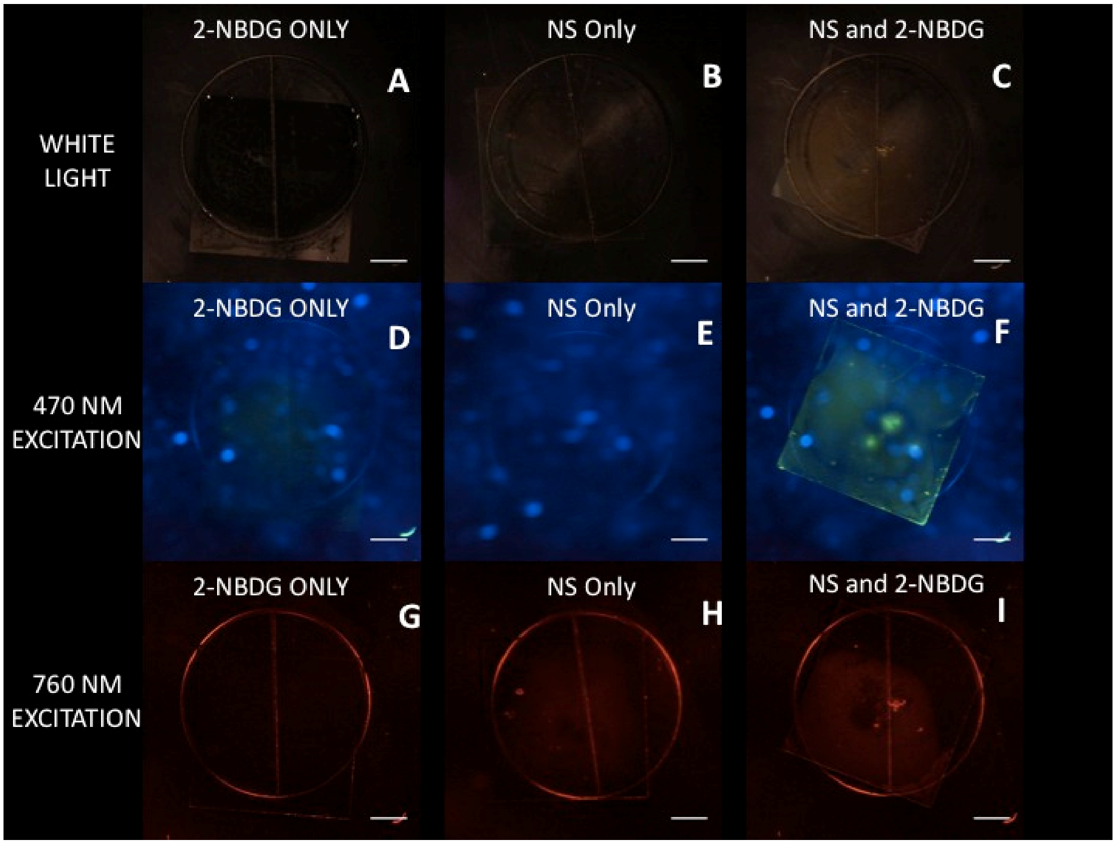

**Figure 6.4.** Images acquired with Sk-Br-3 cells incubated with 2-NBDG only (A,D&G), anti-HER2 NS only (B,E,&H), and both contrast agents (C,F,&I). Green signal from 2-NBDG is seen in both D&F but no in cells incubated with NS only. Additionally, for cells in NIR imaging settings (G-I), there is no signal from cells incubated with 2-NBDG only but cells incubated with NS only had similar signal to cells incubated with both contrast agents. Cells with no signal (Fig. 7.3(E&G)) had the same signal as negative control cells. Scale bar = 5 mm.

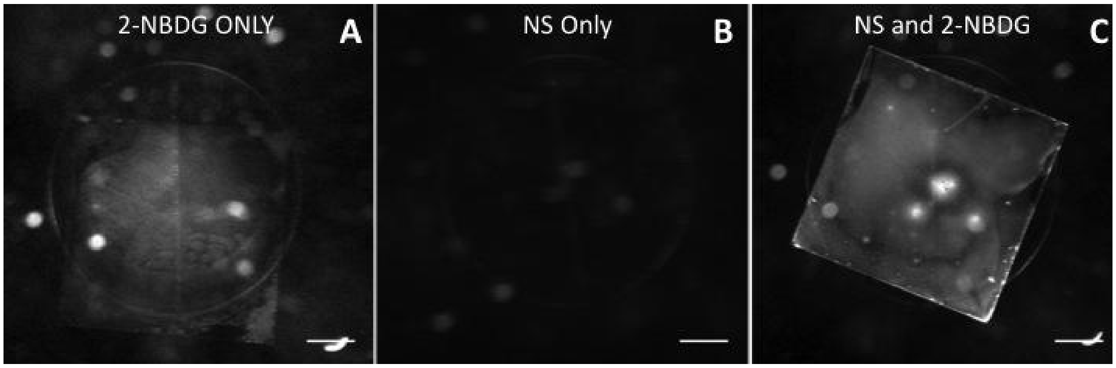

**Figure 6.5.** Green channel images from Figure 7.4(D-F) that have had contrast enhanced. Image show high signal in the green channel from both cells incubated with 2-NBDG and no signal from cells incubated with anti-HER2 NS only. This confirmed that green signal seen in Figure 7.4 is from the 2-NBDG. Scale bar = 5 mm.

This is an important proof of concept that shows multiple contrast agents can be captured using this system and that these contrast agents can be accurately distinguished. As the green signal from the 2-NBDG only cells was very faint, each blue light image was split into its respective RGB channels and the green channel was used for comparison. The results after enhancing the contrast in each image to further delineate cell signal are shown in Figure 6.5. These results clearly show the 2-NBDG signal in both Figure 5(A&C) and no signal from 2-NBDG in cells incubated with NS only. A possible reason for the lower signal from the 2-NBDG only cells is that a limited amount of cells were transferred to the coverslip, lowering the overall signal detected. However, Figure 6.5(C) clearly shows high 2-NBDG signal from cells on the coverslip.

### *2-NBDG and anti-HER2 NS in ex vivo specimens*

Figure 7.6 displays the initial attempt to visualize both 2-NBDG and anti-HER2 NS in *ex vivo* tissue samples. As the tissue was frozen, the signal from 2-NBDG seen in Figure 6(E) is from tissue that was not rinsed after incubation as most of the 2-NBDG would have been rinsed away. However, it is important as it illustrates that 2-NBDG signal on the tissue is much stronger than the autofluorescent signal seen in Figure 6.6(B). These are similar to the images we displayed in chapter 5 which demonstrated the enhanced fluorescent signal after incubation with 2-NBDG. This shows that we are able to use our inexpensive, portable system can create images very similar to the expensive Maestro system. Figure 6.6(C&F) show no difference between tissues after anti-HER2 NS incubation NS showing that the system is unable to resolve the NS scattering signal at this low camera exposure time.

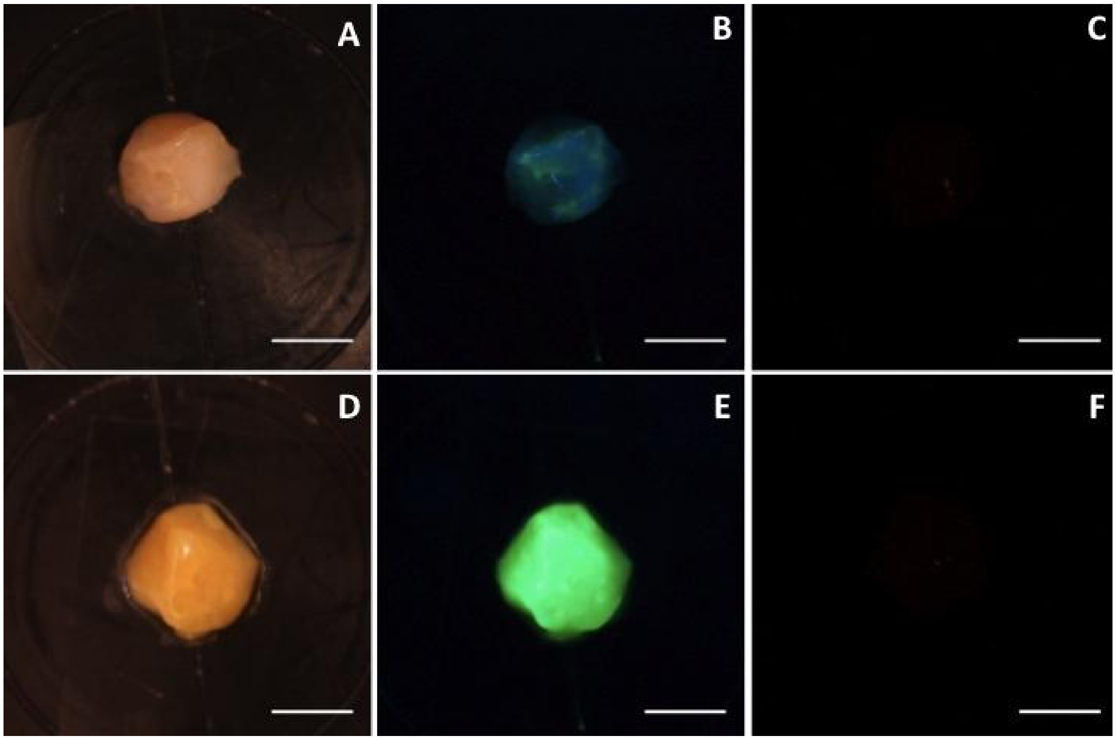

**Figure 6.6** Pre (A-C) and post (D-F) incubation images of HER2-positive tissue after incubation with 2-NBDG (B&E) then anti-HER2 NS (C&F). Images display the system's ability to differentiate 2-NBDG signal from autofluorescence. However, anti-HER2 NS binding was not visualized through NIR scattering. Scale bar = 5 mm.

The inability to visualize NS scattering at low exposure settings created a problem as increasing exposure time on the camera not only increased NS scatter but also signal from tissue (Fig. 6.7). At 10 ms exposure with a 720 LP filter, the average signal for HER2-positive tissue was calculated to be (48 (a.u), n=3). Using the graph presented in Figure 3(A), we see that to visualize NS due to their high scattering, we would need approximately 500 million particles to bind in a concentrated area to have enhanced scattering from the tissue. As this high concentration is not feasible, we hypothesized that we could decrease tissue signal through the use of the optical clearing agent, glycerol. Figure 8(A&B) demonstrates the reduced signal in tissue after incubation for 10 minutes in glycerol. The 10-minute time point was chosen to minimize incubation time in the glycerol to maintain our goal of developing a system to rapidly differentiate *ex vivo* tissue. However, we were still unable to show increased NIR signal after incubation with anti-HER2 NS (Fig. 8(C&D).

*Application of FITC-functionalized NS to co-localize NS in tissue*

As we were unable to show increased scatter signal after glycerol and NS incubation, we wanted to confirm that the NS were on the tissue. To do this, we back-filled the NS with a fluorescent PEG (FITC-PEG) that could be visualized using the blue imaging settings on the device. We first incubated non-targeted NS (backfilled with either FITC-PEG or non-flourescent PEG) with HER2-negative tissue and imaged the tissues without rinsing the NS. Blue and NIR images comparing the tissues are shown in Figure 9(A&B). The FITC labeled NS (F) have a much higher signal in Figure 6.9(A) due to the presence of FITC on the NS incubating the tissue. The NIR images in Figure 6.9(B) show that there is no difference between the tissues' NIR scattering. Due to autofluorescent differences in the tissues, we also calculated the change in green channel intensity for each tissue pre and post NS incubation. The tissue incubated with FITC-NS did have higher autofluorescence; however, the signal difference between the tissues is much higher after incubation with the particles (10 vs. 35). This confirms the NS location on the surface of the tissue but that we were unable to differentiate their scattering signal from the endogenous tissue signal.

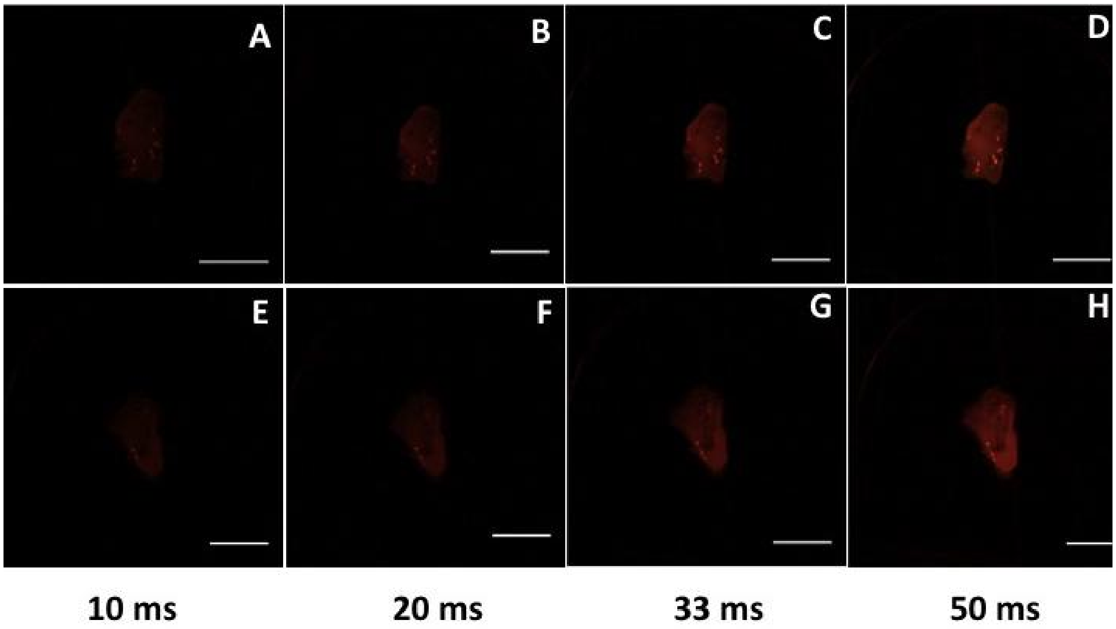

**Figure 6.7.**HER2-positive tissue pre (A-D) and post (E-H) incubation with anti-HER2 NS at different exposure times for the imaging system. Increasing exposure time increased signal from the tissue and did not improve the scatter signal from the anti-HER2 NS on the tissue. Scale bar = 5 mm

After confirming NS presence via FITC signal, we attempted to use targeted anti-HER2 NS with FITC –PEG to visualize the distribution of targeted NS on tissue. Our goal was to show that even if there was minimal NIR scatter from the NS, we would still be able to demonstrate binding of the NS to tissue through the FITC signal. If we were able to show this, then it would confirm that our optical configuration was not ideal for differentiating the binding of the anti-HER2 NS via their NIR scattering.

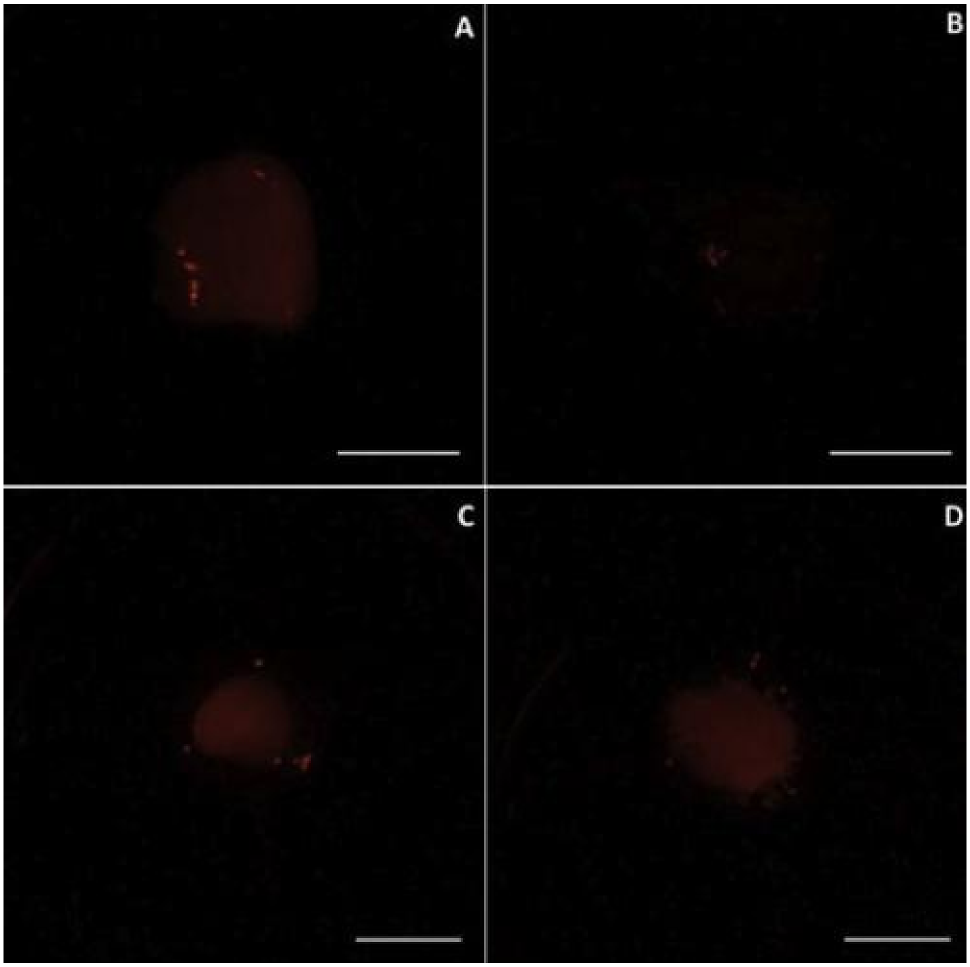

**Figure 6.8.** Images displaying NIR scatter reduction in HER2-positive tissue after incubation with 99.9% glycerol for 10 minutes. C&D demonstrate that anti-HER2 NS scatter signal could still not be separated from tissue that had been incubated in glycerol (C) and then incubated with anti-HER2 NS (D). Scale bar = 5 mm

Figure 6.10 displays the results from these incubation experiments. As can be seen in the images, the glycerol lowered the NIR signal from the tissue. And as observed in previous experiments, the addition of the anti-HER2 NS failed to increase the NIR signal from the tissue. However, the images that display the green channel of the blue imaging settings (Fig 10 (C,F,&I)) show increased intensity that is due to the presence of the NS throughout the tissue. Figure 10(J) displays the average signal intensity of the tissue in the blue imaging settings during each step of the experiment. As expected, the total signal from the tissue decreases after incubation with glycerol, and there is an increase in signal after the addition of NS but the overall signal intensity is still much less than the normal autofluorescent signal of the tissue. However, this graph shows a sharp increase in green channel intensity that occurs after incubation with FITC-NS. This indicates a presence of NS throughout the tissue that was not visualized through NIR scatter but through FITC signal, confirming our hypothesis that this optical set-up could not visualize enhanced scattering from targeted silica-gold NS in HER2-positive breast cancer.

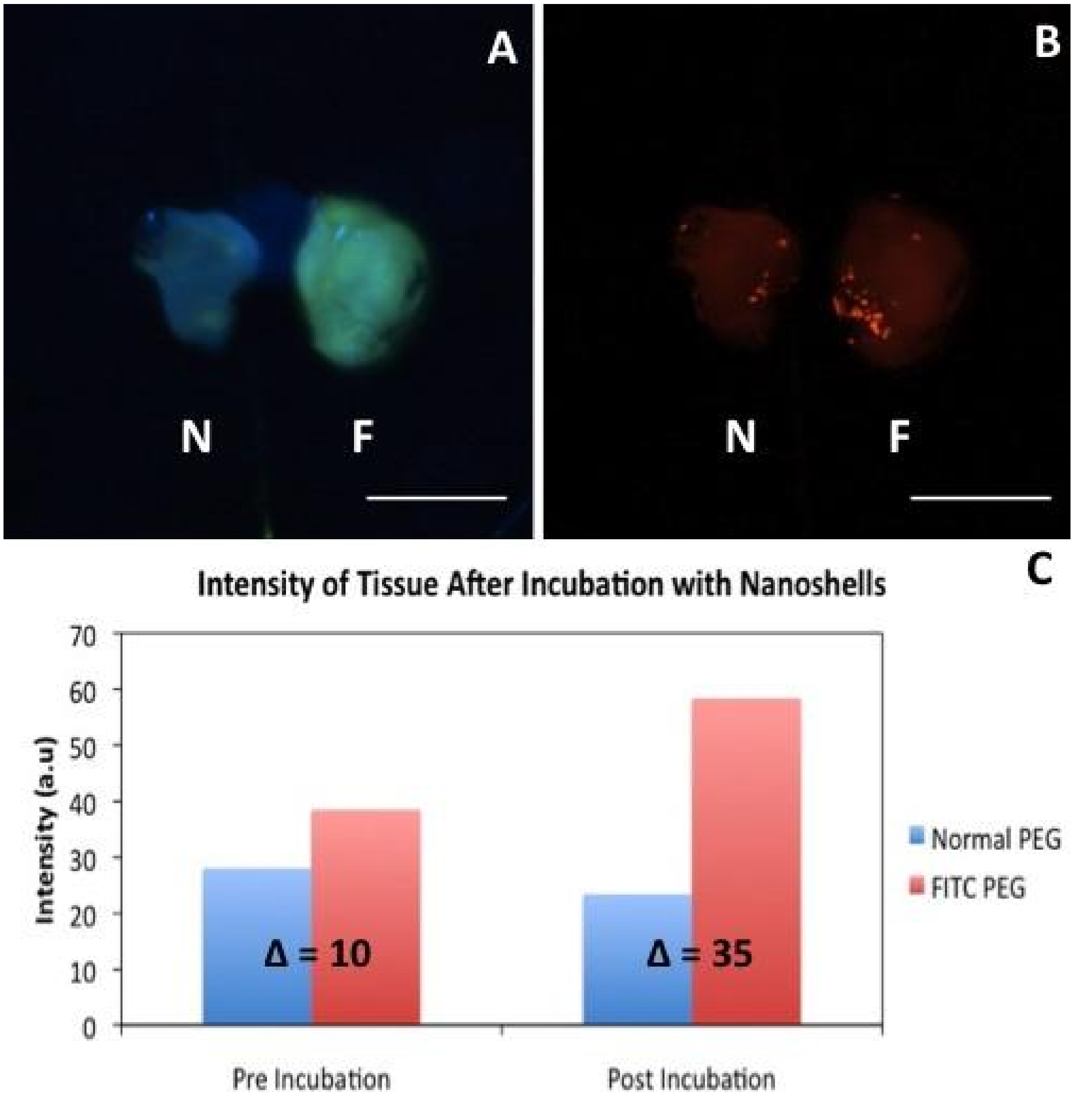

**Figure 6.9.**NS backfilled with FITC (F) or unmodified (N) PEG on tissue from the same patient. Figure 7.9(A) displays the increased signal from FITC in the blue imaging setup tissue labeled F. However, NIR imaging of the tissues showed minimal difference in scatter from the tissues, demonstrating that increased signal in A is due to FITC. Scale bar = 5 mm. Figure 7.9(C) quantifies the signal difference between the tissues before and after incubation with NS. Increased signal in the FITC NS was due to the presence of FITC on the NS.

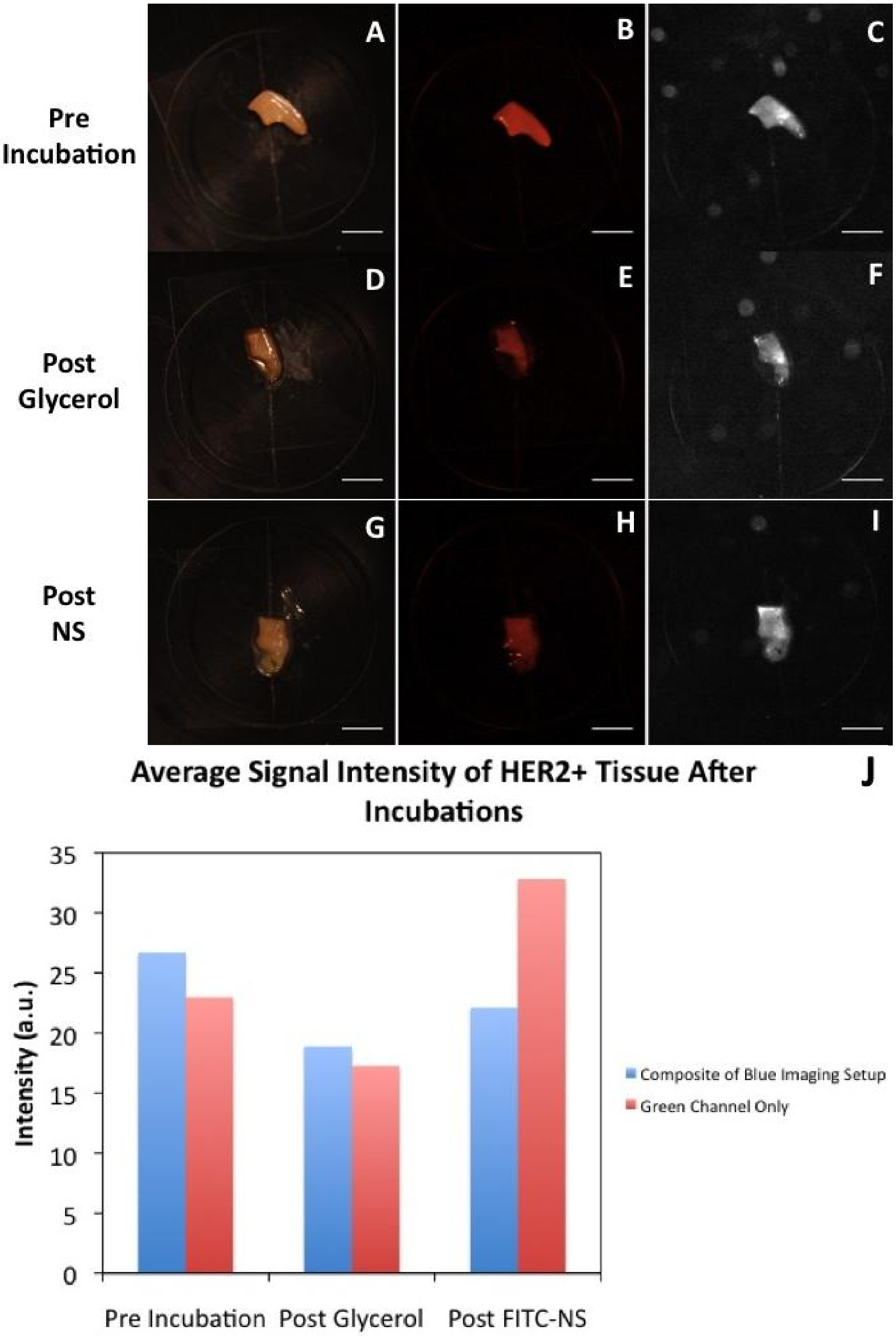

**Figure 6.10.**Images of HER2-positive tissue after incubation with glycerol (D-F) and anti-HER2 NS backfilled with FITC-PEG. Images demonstrate increased signal from FITC-NS showing distribution throughout the tissue. However, even with widespread tissue distribution, there was little increase in NIR signal from the tissue. Scale bar = 5 mm. Figure 7.10(J) displays intensities from FITC image composites and the green channel. Increased signal is due to FITC presence on the NS distributed throughout the tissue.

Even though we were unable to localize the anti-HER2 NS through NIR scattering, we were able to use white light imaging to visualize small pockets of NS using their absorbance (Fig 6.11). This demonstrates the system's ability to localize contrast agents through white light imaging, as long as the agent con provide ample contrast against the tissue without any special excitation and emission filters. These results are similar to data presented in prior years that showed absorbance of targeted NS on the surface of HER2-positive tissue.

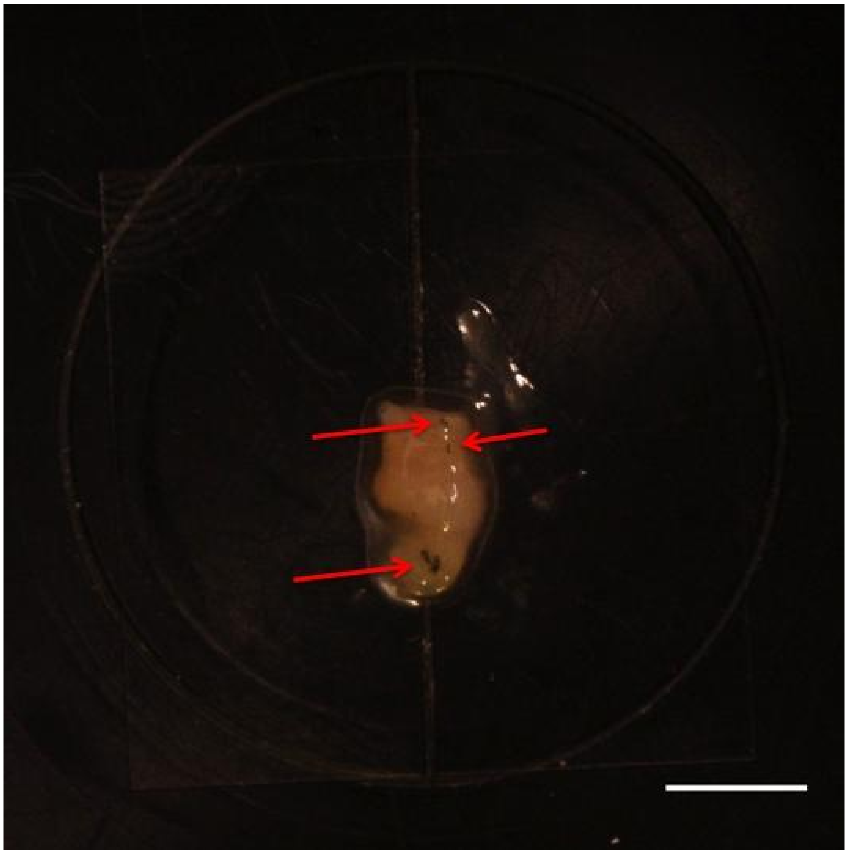

**Figure 6.11.** White light image of tissue presented in presented in 7.10(G) showing pockets of anti-HER2 NS binding, demonstrating the ability of our system to visualize the absorbance of targeted silica-gold NS in tissue. Scale ber = 5 mm.

To further demonstrate the compatibility of the system with other diagnostic agents, we incubated HER2-positive tissue with an NIR fluorescent dye that stains for EGFR. Recent studies by Xie, Ke, and Kovar et al. have demonstrated the intratumoral specificity of this dye in EGFR-overexpressing tumor xenografts(Xie et al. 2012; Ke et al. 2003; Kovar et al. 2007). The dye has an excitation maximum of 774 nm and emission maximum of 805 nm (Kovar et al. 2007), allowing us to visualize the fluorophore in our NIR setting with an LP800 filter. In Figure 12, pre (A) and post-incubation (B) results show distinct differences between tissues after incubation with the contrast agent. The blue hue seen in the tissue incubated with the dye is consistent with the signal observed when the fluorophore was suspended in a quartz cuvette (data not shown). This figure demonstrates the proof-of-concept that the imaging system can be used with a contrast agent that is not custom made (as was the case with the NS), but rather a commercially available product that has already demonstrated high specificity *in vivo*(Xie et al. 2012; Ke et al. 2003; Kovar et al. 2007).

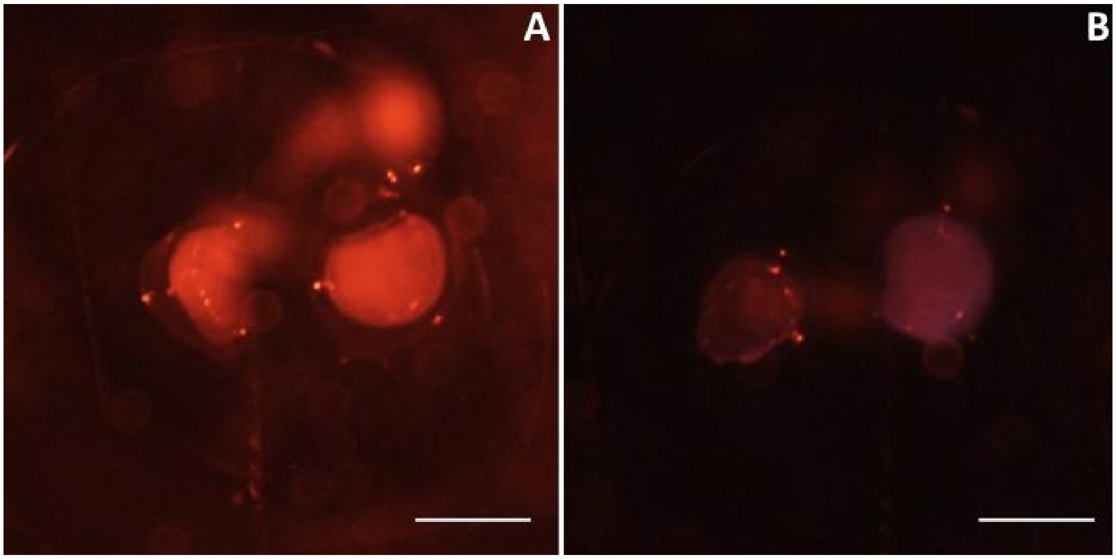

**Figure 6.12.**HER2-positive tissues before (A) and after (B) incubation with an NIR fluorescent EGFR dye. The tissue on the right of each image was the tissue incubated with the dye and the tissue on the left served as a control. There is a large difference in the tissues after incubation that was not seen in the pre-incubation images. Scale bar = 5 mm.

## Discussion

Our results indicate that we have developed a system that has the ability to image multiple wavelengths and contrast agents on the same tissue. The original design of the system was to visualize 2-NBDG fluorescence and NIR scattering from targeted silica-gold NS. We were unable to develop a method to differentiate NS scatter from tissue scatter; however, we were able to visualize NS absorbance from large aggregates using white light. Even though our system did not differentiate NIR scatter from tissue, we were able to show that we could visualize NIR fluorescence from the optical probe IRDye 800CW EGF. As its excitation and emission maxima are located in the middle of the water window (700-900 nm) (Bhushan et al. 2008) , IRDye 800CW is thought to have optimal characteristics for *in vivo* imaging (Kovar et al. 2007). In addition to imaging EGF, IRDye 800 CW has been conjugated to deoxy-glucose to visualize GLUT1 expression in the same manner as 2-NBDG (Xie et al. 2012; Kovar et al. 2009; Chatni et al. 2012). As the system can visualize contrast agents in three different modes (white light and visible/NIR fluorescence), it is conceivable that this system could be used to visualize three separate contrast agents on one tissue. However, this system is designed as a portable device to be used intra-operatively and provide surgeons with rapid visualization of cancerous tissue, so appropriate contrast agents would need to be selected.

One design parameter for the device was to develop the system using inexpensive components with minimum costs for customized parts and contrast agents. The total cost of the materials was $2,954.00. Additionally, two of the contrast agents that we used (2-NBDG and IRDye 800CW EGF) were commercially available products that required only re-suspension in PBS upon receipt, and their cost was $171.00 and $325.00, respectively. Our silica-gold NS were manufactured by Nanospectra and required functionalization with both an OPSS-PEG-antibody linker and PEG-SH. The integration of inexpensive imaging components with commercially available contrast agents dramatically decreases the overall construction and operation for this system while also providing enhanced visualization of contrast agents in cancerous tissue.

Another positive characteristic of this system is the ability to customize the system to contrast agents by replacing LEDs, excitation filters, and emission filters. As the majority of optical contrast agents have been focused in the NIR range due to their optimal signal-to-background (Kobayashi et al. 2010; Kovar et al. 2007), one could design the system so that multiple NIR dyes (such as Cy 5.5 and IRDye 800CW) with different molecular targets are imaged using different combinations of NIR LEDs and emission filters.

Finally, the speed with which tissues were incubated and imaged is a promising indication for the future use of this system. The goal of this project was to develop an imaging device that would provide surgeons with a rapid detection method of cancerous tissue using molecular contrast agents as a tool to lower positive margin rates. We do not envision this technology as a replacement for intraoperative pathology, but rather as a tool to help surgeons who do not have any method to visualize microscopic disease.

This device can also be thought of as a tool to supplement intraoperative pathology. As discussed earlier, a recent study by Vosoughhosseini et al. demonstrated that patients diagnosed with negative margins via standard H&E pathology were found to have positive margins when EGFR staining was performed on the same specimens (Vosoughhosseini et al. 2012). If the pathologists had a method of visualizing specific receptors in a rapid method, there is a greater possibility that these false negatives would have been avoided. Additionally, the system could also be used to pre-screen resected specimens by helping the surgical team visualize the specific areas of the margin that need H&E performed and not spend unnecessary resources and time on areas that are benign.

There are system limitations. As it is a wide-field imaging system, there are limitations to the resolution of the system. While we were able to visualize the signal from cells incubated with molecular contrast agents, individual cells could not be resolved. Additionally, this system can only visualize the surface of the tissues. However, this is also a limitation of the anti-HER2 NS, as the contrast agents do not penetrate the surface of the tissue in the limited incubation time (L. R. Bickford et al. 2012). Additionally, the operation of the system is done by hand. The system could be improved by integration with a data acquisition (DAQ) board so that control of the camera and image processing would be performed with a graphical user interface (GUI) that would easily translate clinically. An example of this interface is the MDM created by Roblyer at al(Roblyer et al. 2008). Futhermore, changing the filters between different wavelengths is also done by hand, and the use of a filter wheel to control the filters placement would also improve the translational ability of the system. Finally, we were unable to differentiate the NIR scatter of silica-gold NS from tissue, but we were still able to image the NS via their absorbance after aggregation on the tissue surface. In addition, we were still able to use the system to visualize the NIR fluorescence of a commercially available and highly specific contrast agent that has demonstrated enhanced contrast *in vivo*.

This system is an important first step in development of a translatable device that can be combined with highly specific contrast agents. It demonstrates that readily available components can be engineered to create a system that has the ability to provide physicians with a tool to visualize molecular expression in resected tissue in a limited amount of time. As it is low-cost and portable, one can imagine this system located in the surgical suite with a technician performing the tissue processing while the surgeon continues operating on the patient. The system can also be customized to visualize different contrast agents for other molecular markers that are more common in other cancers.

## Conclusion

The portable imaging device developed in this section was designed for compatibility with contrast agents that were characterized in previous work in our research group (L. R. Bickford et al. 2012; Langsner et al. 2011; L. R. Bickford et al. 2010; L. Bickford et al. 2008). Previously, we had found that optical contrast agents 2-NBDG and anti-HER2 silica-gold NS could differentiate cancerous tissue due to the overexpression of GLUT1 and HER2 proteins. We had also demonstrated that the contrast provided by these agents was done in a rapid manner (≤ 20 minutes), demonstrating possible use as an intraoperative agent. However, previous methods to visualize these agents were performed with non-portable and expensive equipment. Our system was designed to overcome these issues by developing a platform in which these agents could be visualized in tissue using inexpensive and portable components. By using LEDs, a DSLR, and commercially available optical filters, we were able to visualize the enhanced contrast of three different contrast agents, 2-NBDG, anti-HER2 silica-gold NS, and IRDye 800CW.

## KEY RESEACH ACCOMPLISHMENTS

### 2008

- Design of needle-based fiber optic imaging system completed and development of first generation system is ahead of schedule (Project 1)
- Demonstrated micron level resolution imaging using needle-compatible system (Project 1)
- Demonstrated system has the resolution and contrast to image individual cells (Project 1)
- Developed cadmium-free NIR qdots and demonstrated imaging benefits compared to conventional emissive nanomaterials (Project 2)
- Developed a synthesis method including scale up for gold nanorods (Project 2)
- Developed and published a method for quantifying gold nanomaterial cellular binding which will be broadly useful for evaluating gold materials developed in this project)
- Investigated how quickly we can achieve image contrast using antiHER2 gold nanomaterials and published these results (Project 2) demonstrating a 5 minute read out period is highly feasible (compared to the 60 minute read out used currently which is too long to be clinically feasible)
- Demonstrated two photon luminescence provides a potential contrast mechanism for targeted gold nanomaterials (Project 2) and published these results
- Demonstrated feasibility of nanotechnology-based optical scattering approach to radiation therapy direct dosimetry measurements although currently the level of radiation required for the approach to work is beyond what would be clinically feasible (Project 3)
- Worked with breast oncologists, surgeons, and pathologists to refine clinical applications and develop a process to move forward towards translation much work quickly than anticipated in the original SOW; in Year 2, we will request approval to changes in SOW so that additional tissue studies and, if possible, in vivo clinical trials can be completed during the time frame of the award
- Participated in the Breast Optical Imaging Working Group at MD Anderson Cancer Center to refine clinical strategies and will be attending this year's full Baylor College of Medicine Breast Cancer retreat as an invited speaker on the Era of Hope project to develop additional breast cancer collaborations to facilitate future clinical work
- First papers on work conducted as a part of this award have been published including joint work with the MD Anderson Cancer Center collaborators involved in the project

### 2009

- Development of a second generation needle-compatible fiber optic imaging system prototype for breast cancer applications. Unlike our first year design, this system is readily reconfigurable (modular illumination, detection, etc.) to provide flexibility as our design requirements evolve. The goal of this system is to provide an inexpensive method ($< 5K cost/instrument) for *in situ* tissue analysis with micron level resolution in a sub-mm package to provide optical biopsy without tissue removal. (Project 1)

- Demonstration of targeted molecular imaging using a novel gold nanorodbioconjugation method. These structures may be used for both the imaging experiments which comprise the last tasks in Project 2 and for the activatable radiation monitoring applications throughout Project 3. Nanorods are more attractive than conventional silica-gold nanoshells for some types of imaging/therapy applications due to smaller size and enhanced absorption. A heterobifunctional PEG with exposed carboxyl groups for antibody conjugation was used to generate surface modified nanorods for HER2 targeted imaging applications. Proof of principle cellular imaging results are reported. (Project 2/Project 3)

- As an alternative to shaping gold (gold nanorods), we have demonstrated both by simulation and now experimentally similar NIR tunability can be achieved through a new type of gold nanoshell (multilayered gold-silica-gold nanoshells). An *Optics Express* paper reports on the physics governing these particles' properties. Synthesis efforts are underway and it is expected these particles may be used in breast cancer imaging and radiation monitoring applications in Projects 2 and 3 in future years. (Project 2/3)

- As part of the biological characterization component of Project 2, we evaluated a number of cells lines including herceptin-resistant lines.We unexpectedly discovered targeted nanoshells bind to herceptin-resistant cell lines much more strongly than we would have anticipated for the line where one might expect MUC interference. This ispossibly due to the high surface area/volume allowing large numbers of potential binding sites on the nanoparticle to be present and opens up intriguing new possibilities for the use of these types of particles as nanotheranostics for treatment of HER2+, herceptin resistant women (Project 2)

- Evaluated strategy for dose measurement during radiation treatment for breast cancer (Project 3)

- My proposal expressed a desire to build connections between my group with the breast centers at both MD Anderson Cancer Center and Baylor College of Medicine to create a sustainable infrastructure for breast cancer research that will continue after the present grant ends. I attended the Baylor College of Medicine Breast Cancer Center Annual Retreat this year and gave a talk on my work resulting in a number of new collaborations. Based on these presentations, I was recently invited by the head of the center to become an adjunct faculty member which will facilitate my future involvement and provide access to all of Baylor's shared cores at internal prices.

**2010**

- Development of a second generation needle-compatible fiber optic imaging system prototype for breast cancer applications. Unlike our first year design, this system is readily reconfigurable (modular illumination, detection, etc.) to provide flexibility as our design requirements evolve. The goal of this system is to provide an inexpensive method ($< 5K cost/instrument) for *in situ* tissue analysis with micron level resolution in a sub-mm package to provide optical biopsy without tissue removal. (Project 1)

- Demonstration of targeted molecular imaging using a novel gold nanorodbioconjugation method. These structures may be used for both the imaging experiments which comprise the last tasks in Project 2 and for the activatable radiation monitoring applications throughout Project 3. Nanorods are more attractive than conventional silica-gold nanoshells for some types of imaging/therapy applications due to smaller size and enhanced absorption. A heterobifunctional PEG with exposed carboxyl groups for antibody conjugation was used to generate surface modified nanorods for HER2 targeted imaging applications. Proof of principle cellular imaging results are reported. (Project 2/Project 3)

- As an alternative to shaping gold (gold nanorods), we have demonstrated both by simulation and now experimentally similar NIR tunability can be achieved through a new type of gold nanoshell (multilayered gold-silica-gold nanoshells). An *Optics Express* paper reports on the physics governing these particles' properties. Synthesis efforts are underway and it is expected these particles may be used in breast cancer imaging and radiation monitoring applications in Projects 2 and 3 in future years. (Project 2/3)

- As part of the biological characterization component of Project 2, we evaluated a number of cells lines including herceptin-resistant lines.We unexpectedly discovered targeted nanoshells bind to herceptin-resistant cell lines much more strongly than we would have anticipated for the line where one might expect MUC interference. This ispossibly due to the high surface area/volume allowing large numbers of potential binding sites on the nanoparticle to be present and opens up intriguing new possibilities for the use of these types of particles as nanotheranostics for treatment of HER2+, herceptin resistant women (Project 2)

- Evaluated strategy for dose measurement during radiation treatment for breast cancer (Project 3)

- My proposal expressed a desire to build connections between my group with the breast centers at both MD Anderson Cancer Center and Baylor College of Medicine to create a sustainable infrastructure for breast cancer research that will continue after the present grant ends. I attended the Baylor College of Medicine Breast Cancer Center Annual Retreat this year and gave a talk on my work resulting in a number of new collaborations. Based on these presentations, I was recently invited by the head of the center to become an adjunct faculty member which will facilitate my future involvement and provide access to all of Baylor's shared cores at internal prices.

**2011**

- As noted in our Year 3 report, we received approval from Rice University and DoD for an exemption protocol for acquisition of breast tissue from the NCI Cooperative Human Tissue Network so that we could test our imaging systems and agents using more biologically relevant samples. This allowed us to conduct a series of tissue studies in Year 4 providing preliminary results demonstrating the potential clinical utility of the methods and imaging agents being developed. As we expected, critical issues to ultimate clinical implementation, such as the impact of neoadjuvant chemotherapy on our proposed methods were able to be identified from working with human breast tissue samples rather than simpler mimics.

- We have continued to improve performance of the needle compatible system for microscopic, high resolution imaging (United States provisional patent submitted) incorporating an improved illumination set up over the past reporting period (**Project 1**)

- We have continued development of the macroscopic imaging system suitable for visualization of large regions of the breast at once. In Year 3, we demonstrated the first generation device. In Year 4, we have designed and began assembly of the second generation device. This is designed to be a handheld device surgeons could ultimately use to guide tumor resection. (**Project 2**)

- We have synthesized cadmium-free NIR quantum dots for molecular targeted fluorescence imaging at wavelengths high enough that there will not be interference from autofluorescence (**Project 3**)

- We have designed a new type of layered nanoparticle which we envision to be of particular use for multiplexed molecular imaging. The particles consist of a gold core, silica middle layer, and outer gold shell with the core offset with respect to the center of the particle, providing ability to sculpt optical properties to meet specific design criteria (**Project 3** – described in ACS Nano paper)

- We have begun assessment of glucose conjugated gold nanoparticles as a means to assess metabolic activity in order to broaden the range of molecular features of cancer we are able to probe. This work was initiated in response to a suggestion received at the DoD LINKS meeting. (**Project 3**)

**2012**

- During Year 5, we have continued to benefit from receiving protocol approval for the use of human tissue from the NCI Cooperative Human Tissue Network. Building on our prior published work using tissue slices, we were able to continue a shift to more translational work through working with whole tissue imaging, mimicking the conditions we would expect to encounter in the future in the surgical suite setting. A paper on our most recent work in now under review at *Journal of Oncology.*

- We have completed verification using a hyperspectral imaging approach that targeted nanoparticle binding was the origin of increased contrast in HER2+ tissue.

- Over the past year, we have completed construction of the final hand held instrument for intraoperative tumor margin delineation. This is the final macroscopic imaging system we have developed via Project 2 of this award. The device is fully functioning. During the next year, we will complete imaging studies using this system.

- We have continued to make progress on enhancing the range of molecular markers being addressed using gold nanoparticle technology in Project 3. We presented development of the glucose nanoparticles for metabolic imaging in Year 4. In Year 5, we progressed to cellular level studies described in the prior section. During the upcoming year we plan to conduct TEM studies to verify we understand our imaging data and write a manuscript on this work.

- A provisional patent was submitted on a new gold nanoparticle synthesis strategy. A paper describing the strategy was published and is included in the appendix. The method allows synthesis of gold nanoparticles over a broad range of sizes in a rapid and inexpensive fashion facilitating many of the theranostic applications now under development.

## Reportable Outcomes

## 2008

### Journal Articles (acknowledging DOD Era of Hope Scholar support)

- Sun, J., Fu, F., Zhu, MQ, Bickford, L., Post, E., and Drezek, R. "Near-Infrared Quantum Dot Contrast Agents for Fluorescence Tissue Imaging: A Phantom Study." *Current Nanoscience*. Submitted. July 2008.

- Bickford, L., Chang, J., Fu, K., Sun, J., Hu, Y., Gobin, A., Yu, TK, and Drezek, R. "Evaluation of Immunotargeted Gold Nanoshells as Rapid Diagnostic Imaging Agents for HER2-Overexpressing Breast Cancer Cells: A Time-Based Analysis." *Nanobiotechnology*. Published online (5/13/2008). Print issue in press.

- Bickford, L., Sun, J., Fu, K., Lewinski, N., Nammalvar, V., Chang, J., Drezek, R. "Enhanced Multi-Spectral Imaging of Live Breast Cancer Cells Using Immunotargeted Gold Nanoshells and Two-Photon Excitation Microscopy." *Nanotechnology*. 19: 315102 (6pp) doi: 10.1088/0957-4484/19/31/315102 (2008).

- Fu, K., Sun, J., Bickford, L., Lin, A., Halas, N., Yu, TK, and Drezek, R. "Measurement of ImmunotargetedPlasmonic Nanoparticle Cellular Binding: A Key Factor in Optimizing Diagnostic Efficacy." *Nanotechnology.* 19: 045103 (2008).

### Abstracts

- Sun, J., Fu, F., Zhu, M-Q., Bickford, L., Post, E., and Drezek, R. "PbS Quantum Dots for Near-infrared Fluorescence Imaging." OSA 2008 Frontiers in Optics (FiO)/Laser Science XXIV Conference. Rochester, NY. 2008.
- Drezek, R. "Nanotechnology-Enabled Optical Molecular Imaging of Cancer." Department of Defense Breast Cancer Research Program Era of Hope Conference. Baltimore, MD. June 2008.
- Bickford, L., Chang, J., Fu, K., Sun, J., Hu, Y., Yu, T.K., Drezek R. "ImmunotargetedNanoshells for Point of Care Diagnostic Applications." Biomedical Optics. St. Petersburg, FL. March 2008.

### Invited Presentations

- Nanotechnology-Enabled Optical Molecular Imaging of Breast Cancer. Baylor College of Medicine Breast Center Annual Retreat. 2008.
- Nanotechnology-Enabled Optical Molecular Imaging of Cancer. Department Seminar. Duke University Fitzpatrick Optics Institute. 2008-2009 seminar series.
- Rice/Texas Medical Center Translational Research in Optical Molecular Imaging of Cancer. Rice University President's House "Something New for Lunch" Lecture. 2008.

- Nanotechnology-Enabled Optical Molecular Imaging of Cancer. Department Seminar.

University of Rochester. 2008-2009 seminar series.

- Applications of Gold Nanoparticles in Cancer Diagnostics. IEEE LEOS Summer Topical Conference: Advances in Nanobiophotonics. Mexico. July 2008.
- Applications of Gold Nanoparticles in Cancer Diagnostics. American Society of Photobiology Annual Meeting. June 2008.
- Optically Activated Nanoparticles for Imaging and Therapy of Cancer. Department Seminar. Beckman Laser Institute, University of California at Irvine. March 2008.
- Optically Activated Nanoparticles for Imaging and Therapy of Cancer. Department Seminar. Rutgers Department of Bioengineering. March 2008.
- Optically Activated Nanoparticles for Imaging and Therapy of Cancer. Department Seminar. University of Washington. Nanotechnology Seminar Series. February 2008.
- Optically Activated Nanoparticles for Imaging and Therapy of Cancer. Department Seminar. MD Anderson Cancer Center Radiology Department. February 2008.
- Hot Topic Nanomedicine Workshop. SPIE Photonics West. San Jose, CA. January 2008.
- Biomedical Applications of Quantum Dots. SPIE Photonics West. San Jose, CA. January 2008.
- Nanotechnology Enabled Optical Imaging of Cancer. The Materials/Biology Interface. Material Research Society (MRS) Annual Meeting. Boston, MA. November 2007.
- Needle Compatible Fiber Probe for Optical Imaging of Cancer. Department of Interventional Radiology. November 2007.
- Nanotechnology Enabled Molecular Targeted Optical Imaging of Cancer. Department Seminar. University of Texas at Austin. October 2007.
- Nanotechnology Enabled Optical Imaging of Cancer. United States/France Nanomedicine Symposium. October 2007.

**2009**

**Journal Articles Acknowledging DOD Era of Hope Scholar Support**

- Sun, J., Fu, K., Zhu, MQ, Bickford, L., Post, E., and Drezek, R. “Near-infrared quantum dots for fluorescence tissue imaging” *Current Nanoscience*, 5 (2), 160-166 (2009). *(Last year this work was reported as submitted. It has now been accepted and published. A pdf of the published version is included.)*

- Hu, Y., Fleming, R., and Drezek, R. “Optical properties of gold-silica-gold multilayered nanoshells.” *Optics Express.* Vol 16, 24,19579 (2008).

- Hleb, E., Hu, Y., Drezek, R., Hafner, J., and Lapotko, D. “Photothermal bubbles as optical scattering probes for imaging live cells.” *Nanomedicine.* 3(6), 797-812 (2008). (doi:10.2217/17435889.3.6.797)

- Rostro-Kohanloo, B., Bickford, L., Payne, C., Day, E., Anderson, L., Zhong, M., Zhong, Lee, S., Mayer, K., Zal, T., Adam, L., Dinney, C., Drezek, R., West, J., and Hafner, J. "Stabilization and Targeting of Surfactant-Synthesized Gold Nanorods."

*Nanotechnology*. Accepted for publication in 2009 (*A copy of the accepted manuscript is included. Page proofs have not arrived yet.)*

- Bickford, L., Chang, J., Fu, K., Sun, J., Hu, Y., Gobin, A., Yu, TK, and Drezek, R. "Evaluation of Immunotargeted Gold Nanoshells as Rapid Diagnostic Imaging Agents for HER2+ Breast Cancers." *Nanobiotechnology*. 1551-1286 (Print) 1551-1294 (Online); DOI 10.1007/s12030-008-9010-4 (2008). *Became available online in 2008 and in print 2009.*

- Bickford, L., Sun, J., Fu, K., Lewinski, N., Nammalvar, V., Chang, J., Drezek, R. "Enhanced Multi-Spectral Imaging of Live Breast Cancer Cells Using Immunotargeted Gold Nanoshells and Two-Photon Excitation Microscopy." *Nanotechnology*. 19: 315102 (6pp) doi: 10.1088/0957-4484/19/31/315102 (2008). *Published June 24, 2008.*

## Abstracts

- Bickford, L. and Drezek, R. Gold Nanoshells as Potential Real-Time Intraoperative Molecular Probes for HER2/NEU Overexpression Using Near-Infrared Reflectance Confocal Microscopy. Annual Houston Conference on Biomedical Engineering Research. Houston, TX. March 2009.

- Hu, Y., and Drezek, R. Angular scatter patterns from multi-layered gold nanoshells. Materials Research Society Spring Annual National Meeting. San Francisco, CA. April 2009.

- Sun, J., Fu, F., Zhu, M-Q., Bickford, L., Post, E., and Drezek, R. "PbS quantum dots for near-infrared fluorescence imaging." OSA 2008 Frontiers in Optics (FiO)/Laser Science XXIV Conference. Rochester, NY. October 19-23, 2008.

## Invited Presentations

- Optical activatable nanoparticles for imaging and therapy of cancer. Department Seminar. Duke University Fitzpatrick Optics Institute 2008-2009 Seminar Series. Durham, NC. March 2009.

- Optical molecular imaging of breast cancer. Baylor College of Medicine Cancer Center Annual Retreat. Cleveland, TX. November 2008.

- Optical molecular imaging and therapy of breast cancer. Distinguished Speaker Seminar Series. Department of Pharmacology. University of Houston. April 2009.

- Optically activatable nanoparticles for imaging and therapy of cancer. Department Seminar. University of Rochester. Department of Biomedical Engineering. Rochester, NY. November 2008.

- Translational research in optical molecular imaging of breast cancer. Rice University Something New for Lunch Lecture Series. Houston, TX. October 2008.

- Invited talked "Advances in Nanobiophotonics" IEEE LEOS Summer Topical Conference. July 2008.

## Employment

- The PI was promoted to Professor of Biomedical Engineering in large part because of results obtained through this research project.

- The PI has been invited to become Adjunct Faculty at Baylor College of Medicine because of the breast cancer collaborations initiated as part of this research

## 2010

## Journal Articles Acknowledging DOD Era of Hope Scholar Support

- Sun, J., Fu, K., Zhu, MQ, Bickford, L., Post, E., and Drezek, R. "Near-infrared quantum dots for fluorescence tissue imaging" *Current Nanoscience*, 5 (2), 160-166 (2009). *(Last year this work was reported as submitted. It has now been accepted and published. A pdf of the published version is included.)*

- Hu, Y., Fleming, R., and Drezek, R. "Optical properties of gold-silica-gold multilayered nanoshells." *Optics Express.* Vol 16, 24,19579 (2008).

- Hleb, E., Hu, Y., Drezek, R., Hafner, J., and Lapotko, D. "Photothermal bubbles as optical scattering probes for imaging live cells." *Nanomedicine.* 3(6), 797-812 (2008). (doi:10.2217/17435889.3.6.797)

- Rostro-Kohanloo, B., Bickford, L., Payne, C., Day, E., Anderson, L., Zhong, M., Zhong, Lee, S., Mayer, K., Zal, T., Adam, L., Dinney, C., Drezek, R., West, J., and Hafner, J. "Stabilization and Targeting of Surfactant-Synthesized Gold Nanorods." *Nanotechnology.* Accepted for publication in 2009 (*A copy of the accepted manuscript is included. Page proofs have not arrived yet.)*

- Bickford, L., Chang, J., Fu, K., Sun, J., Hu, Y., Gobin, A., Yu, TK, and Drezek, R. "Evaluation of Immunotargeted Gold Nanoshells as Rapid Diagnostic Imaging Agents for HER2+ Breast Cancers." *Nanobiotechnology*. 1551-1286 (Print) 1551-1294 (Online); DOI 10.1007/s12030-008-9010-4 (2008). *Became available online in 2008 and in print 2009.*

- Bickford, L., Sun, J., Fu, K., Lewinski, N., Nammalvar, V., Chang, J., Drezek, R. "Enhanced Multi-Spectral Imaging of Live Breast Cancer Cells Using Immunotargeted Gold Nanoshells and Two-Photon Excitation Microscopy." *Nanotechnology*. 19: 315102 (6pp) doi: 10.1088/0957-4484/19/31/315102 (2008). *Published June 24, 2008.*

## Abstracts

- Bickford, L. and Drezek, R. Gold Nanoshells as Potential Real-Time Intraoperative Molecular Probes for HER2/NEU Overexpression Using Near-Infrared Reflectance Confocal Microscopy. Annual Houston Conference on Biomedical Engineering Research. Houston, TX. March 2009.

- Hu, Y., and Drezek, R. Angular scatter patterns from multi-layered gold nanoshells. Materials Research Society Spring Annual National Meeting. San Francisco, CA. April 2009.

- Sun, J., Fu, F., Zhu, M-Q., Bickford, L., Post, E., and Drezek, R. "PbS quantum dots for near-infrared fluorescence imaging." OSA 2008 Frontiers in Optics (FiO)/Laser Science XXIV Conference. Rochester, NY. October 19-23, 2008.

## Invited Presentations

- Optical activatable nanoparticles for imaging and therapy of cancer. Department Seminar. Duke University Fitzpatrick Optics Institute 2008-2009 Seminar Series. Durham, NC. March 2009.

- Optical molecular imaging of breast cancer. Baylor College of Medicine Cancer Center Annual Retreat. Cleveland, TX. November 2008.

- Optical molecular imaging and therapy of breast cancer. Distinguished Speaker Seminar Series. Department of Pharmacology. University of Houston. April 2009.

- Optically activatable nanoparticles for imaging and therapy of cancer. Department Seminar. University of Rochester. Department of Biomedical Engineering. Rochester, NY. November 2008.

- Translational research in optical molecular imaging of breast cancer. Rice University Something New for Lunch Lecture Series. Houston, TX. October 2008.

- Invited talked "Advances in Nanobiophotonics" IEEE LEOS Summer Topical Conference. July 2008.

## Employment

- The PI was promoted to Professor of Biomedical Engineering in large part because of results obtained through this research project.

- The PI has been invited to become Adjunct Faculty at Baylor College of Medicine because of the breast cancer collaborations initiated as part of this research

## 2011

## Peer Reviewed Journal Papers

Sun, J., C. Shu, et al. (2010). "Needle-compatible single fiber bundle image guide reflectance endoscope." J Biomed Opt**15**(4): 040502. (A Word document of the version of this manuscript in place prior to publication was submitted in last year's report. This year we include the published paper.)

Hu, Y., Noelck, S., and Drezek, R. "Symmetry breaking in gold-silica-gold multilayer nanoshells." ACS Nano. 4(3): 1521-1528 (2010).

Carpin, L. B., L. R. Bickford, et al. (2011). "Immunoconjugated gold nanoshell-mediated photothermal ablation of trastuzumab-resistant breast cancer cells."Breast Cancer Res Treat**125**(1): 27-34.

## Abstracts

Bickford, L., and Drezek, R. Gold-silica nanoshells for targeted imaging of tumor margins.Biomedical Engineering Society Annual National Meeting. Austin, TX. October 2010.

Langsner, R., Yu,K., and Drezek, R. The Use of 2-NBDG for Optical Assessment of Breast Tumor Margins.Biomedical Engineering Society Annual National Meeting. Austin, TX. October 2010.

Noelck, S. and Drezek, R.Optical Properties of Gold-Silica-Gold Nanoshells.Biomedical Engineering Society Annual National Meeting. Austin, TX. October 2010.

Noelck, S., Hu, Y., and Drezek, R.Probing Optical Properties of Gold-Silica-Gold Multilayer Nanoshells with Broken Symmetry, 2010 Inter IGERT Nanoscience and Professional Development Workshop. Austin, TX. 2010.

Langsner, R., Drezek, R,and Yu, K. Towards 2-NBDG for Intraoperative Assessment of Tumor Margins.Gordon Conference on Lasers in Surgery and Medicine. 2010.

## Other Presentations

Drezek, R. Nanotechnology Enabled Optical Molecular Imaging of Cancer. DoD Links Meeting. 2011. Small group presentations.

## Jobs

Dr. Jiantang Sun, a postdoctoral fellow funded by this project, became an Associate Professor at the Chinese Academy of Sciences Suszhou Institute of Biomedical Engineering

Dr. Lissett Bickford, a graduate student who worked on this project, completed her PhD degree in Biomedical Engineering and joined the cancer nanotechnology lab of Dr. Joe DeSimone, a NIH Pioneer Award winner

## Awards

Robert Langsner, a graduate student funded by this project, received the 2010 Edgar O'Rear Travel Award for conference travel support

## 2012

### Peer Reviewed Publications

Lissett R. Bickford*, Robert J. Langsner*, Joseph Chang, Laura C. Kennedy, Germaine D. Agollah, Rebekah A. Drezek."Rapid stereomicroscopic imaging of HER overexpression in *ex vivo* breast tissue using topically applied silica-based gold nanoshells." J of Oncology.In review (2012).

Young, J. K., Figueroa, E. R., & Drezek, R. A. (2012).Tunable nanostructures as photothermaltheranostic agents.*Annals of biomedical engineering*, *40*(2), 438-59.doi:10.1007/s10439-011-0472-5 (2012).

Joseph K Young, Nastassja A Lewinski, Robert J Langsner, Laura C Kennedy, ArthiSatyanarayan, VengadesanNammalvar, Adam Y Lin and Rebekah A Drezek. "Size-controlled synthesis of monodispersed gold nanoparticles via carbon monoxide gas reduction" Nanoscale Research Letters (2011). 6:428. doi:10.1186/1556-276X-6-428

### Book Chapter

Bickford, L., Carpin, L, Sun, J., Lin, A., Loo, C., Yu, T., and Drezek, R."Chapter 95: Non-invasive Optical and Functional Imaging of Breast Tissue" Book chapter in *Advanced Therapy of Breast Disease.*BC Decker (2012).*(This chapter is for a revised edition of this book. While it is not research based so not directly supported by DoD CDMRP, as part of our Era of Hope project we have been participating in writing opportunities that provide clinicians focused on breast cancer background on the potential of emerging optical technologies.)*

### Abstracts

Drezek, R. Optical Molecular Imaging of Breast Cancer Using Nanoengineered Agents.Era of Hope Meeting. Florida. August 2011.

Joseph K. Youngand Rebekah Drezek."Synthesis and Characterization of Au2S/Au Core/Shell Nanostructures" 2011 Joint Annual Conference of NSBP and NSHP (2011).

### Provisional Patent Application

Size Controlled Synthesis of Gold Nanoparticles Using Carbon Monoxide Based Reduction. 61/500,376. June 23, 2011 (Joseph Young)

### Jobs

Lissett Bickford, whose PhD research as a graduate student was funded by this award, has accepted a faculty position at Virginia Tech beginning July 2012

## Awards

Joseph Young,  a portion of whose PhD research as a graduate student was funded by this award. was 1 of 20 United States graduate students selected by National Nanotechnology Initiative to attend global nanotechnology winter school in Brazil, Joseph Young (Winter 2012)**;** Joseph Young received the OSA/SPIE award for best presentation in photonics (2011);Joseph Young received the American Physical Society, Condensed Matter Division, 1st place poster (2011)

## Conclusion

Our research team has focused the majority of its Era of Hope research efforts specifically in areas of breast cancer care where the combination of ***miniaturized optical devices*** and ***molecular-specific imaging agents*** offer the potential to address current gaps in care. There are two primary areas where I believe our technologies can make the biggest difference: ***early detection*** and ***integrated delivery and monitoring of therapy.*** Optical spectroscopy, implemented through small fiber optics, can provide clinically valuable information ranging from cellular metabolic status (via endogenous fluorescence) to nuclear size (correlated to optical scatter) to quantitative measurements of molecular markers (through targeted imaging agents under development in our lab). Most of our effort has focused on development of needle-compatible spectroscopic and direct imaging probes for breast cancer applications. The technology is being designed for clinical applications for which it is valuable to have a local high resolution imaging method to complement a more macroscopic imaging modality (for example, during ultrasound guided breast biopsy). Progressive design and evaluation of the needle-based technologies has been the focus of **Project 1** of our DOD project. In Year 3, we added in a new project, **Project 2**, to allow us to further develop a multi-modal, widefield optical imaging device. To complement our imaging technology development projects, the second primary effort underway is development of molecular-specific optical imaging probes (**Projects 3**). Much of the work underway in **Project 3** has been directly applicable to tumor margins assessment, and we have presented our results in this area in our series of annual reports.

## References

### Year 1

[1] Sausville, Edward A. and Longo, Dan L.: Principles of Cancer Treatment: Surgery, Chemotherapy, and Biologic Therapy in Harrison's Principles of Internal Medicine, 16th Ed. Kaspar, Dennis L. et al., editors. p.446 (2005)

[2] Ward, DE and Sapecki, R. “Innocent Bystanders or Partners in Crime.” Ohio State University Frontiers Magazine Archive 2005; accessed online. http://www.jamesline.com/news/publications/frontiers/archives/?ID=1570&CID=0

[3] Bancroft JD, Gamble M, editors. Theory and Practice of Histological Techniques, 5th edition. Edinburgh: Churchill Livingstone, 2002.

[4] Ross MH, Romrell LJ, Kaye GI. Histology A Text and Atlas. Third ed. Baltimore: Williams & Wilkins, 1995.

[5] Parker SH, Lovin JD, Jobe WE, et al. Stereo-tactic breast biopsy with a biopsy gun. Radiology 1990; 176:741-747.

[6] Parker SH, Jobe WE, Dennis MA, et al. US-guided automated large-core biopsy. Radiology 1993; 187:507-511.

[7] Schueller G, Jaromi S, Ponhold L, et al. US-guided 14-gauge core-needle breast biopsy: results of a validation study in 1352 cases. Radiology 2008; 248(2); 406-413.

[8] Dowlatshahi K, Jokich PM, Schmidt R, Bibbo M, Dawson PJ. Cytologic diagnosis of occult breast lesions using steriotaxic needle aspiration. Arch. Surg. 1987; 122: 1343-1346.

[9] The Uniform Approach to Breast Fine-Needle Aspiration Biopsy (adopted from proceedings of a NCI sponsored conference in 1996). Am. J. Surg. 1997; 174: 371-385.

[10] Barra A, Gobbi H, Rezende CA, et al. A Comparison of Aspiration Cytology and Core Needle Biopsy According to Tumor Size of Suspicious Breast Lesions. Diagn. Cytopathol. 2007; 36(1): 26-31.

[11] Dowlatshahi K, Yaremko ML, Kluskens LF, and Jokich PM. Nonpalpable Breast Lesions: Findings of Stereotaxic Needle-Core Biopsy and Fine-Needle Aspiration Cytology. Radiology 1991: 181:745-750.

[12] Spaner SJ and Warnock GL. A brief history of endoscopy, laparoscopy, and laparoscopic surgery. J Laparoendosc Adv Surg Tech A. 1997 Dec;7(6):369-373.

[13] Flusberg BA, Cocker ED, Piyawattanametha WP, Jung JC, Cheung ELM, and Schnitzer MJ. Fiber-optic fluorescence imaging. Nat. Methods 2005;2:941-950.

[14] Kimura S and Wilson T. Confocal scanning optical miscroscope using single-mode fiber for signal detection. Appl. Opt. 1991;30:2143-2150

[15] Delaney PM, Harris MR, and King RG. Fibre-optic laser scanning confocal microscope suitable for fluorescence imaging. Appl. Opt. 1994;33:573-577.

[16] Dickensheets DL and Kino GS. Micromachined scanning confocal optical microscope. Electron Lett 1991;27:724-726

[17] Liu JTC, Mandella MJ, Ra H, Wong LK et al. Miniature near-infrared dual-axes confocal microscope utilizing a two-dimensional microelectromechanical systems scanner. Opt Lett. 2007;32:256-258.

[18] Shin HJ, Pierce MC, Lee D, Ra H, Solgaard O, and Richard-Kortum R. Fiber-optic confocal microscope using a MEMS scanner and miniature objective lens. Opt Express 2007;15:9113-9122.

[19] Seibel EJ and Smithwick QYJ. Unique Features of Optical Scanning, Single Fiber Endoscopy. Lasers Surg Med 2002;30:177-183

[20] Polglase AL, McLaren WJ, Skinner SA, Kiesslich R, Neurath MF, and Delaney PM. Fluorescence confocal endomicroscope for in vivo microscopy of the upper and lower gastrointestinal tract. Gastrointest Endosc 2005;62:686-695.

[21] Kiesslich R, Goetz M, Vieth M, Galle PR, and Neurath MF. Technology Insight: confocal laser endoscopy for in vivo diagnosis of colorectal cancer. Nat Clin Pract Oncol 2007;4:480-490.

[22] Harris MR. UK patent 2001:GB2340332B.

[23] Yelin D, Rizvi I, White WM et al. Three-dimensional miniature endoscopy. Nature 2006;443:765.

[24] Gmitro AF and Aziz DJ. Confocal microscopy through a fiber-optic imaging bundle. Opt. Lett. 1993;18:565-567.

[25] Sumitomo Electric. Silica Image Guide for Fiberscope. Proprietary Technical Document 2008.

[26] Juskaitis R, Wilson T, and Watson TF. “Real-time white light reflection confocal microscopy using a fibre-optic bundle” Scanning 1997;19:15-19.

[27] Liang C, Descour M, Sun KB, and Richards-Kortum R. Fiber confocal reflectance microscope (FCRM) for in-vivo imaging. Opt. Express 2001;9:821-830.

[28] Jean F, Bourg-Heckly G, and Viellerobe B. Fibered confocal spectroscopy and multicolor imaging system for in vivo fluorescence analysis. Opt. Express 2007;15:4008-4017.

[29] Dubaj V, Mazzolini A, Wood A, and Harris M. Optic fibre bundle contact imaging probe employing a laser scanning confocal microscope. J. Microsc. 2002;207:108-117.

[30] Sabharwal YS, Rouse AR, Donaldson L, Hopkins MF, and Gmitro AF. Slit-Scanning Confocal Microendoscope for high-Resolution In Vivo Imaging. Appl. Opt. 1999;38:7133-7144.

[31] Muldoon TJ, Pierce MC, Nida DL, Williams MD, Gillenwater A, and Richards-Kortum R. Subcellular-resolution molecular imaging within living tissue by fiber microendoscopy. Opt. Express 2007;15(25):16413-16423.

[32] Oppenheim AV, Wilsky AS, and Hamid S. Signals and Systems, 2nd Ed. New Jersey: Prentice Hall; 1996.

[33] Oppenheim AV, Schafer RW, and Buck JR. Discrete-Time Signal Processing, 2nd Ed. New Jersey: Prentice Hall 1999.

[34] Laemmel E, Genet M, Le Goualher G, Perchant A, Le Gargasson JF, and Vicaut E. Fibered confocal fluorescence microscopy (Cell-viZio) facilitates extended imaging in the field of microcirculation. A comparison with intravital microscopy. J. Vasc. Res. 2004;41:400-411.

[35] Delaney P and Harris M. Handbook of Biological Confocal Microscopy, 3rd Ed. New York: Springer 2007.

[36] Wahlby C, Sintorn IM, Erlandsson F, and Bengtsson E. Combining intensity, edge and shape information for 2D and 3D segmentation of cell nuclei in tissue sections. J Microsc 2004;215:67-76.

[37] Sahoo PK, Soltani S, Wong AKC, and Chen YC. A survey of thresholding techniques. Comp. Vision, Graphics Image Proc. 1988;41:233-260.

[38] Krtolic A, Ortiz de Solorzano C., Lockett S, and Campisi J. Quantification of epithelial cells in coculture with fibroblasts by fluorescence image analysis. Cytometry 2002;49:73-82.

[39] Lindblad J and Bengtsson E. A comparison of methods for estimation of intensity nonuniformities in 2D and 3D microscope images of fluorescence stained cells. Proceedings of the 12th Scandinavian Conference on Image Anlysis (SCIA), Norway. NOBIM;264-271.

[40] Ortiz de Solorzano C, Garcia Rodriguez E, Jones A et al. Segmentation of confocal microscope images of cell nuclei in thick tissue sections. J Microsc 1999;193:212-226.

[41] Beucher S and Lanteujoul CH. Use of watersheds in contour detection. Int. Workshop on Image Processing: Real-Time and Motion Detection/Estimation, Rennes, France. IRISA Report 1979;132.

[42] Meyer F and Beucher S. Morphological Segmentation. J Vis Comm Image Report 1990;1:21-46.

[43] Vincent L. Morphological grayscale reconstruction in image analysis: applications and efficient algorithms. IEEE Trans. Image Processing 1993;2:176-201.

[44] Beucher S. The watershed transformation applied to image segmentation. Scanning Microsc 1992;6:299-314

[45] Lockett SJ, Sudar D, Thompson CT, Pinkel D, and Gray JW. Efficient, interactive, and three-dimensional segmentation of cell nuclei in thick tissue sections. Cytometry 1998;31:275-286.

[46] Stoev SL and Straaer W. Extracting regions of interest applying local watershed transformation. Proceedings of IEEE Visualization 2000, Salt Lake City;21-29.

[47] Landini G and Othman IE. Estimation of tissue layer level by sequential morphological reconstruction. J Microsc 2003;209:118-125.

[48] Baggett D, Nakaya M, McAuliffe M, Yamaguchi T, and Lockett S. Whole Cell Segmentation in Solid Tissue Sections. Cytometry Part A 2005;67(A):137-143

[49] Dreyfus S. Richard Bellman on the birth of dynamic programming. Operations Research 2002;50(1):48-51.

[50] Bellman R, 1957, *Dynamic Programming*, Princeton University Press. Dover paperback edition (2003),

[51] Bertsekas, D. P., 2000. *Dynamic Programming and Optimal Control, Vols. 1 & 2*, 2nd ed. Athena Scientific.

[52] Montanari U. On the optimal detection of curves in noisy pictures. Commun ACM 1971;14:335-345.

[53] Verwer BJH, Verbeek PW, and Dekker ST. An efficient uniform cost algorithm applied to distance transforms. IEE Trans Pattern Anal Mach Intell 1989;11:425-429.

[54] Geusebroek J-M, Smeulders AWM, and Geerts H. A minimum cost approach for segmenting networks of lines. Int J Comput Vis 2001;43:99-111.

[55] Kampe T and Kober R. Nonparametric Image segmentation. Pattern Anal Appl 1998;1:145-154.

[56] Zeng A, Staib LH, Schultz RT, Tagare H, Win L, and Duncan JS. A new approach to 3D sulcal ribbon finding from MR images. Medical image computing and computer-assisted intervention, MICCAI'99 Proc. Lect Notes Comput Sci 1999;1679:148-157.

[57] McCullough DP, Gudla PR, Harris BS et al. Segmentation of whole cells and cell nuclei from 3-D optical microscope images using dynamic programming. IEEE Transactions on Medical Imaging 2008;27(5):723-734.

[58] Duda RO and Hart PE. Use of the Hough Transformation to Detect Lines and Curves in Pictures. Comm. ACM 1972;15:11-15.

[59] Shapiro L and Stockman G. Computer Vision. New Jersey: Prentice Hall; 2001.

[60] Mouroutis T, Roberts SJ, and Bharath AA. Robust cell nuclei segmentation using statistical modeling. Bioimaging 1998;6(2):79-91.

[61] Uchino E, Yamakawa T, and Hirakawa K. Effective detection of nucleus in cytodiagnosis by employing combinatorial fuzzy hough transform. J Intell Fussy Syst 1997;5(4):333-343.

[62] Garrido A and de la Blanca NP. Applying deformable templates for cell image segmentation. Pattern Recognition 2000;33(5):821-832.

### Year 2

Bickford, L., Chang, J., Fu, K., Sun, J., Hu, Y., Gobin, A., Yu, TK, and Drezek, R. “Evaluation of Immunotargeted Gold Nanoshells as Rapid Diagnostic Imaging Agents for HER2+ Breast Cancers.” *Nanobiotechnology*. 1551-1286 (Print) 1551-1294 (Online); DOI 10.1007/s12030-008-9010-4 (2008).

Bickford, L., Sun, J., Fu, K., Lewinski, N., Nammalvar, V., Chang, J., Drezek, R. “Enhanced Multi-Spectral Imaging of Live Breast Cancer Cells Using Immunotargeted Gold Nanoshells and Two-Photon Excitation Microscopy.” *Nanotechnology*. 19: 315102 (6pp) doi: 10.1088/0957-4484/19/31/315102 (2008).

Hleb, E., Hu, Y., Drezek, R., Hafner, J., and Lapotko, D. “Photothermal bubbles as optical scattering probes for imaging live cells.” *Nanomedicine.* 3(6), 797-812 (2008). (doi:10.2217/17435889.3.6.797)

Hu, Y., Fleming, R., and Drezek, R. “Optical properties of gold-silica-gold multilayered nanoshells.” *Optics Express.* Vol 16, 24, 19579 (2008).

Rostro-Kohanloo, B., Bickford, L., Payne, C., Day, E., Anderson, L., Zhong, M., Zhong, Lee, S., Mayer, K., Zal, T., Adam, L., Dinney, C., Drezek, R., West, J., and Hafner, J. "Stabilization and Targeting of Surfactant-Synthesized Gold Nanorods." *Nanotechnology.*

Sun, J., Fu, K., Zhu, MQ, Bickford, L., Post, E., and Drezek, R. “Near-infrared quantum dots for fluorescence tissue imaging” *Current Nanoscience*, 5 (2), 160-166 (2009).

### Year 3

Sun, J., Shu, C., Appiah, B., and Drezek, R. A Needle Compatible Single Fiber Reflectance Endoscope. *Journal of Biomedical Optics*. In press (2010).

Rostro-Kohanloo, B., Bickford, L., Payne, C., Day, E., Anderson, L., Zhong, M., Zhong, Lee, S., Mayer, K., Zal, T., Adam, L., Dinney, C., Drezek, R., West, J., and Hafner, J. "Stabilization and Targeting of Surfactant-Synthesized Gold Nanorods." *Nanotechnology.* 20:434005 (2009).

Hu, Y., Noelck, S., and Drezek, R. "Symmetry breaking in gold-silica-gold multilayer nanoshells." ACS Nano. 4(3): 1521-1528 (2010).

**Year 4**

Aaron, J., N. Nitin, et al. (2007). "Plasmon resonance coupling of metal nanoparticles for molecular imaging of carcinogenesis in vivo." J Biomed Opt **12**(3): 034007.

Bickford, L., G. Agollah, et al. (2009). "Silica-gold nanoshells as potential intraoperative molecular probes for HER2-overexpression in ex vivo breast tissue using near-infrared reflectance confocal microscopy." Breast Cancer Research and Treatment: 1-9.

Bickford, L., G. Agollah, et al. (2010). "Silica-gold nanoshells as potential intraoperative molecular probes for HER2-overexpression in ex vivo breast tissue using near-infrared reflectance confocal microscopy." Breast Cancer Research and Treatment **120**(3): 547-555.

Bickford, L., J. Chang, et al. (2008a). "Evaluation of Immunotargeted Gold Nanoshells as Rapid Diagnostic Imaging Agents for HER2-Overexpressing Breast Cancer Cells: A Time-based Analysis." NanoBioTechnology **4**(1): 1-8.

Bickford, L. and et al. (2008b). "Enhanced multi-spectral imaging of live breast cancer cells using immunotargeted gold nanoshells and two-photon excitation microscopy." Nanotechnology **19**(31): 315102.

Brewer, M., U. Utzinger, et al. (2001). "Fluorescence spectroscopy for in vivo characterization of ovarian tissue." Lasers Surg Med **29**(2): 128-135.

Buckman, R. (1997). What You Really Need to Know About Cancer. Baltimore, The Johns Hopkins University Press.

Cabioglu, N., K. Hunt, et al. (2007). "Role for Intraoperative Margin Assessment in Patients Undergoing Breast-Conserving Surgery." Annals of Surgical Oncology **14**(4): 1458-1471.

Cancer, S. A. (2005). "Breast Cancer Facts and Figures 2005-2006." Atlanta ACS, Inc.

Chithrani, B. D. and W. C. W. Chan (2007). "Elucidating the Mechanism of Cellular Uptake and Removal of Protein-Coated Gold Nanoparticles of Different Sizes and Shapes." Nano Letters **7**(6): 1542-1550.

Connor, E. E., J. Mwamuka, et al. (2005). "Gold Nanoparticles Are Taken Up by Human Cells but Do Not Cause Acute Cytotoxicity13." Small **1**(3): 325-327.

Duff, D. G., A. Baiker, et al. (1993). "A new hydrosol of gold clusters. 1. Formation and particle size variation." Langmuir **9**(9): 2301-2309.

El-Sayed, I. H., X. Huang, et al. (2005). "Surface plasmon resonance scattering and absorption of anti-EGFR antibody conjugated gold nanoparticles in cancer diagnostics: applications in oral cancer." Nano Lett **5**(5): 829-834.

Fisher, B., S. Anderson, et al. (2002). "Twenty-Year Follow-up of a Randomized Trial Comparing Total Mastectomy, Lumpectomy, and Lumpectomy plus Irradiation for the Treatment of Invasive Breast Cancer." New England Journal of Medicine **347**(16): 1233-1241.

Geiser, M., B. Rothen-Rutishauser, et al. (2005). "Ultrafine particles cross cellular membranes by nonphagocytic mechanisms in lungs and in cultured cells." Environ Health Perspect **113**(11): 1555-1560.

Graham, R. A., M. J. Homer, et al. (1994). "The efficacy of specimen radiography in evaluating the surgical margins of impalpable breast carcinoma." AJR Am J Roentgenol **162**(1): 33-36.

Kong, T., J. Zeng, et al. (2008). "Enhancement of radiation cytotoxicity in breast-cancer cells by localized attachment of gold nanoparticles." Small **4**(9): 1537-1543.

Lane, P. M., T. Gilhuly, et al. (2006). "Simple device for the direct visualization of oral-cavity tissue fluorescence." Journal of Biomedical Optics **11**(2): 024006-024007.

Liu, H., B. Beauvoit, et al. (1996). "Dependence of tissue optical properties on solute-induced changes in refractive index and osmolarity." Journal of Biomedical Optics **1**(2): 200-211.

Loo, C., L. Hirsch, et al. (2005a). "Gold nanoshell bioconjugates for molecular imaging in living cells." Opt Lett **30**(9): 1012-1014.

Loo, C., A. Lin, et al. (2004). "Nanoshell-enabled photonics-based imaging and therapy of cancer." Technol Cancer Res Treat **3**(1): 33-40.

Loo, C., A. Lowery, et al. (2005b). "Immunotargeted nanoshells for integrated cancer imaging and therapy." Nano Lett **5**(4): 709-711.

Mironava, T., M. Hadjiargyrou, et al. (2010). "Gold nanoparticles cellular toxicity and recovery: Effect of size, concentration and exposure time." Nanotoxicology **4**(1): 120-137.

Mojica CM, B. R., Boscardin WJ, Ponce NA (2007). "Low-Income Women with Breast Abnormalitis: System Predictors of Timely Diagnostic Resolution." Cancer Control **14**(2): 176-182.

Nahta, R., D. Yu, et al. (2006). "Mechanisms of disease: understanding resistance to HER2-targeted therapy in human breast cancer." Nat Clin Pract Oncol **3**(5): 269-280.

Nitin, N., A. L. Carlson, et al. (2009a). "Molecular imaging of glucose uptake in oral neoplasia following topical application of fluorescently labeled deoxy-glucose." Int J Cancer **124**(11): 2634-2642.

Nitin, N., D. J. Javier, et al. (2007). "Widefield and high-resolution reflectance imaging of gold and silver nanospheres." J Biomed Opt **12**(5): 051505.

Nitin, N., K. J. Rosbach, et al. (2009b). "Optical molecular imaging of epidermal growth factor receptor expression to improve detection of oral neoplasia." Neoplasia **11**(6): 542-551.

Ntziachristos, V., C. Bremer, et al. (2003). "Fluorescence imaging with near-infrared light: new technological advances that enable in vivo molecular imaging." Eur Radiol **13**(1): 195-208.

O'Neil, R., L. Wu, et al. (2005). "Uptake of a Fluorescent Deoxyglucose Analog (2-NBDG) in Tumor Cells." Molecular Imaging and Biology **7**(6): 388-392.

Oouchi, A., K.-i. Sakata, et al. (2009). "The treatment outcome of patients undergoing breast-conserving therapy: the clinical role of postoperative radiotherapy." Breast Cancer **16**(1): 49-57.

Pierce, M. C., D. J. Javier, et al. (2008). "Optical contrast agents and imaging systems for detection and diagnosis of cancer." Int J Cancer **123**(9): 1979-1990.

Rasbridge, S. A., C. E. Gillett, et al. (1994). "The effects of chemotherapy on morphology, cellular proliferation, apoptosis and oncoprotein expression in primary breast carcinoma." Br J Cancer **70**(2): 335-341.

Roblyer, D., C. Kurachi, et al. (2009). "Objective detection and delineation of oral neoplasia using autofluorescence imaging." Cancer Prev Res (Phila Pa) **2**(5): 423-431.

Roblyer, D., R. Richards-Kortum, et al. (2008). "Multispectral optical imaging device for in vivo detection of oral neoplasia." J Biomed Opt **13**(2): 024019.

Rosbach, K. J., D. Shin, et al. (2010). "High-resolution fiber optic microscopy with fluorescent contrast enhancement for the identification of axillary lymph node metastases in breast cancer: a pilot study." Biomed. Opt. Express **1**(3): 911-922.

Rylander, C. G., T. E. Milner, et al. (2008). "Mechanical tissue optical clearing devices: enhancement of light penetration in ex vivo porcine skin and adipose tissue." Lasers Surg Med **40**(10): 688-694.

Salas-Burgos, A., P. Iserovich, et al. (2004). "Predicting the three-dimensional structure of the human facilitative glucose transporter glut1 by a novel evolutionary homology strategy: insights on the molecular mechanism of substrate migration, and binding sites for glucose and inhibitory molecules." Biophys J **87**(5): 2990-2999.

Sheth, R. A., L. Josephson, et al. (2009). "Evaluation and clinically relevant applications of a fluorescent imaging analog to fluorodeoxyglucose positron emission tomography." J Biomed Opt **14**(6): 064014.

Slamon, D. J., G. M. Clark, et al. (1987). "Human breast cancer: correlation of relapse and survival with amplification of the HER-2/neu oncogene." Science **235**(4785): 177-182.

Smitt, M. C., K. W. Nowels, et al. (1995). "The importance of the lumpectomy surgical margin status in long term results of breast conservation." Cancer **76**(2): 259-267.

Sokolov, K., M. Follen, et al. (2003). "Real-Time Vital Optical Imaging of Precancer Using Anti-Epidermal Growth Factor Receptor Antibodies Conjugated to Gold Nanoparticles." Cancer Res **63**(9): 1999-2004.

Staros, J. V., R. W. Wright, et al. (1986). "Enhancement by N-hydroxysulfosuccinimide of water-soluble carbodiimide-mediated coupling reactions." Analytical Biochemistry **156**(1): 220-222.

Steen, R. (1993). A Conspiracy of Cells. New York, Plenum Press.

Stober, W., A. Fink, et al. (1968). "Controlled growth of monodisperse silica spheres in the micron size range." Journal of Colloid and Interface Science **26**(1): 62-69.

Sun, L., D. Liu, et al. (2008). "Functional Gold Nanoparticle,àíPeptide Complexes as Cell-Targeting Agents." Langmuir **24**(18): 10293-10297.

Tanaka, E., H. S. Choi, et al. (2006). "Image-guided oncologic surgery using invisible light: completed pre-clinical development for sentinel lymph node mapping." Ann Surg Oncol **13**(12): 1671-1681.

Tkachenko, A. G., H. Xie, et al. (2003). "Multifunctional Gold Nanoparticle,àíPeptide Complexes for Nuclear Targeting." Journal of the American Chemical Society **125**(16): 4700-4701.

Vargas, G., K. F. Chan, et al. (2001). "Use of osmotically active agents to alter optical properties of tissue: Effects on the detected fluorescence signal measured through skin." Lasers in Surgery and Medicine **29**(3): 213-220.

Vargas, O., E. K. Chan, et al. (1999). "Use of an agent to reduce scattering in skin." Lasers in Surgery and Medicine **24**(2): 133-141.

Ven, A. L. v. d., K. Adler-Storthz, et al. (2009a). "Delivery of optical contrast agents using Triton-X100, part 1: reversible permeabilization of live cells for intracellular labeling." Journal of Biomedical Optics **14**(2): 021012.

Ven, A. L. v. d., K. Adler-Storthz, et al. (2009b). "Delivery of optical contrast agents using Triton-X100, part 2: enhanced mucosal permeation for the detection of cancer biomarkers." Journal of Biomedical Optics **14**(2): 021013.

Wu, B.-Y., S.-H. Hou, et al. (2007). "Amperometric glucose biosensor based on multilayer films via layer-by-layer self-assembly of multi-wall carbon nanotubes, gold nanoparticles and glucose oxidase on the Pt electrode." Biosensors and Bioelectronics **22**(12): 2854-2860.

Zhou, L. and W. S. El-Deiry (2009). "Multispectral fluorescence imaging." J Nucl Med **50**(10): 1563-1566.

## Year 5

Al-Ghazal, S K, L Fallowfield, and R W Blamey. 2000. "Comparison of psychological aspects and patient satisfaction following breast conserving surgery, simple mastectomy and breast reconstruction." *European journal of cancer (Oxford, England : 1990)* 36 (15) (October): 1938-43. http://www.ncbi.nlm.nih.gov/pubmed/11000574.

Ali, A N, N Vapiwala, M Guo, W T Hwang, E E Harris, and L J Solin. 2011. "The impact of re-excision and residual disease on local recurrence after breast conservation treatment for patients with early stage breast cancer." *Clin Breast Cancer* 11 (6): 400-405. doi:S1526-8209(11)00160-1 [pii] 10.1016/j.clbc.2011.08.003. http://www.ncbi.nlm.nih.gov/entrez/query.fcgi?cmd=Retrieve&db=PubMed&dopt=Citation&list_uids=21993010.

Allweis, Tanir M, Zvi Kaufman, Shlomo Lelcuk, Itzhak Pappo, Tami Karni, Shlomo Schneebaum, Rona Spector, et al. 2008. "A prospective, randomized, controlled, multicenter study of a real-time, intraoperative probe for positive margin detection in breast-conserving surgery." *American journal of surgery* 196 (4) (October): 483-9. doi:10.1016/j.amjsurg.2008.06.024. http://www.ncbi.nlm.nih.gov/pubmed/18809049.

Altintas, Sevilay, Kathleen Lambein, Manon T Huizing, Geert Braems, Fernando Tjin Asjoe, Hilde Hellemans, Eric Van Marck, et al. 2009. "Prognostic significance of oncogenic markers in ductal carcinoma in situ of the breast: a clinicopathologic study." *The breast journal* 15 (2): 120-32. doi:10.1111/j.1524-4741.2009.00686.x. http://www.ncbi.nlm.nih.gov/pubmed/19292797.

Aoyama, Kei, Takako Kamio, Tetsuya Ohchi, Masako Nishizawa, and Shingo Kameoka. 2011. "Sentinel lymph node biopsy for breast cancer patients using fluorescence navigation with indocyanine green." *World journal of surgical oncology* 9 (January): 157. doi:10.1186/1477-7819-9-157. http://www.pubmedcentral.nih.gov/articlerender.fcgi?artid=3269998&tool=pmcentrez&rendertype=abstract.

Arthur, Douglas W, Kathryn Winter, Robert R Kuske, John Bolton, Rachel Rabinovitch, Julia White, William F Hanson, Raymond M Wilenzick, and Beryl McCormick. 2008. "A Phase II trial of brachytherapy alone after lumpectomy for select breast cancer: tumor control and survival outcomes of RTOG 95-17." *International journal of radiation oncology, biology, physics* 72 (2) (October 1): 467-73. doi:10.1016/j.ijrobp.2007.12.056.

http://www.pubmedcentral.nih.gov/articlerender.fcgi?artid=2604132&tool=pmcentrez&rendertype=abstract.

Atkins, Jordan, Fatema Al Mushawah, Catherine M Appleton, Amy E Cyr, William E Gillanders, Rebecca L Aft, Timothy J Eberlein, Feng Gao, and Julie A Margenthaler. 2012. "Positive margin rates following breast-conserving surgery for stage I-III breast cancer: Palpable versus nonpalpable tumors." *The Journal of surgical research* (April 10). doi:10.1016/j.jss.2012.03.045. http://www.ncbi.nlm.nih.gov/pubmed/22516344.

Audisio, Riccardo A, and Leena S Chagla. 2007. "Oncoplastic fellowship: can we do better?" *Breast (Edinburgh, Scotland)* 16 (1) (February): 11-2. doi:10.1016/j.breast.2006.07.001. http://www.ncbi.nlm.nih.gov/pubmed/16987663.

Avril, N, C a Rosé, M Schelling, J Dose, W Kuhn, S Bense, W Weber, S Ziegler, H Graeff, and M Schwaiger. 2000. "Breast imaging with positron emission tomography and fluorine-18 fluorodeoxyglucose: use and limitations." *Journal of clinical oncology : official journal of the American Society of Clinical Oncology* 18 (20) (October): 3495-502. http://www.ncbi.nlm.nih.gov/pubmed/11032590.

Avril, Norbert, Manuela Menzel, Marcus Schelling, Wolfgang Weber, Fritz Ja, Walter Nathrath, and Markus Schwaiger. 2001. "Glucose Metabolism of Breast Cancer Assessed by 18 F-FDG PET : Histologic and Immunohistochemical Tissue Analysis." *Journal of Nuclear Medicine*: 9-16.

Aziz, Dalal, Ellen Rawlinson, Steven A Narod, Ping Sun, H Lavina A Lickley, David R McCready, and Claire M B Holloway. 2006. "The role of reexcision for positive margins in optimizing local disease control after breast-conserving surgery for cancer." *The breast journal* 12 (4): 331-7. doi:10.1111/j.1075-122X.2006.00271.x. http://www.ncbi.nlm.nih.gov/pubmed/16848842.

Bakhshandeh, Maryam, S Osman Tutuncuoglu, Gabor Fischer, and Shahla Masood. 2007. "Use of imprint cytology for assessment of surgical margins in lumpectomy specimens of breast cancer patients." *Diagnostic cytopathology* 35 (10) (October): 656-9. doi:10.1002/dc.20704. http://www.ncbi.nlm.nih.gov/pubmed/17854083.

Baselga, José, José M Trigo, Jean Bourhis, Jacques Tortochaux, Hernán Cortés-Funes, Ricardo Hitt, Pere Gascón, Nadia Amellal, Andreas Harstrick, and André Eckardt. 2005. "Phase II multicenter study of the antiepidermal growth factor receptor monoclonal antibody cetuximab in combination with platinum-based chemotherapy in patients with platinum-refractory metastatic and/or recurrent squamous cell carcinoma of the head and n." *Journal of clinical oncology : official journal of the American Society of Clinical Oncology* 23 (24) (August 20): 5568-77. doi:10.1200/JCO.2005.07.119. http://www.ncbi.nlm.nih.gov/pubmed/16009950.

Beadle, Beth M, Wendy A Woodward, Susan L Tucker, Elesyia D Outlaw, Pamela K Allen, Julia L Oh, Eric A Strom, et al. 2009. "Ten-year recurrence rates in young women with breast cancer by locoregional treatment approach." *International journal of radiation oncology, biology, physics* 73 (3) (March 1): 734-44. doi:10.1016/j.ijrobp.2008.04.078. http://www.pubmedcentral.nih.gov/articlerender.fcgi?artid=3041273&tool=pmcentrez&rendertype=abstract.

Bennett, I C, J Greenslade, and H Chiam. 2005. "Intraoperative ultrasound-guided excision of nonpalpable breast lesions." *World journal of surgery* 29 (3) (March): 369-74. doi:10.1007/s00268-004-7554-6. http://www.ncbi.nlm.nih.gov/pubmed/15706446.

Bickford, L, J Chang, K Fu, J Sun, Y Hu, A Gobin, Tse-Kuan Yu, and R Drezek. 2008. “Evaluation of Immunotargeted Gold Nanoshells as Rapid Diagnostic Imaging Agents for HER2-Overexpressing Breast Cancer Cells: A Time Based Analysis.” *Nanobiotechnology* 4 (1-4): 1-8.

Bickford, L, J Sun, K Fu, N Lewinski, V Nammalvar, J Chang, and R Drezek. 2008. “Enhanced multi-spectral imaging of live breast cancer cells using immunotargeted gold nanoshells and two-photon excitation microscopy.” *Nanotechnology* 19 (31): -. doi:Artn 315102 Doi 10.1088/0957-4484/19/31/315102. <Go to ISI>://000257166800002.

Bickford, Lissett R, Germaine Agollah, Rebekah Drezek, and Tse-Kuan Yu. 2010. “Silica-gold nanoshells as potential intraoperative molecular probes for HER2-overexpression in ex vivo breast tissue using near-infrared reflectance confocal microscopy.” *Breast cancer research and treatment* 120 (3) (April): 547-55. doi:10.1007/s10549-009-0408-z. http://www.ncbi.nlm.nih.gov/pubmed/19418216.

Bos, Reinhard, Jacobus J M van Der Hoeven, Elsken van Der Wall, Petra van Der Groep, Paul J van Diest, Emile F I Comans, Urvi Joshi, et al. 2002. “Biologic correlates of (18)fluorodeoxyglucose uptake in human breast cancer measured by positron emission tomography.” *Journal of clinical oncology : official journal of the American Society of Clinical Oncology* 20 (2) (January): 379-87. http://www.ncbi.nlm.nih.gov/pubmed/11786564.

Bria, Emilio, Diana Giannarelli, Alessandra Felici, William P Peters, Cecilia Nisticò, Barbara Vanni, Federica Cuppone, Francesco Cognetti, and Edmondo Terzoli. 2005. “Taxanes with anthracyclines as first-line chemotherapy for metastatic breast carcinoma.” *Cancer* 103 (4) (February 15): 672-9. doi:10.1002/cncr.20757. http://www.ncbi.nlm.nih.gov/pubmed/15637696.

Burkholder, Hans C, Laura E Witherspoon, R Phillip Burns, Jeffrey S Horn, and Michael D Biderman. 2007. “Breast surgery techniques: preoperative bracketing wire localization by surgeons.” *The American surgeon* 73 (6) (June): 574-8; discussion 578-9. http://www.ncbi.nlm.nih.gov/pubmed/17658094.

Bydlon, Torre M, Stephanie A Kennedy, Lisa M Richards, J Quincy Brown, Bing Yu, Marlee K Junker, Jennifer Gallagher, Joseph Geradts, Lee G Wilke, and Nimmi Ramanujam. 2010. “Performance metrics of an optical spectral imaging system for intra-operative assessment of breast tumor margins.” *Optics express* 18 (8) (April 12): 8058-76. http://www.pubmedcentral.nih.gov/articlerender.fcgi?artid=2939901&tool=pmcentrez&rendertype=abstract.

Cabioglu, N, K K Hunt, A A Sahin, H M Kuerer, G V Babiera, S E Singletary, G J Whitman, et al. 2007. “Role for intraoperative margin assessment in patients undergoing breast-conserving surgery.” *Ann Surg Oncol* 14 (4): 1458-1471. doi:10.1245/s10434-006-9236-0. http://www.ncbi.nlm.nih.gov/entrez/query.fcgi?cmd=Retrieve&db=PubMed&dopt=Citation&list_uids=17260108.

Cameron, David, Michelle Casey, Cristina Oliva, Beth Newstat, Bradley Imwalle, and Charles E Geyer. 2010. “Lapatinib plus capecitabine in women with HER-2-positive advanced breast cancer: final survival analysis of a phase III randomized trial.” *The oncologist* 15 (9) (January): 924-34. doi:10.1634/theoncologist.2009-0181. http://www.pubmedcentral.nih.gov/articlerender.fcgi?artid=3228041&tool=pmcentrez&rendertype=abstract.

Camp, E Ramsay, Priscilla F McAuliffe, Jeffrey S Gilroy, Christopher G Morris, D Scott Lind, Nancy P Mendenhall, and Edward M Copeland. 2005. “Minimizing local recurrence after breast conserving therapy using intraoperative shaved margins to determine pathologic tumor clearance.” *Journal of the American College of Surgeons* 201 (6) (December): 855-61. doi:10.1016/j.jamcollsurg.2005.06.274. http://www.ncbi.nlm.nih.gov/pubmed/16310688.

Carlson, Robert W, D Craig Allred, Benjamin O Anderson, Harold J Burstein, W Bradford Carter, Stephen B Edge, John K Erban, et al. 2009. “Breast cancer. Clinical practice guidelines in oncology.” *Journal of the National Comprehensive Cancer Network : JNCCN* 7 (2) (February): 122-92. http://www.ncbi.nlm.nih.gov/pubmed/19200416.

Carpin, L B, L R Bickford, G Agollah, T K Yu, R Schiff, Y Li, and R A Drezek. 2011. “Immunoconjugated gold nanoshell-mediated photothermal ablation of trastuzumab-resistant breast cancer cells.” *Breast Cancer Res Treat* 125 (1): 27-34. doi:10.1007/s10549-010-0811-5. http://www.ncbi.nlm.nih.gov/entrez/query.fcgi?cmd=Retrieve&db=PubMed&dopt=Citation&list_uids=20217215.

Cendán, Juan C, Dominique Coco, and Edward M Copeland. 2005. “Accuracy of intraoperative frozen-section analysis of breast cancer lumpectomy-bed margins.” *Journal of the American College of Surgeons* 201 (2) (August): 194-8. doi:10.1016/j.jamcollsurg.2005.03.014. http://www.ncbi.nlm.nih.gov/pubmed/16038815.

Chakravorty, A, A K Shrestha, N Sanmugalingam, F Rapisarda, N Roche, G Querci Della Rovere, and F A Macneill. 2012. “How safe is oncoplastic breast conservation? Comparative analysis with standard breast conserving surgery.” *European journal of surgical oncology : the journal of the European Society of Surgical Oncology and the British Association of Surgical Oncology* 38 (5) (May): 395-8. doi:10.1016/j.ejso.2012.02.186. http://www.ncbi.nlm.nih.gov/pubmed/22436560.

Cho, Kyu Ran, Bo Kyoung Seo, Chul Hwan Kim, Kyu Won Whang, Yun Hwan Kim, Baek Hyun Kim, Ok Hee Woo, Young Hen Lee, and Kyoo Byung Chung. 2008. “Non-calcified ductal carcinoma in situ: ultrasound and mammographic findings correlated with histological findings.” *Yonsei medical journal* 49 (1) (February 29): 103-10. doi:10.3349/ymj.2008.49.1.103. http://www.pubmedcentral.nih.gov/articlerender.fcgi?artid=2615255&tool=pmcentrez&rendertype=abstract.

Chung, Alice, Doug Liou, Scott Karlan, Alan Waxman, Kayo Fujimoto, Masanobu Hagiike, and Edward H Phillips. 2006. “Preoperative FDG-PET for axillary metastases in patients with breast cancer.” *Archives of surgery (Chicago, Ill. : 1960)* 141 (8) (August): 783-8; discussion 788-9. doi:10.1001/archsurg.141.8.783. http://www.ncbi.nlm.nih.gov/pubmed/16924086.

De Cicco, C, M Pizzamiglio, G Trifirò, A Luini, M Ferrari, G Prisco, V Galimberti, et al. 2002. “Radioguided occult lesion localisation (ROLL) and surgical biopsy in breast cancer. Technical aspects.” *The quarterly journal of nuclear medicine : official publication of the Italian Association of Nuclear Medicine (AIMN) [and] the International Association of Radiopharmacology (IAR)* 46 (2) (June): 145-51. http://www.ncbi.nlm.nih.gov/pubmed/12114878.

Clarke, M, R Collins, S Darby, C Davies, P Elphinstone, E Evans, J Godwin, et al. 2005. “Effects of radiotherapy and of differences in the extent of surgery for early breast cancer on local recurrence and 15-year survival: an overview of the randomised trials." *Lancet* 366 (9503): 2087-2106. doi:S0140-6736(05)67887-7 [pii] 10.1016/S0140-6736(05)67887-7. http://www.ncbi.nlm.nih.gov/entrez/query.fcgi?cmd=Retrieve&db=PubMed&dopt=Citation&list_uids=16360786.

Clough, Krishna B, Gabriel J Kaufman, Claude Nos, Ines Buccimazza, and Isabelle M Sarfati. 2010. "Improving breast cancer surgery: a classification and quadrant per quadrant atlas for oncoplastic surgery." *Annals of surgical oncology* 17 (5) (May): 1375-91. doi:10.1245/s10434-009-0792-y. http://www.ncbi.nlm.nih.gov/pubmed/20140531.

Cobleigh, Melody A, Virginia K Langmuir, George W Sledge, Kathy D Miller, Latrice Haney, William F Novotny, James D Reimann, and Amy Vassel. 2003. "A phase I/II dose-escalation trial of bevacizumab in previously treated metastatic breast cancer." *Seminars in oncology* 30 (5 Suppl 16) (October): 117-24. http://www.ncbi.nlm.nih.gov/pubmed/14613032.

Cohn, David E, Nathan C Hall, Stephen P Povoski, Leigh G Seamon, William B Farrar, and Edward W Martin. 2008. "Novel perioperative imaging with 18F-FDG PET/CT and intraoperative 18F-FDG detection using a handheld gamma probe in recurrent ovarian cancer." *Gynecologic oncology* 110 (2) (August): 152-7. doi:10.1016/j.ygyno.2008.04.026. http://www.ncbi.nlm.nih.gov/pubmed/18539314.

Connor, Ellen†E., Judith Mwamuka, Anand Gole, Catherine†J. Murphy, and Michael†D. Wyatt. 2005. "Gold Nanoparticles Are Taken Up by Human Cells but Do Not Cause Acute Cytotoxicity13." *Small* 1 (3): 325-327. http://dx.doi.org/10.1002/smll.200400093.

Creager, Andrew J, Jo Ann Shaw, Peter R Young, and Kim R Geisinger. 2002. "Intraoperative evaluation of lumpectomy margins by imprint cytology with histologic correlation: a community hospital experience." *Archives of pathology & laboratory medicine* 126 (7) (July): 846-8. doi:10.1043/0003-9985(2002)126<0846:IEOLMB>2.0.CO;2. http://www.ncbi.nlm.nih.gov/pubmed/12088456.

Cèfaro, Giampiero Ausili, Domenico Genovesi, Rita Marchese, Lucia Anna Ursini, Ettore Cianchetti, Enzo Ballone, and Marta Di Nicola. 2006. "Predictors of local recurrence after conservative surgery and whole-breast irradiation." *Breast cancer research and treatment* 98 (3) (August): 329-35. doi:10.1007/s10549-006-9169-0. http://www.ncbi.nlm.nih.gov/pubmed/16555125.

DeSantis, Carol, Rebecca Siegel, Priti Bandi, and Ahmedin Jemal. 2011. "Breast cancer statistics, 2011." *CA: a cancer journal for clinicians* 61 (6): 409-18. doi:10.3322/caac.20134. http://www.ncbi.nlm.nih.gov/pubmed/21969133.

Duff, Daniel G, Alfons Baiker, and Peter P Edwards. 1993. "A new hydrosol of gold clusters. 1. Formation and particle size variation." *Langmuir* 9 (9): 2301-2309. doi:10.1021/la00033a010. http://dx.doi.org/10.1021/la00033a010.

Duffy, Michael J, Patricia M McGowan, and John Crown. 2012. "Targeted therapy for triple-negative breast cancer: where are we?" *International journal of cancer. Journal international du cancer* (May 14). doi:10.1002/ijc.27632. http://www.ncbi.nlm.nih.gov/pubmed/22581656.

D'Halluin, François, Patrick Tas, Sophie Rouquette, Cécile Bendavid, Fabrice Foucher, Habiba Meshba, Jérôme Blanchot, Olivier Coué, and Jean Levêque. 2009. "Intra-operative touch preparation cytology following lumpectomy for breast cancer: a series of 400 procedures." *Breast (Edinburgh, Scotland)* 18 (4) (August): 248-53. doi:10.1016/j.breast.2009.05.002. http://www.ncbi.nlm.nih.gov/pubmed/19515566.

Fentiman, I S. 2011. "Marginal effect in breast-conserving surgery." *International journal of clinical practice* 65 (5) (May): 519-20. doi:10.1111/j.1742-1241.2011.02608.x. http://www.ncbi.nlm.nih.gov/pubmed/21489074.

Fisher, Bernard, Stewart Anderson, John Bryant, Richard G Margolese, Melvin Deutsch, Edwin R Fisher, Jong-Hyeon Jeong, and Norman Wolmark. 2002. "Twenty-year follow-up of a randomized trial comparing total mastectomy, lumpectomy, and lumpectomy plus irradiation for the treatment of invasive breast cancer." *The New England journal of medicine* 347 (16) (October 17): 1233-41. doi:10.1056/NEJMoa022152. http://www.ncbi.nlm.nih.gov/pubmed/12393820.

Geyer, Charles E, John Forster, Deborah Lindquist, Stephen Chan, C Gilles Romieu, Tadeusz Pienkowski, Agnieszka Jagiello-Gruszfeld, et al. 2006. "Lapatinib plus capecitabine for HER2-positive advanced breast cancer." *The New England journal of medicine* 355 (26) (December 28): 2733-43. doi:10.1056/NEJMoa064320. http://www.ncbi.nlm.nih.gov/pubmed/17192538.

Van Goethem, M, K Schelfout, E Kersschot, C Colpaert, I Verslegers, I Biltjes, W A Tjalma, A De Schepper, J Weyler, and P M Parizel. 2007. "MR mammography is useful in the preoperative locoregional staging of breast carcinomas with extensive intraductal component." *European journal of radiology* 62 (2) (May): 273-82. doi:10.1016/j.ejrad.2006.12.004. http://www.ncbi.nlm.nih.gov/pubmed/17223002.

Gomez, Henry L, Dinesh C Doval, Miguel A Chavez, Peter C-S Ang, Zeba Aziz, Shona Nag, Christina Ng, et al. 2008. "Efficacy and safety of lapatinib as first-line therapy for ErbB2-amplified locally advanced or metastatic breast cancer." *Journal of clinical oncology : official journal of the American Society of Clinical Oncology* 26 (18) (June 20): 2999-3005. doi:10.1200/JCO.2007.14.0590. http://www.ncbi.nlm.nih.gov/pubmed/18458039.

Groheux, David, Sylvie Giacchetti, Jean-Luc Moretti, Raphael Porcher, Marc Espié, Jacqueline Lehmann-Che, Anne de Roquancourt, et al. 2011. "Correlation of high 18F-FDG uptake to clinical, pathological and biological prognostic factors in breast cancer." *European journal of nuclear medicine and molecular imaging* 38 (3) (March): 426-35. doi:10.1007/s00259-010-1640-9. http://www.ncbi.nlm.nih.gov/pubmed/21057787.

Guidroz, Julie A, Gregory Larrieux, Junlin Liao, Sonia L Sugg, Carol E H Scott-Conner, and Ronald J Weigel. 2011. "Sampling of secondary margins decreases the need for re-excision after partial mastectomy." *Surgery* 150 (4) (October): 802-9. doi:10.1016/j.surg.2011.07.064. http://www.ncbi.nlm.nih.gov/pubmed/22000194.

Gulec, Seza A, Farhad Daghighian, and Richard Essner. 2006. "PET-Probe: Evaluation of Technical Performance and Clinical Utility of a Handheld High-Energy Gamma Probe in Oncologic Surgery." *Annals of surgical oncology* (July 24). doi:10.1245/ASO.2006.05.047. http://www.ncbi.nlm.nih.gov/pubmed/16865592.

Gülben, Kaptan, Uğur Berberoğlu, Aziz Cengiz, and Hüseyin Altinyollar. 2007. "Prognostic factors affecting locoregional recurrence in patients with stage IIIB noninflammatory breast cancer." *World journal of surgery* 31 (9) (September 1): 1724-30. doi:10.1007/s00268-007-9139-7. http://www.springerlink.com/content/n752170246r84660/.

Hall, Nathan C, Stephen P Povoski, Douglas A Murrey, Michael V Knopp, and Edward W Martin. 2007. "Combined approach of perioperative 18F-FDG PET/CT imaging and intraoperative 18F-FDG handheld gamma probe detection for tumor localization and verification of complete tumor resection in breast cancer." *World journal of surgical oncology* 5 (January): 143. doi:10.1186/1477-7819-5-143.

http://www.pubmedcentral.nih.gov/articlerender.fcgi?artid=2235860&tool=pmcentrez&rendertype=abstract.

Heckathorne, Elena, Colin Dimock, and Magnus Dahlbom. 2008. “Radiation dose to surgical staff from positron-emitter-based localization and radiosurgery of tumors.” *Health physics* 95 (2) (August): 220-6. doi:10.1097/01.HP.0000310962.96089.44. http://www.ncbi.nlm.nih.gov/pubmed/18617803.

Houssami, Nehmat, Stefano Ciatto, Petra Macaskill, Sarah J Lord, Ruth M Warren, J Michael Dixon, and Les Irwig. 2008. “Accuracy and surgical impact of magnetic resonance imaging in breast cancer staging: systematic review and meta-analysis in detection of multifocal and multicentric cancer.” *Journal of clinical oncology : official journal of the American Society of Clinical Oncology* 26 (19) (July 1): 3248-58. doi:10.1200/JCO.2007.15.2108. http://www.ncbi.nlm.nih.gov/pubmed/18474876.

Houssami, Nehmat, Petra Macaskill, M Luke Marinovich, J Michael Dixon, Les Irwig, Meagan E Brennan, and Lawrence J Solin. 2010. “Meta-analysis of the impact of surgical margins on local recurrence in women with early-stage invasive breast cancer treated with breast-conserving therapy.” *European journal of cancer (Oxford, England : 1990)* 46 (18) (December): 3219-32. doi:10.1016/j.ejca.2010.07.043. http://dx.doi.org/10.1016/j.ejca.2010.07.043.

Huynh, P T, A M Jarolimek, and S Daye. 1998. “The false-negative mammogram.” *Radiographics : a review publication of the Radiological Society of North America, Inc* 18 (5): 1137-54; quiz 1243-4. http://www.ncbi.nlm.nih.gov/pubmed/9747612.

Ikeda, Debra M, Robyn L Birdwell, Kathryn F O’Shaughnessy, R James Brenner, and Edward A Sickles. 2003. “Analysis of 172 subtle findings on prior normal mammograms in women with breast cancer detected at follow-up screening.” *Radiology* 226 (2) (February): 494-503. http://www.ncbi.nlm.nih.gov/pubmed/12563145.

Jacobs, L. 2008. “Positive margins: the challenge continues for breast surgeons.” *Ann Surg Oncol* 15 (5): 1271-1272. doi:10.1245/s10434-007-9766-0. http://www.ncbi.nlm.nih.gov/entrez/query.fcgi?cmd=Retrieve&db=PubMed&dopt=Citation&list_uids=18320287.

Jassem, J, T Pieńkowski, A Płuzańska, S Jelic, V Gorbunova, Z Mrsic-Krmpotic, J Berzins, et al. 2001. “Doxorubicin and paclitaxel versus fluorouracil, doxorubicin, and cyclophosphamide as first-line therapy for women with metastatic breast cancer: final results of a randomized phase III multicenter trial.” *Journal of clinical oncology : official journal of the American Society of Clinical Oncology* 19 (6) (March 15): 1707-15. http://www.ncbi.nlm.nih.gov/pubmed/11251000.

Kaida, Hayato, Masatoshi Ishibashi, Teruhiko Fuji, Seiji Kurata, Masafumi Uchida, Kenkichi Baba, Teruo Miyagawa, et al. 2008. “Improved breast cancer detection of prone breast fluorodeoxyglucose-PET in 118 patients.” *Nuclear medicine communications* 29 (10) (October): 885-93. doi:10.1097/MNM.0b013e32830439d9. http://www.ncbi.nlm.nih.gov/pubmed/18769306.

Karni, T, I Pappo, J Sandbank, O Lavon, V Kent, R Spector, S Morgenstern, and S Lelcuk. 2007. “A device for real-time, intraoperative margin assessment in breast-conservation surgery.” *Am J Surg* 194 (4): 467-473. doi:S0002-9610(07)00530-2 [pii] 10.1016/j.amjsurg.2007.06.013. http://www.ncbi.nlm.nih.gov/entrez/query.fcgi?cmd=Retrieve&db=PubMed&dopt=Citation&list_uids=17826057.

Kaufmann, Manfred, Gabriel N Hortobagyi, Aron Goldhirsch, Suzy Scholl, Andreas Makris, Pinuccia Valagussa, Jens-Uwe Blohmer, et al. 2006. "Recommendations from an international expert panel on the use of neoadjuvant (primary) systemic treatment of operable breast cancer: an update." *Journal of clinical oncology : official journal of the American Society of Clinical Oncology* 24 (12) (April 20): 1940-9. doi:10.1200/JCO.2005.02.6187. http://www.ncbi.nlm.nih.gov/pubmed/16622270.

Kaufmann, Manfred, Monica Morrow, Gunter von Minckwitz, and Jay R Harris. 2010. "Locoregional treatment of primary breast cancer: consensus recommendations from an International Expert Panel." *Cancer* 116 (5) (March 1): 1184-91. doi:10.1002/cncr.24874. http://www.ncbi.nlm.nih.gov/pubmed/20087962.

Kelly, P, and E H Winslow. 1996. "Needle wire localization for nonpalpable breast lesions: sensations, anxiety levels, and informational needs." *Oncology nursing forum* 23 (4) (May): 639-45. http://www.ncbi.nlm.nih.gov/pubmed/8735322.

Kim, Mi-Jung, Jae Y Ro, Sei-Hyun Ahn, Hak Hee Kim, Sung-Bae Kim, and Gyungyub Gong. 2006. "Clinicopathologic significance of the basal-like subtype of breast cancer: a comparison with hormone receptor and Her2/neu-overexpressing phenotypes." *Human pathology* 37 (9) (September): 1217-26. doi:10.1016/j.humpath.2006.04.015. http://www.ncbi.nlm.nih.gov/pubmed/16938528.

Komoike, Yoshifumi, Futoshi Akiyama, Yuichi Iino, Tadashi Ikeda, Sadako Akashi-Tanaka, Shozo Ohsumi, Mikihiro Kusama, et al. 2006. "Ipsilateral breast tumor recurrence (IBTR) after breast-conserving treatment for early breast cancer: risk factors and impact on distant metastases." *Cancer* 106 (1) (January 1): 35-41. doi:10.1002/cncr.21551. http://www.ncbi.nlm.nih.gov/pubmed/16333848.

Kong, T, J Zeng, X Wang, X Yang, J Yang, S McQuarrie, A McEwan, W Roa, J Chen, and J Z Xing. 2008. "Enhancement of radiation cytotoxicity in breast-cancer cells by localized attachment of gold nanoparticles." *Small* 4 (9): 1537-1543. doi:10.1002/smll.200700794. http://www.ncbi.nlm.nih.gov/entrez/query.fcgi?cmd=Retrieve&db=PubMed&dopt=Citation&list_uids=18712753.

Kreike, Bas, Augustinus A M Hart, Tony van de Velde, Jacques Borger, Hans Peterse, Emiel Rutgers, Harry Bartelink, and Marc J van de Vijver. 2008. "Continuing risk of ipsilateral breast relapse after breast-conserving therapy at long-term follow-up." *International journal of radiation oncology, biology, physics* 71 (4) (July 15): 1014-21. doi:10.1016/j.ijrobp.2007.11.029. http://www.ncbi.nlm.nih.gov/pubmed/18234444.

Kukreti, Shwayta, Albert E Cerussi, Wendy Tanamai, David Hsiang, Bruce J Tromberg, and Enrico Gratton. 2010. "Characterization of metabolic differences between benign and malignant tumors: high-spectral-resolution diffuse optical spectroscopy." *Radiology* 254 (1) (January): 277-84. doi:10.1148/radiol.09082134. http://www.pubmedcentral.nih.gov/articlerender.fcgi?artid=2797652&tool=pmcentrez&rendertype=abstract.

Kumar, A, R Kumar, V Seenu, S D Gupta, M Chawla, A Malhotra, and S N Mehta. 2009. "The role of 18F-FDG PET/CT in evaluation of early response to neoadjuvant chemotherapy in patients with locally advanced breast cancer." *Eur Radiol* 19 (6): 1347-1357. doi:10.1007/s00330-009-1303-z. http://www.ncbi.nlm.nih.gov/entrez/query.fcgi?cmd=Retrieve&db=PubMed&dopt=Citation&list_uids=19214522.

Langsner, R J, L P Middleton, J Sun, F Meric-Bernstam, K K Hunt, R A Drezek, and T K Yu. 2011. “Wide-field imaging of fluorescent deoxy-glucose in ex vivo malignant and normal breast tissue.” *Biomed Opt Express* 2 (6): 1514-1523. doi:10.1364/BOE.2.001514 145022 [pii]. http://www.ncbi.nlm.nih.gov/entrez/query.fcgi?cmd=Retrieve&db=PubMed&dopt=Citation&list_uids=21698015.

Laurinavicius, Arvydas, Aida Laurinaviciene, Valerijus Ostapenko, Darius Dasevicius, Sonata Jarmalaite, and Juozas Lazutka. 2012. “Immunohistochemistry profiles of breast ductal carcinoma: factor analysis of digital image analysis data.” *Diagnostic pathology* 7 (January): 27. doi:10.1186/1746-1596-7-27. http://www.pubmedcentral.nih.gov/articlerender.fcgi?artid=3319425&tool=pmcentrez&rendertype=abstract.

Lee, Hyeran, Walter Akers, Kumar Bhushan, Sharon Bloch, Gail Sudlow, Rui Tang, and Samuel Achilefu. 2011. “Near-infrared pH-activatable fluorescent probes for imaging primary and metastatic breast tumors.” *Bioconjugate chemistry* 22 (4) (April 20): 777-84. doi:10.1021/bc100584d. http://www.pubmedcentral.nih.gov/articlerender.fcgi?artid=3080440&tool=pmcentrez&rendertype=abstract.

Lee, Jun H, and Anjan Nan. 2012. “Combination drug delivery approaches in metastatic breast cancer.” *Journal of drug delivery* 2012 (January): 915375. doi:10.1155/2012/915375. http://www.ncbi.nlm.nih.gov/pubmed/22619725.

Lee, Larissa J, and Jay R Harris. 2009. “Innovations in radiation therapy (RT) for breast cancer.” *Breast (Edinburgh, Scotland)* 18 Suppl 3 (October): S103-11. doi:10.1016/S0960-9776(09)70284-X. http://www.ncbi.nlm.nih.gov/pubmed/19914528.

Lester, Susan C. 2004. The Breast. In *Pathologic Basis of Disease*, ed. Vinay Kumar, Abul Abbas, and Nelson Fausto, 1119-1154. 7th ed. Philadelphia: Elsevier Inc.

Lim, Hyo Soon, Woong Yoon, Tae Woong Chung, Jae Kyu Kim, Jin Gyoon Park, Heoung Keun Kang, Hee Seung Bom, and Jung Han Yoon. 2007. “FDG PET/CT for the detection and evaluation of breast diseases: usefulness and limitations.” *Radiographics : a review publication of the Radiological Society of North America, Inc* 27 Suppl 1 (October): S197-213. doi:10.1148/rg.27si075507. http://www.ncbi.nlm.nih.gov/pubmed/18180227.

Linderholm, B, B Tavelin, K Grankvist, and R Henriksson. 1999. “Does vascular endothelial growth factor (VEGF) predict local relapse and survival in radiotherapy-treated node-negative breast cancer?” *British journal of cancer* 81 (4) (October): 727-32. doi:10.1038/sj.bjc.6690755. http://www.pubmedcentral.nih.gov/articlerender.fcgi?artid=2362894&tool=pmcentrez&rendertype=abstract.

Livi, Lorenzo, Icro Meattini, Carla De Luca Cardillo, Monica Mangoni, Daniela Greto, Alessia Petrucci, Andrea Rampini, et al. 2009. “Non-pegylated liposomal doxorubicin in combination with cyclophosphamide or docetaxel as first-line therapy in metastatic breast cancer: a retrospective analysis.” *Tumori* 95 (4): 422-6. http://www.ncbi.nlm.nih.gov/pubmed/19856650.

Loo, C, L Hirsch, M H Lee, E Chang, J West, N Halas, and R Drezek. 2005. “Gold nanoshell bioconjugates for molecular imaging in living cells.” *Opt Lett* 30 (9): 1012-1014. http://www.ncbi.nlm.nih.gov/entrez/query.fcgi?cmd=Retrieve&db=PubMed&dopt=Citation&list_uids=15906987.

Loo, C, A Lin, L Hirsch, M H Lee, J Barton, N Halas, J West, and R Drezek. 2004. "Nanoshell-enabled photonics-based imaging and therapy of cancer." *Technol Cancer Res Treat* 3 (1): 33-40. doi:d=3018&c=4130&p=12032&do=detail [pii]. http://www.ncbi.nlm.nih.gov/entrez/query.fcgi?cmd=Retrieve&db=PubMed&dopt=Citation&list_uids=14750891.

Loo, C, A Lowery, N Halas, J West, and R Drezek. 2005. "Immunotargeted nanoshells for integrated cancer imaging and therapy." *Nano Lett* 5 (4): 709-711. doi:10.1021/nl050127s. http://www.ncbi.nlm.nih.gov/entrez/query.fcgi?cmd=Retrieve&db=PubMed&dopt=Citation&list_uids=15826113.

Lowery, Aoife J, Malcolm R Kell, Ronan W Glynn, Michael J Kerin, and Karl J Sweeney. 2011. "Locoregional recurrence after breast cancer surgery: a systematic review by receptor phenotype." *Breast cancer research and treatment* (December 7). doi:10.1007/s10549-011-1891-6. http://www.ncbi.nlm.nih.gov/pubmed/22147079.

Luini, Alberto, Joel Rososchansky, Giovanna Gatti, Stefano Zurrida, Pietro Caldarella, Giuseppe Viale, Gabriela Rosali dos Santos, and Antonio Frasson. 2009. "The surgical margin status after breast-conserving surgery: discussion of an open issue." *Breast cancer research and treatment* 113 (2) (January): 397-402. doi:10.1007/s10549-008-9929-0. http://www.ncbi.nlm.nih.gov/pubmed/18386174.

MacDonald, Shannon, and Alphonse G Taghian. 2009. "Prognostic factors for local control after breast conservation: does margin status still matter?" *Journal of clinical oncology : official journal of the American Society of Clinical Oncology* 27 (30) (October 20): 4929-30. doi:10.1200/JCO.2009.23.6679. http://www.ncbi.nlm.nih.gov/pubmed/19720895.

Macheda, Maria L, Suzanne Rogers, and James D Best. 2005. "Molecular and cellular regulation of glucose transporter (GLUT) proteins in cancer." *Journal of cellular physiology* 202 (3) (March): 654-62. doi:10.1002/jcp.20166. http://www.ncbi.nlm.nih.gov/pubmed/15389572.

Mahmood, Usama, Christopher Morris, Geoffrey Neuner, Matthew Koshy, Susan Kesmodel, Robert Buras, Saranya Chumsri, Ting Bao, Katherine Tkaczuk, and Steven Feigenberg. 2012. "Similar Survival with Breast Conservation Therapy or Mastectomy in the Management of Young Women with Early-Stage Breast Cancer." *International Journal of Radiation Oncology*Biology*Physics* (January). doi:10.1016/j.ijrobp.2011.10.075. http://linkinghub.elsevier.com/retrieve/pii/S0360301611034833.

Manders, Peggy, Fred C G J Sweep, Vivianne C G Tjan-Heijnen, Anneke Geurts-Moespot, Doorléne T H van Tienoven, John A Foekens, Paul N Span, Jan Bussink, and Louk V A M Beex. 2003. "Vascular endothelial growth factor independently predicts the efficacy of postoperative radiotherapy in node-negative breast cancer patients." *Clinical cancer research : an official journal of the American Association for Cancer Research* 9 (17) (December 15): 6363-70. http://www.ncbi.nlm.nih.gov/pubmed/14695136.

Mannell, Aylwyn. 2005. "Breast-conserving therapy in breast cancer patients--a 12-year experience." *South African journal of surgery. Suid-Afrikaanse tydskrif vir chirurgie* 43 (2) (May): 28-30; discussion 30, 32. http://www.ncbi.nlm.nih.gov/pubmed/16035379.

Margenthaler, Julie A. 2011. "Optimizing conservative breast surgery." *Journal of surgical oncology* 103 (4) (March 15): 306-12. doi:10.1002/jso.21700. http://www.ncbi.nlm.nih.gov/pubmed/21337563.

McGuire, K P, A A Santillan, P Kaur, T Meade, J Parbhoo, M Mathias, C Shamehdi, M Davis, D Ramos, and C E Cox. 2009. "Are mastectomies on the rise? A 13-year trend analysis of the selection of mastectomy versus breast conservation therapy in 5865 patients." *Ann Surg*

*Oncol* 16 (10): 2682-2690. doi:10.1245/s10434-009-0635-x. http://www.ncbi.nlm.nih.gov/entrez/query.fcgi?cmd=Retrieve&db=PubMed&dopt=Citation&list_uids=19653046.

Medina-Franco, Heriberto, Leonardo Abarca-Pérez, Miriam N García-Alvarez, José L Ulloa-Gómez, Cecilia Romero-Trejo, and Jesús Sepúlveda-Méndez. 2008. "Radioguided occult lesion localization (ROLL) versus wire-guided lumpectomy for non-palpable breast lesions: a randomized prospective evaluation." *Journal of surgical oncology* 97 (2) (February 1): 108-11. doi:10.1002/jso.20880. http://www.ncbi.nlm.nih.gov/pubmed/18181162.

Mieog, J Sven D, Susan L Troyan, Merlijn Hutteman, Kevin J Donohoe, Joost R van der Vorst, Alan Stockdale, Gerrit-Jan Liefers, et al. 2011. "Toward optimization of imaging system and lymphatic tracer for near-infrared fluorescent sentinel lymph node mapping in breast cancer." *Annals of surgical oncology* 18 (9) (September): 2483-91. doi:10.1245/s10434-011-1566-x. http://www.pubmedcentral.nih.gov/articlerender.fcgi?artid=3139732&tool=pmcentrez&rendertype=abstract.

Miles, Randy C, Rachel E Gullerud, Christine M Lohse, James W Jakub, Amy C Degnim, and Judy C Boughey. 2012. "Local recurrence after breast-conserving surgery: multivariable analysis of risk factors and the impact of young age." *Annals of surgical oncology* 19 (4) (April): 1153-9. doi:10.1245/s10434-011-2084-6. http://www.ncbi.nlm.nih.gov/pubmed/21989658.

Miller, Alexander R, Guillermo Brandao, Thomas J Prihoda, Cheryl Hill, Anatolio B Cruz, and I-Tien Yeh. 2004. "Positive margins following surgical resection of breast carcinoma: analysis of pathologic correlates." *Journal of surgical oncology* 86 (3) (June 1): 134-40. doi:10.1002/jso.20059. http://www.ncbi.nlm.nih.gov/pubmed/15170651.

Minamimoto, R, M Senda, K Uno, S Jinnouchi, T Iinuma, K Ito, C Okuyama, et al. 2007. "Performance profile of FDG-PET and PET/CT for cancer screening on the basis of a Japanese Nationwide Survey." *Ann Nucl Med* 21 (9): 481-498. doi:10.1007/s12149-007-0061-8. http://www.ncbi.nlm.nih.gov/entrez/query.fcgi?cmd=Retrieve&db=PubMed&dopt=Citation&list_uids=18030580.

Mironava, T, M Hadjiargyrou, M Simon, V Jurukovski, and M H Rafailovich. 2010. "Gold nanoparticles cellular toxicity and recovery: Effect of size, concentration and exposure time." *Nanotoxicology* 4 (1): 120-137. doi:Doi 10.3109/17435390903471463. <Go to ISI>://000275061000009.

Moore, M M, L A Whitney, L Cerilli, J Z Imbrie, M Bunch, V B Simpson, and J B Hanks. 2001. "Intraoperative ultrasound is associated with clear lumpectomy margins for palpable infiltrating ductal breast cancer." *Annals of surgery* 233 (6) (June): 761-8. http://www.pubmedcentral.nih.gov/articlerender.fcgi?artid=1421318&tool=pmcentrez&rendertype=abstract.

Moran, Meena S, Qifeng Yang, Sharad Goyal, Lyndsay Harris, Gina Chung, and Bruce G Haffty. 2011. "Evaluation of vascular endothelial growth factor as a prognostic marker for local relapse in early-stage breast cancer patients treated with breast-conserving therapy." *International journal of radiation oncology, biology, physics* 81 (5) (December 1): 1236-43. doi:10.1016/j.ijrobp.2010.07.031. http://www.ncbi.nlm.nih.gov/pubmed/21093162.

Morrow, Monica, and Gary Freedman. 2006. “A clinical oncology perspective on the use of breast MR.” *Magnetic resonance imaging clinics of North America* 14 (3) (August): 363-78, vi. doi:10.1016/j.mric.2006.07.006. http://www.ncbi.nlm.nih.gov/pubmed/17098177.

Munirah, M A, M A Siti-Aishah, M Z Reena, N A Sharifah, M Rohaizak, A Norlia, M K M Rafie, et al. 2011. “Identification of different subtypes of breast cancer using tissue microarray.” *Romanian journal of morphology and embryology = Revue roumaine de morphologie et embryologie* 52 (2) (January): 669-77. http://www.ncbi.nlm.nih.gov/pubmed/21655659.

Nguyen, Freddy T, Adam M Zysk, Eric J Chaney, Jan G Kotynek, Uretz J Oliphant, Frank J Bellafiore, Kendrith M Rowland, Patricia A Johnson, and Stephen A Boppart. 2009. “Intraoperative evaluation of breast tumor margins with optical coherence tomography.” *Cancer research* 69 (22) (November 15): 8790-6. doi:10.1158/0008-5472.CAN-08-4340. http://www.pubmedcentral.nih.gov/articlerender.fcgi?artid=2782920&tool=pmcentrez&rendertype=abstract.

Ngô, Charlotte, Aymeric G Pollet, Juliette Laperrelle, Gregory Ackerman, Sandra Gomme, Fabienne Thibault, Virginie Fourchotte, and Remy J Salmon. 2007. “Intraoperative ultrasound localization of nonpalpable breast cancers.” *Annals of surgical oncology* 14 (9) (September): 2485-9. doi:10.1245/s10434-007-9420-x. http://www.ncbi.nlm.nih.gov/pubmed/17541694.

Nitin, Nitin, Alicia L Carlson, Tim Muldoon, Adel K El-Naggar, Ann Gillenwater, and Rebecca Richards-Kortum. 2009. “Molecular imaging of glucose uptake in oral neoplasia following topical application of fluorescently labeled deoxy-glucose.” *International journal of cancer. Journal international du cancer* 124 (11) (June): 2634-42. doi:10.1002/ijc.24222. http://www.pubmedcentral.nih.gov/articlerender.fcgi?artid=2700039&tool=pmcentrez&rendertype=abstract.

Nottage, Michelle K, Karen A Kopciuk, Anjela Tzontcheva, Irene L Andrulis, Shelley B Bull, and Martin E Blackstein. 2006. “Analysis of incidence and prognostic factors for ipsilateral breast tumour recurrence and its impact on disease-specific survival of women with node-negative breast cancer: a prospective cohort study.” *Breast cancer research : BCR* 8 (4) (January): R44. doi:10.1186/bcr1531. http://www.pubmedcentral.nih.gov/articlerender.fcgi?artid=1779479&tool=pmcentrez&rendertype=abstract.

Ogasawara, Yutaka, Hirokuni Ikeda, Mina Takahashi, Kensuke Kawasaki, and Hiroyoshi Doihara. 2008. “Evaluation of breast lymphatic pathways with indocyanine green fluorescence imaging in patients with breast cancer.” *World journal of surgery* 32 (9) (September): 1924-9. doi:10.1007/s00268-008-9519-7. http://www.ncbi.nlm.nih.gov/pubmed/18330628.

Olson, T P, J Harter, A Muñoz, D M Mahvi, and Tm Breslin. 2007. “Frozen section analysis for intraoperative margin assessment during breast-conserving surgery results in low rates of re-excision and local recurrence.” *Annals of surgical oncology* 14 (10) (October): 2953-60. doi:10.1245/s10434-007-9437-1. http://www.ncbi.nlm.nih.gov/pubmed/17674109.

Osborn, John B, Gary L Keeney, James W Jakub, Amy C Degnim, and Judy C Boughey. 2011. “Cost-effectiveness analysis of routine frozen-section analysis of breast margins compared with reoperation for positive margins.” *Annals of surgical oncology* 18 (11) (October): 3204-9. doi:10.1245/s10434-011-1956-0. http://www.ncbi.nlm.nih.gov/pubmed/21861234.

O’Neil, Roger G, Ling Wu, and Nizar Mullani. 2005. “Uptake of a fluorescent deoxyglucose analog (2-NBDG) in tumor cells.” *Molecular imaging and biology : MIB : the official publication of the Academy of Molecular Imaging* 7 (6): 388-92. doi:10.1007/s11307-005-0011-6. http://www.ncbi.nlm.nih.gov/pubmed/16284704.

Pansare, Vikram J., Shahram Hejazi, William J. Faenza, and Robert K. Prud’homme. 2012. “Review of Long-Wavelength Optical and NIR Imaging Materials: Contrast Agents, Fluorophores, and Multifunctional Nano Carriers.” *Chemistry of Materials* 24 (5) (March 13): 812-827. doi:10.1021/cm2028367. http://pubs.acs.org/doi/abs/10.1021/cm2028367.

Pengel, K E, C E Loo, H J Teertstra, S H Muller, J Wesseling, J L Peterse, H Bartelink, E J Rutgers, and K G A Gilhuijs. 2009. “The impact of preoperative MRI on breast-conserving surgery of invasive cancer: a comparative cohort study.” *Breast cancer research and treatment* 116 (1) (July): 161-9. doi:10.1007/s10549-008-0182-3. http://www.ncbi.nlm.nih.gov/pubmed/18807269.

Pierce, Mark C, Peter M Vila, Alexandros D Polydorides, Rebecca Richards-Kortum, and Sharmila Anandasabapathy. 2011. “Low-cost endomicroscopy in the esophagus and colon.” *The American journal of gastroenterology* 106 (9) (September): 1722-4. doi:10.1038/ajg.2011.140. http://www.pubmedcentral.nih.gov/articlerender.fcgi?artid=3191066&tool=pmcentrez&rendertype=abstract.

Pierce, Mark C., Richard a. Schwarz, Dong-Suk Shin, Darren Roblyer, Tim Muldoon, Mohammed Rahman, Ann M. Gillenwater, Sharmila Anandasabapathy, and Rebecca Richards-Kortum. 2010. “Low-cost, portable imaging systems for cancer detection.” *Quality* 7556: 755606-755606-5. doi:10.1117/12.848553. http://link.aip.org/link/PSISDG/v7556/i1/p755606/s1&Agg=doi.

Pleijhuis, R G, M Graafland, J de Vries, J Bart, J S de Jong, and G M van Dam. 2009. “Obtaining adequate surgical margins in breast-conserving therapy for patients with early-stage breast cancer: current modalities and future directions.” *Ann Surg Oncol* 16 (10): 2717-2730. doi:10.1245/s10434-009-0609-z. http://www.ncbi.nlm.nih.gov/entrez/query.fcgi?cmd=Retrieve&db=PubMed&dopt=Citation&list_uids=19609829.

Pleijhuis, R G, G C Langhout, W Helfrich, G Themelis, A Sarantopoulos, L M A Crane, N J Harlaar, J S de Jong, V Ntziachristos, and G M van Dam. 2011. “Near-infrared fluorescence (NIRF) imaging in breast-conserving surgery: assessing intraoperative techniques in tissue-simulating breast phantoms.” *European journal of surgical oncology : the journal of the European Society of Surgical Oncology and the British Association of Surgical Oncology* 37 (1) (January): 32-9. doi:10.1016/j.ejso.2010.10.006. http://www.ncbi.nlm.nih.gov/pubmed/21106329.

Pons, F, J Duch, and D Fuster. 2009. “Breast cancer therapy: the role of PET-CT in decision making.” *Q J Nucl Med Mol Imaging* 53 (2): 210-223. http://www.ncbi.nlm.nih.gov/entrez/query.fcgi?cmd=Retrieve&db=PubMed&dopt=Citation&list_uids=19293769.

Provenzano, E, J L Hopper, G G Giles, G Marr, D J Venter, and J E Armes. 2003. “Biological markers that predict clinical recurrence in ductal carcinoma in situ of the breast.” *European journal of cancer (Oxford, England : 1990)* 39 (5) (March): 622-30. http://www.ncbi.nlm.nih.gov/pubmed/12628841.

Purmonen, Timo T, Emma Pänkäläinen, Juha H O Turunen, Christian Asseburg, and Janne A Martikainen. 2011. “Short-course adjuvant trastuzumab therapy in early stage breast cancer in Finland: cost-effectiveness and value of information analysis based on the 5-year follow-up results of the FinHer Trial.” *Acta oncologica (Stockholm, Sweden)* 50 (3) (April): 344-52. doi:10.3109/0284186X.2011.553841. http://www.ncbi.nlm.nih.gov/pubmed/21299447.

Rahusen, Frans D, Andre J A Bremers, Hans F J Fabry, A H M Taets van Amerongen, Rob P A Boom, and S Meijer. 2002. “Ultrasound-guided lumpectomy of nonpalpable breast cancer versus wire-guided resection: a randomized clinical trial.” *Annals of surgical oncology* 9 (10) (December): 994-8. http://www.ncbi.nlm.nih.gov/pubmed/12464592.

Rampaul, R S, M Bagnall, H Burrell, S E Pinder, A J Evans, and R D Macmillan. 2004. “Randomized clinical trial comparing radioisotope occult lesion localization and wire-guided excision for biopsy of occult breast lesions.” *The British journal of surgery* 91 (12) (December): 1575-7. doi:10.1002/bjs.4801. http://www.ncbi.nlm.nih.gov/pubmed/15505875.

Rauscher, Garth H, Timothy P Johnson, Young Ik Cho, and Jennifer A Walk. 2008. “Accuracy of self-reported cancer-screening histories: a meta-analysis.” *Cancer epidemiology, biomarkers & prevention : a publication of the American Association for Cancer Research, cosponsored by the American Society of Preventive Oncology* 17 (4) (April): 748-57. doi:10.1158/1055-9965.EPI-07-2629. http://www.ncbi.nlm.nih.gov/pubmed/18381468.

Riedl, O, F Fitzal, N Mader, P Dubsky, M Rudas, M Mittlboeck, M Gnant, and R Jakesz. 2009. “Intraoperative frozen section analysis for breast-conserving therapy in 1016 patients with breast cancer.” *European journal of surgical oncology : the journal of the European Society of Surgical Oncology and the British Association of Surgical Oncology* 35 (3) (March): 264-70. doi:10.1016/j.ejso.2008.05.007. http://www.ncbi.nlm.nih.gov/pubmed/18706785.

Roblyer, Darren, Cristina Kurachi, Vanda Stepanek, Michelle D Williams, Adel K El-Naggar, J Jack Lee, Ann M Gillenwater, and Rebecca Richards-Kortum. 2009. “Objective detection and delineation of oral neoplasia using autofluorescence imaging.” *Cancer Prev Res (Phila Pa)* 2 (5) (May): 423-431. doi:1940-6207.CAPR-08-0229 [pii] 10.1158/1940-6207.CAPR-08-0229. http://www.pubmedcentral.nih.gov/articlerender.fcgi?artid=2719708&tool=pmcentrez&rendertype=abstract.

Rodríguez Lajusticia, Laura, Miguel Martín Jiménez, and Sara López-Tarruella Cobo. 2008. “Endocrine therapy of metastatic breast cancer.” *Clinical & translational oncology : official publication of the Federation of Spanish Oncology Societies and of the National Cancer Institute of Mexico* 10 (8) (August): 462-7. http://www.ncbi.nlm.nih.gov/pubmed/18667376.

de Roos, Marnix A, Geertruida H de Bock, Jaap de Vries, Bert van der Vegt, and Jelle Wesseling. 2007. “p53 overexpression is a predictor of local recurrence after treatment for both in situ and invasive ductal carcinoma of the breast.” *The Journal of surgical research* 140 (1) (June 1): 109-14. doi:10.1016/j.jss.2006.10.045. http://www.ncbi.nlm.nih.gov/pubmed/17291532.

Rosbach, Kelsey J, Dongsuk Shin, Timothy J Muldoon, Mohammad A Quraishi, Lavinia P Middleton, Kelly K Hunt, Funda Meric-Bernstam, Tse-Kuan Yu, Rebecca R Richards-Kortum, and Wei Yang. 2010. “High-resolution fiber optic microscopy with fluorescent contrast enhancement for the identification of axillary lymph node metastases in breast cancer: a pilot study.” *Biomed. Opt. Express* 1 (3): 911-922. http://www.opticsinfobase.org/boe/abstract.cfm?URI=boe-1-3-911.

Rowland, J H, K A Desmond, B E Meyerowitz, T R Belin, G E Wyatt, and P A Ganz. 2000. “Role of breast reconstructive surgery in physical and emotional outcomes among breast cancer survivors.” *Journal of the National Cancer Institute* 92 (17) (September 6): 1422-9. http://www.ncbi.nlm.nih.gov/pubmed/10974078.

Rusby, Jennifer E, Nirmala Paramanathan, Siobhan A M Laws, and Richard M Rainsbury. 2008. “Immediate latissimus dorsi miniflap volume replacement for partial mastectomy: use of intra-operative frozen sections to confirm negative margins.” *American journal of surgery* 196 (4) (October): 512-8. doi:10.1016/j.amjsurg.2008.06.026. http://www.ncbi.nlm.nih.gov/pubmed/18809053.

Salas-Burgos, Alexis, Pavel Iserovich, Felipe Zuniga, Juan Carlos Vera, and Jorge Fischbarg. 2004. “Predicting the three-dimensional structure of the human facilitative glucose transporter glut1 by a novel evolutionary homology strategy: insights on the molecular mechanism of substrate migration, and binding sites for glucose and inhibitory molecules.” *Biophysical journal* 87 (5) (November): 2990-9. doi:10.1529/biophysj.104.047886. http://www.ncbi.nlm.nih.gov/pubmed/15326030.

Sano, Kohei, Makoto Mitsunaga, Takahito Nakajima, Peter L Choyke, and Hisataka Kobayashi. 2012. “In vivo breast cancer characterization imaging using two monoclonal antibodies activatably labeled with near infrared fluorophores.” *Breast cancer research : BCR* 14 (2) (April 17): R61. doi:10.1186/bcr3167. http://www.ncbi.nlm.nih.gov/pubmed/22510481.

Sarlos, D, L D Frey, H Haueisen, G Landmann, L A Kots, and G Schaer. 2009. “Radioguided occult lesion localization (ROLL) for treatment and diagnosis of malignant and premalignant breast lesions combined with sentinel node biopsy: a prospective clinical trial with 100 patients.” *European journal of surgical oncology : the journal of the European Society of Surgical Oncology and the British Association of Surgical Oncology* 35 (4) (April): 403-8. doi:10.1016/j.ejso.2008.06.016. http://www.ncbi.nlm.nih.gov/pubmed/18692358.

Schelling, M, N Avril, J Nahrig, W Kuhn, W Romer, D Sattler, M Werner, et al. 2000. “Positron Emission Tomography Using [18F]Fluorodeoxyglucose for Monitoring Primary Chemotherapy in Breast Cancer.” *J Clin Oncol* 18 (8): 1689-1695. http://jco.ascopubs.org/cgi/content/abstract/18/8/1689.

Schwartz, Gordon F, Umberto Veronesi, Krishna B Clough, J Michael Dixon, Ian S Fentiman, Sylvia H Heywang-Köbrunner, Roland Holland, et al. 2006. “Consensus conference on breast conservation.” *Journal of the American College of Surgeons* 203 (2) (August): 198-207. doi:10.1016/j.jamcollsurg.2006.04.009. http://www.ncbi.nlm.nih.gov/pubmed/16864033.

Sevick-Muraca, Eva M, Ruchi Sharma, John C Rasmussen, Milton V Marshall, Juliet A Wendt, Hoang Q Pham, Elizabeth Bonefas, et al. 2008. “Imaging of lymph flow in breast cancer patients after microdose administration of a near-infrared fluorophore: feasibility study.” *Radiology* 246 (3) (March): 734-41. doi:10.1148/radiol.2463070962. http://www.pubmedcentral.nih.gov/articlerender.fcgi?artid=3166516&tool=pmcentrez&rendertype=abstract.

Shao, Wenlin, and Myles Brown. 2004. “Advances in estrogen receptor biology: prospects for improvements in targeted breast cancer therapy.” *Breast cancer research : BCR* 6 (1) (January): 39-52. doi:10.1186/bcr742. http://www.pubmedcentral.nih.gov/articlerender.fcgi?artid=314456&tool=pmcentrez&rendertype=abstract.

Singletary, S Eva. 2002. “Surgical margins in patients with early-stage breast cancer treated with breast conservation therapy.” *The American Journal of Surgery* 184 (5) (November): 383-393. http://www.sciencedirect.com/science/article/B6VHS-475NT83-3/2/62cd2a2269bef4ab66bd98f94184a246.

Smith, Ian, Marion Procter, Richard D Gelber, Sébastien Guillaume, Andrea Feyereislova, Mitch Dowsett, Aron Goldhirsch, et al. 2007. “2-year follow-up of trastuzumab after adjuvant chemotherapy in HER2-positive breast cancer: a randomised controlled trial.” *Lancet* 369 (9555) (January 6): 29-36. doi:10.1016/S0140-6736(07)60028-2. http://www.ncbi.nlm.nih.gov/pubmed/17208639.

Solin, Lawrence J, Susan G Orel, Wei-Ting Hwang, Eleanor E Harris, and Mitchell D Schnall. 2008. “Relationship of breast magnetic resonance imaging to outcome after breast-conservation treatment with radiation for women with early-stage invasive breast carcinoma or ductal carcinoma in situ.” *Journal of clinical oncology : official journal of the American Society of Clinical Oncology* 26 (3) (January 20): 386-91. doi:10.1200/JCO.2006.09.5448. http://www.ncbi.nlm.nih.gov/pubmed/18202414.

Stewart, Alexandra J, Desmond A O’Farrell, Robert A Cormack, Jorgen L Hansen, Atif J Khan, Subhakar Mutyala, and Phillip M Devlin. 2008. “Dose volume histogram analysis of normal structures associated with accelerated partial breast irradiation delivered by high dose rate brachytherapy and comparison with whole breast external beam radiotherapy fields.” *Radiation oncology (London, England)* 3 (January): 39. doi:10.1186/1748-717X-3-39. http://www.pubmedcentral.nih.gov/articlerender.fcgi?artid=2612673&tool=pmcentrez&rendertype=abstract.

Stober, W, A Fink, and E Bohn. 1968. “Controlled Growth of Monodisperse Silica Spheres in Micron Size Range.” *Journal of Colloid and Interface Science* 26 (1): 62-& <Go to ISI>://A1968A684600009.

Strong, Vivian E, John Humm, Paul Russo, Achim Jungbluth, W Douglas Wong, Farhad Daghighian, Lloyd Old, Yuman Fong, and Steven M Larson. 2008. “A novel method to localize antibody-targeted cancer deposits intraoperatively using handheld PET beta and gamma probes.” *Surgical endoscopy* 22 (2) (February): 386-91. doi:10.1007/s00464-007-9611-3. http://www.ncbi.nlm.nih.gov/pubmed/18027053.

Sørum, Ragnhild, Solveig Hofvind, Per Skaane, and Tor Haldorsen. 2010. “Trends in incidence of ductal carcinoma in situ: the effect of a population-based screening programme.” *Breast (Edinburgh, Scotland)* 19 (6) (December): 499-505. doi:10.1016/j.breast.2010.05.014. http://www.ncbi.nlm.nih.gov/pubmed/21071225.

Tafra, Lorraine, Richard Fine, Pat Whitworth, Michael Berry, James Woods, Gregory Ekbom, Jennifer Gass, et al. 2006. “Prospective randomized study comparing cryo-assisted and needle-wire localization of ultrasound-visible breast tumors.” *American journal of surgery* 192 (4) (October): 462-70. doi:10.1016/j.amjsurg.2006.06.012. http://www.sciencedirect.com/science/article/pii/S0002961006004405.

Tagaya, Nobumi, Rie Yamazaki, Aya Nakagawa, Akihito Abe, Kiyoshige Hamada, Keiichi Kubota, and Tetsunari Oyama. 2008. “Intraoperative identification of sentinel lymph nodes by near-infrared fluorescence imaging in patients with breast cancer.” *American journal of surgery* 195 (6) (June): 850-3. doi:10.1016/j.amjsurg.2007.02.032. http://www.ncbi.nlm.nih.gov/pubmed/18353274.

Tamimi, Rulla M, Heather J Baer, Jonathan Marotti, Mark Galan, Laurie Galaburda, Yineng Fu, Anne C Deitz, et al. 2008. “Comparison of molecular phenotypes of ductal carcinoma in situ and invasive breast cancer." *Breast cancer research : BCR* 10 (4) (January): R67. doi:10.1186/bcr2128. http://www.pubmedcentral.nih.gov/articlerender.fcgi?artid=2575540&tool=pmcentrez&rendertype=abstract.

Tanis, E, C J H van de Velde, H Bartelink, M J van de Vijver, H Putter, and J A van der Hage. 2012. "Locoregional recurrence after breast-conserving therapy remains an independent prognostic factor even after an event free interval of 10years in early stage breast cancer." *European journal of cancer (Oxford, England : 1990)* (March 23). doi:10.1016/j.ejca.2012.02.051. http://www.ncbi.nlm.nih.gov/pubmed/22446021.

Thekkek, N, D M Maru, A D Polydorides, M S Bhutani, S Anandasabapathy, and R Richards-Kortum. 2011. "Pre-clinical evaluation of fluorescent deoxyglucose as a topical contrast agent for the detection of Barrett's-associated neoplasia during confocal imaging." *Technology in cancer research & treatment* 10 (5) (October): 431-41. http://www.pubmedcentral.nih.gov/articlerender.fcgi?artid=3193280&tool=pmcentrez&rendertype=abstract.

Thekkek, Nadhi, Sharmila Anandasabapathy, and Rebecca Richards-Kortum. 2011. "Optical molecular imaging for detection of Barrett's-associated neoplasia." *World journal of gastroenterology : WJG* 17 (1) (January 7): 53-62. doi:10.3748/wjg.v17.i1.53. http://www.pubmedcentral.nih.gov/articlerender.fcgi?artid=3016680&tool=pmcentrez&rendertype=abstract.

Thind, C R, S Desmond, O Harris, R Nadeem, L S Chagla, and R A Audisio. 2005. "Radio-guided localization of clinically occult breast lesions (ROLL): a DGH experience." *Clinical radiology* 60 (6) (June): 681-6. doi:10.1016/j.crad.2004.12.004. http://www.ncbi.nlm.nih.gov/pubmed/16038695.

Tromberg, Bruce J, and Albert E Cerussi. 2010. "Imaging breast cancer chemotherapy response with light. Commentary on Soliman et al., p. 2605." *Clinical cancer research : an official journal of the American Association for Cancer Research* 16 (9) (May 1): 2486-8. doi:10.1158/1078-0432.CCR-10-0397. http://www.pubmedcentral.nih.gov/articlerender.fcgi?artid=3204881&tool=pmcentrez&rendertype=abstract.

Tromberg, Bruce J, Brian W Pogue, Keith D Paulsen, Arjun G Yodh, David A Boas, and Albert E Cerussi. 2008. "Assessing the future of diffuse optical imaging technologies for breast cancer management." *Medical physics* 35 (6) (June): 2443-51. http://www.pubmedcentral.nih.gov/articlerender.fcgi?artid=2809725&tool=pmcentrez&rendertype=abstract.

Troyan, Susan L, Vida Kianzad, Summer L Gibbs-Strauss, Sylvain Gioux, Aya Matsui, Rafiou Oketokoun, Long Ngo, Ali Khamene, Fred Azar, and John V Frangioni. 2009. "The FLARE intraoperative near-infrared fluorescence imaging system: a first-in-human clinical trial in breast cancer sentinel lymph node mapping." *Annals of surgical oncology* 16 (10) (October): 2943-52. doi:10.1245/s10434-009-0594-2. http://www.pubmedcentral.nih.gov/articlerender.fcgi?artid=2772055&tool=pmcentrez&rendertype=abstract.

Tse, Gary M K, Philip C W Lui, Joaquim S L Vong, Kin-Mang Lau, Thomas C Putti, Rooshdiya Karim, Richard A Scolyer, et al. 2009. "Increased epidermal growth factor receptor (EGFR) expression in malignant mammary phyllodes tumors." *Breast cancer research and* *treatment* 114 (3) (April): 441-8. doi:10.1007/s10549-008-0030-5. http://www.ncbi.nlm.nih.gov/pubmed/18443904.

Valdes, Edna K, Susan K Boolbol, Jean-Marc Cohen, and Sheldon M Feldman. 2007. "Intra-operative touch preparation cytology; does it have a role in re-excision lumpectomy?" *Annals of surgical oncology* 14 (3) (March): 1045-50. doi:10.1245/s10434-006-9263-x. http://www.ncbi.nlm.nih.gov/pubmed/17206481.

Vanden Bempt, Isabelle, Peter Van Loo, Maria Drijkoningen, Patrick Neven, Ann Smeets, Marie-Rose Christiaens, Robert Paridaens, and Christiane De Wolf-Peeters. 2008. "Polysomy 17 in breast cancer: clinicopathologic significance and impact on HER-2 testing." *Journal of clinical oncology : official journal of the American Society of Clinical Oncology* 26 (30) (October 20): 4869-74. doi:10.1200/JCO.2007.13.4296. http://www.ncbi.nlm.nih.gov/pubmed/18794552.

Vargas, Carlos, Larry Kestin, Nel Go, Daniel Krauss, Peter Chen, Neal Goldstein, Alvaro Martinez, and Frank A Vicini. 2005. "Factors associated with local recurrence and cause-specific survival in patients with ductal carcinoma in situ of the breast treated with breast-conserving therapy or mastectomy." *International journal of radiation oncology, biology, physics* 63 (5) (December 1): 1514-21. doi:10.1016/j.ijrobp.2005.04.045. http://www.ncbi.nlm.nih.gov/pubmed/16005576.

Veronesi, Umberto, Natale Cascinelli, Luigi Mariani, Marco Greco, Roberto Saccozzi, Alberto Luini, Marisel Aguilar, and Ettore Marubini. 2002. "Twenty-year follow-up of a randomized study comparing breast-conserving surgery with radical mastectomy for early breast cancer." *The New England journal of medicine* 347 (16) (October 17): 1227-32. doi:10.1056/NEJMoa020989. http://www.ncbi.nlm.nih.gov/pubmed/12393819.

Vicini, Frank A, Vincent Remouchamps, Michelle Wallace, Michael Sharpe, Julie Fayad, Laura Tyburski, Nicola Letts, et al. 2003. "Ongoing clinical experience utilizing 3D conformal external beam radiotherapy to deliver partial-breast irradiation in patients with early-stage breast cancer treated with breast-conserving therapy." *International journal of radiation oncology, biology, physics* 57 (5) (December 1): 1247-53. http://www.ncbi.nlm.nih.gov/pubmed/14630258.

Vinh-Hung, Vincent, and Claire Verschraegen. 2004. "Breast-conserving surgery with or without radiotherapy: pooled-analysis for risks of ipsilateral breast tumor recurrence and mortality." *Journal of the National Cancer Institute* 96 (2) (January 21): 115-21. http://www.ncbi.nlm.nih.gov/pubmed/14734701.

Virnig, Beth A, Todd M Tuttle, Tatyana Shamliyan, and Robert L Kane. 2010. "Ductal carcinoma in situ of the breast: a systematic review of incidence, treatment, and outcomes." *Journal of the National Cancer Institute* 102 (3) (February 3): 170-8. doi:10.1093/jnci/djp482. http://www.ncbi.nlm.nih.gov/pubmed/20071685.

Voogd, A C, F J van Oost, E J T Rutgers, P H M Elkhuizen, A N van Geel, L J E E Scheijmans, M J C van der Sangen, et al. 2005. "Long-term prognosis of patients with local recurrence after conservative surgery and radiotherapy for early breast cancer." *European journal of cancer (Oxford, England : 1990)* 41 (17) (November): 2637-44. doi:10.1016/j.ejca.2005.04.040. http://www.ncbi.nlm.nih.gov/pubmed/16115758.

Vosoughhosseini, S, M Lotfi, A Fakhrjou, A Aghbali, M Moradzadeh, M Sina, and P Emamverdizadeh. 2012. "Analysis of epidermal growth factor receptor in histopathologically tumor-free surgical margins in patients with oral squamous cell carcinoma." *African Journal of Biotechnology* 11 (2): 516-520. doi:10.5897/AJB 10.489.

Vranic, Semir, Ossama Tawfik, Juan Palazzo, Nurija Bilalovic, Eduardo Eyzaguirre, Lisa Mj Lee, Patrick Adegboyega, Jill Hagenkord, and Zoran Gatalica. 2010. "EGFR and HER-2/neu expression in invasive apocrine carcinoma of the breast." *Modern pathology : an official journal of the United States and Canadian Academy of Pathology, Inc* 23 (5) (May): 644-53. doi:10.1038/modpathol.2010.50. http://www.ncbi.nlm.nih.gov/pubmed/20208479.

Wahl, R L, R L Cody, G D Hutchins, and E E Mudgett. 1991. "Primary and metastatic breast carcinoma: initial clinical evaluation with PET with the radiolabeled glucose analogue 2-[F-18]-fluoro-2-deoxy-D-glucose." *Radiology* 179 (3): 765-770. http://radiology.rsna.org/content/179/3/765.abstract.

Wang, Shi-Yi, Tatyana Shamliyan, Beth A Virnig, and Robert Kane. 2011. "Tumor characteristics as predictors of local recurrence after treatment of ductal carcinoma in situ: a meta-analysis." *Breast cancer research and treatment* 127 (1) (May): 1-14. doi:10.1007/s10549-011-1387-4. http://www.ncbi.nlm.nih.gov/pubmed/21327465.

Weinberg, Elizabeth, Charles Cox, Elisabeth Dupont, Laura White, Mark Ebert, Harvey Greenberg, Nils Diaz, et al. 2004. "Local recurrence in lumpectomy patients after imprint cytology margin evaluation." *American journal of surgery* 188 (4) (October): 349-54. doi:10.1016/j.amjsurg.2004.06.024. http://www.ncbi.nlm.nih.gov/pubmed/15474425.

Wilke, Lee G, J Quincy Brown, Torre M Bydlon, Stephanie a Kennedy, Lisa M Richards, Marlee K Junker, Jennifer Gallagher, William T Barry, Joseph Geradts, and Nimmi Ramanujam. 2009. "Rapid noninvasive optical imaging of tissue composition in breast tumor margins." *American journal of surgery* 198 (4) (October): 566-74. doi:10.1016/j.amjsurg.2009.06.018. http://www.pubmedcentral.nih.gov/articlerender.fcgi?artid=2764289&tool=pmcentrez&rendertype=abstract.

Yang, Hae-Chung, Lisa M Thornton, Charles L Shapiro, and Barbara L Andersen. 2008. "Surviving recurrence: psychological and quality-of-life recovery." *Cancer* 112 (5) (March 1): 1178-87. doi:10.1002/cncr.23272. http://www.pubmedcentral.nih.gov/articlerender.fcgi?artid=2435301&tool=pmcentrez&rendertype=abstract.

Yang, Xiaohong R, Mark E Sherman, David L Rimm, Jolanta Lissowska, Louise A Brinton, Beata Peplonska, Stephen M Hewitt, et al. 2007. "Differences in risk factors for breast cancer molecular subtypes in a population-based study." *Cancer epidemiology, biomarkers & prevention : a publication of the American Association for Cancer Research, cosponsored by the American Society of Preventive Oncology* 16 (3) (March): 439-43. doi:10.1158/1055-9965.EPI-06-0806. http://www.ncbi.nlm.nih.gov/pubmed/17372238.

Yildirim, E. 2009. "Locoregional recurrence in breast carcinoma patients." *European journal of surgical oncology : the journal of the European Society of Surgical Oncology and the British Association of Surgical Oncology* 35 (3) (March): 258-63. doi:10.1016/j.ejso.2008.06.010. http://www.ncbi.nlm.nih.gov/pubmed/18644692.

Yoshioka, K, K B Oh, M Saito, Y Nemoto, and H Matsuoka. 1996. "Evaluation of 2-[N-(7-nitrobenz-2-oxa-1,3-diazol-4-yl)amino]-2-deoxy-D-glucose, a new fluorescent derivative of glucose, for viability assessment of yeast Candida albicans." *Appl Microbiol Biotechnol* 46 (4): 400-404. http://www.ncbi.nlm.nih.gov/entrez/query.fcgi?cmd=Retrieve&db=PubMed&dopt=Citation&list_uids=8987729.

Yu, Jennifer, Fatema Al Mushawah, Marie E Taylor, Amy E Cyr, William E Gillanders, Rebecca L Aft, Timothy J Eberlein, Feng Gao, and Julie A Margenthaler. 2012. "Compromised margins following mastectomy for stage I-III invasive breast cancer." *The Journal of surgical research* (April 10). doi:10.1016/j.jss.2012.03.046. http://www.ncbi.nlm.nih.gov/pubmed/22520579.

Zavagno, Giorgio, Elena Goldin, Roberto Mencarelli, Giovanni Capitanio, Paola Del Bianco, Renato Marconato, Simone Mocellin, et al. 2008. "Role of resection margins in patients treated with breast conservation surgery." *Cancer* 112 (9) (May 1): 1923-31. doi:10.1002/cncr.23383. http://www.ncbi.nlm.nih.gov/pubmed/18327818.

## Year 6

Baeten, John, Jodi Haller, Helen Shih, and Vasilis Ntziachristos. 2009. "In Vivo Investigation of Breast Cancer Progression by Use of an Internal Control." *Neoplasia (New York, N.Y.)* 11 (3) (March): 220–7. http://www.pubmedcentral.nih.gov/articlerender.fcgi?artid=2647724&tool=pmcentrez&rendertype=abstract.

Bedard, Noah, Mark Pierce, Adel El-Nagger, S Anandasabapathy, Ann Gillenwater, and R Richards-Kortum. 2010. "Emerging Roles for Multimodal Optical Imaging in Early Cancer Detection: a Global Challenge." *Technology in Cancer Research & Treatment* 9 (2) (April): 211–7. http://www.pubmedcentral.nih.gov/articlerender.fcgi?artid=2906814&tool=pmcentrez&rendertype=abstract.

Bhushan, Kumar R, Preeti Misra, Fangbing Liu, Sanjeev Mathur, Robert E Lenkinski, and John V Frangioni. 2008. "Detection of Breast Cancer Microcalcifications Using a Dual-modality SPECT/NIR Fluorescent Probe." *Journal of the American Chemical Society* 130 (52) (December 31): 17648–9. doi:10.1021/ja807099s. http://www.pubmedcentral.nih.gov/articlerender.fcgi?artid=2696399&tool=pmcentrez&rendertype=abstract.

Bickford, L, J Chang, K Fu, J Sun, Y Hu, A Gobin, Tse-Kuan Yu, and R Drezek. 2008. "Evaluation of Immunotargeted Gold Nanoshells as Rapid Diagnostic Imaging Agents for HER2-Overexpressing Breast Cancer Cells: A Time Based Analysis." *Nanobiotechnology* 4 (1-4): 1–8.

Bickford, Lissett R, Germaine Agollah, Rebekah Drezek, and Tse-Kuan K Yu. 2010. "Silica-gold Nanoshells as Potential Intraoperative Molecular Probes for HER2-overexpression in Ex Vivo Breast Tissue Using Near-infrared Reflectance Confocal Microscopy." *Breast Cancer Research and Treatment* 120 (3) (April): 1–9. doi:10.1007/s10549-009-0408-z. http://www.ncbi.nlm.nih.gov/pubmed/19418216.

Bickford, Lissett R., Robert J. Langsner, Joseph Chang, Laura C. Kennedy, Germaine D. Agollah, and Rebekah Drezek. 2012. "Rapid Stereomicroscopic Imaging of HER2 Overexpression in Ex Vivo Breast Tissue Using Topically Applied Silica-Based Gold Nanoshells." *Journal of Oncology* 2012: 1–10. doi:10.1155/2012/291898. http://www.hindawi.com/journals/jo/2012/291898/.

Chatni, Muhammad Rameez, Jun Xia, Rebecca Sohn, Konstantin Maslov, Zijian Guo, Yu Zhang, Kun Wang, et al. 2012. "Tumor Glucose Metabolism Imaged in Vivo in Small Animals with Whole-body Photoacoustic Computed Tomography." *Journal of Biomedical*

*Optics* 17 (7) (July): 076012. doi:10.1117/1.JBO.17.7.076012. http://www.ncbi.nlm.nih.gov/pubmed/22894495.

Genina, E. A., A. N. Bashkatov, Yu. P. Sinichkin, and V. V. Tuchin. 2010. "Optical Clearing of Skin Under Action of Glycerol: Ex Vivo and in Vivo Investigations." *Optics and Spectroscopy* 109 (2) (August 19): 225–231. doi:10.1134/S0030400X10080126. http://www.springerlink.com/index/10.1134/S0030400X10080126.

Genina, Elina A, Alexy N Bashkatov, Anastasiya A Korobko, Elena A Zubkova, Valery V Tuchin, Ilya Yaroslavsky, and Gregory B Altshuler. "Optical Clearing of Human Skin: Comparative Study of Permeability and Dehydration of Intact and Photothermally Perforated Skin." *Journal of Biomedical Optics* 13 (2): 021102. doi:10.1117/1.2899149. http://www.ncbi.nlm.nih.gov/pubmed/18465951.

Hirshburg, Jason, Bernard Choi, J Stuart Nelson, and Alvin T Yeh. "Collagen Solubility Correlates with Skin Optical Clearing." *Journal of Biomedical Optics* 11 (4): 040501. doi:10.1117/1.2220527. http://www.ncbi.nlm.nih.gov/pubmed/16965124.

Ke, Shi, Xiaoxia Wen, Michael Gurfinkel, Chusilp Charnsangavej, Sidney Wallace, Eva M Sevick-Muraca, and Chun Li. 2003. "Near-infrared Optical Imaging of Epidermal Growth Factor Receptor in Breast Cancer Xenografts." *Cancer Research* 63 (22) (November 15): 7870–5. http://www.ncbi.nlm.nih.gov/pubmed/14633715.

Kobayashi, Hisataka, Mikako Ogawa, Raphael Alford, Peter L Choyke, and Yasuteru Urano. 2010. "New Strategies for Fluorescent Probe Design in Medical Diagnostic Imaging." *Chemical Reviews* 110 (5) (May 12): 2620–40. doi:10.1021/cr900263j. http://www.pubmedcentral.nih.gov/articlerender.fcgi?artid=3241938&tool=pmcentrez&rendertype=abstract.

Kovar, Joy L, Melanie A Simpson, Amy Schutz-Geschwender, and D Michael Olive. 2007. "A Systematic Approach to the Development of Fluorescent Contrast Agents for Optical Imaging of Mouse Cancer Models." *Analytical Biochemistry* 367 (1) (August 1): 1–12. doi:10.1016/j.ab.2007.04.011. http://www.ncbi.nlm.nih.gov/pubmed/17521598.

Kovar, Joy L, William Volcheck, Eva Sevick-Muraca, Melanie a Simpson, and D Michael Olive. 2009. "Characterization and Performance of a Near-infrared 2-deoxyglucose Optical Imaging Agent for Mouse Cancer Models." *Analytical Biochemistry* 384 (2) (January): 254–62. doi:10.1016/j.ab.2008.09.050. http://www.pubmedcentral.nih.gov/articlerender.fcgi?artid=2720560&tool=pmcentrez&rendertype=abstract.

Lam, Stephen, Beau Standish, Corisande Baldwin, Annette McWilliams, Jean LeRiche, Adi Gazdar, Alex I Vitkin, Victor Yang, Norihiko Ikeda, and Calum MacAulay. 2008. "In Vivo Optical Coherence Tomography Imaging of Preinvasive Bronchial Lesions." *Clinical Cancer Research : an Official Journal of the American Association for Cancer Research* 14 (7) (April 1): 2006–11. doi:10.1158/1078-0432.CCR-07-4418. http://www.pubmedcentral.nih.gov/articlerender.fcgi?artid=2849640&tool=pmcentrez&rendertype=abstract.

Langsner, R J, L P Middleton, J Sun, F Meric-Bernstam, K K Hunt, R A Drezek, and T K Yu. 2011. "Wide-field Imaging of Fluorescent Deoxy-glucose in Ex Vivo Malignant and Normal Breast Tissue." *Biomed Opt Express* 2 (6): 1514–1523. doi:10.1364/BOE.2.001514 145022 [pii]. http://www.ncbi.nlm.nih.gov/entrez/query.fcgi?cmd=Retrieve&db=PubMed&dopt=Citation&list_uids=21698015.

Liotta, L, and E Petricoin. 2000. “Molecular Profiling of Human Cancer.” *Nature Reviews. Genetics* 1 (1) (October): 48–56. doi:10.1038/35049567. http://www.ncbi.nlm.nih.gov/pubmed/11262874.

Milas, Luka, and Walter N Hittelman. 2009. “Cancer Stem Cells and Tumor Response to Therapy: Current Problems and Future Prospects.” *Seminars in Radiation Oncology* 19 (2) (April): 96–105. doi:10.1016/j.semradonc.2008.11.004. http://www.ncbi.nlm.nih.gov/pubmed/19249647.

Montet, Xavier, Jose-Luiz Figueiredo, Herlen Alencar, Vasilis Ntziachristos, Umar Mahmood, and Ralph Weissleder. 2007. “Tomographic Fluorescence Imaging of Tumor Vascular Volume in Mice.” *Radiology* 242 (3) (March): 751–8. doi:10.1148/radiol.2423052065. http://www.ncbi.nlm.nih.gov/pubmed/17325064.

Muldoon, Timothy J, Mark C Pierce, Dawn L Nida, Michelle D Williams, Ann Gillenwater, and Rebecca Richards-Kortum. 2007. “Subcellular-resolution Molecular Imaging Within Living Tissue by Fiber Microendoscopy.” *Optics Express* 15 (25) (December 10): 16413–23. http://www.pubmedcentral.nih.gov/articlerender.fcgi?artid=3065245&tool=pmcentrez&rendertype=abstract.

Nitin, Nitin, David J Javier, Darren M Roblyer, and Rebecca Richards-Kortum. 2010. “Widefield and High-resolution Reflectance Imaging of Gold and Silver Nanospheres.” *Journal of Biomedical Optics* 12 (5): 051505. doi:10.1117/1.2800314. http://www.ncbi.nlm.nih.gov/pubmed/17994869.

Patel, Rakesh, Ashraf Khan, Dennis Wirth, Michal Kamionek, Dina Kandil, Robert Quinlan, and Anna N Yaroslavsky. 2012. “Multimodal Optical Imaging for Detecting Breast Cancer.” *Journal of Biomedical Optics* 17 (6) (June): 066008. doi:10.1117/1.JBO.17.6.066008. http://www.ncbi.nlm.nih.gov/pubmed/22734764.

Roblyer, Darren, Rebecca Richards-Kortum, Konstantin Sokolov, Adel K El-Naggar, Michelle D Williams, Ann M Gillenwater, and Cristina Kurachi. 2008. “Multispectral Optical Imaging Device for in Vivo Detection of Oral Neoplasia.” *Journal of Biomedical Optics* 13 (2): 1–11. doi:10.1117/1.2904658. http://www.ncbi.nlm.nih.gov/pubmed/18465982.

Rylander, Christopher G, Oliver F Stumpp, Thomas E Milner, Nate J Kemp, John M Mendenhall, Kenneth R Diller, and A J Welch. “Dehydration Mechanism of Optical Clearing in Tissue.” *Journal of Biomedical Optics* 11 (4): 041117. doi:10.1117/1.2343208. http://www.ncbi.nlm.nih.gov/pubmed/16965145.

Shipitsin, Michail, Lauren L Campbell, Pedram Argani, Stanislawa Weremowicz, Noga Bloushtain-Qimron, Jun Yao, Tatiana Nikolskaya, et al. 2007. “Molecular Definition of Breast Tumor Heterogeneity.” *Cancer Cell* 11 (3) (March): 259–73. doi:10.1016/j.ccr.2007.01.013. http://www.ncbi.nlm.nih.gov/pubmed/17349583.

Vargas, O, E K Chan, J K Barton, H G Rylander, and A J Welch. 1999. “Use of an Agent to Reduce Scattering in Skin.” *Lasers in Surgery and Medicine* 24 (2): 133–141. <Go to ISI>://000079003900009.

Vermeulen, Jeroen F, Aram S A van Brussel, Petra van der Groep, Folkert H M Morsink, Peter Bult, Elsken van der Wall, and Paul J van Diest. 2012. “Immunophenotyping Invasive Breast Cancer: Paving the Road for Molecular Imaging.” *BMC Cancer* 12 (January): 240. doi:10.1186/1471-2407-12-240. http://www.pubmedcentral.nih.gov/articlerender.fcgi?artid=3430576&tool=pmcentrez&rendertype=abstract.

Vosoughhosseini, S, M Lotfi, A Fakhrjou, A Aghbali, M Moradzadeh, M Sina, and P Emamverdizadeh. 2012. "Analysis of Epidermal Growth Factor Receptor in Histopathologically Tumor-free Surgical Margins in Patients with Oral Squamous Cell Carcinoma." *African Journal of Biotechnology* 11 (2): 516–520. doi:10.5897/AJB 10.489.

Xie, Bang-Wen, Isabel M Mol, Stijn Keereweer, Ermond R van Beek, Ivo Que, Thomas J A Snoeks, Alan Chan, Eric L Kaijzel, and Clemens W G M Löwik. 2012. "Dual-wavelength Imaging of Tumor Progression by Activatable and Targeting Near-infrared Fluorescent Probes in a Bioluminescent Breast Cancer Model." *PloS One* 7 (2) (January): e31875. doi:10.1371/journal.pone.0031875. http://www.pubmedcentral.nih.gov/articlerender.fcgi?artid=3278453&tool=pmcentrez&rendertype=abstract.

Yeh, Alvin T, Bernard Choi, J Stuart Nelson, and Bruce J Tromberg. 2003. "Reversible Dissociation of Collagen in Tissues." *The Journal of Investigative Dermatology* 121 (6) (December): 1332–5. doi:10.1046/j.1523-1747.2003.12634.x. http://www.ncbi.nlm.nih.gov/pubmed/14675178.

## Bibliography

### *Publications*

Bickford, L., Chang, J., Fu, K., Sun, J., Hu, Y., Gobin, A., Yu, TK, and Drezek, R. "Evaluation of Immunotargeted Gold Nanoshells as Rapid Diagnostic Imaging Agents for HER2-Overexpressing Breast Cancer Cells: A Time-Based Analysis." Nanobiotechnology. 1551-1286 (print) 1551-1294 (online) (2008)

Bickford, L., Sun, J., Fu, K., Lewinski, N., Nammalvar, V., Chang, J., Drezek, R. "Enhanced Multi-Spectral Imaging of Live Breast Cancer Cells Using Immunotargeted Gold Nanoshells and Two-Photon Excitation Microscopy." Nanotechnology. 19: 315102 (2008)

Fu, K., Sun, J., Bickford, L., Lin, A., Halas, N., Yu, TK, and Drezek, R. "Measurement of Immunotargeted Plasmonic Nanoparticle's Cellular Binding: A Key Factor in Optimizing Diagnostic Efficacy." Nanotechnology. 19: 045103 (2008)

Sun, J., Fu, K., Zhu, MQ, Bickford, L., Post, E., and Drezek, R. "Near-infrared quantum dots for fluorescence tissue imaging" Current Nanoscience. 5: 160-166 (2009).

Hleb, E., Hu, Y., Drezek, R., Hafner, J., and Lapotko, D. "Photothermal bubbles as optical scattering probes for imagine live cells." Nanomedicine. 3: 797-812. (2008)

Hu, Y., Fleming, R., and Drezek, R. "Optical properties of gold-silica-gold multilayer nanoshells." Optics Express. 16: (2008)

Rostro-Kohanloo, B., Bickford, L., Payne, C., Day, E., Anderson, L., Zhong, M., Zhong, Lee, S., Mayer, K., Zal, T., Adam, L., Dinney, C., Drezek, R., West, J., and Hafner, J. "Stabilization and Targeting of Surfactant-Synthesized Gold Nanorods." Nanotechnology. 20:434005 (2009).

Sun J, Shu C, Appiah B, and Drezek R, Needle-compatible single fiber bundle image guide reflectance endoscope, Journal of Biomedical Optics Letters, 15 (4), 040502 (2010).

Carpin, LB., Bickford LR.,Agollah, G., Yu, TK., Schiff, R, Li, Y, Drezek RA. "Immunoconjugated gold nanoshell-mediated photothermal ablation of trastuzumab-resistant breast cancer cells." Breast Cancer Research and Treatment. 125(1):27-34. (2011)

Hu, Y., Noelck, S., and Drezek, R. "Symmetry breaking in gold-silica-gold multilayer nanoshells." ACS Nano. 4:1521-8 (2010).

### *Abstracts*

Sun, J., Fu, F., Zhu, M-Q., Bickford, L., Post, E., and Drezek, R. "PbS Quantum Dots for Near-infrared Fluorescence Imaging." OSA 2008 Frontiers in Optics (FiO)/Laser Science XXIV Conference. Rochester, NY. 2008.

Drezek, R. "Nanotechnology-Enabled Optical Molecular Imaging of Cancer." Department of Defense Breast Cancer Research Program Era of Hope Conference. Baltimore, MD. June 2008.

Bickford, L., Chang, J., Fu, K., Sun, J., Hu, Y., Yu, T.K., Drezek R. “Immunotargeted Nanoshells for Point of Care Diagnostic Applications.” Biomedical Optics. St. Petersburg, FL. March 2008.

Bickford, L. and Drezek, R. Gold Nanoshells as Potential Real-Time Intraoperative Molecular Probes for HER2/NEU Overexpression Using Near-Infrared Reflectance Confocal Microscopy. Annual Houston Conference on Biomedical Engineering Research. Houston, TX. March 2009.

Hu, Y., and Drezek, R. Angular scatter patterns from multi-layered gold nanoshells. Materials Research Society Spring Annual National Meeting. San Francisco, CA. April 2009.

Day, E., Bickford, L., Drezek, R., and West, J. Use of Nanoshells for Combined Two-Photon Imaging and Therapy of Cancer. NanoMed: 6th International Conference on Biomedical Applications of Nanotechnology. March 2009.

Day, E., Bickford, L., Drezek, R., and West, J. Multiphoton Imaging and Therapy of Cancer with Gold-Sulfide Nanoparticles. Frontiers of Cancer Research. March 2009.

Sun, J., Fu, F., Zhu, M-Q., Bickford, L., Post, E., and Drezek, R. “PbS quantum dots for near-infrared fluorescence imaging.” OSA 2008 Frontiers in Optics (FiO)/Laser Science XXIV Conference. Rochester, NY. October 19-23, 2008.

Bickford, L., Yu, K., and Drezek, R. Intraoperative Tumor Margin Detection Using Targeted Gold Nanoparticles, Baylor College of Medicine Translational Research Conference. September 2009.

Day, E., Bickford, L, Drezek, R., and West, J. Cancer Imaging and Thermal Therapy Facilitated by Nanoparticles and Multiphoton Microscopy. ASME 2010 First Global Conference on Nanonengineering for Medicine and Biology. Houston, TX. Spring 2010.

Langsner, R., Drezek, R., and Yu, T. A Fluorescent Deoxyglucose Analog for Detection of Cancer in Breast Tissue. Rice Quantum Institute Summer Conference. August 2009.

Bickford, L., and Drezek, R. Gold-silica nanoshells for targeted imaging of tumor margins. Biomedical Engineering Society Annual National Meeting. Austin, TX. October 2010.

Langsner, R., Yu,K., and Drezek, R. The Use of 2-NBDG for Optical Assessment of Breast Tumor Margins. Biomedical Engineering Society Annual National Meeting. Austin, TX. October 2010.

Noelck, S. and Drezek, R. Optical Properties of Gold-Silica-Gold Nanoshells. Biomedical Engineering Society Annual National Meeting. Austin, TX. October 2010.

Noelck, S., Hu, Y., and Drezek, R. Probing Optical Properties of Gold-Silica-Gold Multilayer Nanoshells with Broken Symmetry, 2010 Inter IGERT Nanoscience and Professional Development Workshop. Austin, TX. 2010.

Langsner, R., Drezek, R, and Yu, K. Towards 2-NBDG for Intraoperative Assessment of Tumor Margins. Gordon Conference on Lasers in Surgery and Medicine. 2010.

## Personnel List

Michael Albers
Eleni Balakrishnan
Vijetha Bhat
Lissett Bickford
Joseph Chang
Allen Chen
Rebekah Drezek
Liz Figueroa
Ying Hu
Marcos Hung
Laura Kennedy
Laura Krone
Robert Langsner
Adam Lin
Nastassja Lewinski
Vengadesan Nammalvar
Clare Ouyang
Chenghau Shu
Jiantang Sun
Joseph Young
Michael Zhao

Hindawi Publishing Corporation
Journal of Oncology
Volume 2012, Article ID 291898, 10 pages
doi:10.1155/2012/291898

*Research Article*

# Rapid Stereomicroscopic Imaging of HER2 Overexpression in *Ex Vivo* Breast Tissue Using Topically Applied Silica-Based Gold Nanoshells

**Lissett R. Bickford,[1,2,3] Robert J. Langsner,[1] Joseph Chang,[4] Laura C. Kennedy,[1,5] Germaine D. Agollah,[6] and Rebekah Drezek[1,7]**

[1] *Department of Bioengineering, Rice University, 6100 Main Street, MS 142, Houston, TX 77005, USA*
[2] *School of Biomedical Engineering and Sciences, Virginia Polytechnic Institute and State University, Blacksburg, VA 24061, USA*
[3] *Department of Mechanical Engineering, Virginia Polytechnic Institute and State University, Blacksburg, VA 24061, USA*
[4] *School of Medicine, University of California San Francisco, San Francisco, CA 94143, USA*
[5] *School of Medicine, Baylor College of Medicine, Houston, TX 77030, USA*
[6] *Department of Chemistry and Process Development, Nanospectra Biosciences, Inc., Houston, TX 77054, USA*
[7] *Department of Electrical and Computer Engineering, Rice University, Houston, TX 77005, USA*

Correspondence should be addressed to Rebekah Drezek, drezek@rice.edu

Received 5 April 2012; Accepted 11 September 2012

Academic Editor: José María Benlloch

Tumor margin detection for patients undergoing breast conservation surgery primarily occurs postoperatively. Previously, we demonstrated that gold nanoshells rapidly enhance contrast of HER2 overexpression in *ex vivo* tissue sections. Our ultimate objective, however, is to discern HER2 overexpressing tissue from normal tissue in whole, nonsectioned, specimens to facilitate rapid diagnoses. Here, we use targeted nanoshells to quickly and effectively visualize HER2 receptor expression in intact *ex vivo* human breast tissue specimens. Punch biopsies of human breast tissue were analyzed after a brief 5-minute incubation with and without HER2-targeted silica-gold nanoshells using two-photon microscopy and stereomicroscopy. Labeling was subsequently verified using reflectance confocal microscopy, darkfield hyperspectral imaging, and immunohistochemistry to confirm levels of HER2 expression. Our results suggest that anti-HER2 nanoshells used in tandem with a near-infrared reflectance confocal microscope and a standard stereomicroscope may potentially be used to discern HER2-overexpressing cancerous tissue from normal tissue in near real time and offer a rapid supplement to current diagnostic techniques.

## 1. Introduction

Currently, breast cancer is the second leading cause of cancer-related deaths in women, and it accounts for approximately one-third of all cancers diagnosed in women in the United States [1]. To reduce cancer recurrence and progression, cancerous tissue must be completely eliminated, regardless of grade [2]. Surgical breast cancer therapy focuses on removing the primary tumor and identifying the possibility of metastatic disease from the evaluation of sentinel lymph nodes. Although some patients may require modified radical mastectomy, many patients with less-advanced breast cancer elect breast-conserving surgery. The presence of a positive surgical margin during these surgeries has been associated with lower rates of patient survival [3]. Due to residual cancer cells being left in many patients that undergo breast conservation therapy, as many as 40% of patients have experienced local breast cancer recurrence near the site of the original tumor [4]. Intraoperative treatment decisions are, therefore, absolutely critical.

Presently, intraoperative tumor margin detection occurs primarily in specialized tertiary centers, such as The University of Texas M.D. Anderson Cancer Center (MDACC). In these centers, the resected tissue receives a preliminary evaluation by a pathologist while the patient remains in the operating room; if necessary, additional tissue can be removed until the pathologist determines that the tumor margins are negative. In community hospitals, however, pathologic analysis of excised tissue only occurs postoperatively [5]. Patients who consequently have positive tumor margins must return for surgical reexcision and receive increased doses of adjuvant radiation therapy [6, 7]. Thus, the existence of positive tumor margins portends additional risks and costs to the patient. Due to the existing limitations of current intraoperative tumor margin detection, there is an opportunity to develop superior diagnostic tools to assist in reducing the recurrence and progression of cancer due to inadequate tissue removal during primary surgery.

While histologic analysis remains the gold standard for tumor margin assessment, the macroscopic evaluation of whole, nonsectioned tissue specimens may also be used to provide an intraoperative estimate of tumor margin status prior to subsequent processing. This would be an invaluable tool in hospitals without onsite pathology suites. Macroscopic visualization of questionable tissue is attractive for enhancing the sensitivity and specificity of tumor margin delineation: if the number of suspicious regions that require further microscopic processing can be reduced, surgeons and pathologists can focus their attention and resources on areas that remain inconclusive. Currently, macroscopic evaluation only occurs for breast cancer specimens that involve microcalcifications or nonpalpable masses and does not occur for palpable breast masses [8]. For nonpalpable masses that have been resected, radiographic images are used to determine the extent of the breast disease and the proximity to the resected margins. Although specimen radiography appears to increase the accuracy of tumor margin detection, limitations have been noted. For instance, microcalcifications that appear as tumor on radiographic images may actually be areas of lymphocytic accumulation [9]. The use of contrast agents targeted to specific biomarkers associated with disease may present an opportunity to increase the sensitivity and specificity of macroscopic evaluations.

In preceding studies, we confirmed that silica-based gold nanoshells targeted to the Human Epidermal growth factor Receptor 2 (HER2) could be used for the rapid contrast enhancement of both cells [10] and tissue sections [11] which overexpress HER2 biomarkers. While gold nanoshells can be conjugated to a variety of biomarkers [12, 13], we have selected HER2 due to its association with increased cancer aggression, recurrence, and progression when amplified [14, 15]. Amplification of this cell-surface bound tyrosine kinase receptor occurs in up to a quarter of all human breast cancer cases [16]. Importantly, using biomarkers for tumor margin detection has recently been shown to better identify patients at high risk of cancer recurrence over standard histological analysis [17].

To facilitate prompt tumor margin detection intraoperatively, the ability to assess tumor margins without physical sectioning is highly desirable as sectioning may incur significant time to the surgical procedure [5]. Thus, in this study, we advance our previous findings by examining the ability to rapidly target HER2 receptors in intact *ex vivo* human breast tissue specimens without sectioning. We first confirm the predominance of the surface targeting needed to identify the tumor margins and preferential labeling of HER2-positive tissue using two photon and hyperspectral imaging. Then, we demonstrate that anti-HER2-targeted gold nanoshells can be used as rapid diagnostic imaging agents for HER2 overexpression in intact breast tissue specimens using a standard stereomicroscope and confirm these results through reflectance confocal microscopy and immunohistochemistry.

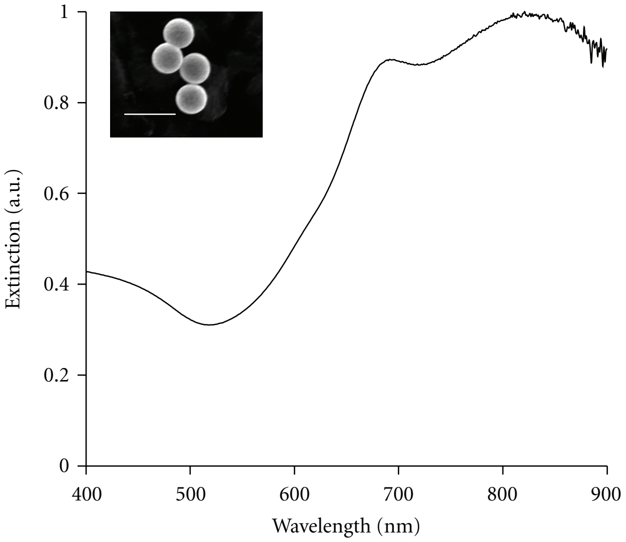

Figure 1: Measured extinction spectra of nanoshells with an average core diameter of 276 nm and average shell thickness of 19 nm. Insert depicts corresponding image from scanning electron microscopy. Scale bar represents 500 nm.

## 2. Materials and Methods

*2.1. Nanoshell Fabrication and Antibody Conjugation.* Nanoshells were fabricated as formerly described [18–20], and only a brief summary will be provided here. Silica cores were made using the Stöber method [21], in which tetraethyl orthosilicate was reduced in the presence of ammonium hydroxide dissolved in 200 proof ethanol. The surfaces of the cores were then modified by reaction with aminopropyltriethoxysilane (APTES) to functionalize reactive amine groups on the surface. The final particles were measured by dynamic light scattering (DLS) to have an average diameter of 276 nm. Next, gold colloid (∼1–3 nm diameter) was fabricated and adsorbed onto the surface of the silica cores via the amine groups to form gold nucleation sites [22]. To fully cover the surface of the silica cores, additional gold was added to these nucleation sites via a reduction reaction in which hydrogen tetrachloroaurate trihydrate ($HAuCl_43H_2O$) was dissolved in potassium carbonate and then added with formaldehyde to help reduce the gold. After the gold layer over the silica cores was formed, the spectrum of the final nanoshell solution was visualized using a UV-VIS spectrophotometer (Varian Cary 300) (Figure 1).

To determine the concentration of nanoshells in solution, the absorption, scattering, and extinction coefficients were determined using Mie theory. The average nanoshell diameter, as validated by scanning electron microscopy (SEM), was 314 nm with a peak surface plasmon resonance at 840 nm. The concentration of the working nanoshell solution was approximately $2.0 \times 10^9$ particles/mL.

Nanoshells were targeted to biological HER2 antigens by linking the surfaces of the nanoshells to anti-HER2 antibodies using previously described methods [18]. Prior to beginning experimental studies, nanoshells were incubated with an anti-HER2-linker cocktail [18] for 2 hours at 4°C. To ensure nanoparticle stabilization in biological media, the nanoshells were next incubated with a 1 mM polyethylene glycolthiol solution (PEG-SH, MW = 5 kD, Nektar) for 12–16 hours at 4°C. Next, unbound antibodies and excess PEG-SH were removed from the nanoshells by centrifugation. Prior to experimental studies, the nanoshells were resuspended in antibody diluent (IHC World, pH 7.4) by gentle pipetting to a final volume of 165 $\mu$L.

### *2.2. Ex Vivo Human Breast Tissue Specimens.*

Normal and cancerous (HER2-negative and HER2-positive) breast tissue specimens were supplied by the Cooperative Human Tissue Network (CHTN) through a protocol approved by the Institutional Review Board (IRB). Tissues were designated as normal or cancerous by pathologists at the medical centers where the tissue samples were obtained. Additionally, HER2 status was previously determined by pathologists at the respective medical centers prior to the patients undergoing any form of medical treatment.

Before use, samples were thawed briefly in a 37°C water bath and cut on a disposable cutting board using a 5 mm punch biopsy to maintain size consistency. At least two punch biopsies were taken from each specimen for control and experimental conditions. Each cut specimen used was 5 mm in diameter with an average thickness of 1 mm. Tissue samples were subsequently incubated in prewarmed antibody diluent for 1 minute at room temperature with gentle agitation in a 24-well plate. After prerinsing, the samples were incubated in either antibody diluent or the aforementioned targeted-nanoshell cocktail in polyethylene sample vials (Sigma Aldrich). The vials were placed on a nutator in an incubator at 37°C for 5 minutes. After incubation, the tissue samples were removed from the vials and rinsed 3 times in 1x PBS briefly in a 24-well plate. Samples were moved to a clean well of 1x PBS prior to imaging.

### *2.3. Two-Photon Imaging of Human Breast Tissue Specimens.*

Both HER2-positive and HER2-negative cancerous samples were evaluated for surface labeling of HER2-targeted nanoshells by employing two-photon imaging of intact breast tissue specimens. Samples were placed directly on a glass coverslip (Fisher Scientific), and an additional coverslip was placed on top of the tissue in order to facilitate moderate tissue compression. For image acquisition, a Zeiss multiphoton confocal microscope (LSM 510 META NLO) was used in tandem with a Coherent Chameleon femtosecond-pulsed, mode-locked Ti: sapphire laser. This system was set to operate as formerly described [23]. Specifically, an excitation wavelength of 780 nm and a power setting of 10% maximum excitation power were used. The collected emission wavelength range was 451–697 nm. Images were collected at a magnification of 20x and a $z$-stack (depth) increment of 5 $\mu$m. In order to calculate the percentage of area covered by nanoshells, ImageJ imaging software was implemented after image acquisition. Recent research has shown that ImageJ can be used to analyze signal intensity of silica-gold nanoshells under different imaging systems [11, 24]. Each pixel in the images had an intensity value in the range of 0–255. To determine the nanoshell level in each image, an intensity threshold of 30 was used to separate areas that did not have nanoshells ($\leq 30$) from those that did have nanoshells ($>30$). The value of 30 was chosen because images of negative controls were found to have a maximum intensity of 30. The number of pixels that were above the threshold value was then used to calculate the area of each image that contained nanoshells.

### *2.4. Darkfield Hyperspectral Imaging of Human Breast Tissue Slices.*

To confirm the presence of nanoshells on the surface of the tissues, HER2-positive cancerous, HER2-negative cancerous and normal tissue samples were incubated with nanoshells as previously described. A thin layer of pathological ink was placed on the tissue surface for orientation. The tissues were embedded in OCT media (BBC chemical) and frozen rapidly over dry ice. The specimens were cut at a section thickness of 8 $\mu$m using a Leica CM1850 UV cryostat. Cancerous specimens were sectioned at −20°C and normal specimens at −30°C. The different temperatures were used to maintain optimal tissue morphology as recommended by Leica. Additionally, Magalhães et al. reported on the use of different temperatures to slice normal and cancerous tissue [25]. The sections were immediately placed on superfrost slides (Fisher Scientific) and allowed to dry overnight. The next day the tissue slices were imaged with a 10x objective on an Olympus darkfield microscope equipped with a Cytoviva high-resolution illuminator. Hyperspectral images of the tissue slices were taken using a hyperspectral camera that provides both spatial and spectral data for each image.

Spectral data of each field of view (FOV) was used to determine if nanoshells were present on each slice of tissue. Comparisons were made between tissue surfaces and tissue beyond the surfaces to determine the presence of nanoshells; spectral data from tissue that was not incubated with nanoshells was also used as a negative control.

### *2.5. Macroscopic Imaging of Human Breast Tissue Specimens.*

Normal and HER2-positive cancerous breast tissue specimens (from patients who had and had not received neoadjuvant chemotherapy) were imaged using a Zeiss Discovery. V8 stereomicroscope equipped with a VisiLED MC1000 light source. For macroscopic imaging of breast tissue specimens, a thin plastic black stage was placed beneath a glass coverslip to enable ease of tissue placement and to provide a consistent black background among all samples. The specimens (controls and respective nanoshell-labeled counterparts) were placed alongside each other on top of the coverslip. Images were taken at both 1x and 2x magnification under the same lighting conditions.

*2.6. Reflectance Confocal Microscopy Imaging of Human Breast Tissue Specimens.* Following widefield imaging, the aforementioned samples were prepared for microscopic analysis under reflectance confocal microscopy. For this component of the study, a Lucid VivaScope 2500 inverted confocal microscope was used. Samples were placed directly on glass slides that were modified by the addition of an adhesive 1 mm deep, 20 mm diameter silicon isolator (Invitrogen). To compress the tissue slightly and consistently among samples, an adhesive tissue cassette (Lucid, Inc.) was placed directly on top of the silicone isolators above the tissue specimens. Multiple images were taken at a power of 0.4 mW and at the same distance from the glass surface for both samples and controls. After reflectance imaging, the samples were prepared for histological processing. Additionally, reflectance intensity measurements were recorded using ImageJ processing software as formerly described [11].

*2.7. Immunohistochemistry and Histology.* Once images were collected under both stereomicroscopy and RCM imaging systems, normal and HER2-positive cancerous samples (with and without previous neoadjuvant chemotherapy) were embedded in OCT media and sectioned to a thickness of 5 $\mu$m. Multiple sections from each specimen were prepared for either immunohistochemistry (IHC) or hematoxylin and eosin (H&E) staining. IHC for the HER2 antigen was executed using the Histostain Plus AEC Broad Spectrum Kit (Invitrogen) per manufacturer's instructions. H&E staining was also performed per manufacturer's instructions (Sigma Aldrich) for the alcoholic Eosin Y solution. For image acquisition, a standard brightfield microscope (Zeiss Axioskop 2 equipped with a Zeiss Axiocam MRc5 color camera) was used at a magnification of 20x.

## 3. Results

*3.1. Distribution and Penetration of Gold Nanoshells in Intact Human Breast Tissue.* The goal of this study was to evaluate the distribution of anti-HER2-conjugated gold nanoshells on resected intact tissue specimens. For comparison, the nanoshell labeling between HER2-positive and HER2-negative tissue samples was evaluated using a two-photon imaging system. As previously reported, this imaging system is capable of enhancing and capturing the luminescence signature of the gold nanoshells [23] while also collecting a stack of images taken through the depth of the tissue of interest. Figure 2 represents such images of HER2-positive and HER2-negative cancerous tissue samples incubated with HER2-targeted nanoshells. Each sequential increment in the $z$-direction represents 5 $\mu$m into the tissue. Qualitatively, the first image (taken at the surface or at 0 $\mu$m) in Figure 2 demonstrates that the nanoshells preferentially label HER2 receptors on the surface of the tissue. Additionally, Figure 2 displays decreased signal as the focal spot from the confocal microscope penetrates further into the tissue. This is believed to be due to a minimal number of nanoshells being able to penetrate the tissue in the limited amount of incubation time, thus decreasing signal collected beyond the surface. A quantitative difference of the nanoshell signal at the surface of the HER2-positive and HER2-negative tissue was calculated. Using ImageJ imaging software, it was determined that approximately 66% of the FOV for HER2-positive tissue was covered in nanoshells versus just 2% for the FOV of the HER2-negative tissue. This confirms the preferential labeling and visualization of HER2-positive tissue using anti-HER2 nanoshells.

To further validate the surface binding of the nanoshells, hyperspectral images of different tissue sections were also acquired. Figure 3(a) shows a representative surface of a HER2-positive tissue section after incubation with anti-HER2 nanoshells. Figure 3(b) illustrates tissue 24 $\mu$m beyond the surface of the same tissue. Spectra from multiple ($n = 3$) specimens that were incubated with anti-HER2 nanoshells were acquired, and analysis showed that tissues without nanoshells had very similar spectra across different patients. Figure 3(c) displays the respective spectral information of each FOV shown in Figures 3(a) and 3(b). Additionally, the spectra of HER2-positive tissue without nanoshells have been included as a control. As can be seen in this graph, the spectra of the surface of the HER2-positive tissue incubated with anti-HER2 nanoshells are distinctive from that of the same tissue 24 $\mu$m beyond the surface. In fact, the spectra of the tissue beyond the surface of the nanoshell-labeled specimen are very similar to the spectra of the surface of the control. These results support our findings that the targeted nanoshells primarily localized to the surface of the tissue.

*3.2. Enhanced Optical Imaging of Intact Ex Vivo Human Breast Cancer Tissue Using Gold Nanoshells.* Based on previous results demonstrating the preferential labeling of HER2-targeted nanoshells on the surface of intact *ex vivo* HER2-positive tissue specimens, we assessed the potential of using a standard stereomicroscope to visualize this enhanced contrast. For this component of the study, human breast tissue specimens that overexpressed HER2 receptors at the time of patient diagnosis were evaluated and compared to normal breast tissue. Due to the ultimate goal of utilizing gold nanoshells to rapidly label tumor margins intraoperatively in diverse patient populations, we examined tissue from patients who had and had not undergone neoadjuvant chemotherapy. All tissue samples were incubated with either antibody diluent buffer or the anti-HER2-targeted nanoshells for 5 minutes at 37°C. As shown in Figure 4, which represents raw images taken with a stereomicroscope, intact tissue specimens incubated with antibody diluent alone showed no markings or features characteristic of nanoshells. However, tissue specimens incubated with the anti-HER2-targeted nanoshells demonstrate numerous particles on the surfaces of the tissues. Qualitatively, the HER2-positive tissue from the patient who did not undergo previous chemotherapy shows the greatest labeling with the targeted nanoshells. The HER2-positive tissue from the patient who did undergo neoadjuvant chemotherapy does demonstrate enriched nanoshell labeling when compared to normal tissue, though not to the same extent as the patient without previous chemotherapy. In contrast, the normal tissue shows the least amount of nanoshell labeling, and only a few areas of nanoshells can be visually perceived.

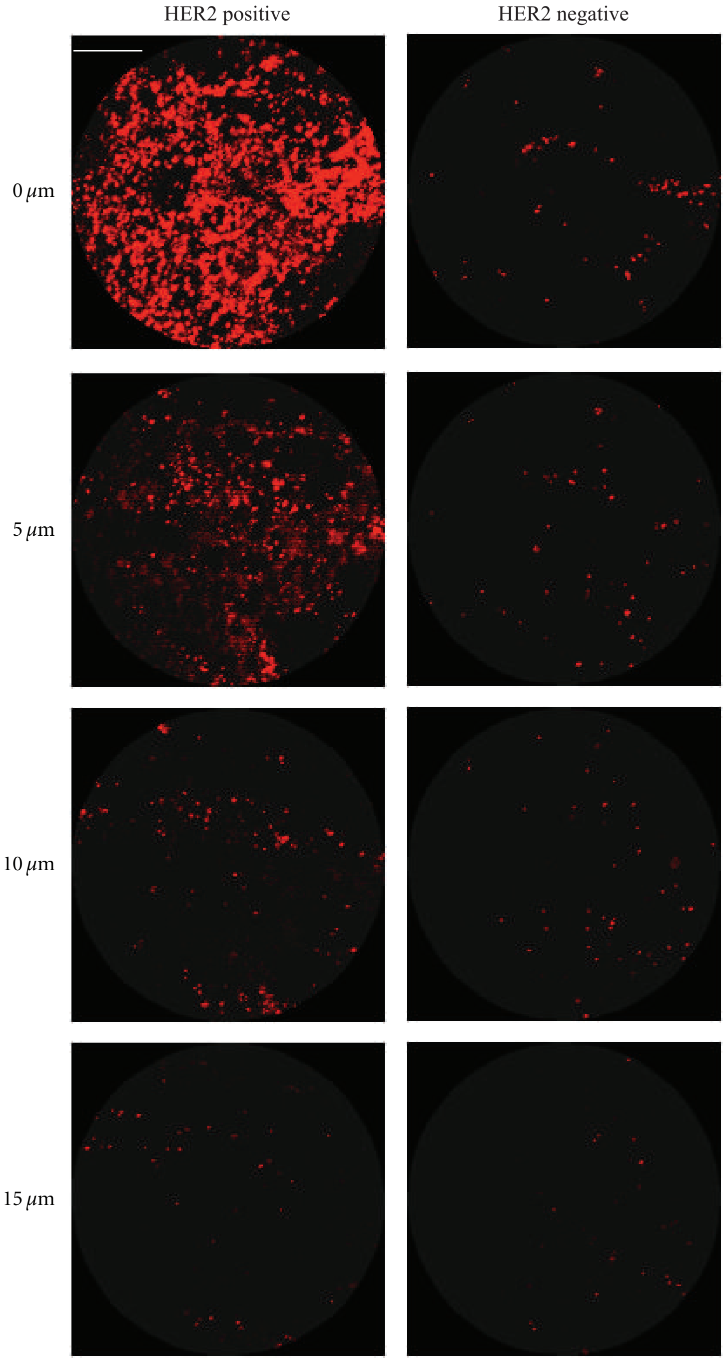

Figure 2: $Z$-stack two-photon luminescence images of HER2-positive and HER2-negative tissue incubated with HER2-targeted nanoshells for 5 minutes at 37°C. Each progressive image represents an increase in depth penetration of 5 μm. Magnification = 20x. Scale bar = 50 μm.

While the degree of nanoshell labeling can be visualized without image adjustments under a standard stereomicroscope, the superior extent of this labeling can be seen more clearly after a simple contrast enhancement using imaging software (ImageJ). As seen in Figure 5(a), the nanoshells are even more discernable against the tissue background regardless of inherent tissue constituents.

To validate the enhanced nanoshell labeling seen by macroscopic imaging, the surfaces of the same tissue samples were also imaged using reflectance confocal microscopy (Figure 5(b)). Concurring with the stereomicroscopic images, we see dramatic nanoshell surface labeling when using targeted nanoshells with previously untreated HER2-positive tissue. For the HER2-positive sample that had formerly undergone chemotherapy, we also see enhanced nanoshell labeling, though to a lesser degree than the untreated sample as suggested by the stereomicroscopy results. The normal breast tissue displays the least amount of

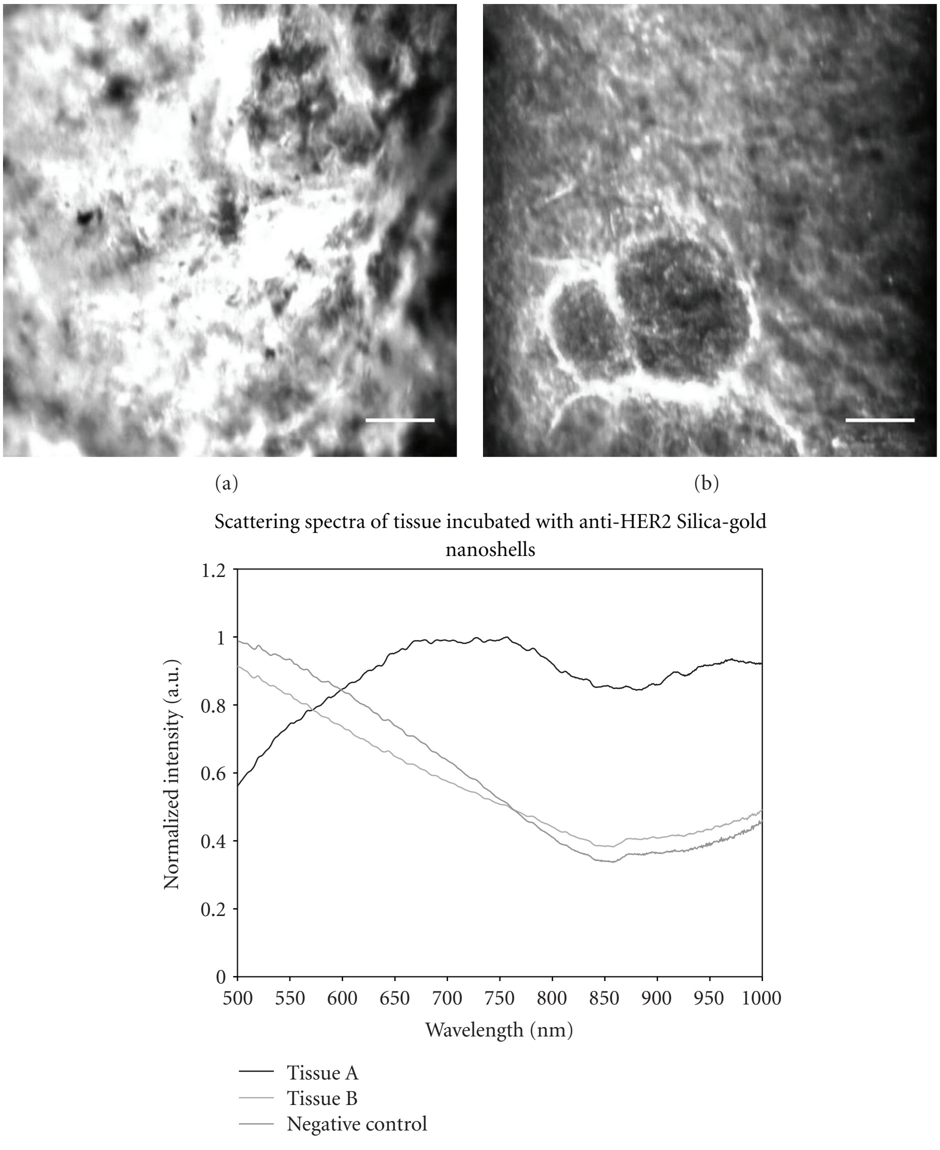

(a) (b)

(c)

Figure 3: Darkfield images of HER2-positive tissue sectioned after incubation with anti-HER2-targeted silica-gold nanoshells. (a) Surface of HER2-positive tissue, (b) 24 $\mu$m beyond the surface of the same tissue. (c) Scattering spectra of the fields of view depicted in (a) and (b). Additionally, spectra from the surface of HER2-positive tissue not incubated with silica-gold nanoshells are shown as a negative control. Scale bar = 50 $\mu$m.

surface labeling with only minimal nanoshells evident with either imaging system. Reflectance intensity measurements (data not shown) were ~2.5 to 3 times greater for both the HER2-positive tissue sample receiving chemotherapy and for the HER2-positive tissue not receiving chemotherapy when compared to the normal tissue sample.

Subsequent histological analysis shown in Figure 5(c) reveals that the distribution of HER2 receptors seen with nanoshell-enabled contrast corresponds to that seen with IHC against HER2. The HER2 expression seen by IHC is greater for the previously untreated HER2-positive tissue sample than for the sample that had undergone neoadjuvant chemotherapy. This is believed to be due to the effects of chemotherapy. Rasbridge et al. previously demonstrated that patient response to chemotherapy is highly variable, with patients previously negative for HER2 overexpression occasionally becoming positive after treatment and patients previously positive for HER2 overexpression subsequently becoming negative [26]. Although patient response to chemotherapy varies, tissues previously identified as overexpressing HER2 receptors during initial diagnosis, regardless of chemotherapy exposure, demonstrate enhanced nanoshell labeling over normal tissue. Additionally, H&E-stained sections of all tissue samples have been included (Figure 5(d)) to illustrate the microscopic characteristics and differences associated with cancerous versus noncancerous conditions.

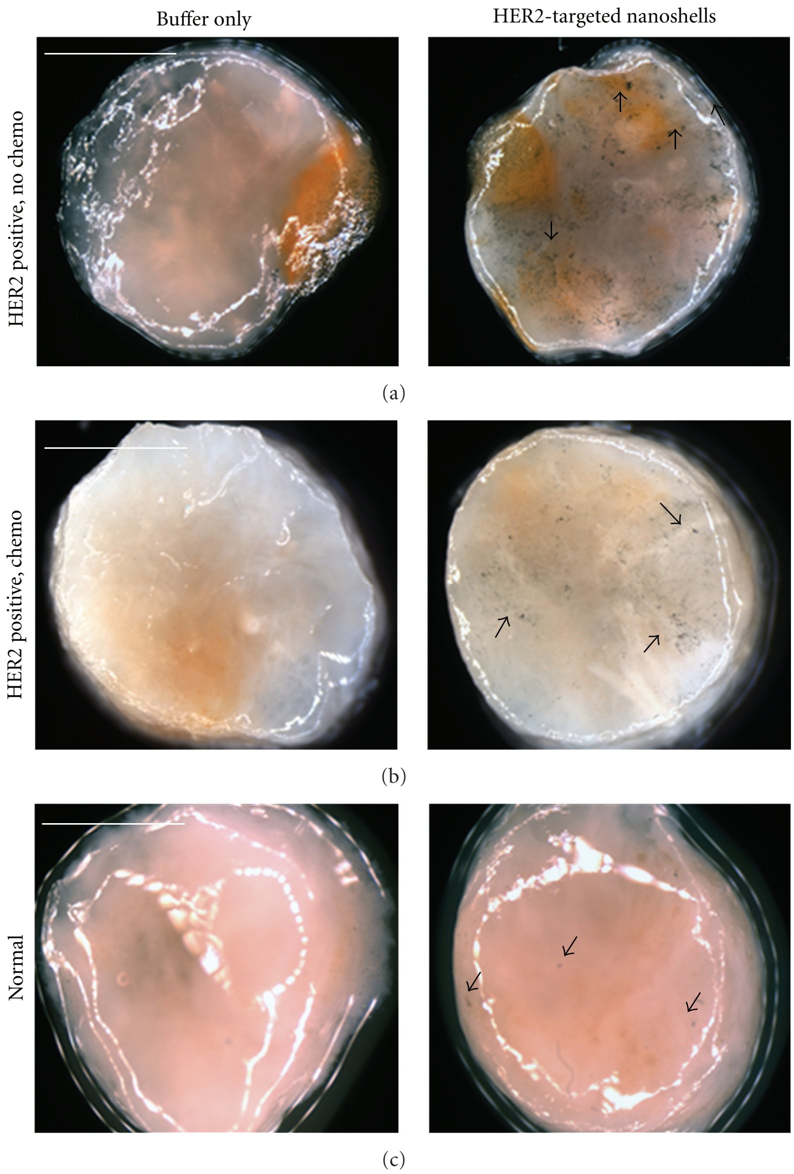

Figure 4: Raw stereomicroscope images of (a) and (b) HER2-overexpressing cancerous and (c) normal tissue incubated with either buffer or HER2-targeted nanoshells for 5 minutes at 37°C. Cancerous tissue taken from a patient (a) without chemotherapy and (b) following neoadjuvant chemotherapy. Arrows represent nanoshells. Images taken at 2x. Scale bars = 2.5 mm.

## 4. Discussion

In this study we demonstrated the ability to use targeted gold nanoshells to rapidly improve visualization of a specific biomarker associated with disease aggression and progression (HER2) in intact *ex vivo* human breast tissue and confirmed binding location via confocal and darkfield hyperspectral microscopy. By utilizing silica-gold nanoshells designed as rapid diagnostic imaging agents, surgeons and pathologists may be able to realize tumor margin status directly in the operating room after both macroscopic and microscopic assessment. While multiple methods of intraoperative tumor margin detection are currently under investigation [27–31], we are developing an inexpensive and portable system for rapidly analyzing *ex vivo* specimens based on the desire to enhance current methodologies without delay in clinical translation due to regulatory concerns associated with *in vivo* systems.

The ability to enhance contrast of malignancy using topically applied agents has previously been demonstrated for oral and breast tissue using fluorescently labeled deoxyglucose and epidermal growth factor (EGF) conjugates [32–34] as well as cervical tissue using fluorescently labeled gold nanoparticles targeted to EGF receptors [35]. However, these studies employed incubation times ranging from 20–45 minutes, which exceeds the length of time currently needed to obtain tumor margin status using frozen section histology. Additionally, the aforementioned studies utilized

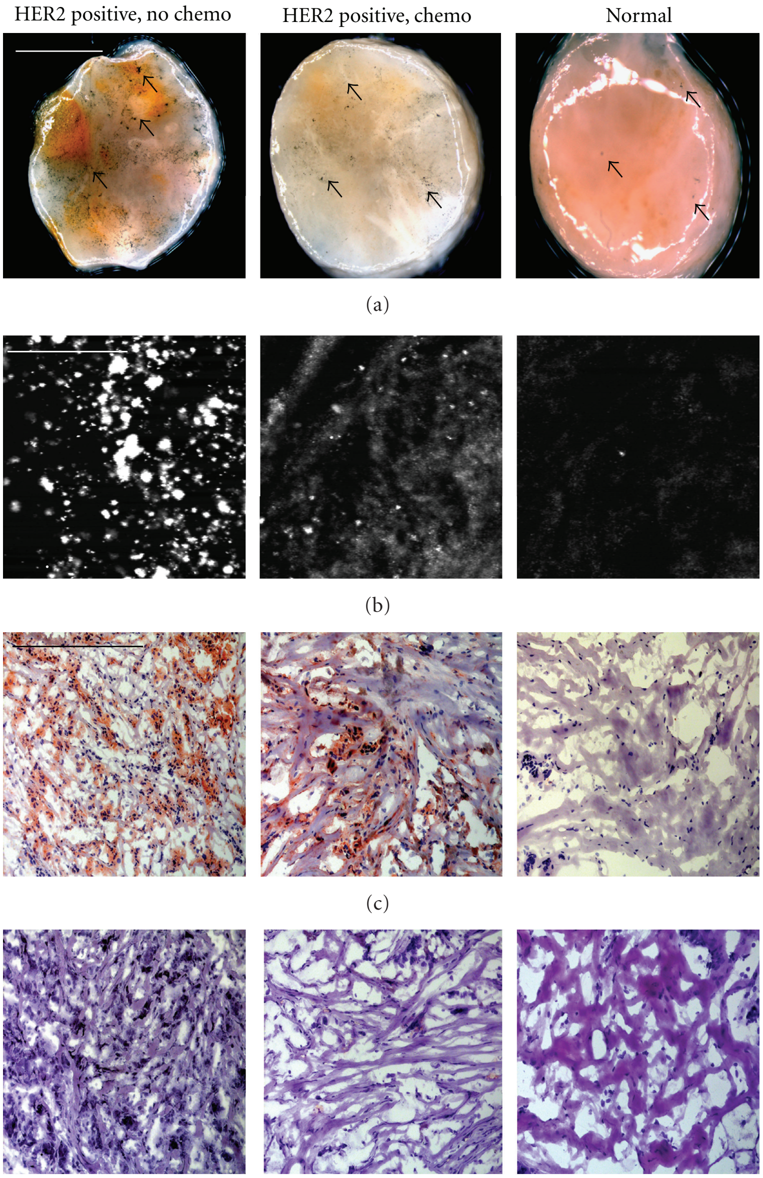

(a)

(b)

(c)

(d)

Figure 5: (a) Stereomicroscopic images of HER2-overexpressing breast tissue (with and without neoadjuvant chemotherapy) and normal breast tissue incubated with HER2-targeted nanoshells for 5 minutes at 37°C after contrast enhancement. Magnification at 2x; scale bar = 2.5 mm. Arrows represent nanoshells. (b) Respective reflectance confocal microscopy images of tissue samples from (a). Power = 0.4 mW and scale bar = 75 $\mu$m. Respective (c) HER2 immunohistochemistry and (d) H&E results taken under brightfield microscopy under 20x magnification. Scale bar = 0.35 mm.

optical clearing agents, which may be necessary for particles that target intracellular biomarkers [36, 37]. Nevertheless, gold nanoshells targeted to extracellular biomarkers may offer more favorable opportunities for *ex vivo* intraoperative tumor margin detection without the need for lengthy incubation times or the use of optical clearing agents.

Recently, we verified that silica-based gold nanoshells could be used to enhance contrast of both HER2-overexpressing cells and tissue sections within 5 minutes of incubation time [10, 11]. However, translating this technology towards clinical relevancy requires the ability to assess whole, unsectioned specimens. Here, we confirm that gold nanoshells, when targeted to HER2 receptors, can be used to distinguish intact HER2-overexpressing *ex vivo* tissue from normal tissue within the same incubation time, and we demonstrate that this difference can be observed macroscopically. These results are supported by microscopic imaging and immunohistochemistry against HER2.

By employing macroscopic imaging intraoperatively, clinicians may be better able to distinguish cancerous and normal breast tissue prior to further microscopic analysis and subsequent histological processing. Ultimately, this system could also be used for other diagnostic applications, for other anatomical locations, and for other biomarkers associated with disease. By facilitating fast and accurate tumor margin results intraoperatively as a supplement to current diagnostic methods, we expect to reduce the amount of time spent in surgery due to inadequate tissue removal.

To translate these findings more readily to the clinic, we are presently developing a low-cost widefield imaging system that can be used to detect the overexpression of HER2 (and other extracellular biomarkers) through contrast enhancement provided by gold nanoshells. In addition, we plan to collect data from diverse patient populations and assess results with fresh tissue samples. In this way, the use of gold nanoshells may demonstrate widespread efficacy or be limited only to specific patient subsets.

## Authors' Contributions

Bickford and Langsner contributed equally to this work.

## Acknowledgments

The authors thank the Cooperative Human Tissue Network for providing fresh frozen tissue samples. The authors thank Glenn P. Goodrich and Nanospectra Biosciences, Inc. for providing nanoshells used in the studies. The authors also thank Nadhi Thekkek for assistance with ImageJ data acquisition. This work was supported by a Department of Defense Congressionally Directed Breast Cancer Research Program Era of Hope Scholar Award to Rebekah Drezek, the Center for Biological and Environmental Nanotechnology (EEC-0118007 and EEC-0647452). L. Bickford thanks the Department of Defense (DoD) for training support through the National Defense Science & Engineering Graduate Fellowship (NDSEG) Program.

## References

[1] A. C. Society, "Breast Cancer Facts and Figures 2005-2006," American Cancer Society, Inc., 2010, http://www.cancer.org/Research/CancerFactsFigures/BreastCancerFactsFigures/breast-cancer-facts–figures-2005-2006.

[2] R. G. Steen, *A Conspiracy of Cells*, Plenum Press, New York, NY, USA, 1993.

[3] C. M. Mojica, R. Bastani, W. J. Boscardin, and N. A. Ponce, "Low-income women with breast abnormalities: system predictors of timely diagnostic resolution," *Cancer Control*, vol. 14, no. 2, pp. 176–182, 2007.

[4] B. Fisher, S. Anderson, J. Bryant et al., "Twenty-year follow-up of a randomized trial comparing total mastectomy, lumpectomy, and lumpectomy plus irradiation for the treatment of invasive breast cancer," *The New England Journal of Medicine*, vol. 347, no. 16, pp. 1233–1241, 2002.

[5] R. G. Pleijhuis, M. Graafland, J. de Vries, J. Bart, J. S. de Jong, and G. M. van Dam, "Obtaining adequate surgical margins in breast-conserving therapy for patients with early-stage breast cancer: current modalities and future directions," *Annals of Surgical Oncology*, vol. 16, no. 10, pp. 2717–2730, 2009.

[6] A. Oouchi, K. I. Sakata, H. Masuoka et al., "The treatment outcome of patients undergoing breast-conserving therapy: the clinical role of postoperative radiotherapy," *Breast Cancer*, vol. 16, no. 1, pp. 49–57, 2009.

[7] C. S. Melanie, W. N. Kent, J. Z. Mark et al., "The importance of the lumpectomy surgical margin status in long term results of breast conservation," *Cancer*, vol. 76, pp. 259–267, 1995.

[8] N. Cabioglu, K. K. Hunt, A. A. Sahin et al., "Role for intraoperative margin assessment in patients undergoing breast-conserving surgery," *Annals of Surgical Oncology*, vol. 14, no. 4, pp. 1458–1471, 2007.

[9] R. A. Graham, M. J. Homer, C. J. Sigler et al., "The efficacy of specimen radiography in evaluating the surgical margins of impalpable breast carcinoma," *American Journal of Roentgenology*, vol. 162, no. 1, pp. 33–36, 1994.

[10] L. R. Bickford, J. Chang, K. Fu et al., "Evaluation of immunotargeted gold nanoshells as rapid diagnostic imaging agents for HER2-overexpressing breast cancer cells: a time-based analysis," *Nanobiotechnology*, vol. 4, no. 1–4, pp. 1–8, 2008.

[11] L. R. Bickford, G. Agollah, R. Drezek, and T.-K. K. Yu, "Silica-gold nanoshells as potential intraoperative molecular probes for HER2-overexpression in ex vivo breast tissue using near-infrared reflectance confocal microscopy," *Breast Cancer Research and Treatment*, vol. 120, no. 3, pp. 547–555, 2010.

[12] K. Sokolov, M. Follen, J. Aaron et al., "Real-time vital optical imaging of precancer using anti-epidermal growth factor receptor antibodies conjugated to gold nanoparticles," *Cancer Research*, vol. 63, no. 9, pp. 1999–2004, 2003.

[13] X. Liu, Q. Dai, L. Austin et al., "A one-step homogeneous immunoassay for cancer biomarker detection using gold nanoparticle probes coupled with dynamic light scattering," *Journal of the American Chemical Society*, vol. 130, no. 9, pp. 2780–2782, 2008.

[14] R. Nahta, D. Yu, M. C. Hung, G. N. Hortobagyi, and F. J. Esteva, "Mechanisms of disease: understanding resistance to HER2-targeted therapy in human breast cancer," *Nature Clinical Practice. Oncology*, vol. 3, no. 5, pp. 269–280, 2006.

[15] D. J. Slamon, G. M. Clark, S. G. Wong, W. J. Levin, A. Ullrich, and W. L. McGuire, "Human breast cancer: correlation of relapse and survival with amplification of the HER-2/neu oncogene," *Science*, vol. 235, no. 4785, pp. 177–182, 1987.

[16] D. G. Hicks and S. Kulkarni, "HER2+ breast cancer," *American Journal of Clinical Pathology*, vol. 129, pp. 263–273, 2008.

[17] S. Vosoughhosseini, M. Lotfi, A. Fakhrjou et al., "Analysis of epidermal growth factor receptor in histopathologically tumor-free surgical margins in patients with oral squamous cell carcinoma," *African Journal of Biotechnology*, vol. 11, pp. 516–520, 2012.

[18] C. Loo, A. Lin, L. Hirsch et al., "Nanoshell-enabled photonics-based imaging and therapy of cancer," *Technology in Cancer Research and Treatment*, vol. 3, no. 1, pp. 33–40, 2004.

[19] C. Loo, L. Hirsch, M. H. Lee et al., "Gold nanoshell bioconjugates for molecular imaging in living cells," *Optics Letters*, vol. 30, no. 9, pp. 1012–1014, 2005.

[20] C. Loo, A. Lowery, N. Halas, J. West, and R. Drezek, "Immunotargeted nanoshells for integrated cancer imaging and therapy," *Nano Letters*, vol. 5, no. 4, pp. 709–711, 2005.

[21] W. Stöber, A. Fink, and E. Bohn, "Controlled growth of monodisperse silica spheres in the micron size range," *Journal of Colloid and Interface Science*, vol. 26, no. 1, pp. 62–69, 1968.

[22] D. G. Duff, A. Baiker, and P. P. Edwards, "A new hydrosol of gold clusters. 1. Formation and particle size variation," *Langmuir*, vol. 9, no. 9, pp. 2301–2309, 1993.

[23] L. Bickford, J. Sun, K. Fu et al., "Enhanced multi-spectral imaging of live breast cancer cells using immunotargeted gold nanoshells and two-photon excitation microscopy," *Nanotechnology*, vol. 19, no. 31, Article ID 315102, 2008.

[24] E. S. Day, L. R. Bickford, J. H. Slater, N. S. Riggall, R. A. Drezek, and J. L. West, "Antibody-conjugated gold-gold sulfide nanoparticles as multifunctional agents for imaging and therapy of breast cancer," *International Journal of Nanomedicine*, vol. 5, no. 1, pp. 445–454, 2010.

[25] T. Magalhães, A. von Bohlen, M. L. Carvalho, and M. Becker, "Trace elements in human cancerous and healthy tissues from the same individual: a comparative study by TXRF and EDXRF," *Spectrochimica Acta B*, vol. 61, no. 10-11, pp. 1185–1193, 2006.

[26] S. A. Rasbridge, C. E. Gillett, A. M. Seymour et al., "The effects of chemotherapy on morphology, cellular proliferation, apoptosis and oncoprotein expression in primary breast carcinoma," *British Journal of Cancer*, vol. 70, no. 2, pp. 335–341, 1994.

[27] A. Haid, M. Knauer, S. Dunzinger et al., "Intra-operative sonography: a valuable aid during breast-conserving surgery for occult breast cancer," *Annals of Surgical Oncology*, vol. 14, no. 11, pp. 3090–3101, 2007.

[28] T. Karni, I. Pappo, J. Sandbank et al., "A device for real-time, intraoperative margin assessment in breast-conservation surgery," *American Journal of Surgery*, vol. 194, no. 4, pp. 467–473, 2007.

[29] L. Tafra, R. Fine, P. Whitworth et al., "Prospective randomized study comparing cryo-assisted and needle-wire localization of ultrasound-visible breast tumors," *American Journal of Surgery*, vol. 192, no. 4, pp. 462–470, 2006.

[30] M. Bakhshandeh, S. O. Tutuncuoglu, G. Fischer, and S. Masood, "Use of imprint cytology for assessment of surgical margins in lumpectomy specimens of breast cancer patients," *Diagnostic Cytopathology*, vol. 35, no. 10, pp. 656–659, 2007.

[31] N. Nitin, L. C. Alicia, M. Tim et al., "Molecular imaging of glucose uptake in oral neoplasia following topical application of fluorescently labeled deoxy-glucose," *International Journal of Cancer*, vol. 124, no. 11, pp. 2634–2642, 2009.

[32] V. E. Strong, J. Humm, P. Russo et al., "A novel method to localize antibody-targeted cancer deposits intraoperatively using handheld PET beta and gamma probes," *Surgical Endoscopy and Other Interventional Techniques*, vol. 22, no. 2, pp. 386–391, 2008.

[33] R. J. Langsner, L. P. Middleton, J. Sun et al., "Wide-field imaging of fluorescent deoxy-glucose in ex vivo malignant and normal breast tissue," *Biomedical Optics Express*, vol. 2, no. 6, pp. 1514–1523, 2011.

[34] N. Nitin, K. J. Rosbach, A. El-Naggar, M. Williams, A. Gillenwaterand, and R. R. Richards-Kortum, "Optical molecular imaging of epidermal growth factor receptor expression to improve detection of oral neoplasia," *Neoplasia*, vol. 11, no. 6, pp. 542–551, 2009.

[35] J. Aaron, N. Nitin, K. Travis et al., "Plasmon resonance coupling of metal nanoparticles for molecular imaging of carcinogenesis in vivo," *Journal of Biomedical Optics*, vol. 12, no. 3, Article ID 034007, 2007.

[36] A. L. van de Ven, K. Adler-Storthz, and R. Richards-Kortum, "Delivery of optical contrast agents using Triton-X100, part 1: reversible permeabilization of live cells for intracellular labeling," *Journal of Biomedical Pptics*, vol. 14, no. 2, Article ID 021012, 2009.

[37] A. L. van de Ven, K. Adler-Storthz, and R. Richards-Kortum, "Delivery of optical contrast agents using Triton-X100, part 2: enhanced mucosal permeation for the detection of cancer biomarkers," *Journal of biomedical optics*, vol. 14, no. 2, Article ID 021013, 2009.

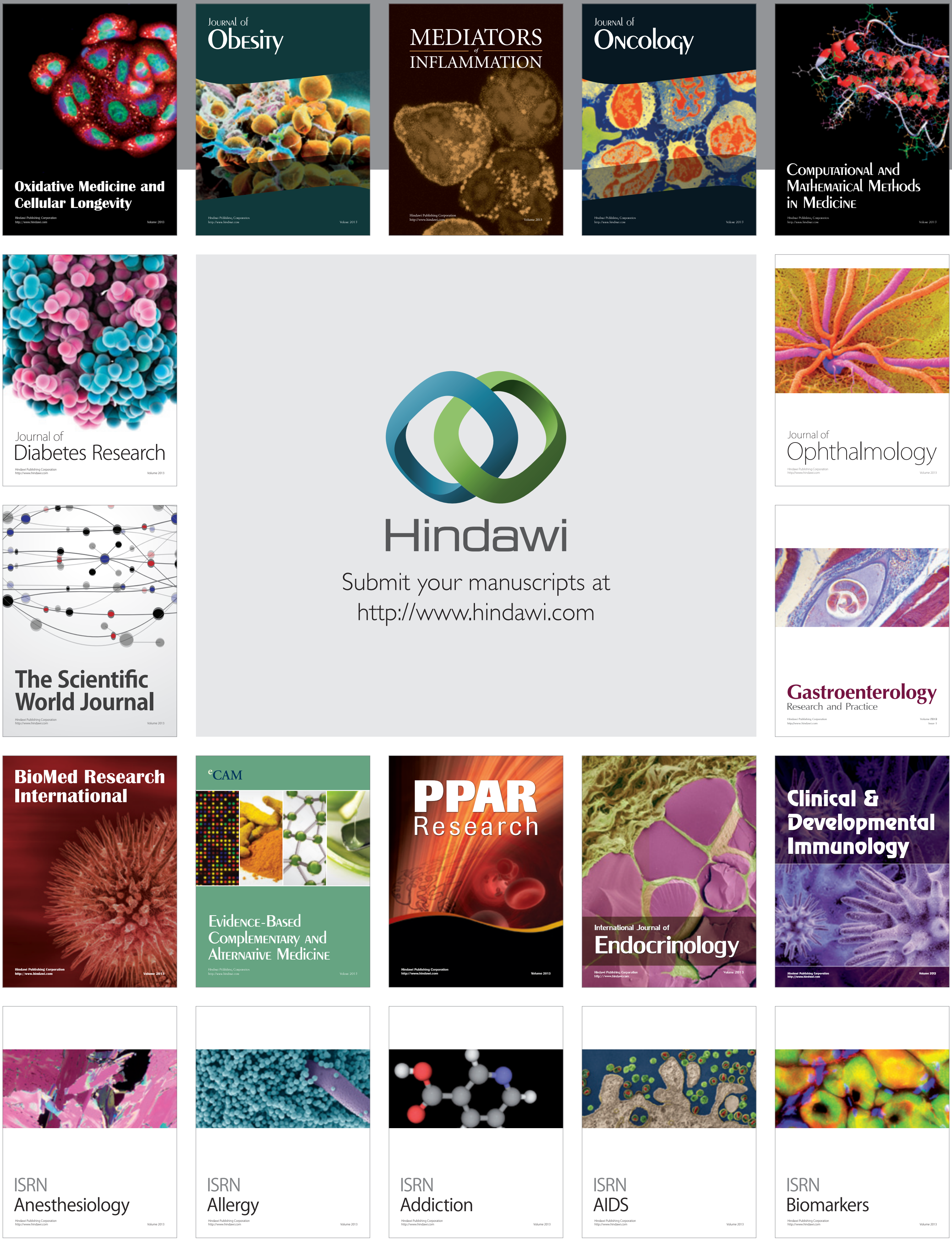
Oxidative Medicine and Cellular Longevity
Journal of Obesity
MEDIATORS of INFLAMMATION
Journal of Oncology
Computational and Mathematical Methods in Medicine
Journal of Diabetes Research
Journal of Ophthalmology
The Scientific World Journal
Gastroenterology Research and Practice
BioMed Research International
eCAM Evidence-Based Complementary and Alternative Medicine
PPAR Research
International Journal of Endocrinology
Clinical & Developmental Immunology
ISRN Anesthesiology
ISRN Allergy
ISRN Addiction
ISRN AIDS
ISRN Biomarkers

Nanobiotechnol
DOI 10.1007/s12030-008-9010-4

# Evaluation of Immunotargeted Gold Nanoshells as Rapid Diagnostic Imaging Agents for HER2-Overexpressing Breast Cancer Cells: A Time-based Analysis

**Lissett R. Bickford · Joseph Chang · Kun Fu · Jiantang Sun · Ying Hu · André Gobin · Tse-Kuan Yu · Rebekah A. Drezek**

**Abstract** Biomedical nanotechnology offers superior potential for diagnostic imaging of malignancy at the microscopic level. In addition to current research focused on dual-imaging and therapeutic applications in vivo, these novel particles may also prove useful for obtaining immediate diagnostic results in vitro at the patient bedside. However, translating the use of nanoparticles for cancer detection to point-of-care applications requires that conditions be optimized such that minimal time is needed for diagnostic results to become available. Thus far, no reports have been published on minimizing the time needed to achieve acceptable optical contrast of cancer cells incubated with nanoparticles. In this study, we demonstrate the use of gold nanoshells targeted to anti-HER2 antibodies that produce sufficient optical contrast with HER2-overexpressing SK-BR-3 breast cancer cells in only 5 min. This work validates the proof of concept that nanoshells targeted to extracellular biomarkers can be used to enhance cancer diagnostic imaging for use in point-of-care applications.

**Keywords** nanoshells · point-of-care diagnostics · optical imaging · cancer diagnosis

## Introduction

Several nanoparticles have been explored for potential applications in cancer diagnosis, including nanoshells [1–4], gold colloid [5, 6], quantum dots [7, 8], carbon dots [9], nanorods [10–12], and nanocrystals [13]. For in vivo applications, several steps will need to be taken to ensure the safe delivery of nanoparticles before they can be used in a clinical setting. However, several opportunities still exist for in vitro applications in which the cytotoxicity of nanoparticles is immaterial. Numerous in vitro technologies that have shown promise for point-of-care diagnostic testing may allow clinicians to provide user-friendly, cost-effective, and rapid results at the patient bedside. Currently, these technologies involve analyzing biological fluids to detect DNA or protein amplification through the use of microarrays or biochip devices [14–16]. In addition to fluid-based modalities, these microscopic advancements can also be used to analyze larger biological components, such as excised tumor specimens, for cancer screening and diagnosis. One particular area of application is the diagnosis of cancer from biopsy samples. For example, after a breast biopsy, the specimen is sent to a pathology laboratory where it is processed and examined microscopically for morphological abnormalities and sometimes analyzed for the presence of molecular biomarkers of

---

T.-K. Yu and R.A. Drezek contributed equally to this work.

L. R. Bickford · J. Chang · K. Fu · J. Sun · Y. Hu ·
R. A. Drezek (✉)
Department of Bioengineering, Rice University,
6100 Main St., MS-142,
Houston, TX 77005, USA
e-mail: drezek@rice.edu

K. Fu · T.-K. Yu
Department of Radiation Oncology,
The University of Texas M.D. Anderson Cancer Center,
Houston, TX 77030, USA

A. Gobin
Department of Bioengineering, University of Louisville,
Louisville, KY 40292, USA

R. A. Drezek
Department of Electrical and Computer Engineering,
Rice University,
Houston, TX 77005, USA

disease, such as hormone receptor expression [17]. This process can take up to several days, during which the patient must cope with the fear of an unknown diagnosis and the potential of treatment delay. Mojica et al. [18] showed that delays between initial breast cancer symptoms and treatment are associated with lower survival rates. Consequently, delays in breast cancer diagnosis top the list of liability claims made against physicians [19].

Another area of opportunity for advancement in point-of-care microscopic analysis of tumor specimens involves the assessment of intraoperative tumor margins. During a lumpectomy, for instance, the surgeon removes the suspected cancerous lesion with a margin of normal tissue. Judgment of the width of this margin is largely based on tactile sensation and visible, macroscopic abnormalities. In advanced hospital systems, the sample is excised and immediately subjected to pathologic analysis to ensure the surgical margins are tumor-free before the procedure is completed. The need to achieve negative margins is critical in minimizing cancer recurrence and progression, particularly for patients undergoing breast conservation therapy [20]. The presence of a positive surgical margin has been associated with lower rates in patient survival [18]. Due to residual cancer cells being left in many patients that undergo breast conservation therapy, as many as 40% of patients have experienced local breast cancer recurrence near the site of the original tumor [21]. Positive margins in a surgical specimen, therefore, necessitate the resection of additional tissue until the margins do not contain tumor. Even if the specimens are examined immediately, this extends the period of anesthesia and hence increases both the cost and risk to the patient. Furthermore, many county hospitals must, by necessity, process tissue samples after the surgery is completed. In that case, the identification of positive surgical margins requires that the patient undergo another surgical procedure to excise the remaining tissue, which further delays the start of adjuvant treatment and increases the risk of cancer recurrence and subsequent patient mortality.

With the expansion of nanotechnology-driven research, opportunities for the use of fast and accurate diagnostic tests outside of the hospital laboratory are likely to increase. To realistically use nanoparticles as a point-of-care tool for the immediate assessment of key cancer gene signatures in excised tissue samples, the time needed to achieve optical contrast must be minimized. Thus far, few published reports have focused on minimizing the time needed to achieve suitable contrast of cancer cells incubated with nanoparticles. Previous studies demonstrating the effectiveness of using gold-based nanoparticles targeted to extracellular cancer biomarkers have involved incubation times ranging from 30 to 90 min [1, 3, 5, 6, 10–12]. The objective of this study was to demonstrate the feasibility of using gold nanoshells targeted to anti-HER2 antibodies to achieve sufficient optical contrast in a HER2-overexpressing breast cancer cell line (SK-BR-3) after a series of incubation times. Overexpression of the HER2 receptor is associated with greater cancer progression and is seen in approximately 15–25% of all breast cancer cases [17]. The nanoshells, made of dielectric silica particles covered with a thin gold shell, were fabricated to scatter strongly in the near-infrared spectrum through manipulation of the silica core/gold shell ratio. We compared the contrast that could be achieved by incubating the nanoshells with both normal and cancerous cells. Our results demonstrate that gold nanoshells targeted to this cell-surface marker can produce enhanced contrast after only 5 min of incubation. This proof of concept supports the initial feasibility of using gold nanoshells for potential point-of-care diagnostic applications.

## Materials and Methods

### Nanoshell Fabrication

Nanoshells were developed and bioconjugated by using previously reported procedures [22]. First, silica cores were prepared with the Stöber method [23], in which tetraethyl orthosilicate (Sigma Aldrich) is reduced in ammonium hydroxide and pure ethanol. Next, aminopropyltriethoxysilane was used to functionalize the particles by terminating the silica core surface with amine groups. The silica particles were then measured by scanning electron microscopy (SEM) to obtain the average silica core diameter of 254 nm.

To create the gold shell overlap for the silica cores, gold colloid of 1–3 nm in diameter was fabricated based on procedures documented by Duff et al. [24]. The gold colloid solution was stored at 4 °C for 2 weeks and subsequently concentrated with a Rotovap. After aging and concentration, the gold colloid solution was added to the aforementioned functionalized silica particles, forming ‘seeds’ in which the gold colloid is adsorbed to the amine groups of the silica cores. To complete nanoshell fabrication, a cocktail of hydrogen tetrachloroaurate trihydrate ($HAuCl_4$) and potassium carbonate was added to the seeds along with formaldehyde to catalyze the formation of the shells. The spectrum of the completed nanoshells was analyzed with a UV-vis spectrophotometer (Varian Cary 300). The relationship between the extinction spectrum obtained by UV-vis spectroscopy and that obtained by application of the Mie scattering theory can be used to approximate the size of the nanoparticles in solution (Fig. 1). Subsequently, Mie Theory can be used to derive the absorption, scattering, and extinction coefficients for nanoparticles of a specific size, and a standard known

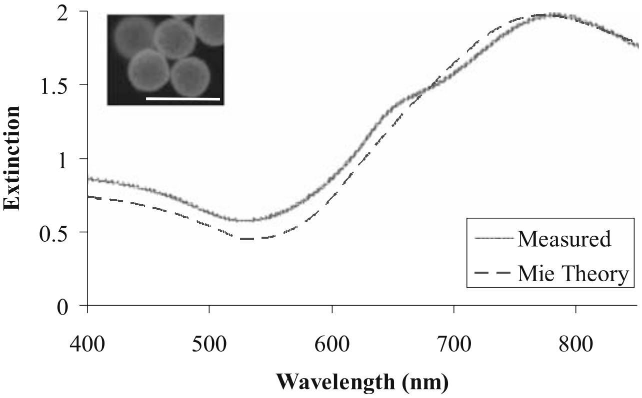

**Fig. 1** Measured spectra of nanoshells (core radius, 127 nm; shell thickness, 19 nm) as compared with that estimated using the Mie scattering theory; the *insert* depicts the corresponding image from scanning electron microscopy. *Scale bar* represents 500 nm.

concentration can be acquired for a particular optical density. In addition to using Mie scattering theory for multilayer spheres, we also used SEM to confirm the size of the nanoshells. The nanoshells used in this study had an average diameter of 292 nm, a peak surface plasmon resonance at 778 nm and a concentration of approximately $1.6\times10^9$ particles/ml.

### Nanoshell Surface Modification

To target the prepared nanoparticles to molecular markers associated with HER2-overexpression, antibodies were first prepared by methods previously described by Hirsch et al. [22]. Briefly, anti-HER2 antibodies (C-erbB-2/HER-2/*neu* Ab-4, Lab Vision Corporation) were conjugated to the heterobifunctionalized polyethylene glycol linker orthopyridyl-disulfide-PEG-*N*-hydroxysuccinimide ester (OPSS-PEG-NHS, MW=2 kD, CreativeBiochem Laboratories) by reaction at a molar ratio of 1:3 in sodium bicarbonate (100 mM, pH 8.5) overnight on ice. Aliquots were stored at −80 °C. The amidohydroxysuccinimide group (NHS) enables conjugation of the PEG linker to the antibodies through amide linkages; the remaining end of the PEG linker, OPSS, allows binding to the nanoshell gold surfaces through sulfur groups. The nanoshells ($1.6\times10^9$ particles/ml) were incubated with the prepared anti-HER2-PEG solution (0.4 mg/ml) for 1 h at 4 °C. The newly conjugated nanoshells were subsequently incubated with a 10 μM polyethylene glycol-thiol solution (PEG-SH, MW=5 kD, Nektar) for 2 additional hours at 4 °C, which stabilized the nanoshells by blocking any unoccupied adsorption sites. The nanoshells were then centrifuged to remove unbound antibodies, resuspended in ultrapure water, and stored at room temperature until use. Before being incubated with cells, the nanoshell solution was supplemented with bovine serum albumin and phosphate-buffered saline (PBS) at final concentrations of 1% each.

### Preparation of Cells

Two cell types were analyzed for this study: the HER2-overexpressing epithelial breast cancer cell line SK-BR-3 and the normal mammary epithelial cell line MCF10A (American Type Culture Collection). The SK-BR-3 cells were grown in McCoy's 5A medium supplemented with 10% fetal bovine serum and 1% penicillin-streptomycin and maintained at 37 °C in a 5% $CO_2$ atmosphere. The MCF10A cells were cultured in Mammary Epithelial Basal Medium (MEBM) supplemented with a BulletKit (Clonetics) and also maintained at 37 °C in 5% $CO_2$. Both cell lines were grown in 25-$cm^2$ culture flasks until confluent. At that time, cells were rinsed once with 1× PBS and incubated with trypsin-ethylenediaminetetraacetic acid for 5 min at 37 °C to detach the cells from the substrate, after which trypsin was neutralized with the appropriate medium and the cells were counted. Approximately $6\times10^5$ cells were placed in each of four conical tubes per cell line for each time point under investigation. The cells were then centrifuged at 115×*g* for 3 min. For each cell line and each time point of interest, three cell pellets were resuspended in the bioconjugated nanoshell solution, and one was resuspended in an equal amount of PBS as a control. The nanoshell–cell suspensions and controls were then incubated in a hybridization chamber (VWR International) at 37 °C and a motor speed of 7 rpm for 5, 10, 30, or 60 min. After incubation, the suspensions were centrifuged at 115×*g* for 3 min, and the unbound nanoshells were collected with a pipette. Cells were then rinsed once with 1× PBS, centrifuged, and the unbound nanoshells were again collected. A small volume (5 μl) of 10% glucose mixed with PBS was added to the remaining cell pellets to prevent cell death during imaging. Approximately 7 μl of each pellet was placed on a glass slide and coverslipped for immediate microscopic analysis.

### Darkfield Imaging and Processing

Images of the two cell types incubated with nanoshells were obtained with a Zeiss Axioskop 2 darkfield microscope outfitted with a color camera (Zeiss AxioCam MRc5). Darkfield microscopy depends on light scattering to achieve contrast. All images were taken under the same lighting conditions and magnification (×20). Optical intensity was quantified by using a Matlab code. Based on this code, an image with a value of 0 was designated pure black and that with a value of 255 pure white. An increase in intensity, therefore, corresponded to an image with a higher numerical value. Average intensity values for each time point and each cell line were calculated from ten independent cell samples that were devoid of scattering influences from neighboring cells and unbound nanoshells. Sample normality was assessed by using Minitab to evaluate the error

**Fig. 2** Darkfield images of MCF10A and SK-BR-3 cells incubated with bioconjugated nanoshells for the indicated times. Images were obtained at ×20. *Scale bar* represents 125 μm.

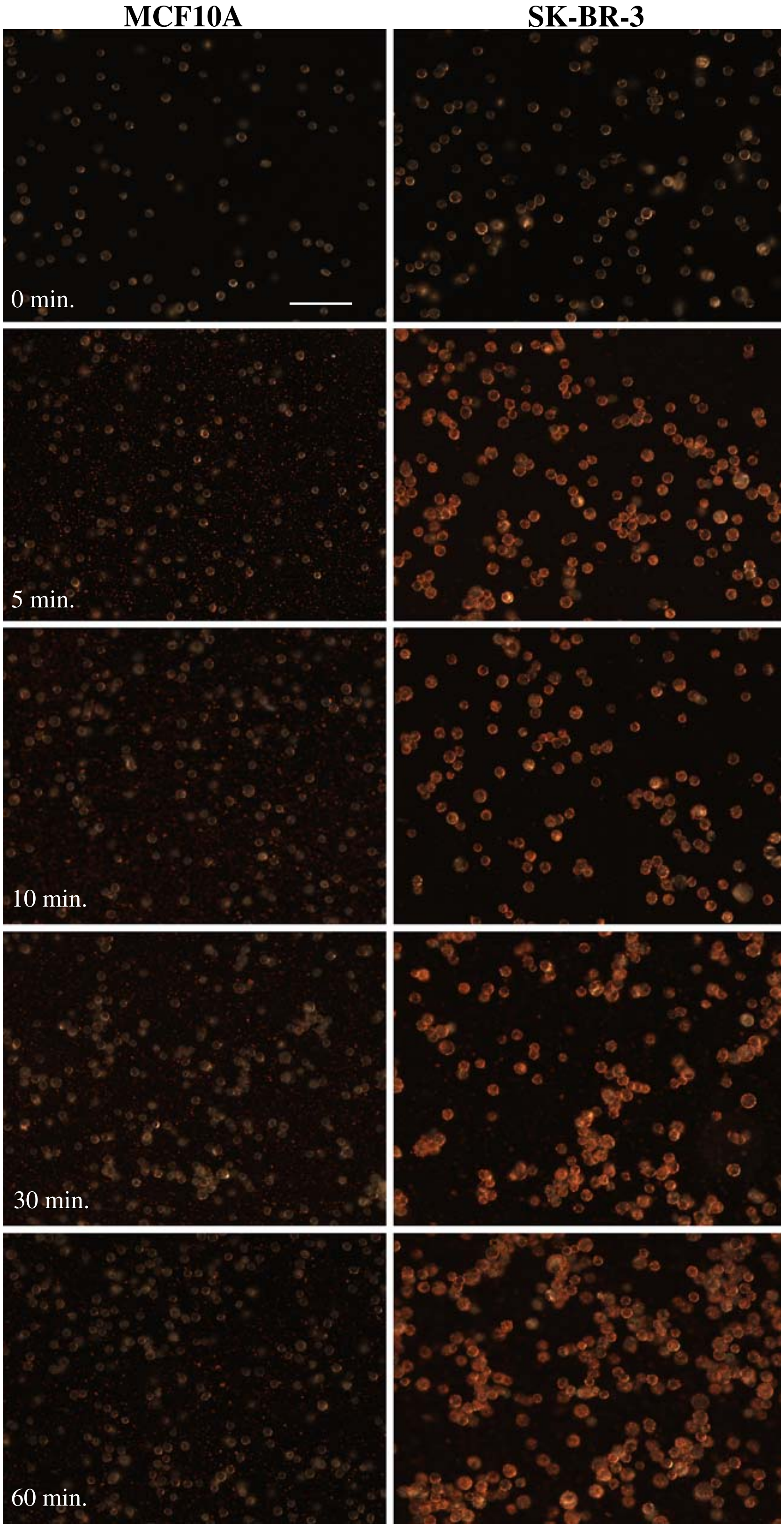

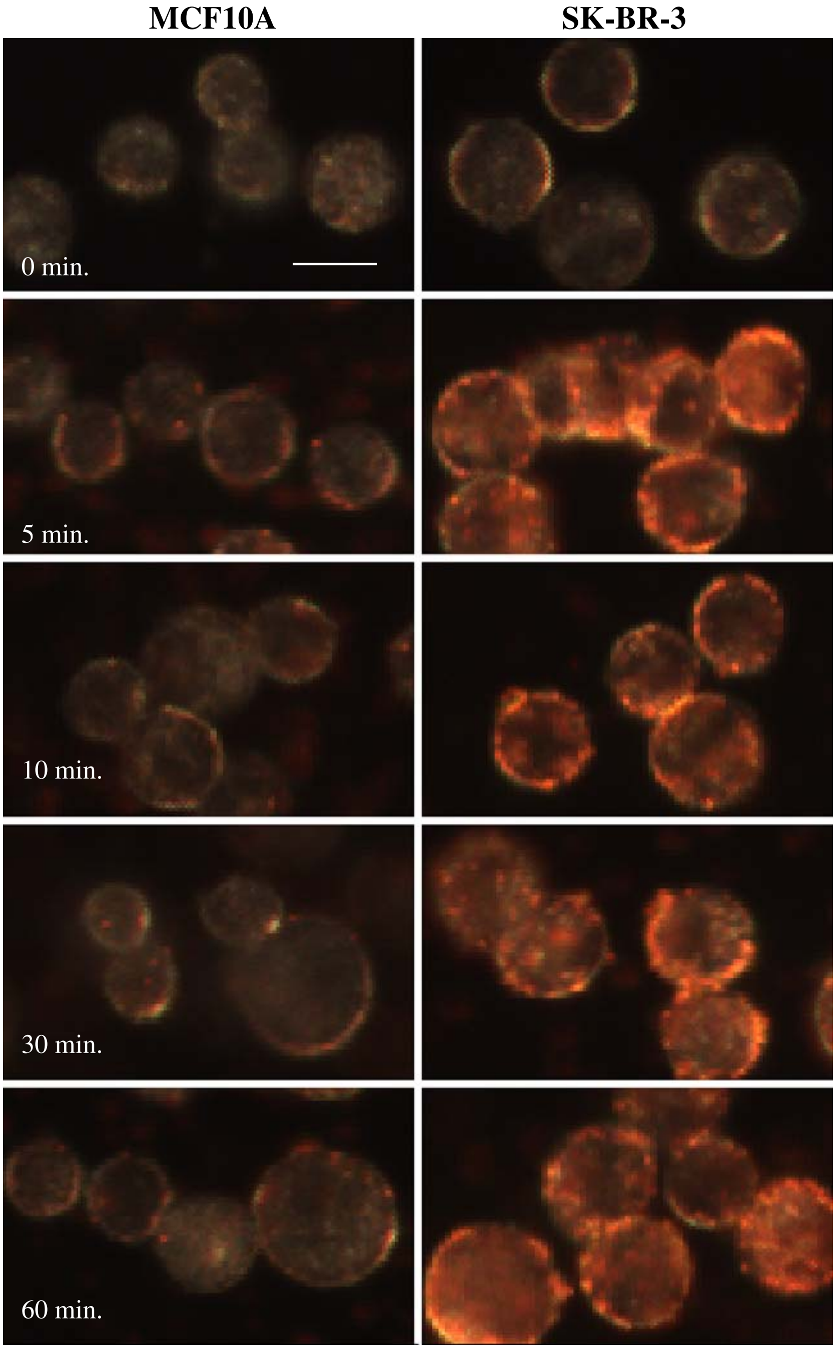

**Fig. 3** Enlarged darkfield images of MCF10A and SK-BR-3 cells incubated with the bioconjugated nanoshells for the indicated times. Original images taken at ×20. *Scale bar* represents 20 μm.

distribution for all data points. A normal probability plot of the residuals verified that the samples followed a normal distribution (data not shown). *F* tests were also used to determine the equality of variance before applying two-tailed paired Student's *t* tests to evaluate significance.

### Derivation of Bound Nanoshell Concentration using Spectroscopy

According to the Beer–Lambert law, the absorbance of particles in solution is directly related to the concentration of those particles in that solution. To validate the ability of spectroscopy to predict the concentration of a solution of nanoshells of known size, we used linear regression analysis. Nanoshells of known concentration, based on the Mie Theory calculations, were serially diluted and, the corresponding peak absorbance values were measured. We considered a concentration of approximately $2.0\times10^9$ particles/ml (optical density=2.4) as a 100× concentration. From this analysis, an equation relating the peak absorbance (independent variable) to each known nanoshell concentration (dependent variable) was used to approxi-

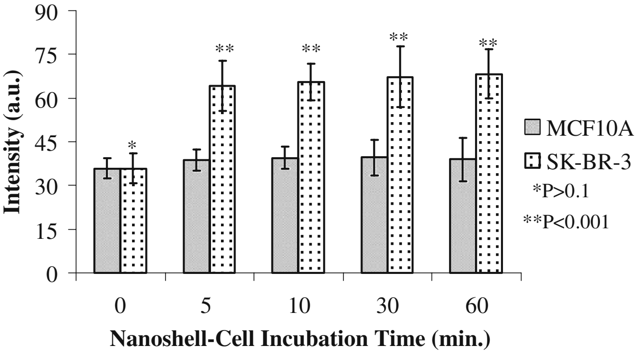

**Fig. 4** Mean quantitative intensity values for samples of MCF10A and SKBR3 cells incubated with nanoshells for the indicated times. Differences between cell types incubated without nanoshells were not statistically significant ($P>0.1$, $n=10$). Differences between cell types incubated with nanoshells were statistically significant at all time points ($P<0.001$, $n=10$). *Error bars* indicate standard deviations.

mate the number of nanoparticles in subsequent solutions of unknown concentration. This derivation was necessary to calculate the approximate number of bound nanoparticles per cell at the different time points.

To determine and compare the number of nanoshells bound after 5 min and 60 min of incubation, the collected unbound nanoshells were centrifuged at 255×*g* for 20 min, resuspended in ultrapure water, transferred to cuvettes and sonicated briefly before being measured with a UV-vis spectrophotometer. The spectrum was recorded and the peak absorbance documented for each sample. Based on the original concentration of nanoshells, the number of cells used, and the concentration of the collected unbound nanoshells, the approximate number of nanoshells bound to each cancer cell was derived. An *F* test was also used to determine the equality of variance before applying a two-tailed paired Student's *t* test to evaluate significance.

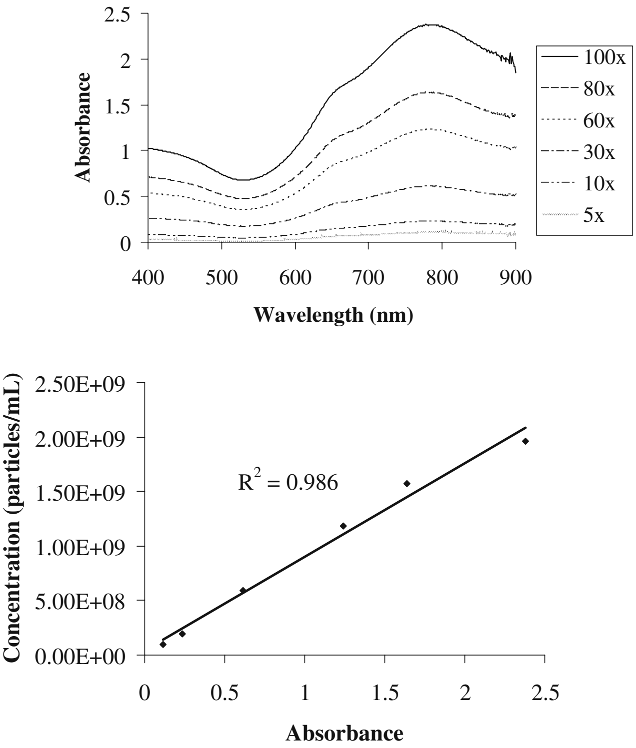

**Fig. 5** *Top* Spectra of serial dilutions of known nanoshells concentrations in suspension. *Bottom* Linear regression analysis of known nanoshell concentrations vs. the corresponding peak absorbance values.

## Results/Discussion

We evaluated the contrast that could be achieved by incubating nanoshells targeted to HER2 receptors with normal breast epithelial cells (MCF10A) or breast cancer cells (SK-BR-3) for four intervals: 5, 10, 30, and 60 min. All procedures were done with triplicate samples and included a control condition (cells to which no nanoshells had been added). Figures 2 and 3 illustrate original and enlarged images obtained at all four time points for both cells lines and for cells incubated without nanoshells (designated as 0 min). Because the optical peak resonance for the fabricated nanoparticles occurred at 778 nm, the nanoshells scattered strongly in the near-infrared range and could be visualized under darkfield illumination as red particles. Qualitative assessment of the imaging results revealed that the MCF10A cells showed little enhanced scattering at any period of incubation with the bioconjugate–nanoshell solution compared with both controls or the cancer cells. However, the SK-BR-3 cancer cells showed enhanced contrast after as little as 5 min of incubation. Typically, SK-BR-3 cells express about $8\times10^5$ receptors per cell and normal MCF10A cells about $1\times10^4$ [25, 26]. The targeted bioconjugated nanoshells apparently bound to cell surface receptors on both cell types; however, because the cancer cells had higher numbers of receptors, the contrast that could be achieved was considerably greater with those HER2-overexpressing cells. Other evidence of the superior contrast achieved with the SK-BR-3 cells was apparent from the difference in the numbers of unbound nanoshells between the two cell types. In the images of the

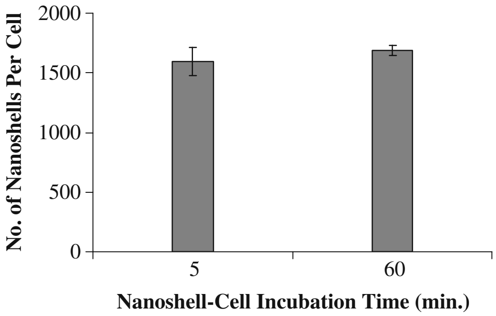

**Fig. 6** Number of nanoshells bound per SK-BR-3 cell after 5 and 60 min of incubation. Values shown are the means of triplicate measurements. *Error bars* indicate standard deviations.

MCF10A cells, several unbound nanoshells could be seen between cells despite our attempts at removing unbound nanoshells by rinsing the cells. Considerably fewer such nanoshells were present in the SK-BR-3-nanoshell images (Fig. 2).

To quantitatively assess the increase in contrast between the normal and cancerous cells at each time point, we used a Matlab code to evaluate the average intensity of ten cells from each condition; an intensity value of 0 was considered pure black and 255 pure white. Statistical analyses indicated no difference between either cell type incubated with only PBS (the control condition; $P>0.1$). However, differences between the MCF10A cells and the SK-BR-3 cells were significant at all four incubation times ($P<0.001$; Fig. 4). An additional analysis of variance showed no differences in the mean intensity of the SK-BR-3 cells at any of the four incubation times ($P>0.5$).

To further compare the differences between contrast that could be achieved at 5 and 60 min for the SK-BR-3 cells, we examined the number of bound nanoshells at both time points. To do so, we first developed a simple UV-vis spectroscopy method to determine the concentration of nanoshells in solution. On the basis of dilutions of known nanoshell concentrations, we used linear regression to estimate the concentration of nanoshells in a given solution (Fig. 5). We confirmed the existence of a linear relationship between absorbance and corresponding concentration of nanoshells for concentrations ranging from $9.8\times10^7$ to $2.0\times10^9$ particles/ml. With a goodness-of-fit ($R^2$) value of 0.986, we concluded that the absorbance accurately predicts the concentration of an unknown suspension of nanoparticles that falls within this range.

We next used this relationship between absorbance and concentration to measure the absorbance of unbound nanoshells collected after incubation and cell rinsing and subsequently resuspended in a volume of water equal to that of the diluted samples of known concentration. Knowing the initial number of nanoshells and cells, we could derive the approximate number of nanoshells bound to each cell, which we did for the triplicate samples of nanoshells plus cells after 5 and 60 min of incubation. At 5 min of incubation, $1{,}593\pm121$ nanoshells were bound per cell; at 60 min, the range was $1{,}686\pm40$ nanoshells per cell ($P>0.1$, not significant; Fig. 6). Thus, roughly 95% of the binding noted at 60 min had occurred within the first 5 min of incubation. Our imaging results suggest that this 5% difference did not seem to affect contrast.

## Conclusions

Our findings support the proof of concept that optical contrast of HER2-overexpressing breast cancer cells can be achieved by brief periods of incubating those cells with nanoshells. Although the ability to detect malignancy by such means is critical for in vivo applications and for in vitro applications associated with biological fluids, other opportunities exist for using such techniques to diagnose solid tumor specimens in vitro. The time between diagnosis and treatment could be drastically shortened by the use of microscopic evaluations of excised tissue samples that provide rapid and reliable results. We have shown both qualitatively and quantitatively that nanoshells can be used to achieve discernible contrast between cancerous and normal breast cells in 5 min. These results suggest that gold nanoshells can be designed and optimized to enhance the scattering signatures of cancer cells at minimal incubation times necessary for potential applications in point-of-care cancer diagnostic imaging. Future studies are underway to extend these findings from the cellular level to tumor specimen models.

**Acknowledgments** We thank Vengadesan Nammalvar and Adrien Wang for expert technical assistance on nanoshell fabrication. We also thank Nastassja Lewinski for SEM imaging and Christine Wogan for editing assistance. This work was supported by a Department of Defense Congressionally Directed Breast Cancer Research Program Era of Hope Scholar Award to Rebekah Drezek and Tse-Kuan Yu, the Center for Biological and Environmental Nanotechnology (EEC-0118007 and EEC-0647452), the Beckman Foundation, and the John and Ann Doerr Fund for Computational Biomedicine.

## References

1. Loo C, Lowery A, Halas N, West J, Drezek R. Nano Lett 2005;5(4):709–11.
2. Loo C, Hirsch L, Lee M-H, Chang E, West J, Halas N, Drezek R. Optics Lett 2005;30:1012–4.
3. Lowery A, Gobin A, et al. Int J Nanomed 2006;1:149–54.
4. Gobin AM, Lee MH, Halas NJ, James WD, Drezek RA, West JL. Nano Lett 2007;7:1929–34.
5. Sokolov K, Follen M, Aaron J, Pavlova I, Malpica A, Lotan R, et al. Cancer Res 2003;63:1999–2004.
6. El-Sayed IH, Huang X, El-Sayed MA. Nano Lett 2005;5(5):829–34.
7. Sun J, Zhu MQ, Fu K, Lewinski N, Drezek R. Int J Nanomed 2007;2(2):235–40.
8. Gao X, Cui Y, Levenson RM, Chung LW, Nie S. Nat Biotechnol 2004;22(8):969–76.
9. Cao L, et al. J Am Chem Soc 2007;129:11318–9.
10. Huang X, El-Sayed IH, Qian W, El-Sayed MA. J Am Chem Soc 2006;128:2115–20.
11. Durr NJ, Larson T, Smith DK, Korgel BA, Sokolov K, Ben-Yakar A. Nano Lett 2007;7:941–5.
12. Yu C, Nakshatri H, Irudayaraj J. Nano Lett 2007;7(8):2300–6.
13. Sukhanova A, Devy J, Venteo L, Kaplan H, et al. Anal Biochem 2004;324:60–7.
14. Zajac A, Song D, Qian W, Zhukov T. Colloids Surf B Biointerfaces 2007;58:309–14.
15. Weigum SE, Floriano PN, Christodoulides N, McDevitt JT. Lab Chip 2007;7(8):995–1003.

16. Culha M, Stokes DL, Griffin GD, Vo-Dinh T. JBO 2004;9(3):439–43.
17. National Comprehensive Cancer Network. Breast cancer treatment guidelines for patients. Version IX. 2007.
18. Mojica CM, Bastani R, Boscardin WJ, Ponce NA. Cancer Control 2007;14(2):176–82.
19. Guthrie TH. Breast J 1995;1(6):376–9.
20. Klimberg VS, Harms S, Korourian S. Surg Oncol 1999;8:77–84.
21. Fisher B, Anderson S, Bryant J, Margolese RG, Deutsch M, Fisher ER, Jeong JH, Wolmark N. NEJM 2002;347:1233–41.
22. Hirsch LR, Halas NJ, West JL. Methods Mol Biol 2005;303:101–11.
23. Stöber W, Fink A, et al. J Colloid Interface Sci 1968;26:62–9.
24. Duff DG, Baiker A, Edwards PP. Langmuir 1993;9:2301–9.
25. Hayes DF, Walker TM, et al. Int J Oncol 2002;21(5):1111–7.
26. Kornilova ES, Taverna D, et al. Oncogene 1992;7(3):511–9.

IOP Publishing Nanotechnology

Nanotechnology **19** (2008) 315102 (6pp) doi:10.1088/0957-4484/19/31/315102

# Enhanced multi-spectral imaging of live breast cancer cells using immunotargeted gold nanoshells and two-photon excitation microscopy

**Lissett Bickford[1,3], Jiantang Sun[1,3], Kun Fu[1,2], Nastassja Lewinski[1], Vengadesan Nammalvar[1], Joseph Chang[1] and Rebekah Drezek[1,2,4]**

[1] Department of Bioengineering, Rice University, Houston, TX 77005, USA
[2] Department of Electrical and Computer Engineering, Rice University, Houston, TX 77005, USA

E-mail: drezek@rice.edu

Received 18 April 2008, in final form 29 May 2008
Published 24 June 2008
Online at stacks.iop.org/Nano/19/315102

**Abstract**
We demonstrate the capability of using immunotargeted gold nanoshells as contrast agents for *in vitro* two-photon microscopy. The two-photon luminescence properties of different-sized gold nanoshells are first validated using near-infrared excitation at 780 nm. The utility of two-photon microscopy as a tool for imaging live HER2-overexpressing breast cancer cells labeled with anti-HER2-conjugated nanoshells is then explored and imaging results are compared to normal breast cells. Five different imaging channels are simultaneously examined within the emission wavelength range of 451–644 nm. Our results indicate that under near-infrared excitation, superior contrast of SK-BR-3 cancer cells labeled with immunotargeted nanoshells occurs at an emission wavelength ranging from 590 to 644 nm. Luminescence from labeled normal breast cells and autofluorescence from unlabeled cancer and normal cells remain imperceptible under the same conditions.

(Some figures in this article are in colour only in the electronic version)

## 1. Introduction

Accurate cancer diagnosis through its multi-stage progression is critical for developing effective and selective cancer treatments. In order to provide clinicians with functional diagnostic results, knowledge of the molecular signatures of carcinogenesis is necessary. Due to their overexpression during the development of cancer, several biomarkers have been identified as a biological means of characterizing these signatures [1]. Although the acquisition of molecular-specific data is typically associated with gene arrays and proteomics [2], there is an opportunity to use such biomarkers as tools for both *in vitro* and *in vivo* diagnostic evaluations of tissue specimens, such as during surgery, in order to identify malignant cells among heterogeneous tissue.

Silica-based gold nanoshells, which are advantageous for several biological applications due to their unique optical tunability and potential as multi-modal agents, have previously demonstrated enhanced diagnostic imaging potential of carcinogenesis at the microscopic scale through the use of extracellular biomarkers [3–6]. By manipulation of the size of their silica cores and gold outer shells, nanoshells can be optically tuned to absorb or scatter light from wavelengths ranging from the visible to the near-infrared, allowing for both imaging and therapy applications [7]. Achieving optimal contrast of gold nanoshells for biological diagnostics includes

---

[3] These authors contributed equally to this work, listed alphabetically by last name.

[4] Address for correspondence: Department of Bioengineering, Rice University, 6100 Main Street, MS-142, Houston, TX 77005, USA.

a combination of developing nanoshells that are tuned to scatter or absorb light in the near-infrared (NIR), where biological chromophores absorb minimal light, and the use of NIR-based imaging systems.

Although several optical devices have been used to validate applications of gold nanoshells as viable contrast agents [3–15], none have focused on evaluating the effectiveness of using immunotargeted nanoshells as contrast agents for cell surface biomarkers using nonlinear excitation microscopy. Nonlinear optics has been used extensively for analyzing fluorescent signals in animal models and tissue samples [16–20]. By using a femtosecond pulsed laser, two photons can be used simultaneously to excite tissue molecules similar to the excitation generated by a single photon, but with twice the energy. Only the molecules at the focus of the femtosecond laser will be excited, resulting in greater resolution than that achievable with single-photon systems, such as conventional confocal microscopy. Additionally, unlike conventional confocal microscopy, a pinhole is not required to reject out-of-focus light and the inherent excitation at only the focal plane means that biological tissue undergoes less photodamage [20]. Although multi-photon microscopy has frequently been used for enhancing fluorescent signals [16, 20], studies have demonstrated that metal particles display photoluminescence as a result of excitation by such multi-photon systems [21, 22]. This photoluminescence is induced by a significant field enhancement that occurs upon multi-photon excitation of the metallic molecules [21]. Thus far in the literature, metallic nanoparticles analyzed for two-photon imaging potential have included gold colloid spheres [23, 24], gold nanorods [25–29], and gold nanoshells [14]. A recent publication on the use of two-photon microscopy for evaluating nanoshell contrast focused on potential dual imaging and therapy applications where unlabeled nanoshells were delivered to murine tumors through extravasations due to the presence of leaky vasculature [14]. However, since nanoshell dimensions are fundamentally variable [7], it is important to further elucidate and confirm the two-photon properties of these highly tunable nanoparticles despite differences in size. Furthermore, since cancer undergoes a multi-stage progression, the ability to track molecular signatures through the overexpression of biomarkers is crucial in obtaining functional and accurate diagnostic results. Therefore, the goal of our study was to demonstrate the nonlinear properties of very different-sized nanoshells and validate the proof of concept that immunotargeted nanoshells can be used to enhance the contrast of malignant human cells *in vitro* through nonlinear excitation prior to our evaluation of this system in excised tissue specimens. Additionally, through the use of two-photon excitation and multi-spectral imaging, the simultaneous acquisition of images at different emission wavelengths was obtained to ascertain the optimal imaging parameters for this system.

We demonstrate the two-photon luminescence properties of two different sizes of gold nanoshell designed with a similar plasmon resonance in the near-infrared. We evaluate the enhanced contrast by comparing HER2-overexpressing breast cancer cells to normal breast cells with and without targeted anti-HER2-bioconjugated gold nanoshells at five different emission wavelength ranges: 451–483, 483–515, 515–547, 558–579, and 590–644 nm. By evaluating imaging results under different ranges, we explore the broad emission properties of silica-based gold nanoshells under two-photon induced luminescence. The anti-HER2 antibody was selected as a model for surface tumor targeting due to the association of HER2-overexpression with more aggressive breast cancers seen in 15–25% of all breast cancer cases [30]. Additionally, studies in our laboratory have previously demonstrated the effectiveness of using immunotargeted nanoshells as diagnostic imaging agents for HER2-overexpressing cancer cells [3, 5, 6, 13]. We show that for immunotargeted nanoshells with a silica core diameter of 254 nm and a gold shell thickness of 19 nm imaged with our specific system, the optimal emission wavelength for observing enhanced contrast of HER2-overexpressing breast cancer cells occurs between 590 and 644 nm at 10% of maximum excitation power. Under similar conditions, normal breast cells are not detectable.

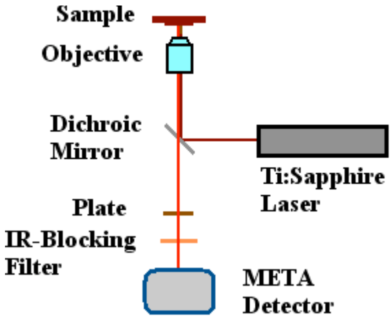

**Figure 1.** Schematic of Zeiss LSM 510 META multi-photon system configuration.

## 2. Method

### *2.1. Multi-photon imaging system*

A Zeiss laser scanning microscope (LSM) 510 META multi-photon system was used in conjunction with a Coherent Chameleon femtosecond mode-locked Ti:sapphire laser to collect two-photon data (figure 1). The wavelength of the polarized output laser beam was tunable between 720 and 950 nm with pulse width of 140 fs at a repetition rate of 90 MHz. A short-pass dichroic mirror (KP700/488, Zeiss) was used to reflect the incident NIR excitation light onto the sample through a 20× or 63× objective and to collect the two-photon-induced luminescence data. To further eliminate the background signal of the excitation light, a wave plate and an IR-blocking filter (BG39, Zeiss) were placed in front of the META detector. The Zeiss LSM META system allowed simultaneous multi-spectral imaging and recording of up to eight emission channels. The maximum output power of the Chameleon femtosecond laser was around 1640 mW for excitation at 780 nm. Based on data from the manufacturer, less than 10% of this power was incident on the sample. The excitation wavelength of 780 nm was chosen as it was within 10 nm of the extinction peak for both nanoshell sizes.

### *2.2. Nanoshell fabrication*

Nanoshells were developed as described in previous publications [3–5]. First, the Stöber method was used to create silica cores by reducing tetraethyl orthosilicate (Sigma Aldrich) in ammonium hydroxide and pure ethanol [31]. Aminopropyltriethoxysilane (APTES) was then added in order to terminate the silica core surfaces with amine groups, which formed functionalized particles. The two different-sized groups of silica particles were measured by scanning electron microscopy (SEM) to obtain the average silica core diameters of 130 and 254 nm. The gold shell overlay on the silica cores was also created using previously described methods [3–5]. First, using procedures outlined by Duff *et al* [32], gold colloid of 1–3 nm in diameter was developed and then aged under refrigeration for two weeks. The colloid was then concentrated using a Rotovap and added to the functionalized silica particles mentioned above. By interacting with the functionalized amine group surfaces of the silica particles, the gold colloid was adsorbed, forming surfaces with partial gold coverage. Addition of more gold completed the formation of the shell through catalysis of formaldehyde with hydrogen tetrachloroaurate trihydrate ($HAuCl_4 3H_2O$) and potassium carbonate. Two groups of nanoshells were fabricated and both were spectrally analyzed using a Varian Cary 300 UV–vis spectrophotometer (figure 2). The final sizes of the nanoshells were determined using SEM imaging (figure 2, inset) and confirmed using Mie theory simulation for multi-layer spheres. The smaller nanoshells had an average gold shell thickness of 21 nm. The larger nanoshells had an average shell thickness of 19 nm. The nanoshells were stored in deionized water at 4 °C until further use.

### *2.3. Nanoshell surface modification and bioconjugation*

For live cell imaging, the larger nanoshells were used and targeted to HER2-overexpressing cells through conjugations with anti-HER2 antibodies. In order to prepare the immunotargeted nanoshells, a heterobifunctionalized polyethylene glycol linker (orthopyridyl-disulfide-PEG-N-hydroxysuccinimide ester, OPSS-PEG-NHS, MW = 2 kD, CreativeBiochem Laboratories) was first conjugated to anti-HER2 antibodies (C-erbB-2/HER-2/neu Ab-4, Lab Vision Corporation) through amide linkages that joined the amidohydroxysuccinimide group (NHS) of the PEG linker to the antibodies. This reaction proceeded at a 3:1 molar ratio in sodium bicarbonate (100 mM, pH 8.5) on ice overnight. Aliquots of the 'PEGylated' antibodies, at a concentration of 0.4 mg $ml^{-1}$, were stored at −80 °C until use. Conjugation of the nanoshells to the PEGylated antibodies was then carried out through sulfur linkages between the gold nanoshell surfaces and the remaining OPSS group of the heterobifunctional PEG linker. This was performed by incubating the nanoshells, at a concentration of $1.6 \times 10^9$ particles $ml^{-1}$, with the PEGylated antibodies for 1 h under refrigeration (4 °C). In order to block vacant adsorption sites, the nanoshells were further incubated with a 10 $\mu$M polyethylene glycol-thiol cocktail (PEG-SH, MW = 5kD, Nektar) for two additional hours under refrigeration. Unbound antibodies were then removed by centrifugation and the immunotargeted nanoshells were then resuspended in deionized water. Prior to incubation with cells, the immunotargeted nanoshell solution was further modified by the addition of bovine serum albumin (BSA) and phosphate-buffered saline (PBS) to a final concentration of 1% each.

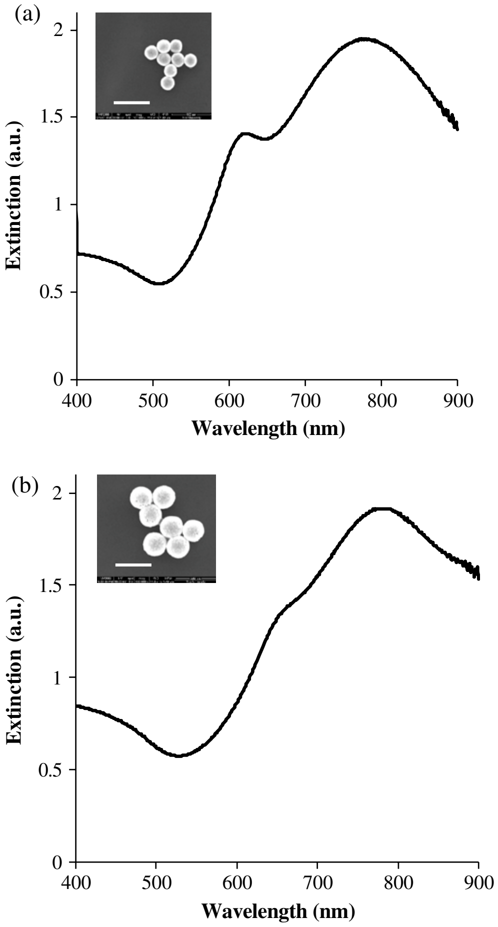

**Figure 2.** Measured extinction spectra of nanoshells. (a) Nanoshells of average core diameter 130 nm and average shell thickness of 21 nm. (b) Nanoshells of average core diameter 254 nm and average shell thickness of 19 nm. The insets depict corresponding images from scanning electron microscopy. Scale bars represent 450 nm.

### *2.4. Cell preparation*

SK-BR-3 cells (American Type Culture Collection, ATCC) were grown at 37 °C in a 5% $CO_2$ atmosphere using McCoy's 5A growth medium supplemented with 1% antibiotics and 10% fetal bovine serum (FBS). MCF10A cells (ATCC) were also grown at 37 °C in a 5% $CO_2$ atmosphere using Mammary Epithelial Basal Medium (MEBM) supplemented with a BulletKit (Clonetics) and 1% antibiotics. Both cell lines were grown in 25 $cm^2$ culture flasks until confluent, rinsed once with 1 × PBS, and incubated with trypsin-EDTA for 5 min at 37 °C in a 5% $CO_2$ atmosphere. The trypsin-EDTA was then neutralized with the appropriate culture medium and the cells were subsequently counted using a hemacytometer. For each cell line, an estimated $6 \times 10^5$ cells were placed in each of two 15 ml conical tubes and then centrifuged at 115 × $g$ for 3 min. One cell pellet was resuspended in the immunotargeted

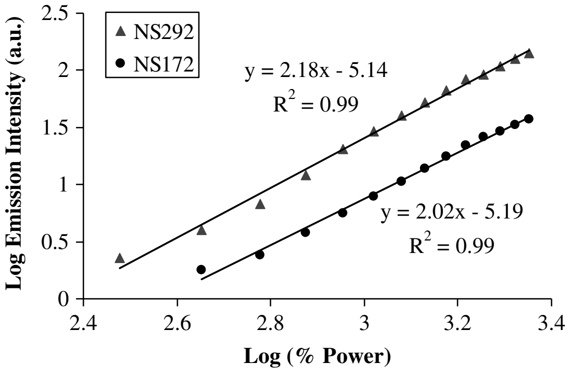

**Figure 3.** Quadratic dependence of luminescence intensity on excitation power at 780 nm for two different-sized nanoshells. Nanoshells of core diameter of 130 nm and shell thickness of 21 nm are designated as NS172. Nanoshells of core diameter of 254 nm and shell thickness of 19 nm are designated as NS292. Data were recorded with a 20× objective.

nanoshell solution and the other pellet was resuspended in an equal volume of 1 × PBS. The cells were then incubated at 37 °C in a hybridization chamber (VWR International) and rotated under a motor speed of 7 rpm for 10 min. Post incubation, the cells were centrifuged at 115 × *g* for 3 min, the supernatant was removed, and the cells were rinsed once with 1 × PBS. Following rinsing, the cells were resuspended in 10% glucose in 1 × PBS in order to maintain cell viability during imaging. The cell suspensions were then placed on chambered coverglasses (Fisher Scientific) prior to two-photon imaging.

## 3. Results and discussion

By manipulation of the core-to-shell ratio, nanoshells can be designed to strongly absorb or scatter light upon near-infrared excitation. In order to validate the two-photon characteristics of silica-based gold nanoshells, we designed two different sizes of nanoshell with a similar peak surface plasmon resonance in the near-infrared. After fabrication of two different-sized silica cores, their average diameters were confirmed through scanning electron microscopy (SEM) as 130 and 254 nm. Once the gold shell was added, the nanoshells were measured by SEM and their optical properties were assessed by UV–vis spectroscopy. The smaller nanoshells had an average diameter of 172 nm and a peak surface plasmon resonance at 772 nm; for the larger nanoshells, the average diameter was 292 nm, with a peak surface plasmon resonance occurring at 778 nm (both shown in figure 2). The two-photon luminescence properties of the gold nanoshells were then observed using a Zeiss LSM 510 META multi-photon system with the configuration shown in figure 1. The two-photon properties were verified by evaluating the dependence of increasing logarithmic emission intensity on increasing logarithmic excitation power. Aliquots of both sizes of bare nanoshell suspended in deionized water were well dispersed with sonication and separately placed on chambered coverglasses (Fisher Scientific). Data were recorded at an excitation wavelength of 780 nm, which corresponded to the peak plasmon resonance of the nanoshells for both sample sizes. The excitation power was varied from 2% to 15% of the maximum laser power with a detection spectral band of 494–634 nm. By using the image processing software inherent in the LSM 510 META system, the average intensities of the nanoshell suspensions were obtained. The dependence of luminescence intensity on excitation power at 780 nm for both smaller- and larger-sized nanoshells was determined (figure 3). The slopes of the fitted linear curves are estimated as 2.02 and 2.18 for the smaller and larger nanoshells, respectively, in accordance with the characteristic two-photon-induced quadratic dependence of emission intensity on excitation power [14, 16, 20]. Specifically, Wang *et al* demonstrated that the dependence of luminescence intensity on excitation power for gold nanorods ranged from 1.97 to 2.17 [27]. This disparity was attributed to possible nanoparticle melting after increasing the power on the nanorod sample and, subsequently, decreasing the power on the same sample. However, in our study, since a difference in quadratic dependence exists for two sizes of gold nanoshell treated under the same conditions, we believe that the nanoshells may actually undergo photophysics which are not yet fully elucidated.

In order to demonstrate the enhanced two-photon optical signatures of breast cancer cells labeled with immunotargeted nanoshells, the HER2-overexpressing epithelial breast cancer cell line, SK-BR-3, was analyzed and compared to the normal breast epithelial cell line, MCF10A, which does not overexpress HER2. For this component of the study, the cells were incubated with the larger nanoshells which were conjugated to anti-HER2 antibodies. Images were taken of the SK-BR-3 cancer cells under three conditions: labeled with nanoshells at 10% of maximum laser power, unlabeled at 10% of maximum laser power, and unlabeled at 100% of maximum laser power. An excitation wavelength of 780 nm was used for all images and five different emission wavelength ranges were analyzed: 451–483, 483–515, 515–547, 558–579, and 590–644 nm. Additionally, images were taken of the MCF10A normal cells under the same labeling and imaging conditions. As shown in figure 4(a), bright two-photon luminescence signals from nanoshells targeted to cell surface receptors provided clear visualization of the SK-BR-3 cancer cells under only 10% of maximum laser power. However, under the same power, unlabeled cancer cells were not perceivable (data not shown due to lack of detectable signal). By increasing the laser power to 100%, the spectral-resolved two-photon-induced autofluorescence is evident at emission wavelengths ranging from 451 to 547 nm (figure 4(b)). However, this autofluorescence, which is only visible at the maximized power, cannot be discerned beyond an emission wavelength of 547 nm. With regard to the normal MCF10A cells labeled with immunotargeted nanoshells under 10% of maximum laser power, clear visualization of the cells is not possible and only a few targeted cell surface receptors can be distinguished (figure 4(c)). Due to the differences in HER2 cell surface receptor expression, which is approximately 8 × 10$^5$ receptors per SK-BR-3 cancer cell [33] and about 1 × 10$^4$ receptors per normal MCF10A cell [34], the contrast was dramatically increased in the cancer cells due to the overexpression of HER2. Similar to the unlabeled

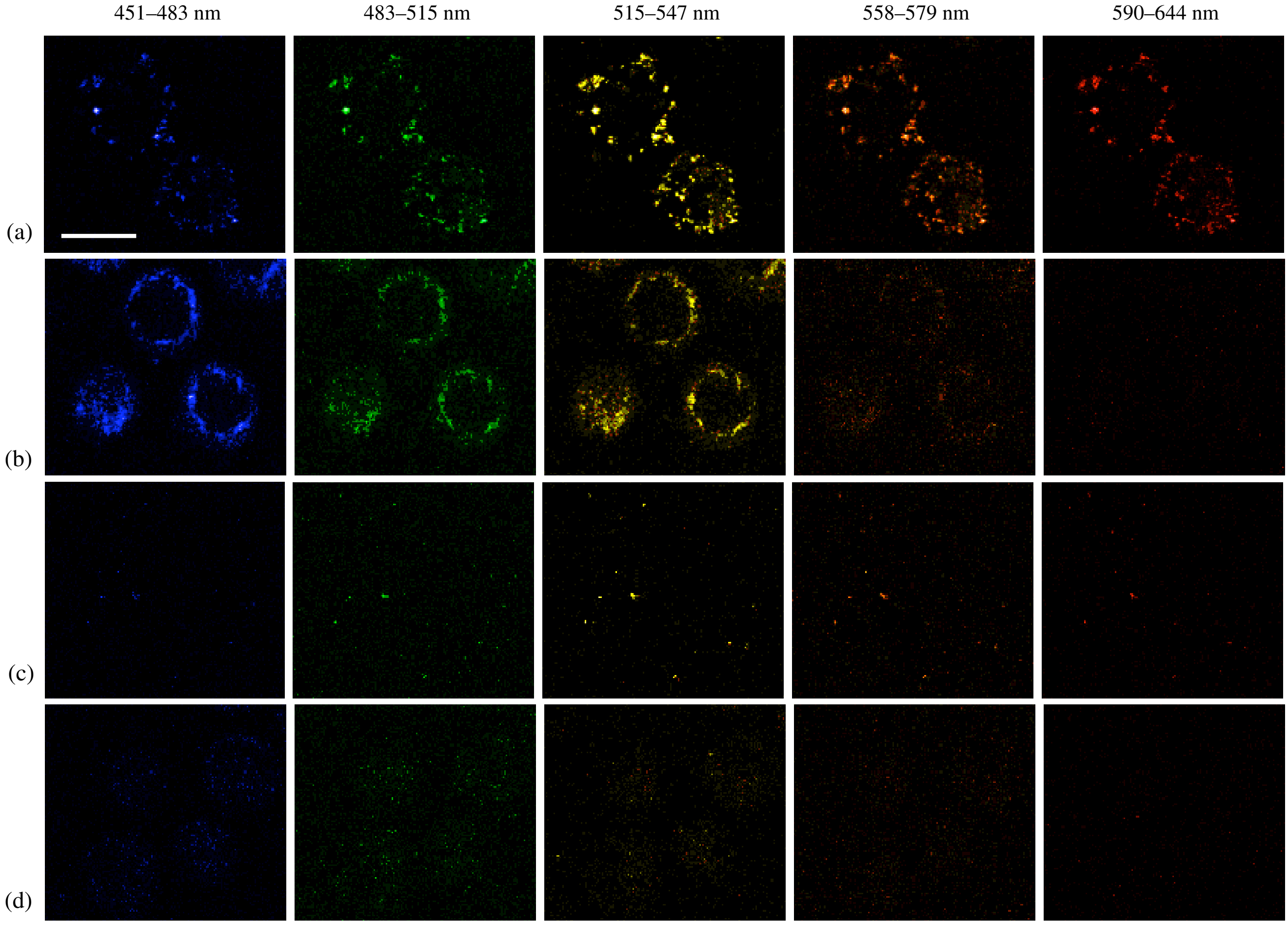

**Figure 4.** Two-photon images (pseudo color) of live SK-BR-3 cancer cells and MCF10A normal cells in suspension taken at different emission wavelengths. (a) Cancer cells labeled with larger nanoshells at 10% of maximum excitation power. (b) Unlabeled cancer cells at 100% of maximum excitation power. (c) Normal cells labeled with larger nanoshells at 10% of maximum excitation power. (d) Unlabeled normal cells at 100% of maximum excitation power. Images taken at 63×. The scale bar represents 20 $\mu$m.

SK-BR-3 cancer cells, unlabeled MCF10A cells imaged at 10% of maximum laser power were not detectable (data not shown due to lack of detectable signal). Furthermore, images collected at 100% of maximum laser power demonstrated that the MCF10A cells exhibited low levels of two-photon-induced autofluorescence (figure 4(d)). Wang *et al* [27] and Durr *et al* [29] have previously shown two-photon imaging results using gold nanorods. However, the images collected were taken over a single emission wavelength range from 400 nm to approximately 700 nm. Based on spectral-resolved image acquisition, however, the unique widely spanning luminescence properties of gold nanoshells demonstrate great flexibility in selecting the emission wavelengths necessary to minimize the influence of background autofluorescence. Photobleaching was also not observed under the two-photon-induced nanoshell luminescence. Based on a comparison of live cell bright-field images observed before and after laser exposure, morphological changes were not detected as a result of the aforementioned laser conditions and, in particular, all cell membranes remained visible and intact.

## 4. Conclusion

Two-photon microscopy is a powerful tool for diagnostic research applications. With advancements in gold-based contrast agent development and flexibility in two-photon excitation wavelength selection readily achieved through tunable laser sources, the potential to use multi-photon imaging for assessment of molecular signatures of malignancy is substantial. In this study, we demonstrate the first use of immunotargeted gold nanoshells as *in vitro* contrast agents for biomarkers of disease using two-photon microscopy. We additionally confirm broad luminescence from gold nanoshells using multi-spectral images to visualize the optical contrast provided by anti-HER2-nanoshells targeted to live HER2-overexpressing breast cancer cells. Our study identifies an additional application of immunotargeted nanoshells and suggests their potential future use as multi-functional probes for molecular imaging.

## Acknowledgments

We thank Dr Robert Raphael for expert technical assistance using a Zeiss LSM META 510 system. We acknowledge support from a Department of Defense Era of Hope Scholar Award to Rebekah Drezek, the Beckman Young Investigator Program, the Welch Foundation (C-1598), and the Center for Biological and Environmental Nanotechnology (EEC-0118007 and EEC-0647452).

## References

[1] Hawk E, Viner J L and Lawrence J A 2000 *Curr. Oncol. Rep.* **2** 242–50
[2] Weinberg R A 2007 *The Biology of CANCER* (New York: Taylor and Francis) pp 727–32
[3] Loo C, Hirsch L, Lee M H, Chang E, West J, Halas N and Drezek R 2005 *Opt. Lett.* **30** 1012–4
[4] Lowery A R, Gobin A M, Day E S, Halas N J and West J L 2006 *Int. J. Nanomed.* **1** 149–54
[5] Loo C, Lowery A, Halas N, West J and Drezek R 2005 *Nano Lett.* **5** 709–11
[6] Fu K, Sun J, Bickford L R, Lin A W H, Halas N J, Yu T K and Drezek R A 2008 *Nanotechnology* **19** 045103
[7] Hirsh L R, Gobin A M, Lowery A R, Tam F, Drezek R A, Halas N J and West J L 2006 *Ann. Biomed. Eng.* **34** 15–22
[8] Gobin A M, Lee M H, Halas N J, James W D, Drezek R A and West J L 2007 *Nano Lett.* **7** 1929–34
[9] Wu C, Liang X and Jiang H 2005 *Opt. Commun.* **253** 214–21
[10] Zaman R T *et al* 2007 *IEEE J. Sel. Top Quantum Electron.* **13** 1715–20
[11] Fournelle M, Maass K, Fonfara H, Welsch H J, Hewener H, Günther C and Lemor R 2007 *IEEE Ultrason. Symp.* **1051-0117/07** 2417–20
[12] Agrawal A, Huang S, Lin A W H, Lee M H, Barton J, Drezek R A and Pfefer T J 2006 *J. Biomed. Opt.* **11** 041121
[13] Loo C 2006 *PhD Thesis* Rice University, Houston, Texas
[14] Park J *et al* 2008 *Opt. Express* **16** 1590–9
[15] Wang Y, Xie X, Wang X, Ku G, Gill K L, O'Neal D P, Stoica G and Wang L 2004 *Nano Lett.* **4** 1689–92
[16] Zipfel W R, Williams R M and Webb W W 2003 *Nat. Biotechnol.* **21** 1369–77
[17] Denk W, Strickler J H and Webb W W 1990 *Science* **248** 73–6
[18] Hell S W, Booth M, Wilms S, Schnetter C M, Kirsch A K, Arndt-Jovin D J and Jovin T M 1998 *Opt. Lett.* **23** 1238–40
[19] Lewis M K, Wolanin P, Gafni A and Steel D G 1998 *Opt. Lett.* **23** 1111–3
[20] Piston D W 1999 *Cell Biol.* **9** 66–9
[21] Boyd G T, Yu Z H and Shen Y R 1986 *Phys. Rev.* B **33** 7923–36
[22] Mooradian A 1969 *Phys. Rev. Lett.* **22** 185–7
[23] Huang X, Qian W, El-Sayed I H and El-Sayed M A 2007 *Lasers Surg. Med.* **39** 747–53
[24] Nagesha D, Laevsky G S, Lampton P, Banyal R, Warner C, DiMarzio C and Sridhar S 2007 *Int. J. Nanomed.* **2** 813–9
[25] Bouhelier A, Bachelot R, Lerondel G, Kostcheev S, Royer P and Wiederrecht G P 2005 *Phys. Rev. Lett.* **95** 267405
[26] Imura K, Nagahara T and Okamoto H 2005 *J. Phys. Chem.* B **109** 13214–20
[27] Wang H, Huff T B, Zweifel D A, He W, Low P S, Wei A and Cheng J X 2005 *Proc. Natl Acad. Sci.* **102** 15752–6
[28] Huff T B, Hansen M N, Zhao Y, Cheng J X and Wei A 2007 *Langmuir* **23** 1596–9
[29] Durr N J, Larson T, Smith D K, Korgel B A, Sokolov K and Ben-Yakar A 2007 *Nano Lett.* **7** 941–5
[30] National Comprehensive Cancer Network 2007 *Breast Cancer Treatment Guidelines for Patients* Version IX http://www.nccn.org
[31] Stöber W, Fink A and Bohn E 1968 *J. Colloid Interface Sci.* **26** 62–9
[32] Duff D G, Baiker A and Edwards P P 1993 *Langmuir* **9** 2301–9
[33] Hayes D F, Walker T M, Singh B, Vitetta E S, Uhr J W, Gross S, Rao C, Doyle G V and Terstappen L W M M 2002 *Int. J. Oncol.* **21** 1111–7
[34] Kornilova E S, Taverna D, Hoeck W and Hynes N E 1992 *Oncogene* **7** 511–9

IOP Publishing Nanotechnology

Nanotechnology **19** (2008) 045103 (6pp) doi:10.1088/0957-4484/19/04/045103

# Measurement of immunotargeted plasmonic nanoparticles' cellular binding: a key factor in optimizing diagnostic efficacy

**Kun Fu[1,3], Jiantang Sun[1], Lissett R Bickford[1], Alex W H Lin[1], Naomi J Halas[2], Tse-Kuan Yu[3] and Rebekah A Drezek[1,2,4]**

[1] Department of Bioengineering, Rice University, 6100 Main Street, MS-142, Houston, TX 77005, USA
[2] Department of Electrical and Computer Engineering, Rice University, 6100 Main Street, MS-142, Houston, TX 77005, USA
[3] Department of Radiation Oncology, University of Texas, M D Anderson Cancer Center, Box 1202, 1515 Holcombe Boulevard, Houston, TX 77030, USA

E-mail: drezek@rice.edu

Received 28 September 2007, in final form 3 December 2007
Published 4 January 2008
Online at stacks.iop.org/Nano/19/045103

**Abstract**
In this study, we use polarized light scattering to study immunotargeted plasmonic nanoparticles which bind to live SK-BR-3 human breast carcinoma cells. Gold nanoparticles can be conjugated to various biomolecules in order to target specific molecular signatures of disease. This specific targeting provides enhanced contrast in scattering-based optical imaging techniques. While there are papers which report the number of antibodies that bind per nanoparticle, there are almost no reports of the key factor which influences diagnostic or therapeutic efficacy using nanoparticles: the number of targeted nanoparticles that bind per cell. To achieve this goal, we have developed a 'negative' method of determining the binding concentration of those antibody/nanoparticle bioconjugates which are targeted specifically to breast cancer cells. Unlike previously reported methods, we collected unbound nanoparticle bioconjugates and measured the light scattering from dilute solutions of these particles so that quantitative binding information can be obtained. By following this process, the interaction effects of adjacent bound nanoparticles on the cell membrane can be avoided simply by measuring the light scattering from the unbound nanoparticles. Specifically, using nanoshells of two different sizes, we compared the binding concentrations of anti-HER2/nanoshell and anti-IgG/nanoshell bioconjugates targeted to HER2-positive SK-BR-3 breast cancer cells. The results indicate that, for anti-HER2/nanoshell bioconjugates, there are approximately 800–1600 nanoshells bound per cell; for anti-IgG/nanoshell bioconjugates, the binding concentration is significantly lower at nearly 100 nanoshells bound per cell. These results are also supported by dark-field microscopy images of the cells labeled with anti-HER2/nanoshell and anti-IgG/nanoshell bioconjugates.

## 1. Introduction

Scattering-based optical imaging techniques offer a new approach to noninvasive cancer diagnosis [1–3]. Targeted optical contrast agents are playing an increasingly significant role in these scattering-based techniques by enabling enhanced molecular-specific optical signals. In particular, gold nanoparticles are attractive for potential *in vivo* applications due to gold's inherent biocompatibility and

---

[4] Author to whom any correspondence should be addressed.

because the gold surface can be readily modified with various molecules. Numerous gold nanomaterials have been investigated as possible optical contrast agents, including colloidal gold nanoparticles [4–6], gold nanoshells [7–11], gold nanorods [12–14] and gold nanocages [15]. As an optical contrast agent for cancer imaging applications, gold nanoshells have shown considerable potential. This potential arises due to the optical tunability of nanoshells from the visible light spectrum through the near-infrared (NIR) region [16].

Previous studies have shown that colloidal gold nanoparticles which have been conjugated with anti-EGFR monoclonal antibodies provide enhanced signals in labeled human cervical tumor cancer (SiHa) cells, as shown in confocal reflectance images [4, 5]. Similar results, when using dark-field microscopy, have also been seen in anti-EGFR/gold nanoparticles' labeled HSC oral cancer cells [6]. Proof-of-concept studies show that gold nanoshells conjugated with anti-HER2 antibodies provide enhanced signals, specifically in labeled HER2-positive human breast cancer SK-BR-3 cells. These have been observed in reflectance confocal and dark-field microscopy images [8, 9]. Given the diagnostic potential of various nanoparticles and their *in vivo* applications, the ability to quantify nanoparticle bioconjugates that can be targeted to cancer cells is significant and critical for improved diagnostic and therapeutic results. Despite this potential, however, the key factor which influences diagnostic or therapeutic efficacy is not even reported: the number of targeted nanoparticles that bind per cell. Thus far in the literature, only Sokolov *et al* have reported $\sim 5 \times 10^4$ nanoparticle bioconjugates bound per cell for human cervical tumor (SiHa) cells labeled with anti-EGFR monoclonal antibodies–conjugated colloidal gold nanoparticles [4]. The method they used to acquire the binding number requires centrifugation of the mixture of labeled cells and nanoparticles, so that those nanoparticles which did not bind to the cell surfaces are separated out. This method may be limited by the size of the nanoparticles and the material from which they are made, i.e. it may not be effective to separate cells and nanoparticles of all varieties by centrifugation. Other people attempted to study the binding efficiency by using the direct measurement of optical signals from nanoparticles which were bound to cells. The limitation of this method is that multiple scattering can occur when nanoparticles are in close proximity to each other on the cell membrane. Due to the nonlinear effect introduced by this multiple scattering, the nanoparticle binding information cannot be accurately assessed. Additionally, measuring the optical signals of nanoparticles which bind to cells does not provide the quantitative information of the binding numbers. It is also difficult to directly count the number of particles that bind to cells. To achieve the binding information effectively and accurately, we have developed a novel method to semi-quantitatively characterize the binding concentration of gold nanoparticle bioconjugate-labeled HER2-positive SK-BR-3 breast cancer cells using polarized angular-dependent light scattering. We have called this method 'negative' quantification because we first obtain concentration information and light scattering spectra from nanoparticles that were originally added to the cells for incubation. We then collect unbound nanoparticles after the incubation period with the cells, and measure the light scattering of these unbound nanoparticles. According to Mie theory, when a single-scattering criterion is satisfied, the intensity of scattered light is linearly proportional to the particle concentration [17, 18]. Under laboratory conditions, a simple way to demonstrate that single-scattering events predominate in a scattering media is to dilute the concentration of particles in the sample by a chosen factor and observe whether the scattered light intensities at all scattering angles also drop by this same factor. If this is true, single scattering predominates in this sample. Therefore, under single-scattering conditions, by comparing the light scattering spectra of the original and the unbound nanoparticles, the concentration of the unbound nanoparticles can effectively be obtained. Combined with cell counting data, the average number of nanoparticles bound per cell can be derived. By following this procedure, cells labeled with immunotargeted nanoparticles can be effectively separated from unbound nanoparticles, as will be discussed later in this paper. Furthermore, multiple light scattering, which may influence the accuracy in deriving the concentration of nanoparticles, can also be avoided simply by measuring light scattering from a diluted suspension of unbound nanoparticles.

## 2. Method

### 2.1. Gold–silica nanoshell fabrication

Detailed description of the fabrication of gold–silica nanoshells can be found in [19]. Generally, spherical $SiO_2$ nanoparticles are synthesized using the Stöber method [20] and functionalized by immersing and boiling the $SiO_2$ nanoparticles with aminopropyl-triethoxysilane (APTES). Gold colloid is prepared as reported by Duff *et al* [21]. The functionalized silica cores are then seeded with concentrated gold colloid, which adsorbs onto the amine groups on the silica surface, to facilitate the growth of the gold shell. Next, nanoshells are grown by mixing a stock solution of $HAuCl_4$ with the seed particles under formaldehyde catalysis. During this process, gold is reduced onto the adsorbed gold colloid on the seed particle and will eventually form a continuous shell over the $SiO_2$ core. The growth of nanoshells is monitored using a UV–vis spectrophotometer (Varian Cary 300) and also by comparing the measured extinction spectra with the calculations from Mie theory; the particle size is further confirmed by using a scanning electron microscope (SEM). Mie theory is used to determine the absorption, as well as scattering and extinction coefficients, of nanoshells with a specific core radius and shell thickness. The concentration of the nanoshells can then be determined by relating the calculated extinction coefficient to the measured extinction from the spectrophotometer. Figure 1 shows the SEM images and the measured extinction spectra of nanoshells used in this study. In this paper, we refer to the size of a gold nanoshell by the notation $R\, r_1/r_2$ nm, where $r_1$ is the core radius in nanometers (nm) and $r_2$ is the overall particle radius in nanometers (nm). Then $(r_2 - r_1)$ is the thickness of the gold shell. Two different sized nanoshells are used in this study. According to Mie theory calculations and SEM images, the smaller nanoshell is $r_1 = 86 \pm 7$ nm and $r_2 = 111 \pm 10$ nm, which is shown as $R86 \pm 7/111 \pm 10$ nm; while the larger one

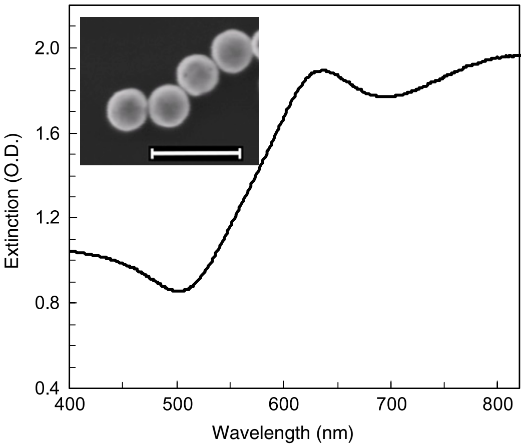

(a) Nanoshells R86±7/111±10nm

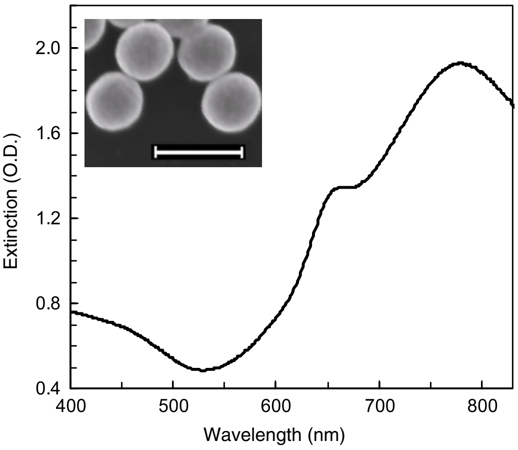

(b) Nanoshells R134±6/157±7nm

**Figure 1.** Measured extinction spectra of gold nanoshells. SEM images of the gold nanoshell are taken at 50 000× and the scale bar is 500 nm. (a) Nanoshells $R86 \pm 7/111 \pm 10$ nm. (b) Nanoshells $R134 \pm 6/157 \pm 7$ nm.

is $r_1 = 134 \pm 6$ nm and $r_2 = 157 \pm 7$ nm, which is displayed as $R134 \pm 6/157 \pm 7$ nm.

### 2.2. Preparation of OPSS-PEG-antibodies

Anti-HER2 (Labvision) or anti-IgG (Sigma) antibodies were tethered to nanoshell surfaces using bifunctional PEG linkers. Orthopyridyl disulfide-PEG-*n*-hydroxysuccinimide (MW 2000, OPSS-PEG-NHS, Shearwater Polymers, Nektar) was allowed to react with each antibody at 1:1 molar ratio in 100 mM sodium bicarbonate (pH 8.5) for 4–8 h, or overnight, on ice. The product was then dialyzed in 100 mM sodium bicarbonate for 2 h using a dialysis cassette with a molecular weight cutoff of 5000, to remove excess reagent. The product was then stored in frozen working aliquots at −20 °C [22, 23].

### 2.3. Nanoshell bioconjugation

The anti-HER2 (anti-IgG)/nanoshell conjugates were obtained by reacting the OPSS-PEG-antibodies with the nanoshells for 1 h at 4 °C. Additional nonspecific adsorption sites on the nanoshell surfaces were then blocked by reacting with PEG-SH (MW 5000) for an additional hour. The nanoshell bioconjugates were subsequently centrifuged so that excess reagent was removed. The nanoshell bioconjugates were then resuspended in phosphate buffered saline (PBS) to prepare for cell targeting. Concentration of nanoshell bioconjugates was determined to be ∼1–1.5 × $10^9$ particles $ml^{-1}$, with peak optical density of the extinction spectra at around 2, depending on the size of the particle.

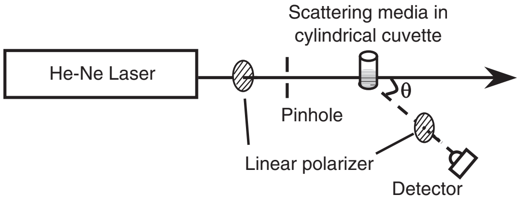

**Figure 2.** Schematic of experimental set-up of the goniometer for the angular-dependent light scattering study. The light from a 633 nm He–Ne laser is incident through the first polarizer onto a cylindrical cuvette containing the samples; the scattered light is then collected by a silicon detector rotating around the cuvette through the second polarizer.

### 2.4. Cell culture and incubation with anti-HER2 (anti-IgG)/gold nanoshell bioconjugates of SK-BR-3 breast cancer cells

HER2-positive human breast epithelial carcinoma SK-BR-3 cells (ATCC) were cultured in McCoy 5A growth medium containing 10% fetal bovine serum (FBS) and 1% antibiotics at 37 °C and 5% $CO_2$. The cells were grown in 25 $cm^2$ cell culture flasks to a concentration of ∼5–8 × $10^4$ cells $cm^{-2}$. Following three washes with PBS, anti-HER2 (anti-IgG)/nanoshell bioconjugates suspended in PBS were added to the cell culture flask together with 1% Bovine Serum Albumin (BSA) as a blocker to eliminate nonspecific interactions. The cells were then incubated with the nanoshell bioconjugates for one hour. After incubation, additional unbound nanoshell conjugates were collected using a pipette. The cells were then rinsed with PBS three times to ensure that all the unbound nanoshells were removed and collected. The rinsing PBS and unbound nanoshells were collected for light scattering measurements. Finally, the labeled cells were removed from the cell culture flask using trypsin-EDTA and resuspended in McCoy 5A growth medium for dark-field imaging and cell counting.

### 2.5. Polarized angular-dependent light scattering measurement

A schematic of the experimental set-up for the light scattering study is shown in figure 2, and details about it can be found in our previous publication [24]. The polarized angular-dependent light scattering spectra of gold nanoshell bioconjugates were studied using an automated goniometer. Light scattering has been shown to be sensitive to both the size and concentration of small particles. Furthermore, it has been proven that light scattering from surface-modified

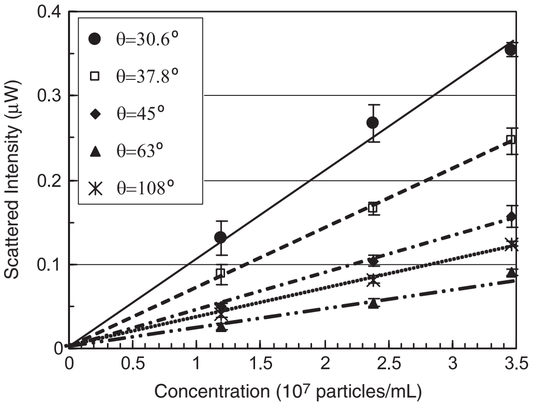

**Figure 3.** Scattered light intensity at different scattering angles showing a linear relationship between the light scattering signal and the concentration for nanoshell $R86 \pm 7/111 \pm 10$ nm. Error bars represent the standard deviation of three separate measurements.

nanoparticles can also be predicted by Mie theory [24–26]. Therefore, the concentration of gold nanoshell bioconjugates can be reliably derived from the light scattering phase function that we measured. We additionally conclude, for the aforementioned reasons, that the goniometer has effectively facilitated our semi-quantitative study and can thus be considered a promising tool with which to characterize the binding concentration of gold nanoshell bioconjugates to SK-BR-3 cells.

## 3. Results and discussion

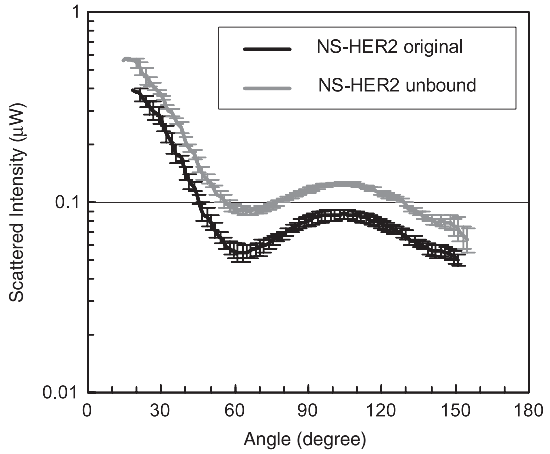

(a) Nanoshells R86±7/111±10nm

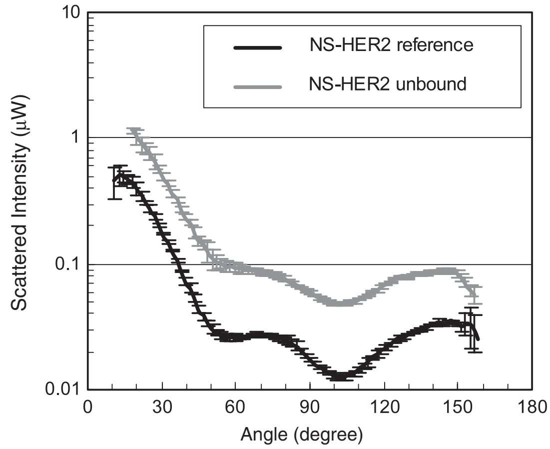

(b) Nanoshells R134±6/157±7nm

**Figure 4.** Parallel polarized angular-dependent light scattering measurements of reference and unbound anti-HER2/nanoshell bioconjugates: the concentration of unbound nanoshells can be derived by comparing the light scattering to that of the reference nanoshells. (a) NS $86 \pm 7/111 \pm 10$ nm. (b) NS $134 \pm 6/157 \pm 7$ nm. Error bars represent the standard deviation of three separate measurements for each sample.

To accomplish our goal of characterizing the number of nanoshells bound on each cancer cell, nanoshell bioconjugates with different concentrations were first prepared, and light scattering from these initial samples was compared. The light scattering study showed a significant linear relationship with the concentration for these samples, as shown in figure 3. This confirms the feasibility of using light scattering to characterize the concentration of unknown nanoshell bioconjugates. One of these diluted nanoshell samples, with known concentration, was then recorded as a standard reference, as shown in figures 4(a) and (b) (black solid curves). After cell targeting, the unbound nanoshell bioconjugates were collected and diluted for light scattering measurements. Once the polarized light scattering of both the unbound and reference nanoshell bioconjugates was obtained, the concentration of the unbound nanoshells could be derived by interpolating the scattered intensity between the lines in figure 3. Specifically, the total number of nanoshells bound to the cell could then be calculated using the volume and concentration data of the unbound nanoshells and the nanoshells originally added to the SK-BR-3 cells. After counting the cells, the number of nanoshells bound per cell could be determined, thus confirming the validity of our 'negative' approach, as referenced above. Figure 4 shows the parallel polarized light scattering from the reference and unbound gold nanoshells (anti-HER2 conjugated only) of different sizes. The number of anti-HER2 (anti-IgG)/nanoshells bound per cell is shown in table 1. The errors in table 1 represent the standard deviations of three separate measurements which come from the summation of the individual errors generated in the light scattering measurements and from cell counting. This data is also supported by the results from a previous study on the use of gold nanoshells for molecular imaging [8]. In that study, Loo and colleagues used nanoshells of $R120/155$ nm for cell labeling, and compared the intensity of dark-field microscopy images taken from different nanoshell-labeled configurations. The author's histogram analysis of the resulting dark-field images shows that nanoshell targeting of the HER2 receptor resulted in significantly greater average contrast values in the anti-HER2 group ($142 \pm 16$) compared with the anti-IgG group ($48 \pm 12$) and with the group lacking nanoshells ($26 \pm 4$) [8]. These results show an average of 5 times greater efficiency in anti-HER2 targeting than in anti-IgG targeting. This reinforces our semi-quantitative results of using the $R134 \pm 6/157 \pm$

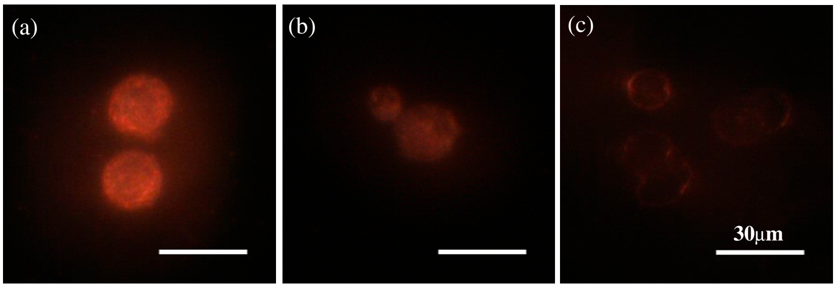

**Figure 5.** Dark-field microscopy images of SK-BR-3 cells with (a) anti-HER2/nanoshell targeting ($R86 \pm 7/111 \pm 10$ nm, specific), (b) anti-IgG/nanoshell targeting ($R86 \pm 7/111 \pm 10$ nm, nonspecific) and (c) without targeting. All images were taken under the same lighting conditions.

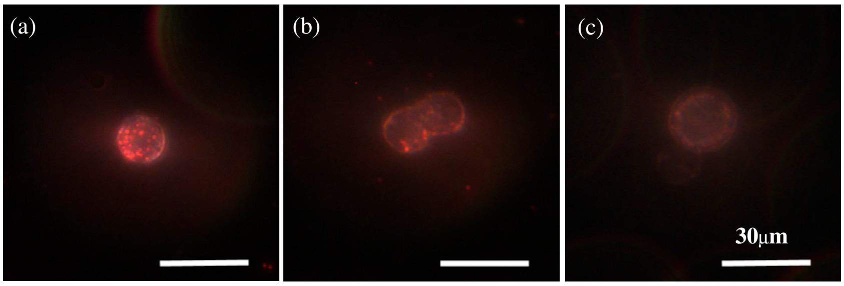

**Figure 6.** Dark-field microscopy images of SK-BR-3 cells with (a) anti-HER2/nanoshell targeting ($R134 \pm 6/157 \pm 7$ nm, specific), (b) anti-IgG/nanoshell targeting ($R134 \pm 6/157 \pm 7$ nm, nonspecific) and (c) without targeting. All images were taken under the same lighting conditions.

**Table 1.** Number of nanoshell bioconjugates bound per cell.

| No. of nanoshells per cell | NS $R86 \pm 7/111 \pm 10$ nm | NS $R134 \pm 6/157 \pm 7$ nm |
|---|---|---|
| Anti-HER2/NS | $1503 \pm 204$ | $883 \pm 101$ |
| Anti-IgG/NS | $90 \pm 11$ | $113 \pm 16$ |

7 nm nanoshells (which are similar in size as reported in [8]) to increase the nanoshell binding efficiency with anti-HER2 targeting. We have found that the anti-HER2 targeting is of the order of 5–9 times more efficient than the anti-IgG targeting for these specific nanoshells, as shown in table 1.

Images of anti-HER2 (anti-IgG)/gold nanoshell bioconjugate-targeted SK-BR-3 breast cancer cells were taken under dark-field microscopy, a type of imaging modality that is only sensitive to the scattered light of visualized objects. This makes dark-field microscopy very suitable for the imaging of biological cells and small particles, as well as for nanoparticle-labeled cells. Images were taken with a Zeiss Axioskop 2 Plus microscope equipped with a color CCD camera using a 40× objective. All images were taken using the same lighting conditions; more specifically, all same-sized nanoshell labeling had images taken under the same conditions. Figures 5 and 6 show the dark-field microscopy images of SK-BR-3 breast cancer cells labeled with anti-HER2 (anti-IgG)/gold nanoshell bioconjugates, as well as SK-BR-3 cells without any labeling. Based on the dark-field images, we can clearly see the difference in both specific (anti-HER2/gold nanoshell) and nonspecific (anti-IgG/gold nanoshell) labeled cells, compared to those cells without any nanoshell labeling. The cells with specific labeling demonstrate greater contrast under dark-field microscopy, due to the increase in targeted nanoshells [8]. This also supports our results on the number of nanoshell bioconjugates bound per cell as shown in table 1.

## 4. Conclusion

In conclusion, we have developed a new technique to semi-quantitatively characterize the binding concentration of nanoparticles to living cancer cells. We have labeled HER2-positive SK-BR-3 human breast cancer cells with gold nanoshells of different sizes, and semi-quantitatively compared the differences in anti-HER2 and anti-IgG conjugated nanoshell labeling. We have provided an easy and reliable method for semi-quantitatively determining the amount of immunotargeted nanoparticles that can be targeted to SK-BR-3 breast cancer cells. Unlike the previous methods which measure cells labeled with nanoparticles, this method only requires the measurement of scattered light from nanoshell bioconjugates and provides accurate information on the number of nanoparticles that actually bind on the cell surfaces. Following this method, multiple scattering effects can be avoided simply by measuring light scattering from the dilute suspension of unbound nanoshells. This study provides important information on characterizing cell labeling with immunotargeted plasmonic nanoparticles for diagnosis and therapeutic applications. As a generalized methodology, it can also be easily applied to studies of other scattering nanoparticles targeted to cells that overexpress other biomarkers.

## Acknowledgments

This work is supported by the Welch Foundation grant C-1598 to RAD, the Department of Defense Congressionally Directed Breast Cancer Research Program Era of Hope Scholar Award, the Center for Biological and Environmental Nanotechnology (CBEN) NSF NSEC grant 0118007, the National Institute of Health (NIH) grant R01CA109385-04, and the Gulf Coast Center for Computational Cancer Research. We would additionally like to thank Mr David Martin for his help with editing the manuscript.

## References

[1] Fujimoto J G 2003 *Nat. Biotechnol.* **21** 1361–7

[2] Lee T M, Oldenburg A L, Sitafalwalla S, Marks D L, Luo W, Toublan F J-J, Suslick K S and Boppart S A 2003 *Opt. Lett.* **28** 1546–8

[3] Palmer G M, Zhu C, Breslin T M, Xu F, Gilchrist K W and Ramanujam N 2003 *IEEE Trans. Biomed. Eng.* **50** 1233–42

[4] Sokolov K, Follen M, Aaron J, Pavlova I, Malpica A, Lotan R and Richartz-Kortum R 2003 *Cancer Res.* **63** 1999–2004

[5] Sokolov K *et al* 2003 *Technol. Cancer Res. Treatment* **2** 491–504

[6] El-Sayed I H, Huang X and El-Sayed M A 2005 *Nano Lett.* **5** 829–34

[7] Loo C, Lin A, Hirsch L, Lee M-H, Barton J, Halas N, West J and Drezek R 2004 *Technol. Cancer Res. Treatment* **3** 33–40

[8] Loo C, Hirsch L R, Lee M-H, Chang E, West J, Halas N and Drezek R 2005 *Opt. Lett.* **30** 1012–4

[9] Loo C, Lowery A, Halas N, West J and Drezek R 2005 *Nano Lett.* **5** 709–11

[10] Jackson J B, Westcott S L, Hirsch L R, West J L and Halas N J 2003 *Appl. Phys. Lett.* **82** 257–9

[11] Jackson J B and Halas N J 2004 *Proc. Natl Acad. Sci. USA* **101** 17930–5

[12] Huang X, El-Sayed I H, Qian W and El-Sayed M A 2006 *J. Am. Chem. Soc.* **128** 2115–20

[13] Stone J W, Sisco P N, Goldsmith E C, Baxter S C and Murphy C J 2007 *Nano Lett.* **7** 116–9

[14] Orendorff C J, Baxter S C, Goldsmith E C and Murphy C J 2005 *Nanotechnology* **16** 2601–5

[15] Chen J *et al* 2005 *Nano Lett.* **5** 473–7

[16] Weissleder R 2001 *Nat. Biotechnol.* **19** 316–7

[17] van de Hulst H C 1981 *Light Scattering by Small Particles* (New York: Dover) pp 5–6

[18] Bohren C and Huffman D R 1983 *Absorption and Scattering of Light by Small Particles* (New York: Wiley) p 9

[19] Oldenburg S J, Averitt R D, Westcott S L and Halas N J 1998 *Chem. Phys. Lett.* **288** 243–7

[20] Stober W and Fink A 1968 *J. Colloid Interface Sci.* **26** 62–6

[21] Duff D G and Baiker A 1993 *Langmuir* **9** 2301–9

[22] Hirsch L R, Jackson J B, Lee A, Halas N J and West J L 2003 *Anal. Chem.* **75** 2377–81

[23] Hirsch L R, Halas N J and West J L 2005 *Methods Mol. Biol.* **303** 101–12

[24] Fu K, Sun J, Lin A W H, Wang H, Halas N J and Drezek R A 2007 *Curr. Nanosci.* **3** 167–70

[25] Khlebtsov N G, Bogatyrev V A, Khlebtsov B N, Dykman L A and Englebienne P 2003 *Colloid. J.* **65** 622–35

[26] Khlebtsov N G 2004 *J. Quant. Spectrosc. Radiat. Transfer* **89** 143–53

# Near-Infrared Quantum Dot Contrast Agents for Fluorescence Tissue Imaging: A Phantom Study

Jiantang Sun[1, 3], Kun Fu[2, 3], Ming-Qiang Zhu[1], Lissett Bickford[1], Eric Post[4] and Rebekah Drezek[1, 2, *]

*[1]Departments of Bioengineering, [2]Electrical and Computer Engineering and [3]Rice Quantum Institute, Rice University, 6100 Main Street, Houston, TX 77005, USA; [4]Biomedical Engineering, Louisiana Tech University, 818 Nelson Avenue, Ruston, LA 71270, USA*

**Abstract:** Due to their small size and red-shifted excitation and emission bands, lead sulfide (PbS) near-infrared (NIR) quantum dots (QDs) are potentially promising optical contrast agents for *in vivo* tumor imaging applications. In this phantom-based study, we correlated PbS NIR QD concentrations to feasible imaging depths. A fluorescence imaging system (FIS) was used to acquire images of QD-filled tumor models, which were embedded in liquid tissue phantoms. For the lowest tested concentration of 200 nM, PbS-QD-filled tumor models could be imaged at a tissue phantom depth of 15 mm. Additionally, the FIS was used to compare the imaging potential of PbS QDs to quantum dots that fluoresce in the visible spectral range. Results indicated that tumor models with photons emitted in the NIR region can be imaged with less distortion than those with photons emitted in the visible spectrum. As the phantom thickness over the tumors was increased from 0 to 1.75 mm, the half-intensity widths of normalized fluorescence images produced by red QDs (acquired peak at ~645 nm) increased by ~300%; for NIR QDs (acquired peak at ~880 nm), the widths increased by ~140%. Due to the decreased scattering effect of the tissue phantoms in the NIR spectral range, the margins of PbS QD images were better defined than those of the corresponding red images.

**Key Words:** Near-infrared, quantum dot, fluorescence, optical imaging, phantom.

## 1. INTRODUCTION

A “therapeutic window” exists in the spectral region of 700 to 1200 nm which allows near-infrared (NIR) light to penetrate several centimeters into human tissue [1-4]. Recently, the development of various NIR fluorescence contrast agents has promoted the application of NIR fluorescence biomedical imaging techniques [4-8]. Among those strategies employing fluorescence contrast agents, the use of lead sulfide (PbS) NIR quantum dots (QDs) is expected to yield promising results for *in vivo* imaging applications. PbS QDs are nanometer-sized, core-shell semiconductor structures that possess a strong emission peak in the NIR region [6, 9, 10]. With specific surface-modification, the water solubility and biocompatibility of PbS QDs can be greatly enhanced [11]. Since the emission peak of these quantum dots can be easily tuned to the desired wavelength by tailoring the particle size, PbS QDs can provide great emission band flexibility for *in vivo* NIR tissue imaging applications [5, 6, 9, 11, 12].

Since the introduction of quantum dots in the late 1970s, numerous reports have been published that examine the use of these nanoparticles as fluorescence imaging contrast agents [6, 10, 12-15]. Compared to quantum dots that fluoresce in the visible spectral range, PbS NIR QDs have their own unique properties for *in vivo* deep tissue fluorescence imaging applications [2, 6, 9, 10, 16]. As reported in previous publications, for PbS QDs that have an emission peak at ~1010 nm, the average particle size is ~4 to 5 nm before surface modification; after surface modification, particles show no significant increase in size when observed by transmission electron microscopy (TEM) [9]. Therefore, it is believed that the relatively small size of PbS QDs will facilitate body clearance of these particles during clinical trials [17]. Moreover, the corresponding excitation spectrum of these QDs spans the range from visible to NIR [9, 11-12] and the emission peak of PbS QDs can be systematically tuned in the NIR spectral range. Thus, both the wide excitation band and the red-shifted emission peak provide flexibility in the choice of proper working wavelength regions; this will, in turn, avoid most of the effects of tissue autofluorescence [18, 19].

A bandpass excitation filter of 671 to 705 nm was selected for the depth-resolved tissue phantom experiments discussed below. This range avoids the major absorption peaks of intrinsic autofluorophores, and therefore permits improved illumination into the samples [18-21]. In this experiment, the fluorescence spectrum of the excited PbS QDs peaks at a wavelength of ~880 nm when acquired with a Maestro imaging system (CRi, Woburn, MA). Under these conditions, the NIR quantum dot signal can be easily distinguished from tissue autofluorescence background [18] and images with improved contrast can then be obtained. Furthermore, in comparison with visible QDs, the minimum absorption and scattering coefficients of tissue samples in the NIR region allow photons emitted from PbS QDs to propagate deeper into tissue [1, 2]. Images of PbS-QD-filled tumor models embedded in tissue phantoms also exhibit minimal blurring at tumor margins due to the reduced scattering effect.

We have previously shown the possibility of using bioconjugated PbS QDs as NIR contrast agents for targeted molecular imaging applications [22]. As a step towards *in vivo* tissue fluorescence screening using PbS NIR quantum dots and the Maestro imaging system, a tissue phantom study was carried out to identify and evaluate the imaging potential of these NIR nanocrystals and to acquire a basic understanding of the contrast agent concentrations required to obtain clear and acceptable images. Additionally, the imaging advantages of NIR QDs have been compared with QDs that fluoresce in the visible spectral range.

## 2. METHODS

### 2.1. NIR Quantum Dot Fabrication and Surface Modification

The lead sulfide NIR QDs used in this study were synthesized [9, 11, 12] and surface modified in accordance with methods presented in previous publications [6, 10, 11]. The NIR fluorescence peak of these PbS quantum dots can be tailored to the desired imaging wavelength range and optimized for the imaging system employed [9, 11].

### 2.2. Tissue Phantom and Tumor Models

Human tissue is a highly turbid media with strong absorption and scattering effects in the ultraviolet (UV) and visible spectral regions [1, 18, 23]. However, it is within the NIR wavelength region of 700 to 1200 nm where most biomolecular absorption coefficients reach their minimum values [1, 2, 5, 18, 24]. To study light propagation and distribution in human tissue, various phantoms have previously been developed that simulate tissue optical proper-

---

*Address correspondence to this author at the Department of Bioengineering, Rice University, 6100 Main Street, Houston, TX 77005, USA; Tel: (713) 348-3011; Fax: (713) 348-5877; E-mail: drezek@rice.edu

1573-4137/09 $55.00+.00

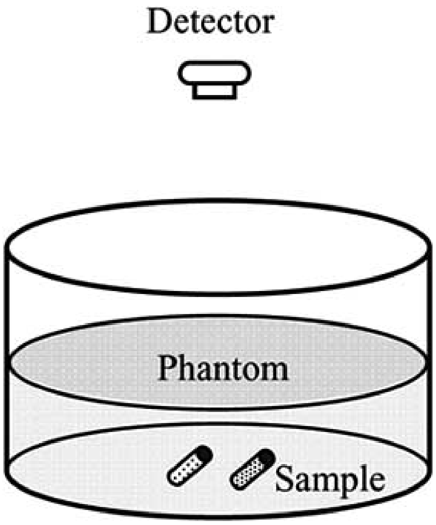

**Fig. (1).** Experimental tissue phantom setup (I).

ties within the visible and NIR spectral regions [23, 25]. In the following experiments, tissue phantoms composed of 1% Liposyn solutions (Abbot Labs, North Chicago, IL) were used to mimic the absorption and scattering properties of human breast tissue [23, 25-27].

Two types of experimental phantom setups were employed. First, different concentrations of PbS-QD filled cylindrical 20 × 8 mm glass vials were embedded in a 1% Liposyn phantom. By changing the volume of the Liposyn solution, tumors with different QD concentrations can be imaged at various phantom thicknesses (Fig. (**1**)). This procedure was used to provide insight into the possibility of using PbS QDs for deep tissue imaging, as well as impart a fundamental understanding of the contrast agent concentrations required for sufficient tumor image acquisition at various depths.

Second, a phantom-filled transparent container was placed above a 384-well microplate (Greiner Bio-one North America, Inc.) which has 3.7 × 3.7 mm square wells that were used to house quantum dot suspensions (see Fig. (**2**)). Two adjacent wells were filled, respectively, with CdSe/CdS red quantum dots and PbS NIR quantum dots of the same concentration (~1 μM) and same volume (100 μL/well). Using the Maestro imaging system, fluorescence images of tumor models with both the red QDs (acquired emission peak at ~645 nm) and the NIR QDs (acquired emission peak at ~880 nm) were analyzed. This procedure was used to obtain specific data about the blurring effect associated with using the tumor margin model for each type of QD, which was assessed by varying phantom thickness (Fig. (**2**)).

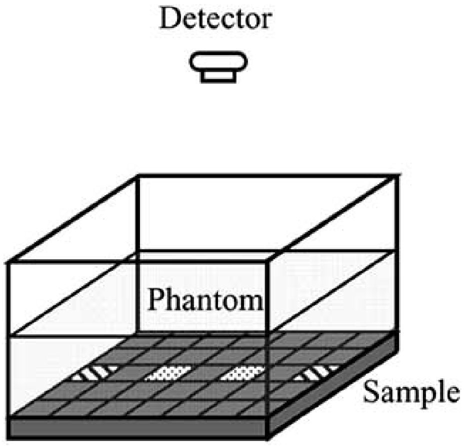

**Fig. (2).** Experimental tissue phantom setup (II).

The second phantom setup was used to simulate relatively small tumor tissue embedded close to superficial skin. To simultaneously image visible and NIR QDs, an excitation band of lower wavelengths was necessary. As a result of using lower wavelengths, however, the excitation photons could not penetrate deep into the tissue phantom. In addition, a strong autofluorescence background was associated with this excitation band. To minimize the influences of the excitation light, a superficial phantom setup was needed. Moreover, the 384-well microplate provided well-defined square geometries and sharp edges, which were necessary for the blurring-effect component of the study.

### 2.3. Fluorescence Image Acquisition and Processing

A Maestro imaging system equipped with proper filter sets (CRi, Woburn, MA) was used to acquire all the fluorescence images in this report. The working wavelength ranges of all the filters used were provided by the Maestro imaging system unless otherwise specified. Table **1** summarizes the filter sets that were used in the study. With the advantages of multispectral acquisition and quantitative data analysis, this system can provide improved imaging flexibility and sensitivity [28]. Therefore, the fluorescence signals from phantom autofluorescence, red QDs, and NIR QDs can be effectively separated from the stack of wavelength-resolved fluorescence images. To further evaluate the dimensions of the image of each square well of QDs, as described in the previous section (Fig. (**2**)), post-acquisition image processing was performed using MatLab codes.

**Table 1. Filter Sets Used in Study**

| | Set 1 | Set 2 | Set 3 |
|---|---|---|---|
| Excitation Filter | 575–605 nm<br>615–665 nm | 671–705 nm | 503–555 nm |
| Emission Filter | 700 nm longpass | 750 nm longpass | 600 nm longpass |

## 3. RESULTS

Four cylindrical 20 × 8 mm glass vials were filled with 0.2 μM, 0.4 μM, 1 μM, and 2 μM PbS quantum dots suspended in phosphate buffered saline (PBS), respectively. For the condition in which there was no phantom above these vials (see Fig. (**1**)), fluorescence images of all four samples were obtained under the exact same acquisition conditions using the fluorescence imaging system. The average signal intensity of the acquired images of each vial of QDs was then extracted using the Maestro image processing program. To assess the influences of acquisition time and quantum dot concentration on the average signal intensities, NIR fluorescence images were taken in a series and then processed. As shown in Fig. (**3a**) and Fig. (**3b**), the average QD image intensity increased linearly as the QD concentration increased. Additionally, the slope also increased linearly as the acquisition time increased for images obtained with acquisition times of 100 ms, 200 ms, and 300 ms. The imaging results show that these same quantum dot image intensities can be affected by the particular applied excitation band [11]. Specifically, Fig. (**3a**) and Fig. (**3b**) show the differences that result from variations in the excitation bands, since the same 700 nm longpass emission filter was utilized. An excitation band from 615 to 665 nm was used for Fig. (**3a**), whereas the corresponding excitation band for Fig. (**3b**) ranged from 575 to 605 nm.

To evaluate the PbS QD concentration needed for an acceptable image at different tissue depths, the thickness of the phantom above each NIR tumor model was systematically varied (Fig. (**1**)). For the visible and near-infrared spectral ranges, the wavelength-dependent reduced scattering coefficient of the 1% Liposyn tissue phantom, as shown in Fig. (**4**), was obtained from previous literature [26, 27, 29-

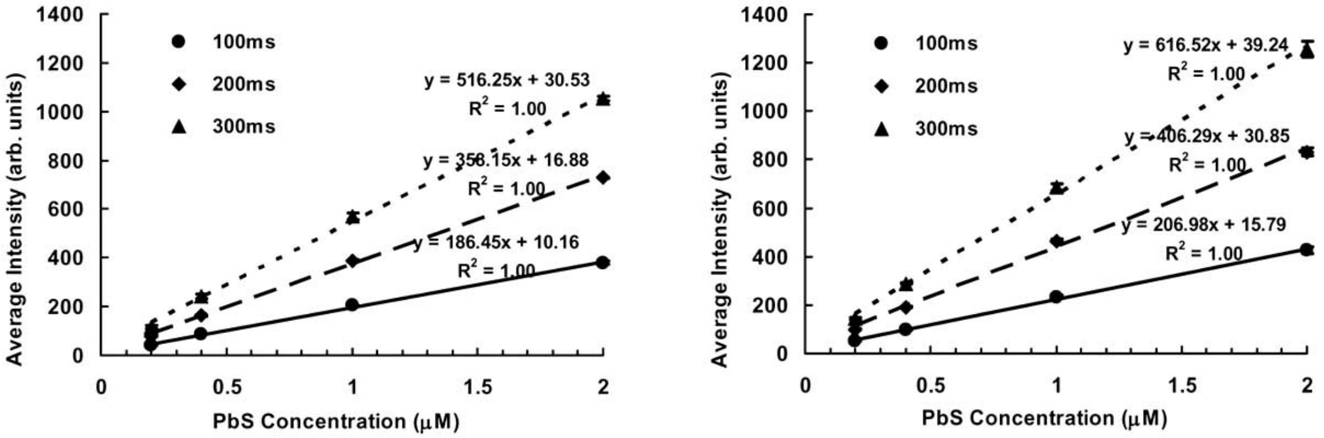

(a) (b)

**Fig. (3).** Average image intensities of PbS NIR QDs acquired with no phantom and a 700 nm longpass emission (Em) filter (**a**) Ex (excitation): 615–665 nm (**b**) Ex: 575–605 nm. (n=3).

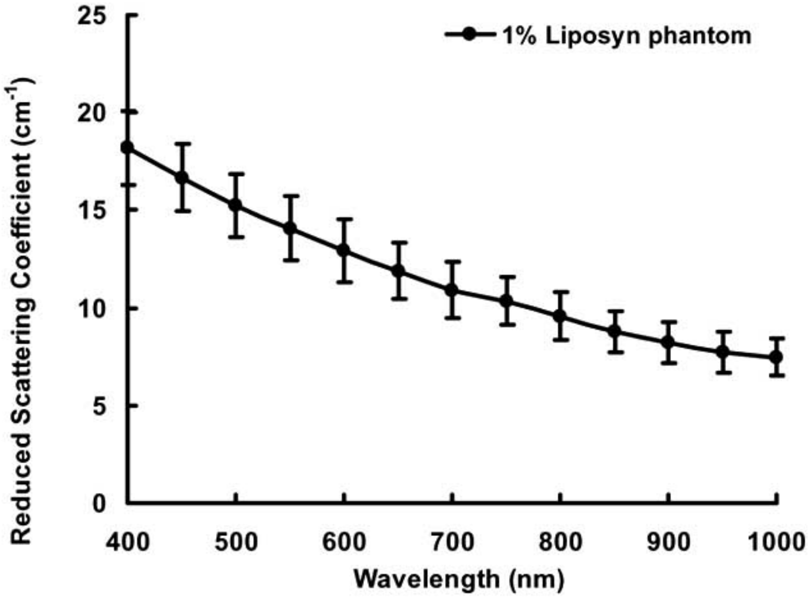

**Fig. (4).** Reduced scattering coefficient of 1% Liposyn tissue phantom.

31]. The corresponding absorption coefficient was dominated by water absorption, which varies from 0.001 to 0.3 $cm^{-1}$ [26, 29, 32]. To demonstrate potential *in vivo* tissue diagnostic applications, the imaging process was optimized by using a bandpass excitation filter of 671 to 705 nm (deep-red excitation filter) coupled with a 750 nm longpass emission filter (deep-red emission filter) to acquire the fluorescence images of PbS-QD-filled tumor models. Both the average QD image intensity and quality decreased with increasing phantom thickness. To assess image quality, the tumor-to-background ratio (TBR) was evaluated. Similar to that described by Adams *et al.* [33], TBR is defined as the ratio of the average tumor region intensity to the average background region intensity. A TBR threshold value of 1.22 was used to distinguish acceptable images from unacceptable ones. Clear fluorescence images (TBR>1.22) of both 1 μM and 2 μM quantum dot suspensions were obtained at a phantom thickness of 25 mm with an acquisition time of 900 ms. However, even with the same imaging conditions, a clear QD image (TBR>1.22) could only be acquired at a phantom thickness of less than 20 mm for the 0.4 μM quantum dots. As for the 0.2 μM QD tumor model, which has a similar order of magnitude of QD concentration as previous reports [34], reasonable images could not be obtained when the phantom was thicker than 15 mm. The normalized average QD image intensities at various concentrations are shown in Fig. (**5**). These normalized average image intensities were obtained by subtracting the average background region intensities from the average tumor region intensities. Although the maximum imaging depths for different concentrations of QDs vary considerably, their normalized average image intensities have the same decreasing trend when plotted as a function of phantom thickness (Fig. (**5**)).

To compare the imaging properties of visible quantum dots and near-infrared quantum dots, the second experimental phantom setup (see Fig. (**2**)), as described in the methods section, was employed. The normalized fluorescence spectra of both CdSe/CdS (red) and PbS (NIR) quantum dots obtained under the same excitation and imaging conditions are shown in Fig. (**6**). A green bandpass excitation filter of 503 to 555 nm and a 600 nm longpass filter were used in tandem to simultaneously obtain the fluorescence images of both types of quantum dots. After spectral unmixing [28], CdSe/CdS

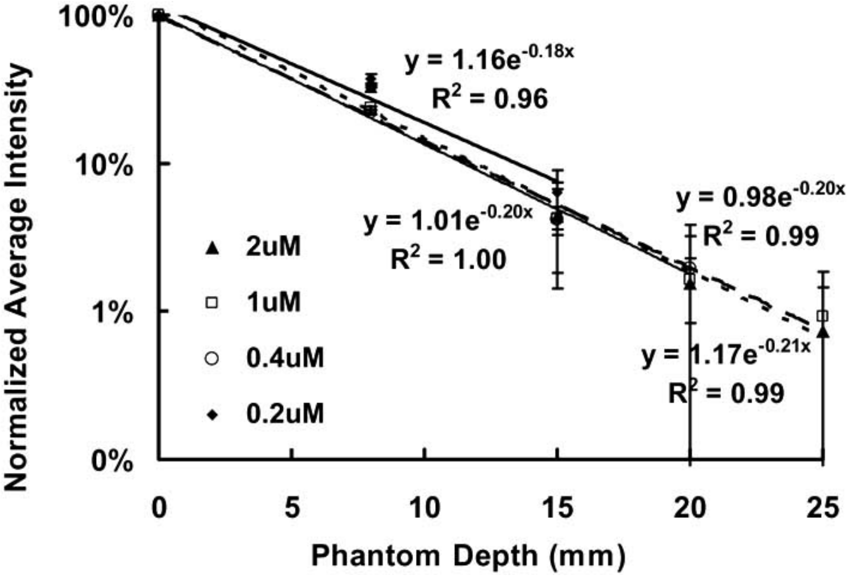

**Fig. (5).** Normalized average intensities of different concentrations of PbS NIR QDs versus phantom thickness (obtained with a bandpass excitation filter of 671 to 705 nm coupled with a 750 nm longpass emission filter, acquisition time: 900 ms) (n=3).

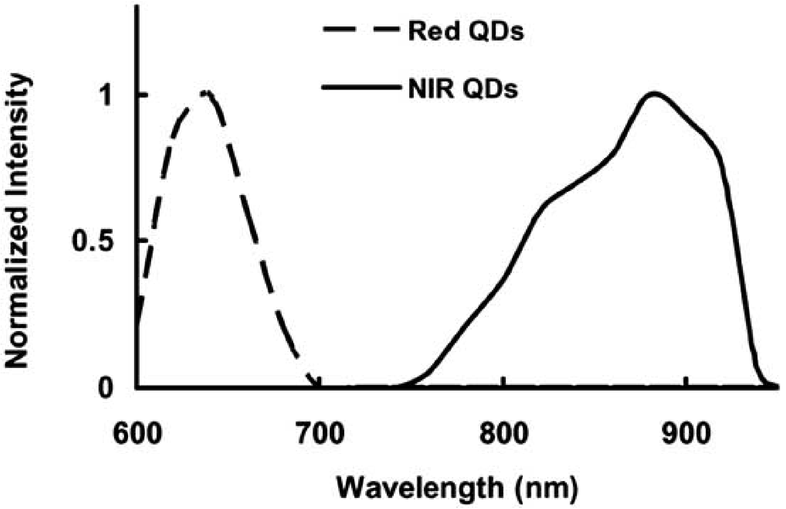

**Fig. (6).** Normalized fluorescence spectra of CdSe/CdS (red) and PbS (NIR) quantum dots (obtained with Maestro Imaging System).

(red) and PbS (NIR) quantum dot images can be isolated from each other as well as from the phantom autofluorescence. A series of fluorescence images, after the spectral unmixing processing for both the red and the NIR Qds, is shown in Fig. (**7**). Initially, when there are no phantoms above the QDs, clear images of the square wells can be acquired, and the image size of these wells is almost exactly the same for both types of QDs. As the phantom thickness gradually increased, the average intensities decreased for both kinds of quantum dot fluorescence images, a finding which supports previous results. Notably, the images of the red QDs are larger and less distinct than those of the NIR QDs, even though they are obtained under the same conditions. To compare the enlarging and blurring effects of these two different types of QDs as a function of the phantom thickness, a section line was drawn for each fluorescence square well in Fig. (**7**). This section line goes directly through the center of every square well image and splits it into two equal rectangular parts. The normalized fluorescence intensity along the section line was plotted as a function of pixel position. Based on the data in Fig. (**8**), it can be observed that when the phantom thickness increased from 0 to 1.75 mm, the half-intensity widths of the red-QD-filled wells expanded by ~300%, while those of the NIR-QD-filled wells expanded by only ~140%. Moreover, the margins of the NIR-QD-filled wells were better defined than the margins of the red-QD-filled wells.

## 4. DISCUSSION AND CONCLUSIONS

The phantom results indicate that lead sulfide NIR quantum dots possess essential properties for fluorescence imaging applications. Increasing either the concentration of QDs used or the image acquisition time can enhance collected image intensities. When PbS QDs are directly excited with yellow or red light and imaged with the Maestro system, clear fluorescence images can be obtained with the lowest tested concentration of 200 nM and the lowest tested acquisition time of 100 ms. In addition to these two factors, PbS QD fluorescence image intensity is also influenced by the excitation band used (Fig. (**3**)). Since tissue absorption and scattering effects are heavily wavelength-dependent [2, 18, 23], an optimized excitation band should be carefully chosen before PbS QDs are used for NIR tissue imaging applications.

For the results shown in Fig. (**5**), clear NIR images were obtained with the lowest tested PbS QD concentration of 200 nM at the phantom depth of 15 mm when imaged with an acquisition time of 900 ms and deep-red excitation and emission filter sets. The red-

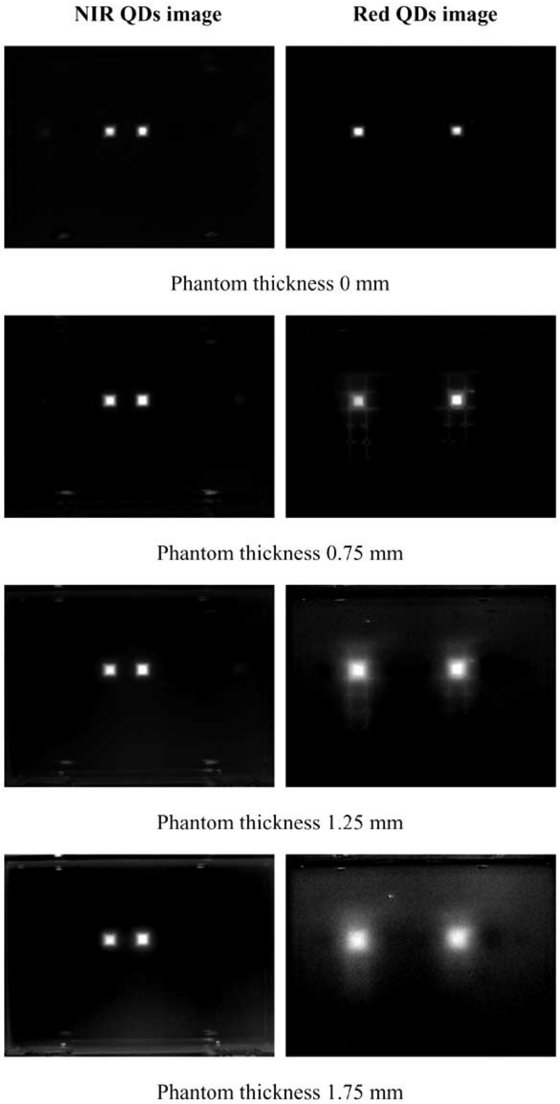

**Fig. (7).** Phantom thickness-resolved florescence images of NIR QDs (spectral unmixed, left column) and red QDs (spectral unmixed, right column).

shifted excitation band of 671 to 705 nm maximizes the illumination penetration depth into the tissue phantom, and the 750 nm longpass emission filter eliminates most phantom autofluorescence. Both factors improved image quality at relatively deep tissue sites. The optimal excitation and emission wavelengths for PbS QD fluorescence imaging were determined using a step-by-step approach. First, the emission wavelengths were selected to be in the NIR region. This region was selected because both tissue absorption and scattering coefficients are minimal in the NIR. For our imaging system, and with the use of PbS QD contrast agents, the optimal emission band of 750 to 950 nm was chosen. Then the optimal excitation wavelengths were selected based on the aforementioned emission band. There were three excitation filters available: one with an excitation band of 575 to 605 nm, a second with 615 to 665 nm, and a third with 671 to 705 nm. The 575 to 605 nm filter was eliminated because it induced a strong autofluorescence background. Although tissue phantom autofluorescence induced by the 615 to 665 and 671 to 705 nm filters were similar to each other, the 671 to 705 nm excitation band resulted in less tissue scattering. The optimal excitation wavelength range of 671 to 705 nm was finally chosen in conjunction with the optimal emission band of 750 to 950 nm. As shown in Fig. (**5**), although the QD concentration and the imaging depth vary over a wide region, the normalized average image intensity for each assessed concentration possesses the same variable trend with respect to the corresponding increase in tissue phantom depth.

Another advantage of using PbS QDs for tissue imaging applications is their red-shifted emission wavelengths in the NIR region. As previously reported, tissue absorbs and scatters NIR light less than UV or visible light [2, 26, 35]. Therefore, most of the NIR emission photons from PbS QDs will pass through the phantom with only a few scattering events and be detected by the camera [1, 19, 36]. This reduced scattering effect will potentially result in an important property of NIR QD imaging: improved margin delineation.

The ability to obtain better-confined tumor images significantly impacts both cancer diagnosis and surgery [37-40]. Currently, surgeons excise both the suspected malignant tumor tissue and the benign tissue surrounding the tumor site to ensure elimination of cancer cells. Aside from causing the patient pain and suffering, this procedure requires extensive recovery time [37-40]. However, if the tumor could be imaged with improved clarity during surgery, for example, with the potential help of bioconjugated PbS NIR QDs, the required tissue excision would be greatly reduced, with promising benefits for both patients and physicians [37-40].

As shown in Fig. (**7**), as the phantom thickness increases, the images of the NIR-QD-filled square wells demonstrate better-

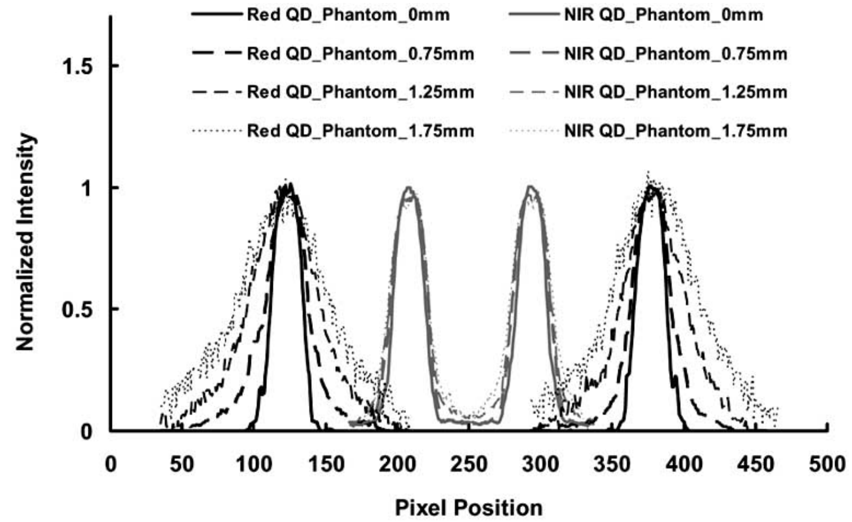

**Fig. (8).** Normalized fluorescence intensity of red and NIR QDs at various phantom depths versus pixel position along section line.

defined margins than those of the red-QD-filled wells. In addition, the images of the red wells with a 1.75 mm phantom are much larger than their initial images taken without a phantom, even though both were obtained under the same imaging conditions. In contrast, the corresponding images of the NIR wells are similar in size regardless of phantom presence. It is believed that the wavelength-dependent phantom optical properties may be one of the most important factors that result in these different red and NIR images.

Although the experimental results shown in Fig. (**7**) are promising, there may be concerns about the green excitation band (503 to 555 nm) used and the maximum imaging depth achieved. A green filter was used for excitation in order to simultaneously excite both the red and NIR QDs and compare the images obtained under the same conditions. With the fluorescence imaging system, a red (615 to 665 nm) or deep-red (671 to 705 nm) excitation band is typically recommended for deep tissue PbS NIR QD imaging because this band maximizes illumination penetration and, simultaneously, avoids the excitation of most tissue autofluorescence. The maximum phantom depth of 1.75 mm was applied in the above experiments in order to obtain reasonable images from both the red and NIR QDs at that depth.

In conclusion, a phantom study in which PbS QDs are used as contrast agents for fluorescence imaging applications is reported. The experiments show that lead sulfide NIR quantum dots possess enhanced fluorescence imaging properties. When collected with the deep-red excitation and emission filter set, adequate NIR QD fluorescence images were obtained with a maximum tissue phantom thickness of 15 mm at a particle concentration of 200 nM and an acquisition time of 900 ms. Furthermore, the improved tumor margin confinement images obtained from PbS QD contrast agents, as explained above, are indicative of their promising surgical applications for future *in vivo* tumor detection.

## ACKNOWLEDGEMENTS

The authors thank financial support for this work by the Department of Defense Congressionally Directed Breast Cancer Research Program Era of Hope Scholar Award, the Center for Biological and Environmental Nanotechnology (EEC-0118007 and EEC-0647452), and the Gulf Coast Center for Computational Cancer Research. We thank Mr. David Martin for his editing assistance.

## ABBREVIATIONS

PbS = lead sulfide
NIR = near-infrared
QDs = quantum dots
FIS = fluorescence imaging system
TEM = transmission electron microscopy
UV = ultraviolet
PBS = phosphate buffered saline
TBR = tumor-to-background ratio
Em = emission
Ex = excitation

## REFERENCES

[1] Wilson, B.C.; Jacques, S.L. Optical reflectance and transmittance of tissue: principles and application. *IEEE J. Quantum Electron.*, **1990**, *26*, 2186.

[2] Cheong, W.F.; Prahl, S.A.; Welch, A.J. Review of the optical properties of biological tissues. *IEEE J. Quantum Electron.*, **1990**, *26*, 2166.

[3] Pogue, B.W.; Geimer, S.; McBride, T.O.; Jiang, S.; Osterberg, U.L.; Paulsen, K.D. Three-dimensional simulation of near-infrared diffusion in tissue: boundary condition and geometry analysis for finite-element image reconstruction. *Appl. Opt.*, **2001**, *40*, 588.

[4] Kim, S.; Lim, Y.T.; Soltesz, E.G.; De Grand, A.M.; Lee, J.; Nakayama, A.; Parker, J.A.; Mihaljevic, T.; Laurence, R.G.; Dor, D.M.; Cohn, L.H.; Bawendi, M.G.; Frangioni, J.V. Near-infrared fluorescent type II quantum dots for sentinel lymph node mapping. *Nat. Biotechnol.*, **2004**, *22*, 93.

[5] Cai, W.; Shin, D.-W.; Chen, K.; Gheysens, O.; Cao, Q.; Wang, S.X.; Gambhir, S.S.; Chen, X. Peptide-labeled near-infrared quantum dots for imaging tumor vasculature in living subjects. *Nano Lett.*, **2006**, *6*, 669.

[6] Michalet, X.; Pinaud, F.F.; Bentolila, L.A.; Tsay, J.M.; Doose, S.; Li, J.J.; Sundaresan, G.; Wu, A.M.; Gambhir, S.S.; Weiss, S. Quantum dots for live cells, in vivo imaging, and diagnostics. *Science*, **2005**, *307*, 538.

[7] Lin, A.W.H.; Lewinski, N.A.; West, J.L.; Halas, N.J.; Drezek, R.A. Optically tunable nanoparticle contrast agents for early cancer detection: model-based analysis of gold nanoshells. *J. Biomed. Opt.*, **2005**, *10*, 064035.

[8] Zuluaga, A.F.; Drezek, R.; Collier, T.; Lotan, R.; Follen, M.; Richards-Kortum, R. Contrast agents for confocal microscopy: how simple chemicals affect confocal images of normal and cancer cells in suspension. *J. Biomed. Opt.*, **2002**, *7*, 398.

[9] Hines, M.A.; Scholes, G.D. Colloidal PbS nanocrystals with size-tunable near-infrared emission: observation of post-synthesis self-narrowing of the particle size distribution. *Adv. Mater.*, **2003**, *15*, 1844.

[10] Medintz, I.L.; Uyeda, H.T.; Goldman, E.R.; Mattoussi, H. Quantum dot bioconjugates for imaging, labeling and sensing. *Nat. Mater.*, **2005**, 435.

[11] Zhu, M.-Q.; Chang, E.; Sun, J.; Drezek, R.A. Surface modification and functionalization of semiconductor quantum dots through reactive coating of silanes in toluene. *J. Mater. Chem.*, **2007**, *17*, 800.

[12] Bakueva, L.; Gorelikov, I.; Musikhin, S.; Zhao, X.S.; Sargent, E.H.; Kumacheva, E. PbS quantum dots with stable efficient luminescence in the near-IR spectral range. *Adv. Mater.*, **2004**, *16*, 926.

[13] Clapp, A.R.; Medintz, I.L.; Mauro, M.; Fisher, B.R.; Bawendi, M.G.; Mattoussi, H. Fluorescence resonance energy transfer between quantum dot donors and dye-labeled protein acceptors. *J. Am. Chem. Soc.*, **2004**, *126*, 301.

[14] Bruchez, M.J.; Moronne, M.; Gin, P.; Weiss, S.; Alivisatos, A.P. Semiconductor nanocrystals as fluorescent biological labels. *Science*, **1998**, *281*, 2013.

[15] Medintz, I.L.; Clapp, A.R.; Mattoussi, H.; Goldman, E.R.; Fisher, B.; Mauro, J.M. Self-assembled nanoscale biosensors based on quantum dot FRET donors. *Nat. Mater.*, **2003**, *2*, 630.

[16] Choi, J.; Wolf, M.; Toronov, V.; Wolf, U.; Polzonetti, C.; Hueber, D.; Safonova, L.P.; Gupta, R.; Michalos, A.; Mantulin, W.; Gratton, E. Noninvasive determination of the optical properties of adult brain: near-infrared spectroscopy approach. *J. Biomed. Opt.*, **2004**, *9*, 22114(14).

[17] Zimmer, J.P.; Kim, S.-W.; Ohnishi, S.; Tanaka, E.; Frangioni, J.V.; Bawendi, M.G. Size series of small indium arsenide-zinc selenide core-shell nanocrystals and their application to in vivo imaging. *J. Am. Chem. Soc.*, **2006**, *128*, 2526.

[18] Richards-Kortum, R.; Sevick-Muraca, E. Quantitative optical spectroscopy for tissue diagnosis. *Annu. Rev. Phys. Chem.*, **1996**, *47*, 555.

[19] Mycek, M.-A.; Pogue, B.W. *Handbook of Biomedical Fluorescence*, Marcel Dekker, Inc.: New York, Basel, **2003**.

[20] Drezek, R.; Sokolov, K.; Utzinger, U.; Boiko, I.; Malpica, A.; Follen, M.; Richards-Kortum, R. Understanding the contributions of NADH and collagen to cervical tissue fluorescence spectra: Modeling, measurements, and imliications. *J. Biomed. Opt.*, **2001**, *6*, 385.

[21] Georgakoudi, I.; Jacobson, B.C.; Mueller, M.G.; Sheets, E.E.; Badizadegan, K.; Carr-Locke, D.L.; Crum, C.P.; Boone, C.W.; Dasari, R.R.; Van Dam, J.; Feld, M.S. NAD(P)H and collagen as in vivo quantitative fluorescent biomarkers of epithelial precancerous changes. *Cancer Res.*, **2002**, *62*, 682.

[22] Sun, J.; Zhu, M.-Q.; Fu, K.; Lewinski, N.; Drezek, R.A. Lead sulfide near-infrared quantum dot bioconjugates for targeted molecular imaging. *Int. J Nanomed.*, **2007**, *2*, 235.

[23] Pogue, B.W.; Patterson, M.S. Review of tissue simulating phantoms for optical spectroscopy, imaging and dosimetry. *J. Biomed. Opt.*, **2006**, *11*, 041102.

[24] Torricelli, A.; Pifferi, A.; Taroni, P.; Giambattistelli, E.; Cubeddu, R. *In vivo* optical characterization of human tissues from 610 to 1010 nm by time-resolved reflectance spectroscopy. *Phys. Med. Biol.*, **2001**, *46*, 2227.

[25] Joshi, A.; Bangerth, W.; Sevick-Muraca, E.M. Non-contact fluorescence optical tomography with scanning patterned illumination. *Opt. Express*, **2006**; 14(14): 6516.

[26] Jacques, S. *Oregon Medical Laser Center, Portland, OR. Available at: http://omlc.ogi.edu/spectra/intralipid*, **1998**.

[27] Hebden, J.C.; Veenstra, H.; Dehghani, H.; Hillman, E.M.C.; Schweiger, M.; Arridge, S.R.; Delpy, D.T. Three-dimensional time-resolved optical tomography of a conical breast phantom. *Appl. Opt.*, **2001**, *40*, 3278.

[28] *User manual for Maestro 2.2 (CRi)*, CRi, **2006**.

[29] Xu, H.; Patterson, M.S. Determination of the optical properties of tissue-simulating phantoms from interstitial frequency domain measurements of relative fluence and phase difference. *Opt. Express*, **2006**, *14*, 6485.

[30] Godavarty, A.; Eppstein, M.J.; Zhang, C.; Theru, A.; Thompson, A.B.; Gurfinkel, M.; Sevick-Muraca, E.M. Fluorescence-enhanced optical imaging in large tissue volumes using a gain-modulated ICCD camera. *Phys. Med. Biol.*, **2003**, *48*, 1701.

[31] van Staveren, H.J.; Moes, C.J.M.; van Marle, J.; Prahl, S.A.; van Gemert, M.J.C. Light scattering in intralipid-10% in the wavelength range of 400-1100 nm. *Appl. Opt.*, **1991**, *30*, 4507.

[32] Palmer, K.F.; Williams, D. Optical properties of water in the near infrared. *J. Opt. Soc. Am.*, **1974**, *64*, 1107.

[33] Adams, K.E.; Ke, S.; Kwon, S.; Liang, F.; Fan, Z.; Lu, Y.; Hirschi, K.; Mawad, M.E.; Barry, M.A.; Sevick-Muraca, E.M. Comparison of visible and near-infrared wavelength-excitable fluorescent dyes for molecular imaging of cancer. *J. Biomed. Opt.*, **2007**, *12*, 024017.

[34] Chu, T.C.; Shieh, F.; Lavery, L.A.; Levy, M.; Richards-Kortum, R.; Korgel, B.A.; Ellington, A.D. Labeling tumor cells with fluorescent nanocrystal-aptamer bioconjugates. *Biosens. Bioelectron.* **2006**, *21*, 1859.

[35] Qu, J.; MacAulay, C.; Lam, S.; Palcic, B. Optical properties of normal and carcinomatous bronchial tissue. *Appl. Opt.*, **1994**, *33*, 7397.

[36] Wang, L.-H.; Jacques, S.L.; Zheng, L.-Q. MCML-Monte Carlo modeling of photon transport in multi-layered tissues. *Comput. Meth. Prog. Biol.*, **1995**, *47*, 131.

[37] Kappas, A.M.; Roukos, D.H. Quality of surgery determinant for outcome of patient with gastric cancer. *Ann. Surg. Oncol.*, **2002**, *9*, 828.

[38] Haka, A.S.; Volynskaya, Z.; Gardecki, J.A.; Nazemi, J.; Lyons, J.; Hicks, D.; Fitzmaurice, M.; Dasari, R.; Crowe, J.P.; Feld, M.S. *In vivo* margin assessment during partial mastectomy breast surgery using Raman spectroscopy. *Cancer Res.*, **2006**, *66*, 3317.

[39] Haglund, M.M.; Hochman, D.W.; Spence, A.M.; Berger, M.S. Enhanced optical imaging of rat gliomas tumor margins. *Neurosurgery*, **1994**, *35*, 930.

[40] McDougal, W.S. Conservative surgery for penile cancer: what surgical excision margins are needed to achieve oncologic control? *Nat. Clin. Pract. Oncol.*, **2006**, *3*, 132.

Received: July 23, 2008 Revised: October 20, 2008 Accepted: December 03, 2008

# Photothermal bubbles as optical scattering probes for imaging living cells

**Aims:** We propose and have experimentally studied a new method with improved sensitivity and specificity of imaging of living cells. **Method:** Intracellular photothermal bubbles generated around gold nanoparticles (NPs) and their clusters were proposed as optical scattering probes for the amplification of scattered light. **Results:** Microbubbles generated around gold spheres and shells with 10-ns 532-nm laser pulses in individual living cells (leukemia cells, lung and squamous carcinoma cancer cells) have amplified optical side scattering up to 1800-times relative to that of intracellular gold NPs, and without detectable damage to host cells. We explain the discovered optical amplification by the endocytosis-mediated clustering of NPs in cells, and by the selective generation of microbubbles (that do not disrupt the host cell) around these clusters at minimal levels of laser pulse fluence. **Conclusions:** Photothermal bubbles generated around laser-activated gold NPs may significantly improve the sensitivity and specificity of cell imaging, and can be considered as a new type of optical cellular probes.

**KEYWORDS: bubble, cell, endocytosis, gold nanoparticle, photothermal, scattering**

Ekaterina Y Hleb[1],
Ying Hu[2], Rebekah A
Drezek[2], Jason H Hafner[3]
& Dmitri O Lapotko[1,3†]
*†Author for correspondence:*
*[1]AV Lykov Heat & Mass*
*Transfer Institute,*
*15 P Brovko Street,*
*Minsk, 220072, Belarus*
*[2]Department of*
*Bioengineering, Rice University,*
*Houston, TX 77005, USA*
*[3]Department of Physics &*
*Astronomy, Rice University,*
*Houston, TX 77005, USA*
*Tel: +375 172 842 483;*
*Fax: +375 172 842 483;*
*E-mail: dmitri.lapotko@*
*rice.edu*

The excellent optical absorption and scattering properties of metal nanoparticles (NPs), combined with their safety and functionality of selective targeting, have stimulated their cytometric and imaging applications as cellular and molecular probes [1]. Gold NPs are the safest imaging nanomaterial [2,3], and their optical properties can be adjusted through their shape and size [2–8]. Functionalized gold NPs can be delivered to target molecules located in the cellular membrane, and potentially to the cytoplasm and nuclei without compromising cell physiology [9,10]. Optical scattering with NPs as cellular probes [11–15] has been applied for microscopy, flow cytometry and endoscopy by coupling strongly scattering NPs with target endogenous molecules, whose scattering properties are too weak for imaging. Results have shown the strong potential of gold NPs as optical probes. Scattered optical signals can be detected *in vivo* and *in situ*. In comparison with fluorescent probes, gold NPs are less toxic and have higher photodamage thresholds. However, gold NPs as optical scattering probes do not provide high sensitivity and specificity at the cellular and molecular levels, especially when being used in a highly heterogeneous environment, which is typical for *in vivo* application. Cellular components provide a strong scattering background. The optical energy that is scattered by NPs depends strongly on the particle's diameter (the sixth power), which requires an increase of probe size by hundreds of nanometers to improve sensitivity. However, this complicates the delivery of the NPs into the cells because biological factors limit the maximal diameter of NPs that can be delivered into living cells by 100 nm for cytoplasm, and by 20 nm for nuclei [9,10]. The scattering efficiency of small single NPs may be relatively low compared with background scattering from endogenous cellular components. Therefore, the cell level scattering imaging (especially for intracellular targets) requires a significant increase in the sensitivity and in the specificity, although without an increase of NP dimensions and laser fluence to avoid photodamage to the cell.

A further increase in the sensitivity of the imaging methods that use NPs as probes may be achieved by using the photothermal (PT) properties of NPs and the secondary phenomena of laser–NP interactions such as thermal diffusion, resulting in heating of the surrounding volume, pressure waves and bubble generation owing to media vaporization [16–18]. The combination of PT-imaging techniques [19–22] with the optical properties of metal NPs has shown promising results in optical microscopy, with a detection limit for probe size of several nanometers and a high signal-to-noise ratio [23,24]. However, optical refractive index gradients (even produced by heated metal NPs) are relatively small, and thus limit the sensitivity and temporal resolution of PT imaging.

10.2217/17435889.3.6.797 © 2008 Future Medicine Ltd *Nanomedicine* (2008) 3(6), 797–812 ISSN 1743-5889

Furthermore the PT methods require increasing the laser-induced temperature for better sensitivity, and this may cause thermal damage to the probe (or target molecule, cell and organ), and also to collateral cells and tissues [25,26]. If the energy is concentrated in too short laser pulses, the risk of optical damage of the probe or cell also increases [27,28].

To be applied for the analysis of single living cells and even molecules, optical scattering methods require a significant increase in sensitivity, although they are attractive owing to their safety, speed and universal applicability. We have proposed a new imaging method based upon using vapor bubbles as optical cellular probes. This approach uses the most universal and natural PT and scattering processes through the amplification of optical scattering with vapor bubbles generated around light-absorbing NPs. The generation of PT bubbles (PTBs) in living tissues is a well-known phenomenon [29–33], but the bubbles were considered to be a damaging factor to the cells. Based on this the bubbles in living cells were detected optically to monitor cell damage [34–36]. As a result, laser-induced intracellular bubbles were not yet considered as cellular-imaging probes, despite their excellent optical scattering properties and high imaging potential, as was demonstrated in other applications [37–43]. Despite the inherent disruptive nature of the bubbles, it has been experimentally determined that optically or acoustically generated bubbles of a small size may not damage the cells [44–47].

In this article, we have used previous knowledge on the scattering imaging of cells, PTB generation around light-absorbing NPs and NP internalization by living cells to propose the new concept of optical cellular probes and scattering imaging. This concept is based on our hypothesis that the PTBs generated around a gold NP in a living cell may significantly amplify the optical scattering without damage to the host cell.

## Methods & materials

### Principle of nanocluster–PTB intracellular amplification of optical signals

The optical scattering signal (S) (Figure 1A) from metal NPs and their clusters is generated through plasmon resonance. The scattering-signal amplitude increases with the probe (NP) diameter to the sixth power. Clustering of small NPs inside the cell [48] increases the total diameter of the scattering probe and over-rides the biological limitation on the maximum diameter of NPs for intracellular delivery. Further amplification of scattering requires an increase in probe diameter and incident optical energy; both parameters are limited for living cells. For this reason, we suggest two mechanisms for increasing optical scattering from intracellular NP probes without damage to cells:

- Small NPs are delivered selectively to the target cells and are internalized through the mechanism of endocytosis, and are concentrated into

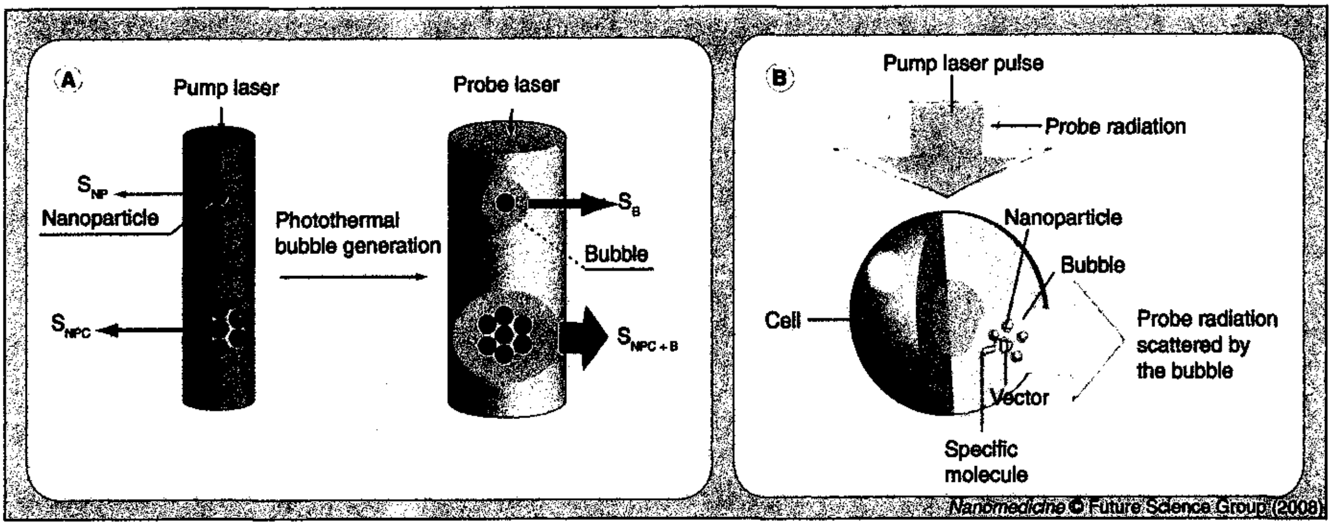

**Figure 1. The principle of amplification of optical scattering and its application for cell imaging. (A)** Nanoparticle (NP) cluster–photothermal bubble (PTB) mechanism of amplification of optical scattering from gold NPs: amplitude of optical S can be increased to $S_{NPC}$ through formation of the NP cluster, and can be further increased to $S_B$ through generating the transient vapor bubble around the NP or NP cluster, resulting in the maximal signal $S_{NPC+B}$. **(B)** The principle *PTB imaging of living cells:* short pump pulse induces a transient intracellular PTB around the molecule-associated NP cluster; scattering of probe laser beam by PTB forms an optical signal.
S: Signal.

the clusters in cellular endosomes. NP clustering as a result of endocytosis were previously studied by our group in detail [48–51]. Additionally, the formation of NP clusters during endocytosis was also experimentally verified by other researchers [52,53]. We define a cluster as a group of tightly packed NPs, with the dimensions spanning 2–50 times the size of the NP;

- Exposure of the cell containing NP clusters to a short laser pulse at the plasmon resonance wavelength of NPs would generate vapor PTBs with larger diameters than those of NP clusters and single NPs, and with high refractive index gradients at the vapor–liquid boundary, thus further increasing optical scattering.

We have previously verified that NP clusters provide more efficient generation of PTBs at lower levels of laser pulse fluencies [48–51,54,55]. For this reason, we do not consider the detailed mechanism of clustering, which is beyond the scope of this current work and can be found in the cited publications. Also, in our previous experimental experience, we have found that the pump wavelength for PT excitation of NP clusters does not differ dramatically from that for single NPs: clusters mainly broaden the absorbance spectrum rather than shift it. Apart from the pump laser beam that is used to generate PTBs, the auxiliary probe laser can be used for optical scattering. The wavelength of the probe laser can be optimized to enable the increase of probe laser fluence (and hence the amplitude of scattered light) without causing damage to the cell. This mechanism of optical amplification is universal, and depends on the properties of gold NPs and laser parameters. It depends less on the cell properties, so that PTB generation can be controlled precisely through the laser and NP parameters.

Optical intracellular amplification can be realized in any living cell where an NP cluster is formed (FIGURE 1B), with irradiation of the cell with pump and probe laser pulses at different wavelengths. The pump pulse generates the bubble and the probe laser provides the scattered signal. An additional advantage of the PTB is its 'on-demand' nature; it does not exist before or after the pump laser pulse. During its nano-to-microsecond lifetime, the PTB can be detected in specific time domains. This would allow the imaging of several PTBs with different lifetimes associated with different molecular targets, and would improve the signal-to-noise ratio relative to the *in vivo* background that may be highly scattering.

## Samples: nanoparticles, cells & their targeting

We have used two types of gold NPs, because gold NPs are the safest for living cells among all nanomaterials and minimally disturb cell physiology. Previously, we have studied the cytotoxicity of gold NPs and their conjugates during NP internalization and endocytotic clustering, and no significant suppression of cell viability was found [48–50]. The nontoxic nature of gold NPs has also been confirmed in many independent studies. However, detailed study of this subject is beyond the scope of this current work, and can be found in several reviews [2,3]. Silica/gold nanoshells (NSs) with a diameter of 170 nm and absorption maximum in the near-infrared (760 nm) range were prepared as described in [56]. Gold spheres with a diameter of 30 nm and the peak absorbance at 530 nm were obtained from Ted Pella, Inc. (#15706, Redding, CA, USA). Extinction spectra of all used NPs were verified with a spectrophotometer (USB 650 Red Tide, Ocean Optics Inc., Dunedin, FL, USA). Three types of tumor cells were used: K562 (leukemia CD33-positive blast cells) and two solid tumor cells, Hep-2C and A549, highly expressing the EGF receptor. All those cells represent different cancers (leukemia, squamous cell carcinoma and lung cancer, respectively), and are of interest in terms of cancer diagnostics and treatment.

NP clusters were formed in cells through nonspecific binding of NPs to the cell membrane and nonspecific endocytotic concentration of the NPs in endosomal compartments. Internalization and clustering of gold NPs into large compact aggregates was previously studied by our group [48–50] and others [52,53]; therefore, we have previously verified clustering protocols. The cells were incubated in the media RPMI 1640 at 37°C for 60 min with 20% (volume) suspension of the NPs at a concentration of $10^9$ NP/ml. This stimulated nonspecific endocytosis of the NPs, and their consequent clustering in endosomal compartments. After preparation, the samples were immediately used in the experiments at room temperature.

## PTB generation & optical detection

We have used a PT microscope previously developed by our group [57] for the generation, imaging and measurement of PTBs in individual cells and in suspensions of NPs [48–51,58–61]. PTBs were generated with a single 10-ns focused laser pulse at 532 nm (Laser LS-2132, Lotis

TII, Minsk, Belarus). This pulse length was short enough compared with the characteristic time of thermal diffusion so that the bubbles could be generated effectively at a submicrometer scale, yet also long enough to ensure that no optical breakdown or two-photon optical absorption would occur. Our recent studies of the PT properties of gold nanorods, NSs and nanospheres have shown that this wavelength (532 nm) is efficient for the excitation of plasmon resonances in NPs under relatively high laser fluencies [62], which is required for PTB generation. In particular, for a gold NS, the laser fluence threshold of PTB generation was several times lower at 532 nm, compared with that at 760 nm. Pulse fluence was varied by rotating Glan prism in the path of a laser beam. Pulse fluence was obtained by measuring pulse energy with a calibrated meter (Ophir PE10-SH, Ophir Optronics, Ltd, Israel), and by measuring the actual pump beam diameter on the sample plane with a CCD image detector (Luca DL-658M, Andor Technology, Ireland). Each individual cell (100 cells for each sample) was irradiated one by one with a single focused laser pulse of the same fluence. PTB generation in NP suspensions was realized by sequential exposure to the laser pulse of the different areas of the suspension.

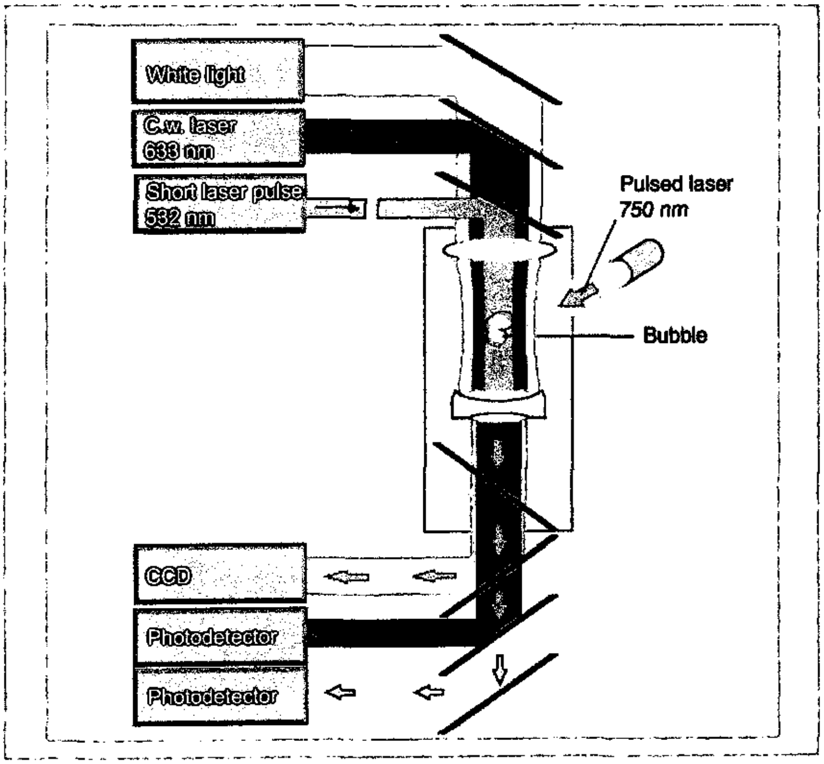

**Figure 2. Block diagram of the experimental set-up: light delivery and collection.** Bubble generation with laser pulse (532 nm), bubble detection with thermal lens method (continuous probe laser is registered with photodetector) and with side-scattering imaging: probe pulse was delivered though the optical fiber and was imaged with a digital camera and registered with a photodetector.
CCD: Charge-coupled camera; c.w.: Continuous wave laser.

PTBs were imaged with an optical side-scattering time-resolved technique, and were also independently monitored with the thermal lens method described by us previously [57,58]. Time–response of the PTB was registered with a continuous probe beam at 633 nm (Figure 2). This type of signal enables PTB dynamics to be monitored, and its lifetime to be measured. Any PTB-related change of the media's refractive index causes a shift of the probe beam phase that influences beam intensity in the input of the photodetector (PDA10A, Thorlabs Inc., Newton, NJ, USA). Electrical output of the photodetector was acquired as a time–response measurement by a high-speed digitizer (Bordo-211, Auris Ltd, Minsk, Belarus) and, in the case of the PTB, this response has a specific negative symmetrical pattern so that the PTB could be distinguished from other optical signals during sample irradiation with the pump laser pulse. Time-resolved side-scattering images of the PTBs were obtained with a pulsed probe laser beam with a wavelength of 750 nm and duration of 10 ns (LT-2211 Ti-Sa laser, Lotis TII). The low-fluence probe pulse was delayed relatively to the pump pulse for 150 ns, thus allowing the detection of the developed PTB (Figure 2). The probe beam was directed into the sample at an angle of approximately 80°, which was optimized to detect scattered signals from gold NPs. Probe pulse scattered by NPs, NP clusters or PTBs was collected with a 60× objective (NA 0.4), and was imaged with a CCD camera. The delay and duration of the probe pulse provided time-resolved imaging without the need for a high-speed camera.

Integral scattered light was also registered with an additional photodetector (PDA55, Thorlabs Inc.) so as to independantly measure the amplitude of the scattered light (Figure 2). The electrical output signal of the photodetector was acquired as a time–response measurement by a high-speed digitizer (Bordo-211, Auris Ltd, Minsk, Belarus), and its maximal amplitude was referred to as the amplitude of integral scattered optical signal.

Using these three optical techniques simultaneously enabled us to detect and monitor the generation of the PTB and to confirm that the main pump laser-induced phenomenon was, in fact, the generation of a vapor bubble around light-absorbing NPs.

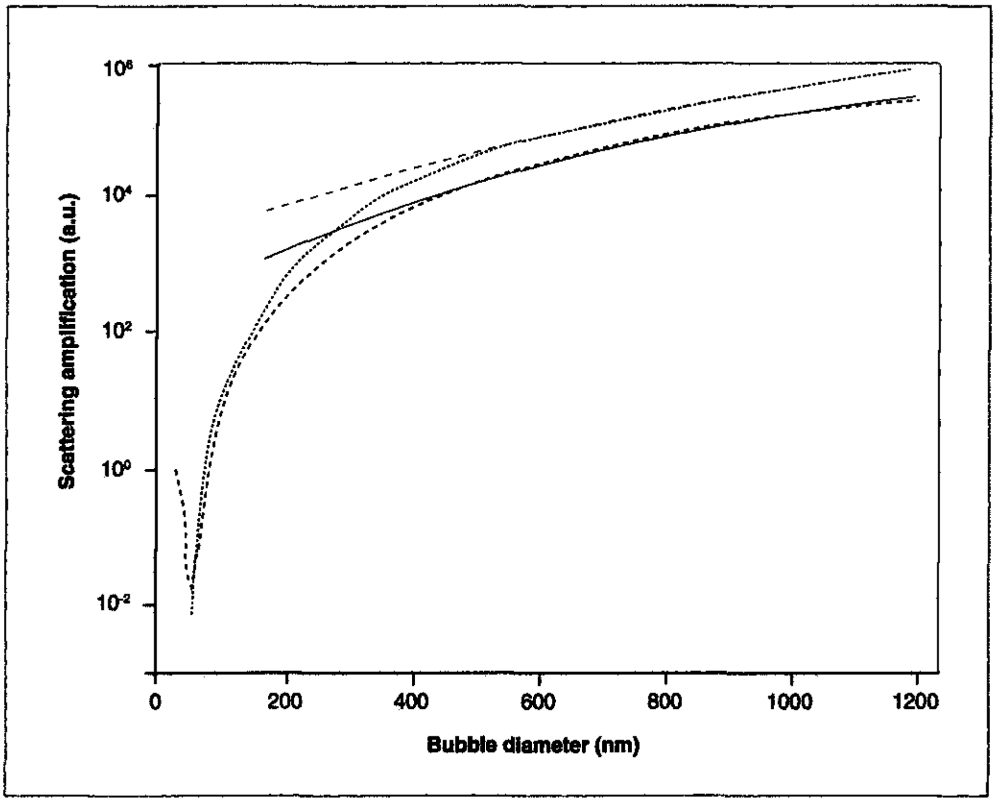

**Figure 3. Theoretical modeling of the amplification of optical side scattering by the air bubble surrounding a 30-nm gold sphere and a 170-nm silica-gold shell as a function of the bubble diameter.** The amplitudes of scattered light were normalized by those for a 30-nm gold sphere (without the bubble) so to demonstrate the bubble effect and are shown for 633 nm (short dash: for gold sphere; solid: for silica-gold nanoshell) and 750 nm (dot: for gold sphere; long dash: for silica-gold nanoshell).

## Results

### ☐ Modeling optical scattering from a bubble versus NP

The theoretical modeling of light scattering from bubbles generated around gold NPs is based on a Mie simulation code developed for multilayer concentric spheres. Subject to general limitations of Mie calculations, the assumptions made here are that NPs and bubbles are rigidly spherical in shape; bubbles are perfectly centered on NPs and the illumination is along a plane wave.

Owing to the nonabsorbent nature of the bubbles, the scattering cross-section ($C_{sca}$) is an effective figure of measurement for their optical properties. The differential scattering cross-section, $dC_{sca}/d\Omega$, is defined as the time-averaged energy projected into a unit solid angle, $d\Omega$, at a direction, $\hat{\Omega}$. It is expressed in terms of scattered irradiance, $I_s$, incident irradiance, $I_i$, and distance, $r$, from the center of the sphere to the detector:

$$\frac{dC_{sca}}{d\Omega} = r^2 \frac{I_s}{I_i}$$

By integrating over all solid angles, $\Omega$, one obtains the $C_{sca}$, which, from the definition above, is also equal to the percentage of scattered power in all directions with respect to the incident power multiplied by $r^2$. Therefore, given $C_{sca}$ and $r$, the percentage of total scattered power can be obtained. Based on Mie coefficients $a_n$ and $b_n$ derived from the aforementioned code, $C_{sca}$ can be calculated by [47]:

$$C_{sca} = \frac{2\pi}{k^2} \sum_{n=1}^{\infty} (2n + 1)(|a_n|^2 + |b_n|^2)$$

where $k$ is the wave number in the surrounding medium and $n$ is the summation index terminated at some $N_{max}$. The detector $r$ can be estimated from the experimental setup.

FIGURE 3 plots the relative levels of total scattered power for a gold sphere with a diameter of 30 nm and a silica–gold NS with an outer diameter of 170 nm and a gold-layer thickness of 8 nm, each NP surrounded by the single air bubble suspended in water. To demonstrate the amplification effect of the bubble, the data were normalized by that for a single 30-nm gold NP without a surrounding bubble. Of note is the general trend of increase in scattering against PTB radius. This can be understood qualitatively from Rayleigh scattering, which states that the scattering intensity is proportional to $d^6/\lambda^4$, where $d$ is the particle diameter and $\lambda$ is the wavelength, provided that $d$ is smaller than $\lambda$. Compared with the scattering from the NPs, PTBs could potentially produce many orders of magnitude amplification in scattering intensity. As air bubbles grow larger, the effect of the particles enclosed diminishes, as can be seen on the 30-nm NP curves versus the 170-nm NS curves. For example, the scattering from a 600-nm bubble that encloses a 30-nm gold NP, and a 600-nm bubble that encloses a 170-nm gold NS gives a nearly identical value of scattered signal. When the bubble becomes comparable to or larger than a particular wavelength, this growth slows down significantly.

The modeling results obtained predict better scattering efficacy of the bubble compared with NPs, mainly owing to the increased diameter of the bubble. A probe of such a large diameter (up to 1 μm) cannot be delivered into the cell without compromising its viability, although it can be temporally generated in the cell for a short time, and possibly without causing damage to the cell.

## ■ Experimental results for water suspensions of NPs

Clustering of 30-nm NPs in water after adding 20% acetone was verified by optical scattering microscopy (Figure 4), and by comparing the extinction spectra of the suspensions (not shown). Clustering of NPs has caused an apparent broadening of the spectrum compared with that of nonclustered (single) NP suspensions. NP clusters were resuspended in water before the study commenced. We have obtained images of optical probe pulses scattered by single NPs (Figure 4A) and by NP clusters (Figure 4B) in the suspensions, and have measured local pixel amplitudes (Table 1). Also, we measured the amplitudes of integral scattered signals using a photodetector in parallel with a CCD camera (Figure 4D & E). Clustering of NPs has increased the amplitude of scattered light, as can be seen by comparing the images and corresponding integral signals in Figure 4A & D (single NPs) and Figure 4B & E (NP clusters). The optical amplification effect was quantified by normalizing the averaged amplitude values of the NP clusters' scattered signals (Table 1) with values obtained from the suspension of single NPs. In our experiment, the clustering of NPs has amplified the scattering by a factor of 2.3–2.4, which can be explained by the increased diameter of the clusters relative to those of the single NPs (30 nm). The values obtained for optical amplification were relatively small compared with what was expected from cluster size versus NP size increase, and from the six-power dependence of the scattering cross-section of the NP upon its size. This discrepancy might have been caused by the spatial averaging of a scattered signal by the photodetector and image sensor over the sample area, which was larger than the cluster size. Because the registered signal delivers the cumulative effect from a specific

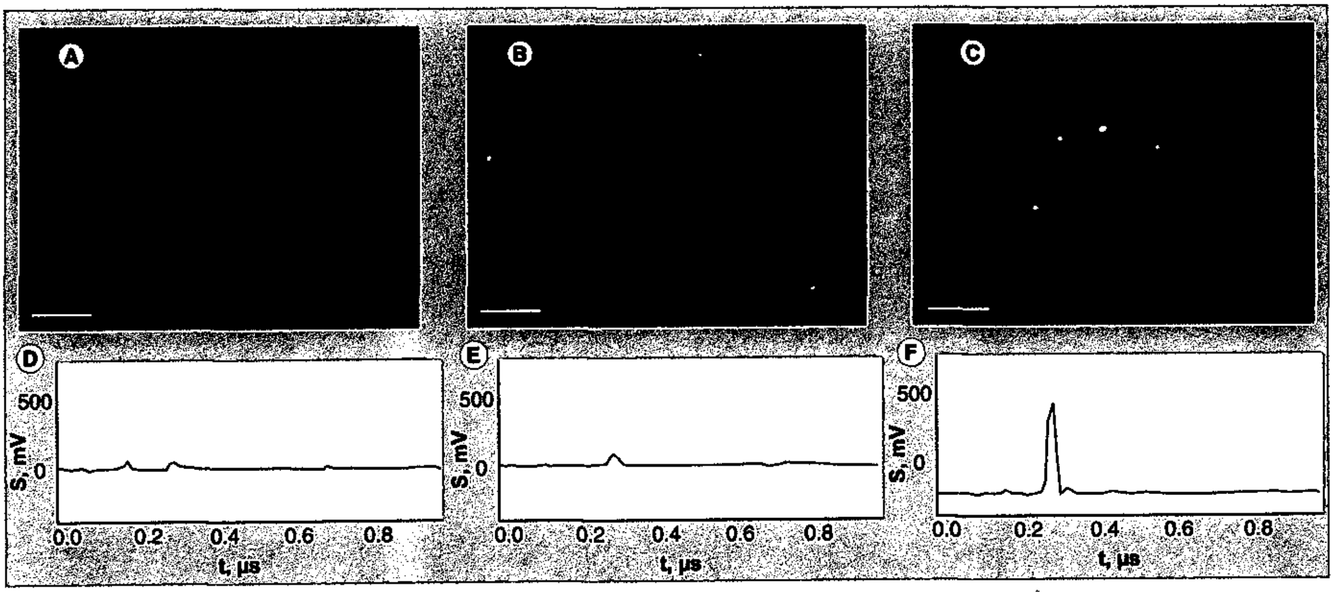

**Figure 4. Optical detection of side scattering of the probe laser pulse by gold nanoparticles and photothermal bubbles.** **(A–C)** Time-resolved images and **(D–F)** integral optical signals of the scattered probe pulse (750 nm, 10 ns). **(A & D)** Suspensions of 30-nm gold nanoparticles (NPs) with pump (532 nm, 10 ns) and probe laser pulses (at 150-ns delay time to pump pulse) applied (no photothermal bubbles were observed). **(B & E)** Suspension of the clusters of 30-nm gold NPs with no pump pulse applied or **(C & F)** with the pump pulse applied at a fluence of 0.45 J/cm². Scale bar: 10 μm.

Table 1. Averaged amplitudes of the scattered signals, obtained with a single probe optical pulse (750 nm, 10 ns) for a water suspension of 30-nm nanoparticles, their clusters and photothermal bubbles.

| Source of optical scattered signal | Single NP suspension/ amplification factor | Suspension of NP clusters/ amplification factor | PTBs around single NPs/ amplification factor | PTBs around NP clusters/amplification factor |
|---|---|---|---|---|
| Image (pixel amplitude, counts) | 231 ± 91/1.0 | 522 ± 289/2.3 | 220 ± 82/1.0<br>(no bubbles) | 10780 ± 2876/47.6 |
| Integral signal (mV) | 21 ± 7/1.0 | 50 ± 12/2.4 | 20 ± 7/1.0<br>(no bubbles) | 700 ± 120/33.3 |

*NP: Nanoparticle; PTB: Photothermal bubble.*

area (~2 μm² for the image sensor and 3–4 μm² for the integral scattering detector), the registered amplitudes of optical scattering increased more slowly than did the scattering from a cluster versus a single NP.

Next, the suspensions of NPs and their clusters were exposed to a single 10-ns pump laser pulse at 532 nm with a fluence of 0.45 J/cm². Exposure of the suspension of single nonclustered NPs to this laser pulse caused no change either in the scattered image (not shown) or in the integral signal. FIGURE 4D shows the two signals: the first peak is for the pump pulse and the second peak is for the probe pulse. The amplitude of the scattered probe pulse did not change (TABLE 1). When the suspension of NP clusters was exposed to the same pump pulse, we observed bright images of the PTBs (FIGURE 4C), with significantly increased image pixel amplitudes. The amplitude of the integral scattered signal has also increased (FIGURE 4F shows the pump- and probe-pulse signals). When considering a relatively rare spatial location of the clusters (their concentration was significantly lower than that for single NPs) and the single pump-pulse irradiation mode, we assume that single PTBs were generated and observed around single NP clusters. Comparing FIGURE 4B (clusters) with FIGURE 4C (PTBs), we have found far fewer PTBs (only four) than the clusters shown in FIGURE 4B. This can be explained by the strong dependence of PTB generation threshold fluence on cluster size: only the largest NP clusters have yielded PTBs. This is in line with our previous results in which the dependence of PTB generation threshold fluence on NP size and clustering was studied in detail [48-50]. Amplification of the scattered signal by PTBs after normalizing the image pixel amplitudes and the integral signal amplitude by the corresponding values obtained for single NPs was 47.6 (local amplification) according to images of individual bubbles, and 33.3 (averaged amplification) for the area probed with the photodetector (TABLE 1).

PTB generation was monitored independently and simultaneously with a thermal lens method. The signal detected (PT response) yielded a bubble-specific symmetrical shape (FIGURE 5B). PT response was obtained with an additional continuous probe laser at 633 nm, which was additionally registered by another photodetector. Its time course shows bubble expansion and collapse, and provides an estimation of bubble lifetime. In the case of NP cluster suspensions, we have detected a bubble-specific response (FIGURE 5B) with a duration of 250 ns. This bubble lifetime is longer than the delay of 150 ns of the probe pulse relative to the pump laser pulse, confirming that the images obtained with the delayed probe pulse (FIGURE 4C) were formed by PTBs. Also, the PT response obtained from the single-NP suspension (FIGURE 5A) under exposure to an equal pump-laser pulse showed no PTBs, which explains the absence of amplification of scattered light in single NP suspension. We gradually increased pump laser fluence until the PTBs were detectible in the single NP suspension; this level was approximately 17 J/cm². This fluence is significantly higher than the one applied to the NP clusters (0.45 J/cm²), which shows the difference between single NPs and their clusters in terms of PTB generation.

The results obtained clearly show that PTBs significantly amplify optical scattering, and that amplification with PTBs has a threshold nature: at a given fluence level of the pump laser pulse, no bubbles were generated around single NPs and there was no amplification of optical scattering from single NPs, while bubbles were generated around NP clusters at the same laser fluence. This demonstrated the selectivity of optical amplification with PTBs, which have provided almost 48-fold amplification of optical scattering amplitude around NP clusters only.

## ■ Scattering by PTBs in living cancer cells

The cluster–bubble mechanism of amplification of optical scattering was studied experimentally in three types of living cancer cells *in vitro*. NP

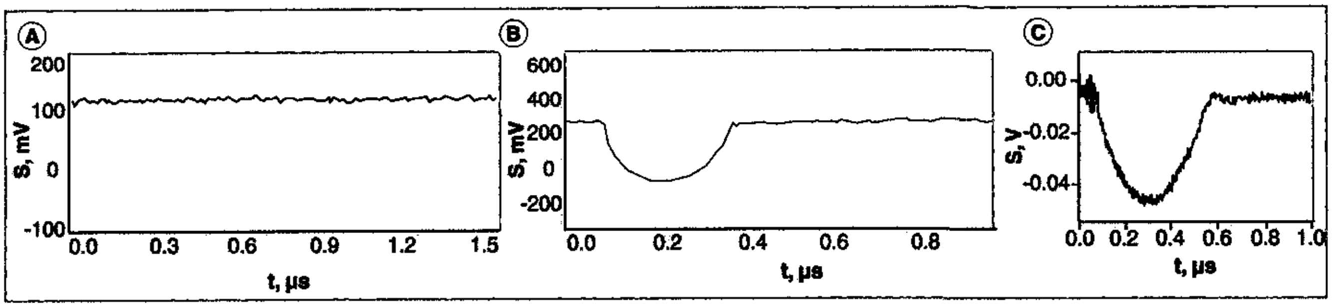

**Figure 5. Photothermal responses obtained from gold nanoparticles and photothermal bubbles.** Thermal lens signals (photothermal responses) obtained during exposure of the samples to a single 10-ns pulse at 532 nm: **(A)** suspension of 30-nm spherical gold nanoparticles (NPs; no bubble); **(B)** suspension of clusters of the same NPs; bubble duration 250 ns; **(C)** individual K562 cell treated with 30-nm gold NPs; bubble duration 380 ns.

clusters were formed in living cells by using nonspecific endocytosis. The suspensions (K562 leukemia-type cells) and monolayers (A549 and Hep-2C cells) of living cells were studied through the amplitude measurements of the integrally scattered signals from individual cells. Signals were obtained for intact, NP-treated and NP- and pump laser-treated cells. Gold 30-nm spheres were used in these experiments. All laser treatments and measurements were performed for individual cells and data were obtained for 150 cells in each population. Generation of the PTB in each individual cell was monitored simultaneously by the thermal lens method as in the aforementioned experiments with NP suspensions. This enabled the interpretation of the scattered signal for each cell during its exposure to the pump laser pulse: scattered signals were attributed to NP clusters when the PT response obtained independently from the same cell

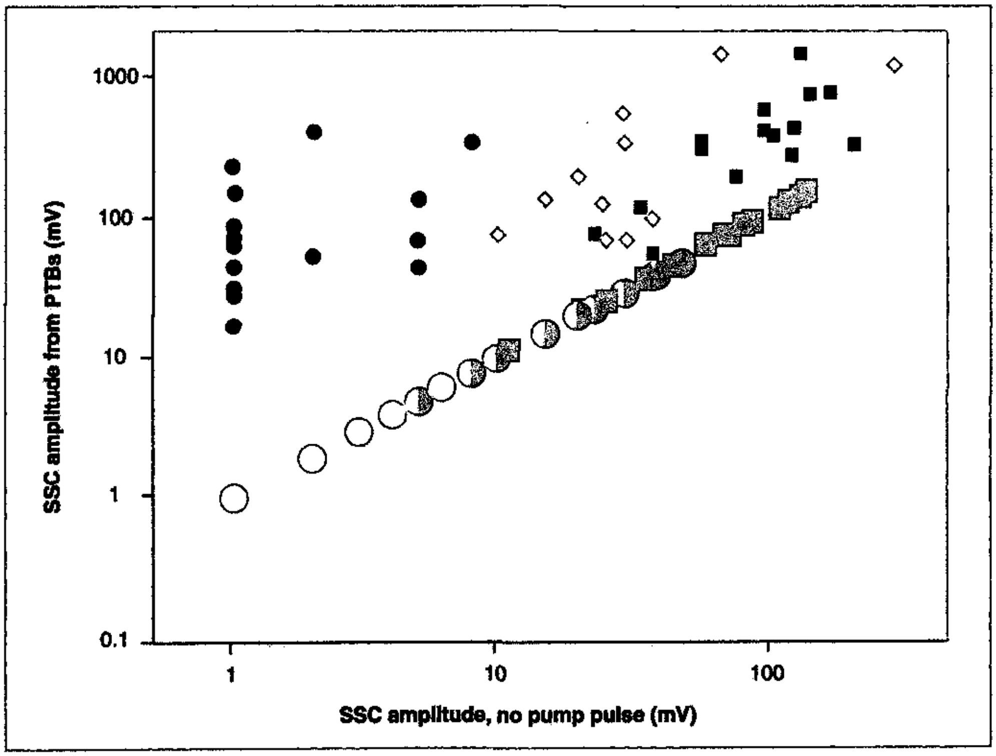

**Figure 6. Optical side-scattering integral signals obtained from intracellular gold nanoparticles (X-axis) and from the photothermal bubbles (Y-axis).** The amplitudes of integral scattering signals obtained from individual cancer cells, pretreated with 30-nm gold spherical NPs, and before and during exposure to a single pump laser pulse that generates PTBs around NP clusters in the living cells: Hep-2C with NP (large square), Hep-2C with PTB (small square), A549 with NP (large two-toned circle), A549 with PTB (small rhombus), K562 with NP (large circles) and K562 with PTB (small circle).

PTB: Photothermal bubble.

showed no sign of PTBs (X-axis, Figure 6), and the scattered signals were attributed to PTBs (Y-axis, Figure 6) when the PT response showed bubble-specific signals (Figure 5C). For each cell type, we have measured the amplitudes of the scattered probe pulse for the four samples: intact cells, intact cells exposed to the 10-ns pump laser pulse at 532 nm, NP-treated cells (cells with NP clusters) and NP-treated cells exposed to the pump laser pulse (Table 2). Optical amplification of PTBs was quantified relative to the scattering of NPs in the same cells.

During the experiments, we adjusted the fluence of the pump laser to the level at which PTBs were generated in 100% of NP-treated cells (Table 2). These fluencies varied slightly for the different types of cells; this may reflect differences in the efficacy of cluster formation (caused by the different efficacy of the endocytosis) in the different types of cells. For each individual cell, we registered a pair of amplitudes of integral scattering signal: before cell irradiation with a pump laser pulse (to characterize NP-related scattering) and during cell irradiation with a pump laser pulse having a fluence above the PTB generation threshold (to characterize PTB-related scattering). These two scattering signals were plotted in a diagram, in which each dot represents an individual cell (Figure 6). This diagram shows a distinct line for 'no PTB' cases. All dots that are above this line correspond to PTBs.

According to the results obtained for all three types of cells, NPs amplify the scattering, but not significantly relative to the scattering by intact cells (Table 2). Also, differences in the amplitudes of an integral scattering signal (X-axis, Figure 6) indicate the differences in cluster size among the three types of cells studied. The smallest signals were observed for K562 suspension-type cells, and the highest scattered signals were observed for the squamous carcinoma Hep-2C cells (Figure 6; Table 2). PTBs yielded a significant increase of scattered signal amplitudes in all studied cells (Figure 6; Table 2). Amplification factors were calculated by normalizing the measured amplitudes by those measured for the intact cells (Table 2). For some specific individual cells in the population, the amplification factor of the integral signal was more than 100 relative to NP scattering. Owing to the heterogeneous nature of cellular properties, the amplification effect was also rather heterogeneous. The higher the NP cluster-related signal, the higher the PTB-related signal. This correlation is in line with physical mechanisms that are involved in PTB generation: the larger the cluster, the larger the bubble.

The imaging potential of PTBs was evaluated in detail for A549 cells incubated with 170-nm NSs. We have studied the influence of PTBs on two main properties of the proposed imaging method: amplification of optical scattering and cell viability. This was achieved by registering and comparing the several optical images for each cell. Cell viability was evaluated optically with two standard microscopy techniques that monitor the integrity of the outer cellular membrane [63]. First, a white light transmittal image was obtained for the cell before and after its exposure to the pump pulse, and the difference between these two images was used to detect any PTB-induced cell shape changes. The coefficient of variation of pixel amplitude $K_{wl}$ of the white light differential image indicated a significant alteration of cell shape and size (which usually accompanies a disruption of the cellular membrane) if its value deviated significantly from zero. Second, cell damage by PTB was detected by monitoring the cellular uptake of ethidium bromide (EtBr). Before the experiment, EtBr was added to the cell samples. This dye penetrates the membranes of compromised cells and produces red fluorescence; however, EtBr does not penetrate the membranes of

**Table 2. Amplitude of the integral optical scattering signal (mV) averaged for cell populations (mV) for intact cells, nanoparticle-treated cells with 30-nm gold spheres and photothermal bubbles generated by a single short pulse (532 nm, 10 ns) in individual living cells.**

| Cancer cell types | Intact cells | Cells treated with single pump laser pulse | NP-treated cells | Cells treated with NPs & single pump laser pulse | Fluence of pump laser pulse (532 nm, 10 ns; J/cm²) |
|---|---|---|---|---|---|
| Hep2C (squamous carcinoma cell) | 68.8 ± 41.6 | 61.5 ± 48.2/1.0 | 95.2 ± 62.8/1.4 | 454 ± 420/6.6 | 1.3 |
| A549 (lung cancer cell) | 20.8 ± 14.3 | 19.4 ± 12.6/1.0 | 36.8 ± 58.8/1.8 | 338 ± 465/17 | 1.3 |
| K562 (acute leukemia cell) | 2.4 ± 1.42 | 2.4 ± 1.85/1.0 | 2.4 ± 2.3/1.0 | 106 ± 111/44 | 1.9 |

*NP: Nanoparticle.*

living cells and hence produces no fluorescence for living cells. For excitation of the fluorescence, we used a single pump pulse (532 nm) with the fluence decreased by 20 times relative to PTB-generation level. Fluorescent images were obtained for each cell before and after PTB generation. Their pixel amplitude ratio was used to quantify the damage: any significant increase of the fluorescence amplitude in the time gap 50–100 s after the generation of PTBs was interpreted as cell damage.

Side-scattering images where obtained before and during the pump pulse with the pulsed probe laser at 750 nm. The former characterized scattering owing to NS, NS clusters and to cellular endogenous structures, and the latter characterized PTB-related scattering. A second scattering image was normalized by the first one and the pixel amplitude of the ratio image ($K_{ssc}$) was considered as the scattering amplification coefficient. It was applied to the image points where the PTBs were detected and was used to quantify the amplification of the scattering by PTBs relative to that related to NSs:

$$K_{ssc} = \frac{(A_{PTB} - B)}{(A_{cl} - B)}$$

where $A_{PTB}$ and $A_{cl}$ are the pixel image amplitudes obtained for the same cell in pulsed mode of scattering for the PTB (pump laser on) and NS (pump laser off), respectively, and $B$ is the constant for the background amplitude. We used, in total, five experimental parameters for each cell: pump laser fluence, white light image ratio, fluorescent image ratio, side-scattering image ratio (as the PTB amplification measure) and the PT response duration (as the PTB lifetime measure).

Influence of the PTBs on optical scattering signal and cell viability is illustrated in Figure 7 & Table 3. The figures and table show data for the two A549 living cells that were exposed to single pump pulses with fluencies of 0.64 J/cm$^2$ (cell 1, top panel of Figure 7) and 0.48 J/cm$^2$ (cell 2, bottom panel of Figure 7). According to the scattering images (Figure 7C) and corresponding PT responses, both cells have yielded submicrometer-sized intracellular PTBs and with PTB durations of 250 ns for cell 2 and 70 ns for cell 1. Both cells have yielded single PTBs, which can be explained by inefficient nonspecific endocytosis of 170-nm NSs by those cells. In general, eight to ten PTBs in individual cells have been observed, and their number increased when pump laser fluence was increased. This was owing to the (aforementioned) dependence of the PTB threshold fluence on cluster size: the larger the cluster, the lower the PTB generation threshold. Cluster size, in turn, depends on the efficacy of endocytosis. Under the given fluence levels, these two cells only yielded a single PTB around the largest NS clusters. Laser-induced PTBs (Figure 7C) have caused an increase of optical scattering by almost three orders of magnitude

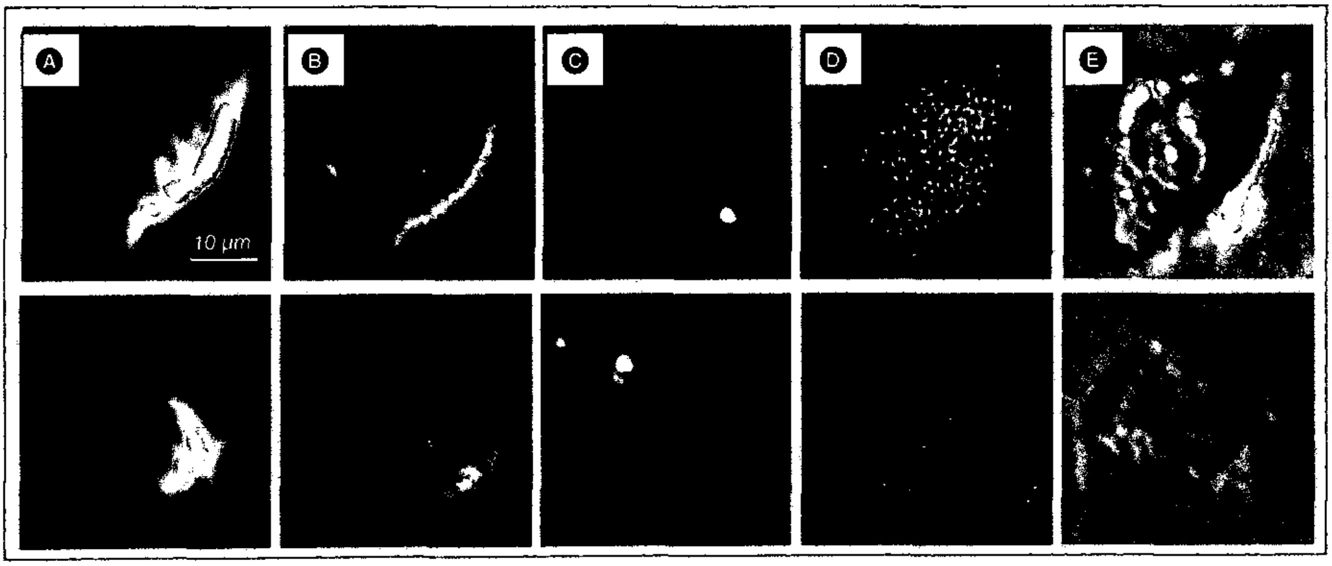

**Figure 7. Images of damaged (top panel) and living (bottom panel) A549 cells after their incubation with 170-nm gold nanoshell and the follow-up exposure to a single pump laser pulse that induced photothermal bubbles.** **(A)** White light image prior to exposure to pump laser pulse; **(B)** Side-scattering image prior to exposure to pump laser pulse shows nanoshell-related signals; **(C)** Side-scattering image during exposure to pump laser pulse shows photothermal bubbles; **(D)** Fluorescent image after the exposure to pump laser pulse shows ethidium bromide fluorescence; **(E)** Differential white light image shows the changes in the cell after exposure to a pump laser pulse.

Table 3. The ratios of the image pixel amplitudes for images of two individual A549 cells: damaged and living after incubation with gold nanoshells, and follow-up exposure to a single laser pulse (*10 ns, 532 nm*) *that has* generated photothermal bubbles in the cells.

| **Parameter** | $K_{ssc}$ | **Relative change of pixel amplitude of ethidium bromide fluorescence** | $K_w$ |
|---|---|---|---|
| Source of the image | Side scattering | Fluorescence | White-light transmittance |
| Damaged cell | 2886 | 3.4 | 0.46 |
| Survived cell | 1779 | 0.7 | 0.05 |

*$K_{ssc}$: Coefficient of amplification of optical side scattering; $K_w$: Relative difference in pixel amplitudes of the transmitted optical images.*

(TABLE 3) relative to the scattering of gold NSs in the same point of the image (FIGURE 7B). Analysis of fluorescent and white light images has shown that cell 1 was damaged by the PTB because its fluorescence has increased (FIGURE 7D, top), and its shape changed significantly (FIGURE 7E, top). Under the lower pump laser fluence, cell 2 survived the pump pulse and PTB: no increase in fluorescence (FIGURE 7D, bottom) nor change in cell shape (FIGURE 7E, top) was detected. PTB lifetime in the surviving cell was shorter than that for a damaged cell, and this difference shows that the maximal diameter of the PTB in the surviving cell was smaller than that for a damaged cell.

Of course, the viability of cells after generation of intracellular PTBs should be verified with a more sensitive method than EtBr staining. Also, the mechanism of selective NS cluster formation around single target molecules has to be studied for receptor-mediated endocytosis of the NPs preconjugated with cell-specific vectors (such as monoclonal antibody C225 for solid tumor cells). *Nevertheless, the results obtained* found that the cluster–bubble mechanism has provided amplification of optical scattering in living cells by more than 1000-times; PTBs have acted as noninvasive cellular optical probes.

Next, we studied the dependence of the image pixel amplitude of scattered light on the incident fluence of the pump laser pulse and the size of NPs (FIGURE 8). We incubated the A549 cancer cells with gold spheres with a diameter of 30 nm and with gold NSs with a diameter of 170 nm. We obtained the scattering amplification coefficient and PTB lifetimes as cell population-averaged values for several different laser fluences. Then, we analyzed the scattering amplification coefficient, $K_{ssc}$, as a function of PTB lifetime. We consider that the bubble lifetime characterizes the PTB more precisely than pump pulse fluence. First, PTB lifetime is proportional to the maximal diameter of the PTB [58], which relates directly to the scattering efficacy of the PTB; second, the generation of the PTBs is provided by several factors, with laser fluence being only one of them. The other important factor that influences PTB diameter and lifetime is the clustering of NPs. The increase of pump laser fluence from 0.5 to 3.5 J/cm$^2$ has caused steady increase of PTB lifetime (not shown) and of the image pixel amplitude of the scattered signal. We plotted both parameters as cell population-averaged values (FIGURE 8). The increase of PTB lifetime (or maximal diameter) causes an increase in optical scattering. Also, experimental data presented in FIGURE 8 correlate with the results of theoretical modeling, as shown in FIGURE 3. Both theoretical and experimental results indicate that the amplification of optical scattering depends on PTB size (lifetime), and does not depend on NP size when the PTB diameter exceeds 300–400 nm or the PTB lifetime exceeds 200 ns. Thus, the NP *diameter does not influence* PTB *scattering* significantly, at least when PTB diameter significantly exceeds the size of the NPs. Additionally, a possible explanation for the absence of a significant difference between the amplitudes of optical scattering provided by 30-nm spheres and 170-nm shells is the clustering of those NPs in the cells: PTBs are generated mainly around the biggest NP clusters, which may be similar in size, although the sizes of the NS and NP are significantly different. It should be noted that the large diameter of gold NSs (170 nm) might not improve scattering owing to poor internalization (and hence clustering) of such large NPs by the cell. Much smaller spheres were better internalized (and clustered) by the cells. This resulted in the relatively similar scattering amplitudes obtained from the cells after their incubation with big NSs and small nanospheres. Therefore, we may conclude that PTB size, not NP size, is important for the amplification of optical scattering, and that NP clustering enables us to improve PTB diameter.

## Discussion

### ■ Amplification of optical scattering with PTBs

There are several basic factors that influence the effect of optical amplification by PTBs. The *in vitro* experimental results have demonstrated

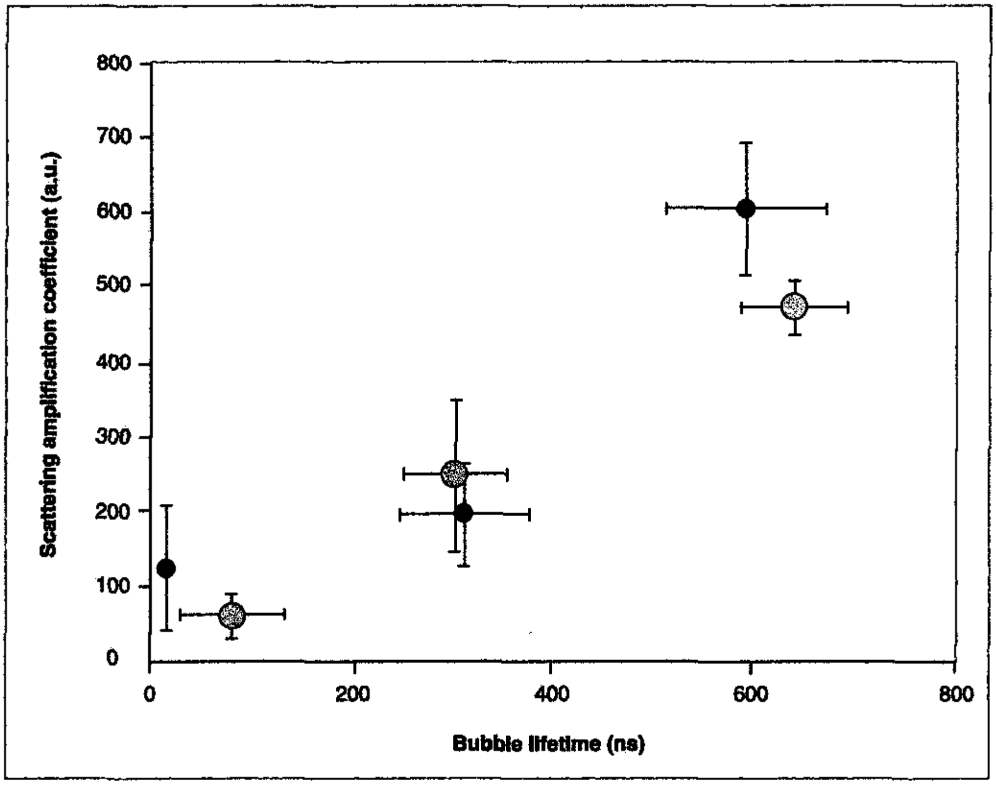

**Figure 8. Influence of the photothermal bubble lifetime on the amplification of optical scattering.** *Experimental dependence of optical scattering amplification coefficient* upon the lifetime of the intracellular photothermal bubbles: large circle for 30-nm gold spheres, small circle for 170-nm gold nanoshells. Population-averaged data are given for A549 cells exposed to a single 10-ns pump pulse at 532 nm.

that a NP cluster generates a much larger PTB than a single NP does under the same laser pulse fluence. This effect and its mechanisms were studied by us previously [48–50]. Under equal laser pulse fluence, the lifetime and maximum diameter of the PTB increase significantly with an increase in NP diameter [30,50]. The larger NPs have high absorbance cross-sections and release more thermal energy, thus expanding the PTB to a larger size. Thus, the increased optical absorbance and diameter of the NP cluster increase the maximum diameter of PTBs, and so contribute to an amplification of optical scattering. Next, for a given NP cluster, the increase of the pump laser fluence also increases the PTB diameter and lifetime (these two PTB parameters are proportional to each other [58]) owing to the increase of the initial laser-induced temperature of the NPs. Finally, scattering can be amplified through an increase of the probe laser fluence, providing that it is safe for the cell.

Besides these three factors that we have considered experimentally, there are several others that also influence PTB size and hence the optical scattering signal. The initial laser-induced temperature also depends on heat loss from the thermal diffusion of heated NPs and from the PTB nuclei. This heat loss into the surrounding media can be alleviated by shortening the length of the laser pulse (10 ns in our experiments). In experiments with picosecond laser pulses, the efficacy of PTB generation was higher compared with that of nanosecond pulses [64]. The initial laser-induced temperature and the laser fluence are limited by two damage thresholds: the threshold of thermal damage for the cell components and the threshold of thermal damage of the NP. Although the thermal damage threshold of cellular molecules may be much lower than the temperatures required for PTB generation, actual thermal damage to the cell can be minimized by localization of the PT effect to the size of the NP cluster and inside the PT bubble. There may be several independent ways of controlling the size and duration of PTBs: through NP properties (NP cluster diameter, absorbance cross-section of individual NPs and laser fluence threshold of NP damage), laser-pulse parameters (duration and fluence of a single laser pulse, and fluence, number and interval for the sequence [train] for several pulses [62]) and through the frequency and amplitude of ultrasound that is applied simultaneously with laser irradiation. Experimental studies of the influence of these factors on the optical amplification is the subject of our ongoing and future work.

## Cell imaging

When PTBs are generated in living cells, viability becomes the most significant factor, and the parameters of the PTB, laser and acoustic radiation must be below cell damage thresholds. This requirement limits the maximal amplitude of optical signal and leads to questions about the signal-to-noise ratio. The source of noise is the scattering from cellular components and tissues (when being carried out *in vivo*). The balance of sensitivity and safety depends not only on PTB-generation factors that were previously considered, but also on the optical scattering properties of specific cells, which is beyond the scope of this article. Nevertheless, the transient nature of the PTB significantly improves the signal-to-noise ratio: the scattered signal amplitude follows the dynamics of PTB radius and, therefore, the PTB can be recognized at specific time domains owing to the specific symmetrical time contour of the optical signal (Figures 5B & C), even in a highly scattering environment.

The generation of laser- and ultrasound-induced bubbles has already been studied in terms of the mechanical damage of cellular outer membranes [33,34]. A cell may repair its membrane if the maximal diameter of the bubble does not exceed 1–2 µm. Optical scattering of a vapor PTB of a 1-µm diameter is several orders of magnitude stronger than optical scattering of the gold NPs that can be delivered into cells (Figure 4). Recent results demonstrating the level of optical scattering from gold NPs in living and fixed cells have shown that scattering from gold NPs is detectable, although it may require many NPs [65–67]. These results, together with our present results, enable prediction of a considerable increase of the sensitivity of scattering imaging owing to PTBs.

When several different cells produce similar PTBs, all those cells viewed through PTB scattering will look alike. An additional way to increase the specificity of optical scattering and so enable differentiation of those cells is to detect an additional signal scattered by NP clusters before PTB generation. The difference in NP cluster scattering can be seen clearly for the three types of cancer cells presented in Figure 6. This difference is caused by different sizes of NP clusters in the three different cell types. However, without a pump laser pulse when no PTB is generated, the difference in cluster scattering is not sufficient, combined with the relatively low scattering signal, and does not provide reliable differentiation among the three groups of cells. Only when the PTB-related signal can be obtained does the difference among cell populations become clear. Therefore, sensitive and specific scatter imaging should combine the two images or the two optical signals. The first image is obtained with probe laser alone and the second image is obtained immediately after the first, by applying pump and probe pulses. With short nanosecond laser pulses, both signals can be acquired in 100 ns. Cluster signals and the second PTB signals can be registered with one photodetector and one probe laser.

The suggested method differs from current optical scattering methods by the double-signal principle. This method may also provide an increase in the signal-to-noise ratio when the target cell or molecule is located among a highly scattered background. The latter is typical for *in vivo* imaging, and thus the suggested method may also improve the efficacy of optical endoscopy. PTBs can be generated inside specific living cells and provide a maximal refractive index gradient that improves optical scattering. Small laser-induced PTBs generated around NP clusters may be safe for the cells, and can be used for the stimulated release of the molecular probes from endosomes and optical imaging of specific single molecules. PTB size can be much larger than that of a single molecule or the other cellular target. Nevertheless, the origin of the PTB can be linked to a specific target molecule through vector-based bonds between NPs that generate the PTB and the molecule. Thus, the suggested method may provide efficient imaging of single intracellular molecules in living cells. The size of the PTB image (up to one µm) may exceed the actual size of the target (the latter may be a size that is well below the diffraction limit), but the PTB would definitely help to detect the presence of such a target as the single molecule in a specific cell.

Our experimental results also suggests that PTB scattering can be applied in cytometry for detecting specific cells. Unlike fluorescent probes, the PTBs do not exist in the cell until after they are generated, and the gold NPs that are present in the cell are much less toxic than any fluorescent probes. Therefore, the influence of PTB imaging on physiological cell processes can be minimized. The threshold mechanism of PTB generation provides selectivity of optical signal, and thus increases the signal-to-noise ratio of imaging. PTBs can be activated with a specific wavelength and energy of a laser pulse, otherwise they do not emerge in a cell, so they would not interfere with cellular processes and other measurements.

## Conclusions

In this work, we have experimentally verified that:

- Optical scattering from metal light-absorbing NPs may be amplified by more than three orders of magnitude by generating PTBs around these NPs;
- Clustering of the NPs around specific molecular targets may significantly improve the specificity of scattering imaging;
- PTBs as cellular optical probes can be used without causing damage to the cell in which they are generated;
- Two-signal scattering method with time-domain detection of the PTBs may significantly enhance the specificity and sensitivity of the imaging of specific targets.

## Future perspective

The universal nature of PTB probes and scattering imaging may enable their applications in microscopy, flow cytometry, endoscopy and other optical methods. Bubble-imaging methods can be applied for optical guidance of therapeutic processes, whereby the bubbles occur as primary or secondary phenomena (in particular, in laser and ultrasound methods). The nontoxic properties of gold NPs, an on-demand feature of the bubbles, may provide noninvasive monitoring and screening of living cells *in vitro* and *in vivo.*

## Financial & competing interests disclosure

*R Drezek acknowledges support from DOD W81XWH-07-1-0428, Welch C-1598, NSF EEC 0647452 and the John and Ann Doer Fund for Computational Biomedicine. D Lapotko has received support for part of this work from the Institute of International Education/SRF (NY, USA). The authors have no other relevant affiliations or financial involvement with any organization or entity with a financial interest in or financial conflict with the subject matter or materials discussed in the manuscript apart from those disclosed.*

*No writing assistance was utilized in the production of this manuscript.*

## Ethical conduct of research

*The authors state that they have obtained appropriate institutional review board approval or have followed the principles outlined in the Declaration of Helsinki for all human or animal experimental investigations. In addition, for investigations involving human subjects, informed consent has been obtained from the participants involved.*

## Executive summary

- Laser-induced vapor microbubbles (photothermal bubbles) when being generated in a living cell with a short laser pulse and around gold nanoparticles (or their clusters) significantly improved the optical scattering (up to three orders of magnitude) relative to that of gold nanoparticles.
- Combination of the intracellular clustering of gold nanoparticles around specific target molecules with the ability of nanoparticle clusters to selectively generate on-demand microbubbles may enable highly sensitive and noninvasive imaging of specific cellular targets and events in living cells.

## Bibliography

1 Hu M, Chen J, Li Z-Y *et al.*: Gold nanostructures: engineering their plasmonic properties for biomedical applications. *Chem. Soc. Rev.* 35(11), 1084–1094 (2006).

2 Oberdorster G, Oberdorster E, Oberdorster J: Nanotoxicology: an emerging discipline evolving from studies of ultrafine particles. *Environ. Health Perspect.* 113(7), 823–839 (2005).

3 Lewinski N, Colvin V, Drezek R: Cytotoxicity of nanoparticles. *Small* 4(1), 26–49 (2008).

4 Gelles J, Schnapp BJ, Sheetz MP: Tracking kinesin-driven movements with nanometre-scale precision. *Nature* 331(6155), 450–453 (1988).

5 Yguerabide J, Yguerabide EE: Light-scattering submicroscopic particles as highly fluorescent analogs and their use as tracer labels in clinical and biological applications. II. Experimental characterization. *Anal. Biochem.* 262(2), 157–176 (1998).

6 El-Sayed IH, Huang X, El-Sayed MA: Surface plasmon resonance scattering and absorption of anti-EGFR antibody conjugated gold nanoparticles in cancer diagnostics: applications in oral cancer. *Nano Lett.* 5(5), 829–834 (2005).

7 Loo C, Lowery A, Halas N, West J, Drezek R: Immunotargeted nanoshells for integrated cancer imaging and therapy. *Nano Lett.* 5(4), 709–711 (2005).

8 West JL, Halas NJ: Engineered nanomaterials for biophotonics applications: improving sensing, imaging, and therapeutics. *Annu. Rev. Biomed. Eng.* 5, 285–292 (2003).

9 Tkachenko AG, Xie H, Liu Y *et al.*: Cellular trajectories of peptide-modified gold particle complexes: comparison of nuclear localization signals and peptide transduction domains. *Bioconjug. Chem.* 15(3), 482–490 (2004).

10 Yang PH, Sun X, Chiu JF, Sun H, He QY: Transferrin-mediated gold nanoparticle cellular uptake. *Bioconjug. Chem.* 16(3), 494–496 (2005).

11 Farokhzad OC, Jon S, Khademhosseini A, Tran TNT, LaVan DA, Langer R: Nanoparticle-aptamer bioconjugates: a new approach for targeting prostate cancer cells. *Cancer Res.* 64(21), 7668–7672 (2004).

12 Sönnichsen C, Geier S, Hecker NE *et al.*: Spectroscopy of single metallic nanoparticles using total internal reflection microscopy. *Appl. Phys. Lett.* 77(19), 2949–2951 (2000).

13 Sokolov K, Follen M, Aaron J *et al.*: Real-time vital optical imaging of precancer using anti-epidermal growth factor receptor antibodies conjugated to gold nanoparticles. *Cancer Res.* 63(9), 1999–2004 (2003).

14 Siiman O, Gordon K, Burshteyn A, Maples J, Whitesell J: Immunophenotyping using gold or silver nanoparticle-polystyrene bead conjugates with multiple light scatter. *Cytometry* 41(4), 298–307 (2000).

15 Nammalvar V, Wang A, Drezek R: Enhanced gold nanoshell scattering contrast in cervical tissue using angled fiber probes. *Proc. SPIE* 6447, 64470H (2007).

16 Hartland G: Measurements of the material properties of metal nanoparticles by time-resolved spectroscopy. *Phys. Chem. Chem. Phys.* 6(23), 5263–5274 (2004).

17 Mohamed MB, Ahmadi TS, Link S, Braun M, El-Sayed MA: Hot electron and phonon dynamics of gold nanoparticles embedded in a gel matrix. *Chem. Phys. Lett.* 343(1–2), 55–63 (2001).

18 Link S, Hathcock DJ, Nikoobakht B, El-Sayed MA: Medium effect on the electron cooling dynamics in gold nanorods and truncated tetrahedral. *Adv. Mater.* 15(5), 393–396 (2003).

19 Rosencwaig A: High-resolution photoacoustic thermal-wave microscopy. *Appl. Phys. Lett.* 36(9), 725–727 (1980).

20 Tam AC: Photothermal investigation of solids and fluids. In: *Overview of Photothermal Spectroscopy.* Sell JA (Ed.). Academic Press, Boston, USA 1–34 (1988).

21 Shibata MM, Kitamori T, Sawada T: Application of coaxial beam photothermal microscopy to the analysis of a single biological cell in water. *Anal. Chim. Acta* 299(3), 343–347 (1995).

22 Cretin B, Daher N, Cavallier B: Thermoelastic modeling: application to superresolution in photothermal and thermoelastic microscopy. *Proc. SPIE* 3098, 466–475 (1997).

23 Boyer D, Tamarat P, Maali A, Lounis B, Orrit M: Photothermal imaging of nanometer-sized metal particles among scatterers. *Science* 297(5584), 1160–1163 (2002).

24 van Dijk MA, Tchebotareva AL, Orrit M *et al.*: Absorption and scattering microscopy of single metal nanoparticles. *Phys. Chem. Chem. Phys.* 8(30), 3486–3495 (2006).

25 Wang FS, Jay DG: Chromophore-assisted laser inactivation (CALI): probing protein function *in situ* with a high degree of spatial and temporal resolution. *Trends Cell. Biol.* 6(11), 442–445 (1996).

26 Seol Y, Carpenter A, Perkins T: Gold nanoparticles: enhanced optical trapping and sensitivity coupled with significant heating. *Optics Lett.* 31(16), 2429–2431 (2006).

27 Doukas AG, Flotte TJ: Physical characteristics and biological effects of laser-induced stress waves. *Ultrasound Med. Biol.* 22(2), 151–164 (1996).

28 Lee S, Anderson T, Zhang H, Flotte TJ, Doukas AG: Alteration of cell membrane by stress waves *in vitro. Ultrasound Med. Biol.* 22(9), 1285–1293 (1996).

29 Pitsillides CM, Joe EK, Wei X, Anderson RR, Lin CP: Selective cell targeting with light absorbing microparticles and nanoparticles. *Biophys. J.* 84(6), 4023–432 (2003).

30 Gerstman BS, Thompson CR, Jacques SL, Rogers ME: Laser-induced bubble formation in the retina. *Lasers Surg. Med.* 18(1), 10–21 (1996).

31 Jacques SL, McAuliffe DJ: The melanosome: threshold temperature for explosive vaporization and internal absorption coefficient during pulsed laser irradiation. *Photochem. Photobiol.* 53(6), 769–775 (1991).

32 Huttmann G, Birngruber R: On the possibility of high-precision optothermal microeffects and the measurement of fast thermal denaturation of proteins. *IEEE J. Select Topics Quant. Electron* 5, 954–962 (1999).

33 Anderson RR, Parrish JA: Selective photothermolysis: precise microsurgery by selective absorption of pulsed radiation. *Science* 220(4596), 524–527 (1983).

34 Roegener J, Brinkmann R, Lin CP: Pump-probe detection of laser-induced microbubble formation in retinal pigment epithelium cells. *J. Biomed. Opt.* 9(2), 367–371 (2004).

35 Lapotko D, Kuchinsky G, Romanovskaya T, Scoromnik H: Photothermal method for cell viability control. In: *Photoacoustica and Photothermal Phenomena.* Scudiery F, Bertolotti M (Eds). AIP, Rome, Italy 582–584 (1998).

36 Lapotko D, Shnip A, Lukianova E: Photothermal detection of laser-induced damage in single intact cells. *Lasers Surg. Med.* 33(5), 320–329 (2003).

37 Hansen GM: Mie scattering as a technique for the sizing of air bubbles. *Applied Optics* 24(19), 3214–3220 (1985).

38 Jeon J-S, Yang I-J, Karng S-W, Kwak H-Y: Radius measurement of a sonoluminescing gas bubble. *Jpn J. Appl. Phys.* 39(3A), 1124–1127 (2000).

39 Zhu Q, Chance B, Jenkins WT, Zhang Y: Enhanced optical scattering by microbubbles. *Proc. SPIE* 2979, 157–162 (1997).

40 Kozuka T, Hatanaka S, Yasui K, Tuziuti T, Mitome H: Simultaneous observation of motion and size of a sonoluminescing bubble. *Jpn J. Appl. Phys.* 41(5B), 3248–3249 (2002).

41 Auger JC, Barrera RG, Stou B: Optical properties of an eccentrically located pigment within an air bubble. *Prog. Organic Coatings* 49(1), 74–83 (2004).

42 Kokhanovsky AA: Optical properties of bubbles. *J. Opt. A Pure Appl. Opt.* 5(1), 47–52 (2003).

43 Yavas O, Leiderer P, Park HK: Optical reflectance and scattering studies of nucleation and growth of bubbles at a liquid-solid interface induced by pulsed laser heating. *Phys. Rev. Lett.* 70(12), 1830–1833 (1993).

44 Stevenson D, Agate B, Tsampoula X *et al.*: Femtosecond optical transfection of cells: viability and efficiency. *Optics Express* 14(16), 7125–7133 (2006).

45 Schlicher RK, Radhakrishna H, Tolentino TP, Apkarian RP, Zarnitsyn V, Prausnitz MR: Mechanism of intracellular delivery by acoustic cavitation. *Ultrasound Med. Biol.* 32(6), 915–924 (2006).

46 Ohl CD, Wolfrum B: Detachment and sonoporation of adherent HeLa cells by shock wave-induced cavitation. *Biochim. Biophys. Acta* 1624(1–3), 131–138 (2003).

47 Prentice P, Cuschieri A, Dholakia K, Prausnitz M, Campbell P: Membrane disruption by optically controlled microbubble cavitation. *Nat. Physics* 1(2), 107–110 (2005).

48 Lapotko D, Lukianova E, Potapnev M, Aleinikova O, Oraevsky A: Method of laser activated nanothermolysis for elimination of tumor cells. *Cancer Lett.* 239, 36–45 (2006).

49 Lapotko D, Lukianova-Hleb E, Oraevsky A: Clustering of nanoparticles during their interaction with living cells. *Nanomed.* 2(2), 241–253 (2007).

50 Lapotko D, Lukianova E, Oraevsky A: Selective laser nano-thermolysis of human leukemia cells with microbubbles generated around clusters of gold nanoparticles. *Lasers Surg. Med.* 38(6), 631–642 (2006).

51 Lapotko D, Lukianova-Hleb E, Hafner J: Nanocluster-bubble photothermal nanotechnology for anti-cancer applications. *Proc. SPIE* 6734, 67340E (2007).

52 Chan WCW, Chithrani BD, Ghazani AA: Determining the size and shape dependence of gold nanoparticle uptake into mammalian cells. *Nano Lett.* 6(4), 662–668 (2006).

53 Chan WCW, Chithrani BD: Elucidating the mechanism of cellular uptake and removal of protein-coated gold nanoparticles of different sizes and shapes. *Nano Lett.* 7(6), 1542–1550 (2007).

54 Lapotko D, Hleb E, Zhdanok S *et al.*: Photothermolysis by laser-induced microbubbles generated around gold nanorod clusters selectively formed in leukemia cells, *Proc. SPIE* 6856, 68560K (2008).

55 Lapotko D, Lukianova-Hleb E, Mitskevich P *et al.*: Photothermal and photoacoustic processes of laser activated nano-thermolysis of cells. *Proc. SPIE* 6437, 64370C (2007).

56 Loo C, Lowery A, Halas N, West J, Drezek R: Immunotargeted nanoshells for integrated cancer imaging and therapy. *Nano Lett.* 5(4), 709–711 (2005).

57 Lapotko D. Kuchinsky G: Optothermal microscope In: *Photoacoustica and Optothermal Phenomena*. Scudiery F, Bertolotti M (Eds). AIP, Rome, Italy 184–186 (1998).

58 Lapotko D, Lukianova K, Shnip A: Photothermal responses of individual cells. *J. Biomed. Opt.* 10(1), 014006 (2005).

59 Lapotko D, Lukianova E, Potapnev M, Aleinikova O, Oraevsky A: Elimination of leukemic cells from human transplants by laser nano-thermolysis. *Proc. SPIE* 6086, 135–142 (2006).

60 Lapotko D, Lukianova K: Laser-induced micro-bubbles in cells. *Int. J. Heat Mass Trans.* 48(1), 227–234 (2005).

61 Lapotko D: Laser-induced bubbles in living cells. *Lasers Surg. Med.* 38(3), 240–248 (2006).

62 Hleb E, Lapotko D: Photothermal properties of gold nanoparticles under exposure to high optical energies. *Nanotechnology* 19(35), 355702 (2008).

63 Rost FWD: Applications of microfluorometry. In: *Quantitative Fluorescence Microscopy*. Cambridge University Press, UK 250 (1991).

64 Francois L, Mostafavi M, Belloni J, Delaire J: Optical limitation induced by gold clusters: mechanism and efficiency. *Phys. Chem. Chem. Phys.* 3(22), 4965–4971 (2001).

65 Drezek R, Faupel M, Pitris C *et al.*: Optical imaging for the detection of cervical precancers *in vivo*. *Cancer* 98(Suppl. 9), 2015–2027 (2003).

66 Jain PK, El-Sayed IH, El-Sayed MA: Au nanoparticles target cancer. *Nano Today* 2(1), 18–29 (2007).

67 Sokolov K, Aaron J, Hsu B *et al.*: Optical systems for *in vivo* molecular imaging of cancer. *Techn. Cancer Res. Treat.* 2(6), 491–504 (2003).

# Optical properties of gold-silica-gold multilayer nanoshells

**Ying Hu,**[1] **Ryan C. Fleming,**[1] **and Rebekah A. Drezek**[1,2]

[1] *Department of Bioengineering,* [2] *Department of Electrical and Computer Engineering,*
*Rice University, Houston, TX 77005*

*hooying@rice.edu*

**Abstract:** The spectral and angular radiation properties of gold-silica-gold multilayer nanoshells are investigated using Mie theory for concentric multilayer spheres. The spectral tunability of multilayer nanoshells is explained and characterized by a plasmon hybridization model and a universal scaling principle. A thinner intermediate silica layer, scaled by particle size, red shifts the plasmon resonance. This shift is relatively insensitive to the overall particle size and follows the universal scaling principle with respect to the resonant wavelength of a conventional silica-gold core-shell nanoshell. The extra tunability provided by the inner core further shifts the extinction peak to longer wavelengths, which is difficult to achieve on conventional sub-100 nm nanoshells due to limitations in synthesizing ultrathin gold coatings. We found multilayer nanoshells to be more absorbing with a larger gold core, a thinner silica layer, and a thinner outer gold shell. Both scattering intensity and angular radiation pattern were found to differ from conventional nanoshells due to spectral modulation from the inner core. Multilayer nanoshells may provide more backscattering at wavelengths where silica-gold core-shell nanoshells predominantly forward scatter.

**OCIS codes:** (290.4020) Mie theory; (240.6680) Surface plasmon; (350.4238) Nanophotonics and photonic crystals.

---

## References and links

1. A. Gulati, H. Liao, and J. H. Hafner, "Monitoring gold nanorod synthesis by localized surface plasmon resonance," J. Phys. Chem. B **110**, 323–22, 327 (2006).
2. C. Nehl, H. Liao, and J. Hafner, "Optical properties of star-shaped gold nanoparticles," Nano Lett. **6**, 683–688 (2006).
3. F. Hao, C. L. Nehl, J. H. Hafner, and P. Nordlander, "Plasmon resonances of a gold nanostar," Nano Lett. **7**, 729–732 (2007).
4. R. Averitt, D. Sarkar, and N. Halas, "Plasmon resonance shifts of Au-coated Au2S nanoshells: Insight into multicomponent nanoparticle growth," Phys. Rev. Lett. **78**, 4217–4220 (1997).
5. R. Averitt, S. Westcott, and N. Halas, "Linear optical properties of gold nanoshells," J. Opt. Soc. Am. B **16**, 1824–1832 (1999).
6. L. Hirsch, A. Gobin, A. Lowery, F. Tam, R. Drezek, N. Halas, and J. West, "Metal nanoshells," Ann. Biomed. Eng. **34**, 15–22 (2006).
7. H. Wang, D. Brandl, F. Le, P. Nordlander, and N. Halas, "Nanorice: A hybrid plasmonic nanostructure," Nano Lett. **6**, 827–832 (2006).
8. H. Cang, T. Sun, Z. Li, J. Chen, B. Wiley, Y. Xia, and X. Li, "Gold nanocages as contrast agents for spectroscopic optical coherence tomography," Opt. Lett. **30**, 3048–3050 (2005).
9. E. Prodan and P. Nordlander, "Structural tunability of the plasmon resonances in metallic nanoshells," Nano Lett. **3**, 543–547 (2003).

#102141 - $15.00 USD Received 29 Sep 2008; revised 7 Nov 2008; accepted 8 Nov 2008; published 12 Nov 2008

10. M. Landsman, G. Kwant, G. Mook, and W. Zijlstra, “Light-absorbing properties, stability, and spectral stabilization of indocyanine green,” J. App. Physiol. **40**, 575–583 (1976).
11. C. Loo, L. Hirsch, M.-H. Lee, E. Chang, J. West, N. Halas, and R. Drezek, “Gold nanoshell bioconjugates for molecular imaging in living cells.” Opt. Lett. **30**, 1012–1014 (2005).
12. A. Lin, N. Lewinski, J. West, N. Halas, and R. Drezek, “Optically tunable nanoparticle contrast agents for early cancer detection: model-based analysis of gold nanoshells,” J. Biomed. Opt. **10**, 315102 (2005).
13. V. Nammalvar, A. Wang, and R. Drezek, “Enhanced gold nanoshell scattering contrast in cervical tissue using angled fiber probes,” in *Nanoscale imaging, spectroscopy, sensing and actuation for biomedical applications IV, Proceedings of SPIE*, A. N. Cartwright and D. V. Nicolau, eds., vol. 6447 (2007).
14. J. Park, A. Estrada, K. Sharp, K. Sang, J. A. Schwatz, D. K. Smith, C. Coleman, J. D. Payne, B. A. Korgel, A. K. Dunn, J. W. Tunnell,“Two-photon-induced photoluminescence imaging of tumors using near-infrared excited gold nanoshells,” Opt. Express **16**, 1590-1599 (2008).
15. L. Bickford, J. Sun, K. Fu, N. Lewinski, V. Nammalvar, J. Chang, and R. Drezek, “Enhanced multi-spectral imaging of live breast cancer cells using immunotargeted gold nanoshells and two-photon excitation microscopy,” Nanotechnology **19**, 315102 (2008).
16. A. R. Lowery, A. M. Gobin, E. S. Day, N. J. Halas, and J. L. West, “Immunonanoshells for targeted photothermal ablation of tumor cells,” Int. J. Nanomed. **1**, 149–154 (2006).
17. M. Bikram, A. M. Gobin, R. E. Whitmire, and J. L. West, “Temperature-sensitive hydrogels with SiO2-Au nanoshells for controlled drug delivery,” J. Control. Release **123**, 219–227 (2007).
18. S. Oldenburg, J. Jackson, S. Westcott, and N. Halas, “Infrared extinction properties of gold nanoshells,” Appl. Phys. Lett. **75**, 2897–2899 (1999).
19. R. Weissleder, “A clearer vision for in vivo imaging,” Nature Biotechnol. **19**, 316-317 (2001).
20. P. K. Jain and M. A. El-Sayed, “Universal scaling of plasmon coupling in metal nanostructures: Extension from particle pairs to nanoshells,” Nano Lett. **7**, 2854–2858 (2007).
21. X. Xia, Y. Liu, V. Backman, and G. A. Ameer, “Engineering sub-100 nm multi-layer nanoshells,” Nanotechnology **17**, 5435–5440 (2006).
22. K. Chen, Y. Liu, G. Ameer, and V. Backman, “Optimal design of structures nanoshperes for ultrasharp light-scattering resonances as molecular imaging multilabels,” J. Biomed. Opt. **10**, 024005 (2005).
23. B. Khlebtsov and N. Khlebtsov, “Ultrasharp light-scattering resonances of structured nanospheres: effects of size-dependent dielectric functions,” J. Biomed. Opt. **11**, 044002 (2006).
24. L. LizMarzan, M. Giersig, and P. Mulvaney, “Synthesis of nanosized gold-silica core-shell particles,” Langmuir **12**, 4329–4335 (1996).
25. Y. Hu, T. A. Nieminen, N. R. Heckenberg, and H. Rubinsztein-Dunlop, “Antireflection coating for improved optical trapping,” J. Appl. Phys. **103**, 093,119 (2008).
26. C. F. Bohren and D. R. Huffman, *Absorption and Scattering of Light by Small Particles* (John Wiley and Sons, 1983).
27. H. C. van de Hulst, *Light Scattering by Small Particles* (Dover Publications, 1981).
28. H. Wang, K. Fu, R. A. Drezek, and N. J. Halas, “Light scattering from spherical plasmonic nanoantennas: effects of nanoscale roughness,” Appl. Phys. B-Lasers O. **84**, 191–195 (2006).
29. H. Wang, Y. Wu, B. Lassiter, C. L. Nehl, J. H. Hafner, P. Nordlander, and N. J. Halas, “Symmetry breaking in individual plasmonic nanoparticles,” P. Natl. Acad. Sci. USA **103**, 10,856–10,860 (2006).
30. J. B. Lassiter, J. Aizpurua, L. I. Hernandez, D. W. Brandl, I. Romero, S. Lal, J. H. Hafner, P. Nordlander, and N. J. Halas, “Close encounters between two nanoshells,” Nano Lett. **8**, 1212–1218 (2008).
31. P. B. Johnson and R. W. Christy, “Optical constants of the noble metals,” Phys. Rev. B **6**, 4370–4379 (1972).
32. U. Kreibig and M. Vollmer, *Optical Properties of Metal Clusters* (Springer, 1995).
33. S. Berciaud, L. Cognet, P. Tamarat, and B. Lounis, “Observation of intrinsic size effects in the optical response of individual gold nanoparticles,” Nano Lett. **5**, 515–518 (2005).
34. B. N. Khlebtsov, V. A. Bogatyrev, L. A. Dykman, and N. G. Khlebtsov, “Spectra of resonance light scattering of gold nanoshells: Effects of polydispersity and limited electron free path,” Opt. Spectrosc. **102**, 233–241 (2007).
35. C. L. Nehl, N. K. Grady, G. P. Goodrich, F. Tam, N. J. Halas, and J. H. Hafner, “Scattering spectra of single gold nanoshells,” Nano Lett. **4**, 2355–2359 (2004).
36. P. Jain, K. Lee, I. El-Sayed, and M. El-Sayed, “Calculated absorption and scattering properties of gold nanoparticles of different size, shape, and composition: Applications in biological imaging and biomedicine,” J. Phys. Chem. B **110**, 7238–7248 (2006).
37. E. Prodan, C. Radloff, N. J. Halas, and P. Nordlander, “A hybridization model for the plasmon response of complex nanostructures,” Science **302**, 419–422 (2003).
38. K. Fu, J. Sun, A. W. H. Lin, H. Wang, N. J. Halas, and R. A. Drezek, “Polarized angular dependent light scattering properties of bare and PEGylated gold nanoshells,” Curr. Nanosci. **3**, 167–170 (2007).
39. P. K. Jain, W. Huang, and M. A. El-Sayed, “On the universal scaling behavior of the distance decay of plasmon coupling in metal nanoparticle pairs: A plasmon ruler equation,” Nano Lett. **7**, 2080–2088 (2007).
40. Y. Wang, W. Qian, Y. Tan, and S. Ding, “A label-free biosensor based on gold nanoshell monolayers for monitoring biomolecular interactions in diluted whole blood,” Biosens. Bioelectron. **23**, 1166–1170 (2008).

41. E. M. Larsson, J. Alegret, M. Käll, D. S. Sutherland, "Sensing characteristics of NIR localized surface plasmon resonances in gold nanorings for application as ultrasensitive biosensors," Nano Lett. **7**, 1256-1263 (2007).
42. M. A. van Dijk, A. L. Tchebotareva, M. Orrit, M. Lippitz, S. Berciaud, D. Lasne, L. Cognet, and B. Lounis, "Absorption and scattering microscopy of single metal nanoparticles," Phys. Chem. Chem. Phys. **8**, 3486–3495 (2006).
43. A. Agrawal, S. Huang, A. W. H. Lin, M.-H. Lee, J. K. Barton, R. A. Drezek, and T. J. Pfefer, "Quantitative evaluation of optical coherence tomography signal enhancement with gold nanoshells," J. Biomed. Opt. **11**, (2006).
44. Y. Han, J. Jiang, S. S. Lee, and J. Y. Ying, "Reverse microemulsion-mediated synthesis of silica-coated gold and silver nanoparticles," Langmuir **24**, 5842–5848 (2008).

---

## 1. Introduction

The human use of gold has been well documented throughout history. Observations have been long made on the unique optical properties of nano-sized particles composed of gold. The rapid development in controlled chemical synthesis and computational modeling has generated an extensive exploration on various gold-related nanostructures, ranging from nanorods [1] and nanostars [2, 3], to core-shell nanoshells [4–6], nanorice [7], and nanocages [8]. Silica-gold core-shell nanoshells have attracted particularly significant research attention due to agile optical tunabilities [4, 9] and absorption and scattering cross sections which can greatly exceed those of organic dyes [10, 11]. Superior photochemical stability in combination with excellent biocompatibility renders gold nanoshells highly attractive for biomedical imaging and spectroscopy applications, such as optical coherence tomography [12], reflectance spectroscopy [13], dark-field and two photon microscopy [11, 14, 15]. Gold nanoshells have also been investigated for photothermal therapy and controlled drug release [16, 17].

Extinction spectra of the core-shell nanoshell can be tuned by varying the gold-shell thickness scaled by particle size. The plasmon resonance of gold nanoshells is related to the interaction between plasmons supported on the inner and outer surface of the gold shell. The strength of their interaction is determined by the shell thickness scaled by particle size. As the gold shell decreases in thickness, a stronger plasmon interaction red shifts the resonance peak compared to that of a solid gold particle. This allows the tuning of nanoshell plasmon resonances into the near-infrared (NIR) region [18] where main biological absorption is minimal [19]. The universal dependence of red shifts upon shell thicknesses scaled by particle size was reported by Jain *et al* [20].

Here we examine the optical properties of gold-silica-gold multilayer nanoshells. Fig. 1. illustrates the structure of multilayer nanoshells and silica-gold core-shell nanoshells. Xia *et al*. were the first to report the synthesis of ∼50 nm multilayer nanoshells that may exhibit NIR absorption peaks [21]. Coating gold colloid with a thin layer of silica was achieved by a modified Stöber method in which silica growth was preceded by a sodium silicate (active silica) treatment in an aqueous solution with a controlled pH. The outer gold coating was produced similarly to the way conventional nanoshells are made. Due to the use of small gold colloids (∼20 nm) and the relative ease of silica coating with various thicknesses, sub-100 nm multilayer nanoshells can be synthesized. While comparable in size with some solid gold spheres, a greater spectral tunability is expected for multilayer nanoshells due to the interaction of plasmons on interfaces between gold and dielectrics. Such nanoshells could also offer a smaller profile than their conventional counterparts, thus provide better vascular permeability and more efficient antibody conjugation owing to the larger surface-to-volume ratio [21].

Thus far, the optical properties of the multilayer nanoshell, composed of a metallic core and two alternating dielectric and metallic layers, have been investigated by Chen *et al*. to achieve ultrasharp resonant peaks across the spectrum for multiplexing applications [22]. In the study, the overall diameter of the nanoshell was kept at 10 nm and the layers were tailored with

#102141 - $15.00 USD Received 29 Sep 2008; revised 7 Nov 2008; accepted 8 Nov 2008; published 12 Nov 2008

subnanometer precision. The thin layers sparked some controversy over spectral broadening due to the intrinsic size effect on metal properties for nano-sized particle simulations [23].

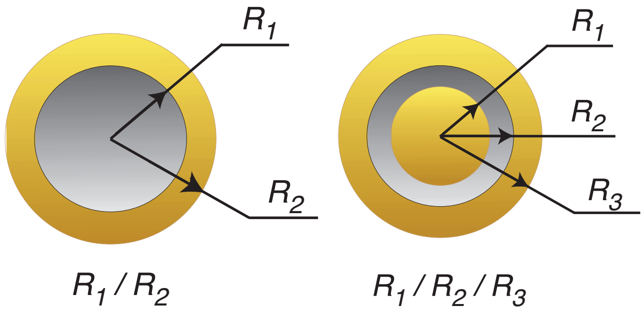

(a) Conventional nanoshell (CNS) (b) Multilayer nanoshell (MNS)

Fig. 1. Geometries of (a) silica-gold core-shell conventional nanoshells, and (b) gold-silica-gold multilayer nanoshells.

The goal of this paper is to examine the spectral and angular scattering properties of gold-silica-gold multilayer nanoshells in the size region where successful particle syntheses have been reported and can be achieved based on currently available protocols [21, 24]. The study is based on what has been done on conventional nanoshells, with the objectives of unveiling and understanding the similar and distinct optical properties of multilayer nanoshells, as well as investigating their potential for bioimaging applications.

## 2. Methodology

A Mie-based computation code has been developed to calculate light scattering from concentric spheres [25–27]. Boundary conditions at each inter-layer interface are expressed in term of vector spherical wave functions and unknown field coefficients. The tangential electric and magnetic fields are stored as alternating rows for each interface in a square matrix and the vector of unknown coefficients is resolved by a matrix division. This approach has a substantial computational advantage as it can handle subjects from spheres with stratification to spheres with gradient index profiles. Extinction, scattering and absorption coefficients were calculated based on Mie scattering coefficients obtained from the Mie code. Angular radiation was calculated for unpolarized light using the approach outlined by van de Hulst [27]. Details of the code can be found in [25].

In this study, plane-wave expansion coefficients are used for illumination. This assumes that particles are located far enough from the light source or that the particles are significantly smaller than the incident beam profile. Other assumptions include that the particles are rigidly spherical and the layers are concentric. It is to be noted that various factors, such as surface topology [28], core eccentricity [29] and interparticle distance [30] have been reported to affect the nanoshell spectra to various degrees.

For gold properties, data from Cristy and Johnson [31] are adapted for the simulation. While the spectral broadening effect from surface scattering in nano-sized particles has been proposed and observed on gold colloids [32,33], the current literature on intrinsic effects of the core-shell nanoshells has not been able to reach a consensus. Common practice at times adds an additional term to the bulk material dielectric constant to acount for the limited free electron path imposed by the thin gold shell [4]. Others propose that this modification is determined by the core radius to shell thickness ratio [34]. However, it was reported that intrinsic effects were not observed on spectral measurement of single silica-gold nanoshells [35]. In light of controversies over this issue, intrinsic size corrections were not considered in this study. In addition, we attempt to construct gold layer geometries outside the region where intrinsic effects prevail.

In simulations presented, water is the surrounding medium unless otherwise noted. The dielectric constant for silica was set to 2.04 and that for water was 1.77. The Mie code was validated against published spectral results for gold particles [36], silica-gold nanoshells [36], and gold-silica-gold-silica nanoshells [37], as well as angular radiation patterns of silica-gold nanoshells [38].

## 3. Spectral properties

### 3.1. Tunability from the inner gold core

In this section, effects from the inner gold core are qualitatively explained by a plasmon hybridization model and quantitatively examined using Mie theory. The goal is to explore the possibilities of synthesizing multilayer nanoshells with enhanced optical properties in the NIR region.

Similar to conventional nanoshells (CNS), multilayer nanoshells (MNS) have tunable optical properties, as explained by plasmon hybridization theory [37]. Briefly stated, the tunability of a CNS is attributed to the interaction between plasmons that reside on the outer and inner surface of the gold shell, also known as the sphere and cavity plasmon. The interaction causes the plasmon to split into a low-energy bonding mode and a high-energy anti-bonding mode. The bonding mode is often visualized by the surface plasmon resonance peak of the nanoshell in the vis-NIR region. The peak can be tuned by varying the ratio of shell thickness to core radius, which essentially tunes the coupling strength between the two plasmons.

In contrast to CNS, MNS have an extra degree of tunability from the inner gold core. This optical tunability can be understood as an interaction between the CNS bonding mode $|BN\rangle$ and the gold core sphere mode $|rC\rangle$. The thickness of the intermediate silica layer determines the degree of interplay between the two modes. An increase in the inner gold core radius on an otherwise fixed geometry will decrease the intermediate silica layer thickness and increase the plasmon interaction. This is accompanied by a red shift of the spectrum that is in agreement with Mie calculation results, shown in Fig. 2 (Media 1).

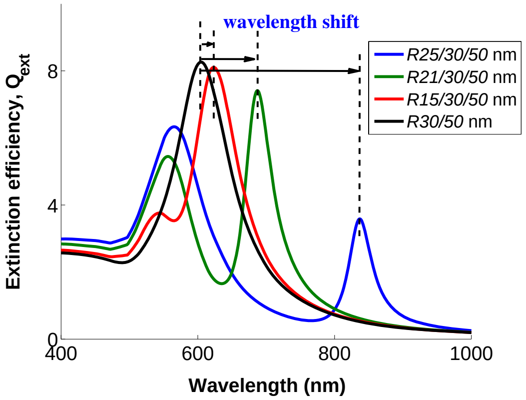

Fig. 2. Calculated spectra of CNS and MNS with various inner core radii while the silica and outer radius remain the same (Media 1). The red shift of MNS from CNS is indicated by lambda shift.

The extra tunability introduced by the inner gold core facilitates the synthesis of small MNS

Received 29 Sep 2008; revised 7 Nov 2008; accepted 8 Nov 2008; published 12 Nov 2008

with NIR extinction peaks. This is not an option for CNS. Near-infrared extinction is difficult to achieve on small CNS because extremely thin outer gold layers are required. The current coating process involves functionalizing the silica core surface with amine groups, then attaching small gold colloids (1–2 nm in size) to form nucleation sites for further reduction of gold to form a continuous layer [6]. However, for sub-10 nm coats, it is often difficult to achieve even layers and smooth surfaces, both of which are needed to avoid drastic deterioration in the overall integrity of the nanoshell spectrum [28,29]. For MNS, these requirements are alleviated because extinction peaks can be further red shifted by having a larger inner gold core with a thin surrounding silica layer. The compromise is a damped peak owing to the increasing plasmon strength associated with the gold core mode $|rC\rangle$.

### 3.2. *Universal scaling principle*

Given that the plasmon coupling strength is qualitatively determined by the intermediate silica layer thickness, a quantitative analysis is desired to characterize the spectrum signature of MNS with various dimensions. Among recently reported observations is the universal scaling principle, which was first reported for metal particle pairs in which plasmon resonance is red shifted from that of an isolated metal sphere by moving the two particles closer together [39]. The shift exhibits a near-exponential decay with increasing interparticle distance. Jain et al. extended this theory to CNS where the gold shell thickness, scaled by particle size, is analogous to the interparticle gap and the two interacting plasmon modes act as a particle pair [20]. A similar exponential decay is observed independent of the overall nanoshell dimension. While MNS support more than two plasmons, their plasmon resonance is mainly determined by the interaction between the bonding mode of CNS and the sphere mode of the gold core. The CNS anti-bonding mode, however, has a very small dipole moment because the cavity plasmon is oppositely aligned with the sphere mode. For this reason, the CNS anti-bonding mode interaction with the core mode is small and becomes too damped to be visible in the spectra. The coupling strength between the two major-playing modes is determined by the intermediate silica layer thickness, scaled by the overall particle size. With $R_2/R_3$ ratio kept constant, a universal decaying curve is observed for MNS of different dimensions.

Figure 3 illustrates an exponential decay insensitive to the overall particle size at a constant ratio of $R_2/R_3 = 0.6$. Results (data not shown) indicate that both the $R_2/R_3$ ratio and the surrounding medium affect the rate of decay. In addition, larger MNS were found to retain the same exponential decay but at slightly different rates. This can be partially attributed to the fact that multiple resonant peaks start to emerge with broad widths and less well-defined shapes. Nevertheless, the universal scaling principle demonstrates that CNS plasmon resonant peaks can be further red shifted on MNS by reducing the silica layer thickness. For particles retaining their overall dimension and outer shell thickness, this translates to the use of large gold cores with thin silica coatings.

It is worth noting that when $t$ is pushed to the zero limit where $R_1 = R_2$, thus the silica layer thickness approaches zero, the plasmon mode red shifts to zero energy. However, the spectral weight becomes negligible due to the cancellation of the dipole moments of the core and of the shell.

### 3.3. *Sensitivity to the surrounding medium*

The plasmon hybridization model can be used to explain the spectral sensitivity of MNS to the surrounding medium. MNS plasmons are resulted from the hybridization between CNS bonding modes $|BN\rangle$ and gold core sphere modes $|rC\rangle$, and since $|rC\rangle$ is not in direct contact with the outside, $|BN\rangle$ is the mode mainly affected by the surrounding medium. For instance, an increase in the refrative index of the medium does not directly affect $|rC\rangle$ but red shift $|BN\rangle$,

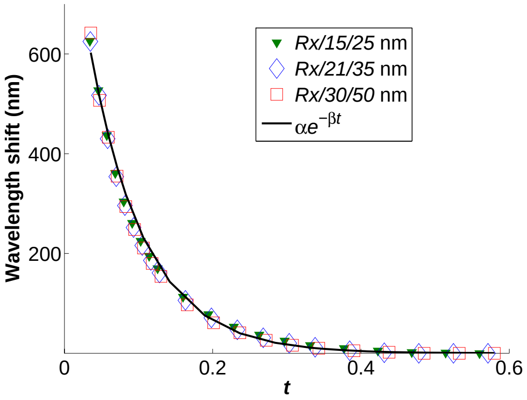

Fig. 3. Mie calculation results for wavelength shifts from the MNS ($R_1/R_2/R_3$) vis-NIR plasmon resonance peak relative to that of CNS ($R_2/R_3$) with the same silica and outer gold radius versus intermediate silica thickness scaled by particle size of MNS. $t = (R_2 - R_1)/R_3$, $\alpha = 972.43$, $\beta = 13.48$.

contributing to an overall red shift as demonstrated in Fig. 4. This suggests that MNS may be used as sensors in various sensing applications based on detecting localized surface plasmon resonances (LSPRs).

While CNS and other nanostructure have been studied for sensing applications [40,41], MNS may offer some unique opportunities given multiple extinction peaks shifted in a synchronous fashion when the surrounding medium is perturbed. Moreover, the degree of shift of each peak was found to be particle-dependent. Table 1 tabulates the wavelength shift for two MNS with an identical size and gold shell thickness. Between the two, MNS2 bears a stronger plasmonic coupling between $|BN\rangle$ and $|rC\rangle$ than MNS1. It can be seen that MNS2 has a larger peak shift at the shorter wavelength and its inter-peak distance decreases with increasing medium indices. The opposite was found for MNS1. Also observed is that the shift of each peak of the MNS approximately adds up to that of the single SPR on an equivalent CNS.

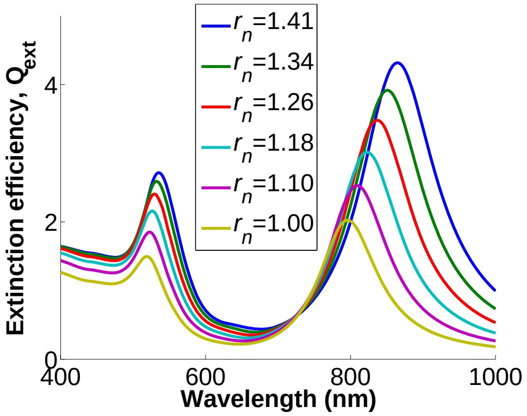

Fig. 4. Calculated extinction spectra of $R20/30/35$ nm MNS immersed in various media with distinct refractive indices.

#102141 - $15.00 USD Received 29 Sep 2008; revised 7 Nov 2008; accepted 8 Nov 2008; published 12 Nov 2008

Table 1. Surface plasmon resonance peak shift of $R20/35/50$ nm (MNS1), $R30/35/50$ nm (MNS2), and $R35/50$ nm (CNS) in different dielectric media ($\lambda_{p2} > \lambda_{p1}$).

| | p1 shift (nm) | | p2 shift (nm) | | p2-p1 (nm) | | p shift (nm) |
|---|---|---|---|---|---|---|---|
| refractive index | MNS1 | MNS2 | MNS1 | MNS2 | MNS1 | MNS2 | CNS |
| 1.0 | 0 | 0 | 0 | 0 | 110 | 424 | 0 |
| 1.1 | 5 | 8 | 10 | 4 | 115 | 420 | 15 |
| 1.2 | 11 | 20 | 22 | 9 | 121 | 413 | 33 |
| 1.3 | 16 | 37 | 38 | 15 | 132 | 402 | 56 |
| 1.4 | 21 | 53 | 56 | 22 | 145 | 393 | 80 |
| 1.5 | 27 | 68 | 77 | 29 | 160 | 385 | 105 |

### *3.4. Tunability on scattering and absorption*

Rayleigh criteria state that, for particles much smaller than the wavelength, the scattering intensity is proportional to $R^6$, where $R$ is the particle radius [42]. However, absorption depends on particle volume, which is proportional to $R^3$ for a sphere. The higher order dependence on particle size makes scattering more sensitive to size variations than absorption. For instance, at 532 nm, 100 nm solid gold spheres have approximately the same absorption and scattering cross sections in water [42]. Scattering attenuates more drastically than absorption when particle size decreases, rendering gold colloids absorption-dominant. In contrast, increasing particle size enhances scattering much faster than absorption; thus, large particles are mainly scattering-based. For inhomogeneous spheres, such as silica-gold core-shell CNS, it has been demonstrated that the scattering-to-absorption ratio rises with increasing core size or outer shell thickness or both [12]. These observations provide very useful guidelines for synthesizing particles to match either scattering- or absorption-based applications at desired wavelengths [16,43].

The scattering and absorption behavior of concentric multilayer spheres can be studied similarly as functions of layer thickness to obtain insight into how changes in each layer affect the overall scattering and absorption. Due to the complexity in displaying results with concurrent variation in each of the three layers, simulations were adapted to geometries in which two layer thicknesses were changed while the third layer remained fixed. Three sets of runs were performed with three combinations of the two variable-layer thicknesses. At each dimension, the extinction, scattering, and absorption spectra were calculated from 400 to 1941 nm. Two plasmon resonance wavelengths $\lambda_{max}$ were chosen at the extinction maxima. The scattering to extinction ratio was calculated at the longer of the two; the one associated with the MNS mode rather than the gold sphere mode. If only one maximum occurred in the wavelength range, then the calculation was performed at that wavelength. Since the resulting plots illustrate the scattering ratio at the longer plasmon resonant wavelengths, we expect the magnitude of the extinction peak to attenuate as it red shifts and it may become weaker than the resonance at shorter wavelengths.

#### 3.4.1. Inner gold core radius fixed at 10 nm

This inner core radius was chosen based on the first experimental synthesis of MNS [21]. Figure 5(a) indicates that scattering increases with thicker silica layers or thicker outer gold shells or both. This behavior resembles that reported for CNS [12]. With a thin silica layer coating (<10 nm) [21, 24, 44], MNS exhibit more absorption than scattering. However, when the silica layer thickness is increased beyond 20 nm, MNS become mainly scattering at practical outer shell

#102141 - $15.00 USD Received 29 Sep 2008; revised 7 Nov 2008; accepted 8 Nov 2008; published 12 Nov 2008

thicknesses.

### 3.4.2. Intermediate silica layer fixed at 10 nm

For these calculations, Fig. 5(b) shows that the general trend still holds that thicker outer shells produce more scattering; however, the role of the inner gold core is less clear. Below 20 nm, an increase in the core radius slowly increases the scattering-to-extinction ratio, but this trend seems to reverse when the core radius goes above 20 nm. Another set of simulations on 20 nm silica layers (not shown here) indicate minimal effects from the gold core below 10 nm in radius and the scattering-to-extinction ratio became relatively insensitive to further increases in core radius. At thin silica layer thicknesses ($<5$ nm), MNS behavior is similar to solid gold colloids in that increasing the inner core radius gradually enhances scattering.

### 3.4.3. Outer shell fixed at 20 nm

Similar to the results in Fig. 5(a) and 5(b), Fig. 5(c) displays a profile in which absorption is dominant or equivalent to scattering for thin silica layers ($<10$ nm). Thicker silica layers ($>10$ nm) quickly turn MNS into scattering particles, with minimal impact from the inner gold core.

### 3.4.4. Outer shell and overall size fixed

To elucidate the core effect, the overall diameter and the outer shell thickness were kept fixed. The inner core radius was gradually increased to the point at which the core made contact with the outer shell. The absorption-to-extinction ratio was obtained at the plasmon resonance, as described above, and results are shown in Fig. 5(d).

Four different geometries with the same $R_1/R_2$ ratio are plotted in Fig. 5(d). As the core radius increases, the absorption component at the plasmon resonance also increases. This is counterintuitive since we expect large gold colloids to exhibit more scattering than absorption. The explanation lies in the interplay between the gold core and other layers of the MNS. For instance, an increasing core size results in a thinner silica coating in this otherwise fixed geometry, and according to Fig. 5(a)–5(c), thinner silica layers produce less scattering; this is consistent with the behavoir in Fig. 5(d). Furthermore, the discontinuities at large $R_1/R_2$ ratios reflect the region where the silica layer becomes so thin that the MNS resonant wavelengths lie outside the region of interest and the gold colloid resonance dominates. MNS demonstrate strong scattering characteristics associated with solid gold spheres. It can be seen that large particles (i.e. $Rx/80/100$ nm) produce more scattering than small particles (i.e. $Rx/24/30$ nm). Because one of the main advantages of MNS over CNS is their relatively small size owing to the use of small gold cores and the possibility of coating them with thin silica layers, sub-100 nm MNS are perceived as advantageous in absorption applications where NIR extinction is desired.

## 4. Angular radiation properties

To understand scattering enhancement by nanoshells in applications where detection angle and angular acceptance range may differ, angular properties need to be considered. Angular properties are commonly characterized by the overall radiation power and its directivity within certain angular ranges. The former is defined by the scattering cross section, $C_{sca}$, and the latter is often described by a single-value parameter: the anisotropy factor $g$, which is a cosine-weighted average over all values of the scattering angle. The scattering cross section is calculated from the Mie coefficients [27]. The anisotropy factor $g$ is calculated as

$$g = \frac{\int_0^\pi S_{11}(\theta) cos\theta 2\pi sin\theta d\theta}{\int_0^\pi S_{11}(\theta) 2\pi sin\theta d\theta} \tag{1}$$

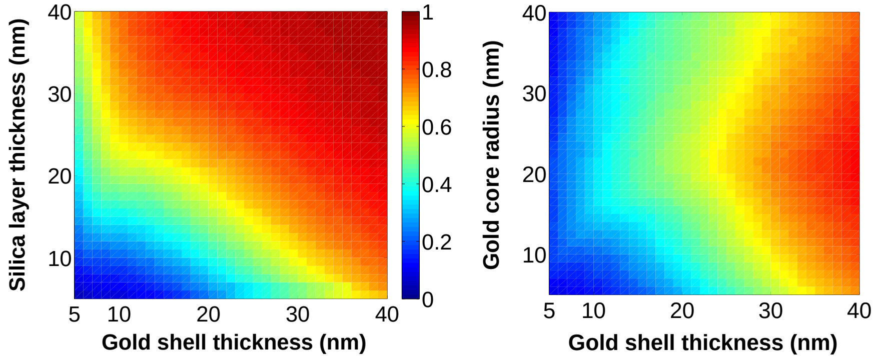

(a) $R_1 = 10$ nm (b) $R_2 - R_1 = 10$ nm

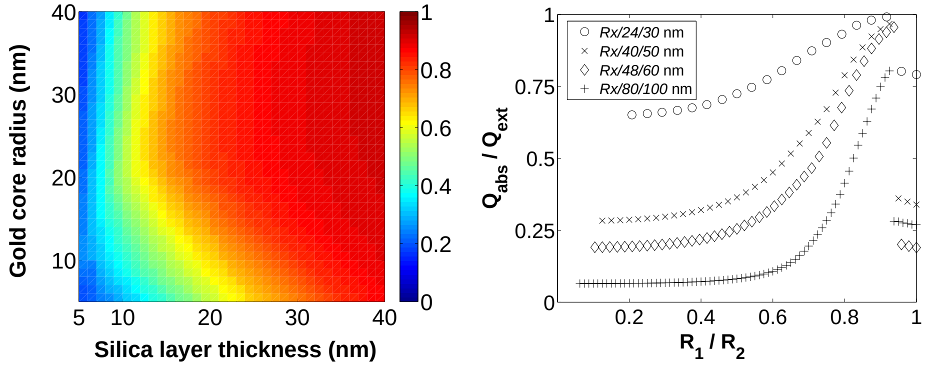

(c) $R_3 - R_2 = 20$ nm (d) $R_3$ fixed

Fig. 5. Scattering-to-extinction ratio at plasmonic resonant wavelengths of MNS with (a) inner gold core radius kept at 10 nm and varying the silica and outer gold layer thickness, (b) silica layer thickness kept at 10 nm and varying the inner gold core radius and outer gold layer thickness, (c) outer gold shell kept at 20 nm and varying the inner gold core radius and silica layer thickness. Absorption-to-extinction ratio (d) at plasmonic resonant wavelengths of MNS with the overall diameter and outer gold shell thickness fixed and varying the inner gold core radius and silica layer thickness.

where $S_{11}$ is the angular radiation power of unpolarized light.

For strongly scattering nanoshells ($> 200$ nm in size), the main extinction peak coincides with the scattering peak where the radiation pattern grows to an overall maximal level. Because MNS and CNS exhibit distinct spectra, as shown in Fig. 2, drastically different radiation patterns are expected at some wavelengths. Figure 6 (Media 2) compares the radiation patterns from MNS and CNS computed as the radiation power normalized to the incident power at one meter from the center of the particle. The radiation power was integrated over all azimuthal angles and plotted in logarithmic form: $\log_{10}(P_{rad}/P_{inc})$. Scattering cross sections are highlighted at selected wavelengths corresponding to the radiation pattern. The overall size and outer shell thickness were chosen so that the corresponding CNS are scattering-dominant.

It can be seen that $R90/125/140$ nm MNS scatters more at 550 nm [Fig. 6(a)], whereas $R125/140$ nm CNS radiates more at 755 nm [Fig. 6(b)] and 1145 nm [Fig. 6(c)]. At 1270 nm the two nanoshells scatter approximately the same [Fig. 6(d)]; this is also indicated by the nearly equivalent scattering cross sections [Fig. 6(e)]. Although optical cross sections give an

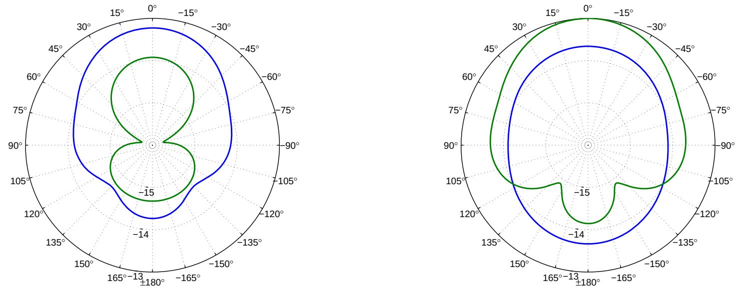

(a) $\lambda$ =550 nm (b) $\lambda$ =755 nm

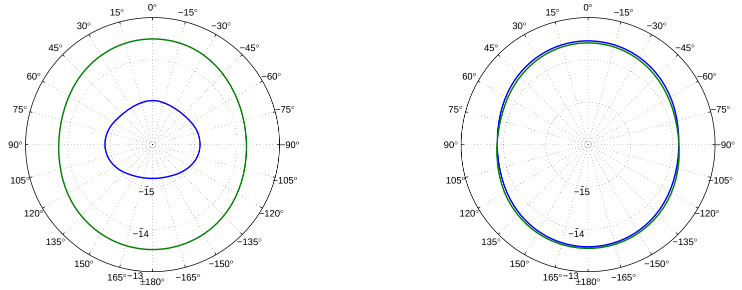

(c) $\lambda$ =1145 nm (d) $\lambda$ =1270 nm

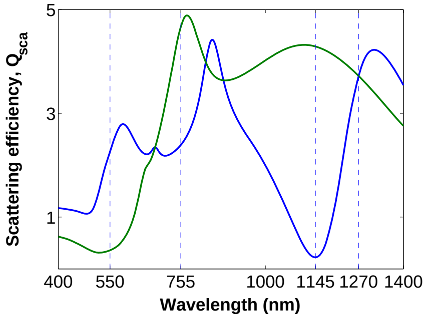

(e) $Q_{sca}$

Fig. 6. Angular radiation pattern of R90/125/140 nm MNS (blue) and R125/140 nm CNS (green) at (a) 550 nm, (b) 755 nm, (c) 1145 nm, (d) 1270 nm and (e) scattering spectra of MNS (blue) and CNS (green) (urlMedia 2). Nanoshells are located in the center of the plot, and the incident wave enters from the bottom (180°).

overall indication of the radiating power, they do not provide angular properties. For instance, despite an overall stronger radiation at 755 nm, $R125/140$ nm CNS does not project as much power in the back direction as $R90/125/140$ nm MNS. From the radiation patterns above, it can also be observed that $R125/140$ nm CNS is more forward-scattering (positive $g$) at shorter wavelengths and becomes isotropic ($g \sim 0$) and slightly back-scattering (negative $g$) at wavelengths longer than the resonance wavelengths. The $R90/125/140$ nm MNS, however, does not exhibit regularities that can be associated with spectral signatures.

To further consolidate this observation, spectral properties are plotted side by side with the anisotropy factor at different wavelengths for 200 nm CNS and MNS with various layer geome-

#102141 - $15.00 USD Received 29 Sep 2008; revised 7 Nov 2008; accepted 8 Nov 2008; published 12 Nov 2008

tries in Fig. 7. A well-defined border between large and near-zero $g$ values is found to follow the general trend of CNS spectra. This suggests the plasmon resonant wavelength is a boundary beyond which CNS primarily scatter isotropically. Nevertheless, MNS seem to reach low $g$ values at shorter wavelengths prior to the plasmon resonance. This may indicate a stronger back scattering profile compared to CNS, as already seen in Fig. 6(b).

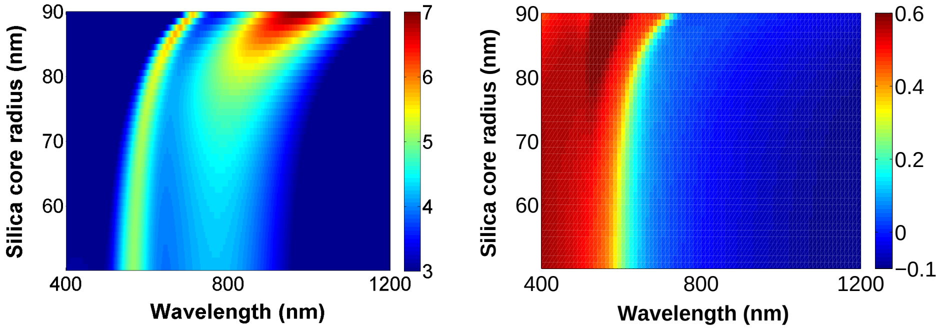

(a) $Q_{ext}$, $Rx/100$ nm CNS

(b) $g$, $Rx/100$ nm CNS

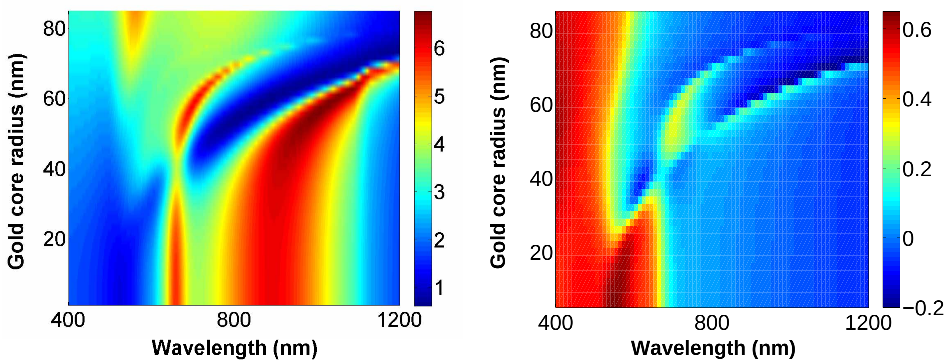

(c) $Q_{ext}$, $Rx/85/100$ nm MNS

(d) $g$, $Rx/85/100$ nm MNS

Fig. 7. (a) Extinction efficiency spectra for $Rx/100$ nm CNS with varying silica core radius x. (b) Anisotropy factor plot for corresponding CNS at different wavelengths. (c) Extinction efficiency spectra for $Rx/85/100$ nm MNS with varying gold core radius x. (d) Anisotropy factor plot for corresponding MNS at different wavelengths.

## 5. Summary

Both spectral and angular radiation properties of gold-silica-gold multilayer nanoshells have been studied using Mie theory. The plasmon hybridization model was employed to explain the spectral tunability due to inner gold core. While the plasmon coupling strength of CNS is known to be determined by a normalized gold shell thickness, that of the MNS was found to be determined by the normalized intermediate silica layer thickness. A thinner silica layer results in a red shift of the plasmon resonance. Furthermore, the MNS spectral shift from CNS without the gold core is characterized by an exponential curve that was found to be insensitive to the particle size, when the outer shell thickness-to-particle size is fixed. This confirms the universal scaling principle reported on particle pair systems and silica-gold core-shell CNS. MNS also demonstrate many characteristics that are similar to CNS. For instance, a thicker silica layer and a thinner gold shell both red shift the MNS spectrum (results not shown) and produce more scattering at the plasmon resonance. MNS are sensitive to the external medium and their multiple extinction peaks with deep spectral valleys may prove valuable for improving the sensitivity and specificity of various biosensing and bioimaging modalities.

Scattering patterns from MNS differ from those of CNS due to the spectral modulation induced by the core. Trends in MNS angular radiation patterns are more intricate than those of CNS. While CNS predominantly forward-scatter at wavelengths shorter than the plasmon resonant wavelength, MNS may radiate more in the back and side directions at these wavelengths.

In summary, this study compares the optical properties of composite multilayer structures with those of CNS, whose properties are well understood. Fully exploiting the potential of MNS requires synthetic studies assessing independent control of each layer, morphological and topological features, size dispersity, and protocol repeatability. It is anticipated that such studies will lead to development of multilayer nanoshells, which, in turn, will accelerate the development of new applications.

## Acknowledgment

This work is supported by the Welch Foundation grant (C-1598), DoD CDMRP (W81XWH-07-1-0428), the Gulf Coast Center for Computational Cancer Research, and the Center for Biological and Environmental Nanotechnology (NSF EEC-0118007 and EEC-0647452). The authors would like to thank Professor Peter Nordlander for his discussion on the plasmon hybridization model and the universal scaling principle, as well as Jim Haile for preparing the manuscript. The polar plots were made based on a modified program initially developed by D. D. Hanselman. Ying Hu is supported by DoE Computational Science Graduate Fellowship program.

#102141 - $15.00 USD Received 29 Sep 2008; revised 7 Nov 2008; accepted 8 Nov 2008; published 12 Nov 2008

IOP Publishing Nanotechnology
Nanotechnology **19** (2008) 315102 (6pp) doi:10.1088/0957-4484/19/31/315102

# Enhanced multi-spectral imaging of live breast cancer cells using immunotargeted gold nanoshells and two-photon excitation microscopy

**Lissett Bickford[1,3], Jiantang Sun[1,3], Kun Fu[1,2], Nastassja Lewinski[1], Vengadesan Nammalvar[1], Joseph Chang[1] and Rebekah Drezek[1,2,4]**

[1] Department of Bioengineering, Rice University, Houston, TX 77005, USA
[2] Department of Electrical and Computer Engineering, Rice University, Houston, TX 77005, USA

E-mail: drezek@rice.edu

Received 18 April 2008, in final form 29 May 2008
Published 24 June 2008
Online at stacks.iop.org/Nano/19/315102

**Abstract**
We demonstrate the capability of using immunotargeted gold nanoshells as contrast agents for *in vitro* two-photon microscopy. The two-photon luminescence properties of different-sized gold nanoshells are first validated using near-infrared excitation at 780 nm. The utility of two-photon microscopy as a tool for imaging live HER2-overexpressing breast cancer cells labeled with anti-HER2-conjugated nanoshells is then explored and imaging results are compared to normal breast cells. Five different imaging channels are simultaneously examined within the emission wavelength range of 451–644 nm. Our results indicate that under near-infrared excitation, superior contrast of SK-BR-3 cancer cells labeled with immunotargeted nanoshells occurs at an emission wavelength ranging from 590 to 644 nm. Luminescence from labeled normal breast cells and autofluorescence from unlabeled cancer and normal cells remain imperceptible under the same conditions.

(Some figures in this article are in colour only in the electronic version)

## 1. Introduction

Accurate cancer diagnosis through its multi-stage progression is critical for developing effective and selective cancer treatments. In order to provide clinicians with functional diagnostic results, knowledge of the molecular signatures of carcinogenesis is necessary. Due to their overexpression during the development of cancer, several biomarkers have been identified as a biological means of characterizing these signatures [1]. Although the acquisition of molecular-specific data is typically associated with gene arrays and proteomics [2], there is an opportunity to use such biomarkers as tools for both *in vitro* and *in vivo* diagnostic evaluations of tissue specimens, such as during surgery, in order to identify malignant cells among heterogeneous tissue.

Silica-based gold nanoshells, which are advantageous for several biological applications due to their unique optical tunability and potential as multi-modal agents, have previously demonstrated enhanced diagnostic imaging potential of carcinogenesis at the microscopic scale through the use of extracellular biomarkers [3–6]. By manipulation of the size of their silica cores and gold outer shells, nanoshells can be optically tuned to absorb or scatter light from wavelengths ranging from the visible to the near-infrared, allowing for both imaging and therapy applications [7]. Achieving optimal contrast of gold nanoshells for biological diagnostics includes

---

[3] These authors contributed equally to this work, listed alphabetically by last name.
[4] Address for correspondence: Department of Bioengineering, Rice University, 6100 Main Street, MS-142, Houston, TX 77005, USA.

0957-4484/08/315102+06$30.00

a combination of developing nanoshells that are tuned to scatter or absorb light in the near-infrared (NIR), where biological chromophores absorb minimal light, and the use of NIR-based imaging systems.

Although several optical devices have been used to validate applications of gold nanoshells as viable contrast agents [3–15], none have focused on evaluating the effectiveness of using immunotargeted nanoshells as contrast agents for cell surface biomarkers using nonlinear excitation microscopy. Nonlinear optics has been used extensively for analyzing fluorescent signals in animal models and tissue samples [16–20]. By using a femtosecond pulsed laser, two photons can be used simultaneously to excite tissue molecules similar to the excitation generated by a single photon, but with twice the energy. Only the molecules at the focus of the femtosecond laser will be excited, resulting in greater resolution than that achievable with single-photon systems, such as conventional confocal microscopy. Additionally, unlike conventional confocal microscopy, a pinhole is not required to reject out-of-focus light and the inherent excitation at only the focal plane means that biological tissue undergoes less photodamage [20]. Although multi-photon microscopy has frequently been used for enhancing fluorescent signals [16, 20], studies have demonstrated that metal particles display photoluminescence as a result of excitation by such multi-photon systems [21, 22]. This photoluminescence is induced by a significant field enhancement that occurs upon multi-photon excitation of the metallic molecules [21]. Thus far in the literature, metallic nanoparticles analyzed for two-photon imaging potential have included gold colloid spheres [23, 24], gold nanorods [25–29], and gold nanoshells [14]. A recent publication on the use of two-photon microscopy for evaluating nanoshell contrast focused on potential dual imaging and therapy applications where unlabeled nanoshells were delivered to murine tumors through extravasations due to the presence of leaky vasculature [14]. However, since nanoshell dimensions are fundamentally variable [7], it is important to further elucidate and confirm the two-photon properties of these highly tunable nanoparticles despite differences in size. Furthermore, since cancer undergoes a multi-stage progression, the ability to track molecular signatures through the overexpression of biomarkers is crucial in obtaining functional and accurate diagnostic results. Therefore, the goal of our study was to demonstrate the nonlinear properties of very different-sized nanoshells and validate the proof of concept that immunotargeted nanoshells can be used to enhance the contrast of malignant human cells *in vitro* through nonlinear excitation prior to our evaluation of this system in excised tissue specimens. Additionally, through the use of two-photon excitation and multi-spectral imaging, the simultaneous acquisition of images at different emission wavelengths was obtained to ascertain the optimal imaging parameters for this system.

We demonstrate the two-photon luminescence properties of two different sizes of gold nanoshell designed with a similar plasmon resonance in the near-infrared. We evaluate the enhanced contrast by comparing HER2-overexpressing breast cancer cells to normal breast cells with and without targeted anti-HER2-bioconjugated gold nanoshells at five different emission wavelength ranges: 451–483, 483–515, 515–547, 558–579, and 590–644 nm. By evaluating imaging results under different ranges, we explore the broad emission properties of silica-based gold nanoshells under two-photon induced luminescence. The anti-HER2 antibody was selected as a model for surface tumor targeting due to the association of HER2-overexpression with more aggressive breast cancers seen in 15–25% of all breast cancer cases [30]. Additionally, studies in our laboratory have previously demonstrated the effectiveness of using immunotargeted nanoshells as diagnostic imaging agents for HER2-overexpressing cancer cells [3, 5, 6, 13]. We show that for immunotargeted nanoshells with a silica core diameter of 254 nm and a gold shell thickness of 19 nm imaged with our specific system, the optimal emission wavelength for observing enhanced contrast of HER2-overexpressing breast cancer cells occurs between 590 and 644 nm at 10% of maximum excitation power. Under similar conditions, normal breast cells are not detectable.

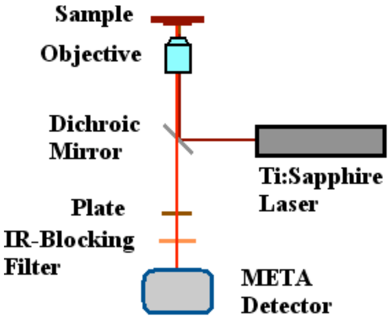

**Figure 1.** Schematic of Zeiss LSM 510 META multi-photon system configuration.

## 2. Method

### 2.1. Multi-photon imaging system

A Zeiss laser scanning microscope (LSM) 510 META multi-photon system was used in conjunction with a Coherent Chameleon femtosecond mode-locked Ti:sapphire laser to collect two-photon data (figure 1). The wavelength of the polarized output laser beam was tunable between 720 and 950 nm with pulse width of 140 fs at a repetition rate of 90 MHz. A short-pass dichroic mirror (KP700/488, Zeiss) was used to reflect the incident NIR excitation light onto the sample through a 20× or 63× objective and to collect the two-photon-induced luminescence data. To further eliminate the background signal of the excitation light, a wave plate and an IR-blocking filter (BG39, Zeiss) were placed in front of the META detector. The Zeiss LSM META system allowed simultaneous multi-spectral imaging and recording of up to eight emission channels. The maximum output power of the Chameleon femtosecond laser was around 1640 mW for excitation at 780 nm. Based on data from the manufacturer, less than 10% of this power was incident on the sample. The excitation wavelength of 780 nm was chosen as it was within 10 nm of the extinction peak for both nanoshell sizes.

### 2.2. Nanoshell fabrication

Nanoshells were developed as described in previous publications [3–5]. First, the Stöber method was used to create silica cores by reducing tetraethyl orthosilicate (Sigma Aldrich) in ammonium hydroxide and pure ethanol [31]. Aminopropyltriethoxysilane (APTES) was then added in order to terminate the silica core surfaces with amine groups, which formed functionalized particles. The two different-sized groups of silica particles were measured by scanning electron microscopy (SEM) to obtain the average silica core diameters of 130 and 254 nm. The gold shell overlay on the silica cores was also created using previously described methods [3–5]. First, using procedures outlined by Duff *et al* [32], gold colloid of 1–3 nm in diameter was developed and then aged under refrigeration for two weeks. The colloid was then concentrated using a Rotovap and added to the functionalized silica particles mentioned above. By interacting with the functionalized amine group surfaces of the silica particles, the gold colloid was adsorbed, forming surfaces with partial gold coverage. Addition of more gold completed the formation of the shell through catalysis of formaldehyde with hydrogen tetrachloroaurate trihydrate ($HAuCl_43H_2O$) and potassium carbonate. Two groups of nanoshells were fabricated and both were spectrally analyzed using a Varian Cary 300 UV–vis spectrophotometer (figure 2). The final sizes of the nanoshells were determined using SEM imaging (figure 2, inset) and confirmed using Mie theory simulation for multi-layer spheres. The smaller nanoshells had an average gold shell thickness of 21 nm. The larger nanoshells had an average shell thickness of 19 nm. The nanoshells were stored in deionized water at 4 °C until further use.

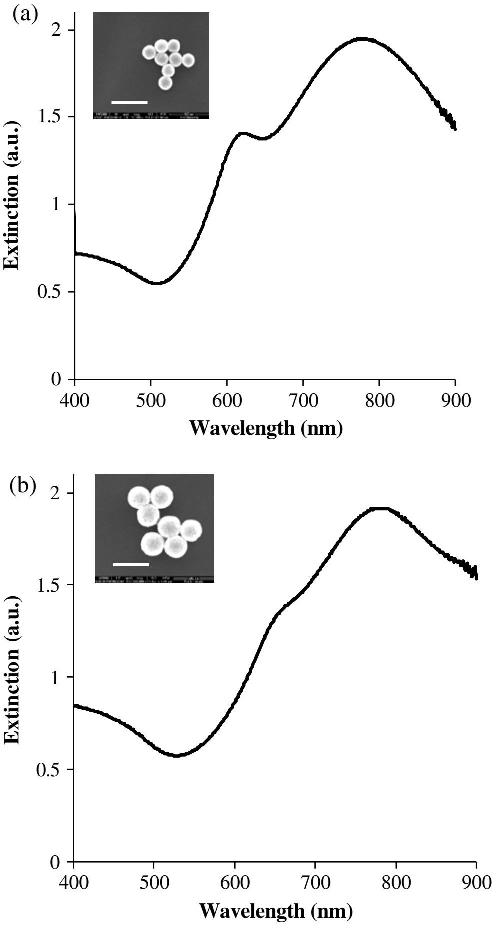

**Figure 2.** Measured extinction spectra of nanoshells. (a) Nanoshells of average core diameter 130 nm and average shell thickness of 21 nm. (b) Nanoshells of average core diameter 254 nm and average shell thickness of 19 nm. The insets depict corresponding images from scanning electron microscopy. Scale bars represent 450 nm.

### 2.3. Nanoshell surface modification and bioconjugation

For live cell imaging, the larger nanoshells were used and targeted to HER2-overexpressing cells through conjugations with anti-HER2 antibodies. In order to prepare the immunotargeted nanoshells, a heterobifunctionalized polyethylene glycol linker (orthopyridyl-disulfide-PEG-N-hydroxysuccinimide ester, OPSS-PEG-NHS, MW = 2 kD, CreativeBiochem Laboratories) was first conjugated to anti-HER2 antibodies (C-erbB-2/HER-2/neu Ab-4, Lab Vision Corporation) through amide linkages that joined the amidohydroxysuccinimide group (NHS) of the PEG linker to the antibodies. This reaction proceeded at a 3:1 molar ratio in sodium bicarbonate (100 mM, pH 8.5) on ice overnight. Aliquots of the 'PEGylated' antibodies, at a concentration of 0.4 mg $ml^{-1}$, were stored at −80 °C until use. Conjugation of the nanoshells to the PEGylated antibodies was then carried out through sulfur linkages between the gold nanoshell surfaces and the remaining OPSS group of the heterobifunctional PEG linker. This was performed by incubating the nanoshells, at a concentration of $1.6 \times 10^9$ particles $ml^{-1}$, with the PEGylated antibodies for 1 h under refrigeration (4 °C). In order to block vacant adsorption sites, the nanoshells were further incubated with a 10 $\mu$M polyethylene glycol-thiol cocktail (PEG-SH, MW = 5kD, Nektar) for two additional hours under refrigeration. Unbound antibodies were then removed by centrifugation and the immunotargeted nanoshells were then resuspended in deionized water. Prior to incubation with cells, the immunotargeted nanoshell solution was further modified by the addition of bovine serum albumin (BSA) and phosphate-buffered saline (PBS) to a final concentration of 1% each.

### 2.4. Cell preparation

SK-BR-3 cells (American Type Culture Collection, ATCC) were grown at 37 °C in a 5% $CO_2$ atmosphere using McCoy's 5A growth medium supplemented with 1% antibiotics and 10% fetal bovine serum (FBS). MCF10A cells (ATCC) were also grown at 37 °C in a 5% $CO_2$ atmosphere using Mammary Epithelial Basal Medium (MEBM) supplemented with a BulletKit (Clonetics) and 1% antibiotics. Both cell lines were grown in 25 $cm^2$ culture flasks until confluent, rinsed once with 1 × PBS, and incubated with trypsin-EDTA for 5 min at 37 °C in a 5% $CO_2$ atmosphere. The trypsin-EDTA was then neutralized with the appropriate culture medium and the cells were subsequently counted using a hemacytometer. For each cell line, an estimated $6 \times 10^5$ cells were placed in each of two 15 ml conical tubes and then centrifuged at $115 \times g$ for 3 min. One cell pellet was resuspended in the immunotargeted

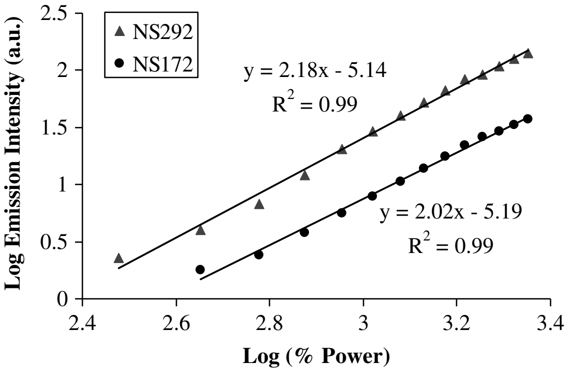

**Figure 3.** Quadratic dependence of luminescence intensity on excitation power at 780 nm for two different-sized nanoshells. Nanoshells of core diameter of 130 nm and shell thickness of 21 nm are designated as NS172. Nanoshells of core diameter of 254 nm and shell thickness of 19 nm are designated as NS292. Data were recorded with a 20× objective.

nanoshell solution and the other pellet was resuspended in an equal volume of 1 × PBS. The cells were then incubated at 37 °C in a hybridization chamber (VWR International) and rotated under a motor speed of 7 rpm for 10 min. Post incubation, the cells were centrifuged at 115 × *g* for 3 min, the supernatant was removed, and the cells were rinsed once with 1 × PBS. Following rinsing, the cells were resuspended in 10% glucose in 1 × PBS in order to maintain cell viability during imaging. The cell suspensions were then placed on chambered coverglasses (Fisher Scientific) prior to two-photon imaging.

## 3. Results and discussion

By manipulation of the core-to-shell ratio, nanoshells can be designed to strongly absorb or scatter light upon near-infrared excitation. In order to validate the two-photon characteristics of silica-based gold nanoshells, we designed two different sizes of nanoshell with a similar peak surface plasmon resonance in the near-infrared. After fabrication of two different-sized silica cores, their average diameters were confirmed through scanning electron microscopy (SEM) as 130 and 254 nm. Once the gold shell was added, the nanoshells were measured by SEM and their optical properties were assessed by UV–vis spectroscopy. The smaller nanoshells had an average diameter of 172 nm and a peak surface plasmon resonance at 772 nm; for the larger nanoshells, the average diameter was 292 nm, with a peak surface plasmon resonance occurring at 778 nm (both shown in figure 2). The two-photon luminescence properties of the gold nanoshells were then observed using a Zeiss LSM 510 META multi-photon system with the configuration shown in figure 1. The two-photon properties were verified by evaluating the dependence of increasing logarithmic emission intensity on increasing logarithmic excitation power. Aliquots of both sizes of bare nanoshell suspended in deionized water were well dispersed with sonication and separately placed on chambered coverglasses (Fisher Scientific). Data were recorded at an excitation wavelength of 780 nm, which corresponded to the peak plasmon resonance of the nanoshells for both sample sizes. The excitation power was varied from 2% to 15% of the maximum laser power with a detection spectral band of 494–634 nm. By using the image processing software inherent in the LSM 510 META system, the average intensities of the nanoshell suspensions were obtained. The dependence of luminescence intensity on excitation power at 780 nm for both smaller- and larger-sized nanoshells was determined (figure 3). The slopes of the fitted linear curves are estimated as 2.02 and 2.18 for the smaller and larger nanoshells, respectively, in accordance with the characteristic two-photon-induced quadratic dependence of emission intensity on excitation power [14, 16, 20]. Specifically, Wang *et al* demonstrated that the dependence of luminescence intensity on excitation power for gold nanorods ranged from 1.97 to 2.17 [27]. This disparity was attributed to possible nanoparticle melting after increasing the power on the nanorod sample and, subsequently, decreasing the power on the same sample. However, in our study, since a difference in quadratic dependence exists for two sizes of gold nanoshell treated under the same conditions, we believe that the nanoshells may actually undergo photophysics which are not yet fully elucidated.

In order to demonstrate the enhanced two-photon optical signatures of breast cancer cells labeled with immunotargeted nanoshells, the HER2-overexpressing epithelial breast cancer cell line, SK-BR-3, was analyzed and compared to the normal breast epithelial cell line, MCF10A, which does not overexpress HER2. For this component of the study, the cells were incubated with the larger nanoshells which were conjugated to anti-HER2 antibodies. Images were taken of the SK-BR-3 cancer cells under three conditions: labeled with nanoshells at 10% of maximum laser power, unlabeled at 10% of maximum laser power, and unlabeled at 100% of maximum laser power. An excitation wavelength of 780 nm was used for all images and five different emission wavelength ranges were analyzed: 451–483, 483–515, 515–547, 558–579, and 590–644 nm. Additionally, images were taken of the MCF10A normal cells under the same labeling and imaging conditions. As shown in figure 4(a), bright two-photon luminescence signals from nanoshells targeted to cell surface receptors provided clear visualization of the SK-BR-3 cancer cells under only 10% of maximum laser power. However, under the same power, unlabeled cancer cells were not perceivable (data not shown due to lack of detectable signal). By increasing the laser power to 100%, the spectral-resolved two-photon-induced autofluorescence is evident at emission wavelengths ranging from 451 to 547 nm (figure 4(b)). However, this autofluorescence, which is only visible at the maximized power, cannot be discerned beyond an emission wavelength of 547 nm. With regard to the normal MCF10A cells labeled with immunotargeted nanoshells under 10% of maximum laser power, clear visualization of the cells is not possible and only a few targeted cell surface receptors can be distinguished (figure 4(c)). Due to the differences in HER2 cell surface receptor expression, which is approximately $8 \times 10^5$ receptors per SK-BR-3 cancer cell [33] and about $1 \times 10^4$ receptors per normal MCF10A cell [34], the contrast was dramatically increased in the cancer cells due to the overexpression of HER2. Similar to the unlabeled

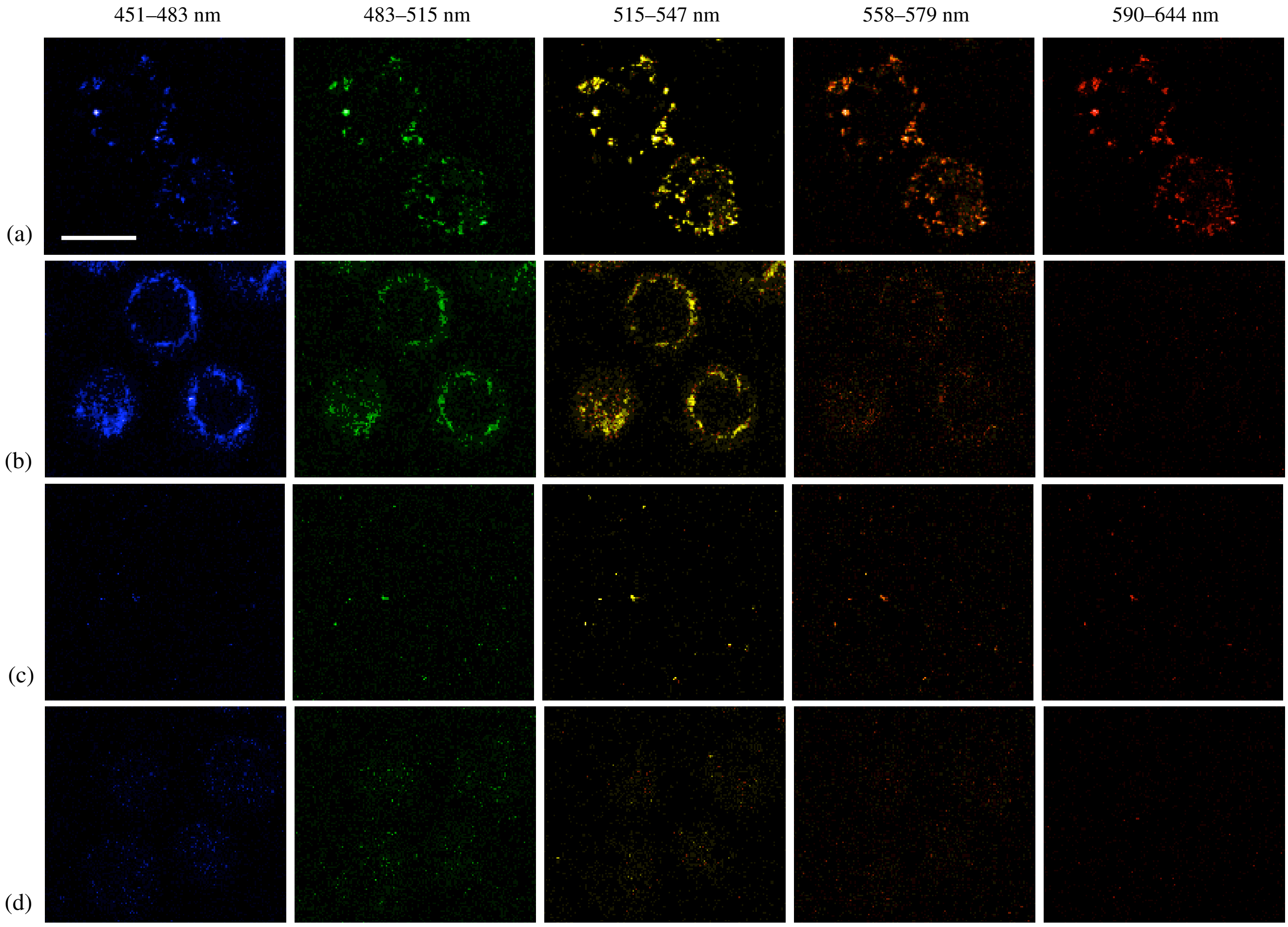

**Figure 4.** Two-photon images (pseudo color) of live SK-BR-3 cancer cells and MCF10A normal cells in suspension taken at different emission wavelengths. (a) Cancer cells labeled with larger nanoshells at 10% of maximum excitation power. (b) Unlabeled cancer cells at 100% of maximum excitation power. (c) Normal cells labeled with larger nanoshells at 10% of maximum excitation power. (d) Unlabeled normal cells at 100% of maximum excitation power. Images taken at 63×. The scale bar represents 20 $\mu$m.

SK-BR-3 cancer cells, unlabeled MCF10A cells imaged at 10% of maximum laser power were not detectable (data not shown due to lack of detectable signal). Furthermore, images collected at 100% of maximum laser power demonstrated that the MCF10A cells exhibited low levels of two-photon-induced autofluorescence (figure 4(d)). Wang *et al* [27] and Durr *et al* [29] have previously shown two-photon imaging results using gold nanorods. However, the images collected were taken over a single emission wavelength range from 400 nm to approximately 700 nm. Based on spectral-resolved image acquisition, however, the unique widely spanning luminescence properties of gold nanoshells demonstrate great flexibility in selecting the emission wavelengths necessary to minimize the influence of background autofluorescence. Photobleaching was also not observed under the two-photon-induced nanoshell luminescence. Based on a comparison of live cell bright-field images observed before and after laser exposure, morphological changes were not detected as a result of the aforementioned laser conditions and, in particular, all cell membranes remained visible and intact.

## 4. Conclusion

Two-photon microscopy is a powerful tool for diagnostic research applications. With advancements in gold-based contrast agent development and flexibility in two-photon excitation wavelength selection readily achieved through tunable laser sources, the potential to use multi-photon imaging for assessment of molecular signatures of malignancy is substantial. In this study, we demonstrate the first use of immunotargeted gold nanoshells as *in vitro* contrast agents for biomarkers of disease using two-photon microscopy. We additionally confirm broad luminescence from gold nanoshells using multi-spectral images to visualize the optical contrast provided by anti-HER2-nanoshells targeted to live HER2-overexpressing breast cancer cells. Our study identifies an additional application of immunotargeted nanoshells and suggests their potential future use as multi-functional probes for molecular imaging.

## Acknowledgments

We thank Dr Robert Raphael for expert technical assistance using a Zeiss LSM META 510 system. We acknowledge support from a Department of Defense Era of Hope Scholar Award to Rebekah Drezek, the Beckman Young Investigator Program, the Welch Foundation (C-1598), and the Center for Biological and Environmental Nanotechnology (EEC-0118007 and EEC-0647452).

## References

[1] Hawk E, Viner J L and Lawrence J A 2000 *Curr. Oncol. Rep.* **2** 242–50

[2] Weinberg R A 2007 *The Biology of CANCER* (New York: Taylor and Francis) pp 727–32

[3] Loo C, Hirsch L, Lee M H, Chang E, West J, Halas N and Drezek R 2005 *Opt. Lett.* **30** 1012–4

[4] Lowery A R, Gobin A M, Day E S, Halas N J and West J L 2006 *Int. J. Nanomed.* **1** 149–54

[5] Loo C, Lowery A, Halas N, West J and Drezek R 2005 *Nano Lett.* **5** 709–11

[6] Fu K, Sun J, Bickford L R, Lin A W H, Halas N J, Yu T K and Drezek R A 2008 *Nanotechnology* **19** 045103

[7] Hirsh L R, Gobin A M, Lowery A R, Tam F, Drezek R A, Halas N J and West J L 2006 *Ann. Biomed. Eng.* **34** 15–22

[8] Gobin A M, Lee M H, Halas N J, James W D, Drezek R A and West J L 2007 *Nano Lett.* **7** 1929–34

[9] Wu C, Liang X and Jiang H 2005 *Opt. Commun.* **253** 214–21

[10] Zaman R T *et al* 2007 *IEEE J. Sel. Top Quantum Electron.* **13** 1715–20

[11] Fournelle M, Maass K, Fonfara H, Welsch H J, Hewener H, Günther C and Lemor R 2007 *IEEE Ultrason. Symp.* **1051-0117/07** 2417–20

[12] Agrawal A, Huang S, Lin A W H, Lee M H, Barton J, Drezek R A and Pfefer T J 2006 *J. Biomed. Opt.* **11** 041121

[13] Loo C 2006 *PhD Thesis* Rice University, Houston, Texas

[14] Park J *et al* 2008 *Opt. Express* **16** 1590–9

[15] Wang Y, Xie X, Wang X, Ku G, Gill K L, O'Neal D P, Stoica G and Wang L 2004 *Nano Lett.* **4** 1689–92

[16] Zipfel W R, Williams R M and Webb W W 2003 *Nat. Biotechnol.* **21** 1369–77

[17] Denk W, Strickler J H and Webb W W 1990 *Science* **248** 73–6

[18] Hell S W, Booth M, Wilms S, Schnetter C M, Kirsch A K, Arndt-Jovin D J and Jovin T M 1998 *Opt. Lett.* **23** 1238–40

[19] Lewis M K, Wolanin P, Gafni A and Steel D G 1998 *Opt. Lett.* **23** 1111–3

[20] Piston D W 1999 *Cell Biol.* **9** 66–9

[21] Boyd G T, Yu Z H and Shen Y R 1986 *Phys. Rev.* B **33** 7923–36

[22] Mooradian A 1969 *Phys. Rev. Lett.* **22** 185–7

[23] Huang X, Qian W, El-Sayed I H and El-Sayed M A 2007 *Lasers Surg. Med.* **39** 747–53

[24] Nagesha D, Laevsky G S, Lampton P, Banyal R, Warner C, DiMarzio C and Sridhar S 2007 *Int. J. Nanomed.* **2** 813–9

[25] Bouhelier A, Bachelot R, Lerondel G, Kostcheev S, Royer P and Wiederrecht G P 2005 *Phys. Rev. Lett.* **95** 267405

[26] Imura K, Nagahara T and Okamoto H 2005 *J. Phys. Chem.* B **109** 13214–20

[27] Wang H, Huff T B, Zweifel D A, He W, Low P S, Wei A and Cheng J X 2005 *Proc. Natl Acad. Sci.* **102** 15752–6

[28] Huff T B, Hansen M N, Zhao Y, Cheng J X and Wei A 2007 *Langmuir* **23** 1596–9

[29] Durr N J, Larson T, Smith D K, Korgel B A, Sokolov K and Ben-Yakar A 2007 *Nano Lett.* **7** 941–5

[30] National Comprehensive Cancer Network 2007 *Breast Cancer Treatment Guidelines for Patients* Version IX http://www.nccn.org

[31] Stöber W, Fink A and Bohn E 1968 *J. Colloid Interface Sci.* **26** 62–9

[32] Duff D G, Baiker A and Edwards P P 1993 *Langmuir* **9** 2301–9

[33] Hayes D F, Walker T M, Singh B, Vitetta E S, Uhr J W, Gross S, Rao C, Doyle G V and Terstappen L W M M 2002 *Int. J. Oncol.* **21** 1111–7

[34] Kornilova E S, Taverna D, Hoeck W and Hynes N E 1992 *Oncogene* **7** 511–9

Nanobiotechnol
DOI 10.1007/s12030-008-9010-4

# Evaluation of Immunotargeted Gold Nanoshells as Rapid Diagnostic Imaging Agents for HER2-Overexpressing Breast Cancer Cells: A Time-based Analysis

**Lissett R. Bickford · Joseph Chang · Kun Fu · Jiantang Sun · Ying Hu · André Gobin · Tse-Kuan Yu · Rebekah A. Drezek**

**Abstract** Biomedical nanotechnology offers superior potential for diagnostic imaging of malignancy at the microscopic level. In addition to current research focused on dual-imaging and therapeutic applications in vivo, these novel particles may also prove useful for obtaining immediate diagnostic results in vitro at the patient bedside. However, translating the use of nanoparticles for cancer detection to point-of-care applications requires that conditions be optimized such that minimal time is needed for diagnostic results to become available. Thus far, no reports have been published on minimizing the time needed to achieve acceptable optical contrast of cancer cells incubated with nanoparticles. In this study, we demonstrate the use of gold nanoshells targeted to anti-HER2 antibodies that produce sufficient optical contrast with HER2-overexpressing SK-BR-3 breast cancer cells in only 5 min. This work validates the proof of concept that nanoshells targeted to extracellular biomarkers can be used to enhance cancer diagnostic imaging for use in point-of-care applications.

**Keywords** nanoshells · point-of-care diagnostics · optical imaging · cancer diagnosis

## Introduction

Several nanoparticles have been explored for potential applications in cancer diagnosis, including nanoshells [1–4], gold colloid [5, 6], quantum dots [7, 8], carbon dots [9], nanorods [10–12], and nanocrystals [13]. For in vivo applications, several steps will need to be taken to ensure the safe delivery of nanoparticles before they can be used in a clinical setting. However, several opportunities still exist for in vitro applications in which the cytotoxicity of nanoparticles is immaterial. Numerous in vitro technologies that have shown promise for point-of-care diagnostic testing may allow clinicians to provide user-friendly, cost-effective, and rapid results at the patient bedside. Currently, these technologies involve analyzing biological fluids to detect DNA or protein amplification through the use of microarrays or biochip devices [14–16]. In addition to fluid-based modalities, these microscopic advancements can also be used to analyze larger biological components, such as excised tumor specimens, for cancer screening and diagnosis. One particular area of application is the diagnosis of cancer from biopsy samples. For example, after a breast biopsy, the specimen is sent to a pathology laboratory where it is processed and examined microscopically for morphological abnormalities and sometimes analyzed for the presence of molecular biomarkers of

---

T.-K. Yu and R.A. Drezek contributed equally to this work.

L. R. Bickford · J. Chang · K. Fu · J. Sun · Y. Hu ·
R. A. Drezek (✉)
Department of Bioengineering, Rice University,
6100 Main St., MS-142,
Houston, TX 77005, USA
e-mail: drezek@rice.edu

K. Fu · T.-K. Yu
Department of Radiation Oncology,
The University of Texas M.D. Anderson Cancer Center,
Houston, TX 77030, USA

A. Gobin
Department of Bioengineering, University of Louisville,
Louisville, KY 40292, USA

R. A. Drezek
Department of Electrical and Computer Engineering,
Rice University,
Houston, TX 77005, USA

disease, such as hormone receptor expression [17]. This process can take up to several days, during which the patient must cope with the fear of an unknown diagnosis and the potential of treatment delay. Mojica et al. [18] showed that delays between initial breast cancer symptoms and treatment are associated with lower survival rates. Consequently, delays in breast cancer diagnosis top the list of liability claims made against physicians [19].

Another area of opportunity for advancement in point-of-care microscopic analysis of tumor specimens involves the assessment of intraoperative tumor margins. During a lumpectomy, for instance, the surgeon removes the suspected cancerous lesion with a margin of normal tissue. Judgment of the width of this margin is largely based on tactile sensation and visible, macroscopic abnormalities. In advanced hospital systems, the sample is excised and immediately subjected to pathologic analysis to ensure the surgical margins are tumor-free before the procedure is completed. The need to achieve negative margins is critical in minimizing cancer recurrence and progression, particularly for patients undergoing breast conservation therapy [20]. The presence of a positive surgical margin has been associated with lower rates in patient survival [18]. Due to residual cancer cells being left in many patients that undergo breast conservation therapy, as many as 40% of patients have experienced local breast cancer recurrence near the site of the original tumor [21]. Positive margins in a surgical specimen, therefore, necessitate the resection of additional tissue until the margins do not contain tumor. Even if the specimens are examined immediately, this extends the period of anesthesia and hence increases both the cost and risk to the patient. Furthermore, many county hospitals must, by necessity, process tissue samples after the surgery is completed. In that case, the identification of positive surgical margins requires that the patient undergo another surgical procedure to excise the remaining tissue, which further delays the start of adjuvant treatment and increases the risk of cancer recurrence and subsequent patient mortality.

With the expansion of nanotechnology-driven research, opportunities for the use of fast and accurate diagnostic tests outside of the hospital laboratory are likely to increase. To realistically use nanoparticles as a point-of-care tool for the immediate assessment of key cancer gene signatures in excised tissue samples, the time needed to achieve optical contrast must be minimized. Thus far, few published reports have focused on minimizing the time needed to achieve suitable contrast of cancer cells incubated with nanoparticles. Previous studies demonstrating the effectiveness of using gold-based nanoparticles targeted to extracellular cancer biomarkers have involved incubation times ranging from 30 to 90 min [1, 3, 5, 6, 10–12]. The objective of this study was to demonstrate the feasibility of using gold nanoshells targeted to anti-HER2 antibodies to achieve sufficient optical contrast in a HER2-overexpressing breast cancer cell line (SK-BR-3) after a series of incubation times. Overexpression of the HER2 receptor is associated with greater cancer progression and is seen in approximately 15–25% of all breast cancer cases [17]. The nanoshells, made of dielectric silica particles covered with a thin gold shell, were fabricated to scatter strongly in the near-infrared spectrum through manipulation of the silica core/gold shell ratio. We compared the contrast that could be achieved by incubating the nanoshells with both normal and cancerous cells. Our results demonstrate that gold nanoshells targeted to this cell-surface marker can produce enhanced contrast after only 5 min of incubation. This proof of concept supports the initial feasibility of using gold nanoshells for potential point-of-care diagnostic applications.

## Materials and Methods

### Nanoshell Fabrication

Nanoshells were developed and bioconjugated by using previously reported procedures [22]. First, silica cores were prepared with the Stöber method [23], in which tetraethyl orthosilicate (Sigma Aldrich) is reduced in ammonium hydroxide and pure ethanol. Next, aminopropyltriethoxysilane was used to functionalize the particles by terminating the silica core surface with amine groups. The silica particles were then measured by scanning electron microscopy (SEM) to obtain the average silica core diameter of 254 nm.

To create the gold shell overlap for the silica cores, gold colloid of 1–3 nm in diameter was fabricated based on procedures documented by Duff et al. [24]. The gold colloid solution was stored at 4 °C for 2 weeks and subsequently concentrated with a Rotovap. After aging and concentration, the gold colloid solution was added to the aforementioned functionalized silica particles, forming ‘seeds’ in which the gold colloid is adsorbed to the amine groups of the silica cores. To complete nanoshell fabrication, a cocktail of hydrogen tetrachloroaurate trihydrate ($HAuCl_4$) and potassium carbonate was added to the seeds along with formaldehyde to catalyze the formation of the shells. The spectrum of the completed nanoshells was analyzed with a UV-vis spectrophotometer (Varian Cary 300). The relationship between the extinction spectrum obtained by UV-vis spectroscopy and that obtained by application of the Mie scattering theory can be used to approximate the size of the nanoparticles in solution (Fig. 1). Subsequently, Mie Theory can be used to derive the absorption, scattering, and extinction coefficients for nanoparticles of a specific size, and a standard known

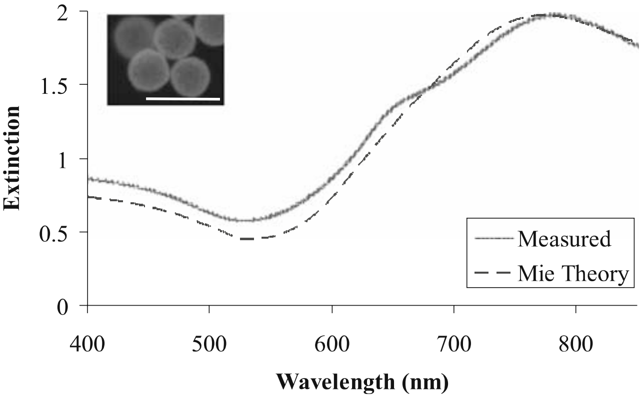

**Fig. 1** Measured spectra of nanoshells (core radius, 127 nm; shell thickness, 19 nm) as compared with that estimated using the Mie scattering theory; the *insert* depicts the corresponding image from scanning electron microscopy. *Scale bar* represents 500 nm.

concentration can be acquired for a particular optical density. In addition to using Mie scattering theory for multilayer spheres, we also used SEM to confirm the size of the nanoshells. The nanoshells used in this study had an average diameter of 292 nm, a peak surface plasmon resonance at 778 nm and a concentration of approximately $1.6\times10^9$ particles/ml.

### Nanoshell Surface Modification

To target the prepared nanoparticles to molecular markers associated with HER2-overexpression, antibodies were first prepared by methods previously described by Hirsch et al. [22]. Briefly, anti-HER2 antibodies (C-erbB-2/HER-2/*neu* Ab-4, Lab Vision Corporation) were conjugated to the heterobifunctionalized polyethylene glycol linker orthopyridyl-disulfide-PEG-*N*-hydroxysuccinimide ester (OPSS-PEG-NHS, MW=2 kD, CreativeBiochem Laboratories) by reaction at a molar ratio of 1:3 in sodium bicarbonate (100 mM, pH 8.5) overnight on ice. Aliquots were stored at −80 °C. The amidohydroxysuccinimide group (NHS) enables conjugation of the PEG linker to the antibodies through amide linkages; the remaining end of the PEG linker, OPSS, allows binding to the nanoshell gold surfaces through sulfur groups. The nanoshells ($1.6\times10^9$ particles/ml) were incubated with the prepared anti-HER2-PEG solution (0.4 mg/ml) for 1 h at 4 °C. The newly conjugated nanoshells were subsequently incubated with a 10 μM polyethylene glycol-thiol solution (PEG-SH, MW=5 kD, Nektar) for 2 additional hours at 4 °C, which stabilized the nanoshells by blocking any unoccupied adsorption sites. The nanoshells were then centrifuged to remove unbound antibodies, resuspended in ultrapure water, and stored at room temperature until use. Before being incubated with cells, the nanoshell solution was supplemented with bovine serum albumin and phosphate-buffered saline (PBS) at final concentrations of 1% each.

### Preparation of Cells

Two cell types were analyzed for this study: the HER2-overexpressing epithelial breast cancer cell line SK-BR-3 and the normal mammary epithelial cell line MCF10A (American Type Culture Collection). The SK-BR-3 cells were grown in McCoy's 5A medium supplemented with 10% fetal bovine serum and 1% penicillin-streptomycin and maintained at 37 °C in a 5% $CO_2$ atmosphere. The MCF10A cells were cultured in Mammary Epithelial Basal Medium (MEBM) supplemented with a BulletKit (Clonetics) and also maintained at 37 °C in 5% $CO_2$. Both cell lines were grown in 25-$cm^2$ culture flasks until confluent. At that time, cells were rinsed once with 1× PBS and incubated with trypsin-ethylenediaminetetraacetic acid for 5 min at 37 °C to detach the cells from the substrate, after which trypsin was neutralized with the appropriate medium and the cells were counted. Approximately $6\times10^5$ cells were placed in each of four conical tubes per cell line for each time point under investigation. The cells were then centrifuged at 115×*g* for 3 min. For each cell line and each time point of interest, three cell pellets were resuspended in the bioconjugated nanoshell solution, and one was resuspended in an equal amount of PBS as a control. The nanoshell–cell suspensions and controls were then incubated in a hybridization chamber (VWR International) at 37 °C and a motor speed of 7 rpm for 5, 10, 30, or 60 min. After incubation, the suspensions were centrifuged at 115×*g* for 3 min, and the unbound nanoshells were collected with a pipette. Cells were then rinsed once with 1× PBS, centrifuged, and the unbound nanoshells were again collected. A small volume (5 μl) of 10% glucose mixed with PBS was added to the remaining cell pellets to prevent cell death during imaging. Approximately 7 μl of each pellet was placed on a glass slide and coverslipped for immediate microscopic analysis.

### Darkfield Imaging and Processing

Images of the two cell types incubated with nanoshells were obtained with a Zeiss Axioskop 2 darkfield microscope outfitted with a color camera (Zeiss AxioCam MRc5). Darkfield microscopy depends on light scattering to achieve contrast. All images were taken under the same lighting conditions and magnification (×20). Optical intensity was quantified by using a Matlab code. Based on this code, an image with a value of 0 was designated pure black and that with a value of 255 pure white. An increase in intensity, therefore, corresponded to an image with a higher numerical value. Average intensity values for each time point and each cell line were calculated from ten independent cell samples that were devoid of scattering influences from neighboring cells and unbound nanoshells. Sample normality was assessed by using Minitab to evaluate the error

**Fig. 2** Darkfield images of MCF10A and SK-BR-3 cells incubated with bioconjugated nanoshells for the indicated times. Images were obtained at ×20. *Scale bar* represents 125 μm.

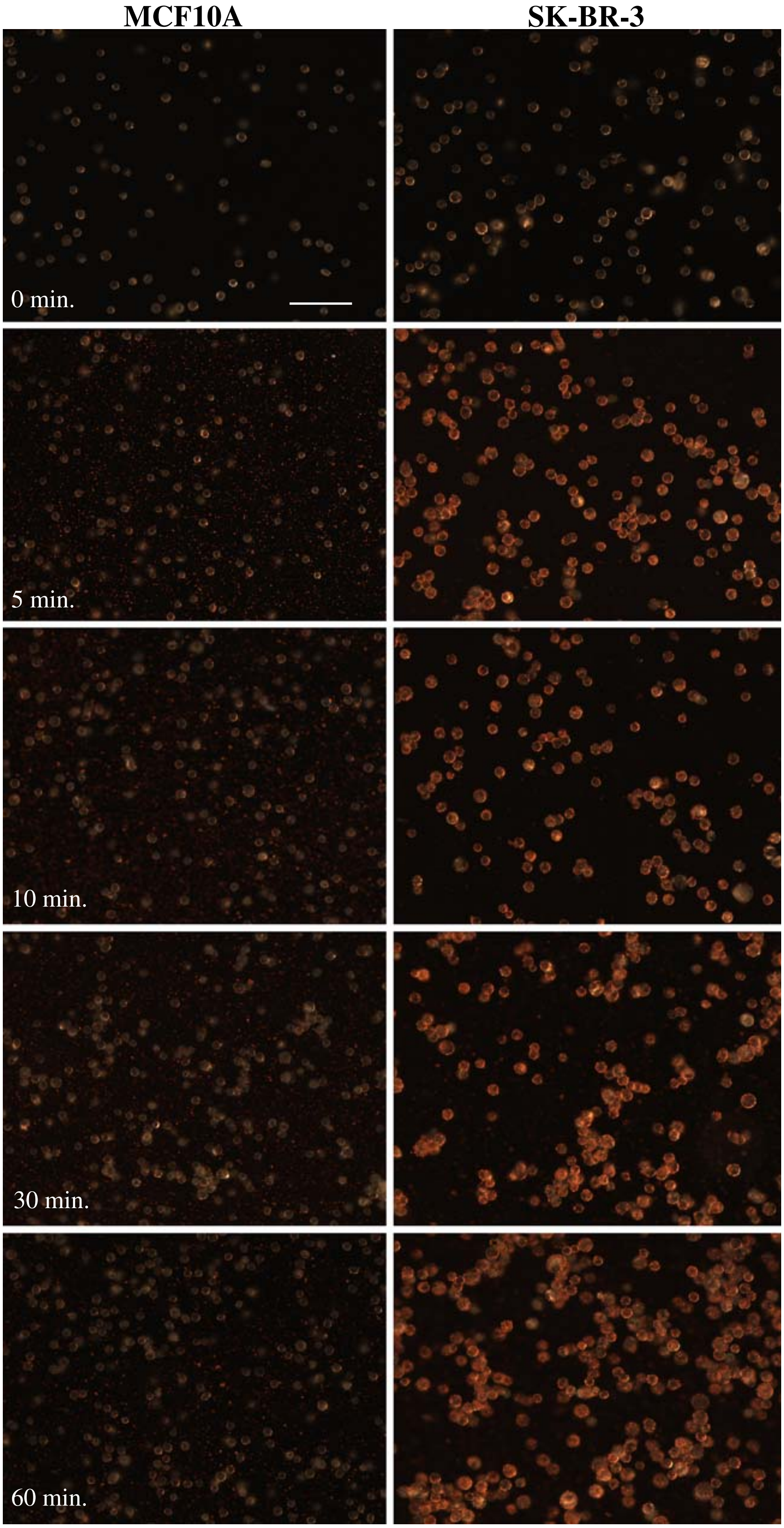

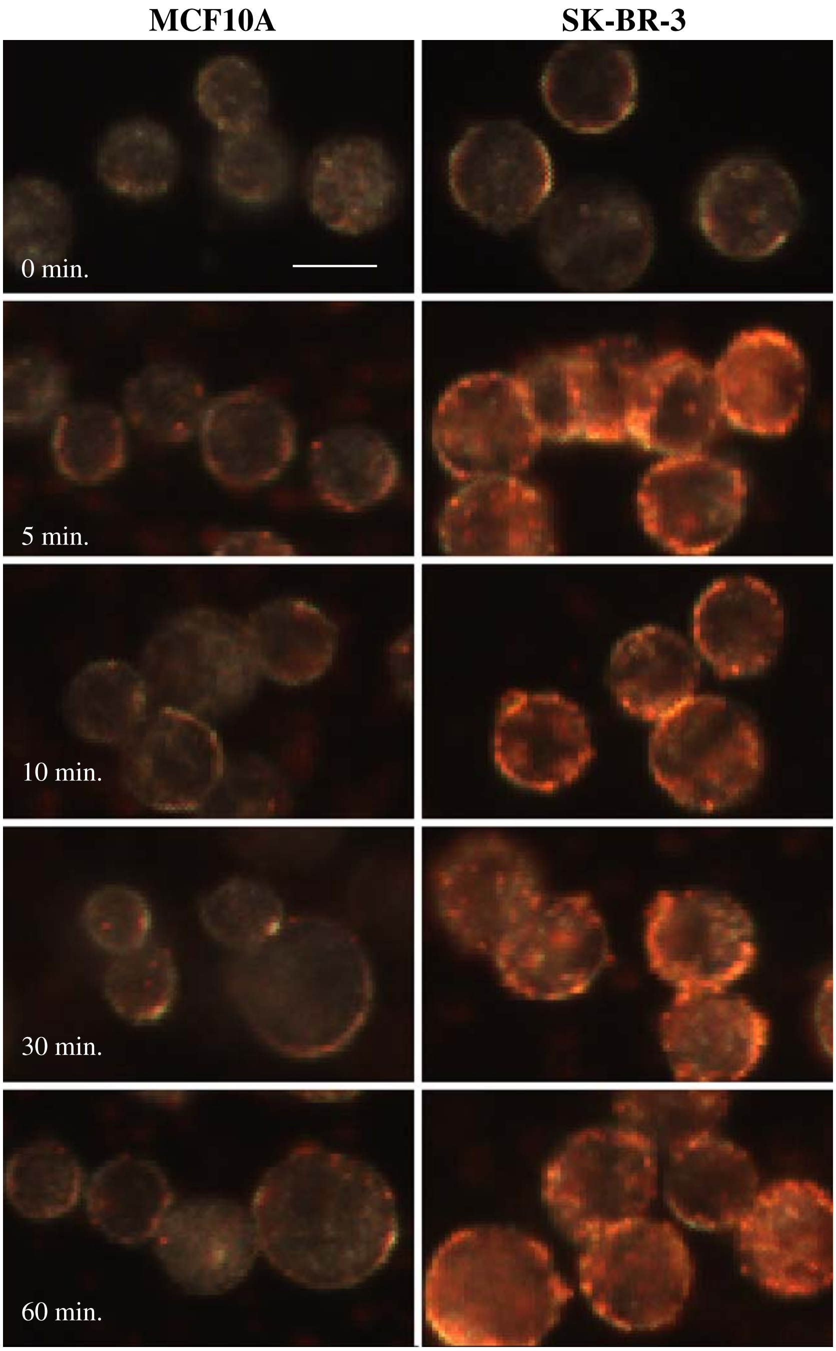

**Fig. 3** Enlarged darkfield images of MCF10A and SK-BR-3 cells incubated with the bioconjugated nanoshells for the indicated times. Original images taken at ×20. *Scale bar* represents 20 μm.

distribution for all data points. A normal probability plot of the residuals verified that the samples followed a normal distribution (data not shown). *F* tests were also used to determine the equality of variance before applying two-tailed paired Student's *t* tests to evaluate significance.

### Derivation of Bound Nanoshell Concentration using Spectroscopy

According to the Beer–Lambert law, the absorbance of particles in solution is directly related to the concentration of those particles in that solution. To validate the ability of spectroscopy to predict the concentration of a solution of nanoshells of known size, we used linear regression analysis. Nanoshells of known concentration, based on the Mie Theory calculations, were serially diluted and, the corresponding peak absorbance values were measured. We considered a concentration of approximately $2.0\times10^9$ particles/ml (optical density=2.4) as a 100× concentration. From this analysis, an equation relating the peak absorbance (independent variable) to each known nanoshell concentration (dependent variable) was used to approxi-

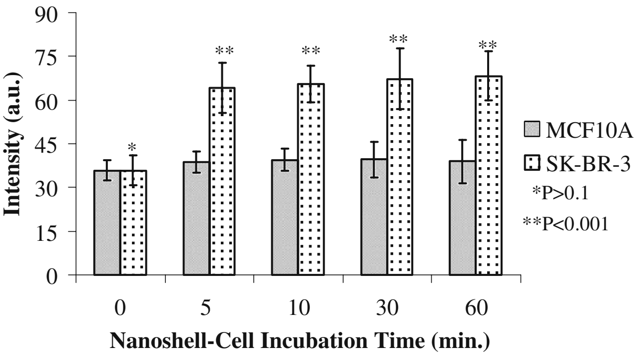

**Fig. 4** Mean quantitative intensity values for samples of MCF10A and SKBR3 cells incubated with nanoshells for the indicated times. Differences between cell types incubated without nanoshells were not statistically significant ($P>0.1$, $n=10$). Differences between cell types incubated with nanoshells were statistically significant at all time points ($P<0.001$, $n=10$). *Error bars* indicate standard deviations.

mate the number of nanoparticles in subsequent solutions of unknown concentration. This derivation was necessary to calculate the approximate number of bound nanoparticles per cell at the different time points.

To determine and compare the number of nanoshells bound after 5 min and 60 min of incubation, the collected unbound nanoshells were centrifuged at 255×*g* for 20 min, resuspended in ultrapure water, transferred to cuvettes and sonicated briefly before being measured with a UV-vis spectrophotometer. The spectrum was recorded and the peak absorbance documented for each sample. Based on the original concentration of nanoshells, the number of cells used, and the concentration of the collected unbound nanoshells, the approximate number of nanoshells bound to each cancer cell was derived. An *F* test was also used to determine the equality of variance before applying a two-tailed paired Student's *t* test to evaluate significance.

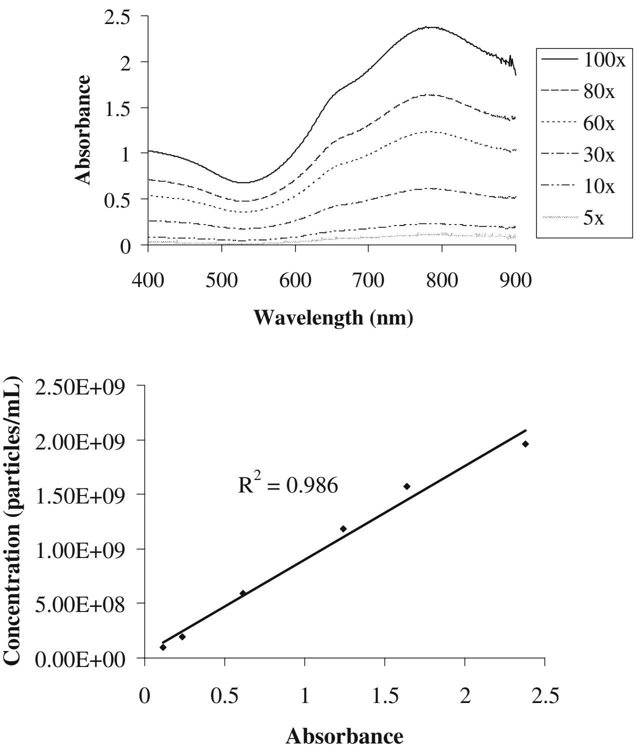

**Fig. 5** *Top* Spectra of serial dilutions of known nanoshells concentrations in suspension. *Bottom* Linear regression analysis of known nanoshell concentrations vs. the corresponding peak absorbance values.

## Results/Discussion

We evaluated the contrast that could be achieved by incubating nanoshells targeted to HER2 receptors with normal breast epithelial cells (MCF10A) or breast cancer cells (SK-BR-3) for four intervals: 5, 10, 30, and 60 min. All procedures were done with triplicate samples and included a control condition (cells to which no nanoshells had been added). Figures 2 and 3 illustrate original and enlarged images obtained at all four time points for both cells lines and for cells incubated without nanoshells (designated as 0 min). Because the optical peak resonance for the fabricated nanoparticles occurred at 778 nm, the nanoshells scattered strongly in the near-infrared range and could be visualized under darkfield illumination as red particles. Qualitative assessment of the imaging results revealed that the MCF10A cells showed little enhanced scattering at any period of incubation with the bioconjugate–nanoshell solution compared with both controls or the cancer cells. However, the SK-BR-3 cancer cells showed enhanced contrast after as little as 5 min of incubation. Typically, SK-BR-3 cells express about $8\times10^5$ receptors per cell and normal MCF10A cells about $1\times10^4$ [25, 26]. The targeted bioconjugated nanoshells apparently bound to cell surface receptors on both cell types; however, because the cancer cells had higher numbers of receptors, the contrast that could be achieved was considerably greater with those HER2-overexpressing cells. Other evidence of the superior contrast achieved with the SK-BR-3 cells was apparent from the difference in the numbers of unbound nanoshells between the two cell types. In the images of the

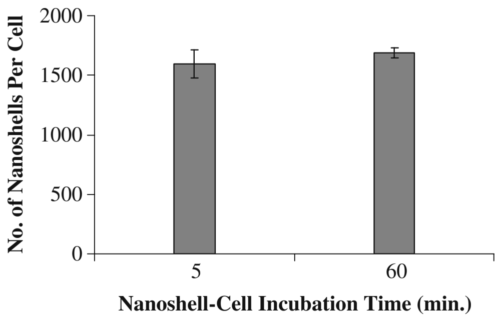

**Fig. 6** Number of nanoshells bound per SK-BR-3 cell after 5 and 60 min of incubation. Values shown are the means of triplicate measurements. *Error bars* indicate standard deviations.

MCF10A cells, several unbound nanoshells could be seen between cells despite our attempts at removing unbound nanoshells by rinsing the cells. Considerably fewer such nanoshells were present in the SK-BR-3-nanoshell images (Fig. 2).

To quantitatively assess the increase in contrast between the normal and cancerous cells at each time point, we used a Matlab code to evaluate the average intensity of ten cells from each condition; an intensity value of 0 was considered pure black and 255 pure white. Statistical analyses indicated no difference between either cell type incubated with only PBS (the control condition; $P > 0.1$). However, differences between the MCF10A cells and the SK-BR-3 cells were significant at all four incubation times ($P < 0.001$; Fig. 4). An additional analysis of variance showed no differences in the mean intensity of the SK-BR-3 cells at any of the four incubation times ($P > 0.5$).

To further compare the differences between contrast that could be achieved at 5 and 60 min for the SK-BR-3 cells, we examined the number of bound nanoshells at both time points. To do so, we first developed a simple UV-vis spectroscopy method to determine the concentration of nanoshells in solution. On the basis of dilutions of known nanoshell concentrations, we used linear regression to estimate the concentration of nanoshells in a given solution (Fig. 5). We confirmed the existence of a linear relationship between absorbance and corresponding concentration of nanoshells for concentrations ranging from $9.8 \times 10^7$ to $2.0 \times 10^9$ particles/ml. With a goodness-of-fit ($R^2$) value of 0.986, we concluded that the absorbance accurately predicts the concentration of an unknown suspension of nanoparticles that falls within this range.

We next used this relationship between absorbance and concentration to measure the absorbance of unbound nanoshells collected after incubation and cell rinsing and subsequently resuspended in a volume of water equal to that of the diluted samples of known concentration. Knowing the initial number of nanoshells and cells, we could derive the approximate number of nanoshells bound to each cell, which we did for the triplicate samples of nanoshells plus cells after 5 and 60 min of incubation. At 5 min of incubation, $1{,}593 \pm 121$ nanoshells were bound per cell; at 60 min, the range was $1{,}686 \pm 40$ nanoshells per cell ($P > 0.1$, not significant; Fig. 6). Thus, roughly 95% of the binding noted at 60 min had occurred within the first 5 min of incubation. Our imaging results suggest that this 5% difference did not seem to affect contrast.

## Conclusions

Our findings support the proof of concept that optical contrast of HER2-overexpressing breast cancer cells can be achieved by brief periods of incubating those cells with nanoshells. Although the ability to detect malignancy by such means is critical for in vivo applications and for in vitro applications associated with biological fluids, other opportunities exist for using such techniques to diagnose solid tumor specimens in vitro. The time between diagnosis and treatment could be drastically shortened by the use of microscopic evaluations of excised tissue samples that provide rapid and reliable results. We have shown both qualitatively and quantitatively that nanoshells can be used to achieve discernible contrast between cancerous and normal breast cells in 5 min. These results suggest that gold nanoshells can be designed and optimized to enhance the scattering signatures of cancer cells at minimal incubation times necessary for potential applications in point-of-care cancer diagnostic imaging. Future studies are underway to extend these findings from the cellular level to tumor specimen models.

**Acknowledgments** We thank Vengadesan Nammalvar and Adrien Wang for expert technical assistance on nanoshell fabrication. We also thank Nastassja Lewinski for SEM imaging and Christine Wogan for editing assistance. This work was supported by a Department of Defense Congressionally Directed Breast Cancer Research Program Era of Hope Scholar Award to Rebekah Drezek and Tse-Kuan Yu, the Center for Biological and Environmental Nanotechnology (EEC-0118007 and EEC-0647452), the Beckman Foundation, and the John and Ann Doerr Fund for Computational Biomedicine.

## References

1. Loo C, Lowery A, Halas N, West J, Drezek R. Nano Lett 2005;5(4):709–11.
2. Loo C, Hirsch L, Lee M-H, Chang E, West J, Halas N, Drezek R. Optics Lett 2005;30:1012–4.
3. Lowery A, Gobin A, et al. Int J Nanomed 2006;1:149–54.
4. Gobin AM, Lee MH, Halas NJ, James WD, Drezek RA, West JL. Nano Lett 2007;7:1929–34.
5. Sokolov K, Follen M, Aaron J, Pavlova I, Malpica A, Lotan R, et al. Cancer Res 2003;63:1999–2004.
6. El-Sayed IH, Huang X, El-Sayed MA. Nano Lett 2005;5(5):829–34.
7. Sun J, Zhu MQ, Fu K, Lewinski N, Drezek R. Int J Nanomed 2007;2(2):235–40.
8. Gao X, Cui Y, Levenson RM, Chung LW, Nie S. Nat Biotechnol 2004;22(8):969–76.
9. Cao L, et al. J Am Chem Soc 2007;129:11318–9.
10. Huang X, El-Sayed IH, Qian W, El-Sayed MA. J Am Chem Soc 2006;128:2115–20.
11. Durr NJ, Larson T, Smith DK, Korgel BA, Sokolov K, Ben-Yakar A. Nano Lett 2007;7:941–5.
12. Yu C, Nakshatri H, Irudayaraj J. Nano Lett 2007;7(8):2300–6.
13. Sukhanova A, Devy J, Venteo L, Kaplan H, et al. Anal Biochem 2004;324:60–7.
14. Zajac A, Song D, Qian W, Zhukov T. Colloids Surf B Biointerfaces 2007;58:309–14.
15. Weigum SE, Floriano PN, Christodoulides N, McDevitt JT. Lab Chip 2007;7(8):995–1003.

16. Culha M, Stokes DL, Griffin GD, Vo-Dinh T. JBO 2004;9(3):439–43.
17. National Comprehensive Cancer Network. Breast cancer treatment guidelines for patients. Version IX. 2007.
18. Mojica CM, Bastani R, Boscardin WJ, Ponce NA. Cancer Control 2007;14(2):176–82.
19. Guthrie TH. Breast J 1995;1(6):376–9.
20. Klimberg VS, Harms S, Korourian S. Surg Oncol 1999;8:77–84.
21. Fisher B, Anderson S, Bryant J, Margolese RG, Deutsch M, Fisher ER, Jeong JH, Wolmark N. NEJM 2002;347:1233–41.
22. Hirsch LR, Halas NJ, West JL. Methods Mol Biol 2005;303:101–11.
23. Stöber W, Fink A, et al. J Colloid Interface Sci 1968;26:62–9.
24. Duff DG, Baiker A, Edwards PP. Langmuir 1993;9:2301–9.
25. Hayes DF, Walker TM, et al. Int J Oncol 2002;21(5):1111–7.
26. Kornilova ES, Taverna D, et al. Oncogene 1992;7(3):511–9.

# The stabilization and targeting of surfactant-synthesized gold nanorods

2009 Nanotechnology 20 434005

(http://iopscience.iop.org/0957-4484/20/43/434005)

IOP Publishing Nanotechnology
Nanotechnology **20** (2009) 434005 (10pp) doi:10.1088/0957-4484/20/43/434005

# The stabilization and targeting of surfactant-synthesized gold nanorods

**Betty C Rostro-Kohanloo[1], Lissett R Bickford[2], Courtney M Payne[4], Emily S Day[2], Lindsey J E Anderson[1], Meng Zhong[3], Seunghyun Lee[4], Kathryn M Mayer[1], Tomasz Zal[5], Liana Adam[3], Colin P N Dinney[3], Rebekah A Drezek[2], Jennifer L West[2] and Jason H Hafner[1,4]**

[1] Department of Physics and Astronomy, Rice University, 6100 Main Street, Houston, TX 77005, USA
[2] Department of Bioengineering, Rice University, 6100 Main Street, Houston, TX 77005, USA
[3] Department of Urology, MD Anderson Cancer Center, 1515 Holcombe Boulevard, Houston, TX 77030, USA
[4] Department of Chemistry, Rice University, 6100 Main Street, Houston, TX 77005, USA
[5] Department of Immunology, MD Anderson Cancer Center, 1515 Holcombe Boulevard, Houston, TX 77030, USA

Received 6 May 2009
Published 2 October 2009
Online at stacks.iop.org/Nano/20/434005

**Abstract**
The strong cetyltrimethylammonium bromide (CTAB) surfactant responsible for the synthesis and stability of gold nanorod solutions complicates their biomedical applications. The critical parameter to maintain nanorod stability is the ratio of CTAB to nanorod concentration. The ratio is approximately 740 000 as determined by chloroform extraction of the CTAB from a nanorod solution. A comparison of nanorod stabilization by thiol-terminal PEG and by anionic polymers reveals that PEGylation results in higher yields and less aggregation upon removal of CTAB. A heterobifunctional PEG yields nanorods with exposed carboxyl groups for covalent conjugation to antibodies with the zero-length carbodiimide linker EDC. This conjugation strategy leads to approximately two functional antibodies per nanorod according to fluorimetry and ELISA assays. The nanorods specifically targeted cells *in vitro* and were visible with both two-photon and confocal reflectance microscopies. This covalent strategy should be generally applicable to other biomedical applications of gold nanorods as well as other gold nanoparticles synthesized with CTAB.

## Abbreviations

| | |
|---|---|
| Ab | antibody |
| AF-Ab | Alexa Fluor labeled antibody |
| CCD | charge coupled device |
| CTAB | cetyltrimethylammonium bromide |
| EDC | 1-ethyl-[3-dimethylaminopropyl]carbodiimide |
| ELISA | enzyme linked immunosorbent assay |
| HRP | horse radish peroxidase |
| LSPR | localized surface plasmon resonance |
| MES | 2-(*N*-morpholino)ethanesulfonic acid (MES) |
| NHS | *N*-hydroxysuccinimide |
| PBS | phosphate buffered saline |
| PEG | poly(ethylene glycol) |
| PSS | poly(sodium 4-stryene-sulfonate) |
| WGA | wheat germ agglutinin |

## 1. Introduction

Localized surface plasmon resonances (LSPR) of gold nanoparticles result in strong optical absorption and scattering at visible and near-infrared wavelengths [1]. These optical properties are of considerable interest for biomedical applications, since the plasmon resonance can affect localized heating and light scattering, and since gold nanoparticles are relatively inert in biological systems. Tunable gold nanoparticles have been recently investigated for applications in photothermal therapy, drug delivery and diagnostic imaging [2–8]. Biomedical applications will ultimately rely on the ability to target the gold nanoparticles specifically to certain tissues or cell types with antibodies, aptamers and peptides [9]. A variety of gold nanoparticle shapes have been fabricated and investigated, including spheres [10], shells [11], rods [12–18], cages [19, 20] and stars [21]. One nanoparticle synthesis that is particularly powerful and versatile is the growth of colloidal gold seeds in the presence of the surfactant cetyltrimethylammonium bromide (CTAB). This method produced gold nanorods at first in low yield [22], and then later in high yield [23, 24] with resonances in the near-infrared. Gold nanorods are of particular interest for biomedical applications due to their small size and potentially improved permeation into tissue, relative to larger tunable gold nanoparticles. However, gold nanorods and other shapes synthesized with CTAB are also stabilized by this strong surfactant, which is thought to form a bilayer on the nanoparticle surface [25]. If the CTAB is removed from solution, the nanorods immediately aggregate [17]. Several strategies have been developed to modify the surface chemistry of nanorods, including polyelectrolyte wrapping to bind the CTAB layer [26], displacement of the CTAB layer by a thiol-terminal polyethylene glycol (PEG) [17] and displacement by alkanethiols [27] and lipids [28]. Even with these options, manipulation and targeting of nanorods has proven difficult, although there has been some recent success with polyelectrolyte wrapping [9, 12, 29–37]. This report describes progress on three aspects of biological targeting of CTAB-synthesized gold nanorods. First, the sensitivity of nanorod stability to CTAB concentration has been carefully characterized. Second, a simple chemical strategy has been developed to create nanorod–antibody conjugates based on strong gold–thiol and amide bonds that specifically target cells. Third, optical imaging modalities to detect nanorods in cells have been compared.

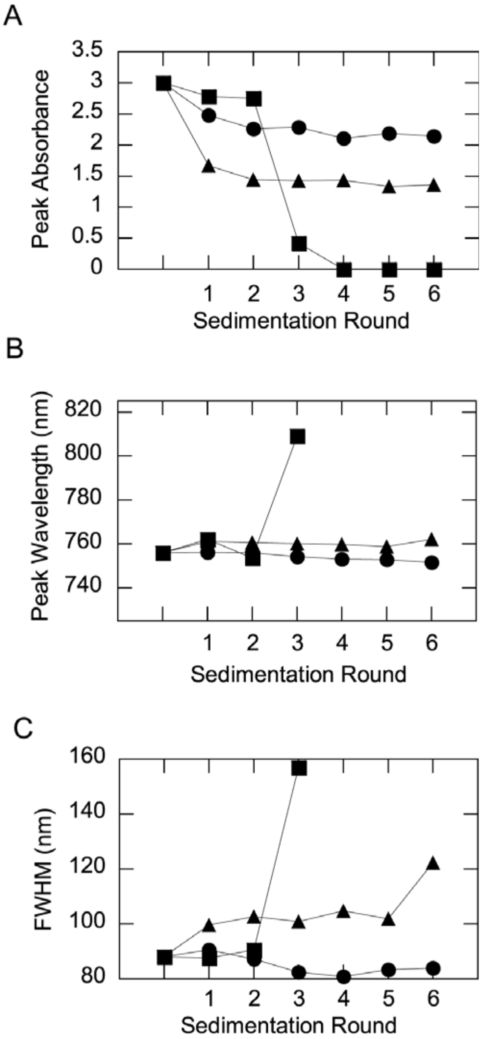

**Figure 1.** The evolution of the plasmon resonant peak of nanorod solutions after reduction of the CTAB concentration by sedimentation. The absorbance peak height (A), peak wavelength (B) and peak width (C) for CTAB-stabilized gold nanorods (■), anionic polymer-stabilized gold nanorods (▲) and PEGylated nanorods (●).

## 2. Materials and methods

### 2.1. Nanorod synthesis

Gold nanorods were prepared as described previously [23, 24], but the procedure was scaled up to increase the quantity. All solutions were prepared fresh for each synthesis, except for the hydrogen tetrachloroaurate(III) (Sigma, #520918), which was prepared as a 28 mM stock solution from a dry ampule and stored in the dark. An aliquot of the stock solution was diluted to 10 mM immediately before use. Gold seed particles were prepared by adding 250 $\mu$l of 10 mM hydrogen tetrachloroaurate(III) to 7.5 ml of 100 mM cetyltrimethylammonium bromide (CTAB) (Sigma, #H9151) in a plastic tube with brief, gentle mixing by inversion. Next, 600 $\mu$l of 10 mM sodium borohydride (Acros, #18930) was prepared from DI water chilled to 2–8 °C in a refrigerator and added to the seed solution *immediately* after preparation, followed by mixing by inversion for 1–2 min. The pale brown seed solution was stable and usable for several hours.

The nanorod growth solution was prepared by adding the following reagents to a plastic tube in the following order and then gently mixing each by inversion: 425 ml of 100 mM CTAB, 18 ml of 10 mM hydrogen tetrachloroaurate(III) and 2.7 ml of 10 mM silver nitrate (Acros, #19768). Next, 2.9 ml of 100 mM ascorbic acid (Fisher, #A61) was added and mixed by inversion, which changed the solution from brownish-yellow to colorless. To initiate nanorod growth, 1.8 ml of seed solution was added to the growth solution, mixed gently by inversion and left still for three hours. During this time, the color changed gradually to dark purple, with most of the color change occurring in the first hour.

### 2.2. Nanorod stabilization

Nanorod solutions were heated to 30 °C to melt CTAB crystals which form at room temperature, and therefore provide a known initial CTAB concentration of 100 mM. 5 ml aliquots were pelleted by centrifugation at 6000 rpm for 60 min. 4.5 ml of the clear supernatants were decanted and the pellets were resuspended with water. The nanorod solutions were pelleted again at 6000 rpm for 60 min and the clear supernatants were decanted. For anionic polymer stabilization, the nanorod pellets were resuspended with 4.5 ml of a solution containing 30 mg ml$^{-1}$ poly(sodium 4-styrene-sulfonate) (PSS, Aldrich, #243051) and 1 mM NaCl. For PEGylation, the nanorod pellets were resuspended with 4.5 ml

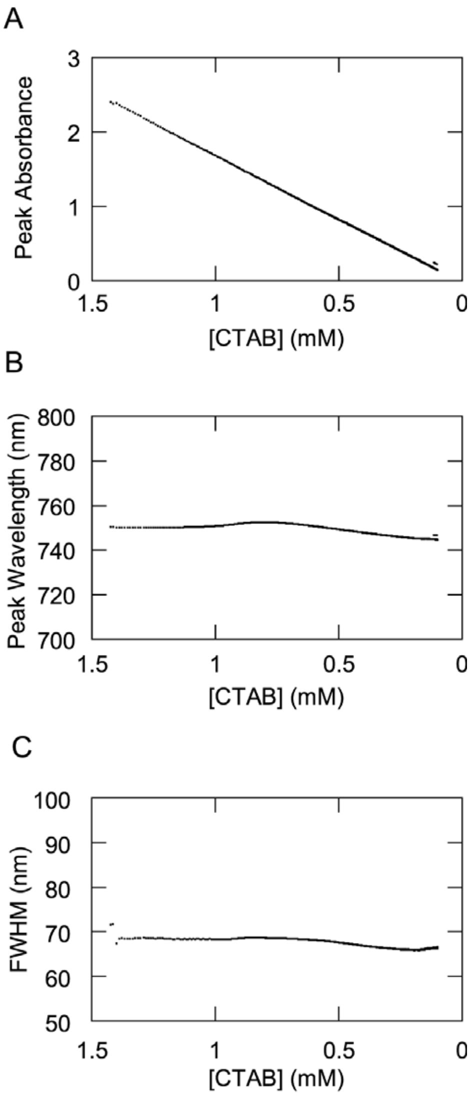

**Figure 2.** The evolution of the plasmon resonant peak height (A), wavelength (B) and width (C) of a nanorod solution during dilution with water.

of a solution containing 200 $\mu$M $K_2CO_3$ and 10 $\mu$M mPEG-SH (Nektar Therapeutics, #2M4E0H01). For both stabilization methods, the nanorod solution was incubated overnight at room temperature. Subsequent rounds of sedimentation, decantation and resuspension with water were then carried out as described above to lower the CTAB concentration.

### 2.3. CTAB dilution

CTAB dilution was carried out by two methods. For the data in figure 1, the CTAB was diluted by subsequent rounds of sedimentation, decantation and resuspension with water as described in the preceding section, except that no stabilizing agent was applied. For the data in figure 2, a 600 $\mu$l aliquot of nanorods diluted to 1.4 mM CTAB was put in a custom 9 ml cuvette for spectral analysis. The plasmon resonant spectral extinction was monitored as water was added to the solution at 20 $\mu$l min$^{-1}$ with a pipette pump.

### 2.4. Chloroform extraction

A separation funnel was filled with 100 ml of chloroform and 10 ml of nanorod solution which contained 30 mM CTAB. The mixture was vigorously shaken and allowed to separate overnight. The aqueous nanorod solution was extracted and 500 $\mu$l aliquots were placed in test tubes. To these tubes were added increasing quantities of chloroform for a second extraction: 0, 50, 100, 150, 200, 250 and 300 $\mu$l. After vigorous mixing, these were allowed to separate overnight. The aqueous nanorod solutions were then removed and analyzed.

### 2.5. Nanorod bioconjugation

Nanorods were stabilized with the heterobifunctional linker $\alpha$-thio-$\omega$-carboxy poly(ethylene glycol) (Iris Biotech, #HOOC-PEG-SH) by the PEGylation method described above and resuspended in 100 mM 2-($N$-morpholino)ethanesulfonic acid (MES) buffer (Sigma, #M-0164) at pH 6.1. The nanorods were concentrated by sedimentation to a volume of 100 $\mu$l with an absorbance value greater than 10 at the LSPR peak wavelength. 96 mg of 1-ethyl-[3-dimethylaminopropyl]carbodiimide (EDC, Sigma, #1769) and 29 mg of $N$-hydroxysuccinimide (NHS, Sigma, #1306762) were added to 10 ml of MES buffer, mixed and then 10 $\mu$l of this solution was immediately added to the 100 $\mu$l nanorod solution. This mixture was allowed to sit for 15 min, during which 0.5 ml of 2-mercaptoethanol was diluted into 14.5 ml MES buffer. After 15 min incubation, 10 $\mu$l of the diluted 2-mercaptoethanol was added to the nanorod solution. This mixture was allowed to sit for 10 min, after which 400 $\mu$l of the antibody solution at 2 mg ml$^{-1}$ in PBS pH 7.1 was added. This final 500 $\mu$l NR/Ab solution was incubated for 2 h at room temperature. Finally, the NR–Ab conjugates were separated from excess reactants and by-products by sedimentation at 10 000 rpm, decantation and resuspension of the pellet in PBS buffer.

### 2.6. Fluorimetry

The procedure above was followed with an Alexa Fluor 488-labeled rabbit IgG (AF-Ab, Invitrogen, #A11059). Upon completion, the AF-Ab–NR conjugates were put through subsequent rounds of sedimentation, 90% decantation and resuspension in PBS. The supernatants and the final AF-Ab–NR conjugate solutions were analyzed in a Horiba Jobin-Yvon FluoroLog-3 fluorimeter with CW xenon excitation. The free AF-Ab in the supernatants served as a standard curve to determine the concentration of AF-Ab bound to the nanorods.

### 2.7. Nanoparticle ELISA

Gold nanorods conjugated to mouse anti-human HER2 antibodies (NeoMarkers, #MS-301-PABX) were incubated with HRP-labeled anti-mouse IgG (Sigma, #A4416) for 1 h. Nonspecific reaction sites were blocked with a 3% solution of bovine serum albumin (BSA). Nanorods were rinsed twice by sedimentation and resuspension in 3% BSA to remove any unbound IgG. The HRP bound to the nanorod conjugates was developed with 3, 3′, 5, 5′-tetramethylbenzidine dihydrochloride (Sigma, #T3405) and compared with an HRP anti-mouse IgG standard curve by determining the absorbance at 450 nm with a spectrophotometer.

### *2.8. Nanorod targeting*

Anti-HER2 nanorod conjugates were incubated with two cell types: the HER2-overexpressing epithelial breast cancer cell line SK-BR-3 and the normal mammary epithelial cell line MCF10A (American Type Culture Collection). The SK-BR-3 cells were grown in McCoy's 5A medium supplemented with 10% fetal bovine serum (FBS) and 1% penicillin–streptomycin and maintained at 37 °C in a 5% $CO_2$ atmosphere. The MCF10A cells were cultured in mammary epithelial basal medium (MEBM) supplemented with a BulletKit (Clonetics) and also maintained at 37 °C in 5% $CO_2$. Both cell lines were prepared for the experiment by putting $6 \times 10^5$ cells in chambered cover slips and allowing them 30 min to attach to the surface. The cells were rinsed once with PBS, then incubated with nanorod conjugates for 1 h in 5% $CO_2$ at 37 °C. The LSPR peak absorbance of the nanorod conjugate solutions was 1.5. After the incubation, cells were rinsed 3× with 1× PBS and then the appropriate cell medium was added prior to imaging. The cells were imaged by two-photon microscopy at 50× with 780 nm illumination and 400–700 nm detection.

KU7 cells were grown in MEM medium supplemented with 10% fetal bovine serum (FBS) and 1% penicillin–streptomycin and maintained at 37 °C in a 5% $CO_2$ atmosphere. The cell line was prepared for the experiment by putting $4 \times 10^5$ cells on cover slips and allowing them 24 h to attach to the surface. Prior to the treatment, the cell media was changed to OptiMEM (Roche Biochemicals) and nanorod-C225 conjugates were added for 4 h. After 4 h, the OptiMEM medium was changed to MEM medium supplemented with 10% serum and incubated in 5% $CO_2$ at 37 °C atmosphere for another 20 h. Twenty minutes prior to fixation, the cells were rinsed once with warm PBS, then incubated with 100 nM Alexa-488-wheat germ agglutinin (WGA) and left for 10 min in the cell incubator for WGA cellular internalization. After 10 min the cells were rinsed three times with warm PBS, fixed in 1:1 methanol:ethanol at 20 °C for 10 min, then washed three times with cold PBS and mounted on slides using slow-fade antifade. All reagents were purchased from Molecular Probes. Imaging was carried out with a Leica SP5RS AOBS confocal microscope using a 63×/1.4 objective. Nanorods were detected with 633 nm illumination in reflection mode. WGA-AF488 was excited at 488 nm and detected at 495–530 nm.

## 3. Results

### *3.1. Nanorod stability*

In order to determine the critical CTAB concentration required for nanorod stability, nanorod solutions were heated to melt the CTAB crystals and provide a well-defined initial concentration of 100 mM. Aliquots of nanorods were then pelleted by sedimentation, 90% of the clear supernatant was removed and the nanorod pellets were resuspended to their initial volume with water. In this way the CTAB concentration was reduced by a factor of 10 on each round of sedimentation. Note that the quantity of CTAB bound to the nanorod surfaces is a negligible fraction of this initial CTAB concentration[6]. The LSPR peak wavelength, width and height were recorded after each round of sedimentation and are plotted in figure 1. There was essentially no nanorod aggregation, i.e. no LSPR peak height reduction, broadening, or redshift, until the third round of sedimentation. Therefore, nanorod aggregation is expected to occur somewhere between 1 and 0.1 mM CTAB.

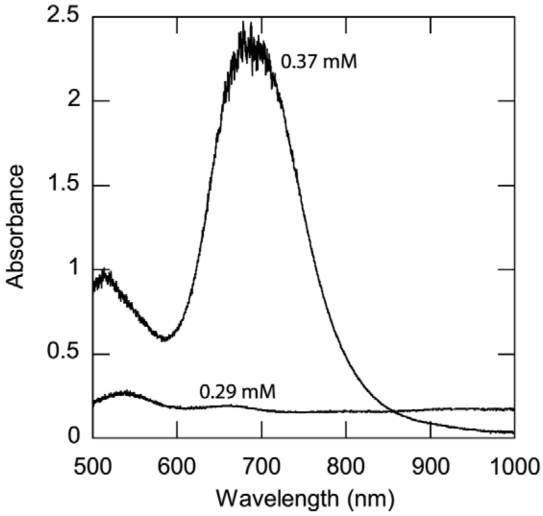

**Figure 3.** The plasmon resonant extinction spectra of nanorod solutions at two CTAB concentrations achieved by chloroform extraction. The nanorod concentration was 0.5 nM.

To further characterize the critical CTAB concentration, the LSPR spectrum of a nanorod solution was monitored during slow dilution with water (figure 2). As expected, the LSPR peak absorbance decreased as the nanorod concentration was reduced. However, the LSPR peak wavelength and width were not affected, indicating that there was no aggregation, although the CTAB concentration was reduced to below 50 $\mu$M. This apparent inconsistency with the results of figure 1 reveals that it is the ratio of CTAB concentration to nanorod concentration that determines stability, not the CTAB concentration alone, which is typical for surfactant-stabilized colloids. To further confirm this point, CTAB was removed from a nanorod solution without reducing the nanorod concentration by extraction with chloroform. As seen in figure 3, there was a critical CTAB concentration at which aggregation occurred. Based on our own measurement of the distribution ratio for CTAB between water and chloroform, the aggregation occurred between 370 and 290 $\mu$M CTAB. Given that the nanorod concentration was 0.5 nM, the critical CTAB/nanorod concentration ratio was approximately 740 000. Note that this number of CTAB molecules per

---

[6] Consider the typical conditions of a nanorod solution with $l = 50$ nm, $d = 15$ nm nanorods at an LSPR peak absorbance of 1, which corresponds to a nanorod concentration of 0.2 nM. The nanorod surface area would be 3063 nm$^2$. The CTAB bilayer packing area is 22 Å$^2$. Therefore, each nanorod would contain 14 000 CTAB molecules on its surface, taking up only 2.8 mM of the CTAB concentration.

**Table 1.** Zeta potential measurements to confirm surface chemistry modification.

| Nanoparticle | ZP (mV) |
|---|---|
| NR–CTAB | +83 |
| NR–S-PEG-COOH | −19 |
| NR–S-PEG-Ab | −6 |

nanorod is much larger than the amount of CTAB needed to simply coat the nanorods with a surfactant bilayer (see the footnote above), so the dynamic interactions between CTAB in solution and in the bilayer must be important for nanorod stability.

Nanorods were stabilized by displacement of the CTAB with a thiol-terminal polyethylene glycol (mPEG-SH), and by wrapping the CTAB bilayer with polystyrene sulfonate (PSS). The LSPR peak wavelength, width and height after successive rounds of sedimentation are displayed in figure 1 to probe the effectiveness of these stabilizers. While the unstabilized nanorods aggregated after the third round of sedimentation as described above, both PEGylation and polyelectrolyte stabilization were effective. However, PEGylation maintained a narrower LSPR peak, indicating a reduced degree of aggregation relative to polyelectrolyte stabilization.

### 3.2. Nanorod bioconjugation

To form stable nanorod bioconjugates, a heterobifunctional polyethylene glycol with thiol and carboxyl end groups (HOOC-PEG-SH) was applied. Nanorod stabilization with HOOC-PEG-SH yielded identical results to mPEG-SH in figure 1. The carboxy-terminal nanorods were conjugated to antibodies using the zero-length crosslinker EDC stabilized by NHS [38]. Standard procedures for EDC protein crosslinking were followed [39], with the following modifications for the unique properties of the carboxy-terminal nanorods. First, since the functionalized nanorod surfaces contain no amines, there is no chance of nanorod aggregation due to amide bond formation between nanorods, which minimizes the criticality of the initial EDC exposure. Second, to avoid the need for buffer exchange or sedimentation, the change in pH from 6.1 for activation to 7.1 for conjugation was accomplished by diluting the nanorods into a larger volume of antibody solution. Finally, sedimentation was performed (rather than buffer exchange) to remove excess reactants and products from the nanorod solution.

As a means to confirm the altered nanorod surface chemistry at various stages, zeta potential measurements (Malvern Zetasizer Nano) were performed on gold nanorods in the original CTAB, after stabilization with HOOC-PEG-SH, and finally after Ab conjugation. The results, presented in table 1, are consistent with the cationic, anionic and zwitterionic surface charges, respectively, associated with these three states of nanorods.

To characterize the final product, nanorods were conjugated to AF-Ab for fluorimetric analysis. After the steps described above, the nanorod conjugates were put through successive rounds of sedimentation, 90% decantation and resuspension in buffer to dilute the unbound AF-Ab by factors of ten. Fluorimetry of unbound AF-Ab in the decants, shown in figure 4, serves as a standard curve and reaches the background fluorescence noise floor by the fourth round at an AF-Ab concentration of 0.1 nM. Fluorimetry of the nanorod conjugates solution indicated a nanorod-bound AF-Ab concentration of 1 nM, which yields approximately two antibodies per nanorod given a nanorod concentration of 0.5 nM based on the LSPR extinction peak [17].

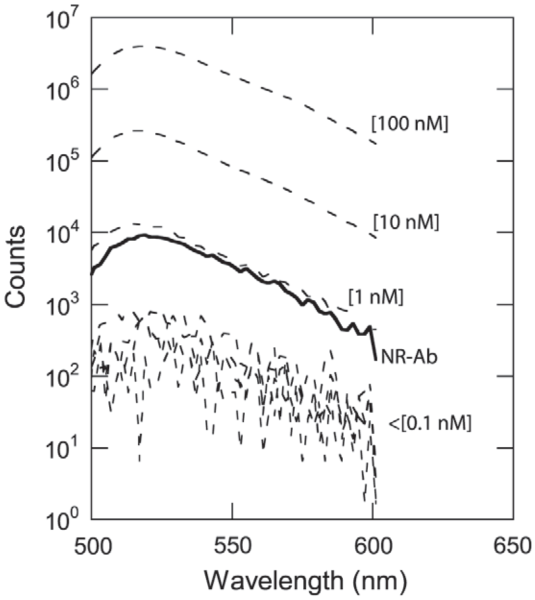

**Figure 4.** Fluorimetric analysis of gold nanorod conjugates. The dashed curves display the signal from free labeled antibodies in solution at the stated concentrations. The solid curve displays the signal from nanorod conjugates.

To further characterize the nanorod conjugates, a nanoparticle ELISA was performed [40]. This method is similar to a traditional ELISA except that the immunosorbent surface is that of the nanoparticles in solution. The nanoparticle ELISA yielded 2.28 ± 0.05 antibodies per nanorod, in reasonable agreement with the fluorimetry results. A simultaneous ELISA on nanorods prepared with mPEG-SH, and therefore no capture antibodies, yielded 0.68 ± 0.2 antibodies per nanorod. This signal may be an artifact due to chemisorption of the label antibody to the available gold surface on the nanorods.

### 3.3. Nanorod targeting and imaging

Nanorod conjugate targeting was tested with two *in vitro* systems. First, nanorods were conjugated to anti-HER2 and also to rabbit IgG as a control. Each conjugate was incubated with both the HER2-overexpressing epithelial breast cancer cell line SK-BR-3 and the normal mammary epithelial cell line MCF10A for 30 min simultaneously and under identical conditions. The cells were washed and immediately imaged live by two-photon luminescence, which highlights the presence of gold particles [18], as well as phase contrast to show the cell locations. Figure 5 demonstrates that only the specific antibody/cell combination produced a significant level

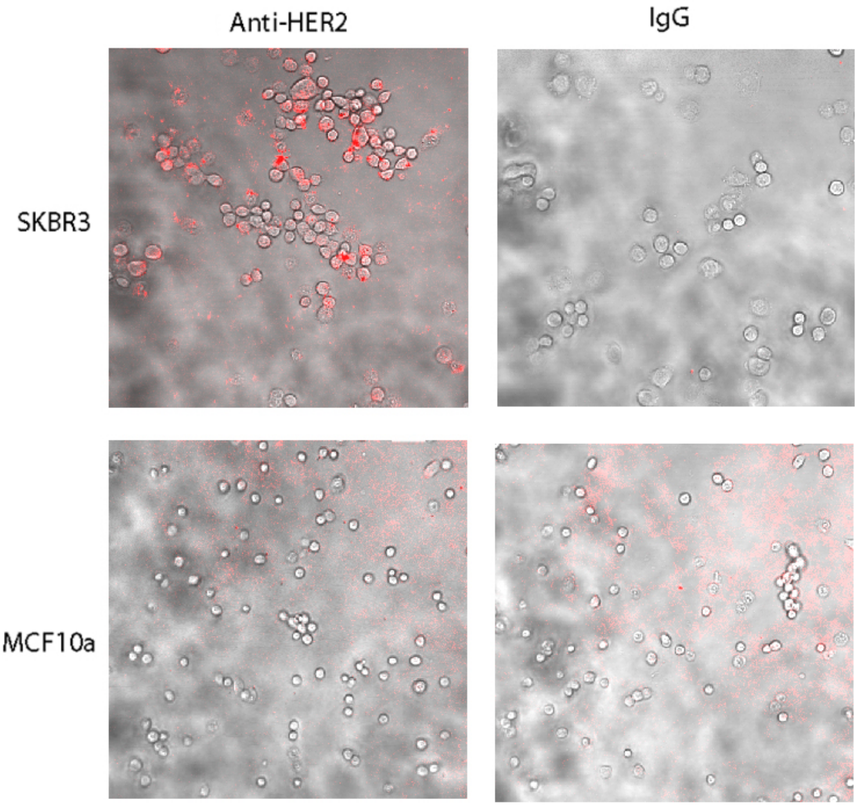

**Figure 5.** Nanorod conjugate targeting. Phase contrast shows the cell locations in grayscale, and two-photon luminescence is displayed in red. Binding was only observed for the anti-HER2 conjugates and SKBR3 cells.

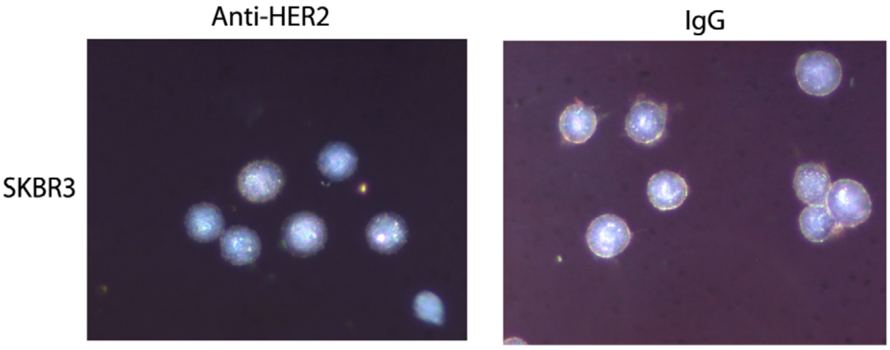

**Figure 6.** Dark-field microscopy images of the same samples as in figure 5.

of nanorod binding to the cells. Figure 6 displays dark-field images of targeted and control cells from the same sample. The nanorods were not visible. To gauge their visibility in dark-field microscopy, isolated nanorods were deposited on glass substrates near alignment marks and easily visible spherical gold nanoparticles so that optical microscopy and AFM could be performed on the same area (see figure 7). The nanorod was not detectable on either a high-sensitivity monochromator or color CCD cameras.

The conjugation method was also tested with C225 and human IgG as a control. In this case, the nanorod conjugates were incubated with the KU7 bladder cancer cell line. The nanorods were imaged by confocal reflectance and the cells were visualized with a fluorescent WGA label. The C225 conjugates were more strongly associated with KU7 cells than the control IgG conjugates, as seen in figure 8.

## 4. Discussion

It is well known that the CTAB surfactant responsible for gold nanorod synthesis is also required to maintain colloidal stability. However, the CTAB concentration at which colloidal stability is lost has not been well characterized. This is due to several factors. First, to reduce the CTAB concentration in a nanorod solution, it is often removed by sedimentation of the nanorods into a pellet, decantation of the CTAB solution and resuspension of the nanorod pellet in water. If this procedure is not performed analytically, the CTAB concentration is

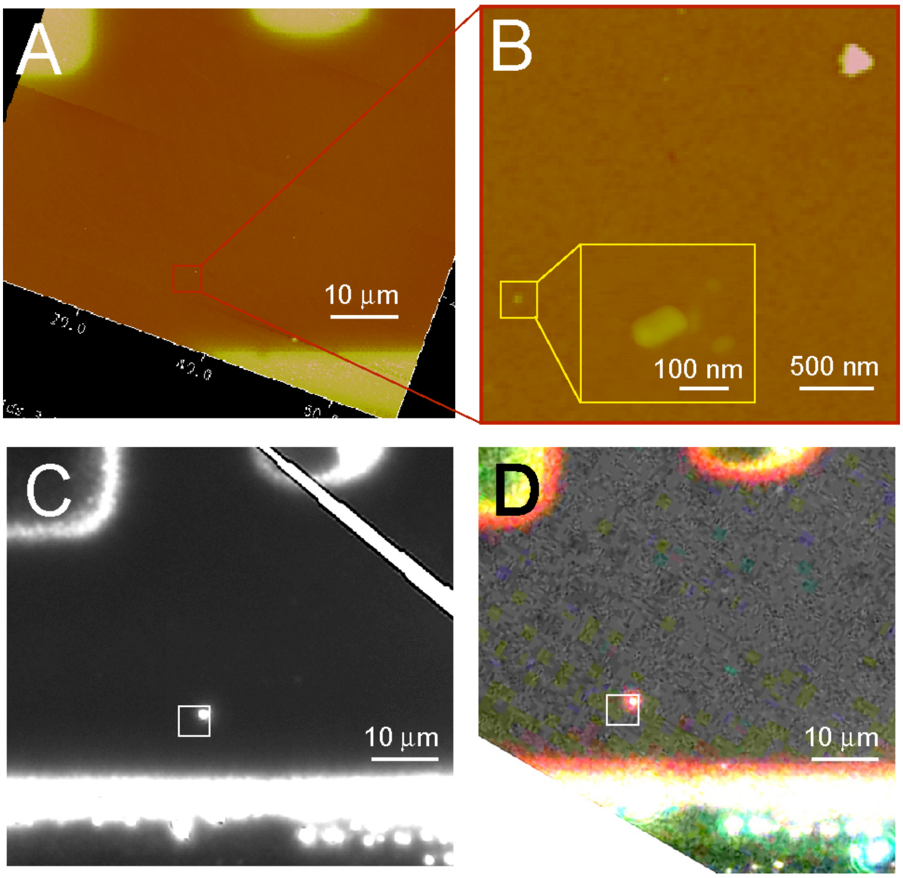

**Figure 7.** Dark-field microscopy images of a single gold nanorod on glass. The first AFM image (A) shows a region near alignment marks that are also visible in the optical images ((C) and (D)). A zoomed AFM image (B) reveals a large nanosphere in the upper right (triangular shape is a tip artifact) and a nanorod in the lower left. The nanorod is clearly revealed in the inset. Its size is exaggerated by the tip. The true size is approximately 50 nm length and 15 nm width. Dark-field images captured with a high-sensitivity CCD (C) and color CCD (D) clearly show the nanosphere, but show no sign of the nanorod in the expected region, even with significant contrast enhancement. The inset boxes in (A), (C) and (D) are all shown at the same size and position.

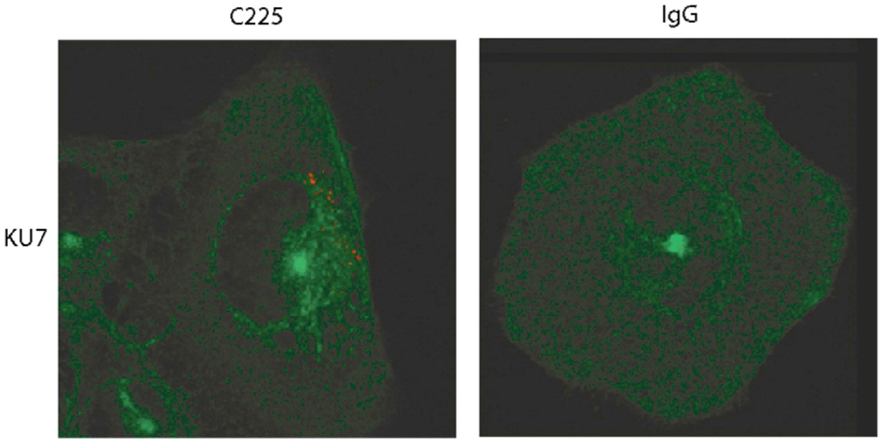

**Figure 8.** *In vitro* nanorod imaging by confocal reflectance. WGA-AF488 fluorescence shows the cell location in green and confocal reflectance at 633 nm is shown in red. Nanorod binding is only observed for the specific C225 conjugates and KU7 cells.

reduced by an unknown amount. Second, nanorod synthesis is carried out at 100 mM CTAB, which is above the saturation concentration at room temperature. Upon storage, some of the CTAB crystallizes, leaving an unknown concentration in the nanorod solution drawn from the solution phase. Finally, attempts at spectroscopic or other analyses of the CTAB concentration are hindered by micellization and association with gold and silver ions in solution.

That the nanorods were found to be entirely stable to a CTAB concentration below 1 mM may confound the development of methods to stabilize nanorods, since the CTAB may stabilize the nanorods when it is thought to have been removed. Nanorod stabilization outside of the CTAB solution is further complicated by several factors. First, the aggregation occurs quite suddenly when the CTAB concentration falls below the critical value, as seen in figure 3. Second, the fact that it is the ratio of CTAB to nanorod concentration that determines stability, rather than the CTAB concentration alone, means that the critical CTAB concentration for a given sample will depend on the nanorod concentration. Third, since CTAB forms a bilayer on the nanorod surface, it is likely that the available nanorod surface area is critical for stability rather than the nanorod concentration. Therefore, the critical CTAB concentration for a given sample also depends on nanorod size. This significant variability of the critical CTAB concentration between samples may in part account for reproducibility issues in stabilizing gold nanorods and forming bioconjugates.

We previously described a strategy to stabilize gold nanorods with a thiol-terminal polyethylene glycol (mPEG-SH) which displaces the CTAB bilayer so that CTAB can be reduced to an arbitrarily low concentration and the nanorods remain in solution [17]. Nanorods can also be stabilized by wrapping them with anionic polymers which are attracted to the cationic CTAB bilayer, as well as by forming multiple polyelectrolyte layers [26]. Figure 1 displays a comparison of the effectiveness of these methods for stabilizing nanorods. Interestingly, after the first and second rounds of sedimentation, the sample with no stabilizing treatment maintained the best spectrum, although aggregation occurred rapidly thereafter. The data demonstrate that, upon removal of CTAB, PEGylation via the thiol–gold bond results in higher yields and a narrower LSPR linewidth than electrostatic stabilization. This spectroscopic result is in agreement with previously reported microscopic characterizations of nanorod substrates. PEGylated nanorod solutions yield highly monodisperse nanorods when deposited on glass substrates [17], while electrostatic wrapping leads to aggregated nanorods [26].

Most gold nanorod targeting experiments to date have been carried out by stabilizing the CTAB-capped gold nanorods with polyelectrolytes, then non-covalently binding antibodies or other targeting agents to the nanoparticles by simply mixing them together [12, 29, 31–33, 35, 36]. This is similar to the original strategies developed to bind antibodies to citrate-capped gold nanoparticles for immunoelectron microscopy [41]. The binding is likely due to weak electrostatic and hydrophobic interactions between the nanoparticles and antibodies. To create more stable nanorod bioconjugates, the strategy described here relies on an amide bond between the linker and antibody, and a strong gold–thiol bond [42] between the linker and nanorod. In some cases polyelectrolytes with exposed carboxyl groups for amide bond formation with antibodies have been employed [30, 37]. In one case an alkanethiol was used in a similar manner to the bifunctional PEG described here [43]. While alkanethiols are more readily available, their low solubility in aqueous solutions required hours of sonication at elevated temperature to achieve sufficient concentration to displace the CTAB bilayer. Although more complicated, conjugates based on gold–thiol and covalent bonds will likely be more stable for *in vivo* applications. Furthermore, we have found the methods described here to be quite reproducible despite the strength of the original gold–CTAB interaction [12]. Tests of the nanorod zeta potential follow the intended surface chemistry, with a negative potential for carboxy-terminated nanorods and a near-neutral potential for the zwitterionic protein conjugates. The fluorimetric assay yields approximately two antibodies per nanorod and the ELISA assay demonstrates that a large fraction of these antibodies are active. Finally, figures 5 and 8 demonstrate successful targeting in two cell types with different antibodies.

We have also investigated the effectiveness of different imaging modalities to visualize nanorods in and around cells. As described previously [18], the images based on two-photon luminescence in figure 5 clearly reveal nanorods in the specific sample. Dark-field microscopy is a much simpler modality that can yield striking images of plasmon resonant nanoparticles [44]. However, the optical scattering which provides dark-field contrast is a strong function of nanoparticle size. Furthermore, the size range at which nanoparticles become visible by dark-field is tens of nanometers, similar to the range of nanoparticles that have been pursued for biomedical applications. Issues of visibility are also sensitive to the illumination and imaging numerical apertures, spectral range, nanoparticle aggregation and background scattering from cells. Therefore, one must be cautious when interpreting nanoparticle targeting results by dark-field microscopy. For example, the dark-field images from figure 6 reveal no evidence of scattering by the nanorods, even though the two-photon images from figure 5 confirm the presence of nanorods. In this case the single 50 nm × 15 nm nanorods do not scatter sufficiently to be visible against the scattering from cells. To further confirm this point, dark-field images of a single nanorod on a glass substrate are displayed in figure 7. Although the location of a single gold nanorod relative to alignment marks is confirmed by atomic force microscopy, one finds that the nanorod is not visible in the dark-field images taken with either a color CCD camera or a back-illuminated electron multiplying CCD camera. If single nanorods are not visible on a flat glass substrate, it is not surprising that they are not visible in the higher background images of cells in figure 6. There are many methods to increase the nanorod imaging signal and contrast without resorting to two-photon luminescence, such as spectrally filtering the scattered light, exciting with monochromatic illumination at the plasmon resonant wavelength and using a higher numerical aperture condensers and objectives. Figure 8 reveals that confocal reflectance microscopy, with monochromatic illumination at the LSPR wavelength and reduced background signal, is sufficient to detect nanorods in cells.

## 5. Conclusions

To maintain colloidal stability, it is the ratio of CTAB to nanorod concentration that must be maintained. Here, the critical CTAB:nanorod ratio was found to be approximately 740 000:1. The CTAB layer can be displaced by thiol-terminal PEG, or wrapped by polyelectrolytes. However, gold–thiol PEGylation results in higher yields and more monodisperse nanorod samples when the CTAB is removed. A bifunctional PEG with thiol and carboxyl end groups results in carboxy-terminal PEGylated nanorods which can be conjugated to antibodies via a carbodiimide linking agent. Fluorimetry and ELISA assays reveal approximately two antibodies per nanorod. The nanorod conjugates demonstrated specific targeting in two different antibody/cell systems. Two-photon luminescence and confocal reflectance microscopies successfully imaged the nanorods in cells.

## Acknowledgments

JHH acknowledges support from the National Science Foundation's Nanoscale Science and Engineering Initiative under award no. EEC-0647452, the US Army Research Office under grant no. W911NF-04-1-0203 and the Welch Foundation under grant C-1556. JHH and LA acknowledge support from the Department of Defense grant W81XWH-06-2-0067 to UTHSC. LJEA acknowledges support from the NSF-funded Integrative Graduate Research and Educational Training program DGE-0750842. RAD acknowledges support from the Department of Defense grant W81XWH-07-1-0428, and the Welch Foundation under grant C-1598.

## References

[1] Link S and El-Sayed M A 1999 Spectral properties and relaxation dynamics of surface plasmon electronic oscillations in gold and silver nanodots and nanorods *J. Phys. Chem.* B **103** 8410–26

[2] Liao H, Nehl C L and Hafner J H 2006 Biomedical applications of plasmon resonant metal nanoparticles *Nanomedicine* **1** 201–8

[3] Jain P K, Huang X H, El-Sayed I H and El-Sayed M A 2008 Noble metals on the nanoscale: optical and photothermal properties and some applications in imaging, sensing, biology, and medicine *Acc. Chem. Res.* **41** 1578–86

[4] Murphy C J, Gole A M, Stone J W, Sisco P N, Alkilany A M, Goldsmith E C and Baxter S C 2008 Gold nanoparticles in biology: beyond toxicity to cellular imaging *Acc. Chem. Res.* **41** 1721–30

[5] Lal S, Clare S E and Halas N J 2008 Nanoshell-enabled photothermal cancer therapy: impending clinical impact *Acc. Chem. Res.* **41** 1842–51

[6] Bikram M and West J L 2008 Thermo-responsive systems for controlled drug delivery *Expert Opin. Drug Deliv.* **5** 1077–91

[7] Tong L, Wei Q S, Wei A and Cheng J X 2009 Gold nanorods as contrast agents for biological imaging: optical properties, surface conjugation and photothermal effects *Photochem. Photobiol.* **85** 21–32

[8] Hleb E Y, Hu Y, Drezek R A, Hafner J H and Lapotko D O 2008 Photothermal bubbles as optical scattering probes for imaging living cells *Nanomedicine* **3** 797–812

[9] Pirollo K F and Chang E H 2008 Does a targeting ligand influence nanoparticle tumor localization or uptake? *Trends Biotechnol.* **26** 552–8

[10] Sokolov K, Follen M, Aaron J, Pavlova I, Malpica A, Lotan R and Richards-Kortum R 2003 Real-time vital optical imaging of precancer using anti-epidermal growth factor receptor antibodies conjugated to gold nanoparticles *Cancer Res.* **63** 1999–2004

[11] Loo C, Lowery A, Halas N, West J and Drezek R 2005 Immunotargeted nanoshells for integrated cancer imaging and therapy *Nano Lett.* **5** 709–11

[12] Javier D J, Nitin N, Roblyer D M and Richards-Kortum R 2008 Metal-based nanorods as molecule-specific contrast agents for reflectance imaging in 3D tissues *J. Nanophoton.* **2** 023506

[13] Yu C X, Nakshatri H and Irudayaraj J 2007 Identity profiling of cell surface markers by multiplex gold nanorod probes *Nano Lett.* **7** 2300–6

[14] Eghtedari M, Oraevsky A, Copland J A, Kotov N A, Conjusteau A and Motamedi M 2007 High sensitivity of *in vivo* detection of gold nanorods using a laser optoacoustic imaging system *Nano Lett.* **7** 1914–8

[15] Huff T B, Hansen M N, Zhao Y, Cheng J X and Wei A 2007 Controlling the cellular uptake of gold nanorods *Langmuir* **23** 1596–9

[16] Chen C C, Lin Y P, Wang C W, Tzeng H C, Wu C H, Chen Y C, Chen C P, Chen L C and Wu Y C 2006 DNA-gold nanorod conjugates for remote control of localized gene expression by near infrared irradiation *J. Am. Chem. Soc.* **128** 3709–15

[17] Liao H and Hafner J 2005 Gold nanorod bioconjugates *Chem. Mater.* **17** 4636–41

[18] Wang H, Huff T B, Zweifel D A, He W, Low P S, Wei A and Cheng J-X 2005 *In vitro* and *in vivo* two-photon luminescence imaging of single gold nanorods *Proc. Natl. Acad. Sci. USA* **102** 15752–6

[19] Cang H, Sun T, Li Z Y, Chen J Y, Wiley B J, Xia Y N and Li X D 2005 Gold nanocages as contrast agents for spectroscopic optical coherence tomography *Opt. Lett.* **30** 3048–50

[20] Skrabalak S E, Chen J, Au L, Lu X, Li X and Xia Y 2007 Gold nanocages for biomedical applications *Adv. Mater.* **19** 3177–84

[21] Nehl C L, Liao H W and Hafner J H 2006 Optical properties of star-shaped gold nanoparticles *Nano Lett.* **6** 683–8

[22] Jana N R, Gearheart L and Murphy C J 2001 Wet chemical synthesis of high aspect ratio cylindrical gold nanorods *J. Phys. Chem.* B **105** 4065–7

[23] Sau T K and Murphy C J 2004 Seeded high yield synthesis of short Au nanorods in aqueous solution *Langmuir* **20** 6414–20

[24] Nikoobakht B and El-Sayed M A 2003 Preparation and growth mechanism of gold nanorods (NRs) using seed-mediated growth method *Chem. Mater.* **15** 1957–62

[25] Nikoobakht B and El-Sayed M A 2001 Evidence for bilayer assembly of cationic surfactants on the surface of gold nanorods *Langmuir* **17** 6368–74

[26] Gole A and Murphy C J 2005 Polyelectrolyte-coated gold nanorods: synthesis, characterization and immobilization *Chem. Mater.* **17** 1325–30

[27] Sun Z H, Ni W H, Yang Z, Kou X S, Li L and Wang J F 2008 pH-controlled reversible assembly and disassembly of gold nanorods *Small* **4** 1287–92

[28] Niidome Y, Honda K, Higashimoto K, Kawazumi H, Yamada S, Nakashima N, Sasaki Y, Ishida Y and Kikuchi J 2007 Surface modification of gold nanorods with synthetic cationic lipids *Chem. Commun.* 3777–9

[29] Tong L, Zhao Y, Huff T B, Hansen M N, Wei A and Cheng J X 2007 Gold nanorods mediate tumor cell death by compromising membrane integrity *Adv. Mater.* **19** 3136

[30] Popovtzer R, Agrawal A, Kotov N A, Popovtzer A, Balter J, Carey T E and Kopelman R 2008 Targeted gold nanoparticles enable molecular CT imaging of cancer *Nano Lett.* **8** 4593–6

[31] Huang X H, El-Sayed I H, Qian W and El-Sayed M A 2007 Cancer cells assemble and align gold nanorods conjugated to antibodies to produce highly enhanced, sharp, and polarized surface Raman spectra: a potential cancer diagnostic marker *Nano Lett.* **7** 1591–7

[32] Huang X H, El-Sayed I H, Qian W and El-Sayed M A 2006 Cancer cell imaging and photothermal therapy in the near-infrared region by using gold nanorods *J. Am. Chem. Soc.* **128** 2115–20

[33] Hu R, Yong K T, Roy I, Ding H, He S and Prasad P N 2009 Metallic nanostructures as localized plasmon resonance enhanced scattering probes for multiplex dark-field targeted imaging of cancer cells *J. Phys. Chem.* C **113** 2676–84

[34] Hauck T S, Ghazani A A and Chan W C W 2008 Assessing the effect of surface chemistry on gold nanorod uptake, toxicity, and gene expression in mammalian cells *Small* **4** 153–9

[35] Durr N J, Larson T, Smith D K, Korgel B A, Sokolov K and Ben-Yakar A 2007 Two-photon luminescence imaging of cancer cells using molecularly targeted gold nanorods *Nano Lett.* **7** 941–5

[36] Ding H, Yong K T, Roy I, Pudavar H E, Law W C, Bergey E J and Prasad P N 2007 Gold nanorods coated with multilayer polyelectrolyte as contrast agents for multimodal imaging *J. Phys. Chem.* C **111** 12552–7

[37] Agarwal A, Huang S W, O'Donnell M, Day K C, Day M, Kotov N and Ashkenazi S 2007 Targeted gold nanorod contrast agent for prostate cancer detection by photoacoustic imaging *J. Appl. Phys.* **102** 064701

[38] Grabarek Z and Gergely J 1990 Zero-length crosslinking procedure with the use of active esters *Anal. Biochem.* **185** 131–5

[39] Hermanson G T 1996 *Bioconjugate Techniques* 1st edn (New York: Academic) p 785

[40] Lowery A R, Gobin A M, Day E S, Halas N J and West J L 2006 Immunonanoshells for targeted photothermal ablation of tumor cells *Int. J. Nanomed.* **1** 149–54

[41] Geoghegan W D and Ackerman G A 1977 Adsorption of horseradish-peroxidase, ovomucoid and antiimmunoglobulin to colloidal gold for indirect detection of concanavalin-a, wheat-germ agglutinin and goat antihuman immunoglobulin-g on cell-surfaces at electron-microscopic level—new method, theory and application *J. Histochem. Cytochem.* **25** 1187–200

[42] Nuzzo R G, Zegarski B R and Dubois L H 1987 Fundamental-studies of the chemisorption of organosulfur compounds on Au(111)—implications for molecular self-assembly on gold surfaces *J. Am. Chem. Soc.* **109** 733–40

[43] Eghtedari M, Liopo A V, Copland J A, Oraevslty A A and Motamedi M 2009 Engineering of hetero-functional gold nanorods for the *in vivo* molecular targeting of breast cancer cells *Nano Lett.* **9** 287–91

[44] Mock J J, Barbic M, Smith D R, Schultz D A and Schultz S 2002 Shape effects in plasmon resonance of individual colloidal silver nanoparticles *J. Chem. Phys.* **116** 6755–9

# Needle-compatible single fiber bundle image guide reflectance endoscope

**Jiantang Sun,[a] Chenghao Shu,[a] Benjamin Appiah,[b] and Rebekah Drezek[a,b,*]**
[a]Rice University, Department of Bioengineering, 6100 Main Street, Houston, Texas 77005
[b]Rice University, Department of Electrical and Computer Engineering, 6100 Main Street, Houston, Texas 77005

**Abstract.** We developed a miniaturized high-resolution low-cost reflectance-mode fiber microscope (RFM) aimed at optical tissue biopsy applications using a polarized imaging configuration to suppress background noise from specular reflectance. The RFM is equipped with an air-cooled light-emitting-diode illumination module and a single 450-$\mu$m outer-diameter fiber bundle image guide compatible with a 20-gauge needle. The dual illumination and image acquisition nature of the fiber bundle simplifies the system and reduces the total cost. Imaging tests with a United States Air Force resolution target demonstrate a lateral resolution of $\sim 3.5\ \mu$m. The performance of the imaging system is evaluated by examining samples of cells and excised human tissue. Still and video rate images are obtainable in reflectance mode using intrinsic contrast. [DOI: 10.1117/1.3465558]

Keywords: reflectance fiber endoscope; optical biopsy.

Paper 10220LR received Apr. 26, 2010; revised manuscript received Jun. 11, 2010; accepted for publication Jun. 23, 2010; published online Jul. 29, 2010.

Standard pathology requires removal of cells or tissue through techniques ranging from fine needle aspiration or core needle biopsy to surgical resection. To allow examination of suspect lesions, a variety of endoscopic imaging techniques may be employed, including fiber-scanning confocal microscopy in reflectance[1,2] and fluorescence[3] modes. These techniques use an optical fiber or fiber bundle to view the surface of interior body cavities. Images are created by scanning mechanisms positioned at either the distal or proximal ends of the fiber. These types of systems can capture point-by-point high-resolution images from a large field of view, and the sensitivity of the systems can be very high.[4,5] Recent advances provide similar high-resolution images using simple, low-cost systems based on coherent fiber bundles with images captured using inexpensive digital cameras.[6–8] Image resolution is limited by the individual fibers of the fiber bundle. A fluorescent-mode fiber endoscope developed by Muldoon et al. achieves a resolution of $\sim 4.4\ \mu$m.[6,7] We are developing a high-resolution ($\sim 3.5\ \mu$m) reflectance-mode endoscope that is flexible, compatible with a 20-gauge needle, and can generate still and video rate images using intrinsic contrast. Reflectance-mode endoscopic imaging can potentially complement fluorescence imaging by capturing information not available in fluorescence mode, and by functioning in situations when fluorescent imaging is not practical.

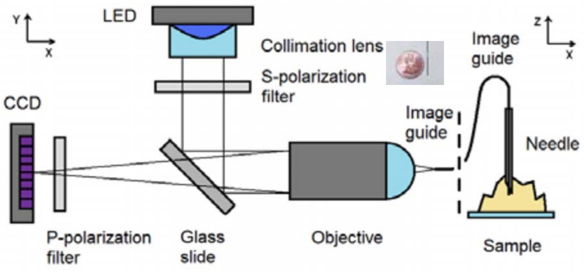

**Fig. 1** Schematic of the reflectance fiber imaging system.

In this work, we present a needle-based, high-resolution reflectance-mode fiber microscope (RFM) developed for optical tissue biopsy applications. The RFM was assembled on a portable $18 \times 24 \times 1/2$ in.$^3$ aluminum breadboard to facilitate eventual clinical trials. As shown in Fig. 1, an air-cooled light-emitting diode (LED) (Luxeon, Brantford, Ontario, Canada; white LED, model LXHL-NWE8; blue LED, model LXHL-NRR8) served as the illumination source to keep the RFM as compact as possible and reduce the system cost. The light from the LED is collimated by an integrated collimating lens and passes through a linear polarizer (Fig. 1), after which the polarized light is reflected by a glass slide positioned at $\sim 45$ deg (with respect to the beam trajectory) and projected onto an infinity-corrected 10× objective lens (Newport, Irvine, California, model L-10×, 0.25 NA). The objective lens and a fiber chuck (Newport, model FPH-DJ) are positioned with a multimode fiber-coupler positioner (Newport, model F-915T). By careful alignment, the illumination light is focused into the incident end of a 450-$\mu$m outer-diameter fiber image guide positioned by the fiber chuck (Sumitomo Electric U.S.A., Los Angeles, California, model IGN-037/10, $10^4$ fiber elements in a picture area of 333 $\mu$m diameter, 0.35 NA).[9] Finally, the imaging end of the fiber image guide is inserted into the core of a 20-gauge needle and positioned in contact with the samples. Light scattered from the samples is collected by the same illumination fiber and passes back through the same 10× objective lens and glass slide described previously (see Fig. 1).

A charge-couple device (CCD) color camera (Edmund Optics, Barrington, New Jersey, model EO-0813C) coupled with a circular polarizer filter (Nikon, 62 mm) is used to sample the fiber bundle elements for image acquisition. Because the polarization orientation of the S-polarized illumination light is perpendicular to the plane of incidence with respect to the glass slide (i.e., the XY plane of Fig. 1), a significant portion is reflected toward the incident end of the fiber bundle to be delivered to the imaging end of the fiber bundle. Specular reflectance from the incident end of fiber bundle is also partly reflected away by the glass slide, and the remaining specular reflectance is further suppressed by the circular polarizer in front of the CCD camera that passes P-polarized light with

---

*Address all correspondence to: Rebekah Drezek, Tel: 713-348-3011; Fax: 713-348-5877; E-mail: drezek@rice.edu

1083-3668/2010/15(4)/040502/3/$25.00 © 2010 SPIE

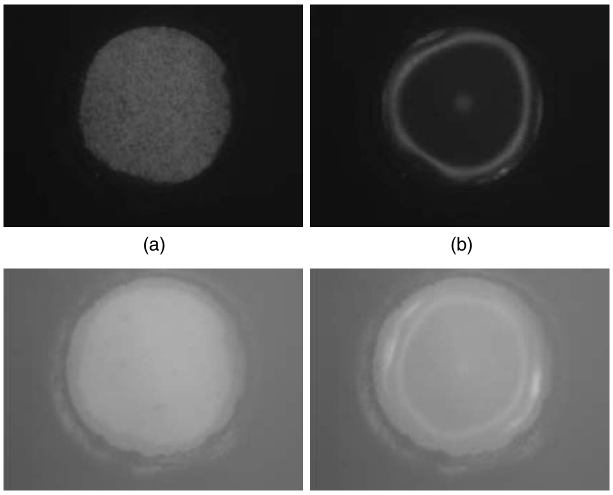

**Fig. 2** Reflectance images of the fiber-bundle tip glass/air interface showing greatly reduced specular background using this RFM system in comparison with the nonpolarized imaging system. Images (a) and (b) were obtained using cross-polarized illumination and imaging filters. For image (a), the fiber tip was in air. For image (b), the fiber tip was covered with a drop of water. Images (c) and (d) were obtained without polarized illumination and imaging filters. Image (c) is with the fiber tip in air, whereas image (d) is with the fiber tip covered with a drop of water.

respect to the plane of incidence. Rays that result from multiple scattering events changing their polarization to the parallel direction can be detected by the CCD camera (e.g., light scattered from the sample). Thus, noise due to specular reflectance from the incident end of the fiber bundle is greatly suppressed, and clearer images are collected.

Figure 2(a) shows a reflectance image of the fiber bundle imaging end when the needle microscope is positioned in air. Light from the white LED that is reflected from the glass-air interface at the imaging end of the fiber bundle is successfully detected by the CCD camera, and individual fibers of the fiber bundle are resolved [Fig. 2(a)]. With the imaging needle of the RFM immersed into a vial of water or phosphate-buffered saline (PBS) solution, the RFM field of view is almost completely dark, because the close match between the refractive indices of water and the glass fiber result in dramatically reduced internal reflection from the imaging end of the fiber bundle.

Figure 2(b) is obtained with a drop of water covering the tip of the imaging fiber bundle, which mimics the immersion of the fiber tip in water, to provide clear image features. Much less internal reflection occurs from the imaging area covered by water [Fig. 2(b)] compared with the same area when it is exposed to air. Figures 2(a) and 2(b) were captured with the same imaging configurations and the index-matching effect is clear. When used in biological or clinical environments, the fiber bundle tip is always in contact with body fluids or tissue. Thus, dipping the fiber bundle tip into water roughly approximates the conditions of realistic imaging applications. In liquid, the reduced internal reflectance leads to a dark field of view and a decrease in background enabling biological imaging. Light scattered by biological structures can be clearly distinguished and cellular images can be obtained. In contrast to the polarized reflectance-mode images in Figs. 2(a) and 2(b), images shown in Figs. 2(c) and 2(d) were captured with a reduced exposure time under the same imaging conditions, but without the illumination and collection polarizers. The specular reflectance from the optical components makes it impossible to obtain useful information from Figs. 2(c) and 2(d).

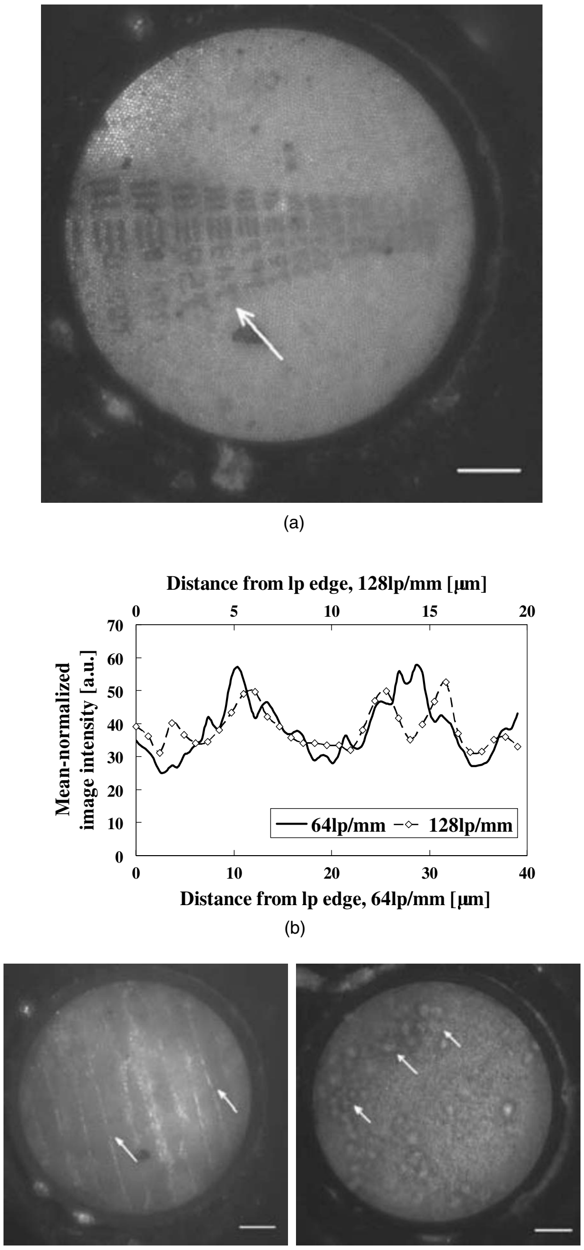

**Fig. 3** Processed endoscopic imaging results of (a) USAF resolution target showing the resolution of ~143 lp/mm, acquired with white LED illumination, (b) cross sections of two resolution line-pair sets showing both the line-pair intensity variation and variation due to probe fibers (3.3 $\mu$m diam), (c) onion skin cells (see also Video 1), where arrows show the resolved cell walls acquired with white LED illumination, and (d) cultured SKBR3 cancer cells (see also Video 2), where the arrows indicate resolved single cells acquired with blue LED illumination. Scale bar is 50 $\mu$m. (Video 1, QuickTime, 754 KB [URL: http://dx.doi.org/10.1117/1.3465558.1]; Video 2, QuickTime, 977 KB [URL: http://dx.doi.org/10.1117/1.3465558.2].)

A white LED was used to acquire the images and plots

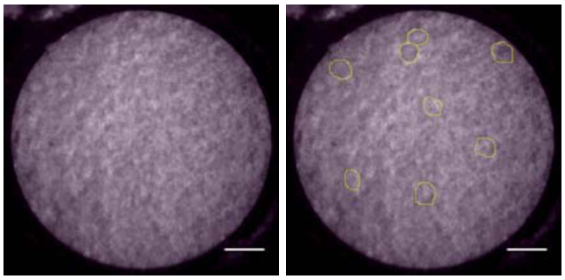

**Fig. 4** Endoscopic images of excised oral cancer tissue including (a) processed image showing cellular structures (see also Video 3, where images move in and out of focus as the imaging tip moves), and (b) processed images with drawn lines superimposed to indicate the estimated cell boundaries. Scale bar is 50 $\mu$m. (Video 3, QuickTime, 2.12 MB [URL: http://dx.doi.org/10.1117/1.3465558.3].)

shown in Figs. 3(a)–3(c) and Video 1. Figure 3(a) shows an imaging resolution of ~3.5 $\mu$m (~143 line pairs/mm) obtained upon imaging the United States Air Force resolution target. Figure 3(b) shows that contrast decreases slightly from low (64 lp/mm) to high (128 lp/mm) resolution, but it also reveals high-frequency components due to the probe fibers (3.3 $\mu$m diam). Figure 3(c) and Video 1 were obtained by using the same white LED-illuminated RFM to image skin tissue from a green onion. The cell walls of the rectangular green onion skin cells[10] are clearly resolved in both the still image and the video. Note that water was used in all the tests to provide refractive index matching.

The LED light source is cost effective and easy to change. An air-cooled blue LED was used to image cultured SKBR3 human carcinoma cells. Before imaging, SKBR3 carcinoma cells were cultured in a 6-mm plate at 37 °C for 2 days. The fiber bundle tip was immersed into the culture medium through a needle and focused onto a group of cells attached to the culture plate. As shown in Fig. 3(d), the cells can be visualized with the RFM using blue-LED illumination. An endoscopic video clip of the SKBR3 cancer cells is provided in Video 2. The same RFM was also used to image excised human oral cancer tissue obtained from the Cooperative Human Tissue Network (CHTN, Rockville, Maryland). The tissue was placed in a culture plate with PBS, which was then placed on a 2-D translation stage. The needle and fiber bundle tip were inserted into the tissue sample, and cellular structures were visualized as shown in Fig. 4 and Video 3. In Video 3, cellular images move in and out of focus as the imaging tip moves closer to or further away from the sample. The same RFM was used to image the reflectance from a dust particle in liquid solution to demonstrate single pixel fiber resolution, as shown in Video 4.

In this work, we describe a high-resolution RFM developed for optical tissue biopsy applications. The resolution of this fiber microscope is limited by the element fiber size of the imaging fiber bundle. For the specific fiber bundle image guide presented, the resolution is ~3.5 $\mu$m. The reported RFM system uses the same fiber bundle guide for both illumination and imaging. A pair of cross-polarized filters is used in addition to the fiber bundle guide to achieve high-resolution reflectance-mode microscopic imaging. The fiber bundle guide is 450 $\mu$m in diameter, making it compatible with current clinical needle tissue biopsy systems. The RFM system can be used without external agents when there is sufficient endogenous imaging contrast. Moreover, with simple filter changes, the RFM system can readily be converted to a fluorescence-mode needle biopsy imaging system similar to that developed by Muldoon et al.[6] Future work will assess whether performance can be improved through the use of simple chemical agents already in routine clinical use.

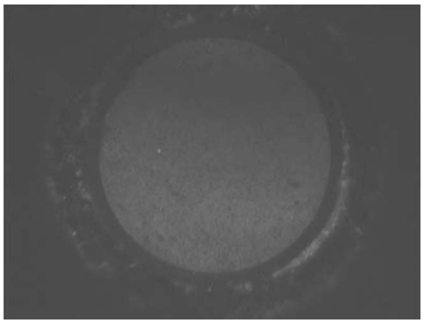

**Video 4** Reflectance endoscopic video of a dust particle in liquid solution showing single pixel fiber resolution. (QuickTime, 950 KB). [URL: http://dx.doi.org/10.1117/1.3465558.4].

## *Acknowledgments*

The authors gratefully acknowledge support from the Department of Defense Congressionally Directed Breast Cancer Research Program Era of Hope Scholar Award (W81XWH-07-1-0428). The NCI Cooperative Human Tissue Network (CHTN) provided specimens used in this project.

## *References*

1. C. Liang, M. Descour, K. B. Sun, and R. Richards-Kortum, “Fiber confocal reflectance microscope (FCRM) for in-vivo imaging,” *Opt. Express* **9**, 821–830 (2001).
2. K. C. Maitland, A. M. Gillenwater, M. D. Williams, A. K. El-Naggar, M. R. Descour, and R. R. Richards-Kortum, “*In vivo* imaging of oral neoplasia using a miniaturized fiber optic confocal reflectance microscope,” *Oral Oncol.* **44**, 1059–1066 (2008).
3. F. Jean, G. Bourg-Heckly, and B. Viellerobe, “Fibered confocal spectroscopy and multicolor imaging system for *in vivo* fluorescence analysis,” *Opt. Express* **15**, 4008–4017 (2007).
4. V. Dubaj, A. Mazzolini, A. Wood, and M. Harris, “Optic fiber bundle contact imaging probe employing a laser scanning confocal microscope,” *J. Microsc.* **207**, 108–117 (2002).
5. R. Kiesslich, M. Goetz, M. Vieth, P. R. Galle, and M. F. Neurath, “Technology Insight: confocal laser endoscopy for *in vivo* diagnosis of colorectal cancer,” *Nat. Clin. Pract. Oncol.* **4**, 480–490 (2007).
6. T. J. Muldoon, M. C. Pierce, D. L. Nida, M. D. Williams, A. Gillenwater, and R. Richards-Kortum, “Subcellular-resolution molecular imaging within living tissue by fiber microendoscopy,” *Opt. Express* **15**, 16413–16423 (2007).
7. T. J. Muldoon, S. Anandasabapathy, D. Maru, and R. Richards-Kortum, “High-resolution imaging in Barrett’s esophagus: a novel, low-cost endoscopic microscope,” *Gastrointest. Endosc.* **68**, 737–744 (2008).
8. T. J. Muldoon, N. Thekkek, D. Roblyer, D. Maru, N. Harpaz, J. Potack, S. Anandasabapathy, and R. Richards-Kortum, “Evaluation of quantitative image analysis criteria for the high-resolution microendoscopic detection of neoplasia in Barrett’s esophagus,” *J. Biomed. Opt.* **15**, 026027 (2010).
9. Sumitomo Electric U.S.A., Image Guide Technical Document ⟨http://www.sumitomoelectricusa.com/scripts/products/ofig/image.cfm⟩ (2010).
10. A. G. von Arnim, X. W. Deng, and M. G. Stacey, “Cloning vectors for the expression of green fluorescent protein fusion proteins in transgenic plants,” *Gene* **221**, 35–43 (1998).

Breast Cancer Res Treat
DOI 10.1007/s10549-010-0811-5

PRECLINICAL STUDY

# Immunoconjugated gold nanoshell-mediated photothermal ablation of trastuzumab-resistant breast cancer cells

**Laura B. Carpin · Lissett R. Bickford · Germaine Agollah · Tse-Kuan Yu · Rachel Schiff · Yi Li · Rebekah A. Drezek**

Received: 4 February 2010 / Accepted: 13 February 2010

**Abstract** Trastuzumab is a FDA-approved drug that has shown clinical efficacy against HER2+ breast cancers and is commonly used in combination with other chemotherapeutics. However, many patients are innately resistant to trastuzumab, or will develop resistance during treatment. Alternative treatments are needed for trastuzumab-resistant patients. Here, we investigate gold nanoparticle-mediated photothermal therapies as a potential alternative treatment for chemotherapy-resistant cancers. Gold nanoshell photothermal therapy destroys the tumor cells using heat, a physical mechanism, which is able to overcome the cellular adaptations that bestow trastuzumab resistance. By adding anti-HER2 to the gold surface of the nanoshells as a targeting modality, we increase the specificity of the nanoshells for HER2+ breast cancer. Silica–gold nanoshells conjugated with anti-HER2 were incubated with both trastuzumab-sensitive and trastuzumab-resistant breast cancer cells. Nanoshell binding was confirmed using two-photon laser scanning microscopy, and the cells were then ablated using a near-infrared laser. We demonstrate the successful targeting and ablation of trastuzumab-resistant cells using anti-HER2-conjugated silica–gold nanoshells and a near-infrared laser. This study suggests potential for applying gold nanoshell-mediated therapy to trastuzumab-resistant breast cancers in vivo.

**Keywords** Nanoshells · Photothermal therapy · Chemotherapy resistance · Breast cancer · Trastuzumab

## Introduction

Despite the advances in the treatment of early-stage breast cancer, patients with advanced Stage III and IV disease have 5-year survival rates of only 57% and 20%, respectively [1]. Although many new chemotherapy drugs and regimens have been developed, little improvement has been seen in the ultimate outcome of these cancer patients. Epidermal growth factor 2 receptor (Erb2 or HER2) is amplified in 20–25% of human breast cancer, and is known to be a marker of poorer prognosis due to HER2+ breast cancers aggressive nature and tendency to recur [2, 3]. In 2006, a therapeutic antibody against HER2 (Trastuzumab) was developed as part of a new class of drugs. Trastuzumab binds to the HER2 receptor and halts tumor cell growth through suppression of HER2 signaling and subsequent elevation of the levels of p27$^{\mathrm{KIP1}}$ protein [2]. Trastuzumab showed positive clinical results as a treatment for HER2+ metastatic breast cancer in clinical trials [4, 5], and after subsequent studies was approved as a treatment for patients with HER2+ metastatic breast

---

L. B. Carpin · L. R. Bickford · T.-K. Yu · R. A. Drezek (✉)
Department of Bioengineering, Rice University, 6100 Main St., MS-142, Houston, TX 77005, USA
e-mail: drezek@rice.edu

G. Agollah
Nanospectra Biosciences Inc., Houston, TX 77054, USA

T.-K. Yu
Department of Radiation Oncology, The University of Texas M.D. Anderson Cancer Center, Houston, TX 77030, USA

R. Schiff · Y. Li
Breast Center, Baylor College of Medicine, Houston, TX 77030, USA

R. A. Drezek
Department of Electrical and Computer Engineering, Rice University, Houston, TX 77005, USA

cancer. Despite the initial success of trastuzumab, the development of drug resistance has presented a major barrier. The majority of patients are intrinsically resistant to trastuzumab prior to starting therapy [6], and most initially responsive patients develop resistance to treatment within a year [2]. Second generation agents like lapatinib, which is small molecule-based tyrosine kinase inhibitor, have been developed for trastuzumab-resistant patients, but chemotherapy resistance continues to be problematic [7]. The development of gold nanoparticle-mediated photothermal cancer therapy presents a new and minimally invasive treatment possibility for chemotherapy-resistant cancers [8]. To date, gold nanoparticle-mediated treatment has only been applied to chemotherapy-sensitive cell lines. Here, we demonstrate the targeting and photothermal ablation of trastuzumab-resistant breast cancer cells in vitro using anti-HER2-conjugated silica–gold nanoshells.

The development of trastuzumab resistance has been attributed to a variety of mechanisms, including overexpression of glycoprotein MUC4 [9], overexpression of insulin-like growth factor 1 (IGF-1) [10], and constitutive P13K/Akt activity [11]. However, even in cases where there is obstructed binding of the extracellular component of the HER2 receptor, the receptor itself remains unchanged. In addition, although a mutation of the extracellular component of the HER2 receptor that results in trastuzumab resistance is theoretically possible, in most cases of resistance this does not occur [2]. This presents the possibility of using an antibody generated against the HER2 receptor as a targeting modality for an alternative form of therapy, such as gold nanoparticle-mediated photothermal therapy.

Gold nanoparticles have great potential in the diagnosis, management, and treatment of cancer due to their versatile scattering and absorbing properties, as well as the ease with which their surfaces can be modified. For therapy applications, a variety of gold nanoparticles can be used, including gold colloid [12], silica–gold nanoshells [8], gold nanorods [13], and gold nanocages [14]. For this study, silica–gold nanoshells are used due to their low cytotoxicity profile and demonstrated efficacy as a therapeutic against HER2+ breast cancer cells [8, 15, 16]. Gold nanoshells usually consist of a dielectric core, such as silica, which is coated with a thin layer of gold. The unique optical properties of nanoshells are due to the localized surface plasmon resonance of the gold metal electrons, and these properties can be modulated by controlling the thickness of the gold coating during synthesis. When designed to primarily absorb light, nanoshells can efficiently convert light energy to heat energy, destroying adjacent cells via thermal ablation [15, 17–19]. Unlike conventional hyperthermia treatments, the use of nanoshells as an absorptive agent has the added benefit of decreasing the laser intensity requirements for therapy, which prevents inadvertent ablation of normal cells.

To further enhance therapy, ligands such as antibodies, polymers, or DNA, can be conjugated to the gold nanoparticle surface. This modification has demonstrated increased target specificity in vitro [8, 17, 20]. In the case of HER2+ breast cancer, Loo et al. demonstrated that gold–silica nanoshells conjugated to anti-HER2 can be successfully used to target and ablate chemotherapy-sensitive breast cancer cells in culture [16]. Here, we demonstrate that anti-HER2-conjugated silica–gold nanoshells can mediate effective targeting and photothermal ablation of two cultured anti-HER2-resistant breast cancer cell lines—JIMT-1 has a lower level of anti-HER2 binding due to overexpression of MUC4 [9], and BT474 AZ LR is resistant to both trastuzumab and lapatinib. Using photothermal therapy, the cancer cells can be destroyed by the conversion of nanoshell-absorbed energy to heat. This physical mechanism of cell ablation effectively evades any developed intracellular resistance mechanism, presenting a new possibility for the treatment of trastuzumab-resistant breast cancers.

## Methods

### Breast cancer cell lines

Three HER2-overexpressing breast cancer cell lines were chosen for this study: SK-BR-3, JIMT-1, and BT474 AZ LR. The MCF10A cell line, which is an immortalized, HER2 negative breast epithelial cell line, was used as a control. The SK-BR-3 and MCF10A cell lines were purchased from American Type Culture Collection. The SK-BR-3 cell line is trastuzumab sensitive. The JIMT-1 cell line was purchased from DSMZ (Germany), and is trastuzumab resistant. The BT474 AZ LR cell line, a subculture of BT474, is resistant to both trastuzumab and lapatinib. The SK-BR-3 and JIMT-1 cell lines were both cultured in McCoy's 5A and Dulbecco's Modified Essential Medium, respectively, supplemented with 10% fetal bovine serum (FBS) and 1% penicillin–streptomycin. The BT474 AZ LR cell line was cultured in Dulbecco's Modified Essential Medium High Glucose supplemented with 10% FBS and 1% penicillin–streptomycin–glutamine and with 1 μM of lapatinib to maintain HER2 therapy resistance. The MCF10A cells were cultured in Mammary Epithelial Basal Medium (MEBM) supplemented with a BulletKit (Clonetics). All cells were maintained at 37°C in a 5% $CO_2$ atmosphere.

### Quantification of HER2 receptor antigens on cell surface

Quantification of HER2 surface receptors was performed as described by Bickford et al. [21]. Cells were grown to confluence, trypsinized, counted, and incubated with either media alone, PE antihuman CD340 (erbB2/HER-2) antibody (BioLegend, San Diego, CA), or PE mouse IgG1 isotype control antibody (BioLegend, San Diego, CA) for 30 min on ice in the dark. The IgG1 isotype serves as background signal correction. The cells were then washed in 1 × PBS, resuspended in 500 µl of cell staining buffer (BioLegend, San Diego, CA, USA), and stored on ice until analysis. Immunofluorescence intensity was determined by flow cytometry at The University of Texas M.D. Anderson Cancer Center (MDACC) flow cytometry core. To correlate the immunofluorescence intensity with the quantity of HER2 antigens available for binding on each cell, a Quantum Simply Cellular anti-Mouse IgG kit (Bangs Laboratories, Inc., Technology Drive Fishers, IN, USA) was used. This kit has four different sets of microbeads possessing a known number of antigen binding sites, which permits the development of a calibration curve correlating immunofluorescence intensity with the quantity of antigen binding sites. The curve is then used to calculate the number of antigen binding sites per cell.

### Silica–gold nanoshells and antibody conjugation

The silica–gold nanoshells were synthesized using previously described methods [15–17, 22]. In brief, silica cores were created using the Stöber method [23], and the silica core surface was functionalized with amine groups. These amine groups were then used to seed 4–7-nm gold colloid onto the silica surface. The size of the silica cores was determined to be 120 nm by scanning electron microscopy (SEM) prior to gold seeding. The gold shell was then completed by adding additional gold solution, potassium carbonate, and formaldehyde. After synthesis, the UV–Vis spectrum of the nanoshells was correlated with Mie Theory to determine the absorption, extinction, and scattering coefficients of the nanoshells, and subsequently the approximate concentration. The average nanoshell diameter was confirmed to be 150 ± 10 nm by SEM. The nanoshell peak absorbance was determined to be 780 nm with a concentration of 3.85 × $10^9$ nanoparticles/ml (Fig. 1).

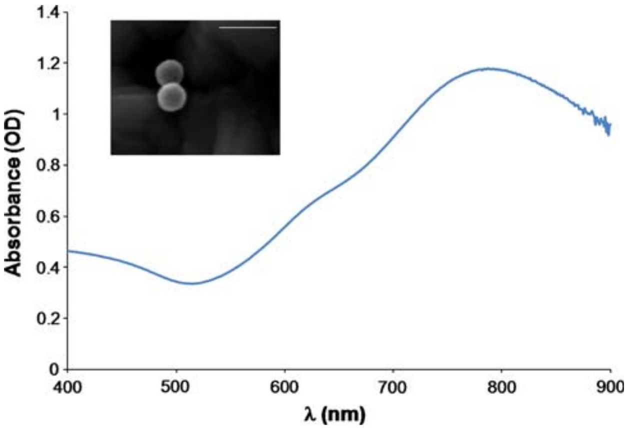

**Fig. 1** Absorbance spectrum of the silica–gold nanoshells (silica core radius = 60 nm, total radius = 75 nm). Inset shows SEM image of the nanoshells; scale bar is 300 nm

To modify the surfaces of the nanoshells with anti-HER2 antibody, the methods of Loo et al. were employed [16]. The anti-HER2 antibody (C-erbB-2/HER-2/*neu* Ab-4, Lab Vision Corporation) was incubated with a custom orthopyridyl-disulfide-polyethylene glycol-*N*-hydroxysuccinimide ester (OPSS-PEG-NHS, MW = 2kD, CreativeBiochem Laboratories, Winston Salem, NC, USA) linker at a molar ratio of 3:1 in sodium bicarbonate (100 mM, pH 8.5) overnight on ice at 4°C. Aliquots were then stored at −80°C until use, when they were thawed on ice. The antibody binds to the OPSS-PEG-NHS linker via the amide group, and adsorbs to the gold surface of the nanoshell via the thiols of the OPSS group. To attach the antibody-linker to the gold nanoshells, nanoshells were incubated with the antibody-linker at 4°C for 2 h, then 1 mM polyethylene glycol-thiol (PEG-SH, MW = 5kD, Nektar) was added and the nanoshells were incubated overnight at 4°C for further stabilization. After nanoshell conjugation, the unreacted PEG-linker and PEG-SH were removed by centrifugation of the nanoshell solution and removal of the supernatant. The anti-HER2 nanoshells were then resuspended in cell-line appropriate media prior to use in cell studies.

### Two-photon laser scanning microscopy to confirm binding efficiency

For in vitro two-photon nanoshell binding studies, 5 × $10^5$ cells in suspension from each cell line (MCF10A, SK-BR-3, JIMT-1, and BT474 AZ LR), were incubated with 1.73 × $10^9$ nanoshells in 1 ml of media for 1 h at 37°C with rotation in a hybridization oven. Cells incubated with media alone were used as a control. After the incubation, the cell lines were washed three times with 1 ml of 1 × phosphate-buffered saline (PBS) to remove unbound nanoshells, and resuspended in 0.5 ml of cell line appropriate media. Each treatment and control group was then seeded onto an inverted coverslip and allowed to attach overnight. A Zeiss Laser Scanning Microscope 510 META multiphoton system (Zeiss, Thornwood, NY, USA) was used in combination with a Coherent Chameleon femtosecond mode locked Ti:sapphire laser (Coherent, Santa Clara, CA, USA) for imaging.

### Nanoshell-mediated photothermal therapy

For in vitro photothermal ablation studies, $5 \times 10^5$ cells in suspension from each cell line (MCF10A, SK-BR-3, JIMT-1, and BT474 AZ LR) were incubated with $1.71 \times 10^{10}$ nanoshells as described above. Media alone was again used as a control. Cells were washed with PBS and seeded in coverslips as described above.

Laser irradiation of the cells was performed in a similar manner to previous photothermal therapy studies [16–18]. After the cells were attached, each well was uncovered, placed on top of a glass microscope slide, and exposed to an 808-nm NIR diode laser (Coherent Inc., Santa Clara, CA, USA) at 80 W/$cm^2$ with a 1.5-mm spot size for 5 min. Following laser irradiation, the cells were returned to the 37°C incubator with 5% $CO_2$ for several hours. Live/dead viability staining was then performed using an Invitrogen Live/Dead viability/cytotoxicity kit (Carlsbad, CA, USA), and cells were imaged using a Zeiss Axiovert 135 Fluorescence microscope (Zeiss, Thornwood, NY, USA). To confirm nanoshell binding, silver staining was performed using Sigma–Aldrich Silver Enhancement solutions (St. Louis, MO, USA), followed by brightfield imaging.

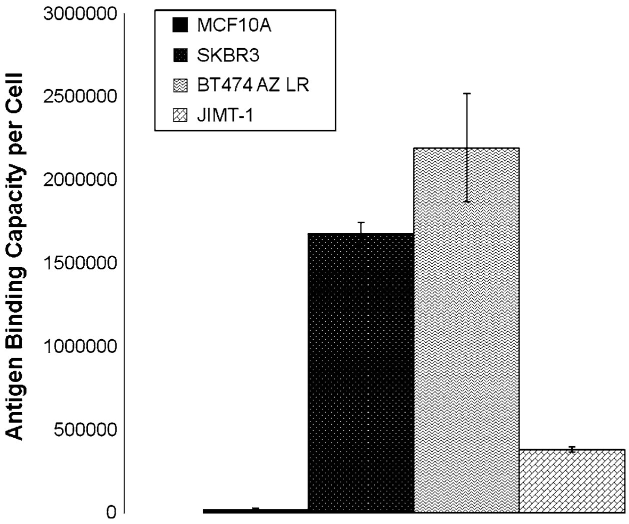

**Fig. 2** Anti-HER2 binding capacity of each breast cancer cell line, determined by flow cytometry. The HER2+ cell lines (SK-BR-3, JIMT-1, BT474 AZ LR) show a significantly higher binding capacity than the HER2-cell line (MCF10A). Data for MCF10A, SK-BR-3, and JIMT-1 reused with permission from [21]. Copyright 2009 from Springer

## Results

### Quantification of antigen binding for each cell line

Using flow cytometry, the number of antigen binding sites for each cell line was determined, as displayed in Fig. 2. Data for the MCF10A, SK-BR3, and JIMT-1 cell lines are being reused with permission from [21]. A one-factor ANOVA test indicated significant differences between cell lines in the number of binding sites ($P < 0.01$). Each of the HER2+ breast cancer lines used in this study had a larger number of anti-HER2 binding sites than the normal epithelial cell line, MCF10A ($2.43 \times 10^4 \pm 3.77 \times 10^3$ receptors), by the Tukey comparison test ($P < 0.01$). The BT474 AZ LR cell line had the greatest anti-HER2 binding capacity ($2.19 \times 10^6 \pm 3.25 \times 10^5$ receptors), followed by the SK-BR-3 ($1.68 \times 10^6 \pm 6.78 \times 10^4$ receptors) and then the JIMT-1 ($3.82 \times 10^5 \pm 1.47 \times 10^4$ receptors) cell lines. Notably, the JIMT-1 cell line has a significantly lower HER2 binding site expression when compared to the SK-BR-3 and BT474 AZ LR cell lines ($P < 0.01$).

### Two-photon microscopy of nanoshell–cell binding

Nanoshell binding is evaluated through two-photon laser scanning microscopy in Fig. 3. The figure shows phase-

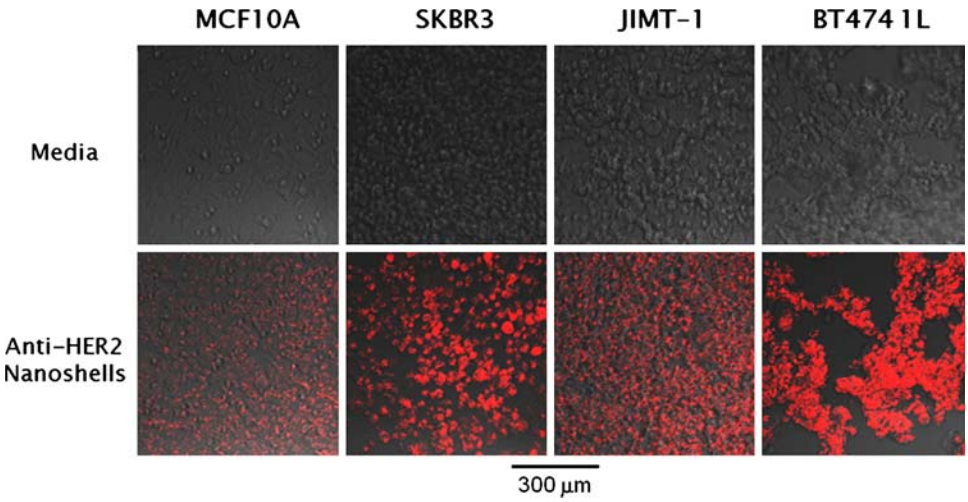

**Fig. 3** Verification of nanoshell binding using two-photon laser scanning microscopy. Images depicted are phase contrast images overlaid with two-photon images. SK-BR-3, JIMT-1, and BT474 AZ LR cell lines, all HER2+, show greater binding of the anti-HER2 nanoshells than the MCF10A normal epithelial cell line

contrast images overlaid with the two-photon images. The cells incubated with media only demonstrate no nanoshell signal. The HER2+ cell lines incubated with nanoshells each show nanoshell signal, while the HER2-cell line shows significantly less. The SK-BR-3 and BT474 AZ LR cell lines show the most nanoshell binding. The JIMT-1 cell line demonstrates less nanoshell binding than the SK-BR-3 and BT474 AZ LR cell lines, but greater nanoshell binding than the MCF10A cell line. There is some degree of binding seen with the MCF10A cell line, but this binding is still significantly less than the HER2+ breast cancer cells.

### Nanoshell-mediated cell destruction of trastuzumab-resistant cell lines

Figure 4 shows the live/dead imaging and silver staining for the treatment and media control group of each cell line. None of the media alone groups show evidence of cell death on the live/dead images or evidence of nanoshell binding on the silver stain. The silver staining confirms that nanoshells are bound to each of the HER2+ cell lines (SK-BR-3, BT474 AZ LR, JIMT-1), with minimal nanoshell binding to the MCF10A cell line. The MCF10A-nanoshell group does not demonstrate localized area of cell death, while each of the HER2+ breast cancer-nanoshell groups show a clearly defined region of dead cells (red) corresponding to the laser spot surrounded by non-irradiated, nanoshell-bound live cells (green).

## Discussion

Anti-HER2 resistance continues to be a challenge for clinicians treating advanced cancers. Gold nanoparticle-mediated photothermal therapy could present new possibilities for cancers that are currently resistant to conventional chemotherapy and radiation treatments. The objective of this study was to demonstrate that immunoconjugated silica–gold nanoshells can effectively destroy both chemotherapy-sensitive and chemotherapy-resistant breast cancer cell lines. Two trastuzumab-resistant breast cancer cell lines were selected for testing, JIMT-1 and BT474 AZ LR. A trastuzumab-sensitive breast cancer cell line, SK-BR-3, and a HER2 negative normal epithelial cell line, MCF10A, were also chosen as positive and negative binding controls. Each of the HER2+ breast cancer cell lines selected was effectively ablated using nanoshell-mediated photothermal therapy. These results suggest gold nanoparticle-mediated photothermal therapy may have potential to be employed against chemotherapy-resistant breast cancers in vivo.

As the first step of this study, we evaluated nanoshell binding efficiency using two-photon laser scanning

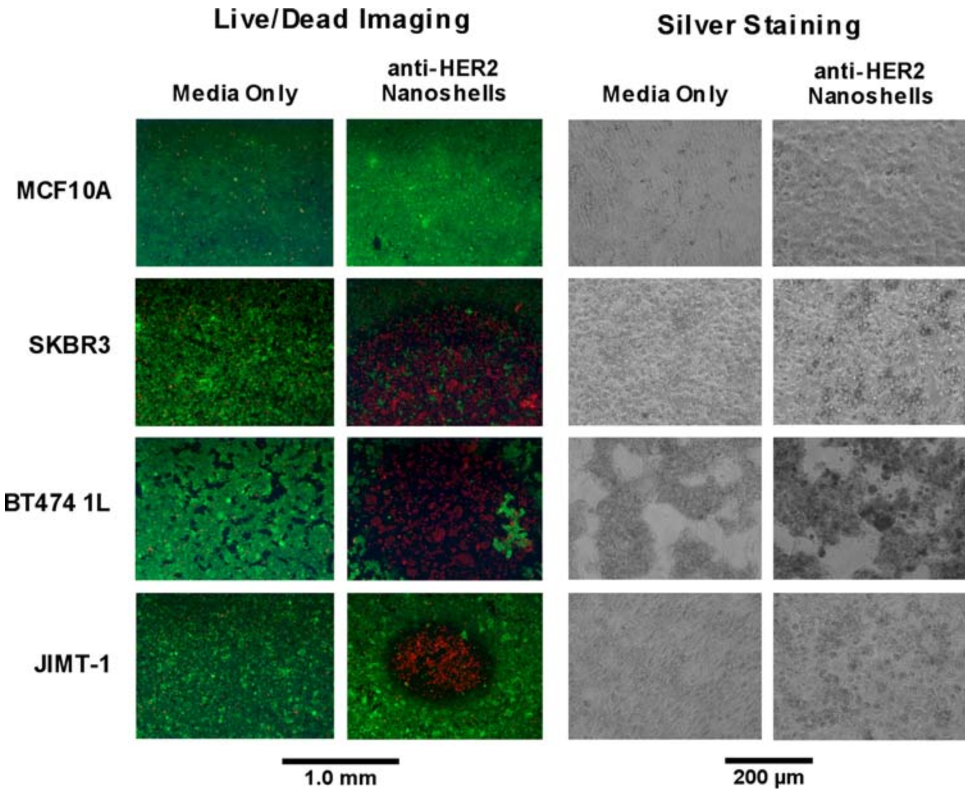

**Fig. 4** Photothermal therapy results. Live/dead imaging demonstrates cell ablation in HER2+ cell lines (SK-BR-3, JIMT-1, BT474 AZ LR) treated with anti-HER2 nanoshells and NIR laser irradiation. Silver staining shows nanoshell binding for each of the HER2+ cell lines

microscopy. Silica–gold nanoshells have demonstrated two-photon properties, and can be used to label HER2+ breast cancer cells in vitro [24, 25]. Nanoshell binding has also been demonstrated using darkfield microscopy [15] and optical coherence tomography [26], which depends on the enhanced scattering of the nanoshells for contrast. However, for future in vivo studies, two-photon luminescence may prove superior in bulk tissue to these scatter-based techniques. This is due to the improved signal to noise ratio of two-photon microscopy, as well as its demonstrated ability to more effectively investigate the nanoshell distribution within the tumor with the assistance of software [25]. In Fig. 3, we observe that the anti-HER2 conjugated silica–gold nanoshells bind specifically to trastuzumab-resistant HER2+ breast cancer cell lines, with very little binding to the normal breast epithelial cell line, MCF10A (Figs. 3, 4). The degree of nanoshell binding shown by both the two-photon and silver stain images seems to correlate with the HER2 antigen binding capacity of the breast cancer cell lines. The JIMT-1 cell line has the lowest anti-HER2 binding capacity of the three breast cancer lines studied. Nagy et al. found that only 20% of HER2 receptors are available for trastuzumab binding due to obstruction of the extracellular component of the HER2 receptor by MUC4 [9]. Despite this, anti-HER2 nanoshell binding is still clearly seen in both the two-photon and silver stain images, though to a lesser degree than the other two HER2+ lines. Importantly, this lesser degree of binding is still sufficient for the photothermal destruction of the JIMT-1 cells, while the action of trastuzumab is impaired against these cells [9]. In the case of the BT474 AZ LR cell line, the nanoshell binding is more than adequate to ensure cell death upon NIR laser irradiation. Photothermal therapy is also effective against the BT474 AZ LR cell line, while the action of both trastuzumab and lapatinib is impaired against these cells.

Using silica–gold nanoshells as a mediating absorptive agent for photothermal therapy has advantages over conventional hyperthermia treatments. In Fig. 4, the ablated areas (red) are surrounded by living, healthy cells (green), and cell lines with minimal or no nanoshell binding show no regions of cell death. Only HER2+ cells with bound nanoshells with in the region of the laser spot are ablated. Targeting the gold nanoparticles with an antibody or peptide permits single cell specificity in vitro [27, 28]. This specificity is important during in vivo studies, when healthy tissues such as skin will be in the laser path to cancerous tissue. Because nanoshells efficiently absorb the irradiating laser energy and convert it to heat, the laser power requirements to induce cell death are lowered. In conventional hyperthermia treatments, this specificity is lacking, as the power of the irradiating energy source must be high enough to kill cells without the assistance of a mediating agent. Thus, using nanoshells as part of photothermal therapy in vitro lowers the power requirements of the irradiating energy, as well as increasing the specificity of therapy for malignant cells.

Figure 4 does demonstrate some variation in the size of the ablated regions. This variation was seen consistently among several replicate experiments. These differences are likely due to variations in the laser intensity distribution, the degree of cell confluence, and density of HER2 receptors on the cell surfaces. In order for cell death to occur, a temperature of 70–80°C must be achieved for approximately 4 min [13]. The net temperature increase of the cells within the laser spot is dependent on a combination of variables, including: the absorptive cross-section of the silica–gold nanoshells, the physical distribution of the nanoshells among the cells, the intensity and duration of the laser illumination, and the heat transfer and dissipation properties of the cells and media [29]. Nonuniform laser intensity could lead to cells at the periphery of the spot receiving less laser power [30], resulting in the minimum temperature and duration needed for cell death not being achieved. However, the laser spot size, power, and duration were held consistent throughout each of the treatment groups and experiments, so it is unlikely that this is a large contributor. The nanoshell binding density could also be playing a significant role, and, based on the information in Figs. 2 and 3, is a likely contributor to the variation in ablated area size.

The low anti-HER2 binding capacity of the JIMT-1 cell line versus the higher binding capacities of the SK-BR-3 and BT474 AZ LR cell lines correlates with the small ablated area for the JIMT-1 cells and the larger ablated areas for the SK-BR-3 and BT474 AZ LR cells. This supports the nanoshell binding density being a major contributor to the variation in ablation size. However, although the SK-BR-3 cell line has a lower anti-HER2 binding capacity than the BT474 AZ LR cell line, the size of the ablated area for this cell line is larger. This could be due to several factors. Some of this variation may be due to the differences in how the SK-BR-3 and BT474 AZ LR cell lines tend to grow. The SK-BR-3 cells grow in a monolayer, while the BT474 AZ LR cell line tends to grow in conglomerates. These growth differences may have resulted in different heating profiles between the two cell lines, affecting the sizes of the ablated regions. Another possible contributing factor is differences in thermal sensitivity between the SK-BR-3 and BT474 AZ LR cell lines, which has been seen in response to conventional hyperthermia treatments in tumors resected from breast cancer patients [31]. Regardless of variation in the size of the ablated regions, each of the HER2+ breast cancer cell lines was successfully ablated using nanoshell-mediated photothermal therapy. Each of these variables (laser intensity profile, nanoshell binding density, the tumor cell density/tumor shape, the thermal sensitivity of the tumor) will need to be considered in applying and optimizing nanoshell-mediated therapy to trastuzumab-resistant cancers in vivo.

The successful application of gold nanoshell-mediated photothermal therapy to trastuzumab-resistant breast cancer cells in vitro suggests a promising new approach for the treatment of advanced HER2+ breast cancers. By virtue of its physical means of destroying cancer, nanoshell-mediated thermal ablation of these types of cancer has an innate advantage over trastuzumab, lapatinib, and other antibody or small molecule-based therapies. Gold nanoparticle-mediated photothermal therapies also have demonstrated synergistic cell killing in combination with chemotherapy in vitro [32]and radiation in vivo [33], suggesting that the combination of conventional treatments and this technology could also be beneficial for cancer therapy. In vivo studies with xenografted trastuzumab-resistant breast cancers are currently underway to further confirm the efficacy and applicability of this nanotechnology to anti-HER2-resistant breast cancers.

**Acknowledgments** We would like to thank Wendy Schober at MDACC for performing the flow cytometry on each cell line. This study was supported by a Department of Defense Congressionally Directed Breast Cancer Research Program Era of Hope Scholar Award to Rebekah Drezek and Tse-Kuan Yu, the Center for Biological and Environmental Nanotechnology (EEC-0118007 and EEC-0647452), the NCI breast cancer SPORE P50 (CA58183), and the Nancy Owens Memorial Foundation (Y. Li). L. Carpin would also like to thank the Medical Scientist Training Program at Baylor College of Medicine for training support.

## References

1. American Cancer Society: Breast Cancer Facts and Figures (2007–2008) In: breast cancer facts and figures 2007–2008. American Cancer Society, Atlanta
2. Nahta R, Yu D, Hung MC, Hortobagyi GN, Esteva FJ (2006) Mechanisms of disease: understanding resistance to HER2-targeted therapy in human breast cancer. Nat Clin Pract 3(5):269–280
3. Slamon DJ, Clark GM, Wong SG, Levin WJ, Ullrich A, McGuire WL (1987) Human breast cancer: correlation of relapse and survival with amplification of the HER-2/neu oncogene. Science 235(1):177–182
4. Cobleigh MA, Vogel CL, Tripathy D, Robert NJ, Scholl S, Fehrenbacher L, Wolter JM, Paton V, Shak S, Lieberman G et al (1999) Multinational study of the efficacy and safety of humanized anti-HER2 monoclonal antibody in women who have HER2-overexpressing metastatic breast cancer that has progressed after chemotherapy for metastatic disease. J Clin Oncol 17(9):2639–2648
5. Vogel CL, Cobleigh MA, Tripathy D, Gutheil JC, Harris LN, Fehrenbacher L, Slamon DJ, Murphy M, Novotny WF, Burchmore M et al (2002) Efficacy and safety of trastuzumab as a single agent in first-line treatment of HER2-overexpressing metastatic breast cancer. J Clin Oncol 20(3):719–726
6. Nahta R, Esteva FJ (2006) HER2 therapy: molecular mechanisms of trastuzumab resistance. Breast Cancer Res 8(6):215
7. Valabrega G, Montemurro F, Aglietta M (2007) Trastuzumab: mechanism of action, resistance and future perspectives in HER2-overexpressing breast cancer. Ann Oncol 18(6):977–984
8. Hirsch LR, Stafford RJ, Bankson JA, Sershen SR, Rivera B, Price RE, Hazle JD, Halas NJ, West JL (2003) Nanoshell-mediated near-infrared thermal therapy of tumors under magnetic resonance guidance. Proc Natl Acad Sci USA 100(23):13549–13554
9. Nagy P, Friedlander E, Tanner M, Kapanen AI, Carraway KL, Isola J, Jovin TM (2005) Decreased accessibility and lack of activation of ErbB2 in JIMT-1, a herceptin-resistant, MUC4-expressing breast cancer cell line. Cancer Res 65(2):473–482
10. Lu Y, Zi X, Zhao Y, Mascarenhas D, Pollak M (2001) Insulin-like growth factor-I receptor signaling and resistance to trastuzumab (Herceptin). J Natl Cancer Inst 93(24):1852–1857
11. Yakes FM, Chinratanalab W, Ritter CA, King W, Seelig S, Arteaga CL (2002) Herceptin-induced inhibition of phosphatidylinositol-3 kinase and Akt Is required for antibody-mediated effects on p27, cyclin D1, and antitumor action. Cancer Res 62(14):4132–4141
12. Huang X, Qian W, El-Sayed IH, El-Sayed MA (2007) The potential use of the enhanced nonlinear properties of gold nanospheres in photothermal cancer therapy. Lasers Surg Med 39(9):747–753
13. Huang X, El-Sayed IH, Qian W, El-Sayed MA (2006) Cancer cell imaging and photothermal therapy in the near-infrared region by using gold nanorods. J Am Chem Soc 128(6):2115–2120
14. Skrabalak SE, Chen J, Au L, Lu X, Li X, Xia Y (2007) Gold nanocages for biomedical applications. Adv Mater 19(20):3177–3184
15. Loo C, Lin A, Hirsch L, Lee MH, Barton J, Halas N, West J, Drezek R (2004) Nanoshell-enabled photonics-based imaging and therapy of cancer. Technol Cancer Res Treat 3(1):33–40
16. Loo C, Lowery A, Halas N, West J, Drezek R (2005) Immunotargeted nanoshells for integrated cancer imaging and therapy. Nano Lett 5(4):709–711
17. Bernardi RJ, Lowery AR, Thompson PA, Blaney SM, West JL (2008) Immunonanoshells for targeted photothermal ablation in medulloblastoma and glioma: an in vitro evaluation using human cell lines. J Neurooncol 86(2):165–172
18. Gobin AM, Moon JJ, West JL (2008) EphrinA I-targeted nanoshells for photothermal ablation of prostate cancer cells. Int J Nanomed 3(3):351–358
19. Stern JM, Stanfield J, Lotan Y, Park S, Hsieh JT, Cadeddu JA (2007) Efficacy of laser-activated gold nanoshells in ablating prostate cancer cells in vitro. J Endourol/Endourol Soc 21(8):939–943
20. Elghanian R, Storhoff JJ, Mucic RC, Letsinger RL, Mirkin CA (1997) Selective colorimetric detection of polynucleotides based on the distance-dependent optical properties of gold nanoparticles. Science 277(5329):1078–1081
21. Bickford LR, Agollah G, Drezek R, Yu TK (2009) Silica-gold nanoshells as potential intraoperative molecular probes for HER2-overexpression in ex vivo breast tissue using near-infrared reflectance confocal microscopy. Breast cancer research and treatment [Epub ahead of print]
22. Oldenburg SJ, Averitt RD, Westcott SL, Halas NJ (1998) Nanoengineering of optical resonances. Chem Phys Lett 288(2–4):243–247
23. Stober W, Fink A, Bohn E (1968) Controlled growth of monodisperse silica spheres in micron size range. J Colloid Interf Sci 26(1):62–69
24. Bickford L, Sun J, Fu K, Lewinski N, Nammalvar V, Chang J, Drezek R (2008) Enhanced multi-spectral imaging of live breast

cancer cells using immunotargeted gold nanoshells and two-photon excitation microscopy. Nanotechnology 19(31): 315102

25. Park J, Estrada A, Sharp K, Sang K, Schwartz JA, Smith DK, Coleman C, Payne JD, Korgel BA, Dunn AK et al (2008) Two-photon-induced photoluminescence imaging of tumors using near-infrared excited gold nanoshells. Opt Express 16(3):1590–1599
26. Gobin AM, Lee MH, Halas NJ, James WD, Drezek RA, West JL (2007) Near-infrared resonant nanoshells for combined optical imaging and photothermal cancer therapy. Nano Lett 7(7):1929–1934
27. Black KC, Kirkpatrick ND, Troutman TS, Xu L, Vagner J, Gillies RJ, Barton JK, Utzinger U, Romanowski M (2008) Gold nanorods targeted to delta opioid receptor: plasmon-resonant contrast and photothermal agents. Mol Imaging 7(1):50–57
28. Tong L, Zhao Y, Huff TB, Hansen MN, Wei A, Cheng JX (2007) Gold nanorods mediate tumor cell death by compromising membrane integrity. Adv Mater 19:3136–3141
29. Cheong SK, Krishnan S, Cho SH (2009) Modeling of plasmonic heating from individual gold nanoshells for near-infrared laser-induced thermal therapy. Med Phys 36(10):4664–4671
30. de Lange DF, Hofman JT, Meijer J (2005) Influence of intensity distribution on the meltpool and clad shape for laser cladding. In: Third international WLT-conference on lasers in manufacturing: 2005; Munich, Germany
31. Rofstad EK (1990) Heat sensitivity and thermotolerance in vitro of human breast carcinoma, malignant melanoma and squamous cell carcinoma of the head and neck. Br J Cancer 61(1):22–28
32. Hauck TS, Jennings TL, Yatsenko T, Kumaradas JC, Chan WCW (2008) Enhancing the toxicity of cancer chemotherapeutics with gold nanorod hyperthermia. Adv Mater 20(20):3832–3838
33. Diagaradjane P, Shetty A, Wang JC, Elliott AM, Schwartz J, Shentu S, Park HC, Deorukhkar A, Stafford RJ, Cho SH et al (2008) Modulation of in vivo tumor radiation response via gold nanoshell-mediated vascular-focused hyperthermia: characterizing an integrated antihypoxic and localized vascular disrupting targeting strategy. Nano Lett 8(5):1492–1500

# Symmetry Breaking in Gold−Silica−Gold Multilayer Nanoshells

**Ying Hu,[†] Sterling J. Noelck,[†] and Rebekah A. Drezek[†,‡,*]**

[†]Department of Bioengineering and [‡]Department of Electrical and Computer Engineering, Rice University, Houston, Texas 77005

**ABSTRACT** We present a computational study of the plasmonic properties of gold−silica−gold multilayer nanoshells with the core offset from the center. Symmetry breaking, due to the core offset, makes plasmon resonances that are dark in concentric geometries visible. Applying plasmon hybridization theory, we explain the origin of these resonances from the interactions of an admixture of both primitive and multipolar modes between the core and the shell. The interactions introduce a dipole moment into the higher order modes and significantly enhance their coupling efficiency to light. To elucidate the symmetry breaking effect, we link the geometrical asymmetry to the asymmetrical distribution of surface charges and demonstrate illustratively the diminishing multipolar characteristic and increasing dipolar characteristic of the higher order modes. The relative amplitudes of the modes are qualitatively related by visual examination of the dipolar component in the surface charge distributions. Using polarization-dependent surface charge plots, we illustrate two distinct mode configurations despite their spectral similarities. We further demonstrate a trend of increasing absorption relative to scattering as the resonant wavelength red shifts in response to a larger core offset.

**KEYWORDS:** plasmonics · multilayer nanoshells · symmetry breaking · plasmon hybridization · surface charge distribution

Up to date, symmetry breaking has been investigated in a variety of gold nanostructures from three-dimensional nanoeggs[1] and nanocups[2] to two-dimensional disk/ring,[3,4] two-layer, and planar nanocavities.[5,6] In nanoeggs, where the silica core is off-centered in a silica−gold core−shell nanoshell, both far-field and near-field properties have been studied as functions of the core offset.[1] It was found that a larger offset correlates with larger red shifts in the low-energy plasmon resonant peaks, a stronger near-field enhancement, and a larger absorption-to-scattering ratio at the dipole resonance.[1] The polarization of light only weakly affects the far-field spectrum.[2] However, in nanocups where the gold shell is partially opened up by the offsetting core, the far-field scattering spectrum strongly depends on polarization owing to its anisotropic geometry.[7] As the core further protrudes from the shell, dipole modes gradually weaken and eventually vanish.[1]

Studies of two-dimensional structures have revealed some interesting phenomena. In geometries with reduced symmetry, the highly damped multipolar modes are excited and interact with the dipole mode. Liu and co-workers demonstrated a carefully designed planar geometry in which the narrow quadrupole resonance of the nanobar/nanoslit dimer destructively interferes with the broad dipole mode of the nanobar/nanoslit monomer that is off-centered, leading to a narrow region where light transmission is significantly enhanced; in atomic physics, this is known as electromagnetically enhanced interference (EIT).[5,6] Similarly, Hao *et al.* reported a nonconcentric ring/disk nanocavity in which the broad dipole mode both constructively and destructively interferes with a sharp quadrupole mode. The interaction results in an asymmetrical sharp Fano-type resonance.[3,4] Due to the sharp nature of the Fano resonance, symmetry-breaking geometries have been proposed for nanoscale optical sensing such as high figure-of-merit metamaterial sensors.[5] It has also been found that offset geometries exhibit significantly larger local-field enhancement, making them promising for surface-enhanced spectroscopies.[1−3]

Multilayer nanoshells (MNS) preserve three-dimensional spherical symmetry, as in nanoeggs, but they also exhibit symmetry-breaking patterns similar to ring/disk nanocavities. Theoretical investigations of concentric MNS have been previously reported using various Mie-based approaches.[8−11] It has been found that the addition of a gold core to the gold shell splits the low-energy plasmon resonance of a conventional silica−gold core−shell nanoshell (CNS) into a high-energy

*Address correspondence to drezek@rice.edu.

Received for review December 1, 2009 and accepted February 02, 2010.

**10.1021/nn901743m**

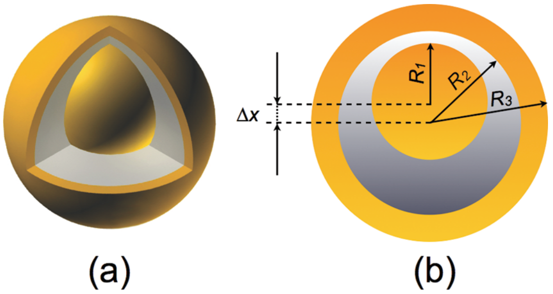

**Figure 1. (a) Three-dimensional illustration of a gold−silica−gold multilayer nanoshell with an offset core. (b) Dimensions of an $R_1/R_2/R_3$ gold−silica−gold multilayer nanoshell with core offset $\Delta x$.**

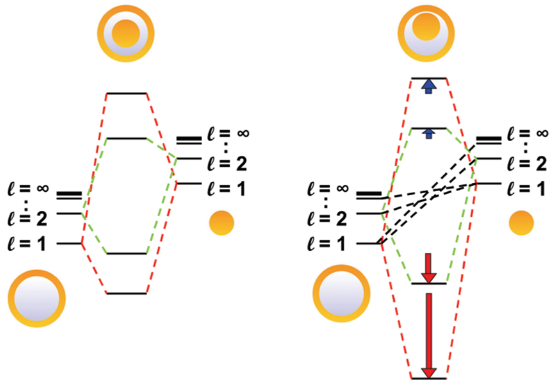

**Figure 2. Hybridization diagrams of MNS with concentric (left) and offset (right) geometries. The left panel illustrates the plasmon hybridization diagram for a concentric MNS with interaction between modes having the same angular momentum (energy increases from bottom to top). The right panel displays the nonconcentric MNS case with black lines showing additional interactions and arrows showing the relative red shift and blue shift (not to scale). Only dipole and quadrupolar interactions are shown for clarity.**

antibonding mode and a low-energy bonding mode that can be tuned from the visible region into the infrared. The red shift of this mode correlates with intermediate silica layer thickness, which determines the strength of coupling between the core mode and the CNS mode. As the mode red shifts, the MNS becomes relatively more absorbing than scattering at the bonding-mode resonance.[10] An experimental study of MNS has also been published. Xia and co-workers reported the chemical synthesis of sub-100 nm multilayer nanoshells.[12] The silica coating on gold was achieved using a modified Stöber method.[13−16] The final gold layer was coated in a way similar to synthesizing silica−gold core−shell nanoshells.[17,18]

Here we use a computational model to investigate MNS with an offset geometry: the inner gold core is moved away from the center but does not touch the gold shell, as illustrated in Figure 1a. The MNS dimensions are denoted by the radius of each layer, $R_1$, $R_2$, and $R_3$, as well as the core offset, $\Delta x$, shown in Figure 1b. We apply plasmon hybridization theory to obtain insight into spectral properties of the MNS. This theory is analogous to molecular orbital theory and describes how the fixed-frequency plasmons of elementary nanostructures hybridize to create more complicated resonances. It has been used to explain the plasmonic properties of structures ranging from concentric nanoshells[19,20] to nanorice[21−24] to nanosphere trimers[25,26] and quadrumers.[25] Some interesting examples of plasmon hybridization applied to nonsymmetrical structures include analyzing the aforementioned nanocups[1,2,7] and nonconcentric ring/disk structures.[3,4]

The far-field properties of MNS were simulated using a finite-element method (FEM) package: COMSOL Multiphysics v3.5a with the RF module. Because the dimensions of the gold core and shell remain unaltered as the location of the core changes, the offset process itself does not require size correction for the dielectric function of gold due to intrinsic effects. It should also be noted that this work does not focus on the spectral width of plasmon resonances, which can be considerably broadened by the surface scattering of electrons in nanostructures.[27−30]

## RESULTS AND DISCUSSION

**Plasmon Hybridization.** An MNS can be modeled as a hybrid between a silica−gold core−shell nanoshell and a solid gold core. We apply plasmon hybridization to explain the optical properties of MNS using these two basic nanostructures. The hybridization diagrams in Figure 2 show, for both the concentric and offset MNS, the interactions between the hybridized modes of the nanoshell and the spherical plasmon modes of the core. For clarity, only the dipolar and quadrupolar interactions are shown. The antibonding modes from the nanoshell are not shown because they are higher energy and have only very weak interactions with the core mode. The left panel of Figure 2 shows the hybridization diagram for the concentric MNS where the modes of different angular momenta are forbidden from interacting. Like the hybridization between the inner and outer layers of a nanoshell, there are two modes for each interaction: a low-energy bonding mode and a higher energy antibonding mode. This can be seen in the left panel of Figure 2 for the dipole−dipole ($l = 1$) and quadrupole−quadrupole ($l = 2$) interaction. For the nonconcentric case, the selection rules for interaction are relaxed, allowing modes of different orders to mix. As depicted in the right panel of Figure 2, the dipole mode ($l = 1$) of the core can now interact with not only the dipole mode ($l = 1$) of the shell but also the quadrupole and higher order modes ($l = 2$, 3, *etc.*) of the shell. Additionally, the quadrupole ($l = 2$) of the shell can now interact with the dipole ($l = 1$) of the core, bringing in the dipole moment into the quadrupole mode.

The hybridization between different modes on the core and the shell also results in red shifts of the hybridized bonding modes of MNS. The lower order modes are red-shifted as they become repelled by the interaction with higher order modes. As shown in the right panel of Figure 2, this yields a shift for the predominately dipole−dipole hybridized modes that is larger than for the quadrupolar−quadrupolar hybridized modes, and so on. In addition to a red shift of the bonding modes, the antibonding hybridized modes are slightly blue-shifted. This leads to a very asymmetrical splitting of the hybridized energy modes. Such asymmetrical splitting is seen in other nanostructures as the symmetry is broken,[2,4,31] as well as in nanoparticle dimers.[32,33] The degree of the shift is determined by the strength of the interactions between the different modes. As the gold core is offset more and approaches the gold nanoshell, the plasmons of the core interact more strongly with plasmons of the shell. These increasing interactions lead to stronger mixing between the different modes, creating a greater shift from the concentric MNS interactions.

**Symmetry Breaking in MNS with Different Geometries.** As seen in the work on concentric multilayer nanoshells, changing the ratio of the core, silica layer, and the outer layer allows tuning of the plasmon resonance.[10] This same effect is seen in offset multilayer nanoshells, as well. Figures 3 and 4 show the extinction spectra of the offset MNS with two different $R_1/R_2/R_3$ ratios as well as different outer radii $R_3$. Figure 3 shows R10/15/25 nm MNS in water with various core offsets. The black stars from the Mie calculation agree very well with the black curve from the FEM calculation of a concentric geometry. Two distinct plasmon resonant peaks can be observed in the concentric spectrum. The high-energy peak around 530 nm is the antibonding mode of the dipole−dipole interaction between the shell and the core along with other higher order modes. The interband transitions of gold lead to a pronounced broadening and damping of all modes in this region.[34−36] The low-energy peak at 643 nm is the bonding mode of the dipolar interaction. Quadrupole modes are not excited as the particle lies in the quasi-static region. When the symmetry is reduced and the mode selection rule for hybridization is relaxed, modes of different angular momenta start to interact.[1,2,31] Among the offset spectra, one can immediately observe a red shift of the dipolar bonding mode. The fact that the dipole of the core is allowed to interact with the quadrupole of the shell and *vice versa* shifts the bonding mode to a lower energy. The blue shift of the antibonding mode, however, is too small to be visualized in the spectrum. In addition to the red shift of the bonding modes and blue shift of the antibonding modes, hybridization results in the appearance of dark modes that were only weakly excited or not excited at all in the concentric MNS. For instance, one can observe the emergence of a new peak at about 592 nm. This peak is likely to be the bonding mode of the quadrupole−quadrupole interaction between the shell and the core (noted by $l = 2$ in the hybridization diagram). This mode can be directly excited because the interaction between the quadrupolar and dipole modes introduces a small overall dipole moment in the plasmon. This mode is not excitable in the concentric case because of the lack of the dipole moment in the quadrupole−quadrupole interaction.

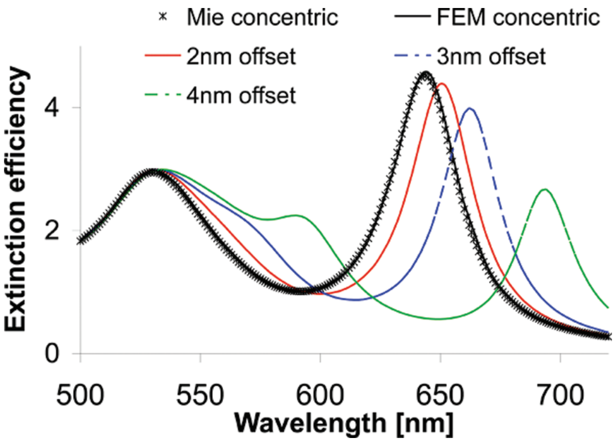

**Figure 3. Extinction spectra of R10/15/25 nm MNS in water with various core offsets. Core offsets in *y*; incident light linearly polarized in *x* and propagates in *z*.**

Although interesting in nature, the quadrupole peak is still not very well-defined at the largest offset we calculated. In Figure 4, we demonstrate the spectra of a larger MNS: R30/40/50 nm in water with a different $R_1/R_2/R_3$ ratio (3/4/5 instead of 2/3/5). The particle lies outside the quasistatic region and can provide opportunities to observe sharp higher order modes. As shown in Figure 4, good agreement was obtained between Mie and FEM calculations on the concentric geometry. The relatively large size of the MNS and limitations from the meshing and scattering boundary condition in COMSOL v3.5a may account for the ∼6% discrepancy on the peak intensity at 890 nm.[37] For clarity, each resonant peak is labeled with a numerical value associated with its mode (*i.e.*, 1 for dipole, 2 for quadrupole, *etc.*), followed by a letter denoting the core offset of that spectrum.

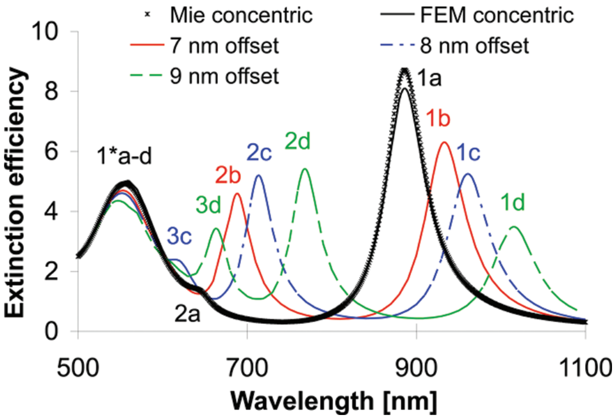

**Figure 4. Extinction spectra of R30/40/50 nm MNS in water with various core offsets. Core offsets in *y*; incident light linearly polarized in *x* and propagates in *z*.**

In the concentric spectrum, in addition to the dipolar modes at 1a and 1*a, a slight quadrupolar peak can be observed at 2a. The excitation of this mode is attributed to the retardation effect as the particle size is comparable to the excitation wavelength. Its small amplitude reflects a lack of the dipole moment. More specifically, the amplitude of the extinction peak is directly proportional to the square of the dipole moment. When the symmetry is reduced, as shown in the 7 nm offset spectrum (red), the dipolar bonding mode is red-shifted from 886 to 934 nm (1a to 1b) and the quadrupolar bonding mode is shifted from ~644 to 688 nm (2a to 2b). While the peak intensity of 1b is decreased, that of 2b is significantly enhanced. The enhancement at 2b is due to the dipole−quadrupole interaction that adds a dipolar component into the quadrupole mode. Likewise, the interaction between the dipole of the core/shell and higher order modes of the core/shell introduces dark characteristics of the multipolar modes into 1b and causes its amplitude to decrease.

From a macroscopic perspective, the *f-sum law* can be used to interpret the relative change of the peak amplitude at each plasmon mode.[38,39] In the MNS system, where the number of oscillating electrons is fixed, the convolution of the amplitudes of plasmon resonances with their energy levels remains a constant. This does not, however, indicate that an increase in one peak necessarily causes a decrease in another peak. In the 7 nm offset spectrum, nevertheless, the significant gain at the high-energy quadrupolar mode demands that the dipolar mode be both down shifted in energy and decreased in amplitude.

As the core continuously moves away from the center, more modes that are completely dark in the concentric spectrum start to emerge. In the 8 nm (blue) and 9 nm (green) offset spectra, the emergence of the 3c mode at ~620 nm and the 3d mode at 664 nm is the octupole mode excited with added dipole components. As previously described by the *f-sum law*, the introduction of this new octupole mode results in a decrease in amplitude of the dipole mode at 1c and 1d.

**Surface Charge Distribution and the Polarization Effect.** While hybridization theory qualitatively explains the plasmon resonances of MNS, it does not provide information regarding charge distributions on metal−dielectric interfaces at each resonant mode. Furthermore, it does not describe the relative amplitude of each peak nor the polarization effect on the spectrum. Therefore, we supplement the hybridization analysis with surface charge distributions at the outer and inner layers of the gold shell as well as the surface of the gold core at resonant wavelengths. We examine both spectral properties and charge distributions of the MNS when the incident light is axially polarized with respect to the core offset and when it is transversely polarized.

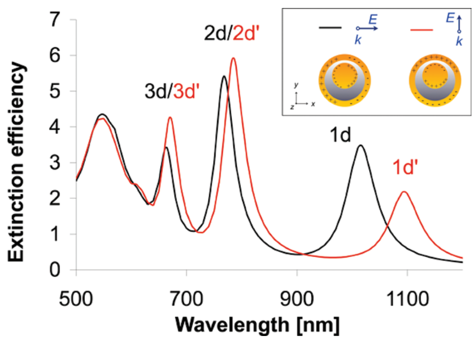

**Figure 5. Extinction spectrum of the R30/40/50 nm MNS in water with 9 nm core offset. Black, incident light is transversely polarized with respect to the offset; red, incident light is axially polarized along the offset.**

Figure 5 shows the extinction spectra of the R30/40/50 nm MNS with a 9 nm offset core at two different polarizations. The dipole, quadrupole, and octupole resonances can be clearly recognized, as described in previous sections. To facilitate the analysis, we denote these modes in the following fashion: dipole modes 1d (transverse) and 1d′ (axial), quadrupole modes 2d (transverse) and 2d′ (axial), and octupole modes 3d (transverse) and 3d′ (axial). One can observe that the two spectra have very similar shapes, indicating minimal impact from polarization. It is worth noting that reported in the literature are three-dimensional nanoparticles whose plasmon resonances do not largely depend on the polarization, such as nanoeggs,[2] and nanoparticles whose spectra bear distinct polarization-dependent characteristics, such as nanocups.[7] We conjecture that, since the offset MNS bear more resemblance to the nanoegg structure, the spectra should be largely polarization independent. One can observe in the axial spectrum slight red shifts in the bonding modes: from 1016 to 1094 nm for the dipole mode, 768 to 785 nm for the quadrupole mode, and 664 to 670 nm for the octupole mode. The red shift implies a stronger interaction between modes with different angular momenta when the light is axially polarized along the small gap between the core and the shell. One can also observe that 1d′ has the largest red shift, whereas 3d′ has the least. This is in agreement with the plasmon hybridization theory shown in Figure 2. In addition, the quadrupole and octupole peaks in the axially polarized spectrum (2d′ and 3d′) appear to be higher than those in the transversely polarized spectrum (2d and 3d), possibly owing to the stronger interaction. In both spectra, the quadrupole peaks (2d and 2d′) appear to be higher than the octupole peaks (3d and 3d′). We will now explore these observations from the surface charge perspective. To calculate the surface charge, Gauss's law was applied to metal−dielectric interfaces. The phase of the solution was swept to find the correct distribution that corresponds to the maximal surface charge density. The extinction spectrum was calculated for the geometry in which the core offset and light polarization were (1) in orthogonal directions (transverse) and (2) along the same direction (axial).

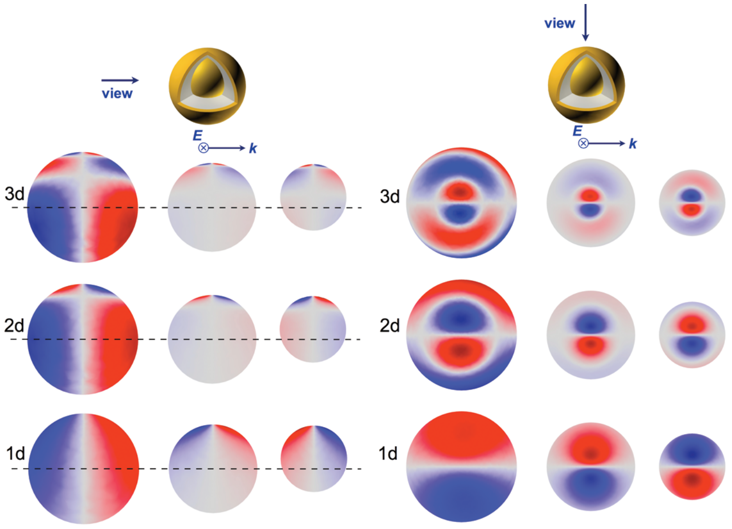

**Figure 6. Side (left) and top (right) views of the surface charge plot of R30/40/50 nm MNS with 9 nm core offset at various hybridized plasmon peaks as the incident light is transversely polarized with respect to the offset. The three columns correspond to the outer gold shell (left), inner gold shell (middle), and inner gold core (right) layers. Red, positive charges; blue, negative charges. Horizontal dashed lines in the left panel mark the center location with respect to the core offset.**

Figure 6 shows the charge distribution on metal–dielectric interfaces for plasmon modes in the transverse spectrum. Side and top views (left and right panel) are provided. The color scales (not shown) on each surface are different for better illustration. Three relevant observations can be made. First, the distributions at 3d, 2d, and 1d resemble octupole, quadrupole, and dipole-like characteristics, respectively. Opposite charges are found on the surface along the *E* field direction in which light is polarized. At each resonance, the charge distribution exhibits an alternating half-ring shape stacked from the top to the bottom of the particle. The pattern is consistent with the predictions we made using plasmon hybridization theory. Second, one observes that the charge polarity is the same along the inner and outer surfaces of the gold shell. This corresponds to the bonding-mode configuration of the shell and indicates that the core is, in fact, interacting with the bonding mode of the shell. Further, the charge polarity on the inner core is oppositely aligned with the outer shell. This also corresponds to the low-energy configuration (bonding) of the MNS and indicates that the plasmon resonance is the low-energy bonding mode from the core–shell interaction. Lastly, the octupole, quadrupole, and dipole distributions appear spatially distorted. The nature of the spatial asymmetry indicates that the hybridized modes are composed of a mixture of modes with different angular momenta. For instance, a perfect quadrupole mode would appear evenly and symmetrically distributed along each quadrant of the spherical surface. The fact that the distribution is skewed, as can be seen in the left panel of Figure 6, is caused by the admixture of a dipole component polarized along the horizontal direction. Since the plasmon resonant peak amplitude is directly proportional to the square of the dipole moment, the quadrupole and octupole modes are enhanced due to the introduction of the dipole interaction and the added dipole components, whereas the dipole mode will have a lower peak owing to the interaction with the multipolar modes and a reduction of the dipole component. Additionally, the degree of asymmetry of the charge distributions for the multipolar modes directly implies the amount of the dipole moment that has been added to the mode. The 2d mode appears to be more asymmetrical in a quadrupole sense than 3d in an octupole sense, suggesting that 2d has a larger dipole moment. This is better revealed in the spectrum in Figure 5, where 2d has a higher amplitude than 3d.

When the incident light is axially polarized, the surface charge distributions exhibit distinct characteristics despite spectral similarities to the transverse polarization case. As shown in the right panel of Figure 7, the octupole and quadrupole distributions appear as whole rings instead of half rings across the entire particle. A larger dipole moment can be recognized in 3d′ and 2d′ as the charge distributions become more dipole-like. Meanwhile, the dipolar distributions in 1d′ also appear distorted, indicating a large multipolar interaction, which attenuates and red shifts the resonant peak. Because the overall degree of asymmetry is larger in Figure 7 than in Figure 6, we conclude that the mode hybridization due to symmetry breaking is stronger when the light is axially polarized. This explains the overall red shift from 1d, 2d, and 3d to

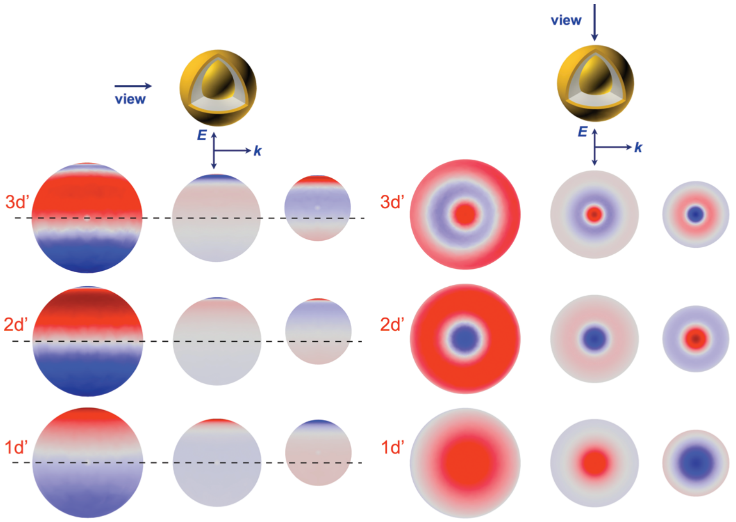

**Figure 7. Side (left) and top (right) views of the surface charge plot of R30/40/50 nm MNS with 9 nm core offset at various hybridized plasmon peaks as the incident light is axially polarized along the offset. The three columns correspond to the outer gold shell (left), inner gold shell (middle), and inner gold core (right) surfaces. Red, positive charges; blue, negative charges. Horizontal dashed lines in the left panel mark the center location with respect to the core offset.**

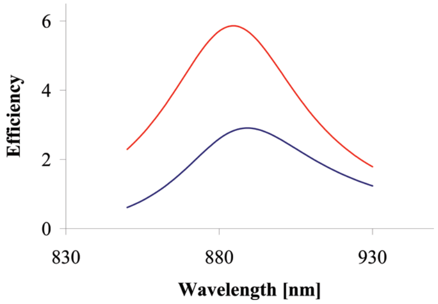

**Figure 8. Mie-based calculation of the absorption (red) and scattering (blue) spectra of the concentric R30/40/50 nm MNS in water near the dipolar resonance.**

1d′, 2d′, and 3d′ and also the higher amplitudes at 2d′, 3d′ *versus* 2d, 3d and the lower amplitude at 1d′ *versus* 1d, as previously described. It is worth noting that, due to the relatively large size of the particle (100 nm), the retardation from the propagating electromagnetic wave comes into play. For instance, in the right panels of Figures 6 and 7, the left−right asymmetry of the charge distribution for the octupole modes reveals this retardation effect. Waves travel in slightly different phase across the particle along the direction of the propagation (indicated by the *k* vector), which yields a slightly asymmetric charge distribution.

When MNS are excited by circularly polarized light (see Supporting Information), the surface charge distribution is a hybrid between the two types described above. The distributions not only appear distorted along the direction of the core offset but also become skewed around the spherical surface. The basic analysis, however, falls in the discussions for the axial and transverse polarizations.

**Absorption Relative to Scattering.** In concentric MNS, an increase of the gold core in an otherwise fixed geometry red shifts the dipolar bonding mode and renders the particle more absorbing than scattering at the plasmon resonance.[10] It is thus of interest to investigate how the absorption of MNS changes with respect to scattering as a function of the core offset. We chose to focus on the dipolar and quadrupolar peaks and compare the absorption and scattering components of overall extinction. It is important to note that the wavelengths of peak values for absorption and scattering are slightly offset from each other. This is manifested not just in the FEM calculations of offset geometries but also in the Mie-based calculations of concentric geometries. The R30/40/50 nm MNS with a 9 nm offset and excited by transversely polarized light has an extinction peak at 886 nm, while the absorption peak is at 885 nm and the scattering peak at 889 nm. The offset is noticeable in Figure 8. The offset value, however, is small enough so the actual scattering and absorption values do not change very much. For consistency, we used the absorption and scattering values at the peak extinction wavelength for the comparisons in Figure 9a,b.

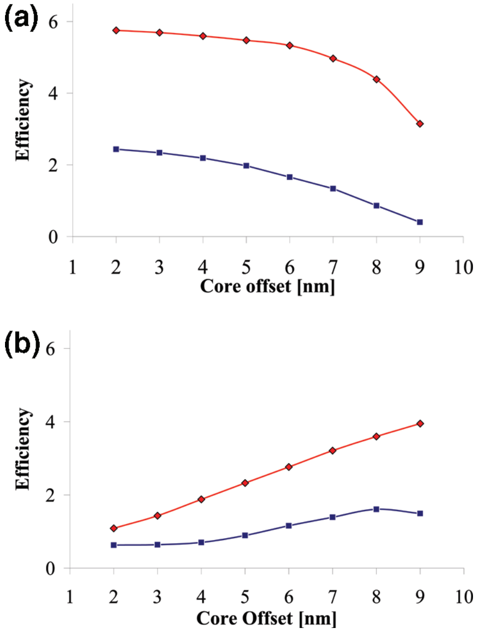

**Figure 9. FEM calculation of the absorption (red) and scattering (blue) efficiency of the R30/40/50 nm MNS with a variable core offset in water (a) at the dipolar resonance and (b) at the quadrupolar resonance. Incident light transversely polarized.**

From Figure 9a, it is clear that both scattering and absorption decrease with increasing offset, and the particle becomes more absorbing relative to scattering at the dipole peak. The scattering component steadily decreases and becomes almost insignificant at large offsets. The quadrupolar peak, shown in Figure 9b, is more complicated as the scattering first increases and then decreases after the 8 nm offset. Although with the decreasing scattering, the overall extinction continues to increase due to the rapidly growing absorption. The stronger absorption of the metal is mainly caused by a larger field confinement within a smaller volume (*i.e.*, the reducing gap between the core and the shell). These general trends are also seen in a R20/30/50 nm MNS (see Supporting Information). Overall, our results show a general trend toward a larger absorption component in the extinction peak as the core offset increases.

## CONCLUSION

In this paper, we used plasmon hybridization theory and demonstrated that an offset of the core in an MNS allows interactions between plasmon resonances of different angular momenta. The mixing of modes allowed by the broken symmetry introduces a dipolar characteristic into higher order multipolar modes and makes them visible in the extinction spectra. We presented qualitatively in a hybridization diagram and quantitatively in the FEM calculations red shifts of the bonding plasmon modes as well as the emergence of the multipolar modes in the offset MNS. While polarization has little effect on the extinction spectra, we demonstrated that different polarizations create distinctly different surface charge distributions. We decomposed the extinction spectra into scattering and absorption and found that MNS tend to have a larger absorption component relative to scattering as the core offset increases. We postulate that offset MNS with larger dimensions will exhibit more interesting multiwavelength plasmon resonances that are associated with even higher order modes. Assuming methods for large-scale synthesis can be developed, such particles may become valuable for multiplexed imaging. The distinctive spectral properties of MNS and their sensitivity to the core offset can also be harnessed to provide proof-of-concept studies for tracking intracellular movements of vessels and capsules that contain gold nanoparticles.

## METHODS

For the FEM simulations, gold properties were obtained from Johnson and Christy.[40] The dielectric constant of silica was set to 2.04, and that for water to 1.33. The surrounding medium of MNS was water. Simulations were performed in COMSOL Multiphysics v3.5a. The simulation space and perfectly matched layer thickness were adjusted until agreement was obtained between the FEM and Mie-based calculations.[10]

For optical spectra, the scattering efficiency was calculated by integrating the normalized *E* field around a far-field transform boundary enclosing the MNS. The absorption efficiency was calculated by summing time-average resistive heating on the inner gold core and other gold shell. For surface charge plots, Gauss's law was applied:

$$\varepsilon_0 \iint \vec{E}\cdot\vec{n}\,dS = \iint \sigma\,dS$$

The gradient operation was realized by implementing the *up* and *down* operators to the metal−dielectric interfaces in COMSOL.

Mie calculations were implemented in an in-house Matlab code written for simulating light scattering from concentric spheres with arbitrary number of layers.[10] The dielectric function of gold was kept the same as the one used in FEM calculations, so were other parameters such as the refractive index of silica and water. The Mie code has been previously validated against literature results.[10,41]

*Acknowledgment.* The authors thank P. Nordlander for insightful discussions on plasmon hybridization, and H. Khakestar for assistance with the COMSOL simulations, both from the Physics Department at Rice University. This work was financially supported by the Welch Foundation Grant C-1598, DoD CDMRP W81XWH-07-1-0428, the Gulf Coast Center for Computational Cancer Research, and the Center for Biological and Environmental Nanotechnology NSF EEC-0118007 and EEC-0647452. Y.H. is supported by the DoE CSGF program. S.J.N. is supported by the NSF IGERT fellowship program. The computational work was supported by the Shared University Grid at Rice University funded by NSF Grant EIA-0216467.

*Supporting Information Available:* Surface charge distributions from circularly polarized light and absorption *vs* scattering for R20/30/50 nm MNS. This material is available free of charge *via* the Internet at http://pubs.acs.org.

## REFERENCES AND NOTES

1. Knight, M. W.; Halas, N. J. Nanoshells to Nanoeggs to Nanocups: Optical Properties of Reduced Symmetry Core−Shell Nanoparticles Beyond the Quasistatic Limit. *New J. Phys.* **2008**, *10*, 105006.
2. Wang, H.; Wu, Y. P.; Lassiter, B.; Nehl, C. L.; Hafner, J. H.; Nordlander, P.; Halas, N. J. Symmetry Breaking in Individual Plasmonic Nanoparticles. *Proc. Natl. Acad. Sci. U.S.A.* **2006**, *103*, 10856–10860.
3. Hao, F.; Nordlander, P.; Sonnefraud, Y.; Van Dorpe, P.; Maier, S. A. Tunability of Subradiant Dipolar and Fano-Type Plasmon Resonances in Metallic Ring/Disk Cavities: Implications for Nanoscale Optical Sensing. *ACS Nano* **2009**, *3*, 643–652.
4. Hao, F.; Sonnefraud, Y.; Van Dorpe, P.; Maier, S. A.; Halas, N. J.; Nordlander, P. Symmetry Breaking in Plasmonic Nanocavities: Subradiant LSPR Sensing and a Tunable Fano Resonance. *Nano Lett.* **2008**, *8*, 3983–3988.
5. Liu, N.; Weiss, T.; Mesch, M.; Langguth, L.; Eigenthaler, U.; Hirscher, M.; Sonnefraud, Y.; Giessen, H. Planar Metamaterial Analogue of Electromagnetically Induced Transparency for Plasmonic Sensing. *Nano Lett.* **2009**, DOI: 10.1021/nl902621d.
6. Liu, N.; Langguth, L.; Weiss, T.; Kastel, J.; Fleischhauer, M.; Pfau, T.; Giessen, H. Plasmonic Analogue of Electromagnetically Induced Transparency at the Drude Damping Limit. *Nat. Mater.* **2009**, *8*, 758–762.
7. Lassiter, J. B.; Knight, M. W.; Mirin, N. A.; Halas, N. J. Reshaping the Plasmonic Properties of an Individual Nanoparticle. *Nano Lett.* **2009**, *9*, 4326–4332.
8. Chen, K.; Liu, Y.; Ameer, G.; Backman, V. Optimal Design of Structured Nanospheres for Ultrasharp Light-Scattering Resonances as Molecular Imaging Multilabels. *J. Biomed. Opt.* **2005**, *10*, 024005.
9. Khlebtsov, B.; Khlebtsov, N. Ultrasharp Light-Scattering Resonances of Structured Nanospheres: Effects of Size-Dependent Dielectric Functions. *J. Biomed. Opt.* **2006**, *11*, 044002.
10. Hu, Y.; Fleming, R. C.; Drezek, R. A. Optical Properties of Gold−Silica−Gold Multilayer Nanoshells. *Opt. Express* **2008**, *16*, 19579–19591.
11. Wu, D. J.; Liu, X. J. Tunable Near-Infrared Optical Properties of Three-Layered Gold−Silica−Gold Nanoparticles. *Appl. Phys. B* **2009**, *97*, 193–197.
12. Xia, X. H.; Liu, Y.; Backman, V.; Ameer, G. A. Engineering Sub-100 nm Multi-layer Nanoshells. *Nanotechnology* **2006**, *17*, 5435–5440.
13. Graf, C.; Vossen, D. L. J.; Imhof, A.; van Blaaderen, A. A General Method to Coat Colloidal Particles with Silica. *Langmuir* **2003**, *19*, 6693–6700.
14. Kobayashi, Y.; Katakami, H.; Mine, E.; Nagao, D.; Konno, M.; Liz-Marzan, L. M. Silica Coating of Silver Nanoparticles Using a Modified Stöber Method. *J. Colloid Interface Sci.* **2005**, *283*, 392–396.
15. Lee, H. B.; Yoo, Y. M.; Han, Y. H. Characteristic Optical Properties and Synthesis of Gold−Silica Core−Shell Colloids. *Scripta Mater.* **2006**, *55*, 1127–1129.
16. LizMarzan, L. M.; Giersig, M.; Mulvaney, P. Synthesis of Nanosized Gold−Silica Core−Shell Particles. *Langmuir* **1996**, *12*, 4329–4335.
17. Westcott, S. L.; Oldenburg, S. J.; Lee, T. R.; Halas, N. J. Formation and Adsorption of Clusters of Gold Nanoparticles onto Functionalized Silica Nanoparticle Surfaces. *Langmuir* **1998**, *14*, 5396–5401.
18. Oldenburg, S. J.; Averitt, R. D.; Westcott, S. L.; Halas, N. J. Nanoengineering of Optical Resonances. *Chem. Phys. Lett.* **1998**, *288*, 243–247.
19. Prodan, E.; Radloff, C.; Halas, N. J.; Nordlander, P. A Hybridization Model for the Plasmon Response of Complex Nanostructures. *Science* **2003**, *302*, 419–422.
20. Radloff, C.; Halas, N. J. Plasmonic Properties of Concentric Nanoshells. *Nano Lett.* **2004**, *4*, 1323–1327.
21. Sealy, C. Nanorice Combines Best of Both Worlds. *Nano Today* **2006**, *1*, 13.

22. Srivastava, D.; Lee, I. Nanorice and Nanospears from Polymer Nanospheres. *Adv. Mater.* **2006**, *18*, 2471–2475.
23. Wang, H.; Brandl, D. W.; Le, F.; Nordlander, P.; Halas, N. J. Nanorice: A Hybrid Plasmonic Nanostructure. *Nano Lett.* **2006**, *6*, 827–832.
24. Wiley, B. J.; Chen, Y. C.; McLellan, J. M.; Xiong, Y. J.; Li, Z. Y.; Ginger, D.; Xia, Y. N. Synthesis and Optical Properties of Silver Nanobars and Nanorice. *Nano Lett.* **2007**, *7*, 1032–1036.
25. Brandl, D. W.; Mirin, N. A.; Nordlander, P. Plasmon Modes of Nanosphere Trimers and Quadrumers. *J. Phys. Chem. B* **2006**, *110*, 12302–12310.
26. Jain, P. K.; El-Sayed, M. A. Surface Plasmon Coupling and Its Universal Size Scaling in Metal Nanostructures of Complex Geometry: Elongated Particle Pairs and Nanosphere Trimers. *J. Phys. Chem. C* **2008**, *112*, 4954–4960.
27. Berciaud, S.; Cognet, L.; Tamarat, P.; Lounis, B. Observation of Intrinsic Size Effects in the Optical Response of Individual Gold Nanoparticles. *Nano Lett.* **2005**, *5*, 515–518.
28. Kreibig, U.; Vollmer, M. *Optical Properties of Metal Clusters*; Springer: New York, 1995.
29. Moroz, A. Electron Mean Free Path in a Spherical Shell Geometry. *J. Phys. Chem. C* **2008**, *112*, 10641–10652.
30. Nehl, C. L.; Grady, N. K.; Goodrich, G. P.; Tam, F.; Halas, N. J.; Hafner, J. H. Scattering Spectra of Single Gold Nanoshells. *Nano Lett.* **2004**, *4*, 2355–2359.
31. Wu, Y. P.; Nordlander, P. Plasmon Hybridization in Nanoshells with a Nonconcentric Core. *J. Chem. Phys.* **2006**, *125*, 124708.
32. Lassiter, J. B.; Aizpurua, J.; Hernandez, L. I.; Brandl, D. W.; Romero, I.; Lal, S.; Hafner, J. H.; Nordlander, P.; Halas, N. J. Close Encounters between Two Nanoshells. *Nano Lett.* **2008**, *8*, 1212–1218.
33. Nordlander, P.; Oubre, C.; Prodan, E.; Li, K.; Stockman, M. I. Plasmon Hybridization in Nanoparticle Dimers. *Nano Lett.* **2004**, *4*, 899–903.
34. Hao, F.; Nordlander, P. Efficient Dielectric Function for FDTD Simulation of the Optical Properties of Silver and Gold Nanoparticles. *Chem. Phys. Lett.* **2007**, *446*, 115–118.
35. Perner, M.; Bost, P.; Lemmer, U.; vonPlessen, G.; Feldmann, J.; Becker, U.; Mennig, M.; Schmitt, M.; Schmidt, H. Optically Induced Damping of the Surface Plasmon Resonance in Gold Colloids. *Phys. Rev. Lett.* **1997**, *78*, 2192–2195.
36. Pinchuk, A.; Kreibig, U.; Hilger, A. Optical Properties of Metallic Nanoparticles: Influence of Interface Effects and Interband Transitions. *Surf. Sci.* **2004**, *557*, 269–280.
37. Khoury, C. G.; Norton, S. J.; Vo-Dinh, T. Plasmonics of 3-D Nanoshell Dimers Using Multipole Expansion and Finite Element Method. *ACS Nano* **2009**, *3*, 2776–2788.
38. Nozieres, P.; Pines, D. Electron Interaction in Solids—General Formulation. *Phys. Rev.* **1958**, *109*, 741–761.
39. Mahan, G. D. *Many-Particle Physics*; Springer: New York, 1990.
40. Johnson, P. B.; Christy, R. W. Optical Constants of the Noble Metals. *Phys. Rev. B* **1972**, *6*, 4370–4379.
41. Bohren, C. F.; Huffman, D. R. *Absorption and Scattering of Light by Small Particles*; Wiley-VCH: Weinheim, Germany, 2004.

Sun, J., Fu, F., Zhu, M-Q., Bickford, L., Post, E., and Drezek, R. "PbS quantum dots for near-infrared fluorescence imaging." OSA 2008 Frontiers in Optics (FiO)/Laser Science XXIV Conference. Rochester, NY. October 19-23, 2008.

# PbS Quantum Dots for Near-Infrared Fluorescence Imaging

**Jiantang Sun**[1, 3], **Kun Fu**[2, 3], **Ming-Qiang Zhu**[1], **Lissett Bickford**[1],
**Eric Post**[4], **and Rebekah Drezek**[1, 2, *]
*[1]Departments of Bioengineering, [2]Electrical and Computer Engineering and [3]Rice Quantum Institute,*
*Rice University, 6100 Main Street, Houston, TX 77005, USA*
*[4]Biomedical Engineering,*
*Louisiana Tech University, 818 Nelson Avenue, Ruston, LA 71270, USA*
*Corresponding author e-mail address: drezek@rice.edu*

**Abstract:** In this phantom-based study, we assessed the imaging potential of lead sulfide (PbS) near-infrared quantum dots (QDs) as novel contrast agents for deep tissue fluorescence imaging applications.

**OCIS codes:** (170.0170) Medical optics and biotechnology

## 1 Introduction

Recently, the development of various near-infrared (NIR) (700-1200 nm) fluorescence contrast agents has greatly promoted the application of NIR fluorescence biomedical imaging techniques. Compared to contrast agents that are fluorescent in the visible spectral range, PbS NIR QDs have their own unique properties for *in vivo* deep tissue fluorescence imaging applications. It is believed that the relatively small size of PbS QDs (~4 to 5 nm) [1] will facilitate body clearance of these particles during clinical trials. Additionally, the emission peak of PbS QDs can be systematically tuned in the NIR spectral range, and the corresponding excitation spectrum of these QDs spans the range from visible to NIR [1, 2]. Thus, both the relatively red-shifted emission peak and wide excitation band provide flexibility in the choice of proper working wavelength regions, which will, in turn, avoid most of the influences from tissue autofluorescence background [1, 3].

## 2 Method and Results

A previous publication has shown the possibility of using bioconjugated PbS QDs as NIR contrast agents for specifically-targeted molecular imaging applications [3]. As a step moving towards *in vivo* tissue fluorescence screening using PbS NIR QDs and fluorescence imaging system (FIS), a tissue phantom study was carried out to identify and evaluate the imaging potentials of these NIR nanocrystals and to acquire a basic understanding of the contrast agent concentrations in relation to obtaining clear and acceptable images. For the lowest tested concentration of 200 nM, PbS-QD-filled tumor models were imageable at a tissue phantom depth of 15 mm. In addition, comparison results indicated that tumor models with photons emitted in the NIR region can be imaged with less distortion than those with photons emitted in the visible spectrum. Due to the decreased scattering effect of the tissue phantoms in the NIR spectral range, well-defined margins of the PbS QD-filled tumor model images were obtained (Fig.1).

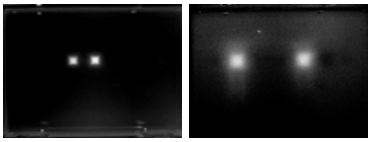

Fig.1. Florescence images of NIR QDs (left) and red QDs (right) at phantom thickness of 1.75mm

## 3 Conclusions

In conclusion, a phantom study in which PbS QDs are used as contrast agents for fluorescence imaging applications is reported. The experiments show that lead sulfide NIR quantum dots possess enhanced deep tissue fluorescence imaging properties. Moreover, the greatly improved tumor margin confinement images obtained from PbS QD contrast agents are indicative of their promising surgical applications for future *in vivo* tumor detection.

## 4 Acknowledgements

The authors thank financial support for this work by the Department of Defense Congressionally Directed Breast Cancer Research Program Era of Hope Scholar Award, and the Gulf Coast Center for Computational Cancer Research.

## 5 References

[1] M. Zhu, E. Chang, J. Sun and R. Drezek, "Surface modification and functionalization of semiconductor quantum dots through reactive coating of silanes in toluene," J Mater Chem **17**: 800-805 (2007).

[2] M. Hines and G. Scholes, "Colloidal PbS nanocrystals with size-tunable near-infrared emission: observation of post-synthesis self-narrowing of the particle size distribution," Adv Mater **15**:1844-1849 (2003).

[3] J. Sun, M. Zhu, K. Fu, N. Lewinski and R. Drezek, "Lead sulfide near-infrared quantum dot bioconjugates for targeted molecular imaging," Int J Nanomedicine **2**(2): 235-240 (2007).

Drezek, R. “Nanotechnology-Enabled Optical Molecular Imaging of Cancer.“ Department of Defense Breast Cancer Research Program Era of Hope Conference. Baltimore, MD. June 2008.

# NANOTECHNOLOGY-ENABLED OPTICAL MOLECULAR IMAGING OF CANCER

**Rebekah Drezek**
Rice University

In this abstract we describe progress during the first year of an Era of Hope Scholar Award focused on the development of miniaturized photonics-based imaging technologies and complementary nanoscale molecular-targeted imaging agents that together have the capability to provide a significant new approach to molecular imaging of breast cancer. While there have been numerous prior published studies using endogenous reflectance and fluorescence spectroscopy for a variety of breast cancer screening, diagnostic, and monitoring applications, there have been far fewer attempts to develop microendoscopes that enable direct visualization of subcellular morphology and no attempts to date to develop a system for simultaneous high-resolution imaging and spectroscopy for breast cancer applications, which is one of the aims of our project. Our poster will provide proof-of-principle data demonstrating the capability for imaging fresh, intact unstained tissue with subcellular resolution using our first generation <1 mm diameter optical fiber probe in which each micron diameter fiber is used as a resolution element. Image processing approaches to remove fiber pixilation effects will also be described. In addition, we will discuss robust new synthesis and bioconjugation approaches for development of NIR scattering and emissive nanomaterials designed to be used in combination with our optical imaging systems. It is our ultiamte goal to develop a simple, inexpensive, needle-compatible, fiber-integrated spectroscopy and imaging system capable of detecting both endogenous biochemical and morphological optical signals and exogenous optical signals created via bright nanoengineered molecular imaging agents. While significant effort has been devoted by the nanotechnology community to developing nanoparticles with progressively more favorable properties for imaging through optimizing “brightness” measured as scatter, absorption, or luminescence, it is our belief that in many cases, optical system design parameters and nanoparticle structure must be simultaneously optimized to achieve optimal imaging results. This is particularly true for the shaped gold nanoparticles being used in this Era of Hope project that have complex angular scattering patterns. Thus, in addition to initial imaging results using the system built in year 1 of our project, we will present additional data demonstrating the dramatic influence optical imaging geometry can have on sensitivity to targeted nanoparticles in tissue. By optimizing geometry, it is possible to obtain equivalent optical contrast using significantly lower nanoparticle dose potentially increasing the clinical viability of nanoparticle-based optical molecular imaging strategies.

---

*This work was supported by the U.S. Army Medical Research and Materiel Command under W81XWH-07-1-0428.*

Bickford, L., Chang, J., Fu, K., Sun, J., Hu, Y., Yu, T.K., Drezek, R. Immunotargeted Nanoshells as Rapid Diagnostic Imaging Agents. Biomedical Optics, St. Petersburg, FL. March 2008.

# Immunotargeted Nanoparticles as Rapid Diagnostic Imaging Agents

**Lissett R. Bickford[a], Joseph Chang[a], Kun Fu[a,b], Ying Hu[a], Tse-Kuan Yu[b], and Rebekah A. Drezek[a,c]**
[a]*Department of Bioengineering, Rice University, 6100 Main. St, MS-142, Houston, TX 77005, USA*
[b]*Department of Radiation Oncology, MD Anderson Cancer Center, Houston, TX 77030, USA*
[c]*Department of Electrical and Computer Engineering, Rice University, Houston, TX 77005, USA*
*Author e-mail address:LR2@rice.edu; Phone: 713.348.5020; Fax: 713.348.5877*

**Abstract:** We demonstrate the potential of using nanoparticles for point of care cancer diagnostic imaging applications by achieving optical contrast between normal and cancerous epithelial cells at minimal incubation times through optimization of nanoshell-cell conjugations.

**OCIS codes**: 300.1030; 160.4236; 170.0170

## Introduction

Point of care diagnostic testing has the potential to assist clinicians by providing user-friendly, cost effective, and rapid results at the patient bedside. Several technologies that demonstrate promise for point of care testing are associated with biological fluids and detection of DNA or protein amplification through the use of microarrays or lab-on-a-chip devices [1,2]. With the expansion of nanotechnology-driven research, opportunities for performing multifaceted diagnostic tests outside of the hospital laboratory is likely to increase. Several nanoparticles have been explored for their potential applications in cancer diagnostic molecular imaging at the single-cell level. These nanoparticles, including nanoshells [3,4], gold colloid [5], quantum dots [6], carbon dots [7], and nanorods [8], can be divided into those that are targeted to cell surface receptors and those that are internalized. For nanoparticles that are internalized, such as quantum dots, the length of incubation time used to achieve contrast has been as high as 4 hours [6]. Other nanoparticles, such as nanoshells, that have targeted cell surface receptors have had incubation times ranging from 30 minutes to 60 minutes [3,4]. Thus far in the literature, few if any, publications have focused on minimizing the time needed to successfully achieve desirable contrast of cancer cells incubated with nanoparticles. In order to realistically use these nanoparticles as a point of care tool for the detection of pathologies, such as cancer, at the single-cell level, the time needed to achieve optical contrast must be dramatically reduced. We demonstrate the use of gold nanoshells targeted to anti-HER2 antibodies to achieve optical contrast in HER2-overexpressing breast cancer cells within ten minutes.

## Preparation of Nanoshell Bioconjugates to Cell Suspensions

Nanoshells, which are silica nanoparticles covered with a thin gold shell, were developed and bioconjugated using previously reported procedures [9]. For the nanoshells used in this research, the radius of the silica core was 127 nm, the total nanoshell radius was 146 nm, and the surface plasmon resonance occurred at 778 nm (Figure 1). Nanoshells were conjugated to anti-HER2 antibodies for cell targeting. Two cell types were analyzed for this study: HER2-overexpressing breast cancer cells (SK-BR-3) and normal mammary epithelial cells (MCF10A). The cells were maintained at 37ºC and 5% $CO_2$ and were grown in $75cm^2$ flasks until confluent. Once cells were confluent, they were rinsed once with phosphate buffered saline and then incubated with trypsin-EDTA for 5 minutes at 37ºC in order to detach the cells from the substrate. Following trypsinization and neutralization with media, cell counting was performed and the cells were then divided into four conical tubes per cell line. The cells were then centrifuged at 110g for 3 minutes. For each cell line, three of the cell pellets were resuspended in the bioconjugate-nanoshell solution and one was resuspended in an equal amount of PBS as a control. For incubation of the nanoshell-cell solution, the cocktails were incubated in a hybridization chamber (VWR) at 37ºC for either 10 minutes, 30 minutes, or 60 minutes. After incubation, the cocktails were centrifuged at 110g for 3 minutes and the unbound nanoshells were collected. Cells were rinsed once with PBS and the unbound nanoshells were again collected. A mixture of 10% glucose in PBS was added to the cell pellet to prevent cell death prior to imaging. The unbound nanoshell solution was then centrifuged at 250g for 20 minutes and the nanoshell pellet was resuspended in water for determination of the unbound concentration (see next section for method). Based on the original known concentration of nanoshells added to a predetermined number of cells, the number of nanoshells bound to the cancer cells was able to be calculated.

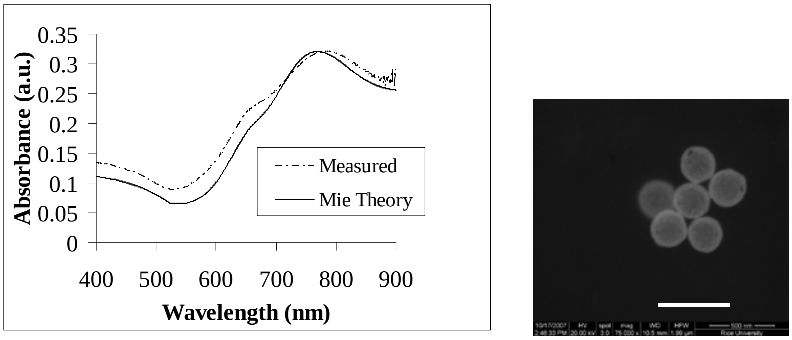

Fig. 1. (L) Measured spectra of nanoshells (size R127/146) as compared with Mie theory. (R) SEM image of nanoshells. (The scale bar is approximately 500 nm.)

## Correlation Between Absorbance and Nanoshell Concentration

In order to obtain approximations for the number of nanoshells bound to cancer cells at different time points, we employed the use of UV-Visible spectroscopy. Spectroscopy can be used following the principles of the Beer-Lambert law demonstrating that the absorbance of particles in solution is directly related to the concentration of those particles in that solution. Nanoshells of known concentration (2E9 particles/mL), based on Beer-Lambert calculations, were varied by serial dilutions and the corresponding absorbance was measured. A linear regression analysis was performed and the results are shown in Figure 2. Based on the $R^2$ value of 0.99, we conclude that the absorbance accurately predicts the concentration of an unknown suspension of nanoparticles.

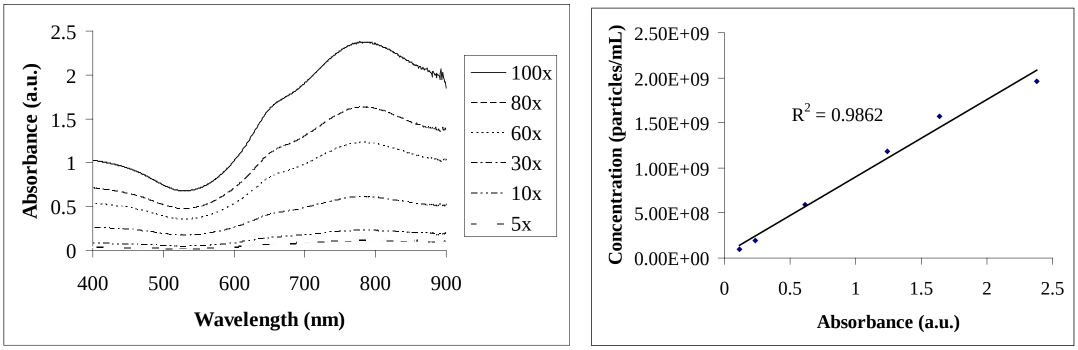

Fig. 2.(L) Spectra of serial dilutions of known nanoshell concentrations in suspension.(R) Linear regression analysis of known concentrations to corresponding peak absorbance values.

## Results / Discussion

Images of the SK-BR-3 cancer cells and MCF10A normal cells for different incubation time points with nanoshells were taken using a Zeiss Axioskop 2 darkfield microscope. Darkfield microscopy is an imaging modality that is dependent on light scattering to achieve contrast. As can be seen in Figure 3, the MCF10A cells incubated with the bioconjugate-nanoshell solution for three different incubation time points show little enhanced scattering when compared to both normal and cancer cell controls. However, for the SK-BR-3 cancer cells, enhanced contrast is perceivable at an incubation time point as low as ten minutes. The number of HER2 receptors on SK-BR-3 and normal cells has been documented as being on the order of $8x10^5$ and $1x10^4$ receptors per cell, respectively [10,11]. The targeted bioconjugated nanoshells reveal binding to the cell surface receptors on both cell types; however, due to the increased number of receptors on the cancer cells, the contrast achievable is considerably greater in the HER2-

overexpressing cells. In order to ascertain the differences in the number of bound nanoshells for each time point, preliminary data on the number of nanoshells bound per cell are reported in Table 1 for SK-BR-3 cancer cells. The collection of additional data for this study is in progress. The binding concentration of nanoshells per cancer cell at 10 minutes is 86% of the binding concentration at 60 minutes. Based on imaging results, this difference in concentration does not appear to drastically affect or reduce contrast. Therefore, this research demonstrates the ability to optimize nanoshell-cell conjugations at minimal incubation times for potential applications in point of care cancer diagnostic imaging.

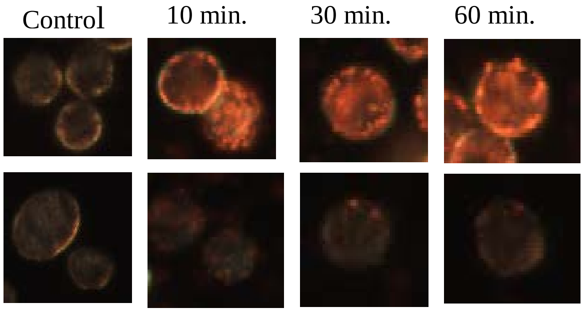

Fig. 3. Darkfield images of SKBR3 cells (top) and MCF10A cells (bottom) at different incubation time points with bioconjugated nanoshells. Images taken at 20x.

Table 1. Preliminary Binding Concentrations of Nanoshells per SKBR3 Cancer Cell

| Incubation Time (min) | No. of Nanoshells |
|---|---|
| 10 | 1873 |
| 30 | 1877 |
| 60 | 2175 |

## References

[1] Zajac A, Song D, Qian W, Zhukov T, “Protein microarrays and quantum dot probes for early cancer detection,” Colloids and Surfaces B:Biointerfaces 58:309-314 (2007).

[2] Weigum SE, Floriano PN, Christodoulides N, McDevitt JT, “Cell-based sensor for analysis of EGFR biomarker expression in oral cancer,” Lab Chip 7(8):995-1003 (2007).

[3] Loo C, Lowery A, Halas N, West J, Drezek R, “Immunotargeted Nanoshells for Integrated Cancer Imaging and Therapy,” Nano Letters 5(4): 709-711 (2005).

[4] Lowery A, Gobin A, et al., “Immunonanoshells for targeted photothermal ablation of tumor cells,” Intl Journal of Nanomedicine 1:149-154 (2006).

[5] Sokolov K, Follen M, Aaron J, Pavlova I, Malpica A, Lotan R, Richartz-Kortum R, “Real-Time Vital Optical Imaging of Precancer Using Anti-Epidermal Growth Factor Receptor Antibodies Conjugated to Gold Nanoparticles,” Cancer Res. 63: 1999-2004 (2003).

[6] Sun J, Zhu MQ, Fu K, Lewinski N, Drezek R, “Lead sulfide near-infrared quantum dot bioconjugates for targeted molecular imaging,” Int J Nanomedicine 2(2):235-40 (2007).

[7] Cao L, et al. “Carbon Dots for Mulitphoton Bioimaging,” JACS 129:11318-11319 (2007).

[8] Huang X, El-Sayed IH, Qian W, El-Sayed MA, “Cancer Cell Imaging and Photothermal Therapy in the Near-Infrared Region by Using Gold Nanorods,” JACS128:2115-2120 (2006).

[9] Hirsch L, Jackson J, “A whole blood immunoassay using gold nanoshells,” Analytical Chemistry 75(10):2377-81 (2003).

[10] Hayes DF, Walker TM, et. al., “Monitoring expression of HER-2 on circulating epithelial cells in patients with advanced breast cancer,” Int J Oncol 21(5):1111-1117 (2002).

[11] Kornilova ES, Taverna D, et al., “Surface expression of erbB-2 protein is post-transcriptionally regulated in mammary epithelial cells by epidermal growth factor and by culture density,” Oncogene 7(3):511-9 (1992).

Bickford, L. and Drezek, R. Gold Nanoshells as Potential Real-Time Intraoperative Molecular Probes for HER2/NEU Overexpression Using Near-Infrared Reflectance Confocal Microscopy. Annual Houston Conference on Biomedical Engineering Research. Houston, TX. March 2009

# GOLD NANOSHELLS AS POTENTIAL REAL-TIME INTRAOPERATIVE MOLECULAR PROBES FOR HER2/NEU OVEREXPRESSION USING NEAR-INFRARED REFLECTANCE CONFOCAL MICROSCOPY

**Lissett R. Bickford** and Rebekah A. Drezek
Department of Bioengineering; Rice University, Houston, TX 77005

6100 Main St., MS-142, Houston, TX 77005; Phone: (713)348-5020; Fax: (713) 348-5877; Email: LR2@rice.edu

## Introduction

Due to residual cancer cells being left in many patients that undergo breast conservation therapy, as many as 40% of patients have experienced local cancer recurrence near the site of the original tumor.[1] Currently, breast cancer tumor margins are examined in a pathology lab either while the patient is anesthetized or after the surgical procedure has been terminated. These methods are expensive, inconvenient, and lengthy. We are developing a nano-biophotonics system to facilitate intraoperative tumor margin assessment at the cellular level. By combining bioconjugated silica-based gold nanoshells, which scatter light in the near-infrared, with a FDA approved reflectance confocal microscope (RCM), we demonstrate the ability to visualize HER-overexpressing cancerous cells and resected human tissue preferentially over normal cells and tissue.

## Materials and Methods

### *Nanoshell Synthesis and Bioconjugation*

Nanoshells were manufactured and bioconjugated to anti-HER2 antibodies as previously described.[2,3] The final size of the silica cores was 276 nm (diameter) with a gold shell thickness of 17 nm. The peak extinction of the nanoshells was 840 nm. The gold nanoshells were conjugated to anti-HER2 antibodies (LabVision) using a heterobifunctional linker as detailed elsewhere.[2,3] This biomarker was selected due to its association with very aggressive breast cancer. To prevent non-specific interactions, PEG-thiol (Nektar) was also added to the nanoshells.

### *In Vitro Cell Studies*

HER2-overexpressing breast cancer cells, HCC1419, and normal breast cells, MCF10A, were incubated with either PBS alone or gold nanoshells targeted to IgG or to anti-HER2 antibodies for 15 minutes at 37ºC. Unbound particles were removed post-incubation through centrifugation. Cells were resuspended in the appropriate growth media and aliquoted onto a glass slide fitted with a 0.12 mm deep spacer (Invitrogen). Samples were coverslipped prior to imaging.

### *Ex Vivo Human Tissue Studies*

Human tissue was obtained through an approved IRB protocol. Normal and HER2-overexpressing cancerous tissue was divided into two halves: one half was incubated with PBS and the other half was incubated with anti-HER2-targeted nanoshells. Incubation occurred at room temperature for 45 minutes. Samples were rinsed with PBS then placed on a glass slide for image acquisition.

## Results and Discussion

A Lucid VivaScope RCM was used to image both cells and tissues. Images of cell studies showed that anti-HER2 nanoshells resulted in enhanced contrast of HER2-overexpressing cells (Fig 1).

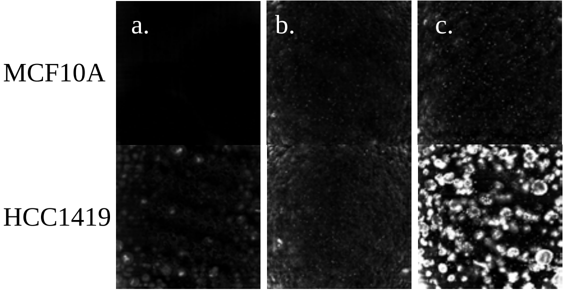

Fig 1. MCF10A and HCC1419 cell lines incubated with (a.) PBS only, (b.) nanoshells conjugated to IgG or (c.) nanoshells conjugated to anti-HER2 antibodies.

For the *ex-vivo* tissue experiment, anti-HER2 nanoshells were also seen to preferentially bind to and enhance contrast of HER2-overexpressing tissue over normal tissue (Fig 2).

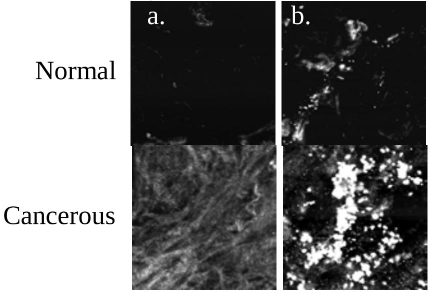

Fig 2. Excised human tissue incubated with (a.) PBS only or (b.) HER2-targeted nanoshells. All images were taken of the tissue surface under 0.7 mW of power.

## Conclusions

These results suggest that anti-HER2-nanoshells used in tandem with a RCM may potentially be applied for discerning HER2-overexpressing cancerous tissue from normal tissue in real time.

## References

1. Fisher, et al. *NEJM*, 347, 16, 2002.
2. Loo, et al. *Tech. Cancer Res. Treat.,* 3, 1, 2004.
3. Lowery, et al. *Int. J. of Nanomed*. 1, 2 2006.

Hu, Y., and Drezek, R. Angular scatter patterns from multi-layered gold nanoshells. Materials Research Society Spring Annual National Meeting. San Francisco, CA. April 2009.

MRS09: Section – Computational nanoscience – how to exploit synergy between predictive simulation and experiment

# A Mie-based simulation study on spectral and angular radiation properties of gold-silica-gold multilayer nanoshells

**Abstract** While gold nanoparticles feature a small size factor and are favored in biomedical imaging studies, their plasmonic resonant wavelength cannot be tuned into the near-infrared (NIR) bioimaging window. Silica-gold core-shell conventional nanoshells (CNS) offer NIR plasmonic resonance at small shell thickness-to-core radius ratios. However, coating on sub-100 nm silica cores with an ultra-thin gold layer is difficult to achieve. This study investigates whether extra tunability can be obtained by introducing an additional gold core in the silica layer.

Xia *et al*. were the first to report the synthesis of ~50 nm multilayer nanoshells (MNS) that may exhibit NIR extinction peaks [*Nanotechnology,* **17** (2006) 5435–5440]. Chen *et al*. simulated the ultrasharp resonant peaks of similar MNS with an overall diameter of 10 nm [*J. Biomed. Opt.*, **10**(2) 024005]. The goal of this paper is to examine the spectral and angular scattering properties of gold-silica-gold MNS in the size region where successful particle syntheses have been reported and can be achieved based on currently available protocols.

A Mie-based computation code was developed to calculate light scattering from concentric spheres. MNS were found to bear an extra degree of tunability from the inner gold core. This optical tunability can be understood as an interaction between the conventional nanoshell bonding mode and the gold core sphere mode. The thickness of the intermediate silica layer determines the degree of interplay between the two modes. An increase in the inner gold core radius on an otherwise fixed geometry decreases the intermediate silica layer thickness and increases the plasmon interaction, thus red shifts the extinction peak. Furthermore, the amount of wavelength shift with respect to the resonant wavelength of an equivalent CNS without the gold core was found independent of the overall particle size and to follow a universal scaling principle. The extinction spectra of MNS were found sensitive to the surrounding medium, with the extinction peaks both red shift and increase in magnitude as the dielectric constant of the medium increases. MNS with a larger gold core, a thinner silica layer, or a thinner outer gold shell were found more absorbing than scattering. Both scattering intensity and angular radiation pattern of MNS differ from CNS due to spectral modulation from the inner core. Angular radiation plots suggest that some MNS may provide more backscattering at wavelengths where CNS predominantly forward scatter.

Bickford, L., Yu, K., and Drezek, R. Nanotechnology-Enabled Optical Molecular Imaging of Breast Cancer, Baylor College of Medicine Translational Research Conference. September 2009.

# Abstract:
# Nanotechnology-Enabled Optical Molecular Imaging of Breast Cancer

*Lissett R. Bickford*[1], *Tse-Kuan Yu*[2] *and Rebekah A. Drezek*[1,3]

[1] Department of Bioengineering; Rice University, Houston, TX 77005

[2] Department of Radiation Oncology; MD Anderson Cancer Center, Houston, TX 77030

[3] Department of Electrical and Computer Engineering; Rice University, Houston, TX 77005

Currently, breast cancer tumor margins are examined in a pathology suite either while the patient is anesthetized (such as in tertiary care centers) or once the surgical procedure has been terminated (such as in community hospitals). Such methodologies are not ideal due to their cost, time to achieve diagnosis, and inconvenience for both surgeons and patients alike. In order to improve upon the current standard of tumor margin assessment in the operating room, which occurs only grossly upon tissue resection, we propose the use of silica-based gold nanoshells in tandem with near-infrared reflectance confocal microscopy (RCM). By collecting backscattered light at different depths from the tissue of interest, where a specialized pinhole is used to eliminate signals from the out-of-focus planes, RCM can be used to image whole tissue specimens without the need for physical sectioning. Gold nanoshells, which have a silica core and a thin, gold outer shell, are beneficial nanoparticles for a variety of biomedical applications due to their biocompatibility and tunable optical properties. Furthermore, they can readily be conjugated to antibodies and, subsequently, used to enhance contrast of specific biomarkers associated with disease progression. In previous studies, we have demonstrated that targeted gold nanoshells can be used to increase contrast of cancer cells that overexpress HER2/neu receptors within only 5 minutes of processing time. In this study, we validate the use of gold nanoshells as effective imaging probes for RCM by evaluating contrast enhancement of three different HER2-overexpressing cells. Additionally, we demonstrate the ability to detect HER2-overexpressing cells in resected tissue specimens from human patients.

**Proceedings of ASME 2010 First Global Congress on NanoEngineering for Medicine and Biology**
**NEMB2010**
**February 7-10, 2010 Houston, TX, USA**

## NEMB2010-13180

# CANCER IMAGING AND THERMAL THERAPY FACILITATED BY NANOPARTICLES AND MULTIPHOTON MICROSCOPY

**Emily S. Day, Lissett R. Bickford, Rebekah A. Drezek, and Jennifer L. West**
Department of Bioengineering, Rice University, Houston, TX, USA

## INTRODUCTION

Despite use of currently available technologies, cancer remains one of the leading causes of death worldwide. Gold-based nanoparticles that strongly absorb near-infrared light, such as nanoshells and nanorods, have shown potential as both diagnostic and therapeutic agents for cancer management (1-3). In this work we explored the use of gold-gold sulfide nanoparticles (mean diameter = 37 nm) with peak plasmon resonance at 800 nm for combined imaging and therapy of breast cancer. Upon excitation with a pulsed laser, these particles exhibit two-photon induced luminescence which may be used to image cancer cells. In addition, by increasing the power output of the laser, cancer cells can be thermally ablated as the gold-gold sulfide nanoparticles convert the light energy into heat.

## MATERIALS AND METHODS

### *Gold-Gold Sulfide Nanoparticle Synthesis*

Gold-gold sulfide nanoparticles were synthesized according to Averitt, *et al.* (4). Solutions of 2 mM $HAuCl_4$ (Alfa Aesar) and 1 mM $Na_2S_2O_3$ (Aldrich) were prepared in milli-Q water and aged two days at room temperature. These solutions were then mixed at volumetric ratios ranging from 1:1 to 1:2 ($Na_2S_2O_3$:$HAuCl_4$). This resulted in a mixture of gold-gold sulfide nanoparticles and small gold colloid. The ratio that produced gold-gold sulfide nanoparticles resonant at 800 nm and with the least colloid contamination was scaled up linearly. To eliminate excess gold colloid, a multi-step centrifugation process was carried out.

### *Antibody Conjugation*

To facilitate cell-specific targeting, antibody can be attached to gold-gold sulfide nanoparticles through a 2000 Da hetero-bifunctional poly(ethylene glycol) (PEG) linker (Creative PEGWorks) with an N-hydroxysuccinimide terminus for antibody coupling and a disulfide terminus for attachment to gold. First the preferred antibodies are attached to the PEG linkers, and then the antibody-PEG conjugates are reacted with the nanoparticles for 1 hour at 4ºC. To help stabilize the particles, 5000 Da mPEG-SH (Laysan Bio, Inc.) is added to empty spaces on the gold surface following antibody attachment. For these studies, three nanoparticle formulations were prepared. Targeted gold-gold sulfide nanoparticles were coated with anti-HER2 antibodies (NeoMarkers) and mPEG-SH. Control nanoparticles were coated with mPEG-SH either with or without anti-IgG antibodies (Sigma).

### *In Vitro Study*

SK-BR-3 breast carcinoma cells, which over-express the HER2 receptor, were incubated with either anti-HER2, anti-IgG, or PEG-SH coated nanoparticles in suspension for 30 minutes. Unbound particles were removed by centrifugation and cells were cultured on coverglass overnight to allow time for adhesion. Samples were then imaged and treated with a Zeiss LSM 510 Meta multiphoton system operated with a Coherent Chameleon femtosecond Ti:sapphire laser. For imaging the laser output was 1 mW at 800 nm. To perform ablating therapy the power was increased to 50 mW. The pixel dwell time was 12.8 μsec in both cases. Following an incubation period, cells were stained with calcein AM (which causes living cells to fluoresce green) and ethidium homodimer (which causes dead cells to fluoresce red) in order to assess cell viability.

## RESULTS

SK-BR-3 cells could be visualized by two-photon microscopy using 1 mW incident laser power only in the presence of anti-HER2 gold-gold sulfide nanoparticles. Cells could not be visualized in the control samples, indicating that luminescence observed in the targeted samples is a result of nanoparticle presence.

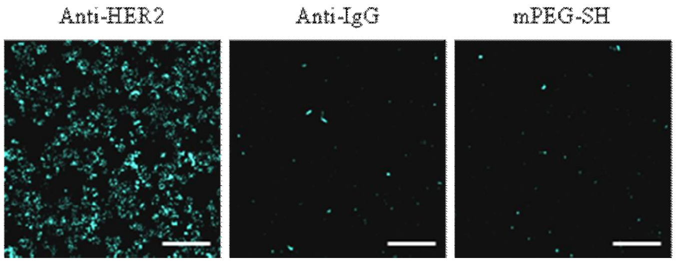

Figure 1. Two-photon images of SK-BR-3 cells with laser power set to 1 mW at 800 nm with 12.8 µsec dwell time. Anti-HER2 coated nanoshells provide the best contrast. Scale bar = 100 µm.

Calcein AM and ethidium homodimer staining verified that the laser power used for imaging (1 mW) was not harmful to cells. Upon increasing the power output to 50 mW, cell death was induced only when targeted nanoparticles and laser exposure were combined (Figure 2).

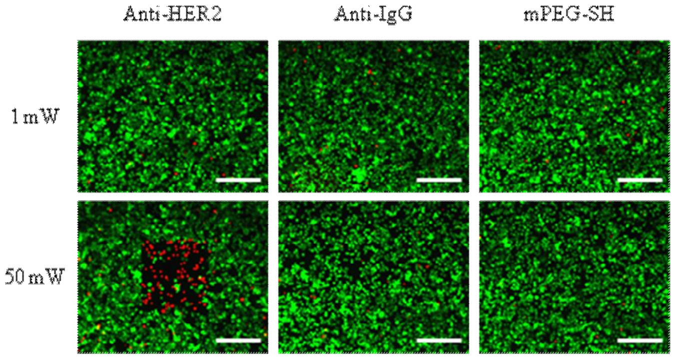

Figure 2. Thermal ablation was observed only when targeted nanoparticles were combined with high laser powers. In the bottom left image red ethidium homodimer staining is present in the square region where the laser was applied. This staining, indicative of cell death, was not observed in control samples. Scale bar = 300 µm.

## CONCLUSIONS

Gold-gold sulfide nanoparticles can be combined with two-photon microscopy to provide both imaging and therapy of cancer. Images of cancerous cells can be obtained at low laser powers, and then by increasing the power output cancerous cells can be destroyed by photothermal ablation. In the future, this technique could be used to treat tumors immediately upon detection.

## REFERENCES

1. Hirsch LR, *et al.* PNAS 2003; 100: 13549-13554.
2. Loo C, *et al.* Nano Letters 2005; 5(4): 709-711.
3. Huang X, *et al.* JACS 2006; 128: 2115-2120.
4. Averitt RD, *et al.* J Opt Soc Am B 1999; 16: 1824-1832.

Langsner, R., Drezek, R., and Yu, T. A Fluorescent Deoxyglucose Analog for Detection of Cancer in Breast Tissue. Rice Quantum Institute Summer Conference. August 2009.

Using the fluorescent glucose analogue, 2-NBDG, we present a method of differentiating cancerous breast tissue from non-cancerous breast tissue. This work is based on the previous work by Richards-Kortum et al, on 2-NBDG imaging of the oral malignant epithelium. In addition to structural and regulatory differences, cancerous tissues also have an altered metabolism. This trait has been utilized in clinic by the use of PET/CT scans, which detect areas of high metabolism using a radioactive deoxyglucose and PET scanner. Our research aims to differentiate tissue on both the microscopic and macroscopic levels by evaluating NBDG fluorescence in both immortalized bresat cell lines and fresh human breast tissue acquired from surgeries performed at MD Anderson.

Bickford, L., and Drezek, R. Gold-silica nanoshells for targeted imaging of tumor margins. Biomedical Engineering Society Annual National Meeting. Austin, TX. October 2010.

Current intraoperative tumor margin assessment occurs only grossly during surgery, often resulting in repeat surgical procedures. To improve existing techniques, we have developed a system employing both gold nanoshells and reflectance confocal microscopy (RCM) for identifying cancerous cells in whole tissue specimens rapidly and intraoperatively. Gold nanoshells, which have a silica core and a gold outer shell, are beneficial nanoparticles for many biomedical applications due to their tunable optical properties. They can also be used to enhance contrast of specific biomarkers associated with disease progression when conjugated to antibodies. Initially, we showed that targeted gold nanoshells can be used to increase contrast of HER2-overexpressing cancer cells within only 5 minutes of processing time. We then confirmed that gold nanoshells could be used as rapid imaging agents for discerning cryosectioned HER2-overexpressing breast tissue and that results are comparable to standard immunohistochemistry. Here, we demonstrate the ability to detect HER2-overexpressing cells in whole, resected tissue specimens using RCM. We also show that the differences in scattering signature between tissues incubated with and without nanoshells can be observed through a standard widefield imaging microscope. Results suggest that anti-HER2-nanoshells used in tandem with a near-infrared reflectance confocal microscope may potentially be used to discern HER2-overexpressing cancerous tissue from normal tissue in near real time and offer a rapid supplement to current diagnostic techniques.

Langsner, R., Yu,K., and Drezek, R. The Use of 2-NBDG for Optical Assessment of Breast Tumor Margins. Biomedical Engineering Society Annual National Meeting. Austin, TX. October 2010.

We present a method of breast cancer tissue differentiation using a contrast agent and wide-field imaging. *Ex vivo* breast specimens were obtained from patients undergoing surgical procedures. We assessed breast tissue fluorescence after application of 2-NBDG, a fluorescent deoxyglucose analog, using a wide-field macroscopic imaging system that created pre and post stain multispectral images of tissue. Fluorescence was evaluated by assessing signal differences between the pre and post stain images at varying emission wavelengths (from 500-720 nm). Also, an area under the curve (AUC) metric was calculated for the spectrums of each tissue, both pre and post stain.

Of the 14 fresh patient samples, there were 2 non-cancerous, 3 ductal carcinoma in situ, 3 invasive lobular carcinoma, 5 invasive ductal carcinoma, and 1 invasive mucinous carcinoma. The average signal difference in cancerous tissue was approximately two times as large as the signal difference for healthy tissue ($p < 0.0001$). The average AUC of the cancerous tissue was approximately three times that of the healthy tissue. The differences were due to the increased presence of 2-NBDG in the malignant tissue.

These initial results indicate that wide-field fluorescence imaging after 2-NBDG application has the potential to aid in discriminating malignant breast tissue from non-cancerous tissue. This is an initial step towards the development of an intra-operative *ex vivo* visualization device that surgeons can use as a tool to improve margin resection when performing Breast Conservation Therapy.

Noelck, S. and Drezek, R. Optical Properties of Gold-Silica-Gold Nanoshells. Biomedical Engineering Society Annual National Meeting. Austin, TX. October 2010.

**Abstract:**

Broken symmetry often leads to interesting features in the plasmonic properties of nanoparticles. This poster presents a computational study of the optical properties of gold-silica-gold multilayer nanoshells (MNSs) with an offset core. Symmetry breaking allows for interactions between the dipolar plasmon resonance and higher order modes, which create additional plasmon peaks in the optical spectrum. We use plasmon hybridization theory to explain the origin of these resonances as a mixture of different order modes between the core and the shell. To further understand the symmetry breaking effect, we plot the distribution of surface changes and link the asymmetry seen to plasmon hybridization theory. These plots illustratively show a mixture of a dipolar mode with higher order modes. Different polarizations had similar optical spectra but excited different mode configurations. Also a trend of increasing absorption relative to scattering is shown as the core offset increases. These non-concentric MNSs could be tuned over a wider range of wavelengths than concentric MNSs because the location of the core can strongly shift the plasmon resonance. This could allow for a small MNS with an offset core to have a resonant peak in the near-infrared for maximal tissue penetration. Also understanding the absorption and scattering properties offers the potential of using offset MNSs for simultaneous imaging and photothermal therapy.

Noelck, S., Hu, Y., and Drezek, R. Probing Optical Properties of Gold-Silica-Gold Multilayer Nanoshells with Broken Symmetry, 2010 Inter IGERT Nanoscience and Professional Development Workshop. Austin, TX. 2010.

**Abstract:**

Broken symmetry often leads to interesting features in the plasmonic properties of nanoparticles. This poster presents a computational study of the optical properties of gold-silica-gold multilayer nanoshells with an offset core. The symmetry breaking allows for interactions between the dipolar plasmon resonance and higher order modes, which create additional plasmon peaks in the optical spectrum. We use plasmon hybridization theory to explain the origin of these resonances as a mixture of different order modes between the core and the shell. To further understand the symmetry breaking effect, we plot the distribution of surface changes and link the asymmetry seen to plasmon hybridization theory. These plots illustratively show a mixture of a dipolar mode with higher order modes. Different polarizations had similar optical spectra but excited different mode configurations. Also a trend of increasing absorption relative to scattering is shown as the core offset increases.

Langsner, R., Drezek, R, and Yu, K. Towards 2-NBDG for Intraoperative Assessment of Tumor Margins. Gordon Conference on Lasers in Surgery and Medicine. 2010.

A significant prognostic factor in breast conserving therapy (BCT) is whether enough disease has been removed from the breast during surgery. Tertiary care centers have the facilities and staff available so that a pathologist can make a proper diagnosis while the patient is anesthetized. Some health centers do not have this luxury and it is not known until 24-48 hours until after surgery if proper margins have been excised. A method of margin visualization would be invaluable to surgeons in these health centers.

2-NBDG is a fluorescent deoxyglucose analog that is preferentially consumed by cells with high metabolism. It has the potential to be used as an effective contrast agent for imaging malignant tissue because of the increased metabolism of cancerous cells. Nitin et al. demonstrated the fluorophore's effectiveness in the delineation of oral neoplasias [1]. The purpose of this preliminary study was to establish a technique to evaluate the ability of 2-NBDG to differentiate normal from cancerous *ex vivo* breast tissue specimens as a first step towards assessing the potential use of 2-NBDG for intra-operative guidance.

We assessed breast tissue fluorescence after application of 2-NBDG using a wide-field macroscopic imaging system that creates multispectral images of tissue that can be qualitatively and quantitatively analyzed. Fresh normal and cancerous breast tissue specimens were collected from patients (n=14). Pre stain and post stain images were acquired. Fluorescence from the tissue was evaluated by assessing signal differences between the pre and post stain images at the peak emission wavelength. In addition, an area under the curve (AUC) metric was calculated for each spectrum.

Of the 14 patient samples, the diagnoses were distributed as follows: 2 non-cancerous, 3 ductal carcinoma in situ (DCIS), 3 invasive lobular carcinoma, 5 invasive ductal carcinoma (IDC), and 1 invasive mucinous carcinoma. At 580 nm emission, the average signal difference in cancerous tissue was approximately two times as large as the signal difference for healthy tissue. The average AUC of the cancerous tissue was approximately three times the AUC of the healthy tissue. These higher differences in the tissues were due to the increased presence of 2-NBDG in the malignant tissue. These initial results indicate that wide-field fluorescence imaging after 2-NBDG application has the potential to aid in discriminating malignant breast tissue from non-cancerous tissue.

1. Nitin, N., L. C. Alicia, et al. (2009). "Molecular imaging of glucose uptake in oral neoplasia following topical application of fluorescently labeled deoxy-glucose." International Journal of Cancer 124(11): 2634-2642.

Title: **Multiphoton Imaging and Therapy of Cancer with Gold-Sulfide Nanoparticles**
Subject Area: Emerging Technologies

Authors: Emily S. Day, Lissett R. Bickford, Rebekah A. Drezek, Jennifer L. West
Affiliation: Department of Bioengineering, Rice University, Houston, Texas, USA

Cancer is one of the leading causes of death worldwide, and therefore development of superior diagnostic and therapeutic tools to manage the disease is crucial. Nanoshells, spherical nanoparticles composed of a thin metal shell surrounding a dielectric core, can be synthesized to absorb light preferentially in the near-infrared, a region where light interacts minimally with tissue components, rendering them useful for near-infrared photothermal cancer therapy. In this work we examined the use of gold-sulfide nanoshells as a combined imaging agent and therapeutic with two-photon microscopy. The particles tested in these studies consisted of a gold-sulfide core and a gold shell (total particle diameter = 40 nm) and were synthesized to have peak extinction at 800 nm. Upon excitation with a pulsed laser, gold-sulfide nanoshells display two-photon induced photoluminescence, verified by the existence of a quadratic dependence of emission intensity on incident laser power. SK-BR-3 breast carcinoma cells, which over-express the HER2 receptor, were incubated with nanoshells coated with either anti-HER2 or anti-IgG antibodies. Unbound particles were rinsed away and samples were then imaged and treated with a Zeiss LSM 510 Meta multiphoton system operated with a Coherent Chameleon femtosecond Ti:sapphire laser. Imaging was performed by exposing the cells to 10 mW for 15 seconds, and enhanced contrast of the cancerous cells was observed only in the presence of anti-HER2 coated nanoshells. In addition, by increasing the power output of the laser to 50 mW, it was determined that the SK-BR-3 cells could be thermally ablated as nanoshells convert the light energy into heat.

Funding Sources: National Science Foundation, National Institutes of Health

## Header

**Title**: Use of Nanoshells for Combined Two-Photon Imaging and Therapy of Cancer
**Authors**: E.S. Day[1], L.R. Bickford[1], J.H. Hafner[2], R.A. Drezek[1], and J.L. West[1]
**Affiliations**: (1) Department of Bioengineering, Rice University, Houston, Texas, USA. (2) Department of Physics & Astronomy, Rice University, Houston, Texas, USA.
**Correspondence Address**: Rice University, Department of Bioengineering, 6100 Main St. MS 142, Houston, Texas, 77005. (Phone): 713-348-5955. (Fax): 713-348-5877.

---

## Short Abstract

Nanoshells, spherical nanoparticles consisting of a dielectric core and a thin gold shell, have unique optical properties that render them useful for near-infrared photothermal cancer therapy. In this work we examined the use of nanoshells as a combined imaging agent and therapeutic. Upon excitation with a pulsed laser, nanoshells exhibit two-photon induced photoluminescence which may be used to image cancer cells. In addition, by increasing the power output of the laser, cancer cells can be thermally ablated as nanoshells convert the light energy into heat.

---

## Extended Abstract

# Use of Nanoshells for Combined Two-Photon Imaging and Therapy of Cancer

E.S. Day, L.R. Bickford, J.H. Hafner, R.A. Drezek, and J.L. West
Rice University, Houston, TX

### Introduction

Development of superior diagnostic and therapeutic tools for cancer is crucial. Nanoshells, spherical nanoparticles consisting of a dielectric core and a thin gold shell, can be synthesized to absorb light in the near-infrared, a region where light penetrates deeply into tissue, rendering them useful for near-infrared photothermal cancer therapy.[1,2] In this work we studied two types of nanoshells, one with a gold sulfide core (total diameter ~50 nm) and one with a silica core (total diameter ~150 nm). In the current work, we examined the use of nanoshells as a combined imaging agent and therapeutic. Upon excitation with a pulsed laser, nanoshells exhibit two-photon induced photoluminescence which may be used to image cancer cells.[3] In addition, by increasing the power output of the laser, cancer cells can be thermally ablated as nanoshells convert the light energy into heat.

### Materials and Methods

*Silica Nanoshell Synthesis*

Nanoshells with silica cores (120 nm diameter) and ultrathin gold shells (14 nm) were manufactured as previously described.[4] After functionalizing the cores with amine groups, colloidal gold particles (~3nm) were adsorbed to the surface. The shell was completed by reduction of additional gold, producing particles with peak absorption at 800 nm and overall diameter of 148 nm.

*Gold Sulfide Nanoshell Synthesis*

Nanoshells consisting of a gold sulfide ($Au_2S$) core and gold shell were made following literature techniques.[5] Solutions of 2 mM $HAuCl_4$ (Alfa Aesar) and 1 mM $Na_2S$ (Aldrich) were mixed at a volumetric ratio of 1:2 ($Na_2S$:$HAuCl_4$), resulting in nanoshells resonant at 800 nm.

*Antibody Conjugation*

Anti-HER2 antibody (NeoMarkers) was conjugated to nanoshells using a poly(ethylene glycol) (PEG) linker purchased from Creative PEGWorks, with an N-hydroxysuccinimide terminus for antibody coupling and a disulfide terminus for attachment to gold. To prevent non-specific interactions, PEG-SH was added to the surface of the nanoshells after antibody addition. Control nanoshells were coated with only PEG-SH to prevent non-specific binding.

*In Vitro Study*

SK-BR-3 breast carcinoma cells, which over-express the HER2 receptor, were incubated with either anti-HER2 or PEG-SH coated nanoshells in suspension for 30 minutes. Unbound particles were removed by centrifugation and cells were cultured on coverglass overnight to allow time for adhesion. Samples were then imaged and treated with a Zeiss LSM 510 Meta multiphoton system operated in conjunction with a Coherent Chameleon femtosecond Ti:sapphire laser. For imaging the laser output was 60 μW at 800 nm. To perform ablating therapy the power was increased to 240 μW. Samples were exposed to the laser for 15 seconds. Following an incubation period of one hour, cell viability was assessed with calcein AM staining.

## Results

SK-BR-3 cells could be visualized by two-photon microscopy only in the presence of anti-HER2 coated nanoshells. Cells that were not incubated with nanoshells could not be discerned by this technique at low laser power output. Two-photon imaging results for gold sulfide nanoshells are shown in Figure 1. Results for silica nanoshells were similar.

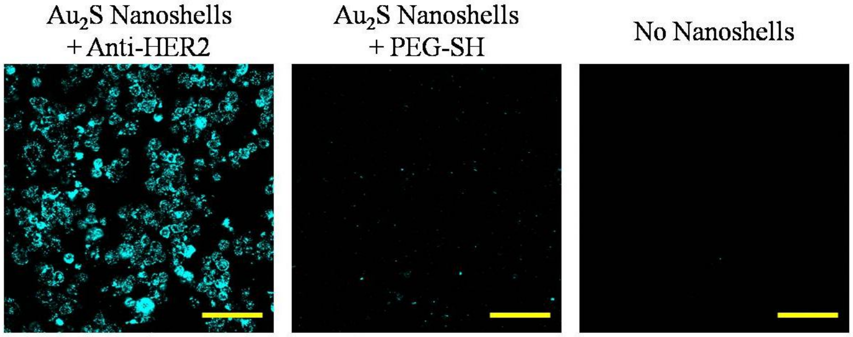

Figure 1. Two-photon images of SK-BR-3 cells taken in the presence or absence of gold sulfide nanoshells. Presence of anti-HER2 coated nanoshells provides the best contrast. Scale bar = 100 μm.

Calcein AM viability staining, which causes living cells to fluoresce green, verified that the laser power used for imaging (60 μW) was not harmful to cells. Upon increasing the power output to 240 μW, cell death was induced only when targeted nanoshells and laser exposure were combined, as seen by the loss of fluorescence in the square region where the laser beam was rastor-scanned (Figure 2).

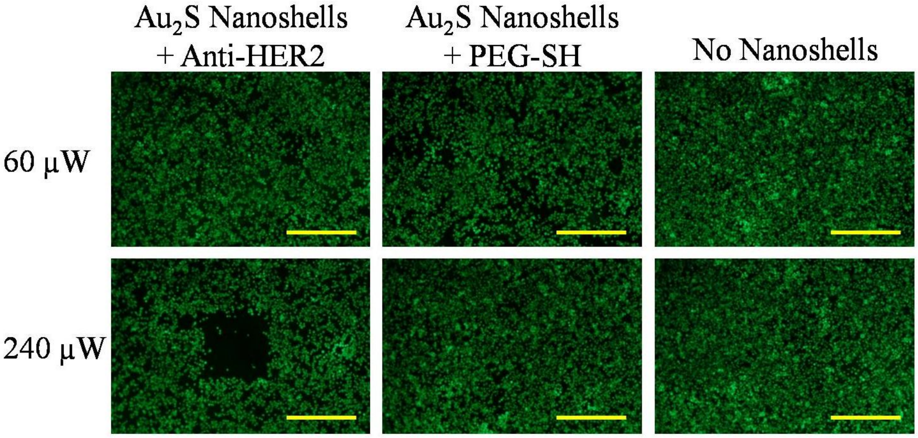

Figure 2. Cell death was observed only when targeted nanoshells were combined with higher laser powers, as seen by loss of fluorescence in the bottom left image. Scale bar = 500 μm.

## Conclusions

Nanoshells can be combined with two-photon microscopy to provide both imaging and therapy of cancer. Images of cancerous cells can be obtained at low laser powers, and then by increasing the power output cancerous cells can be destroyed by photothermal ablation. In the future, this technique could be used to treat tumors immediately upon detection.

## References

1. Hirsch LR. PNAS. 2003; 100: 13549-13554.
2. Weissleder R. Nat Biotechnol. 2001; 19: 316-317.
3. Park J. Opt Express. 2008; 16: 1590-1599.
4. Oldenburg SJ. Chem Phys Lett. 1998; 288: 243-247.
5. Averitt RD. J Opt Soc Am B. 1999; 16: 1824-1832.